

NASA Conference Publication 3123

Flight Mechanics/Estimation Theory Symposium 1991

(NASA-CP-3123) FLIGHT MECHANICS/ESTIMATION
THEORY SYMPOSIUM, 1991 (NASA) 490 p
CSCL 22A

N92-14070

--THRU--

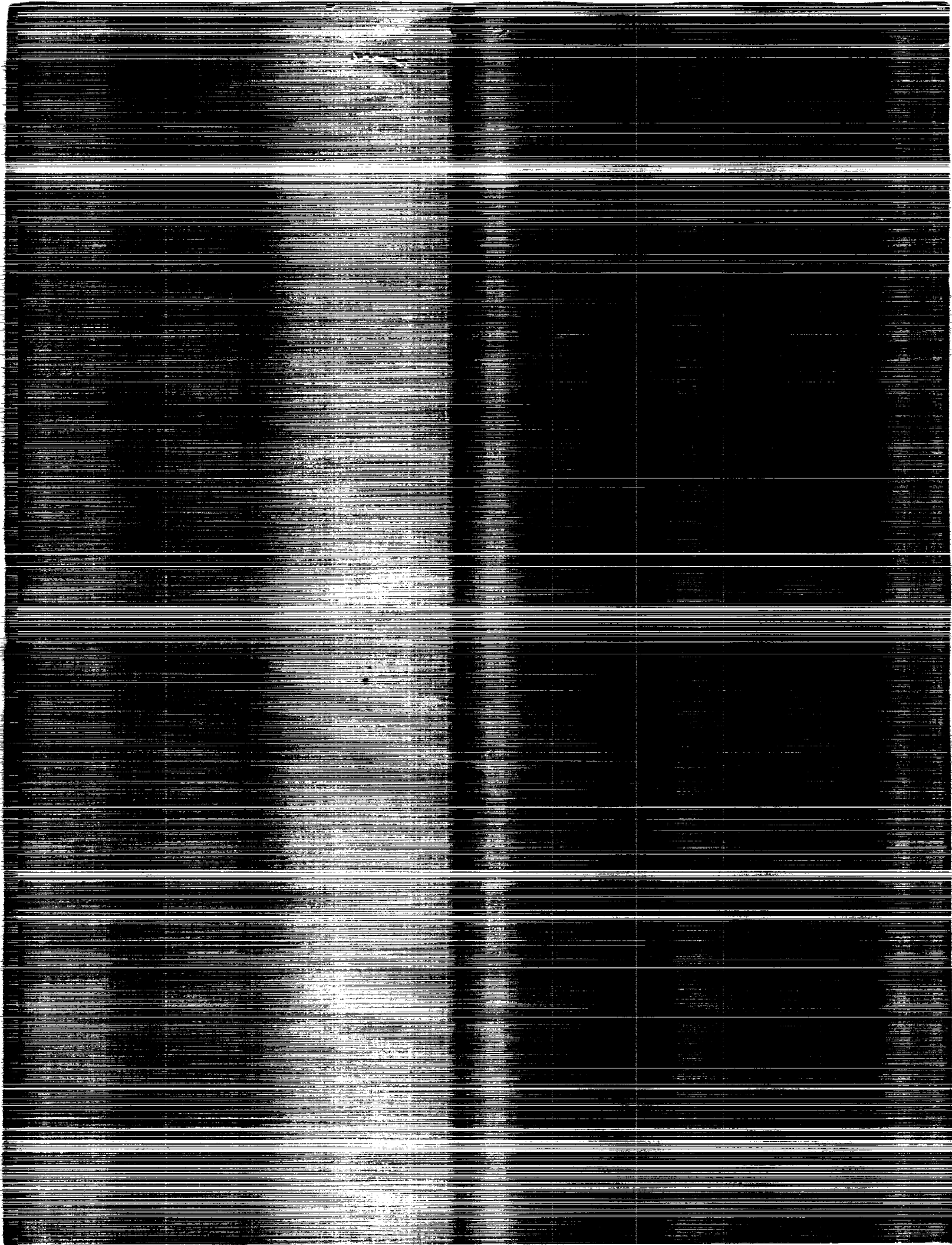
N92-14096

Unclas

H1/13 0057614

*Proceedings of a symposium held at
Langley Research Center
Hampton, Virginia
January 21-28, 1991*

NASA



NASA Conference Publication 3123

Flight Mechanics/Estimation Theory Symposium 1991

Thomas Stengle, *Editor*
Goddard Space Flight Center
Greenbelt, Maryland

Proceedings of a symposium sponsored by
NASA Goddard Space Flight Center and held at
Goddard Space Flight Center
Greenbelt, Maryland
May 21-23, 1991



National Aeronautics and
Space Administration

Office of Management

Scientific and Technical
Information Program

1991

•

FOREWORD

The papers presented here have been derived primarily from speaker's summaries of talks presented at the Flight Mechanics / Estimation Theory Symposium held May 21-23, 1991 at the Goddard Space Flight Center. For completeness, abstracts are included of those talks for which summaries were unavailable at press time. Papers included in this document are presented as received from the authors with little or no editing.

CONTENTS

Page

SESSION 1

Cosmic Background Explorer (COBE) Navigation with TDRSS One-Way Return-Link Doppler in the Post-Helium-Venting Phase M. Nemesure, J. Dunham (CSC), M. Maher (BFEC), J. Teles, J. Jackson (NASA/GSFC)	3
Preliminary Navigation Accuracy Analysis for the TDRSS Onboard Navigation System (TONS) Experiment on EP/EUVE C. Gramling (NASA/GSFC), A. Long, T. Lee, N. Ottenstein, M. Samii (CSC)	23
Analysis of the Navigation Performance for the Earth Observing System (EOS) Using the TDRSS Onboard Navigation System (TONS) B. Elrod, A. Kapoor (STI), D. Folta (NASA/GSFC), K. Liu (CSC)	45
Flight Dynamics Facility Operational Orbit Determination Support for the Ocean Topography Experiment D. Bolvin, A. Schanzle, M. Samii, C. Doll (NASA/GSFC)	65
Comparison of ERBS Orbit Determination Accuracy Using Batch Least-Squares and Sequential Methods D. Oza, T. Jones, S. Fabien (CSC), G. Mistretta, R. Hart, C. Doll (NASA/GSFC)	79
Navigation of the TSS-1 Mission T. Jackson, J. Pido, P. Zimmerman (Rockwell)	97

SESSION 2

New QUESTs for Better Attitudes M. Shuster (APL)	125
COBE Experience With Filter QUEST O. Filla, J. Keat, D. Chu (CSC)	139
COBE Ground Segment Attitude Determination V. Kumar, I. Freedman (ST Systems), E. Wright (UCLA), F. Patt (GSC)	151

COBE Ground Segment Gyro Calibration	
I. Freedman, V. Kumar, A. Rae,	
R. Venkataraman (ST Systems),	
F. Patt (GSC), E. Wright (UCLA)	167

SESSION 3

Evidence of Chaotic Pattern in Solar Flux Through a Reproducible Sequence of Period- Doubling Bifurcations	
S. Ashrafi, L. Roszman (CSC)	189
Ionospheric Refraction Effects on TOPEX Orbit Determination Accuracy Using the Tracking and Data Relay Satellite System (TDRSS)	
M. Radomski (CSC), C. Doll (NASA/GSFC)	209
Study of Geopotential Error Models Used in Orbit Determination Error Analysis	
C. Yee, D. Kelbel, T. Lee, M. Samii (CSC), G. Mistretta, R. Hart (NASA/GSFC)	229
Increased Ephemeris Accuracy Using Attitude- Dependent Aerodynamic Force Coefficients for Inertially Stabilized Spacecraft	
D. Folta, D. Baker (NASA/GSFC)	249
Elimination of Secular Terms from the Differential Equations for the Elements of Perturbed Two-Body Motion	
V. Bond, M. Fraietta (MDSSC)	265
Improved Accuracies for Satellite Tracking	
P. Kammeyer, A. Fiala, P. Seidelmann (Naval Observatory)	285

SESSION 4

Testing of the High Accuracy Inertial Navigation System in the Shuttle Avionics Integration Lab	
R. Strachan, J. Evans (Rockwell)	301
Effectiveness of Large Booms as Nutation Dampers for Spin Stabilized Spacecraft	
F. Eke (Univ. Ca./Davis)	321
An Analysis of the Hubble Space Telescope Fine Guidance Sensor Fine Lock Mode	
L. Taff (ST Science Institute)	333

The In-Flight Calibration of the Hubble Space Telescope Attitude Sensors G. Welter (CSC)	353
--	-----

SESSION 5

An Extended Kalman Filter for Spinning Spacecraft Attitude Estimation D. Baker (NASA/GSFC)	385
Quaternion Normalization in Additive EKF for Spacecraft Attitude Determination I. Bar-Itzhack (Technion), F. Markley, J. Deutschmann (NASA/GSFC)	403
Colored Noise Effects on Batch Attitude Accuracy Estimates S. Bilanow (GSC)	423
Correlation Techniques to Determine Model Form in Robust Nonlinear System Realization/ Identification G. Stry, D. Mook (SUNY)	443
Minimum Fuel Coplanar Aeroassisted Orbital Transfer Using Collocation and Nonlinear Programming Y. Shi, D. Young (MDSSC)	461
Propellant-Remaining Modeling S. Torgovitsky (CSC)	481

FLIGHT MECHANICS/ESTIMATION THEORY SYMPOSIUM

MAY 21-23, 1991

SESSION 1

Cosmic Background Explorer (COBE) Navigation With TDRSS One-Way Return-Link Doppler in the Post-Helium-Venting Phase*

**M. Nemesure and J. Dunham
COMPUTER SCIENCES CORPORATION (CSC)**

**M. Maher
BENDIX FIELD ENGINEERING CORPORATION (BFEC)**

**J. Teles and J. Jackson
GODDARD SPACE FLIGHT CENTER (GSFC)**

ABSTRACT

A navigation experiment has been performed which establishes USO-frequency-stabilized one-way return-link Doppler TDRSS tracking data as a feasible option for mission orbit determination support at the Goddard Space Flight Center Flight Dynamics Facility (GSFC FDF). The study was conducted using both one-way and two-way Tracking and Data Relay Satellite System (TDRSS) tracking measurements for the Cosmic Background Explorer (COBE) spacecraft. Tracking data for a 4-week period immediately following the depletion of the helium supply was used. The study shows that, for both definitive orbit solution and short-term orbit prediction (up to 4 weeks), orbit determination results based on one-way return-link Doppler tracking measurements are comparable to orbit determination results based on two-way range and two-way Doppler tracking measurements.

* This work was supported by the National Aeronautics and Space Administration (NASA)/Goddard Space Flight Center (GSFC), Greenbelt, Maryland, under Contract NAS 5-31500.

INTRODUCTION

This paper discusses orbit determination analysis results that establish Ultra-Stable Oscillator (USO)-frequency-stabilized one-way return-link Doppler Tracking and Data Relay Satellite (TDRS) System (TDRSS) tracking data as a feasible option for mission orbit determination support at the Goddard Space Flight Center Flight Dynamics Facility (GSFC FDF). The study was conducted using TDRSS tracking measurements for the Cosmic Background Explorer (COBE) spacecraft.

COBE is the first, and so far the only, spacecraft supported by the FDF to be tracked with USO-stabilized one-way return-link noncoherent Doppler tracking measurements. COBE orbit determination analysis has therefore served as a flight-test of the one-way tracking system. Future use of TDRSS one-way Doppler tracking measurements will be required by the Ocean Topography Experiment (TOPEX) and the Explorer Platform/Extreme Ultraviolet Explorer (EP/EUVE) TDRSS Onboard Navigation (TONS) experiment. Both of these future experiments will utilize USOs similar to the USO carried by COBE for Doppler frequency reference. TOPEX requires very high precision orbit determination using one-way return-link Doppler tracking. For example, velocity changes brought about by in-plane TOPEX spacecraft maneuvers must be determined to within 0.1 millimeter per second (Reference 1). The EP/EUVE TONS experiment will use one-way forward-link Doppler tracking data for a ground-based emulation of onboard navigation. The EP/EUVE TONS experiment will benefit from the USO performance evaluation techniques discussed in this paper (see Reference 2 for a discussion of the EP/EUVE TONS experiment). Reference 3 provides background information about the COBE spacecraft and describes the USO and its role in one-way orbit determination.

Previous COBE navigation analysis (Reference 3) utilized tracking measurements obtained during the period COBE was venting helium from a Dewar used to cool one of its science experiments. This period began soon after COBE launch on November 18, 1989, and lasted until September 1990. This venting phase work accomplished three objectives: (1) verification of algorithms for one-way navigation with real data, (2) determination of the flight performance of the USO coupled to the second-generation TDRSS transponder, and (3) qualification of TDRSS noncoherent one-way return-link Doppler tracking data for FDF mission support of COBE. Since this work involved analysis of an orbit that was being perturbed by helium venting, the third objective stated above only addressed whether the one-way data can support COBE mission requirements. Overlap ephemeris comparisons on the order of hundreds of meters and 4-week orbit prediction errors on the order of hundreds of kilometers characterized both one-way and two-way orbit determination capabilities during the venting phase. Thus, accuracy assessment was severely limited.

This paper covers the second phase of the COBE navigation experiment, which was initiated on September 27, 1990, after the helium was depleted. One-way tracking measurements for October and the last 4 days of September 1990 were used for orbit determination with a research version of the Goddard Trajectory Determination System (GTDS). The objective of this phase of analysis was to reassess the suitability of one-way tracking measurements for orbit determination during a more quiescent period of the COBE mission, when greater orbit determination accuracy is possible. Orbit solutions were generated using the best force

models and processing options available within the GTDS environment. Such an effort was warranted only when the unmodeled venting perturbations were no longer a factor. Although additional one-way solution accuracy was achieved during the postventing phase analysis, these one-way solutions do not represent the best possible with one-way tracking systems. The primary accuracy-limiting factor during the postventing phase is the poor COBE tracking geometry, which results from limitations of the COBE TDRSS antenna pattern coverage. More discussion of the COBE tracking geometry follows in the analysis section of this paper.

This paper discusses the consistency, compatibility, and predictive capability of one-way solutions relative to two-way solutions. Additionally, the performance of the USO in the in-flight environment is addressed.

REVIEW OF COBE CHARACTERISTICS RELEVANT TO ORBIT DETERMINATION

The COBE spacecraft was placed in a nearly circular Sun-synchronous orbit with an altitude of 900 kilometers and an inclination of 99 degrees. The spacecraft has no orbit maneuver capability. The primary influences on the orbit evolution are the gravitational, atmospheric drag, and (prior to September 27, 1990) helium venting forces.

The USO onboard COBE provides a command-selectable external stable reference frequency to either of the two onboard TDRSS user transponders. It has a reference frequency of 19.056393 megahertz and a prelaunch measured long-term drift of -4×10^{-11} parts per day (Reference 4). The drift of the USO, when coupled to the COBE second-generation TDRSS transponder, has been determined from previous flight analysis to be better than 5×10^{-11} parts per day in magnitude. The USO is used as the source frequency for one-way noncoherent Doppler data extracted from the TDRSS return-link signal at the White Sands Ground Terminal (WSGT), as depicted in Figure 1. The TDRSS tracking data for these evaluations were derived from both the S-band Single-Access (SSA) and Multiple-Access (MA) TDRSS services.

Details of the one-way return-link Doppler measurement model can be found in Reference 3.

ANALYSIS PROCEDURE

The orbit determination performed for this analysis was based on the least-squares batch estimation algorithm available in GTDS. (Reference 5 gives a detailed discussion of this algorithm.) In addition to COBE orbit determination using TDRSS tracking measurements, the analysis also involved TDRS-East and TDRS-West orbit determination using Bilateral Ranging Transponder System (BRTS) tracking measurements. Although simultaneous solution of relay and user satellite orbits is possible, the TDRS orbits were predetermined for this study.

This study utilized the the force models summarized in Table 1 and the processing options summarized in Table 2 for user and relay orbit determination. In particular, the Goddard Earth Model (GEM)-T2 geopotential model (Reference 6) provided coefficients through

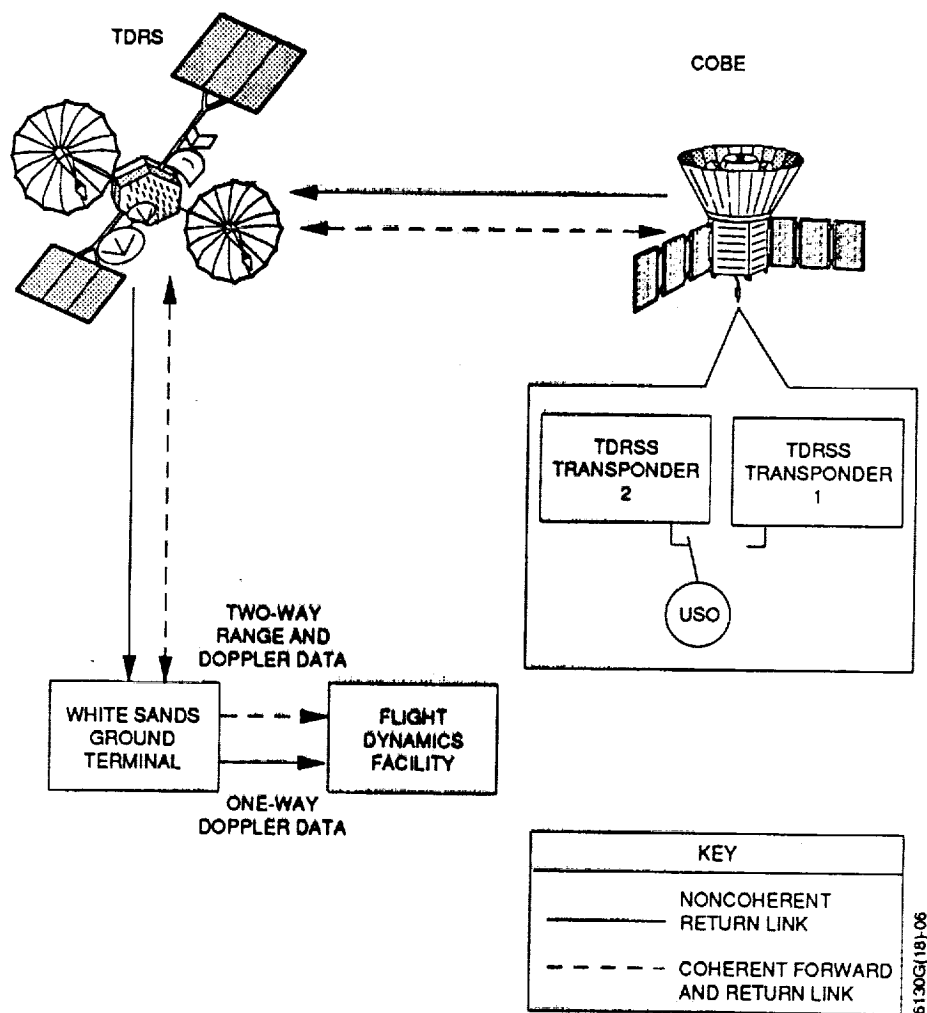


Figure 1. USO COBE Experiment Overview

Table 1. Summary of Modeling Options

OPTION	SPACECRAFT	
	COBE	TDRS-EAST AND TDRS-WEST
GEOPOTENTIAL	GEM-T2 50 x 50, EQUATIONS OF MOTION GEM-T2 4 x 0 (TRUNCATED), VARIATIONAL EQUATIONS	GEM-T2 8 x 8 (TRUNCATED), EQUATIONS OF MOTION GEM-T2 4 x 0 (TRUNCATED), VARIATIONAL EQUATIONS
THIRD-BODY EFFECTS	SUN, MOON (POINT-MASS)	SUN, MOON (POINT-MASS)
SOLAR RADIATION PRESSURE	APPLIED WITH $C_R = 1.42$	COEFFICIENT ESTIMATED
POLAR MOTION	YES	YES
ATMOSPHERIC DRAG	JACCHIA-ROBERTS MODEL; $C_D = 2.3$; HISTORICAL F10.7 SOLAR FLUX, GEOMAGNETIC, AND TEMPERATURE DATA; C_D VARIATION ESTIMATED	NEITHER APPLIED NOR ESTIMATED
EARTH TIDES	GEOPOTENTIAL COMPENSATED; LOVE NUMBER = 0.29; LAG ANGLE = 2.5 DEGREES	GEOPOTENTIAL COMPENSATED; LOVE NUMBER = 0.29; LAG ANGLE = 2.5 DEGREES
SATELLITE AREA	SPHERE WITH DIAMETER = 4.78 METERS	SPHERE WITH DIAMETER = 6.32 METERS
SATELLITE MASS	2055 KILOGRAMS	TDRS-East: 1984.87 KILOGRAMS (9/27/90-10/4/90) 1984.77 KILOGRAMS (10/5/90-10/31/90) TDRS-West: 1981.85 KILOGRAMS

Table 2. Summary of Processing Options

OPTION	SPACECRAFT	
	COBE	TDRS-EAST AND TDRS-WEST
NUMERICAL INTEGRATION	12th-ORDER FIXED-STEP COWELL; 60-SECOND STEPSIZE	12th-ORDER FIXED-STEP COWELL; 600-SECOND STEPSIZE
REFERENCE FRAME	MEAN EQUATOR AND EQUINOX OF J2000.0 FOR INTEGRATION AND SOLAR/LUNAR/PLANETARY (SLP) EPHEMERIS	MEAN EQUATOR AND EQUINOX OF J2000.0 FOR INTEGRATION AND SLP EPHEMERIS
MEASUREMENT DATA AND DATA RATE	ONE-WAY DOPPLER: 10 SECONDS TWO-WAY DOPPLER: 10 SECONDS RANGE: 10 SECONDS	BRTS DOPPLER: 10 SECONDS BRTS RANGE: 10 SECONDS
EDITING CRITERIA	ATMOSPHERIC EDITING: HORP*/CENTRAL ANGLE = 830 KILOMETERS/70 DEGREES (SEE TEXT) RESIDUAL EDITING: 3σ	3σ RESIDUAL EDITING
STANDARD DEVIATIONS USED FOR EDITING AND WEIGHTING	ONE-WAY DOPPLER: 0.13 HERTZ TWO-WAY DOPPLER: 0.25 HERTZ RANGE: 30 METERS	BRTS DOPPLER: 0.003 HERTZ BRTS RANGE: 10 METERS
IONOSPHERIC REFRACTION	NO CORRECTION	GROUND-TO-RELAY LEG CORRECTED
TROPOSPHERIC REFRACTION	GROUND-TO-RELAY LEG CORRECTED	GROUND-TO-RELAY LEG CORRECTED
ESTIMATOR	BATCH WEIGHTED LEAST SQUARES	BATCH WEIGHTED LEAST SQUARES
ESTIMATED PARAMETERS	POSITION, VELOCITY, ATMOSPHERIC VARIATION COEFFICIENT (ρ_1); USO FREQUENCY BIAS AND DRIFT	POSITION, VELOCITY, AND SOLAR REFLECTIVITY COEFFICIENT (C_R)

* HORP = HEIGHT OF RAY PATH

degree and order 50. The complete coefficient set was incorporated in the COBE solutions; the coefficient set was truncated at degree and order 8 for the relay satellites. Additionally, historical solar flux, geomagnetic, and exospheric temperature data were used with the Jacchia-Roberts atmospheric density model. The cross-sectional areas of the COBE and Tracking and Data Relay Satellite (TDRS) spacecraft were assumed constant. The error associated with this assumption was compensated by estimating the atmospheric drag variation coefficient (ρ_1) for COBE and estimating the solar reflectivity coefficient (C_R) for the TDRSs. The effects due to polar motion, Earth tides, and atmospheric refraction of the tracking signal were taken into account. These corrections are discussed in References 7 and 8.

Prior to the orbit determination analysis, error analysis was performed using the Orbit Determination Error Analysis Program (ODEAS) in an attempt to find the optimum data arc length for COBE that would enable estimation of the atmospheric drag variation parameter (ρ_1). High correlations among the state variables were observed in the noise-only covariance matrix for a 34-hour COBE solution arc when ρ_1 was included in the state. The error analysis showed that 4 days of data would allow ρ_1 estimation and acceptable levels of geopotential error (at COBE's altitude of 900 kilometers, drag effects are too small to permit short-arc ρ_1 estimation). The error analysis also showed that the benefits of a long TDRS data arc are diminished by accumulation of gravitational and solar radiation pressure errors. Based on the error analysis, a 4-day, 10-hour arc was selected for COBE and a 40-hour arc was selected for the TDRSs.

Two sets of four separate 40-hour TDRS solutions (one set for TDRS-East and one set for TDRS-West) were utilized for each 4-day, 10-hour COBE solution. The 40-hour arcs were scheduled so that they would overlap by 10 hours.¹ The TDRS solutions involved the estimation of the coefficient of reflectivity, C_R , and were based on BRTS range and Doppler measurements.

Three separate COBE solutions for each of eight 4-day, 10-hour arcs were evaluated: a one-way only solution, a two-way only solution, and a combined one-way and two-way solution. The COBE solutions involved estimation of the drag variation parameter (ρ_1) and, when one-way data were included, the effective USO frequency bias and drift. The bias estimation, in addition to compensating for the USO bias, accounted for relativistic shifts in the frequency during transmission of the tracking signal. The COBE data arcs matched the schedule followed by FDF Orbit Operations personnel for mission support of COBE. Accordingly, each 4-day, 10-hour data arc started at 0 hours on either a Monday or a Thursday. Thus, alternating overlaps periods of 10 hours and 34 hours occurred.

In an attempt to mitigate the effects of ionospheric disturbance on the tracking measurements (see the analysis results section), atmospheric editing was performed. This editing used a geometric criterion based on the height of ray path (HORP) and the central angle. HORP is defined as the height above the surface of the Earth of the point on an imaginary line connecting the relay and TDRS spacecraft that is closest to the Earth's surface. The central angle is

¹ A slight adjustment had to be made to the data arc scheduling so that a TDRS-East maneuver, which occurred on October 4, 1990, could be accommodated.

measured between the user spacecraft and relay spacecraft position vectors with respect to the center of the Earth. Figure 2 illustrates the HORP (h) and central angle (δ) geometry. For this study, a tracking measurement was not used if its associated central angle was greater than 70 degrees at the same time its associated HORP was less than 830 kilometers.

Since simultaneous one-way and two-way tracking was not available, the one-way and two-way tracking measurement distributions were not identical. However, similar tracking schedules and similar quantities of one-way measurements and two-way measurement pairs allowed valid comparisons of one-way and two-way solutions. Figure 3 shows typical one-way and two-way tracking measurement distributions as they were accepted for orbit determination. The figure covers a 4-day period used for one of the solution arcs.

Three types of ephemeris comparisons were used to evaluate solution consistency and solution compatibility: overlap comparisons, parallel comparisons, and predictive comparisons. Overlap and predictive comparisons both involve comparison of solutions based on the same data type. Parallel comparisons involve a comparison of solutions based on different data types. Each comparison scheme is illustrated in Figure 4. In addition to ephemeris comparison results, the byproducts of the estimation process (such as editing statistics), the RMS of the observation residuals, and the atmospheric drag variation parameter provided a basis for comparison between one-way and two-way solutions. Additionally, the performance of the USO in the in-flight environment was ascertained from an evaluation of the tracking data. The effects of the USO bias and drift on the one-way data and on the solution accuracy were analyzed.

TRACKING DATA EVALUATION RESULTS

The noise and bias characteristics of the USO were computed based on the statistical properties of the one-way measurement residuals. A measurement residual is the algebraic difference between the observed value of a tracking measurement and the computed value of the measurement. The residuals, which are computed during the estimation process, effectively remove orbital variations from the tracking data. Thus, such qualities as random noise variation, S-band frequency bias, and S-band frequency drift are more easily discerned from the residuals than from the tracking measurements. The frequency bias and drift were considered reflections of USO performance. The residuals used for the data evaluation were obtained from 24-hour GTDS solutions generated over the course of the period starting with COBE's launch and ending at the end of November 1990 (tracking data evaluation was unaffected by venting effects). Each 24-hour solution provided a mean residual for each batch of data occurring within its solution arc.

The first parameter evaluated was the USO frequency bias. A least-squares quadratic curve was fit to all the Doppler residual mean values that had accumulated during the period under study (from September 27, 1990, through October 1990). The equation for this fit was as follows:

$$b(T) = -226.178 - 0.1583T + 0.000127T^2 \pm 0.1086$$

where T is the number of days from December 31, 1989, and $b(T)$ is in hertz.

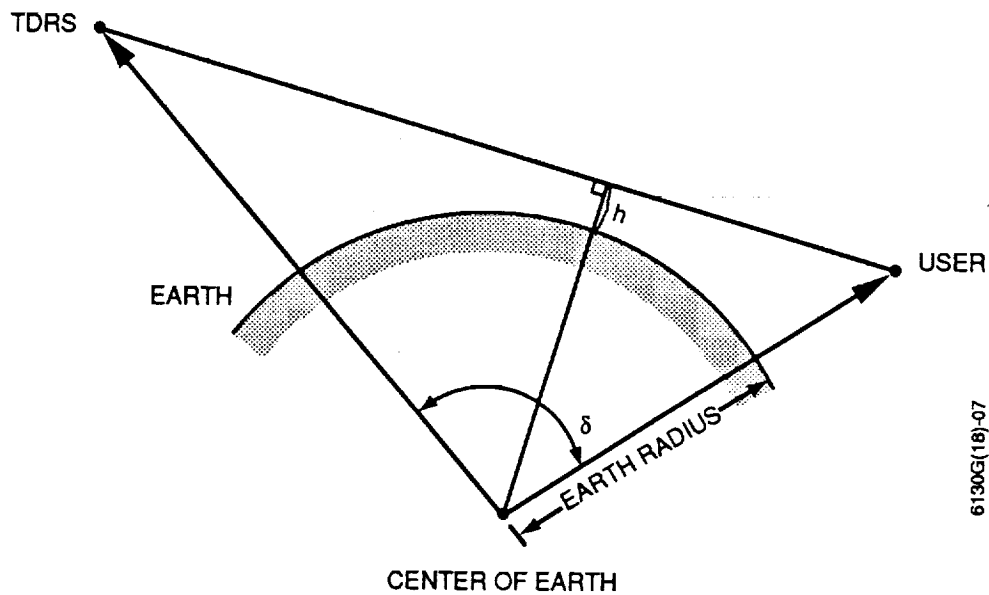


Figure 2. Illustration of the Atmospheric Editing Geometry Showing the Height of Ray Path (h) and the Central Angle (δ)

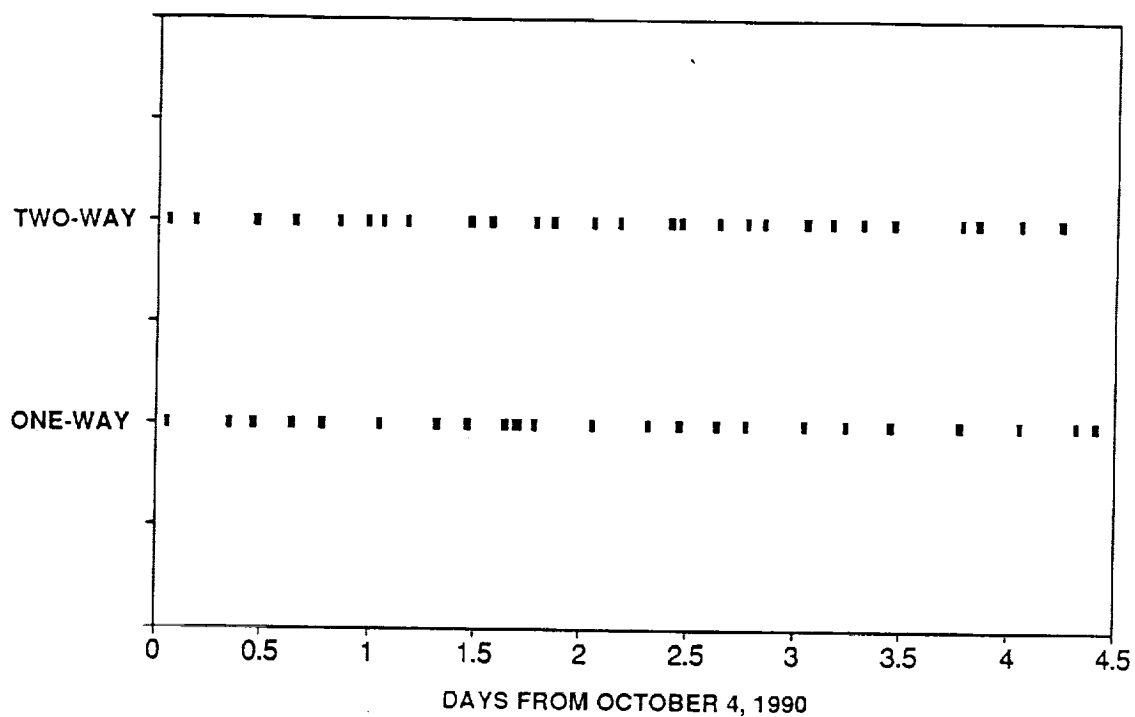


Figure 3. Passes Accepted by the Differential Correction Process for a Typical Solution Arc

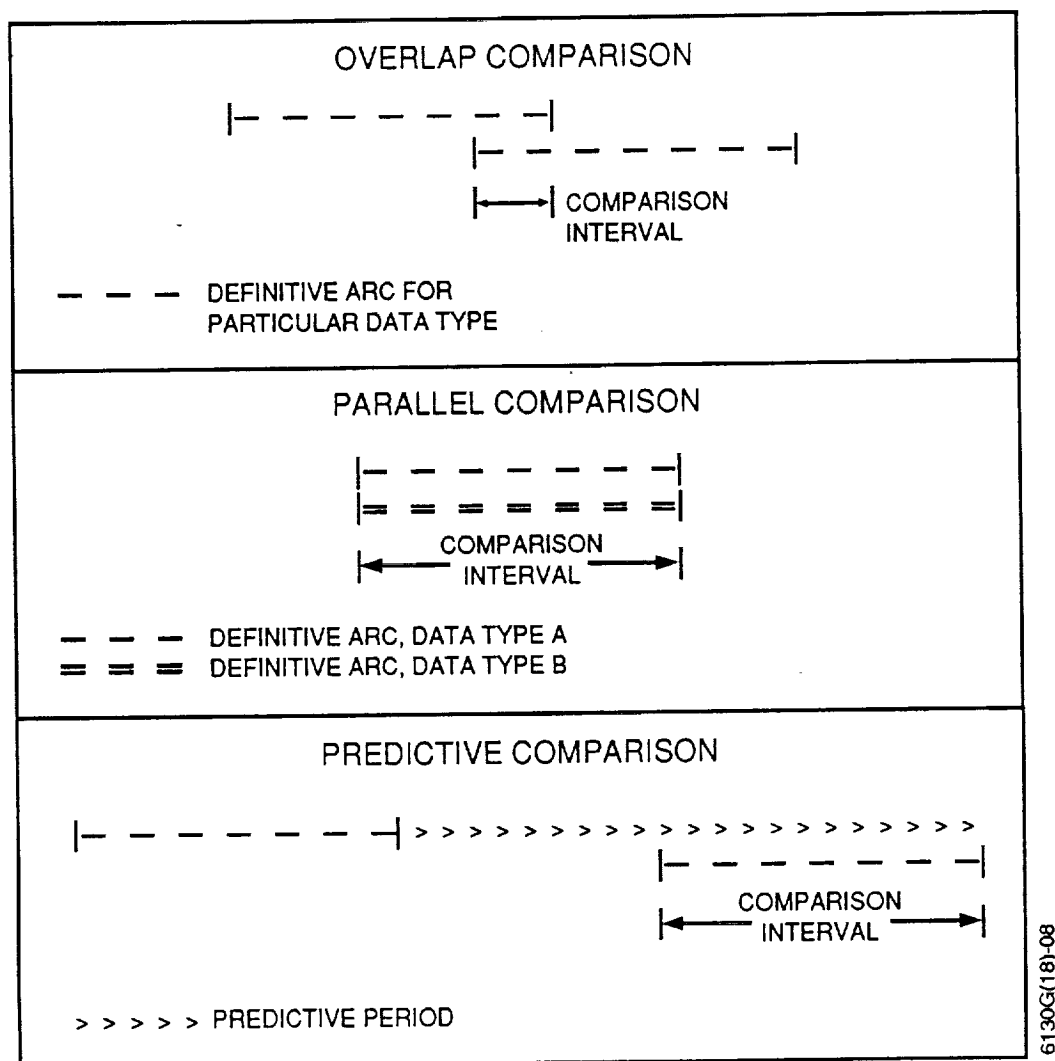


Figure 4. Illustration of Ephemeris Comparison Schemes

Figure 5 shows the fitted parabola along with the mean residual data. The figure also displays the estimated values of the USO frequency bias obtained from the 4-day solutions generated for this study. The curve can be interpreted as the offset from the nominal S-band return-link frequency of 2287.5 megahertz. Spikes in the curve are likely attributable to exceptionally high levels of ionospheric disturbance. It was confirmed that most of the tracking data which produced these spikes were rejected from the orbit determination process either with atmospheric editing or 3σ editing.

The second parameter evaluated was the frequency drift. A least-squares linear curve was fit to the mean residuals over sliding 24-hour intervals. Table 3 lists the drift values obtained from these 24-hour curve fits, from differentiation of the frequency offset equation above, and from the 4-day orbit solutions. The drift is expressed as fractional parts of 2287.5 megahertz per day. Table 3 shows good agreement between the 4-week evaluated drift values and the estimated drift values. The 24-hour evaluated drift values displayed wider fluctuation. All

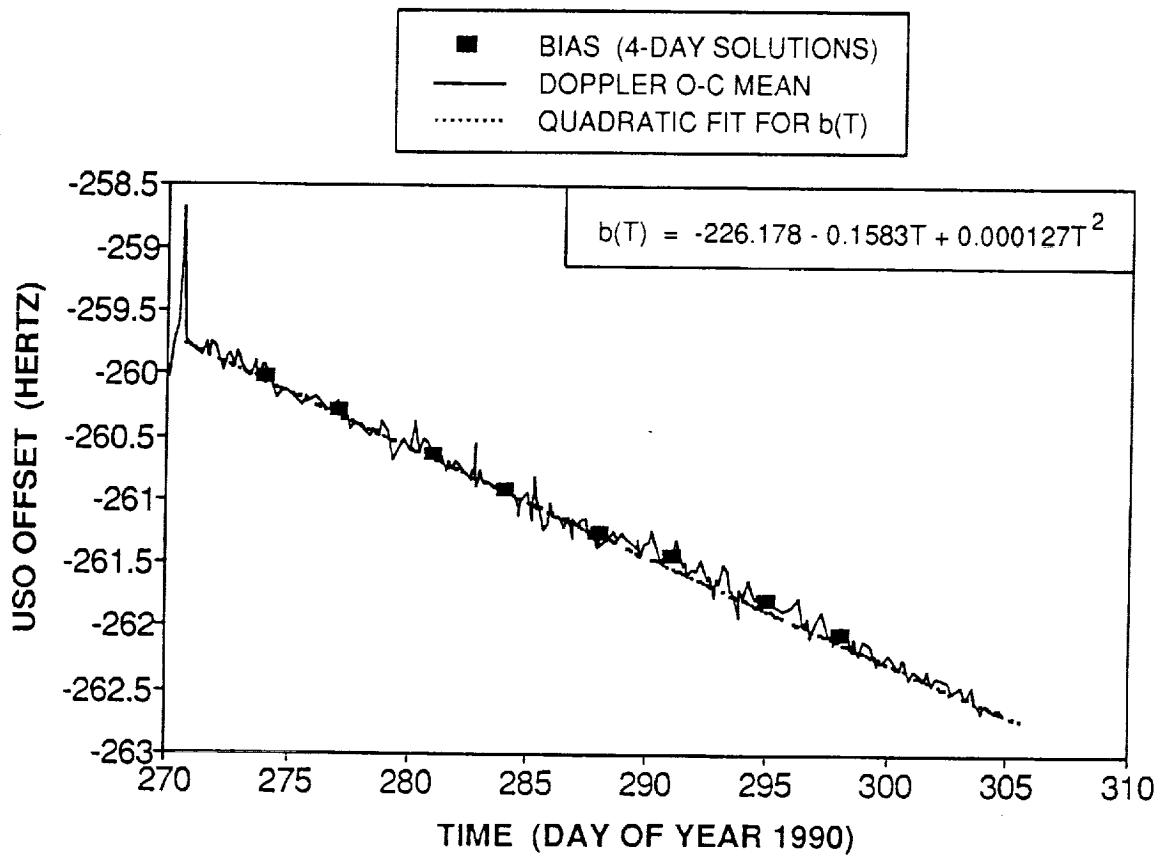


Figure 5. One-Way Doppler Residual Mean Values Used to Estimate the USO Frequency Bias

Table 3. Estimated and Evaluated S-Band Frequency Bias and Drift

A. BIAS

SOLUTION EPOCH (0 HOURS)	ESTIMATED BIAS (HERTZ)		EVALUATED BIAS (HERTZ)
	FROM ONE-WAY SOLUTION	FROM COMBINED ONE- AND TWO-WAY SOLUTIONS	FROM 4-WEEK QUADRATIC FIT
10/01/90	-260.0260	-260.0374	-260.0252
10/04/90	-260.2743	-260.3117	-260.2902
10/08/90	-260.6440	-260.6466	-260.6400
10/11/90	-260.9246	-260.9133	-260.8997
10/15/90	-261.2572	-261.2529	-261.2424
10/18/90	-261.4292	-261.4084	-261.4967
10/22/90	-261.7965	-261.8137	-261.8323
10/25/90	-262.0560	-262.0480	-262.0813

B. DRIFT

SOLUTION EPOCH (0 HOURS)	ESTIMATED DRIFT (PARTS/DAY)		EVALUATED DRIFT (PARTS/DAY)	
	FROM ONE-WAY SOLUTION	FROM COMBINED ONE- AND TWO-WAY SOLUTIONS	FROM 4-WEEK QUADRATIC FIT	FROM 24-HOUR QUADRATIC FIT
10/01/90	-3.9723×10^{-11}	-4.1034×10^{-11}	-3.8785×10^{-11}	-2.9290×10^{-11}
10/04/90	-3.6917×10^{-11}	-3.8953×10^{-11}	-3.8452×10^{-11}	-2.2295×10^{-11}
10/08/90	-3.7234×10^{-11}	-3.6762×10^{-11}	-3.8008×10^{-11}	-6.0328×10^{-11}
10/11/90	-4.3104×10^{-11}	-3.9550×10^{-11}	-3.7675×10^{-11}	-1.6175×10^{-11}
10/15/90	-2.8505×10^{-11}	-3.1803×10^{-11}	-3.7230×10^{-11}	$+5.6831 \times 10^{-11}$
10/18/90	-2.4158×10^{-11}	-2.4320×10^{-11}	-3.6897×10^{-11}	-2.7541×10^{-11}
10/22/90	-3.8783×10^{-11}	-4.1310×10^{-11}	-3.6453×10^{-11}	-19.8470×10^{-11}
10/25/90	-4.2896×10^{-11}	-3.7718×10^{-11}	-3.6119×10^{-11}	$+11.3224 \times 10^{-11}$

three sources of drift values indicate good USO stability. Furthermore, the USO characteristics have so far remained essentially unchanged during the course of COBE's in-flight life.

Finally, an evaluation of the random noise level on the one-way Doppler data was performed. Again, the statistical properties of the mean observation residuals were used to infer characteristics of the raw Doppler data. The 24-hour solutions provided residual data for noise analysis. A technique called Variate Differenced Noise Analysis (VDNA) was applied to the selected set of measurement residuals. A pth-order variate difference, δ_p , is given by

$$\delta_p = \sqrt{\frac{\sum_{i=1}^{n-p} (\Delta_i^p)^2 \frac{n!}{(n-p)!}}{(n-p)(2n)!}}$$

where n = number of data points

Δ_i^p = ith pth-order difference computed from the data points

Since the differencing operation tends to eliminate nonrandom trends in data, the VDNA computation provides a measure of randomness. As the order of the variate difference grows, the elimination of deterministic variation becomes more thorough. On the other hand, fewer terms in the variate summation become available. The third-order variate difference was computed for this study. A discussion of VDNA is provided in Reference 9.

In the current application, the measurement noise levels provided by VDNA can reveal periods of large ionospheric scintillation of the tracking signal. A scatter plot of 10-second one-way Doppler noise from VDNA is provided in Figure 6. The greatest noise levels apparent in Figure 6 coincide with transits of COBE through the Earth's polar regions where tracking measurements are particularly susceptible to ionospheric disturbance.

ORBIT DETERMINATION ANALYSIS RESULTS

Figure 7 shows the maximum total position differences for the one-way, two-way, and combined one-way and two-way overlap comparisons. Figure 8 shows how the comparison varied over time for a typical case. The maximum total position differences for the overlap comparisons fell within similar ranges for the three solution types (10 meters to 73 meters, 20 meters to 75 meters, and 15 meters to 72 meters for the one-way, combined, and two-way cases, respectively). The largest disparity between comparison results for a given comparison interval was 30 meters. An overlap comparison is essentially a consistency measure. While it is true that a poor solution can be self-consistent, a good solution *must* be self-consistent. In fact, overlap comparison results can justifiably be used as a lower bound on definitive orbit accuracy.

Figure 9 summarizes the results of parallel comparisons between solution types, giving the maximum total position differences. The comparison interval corresponds to the 4-day,

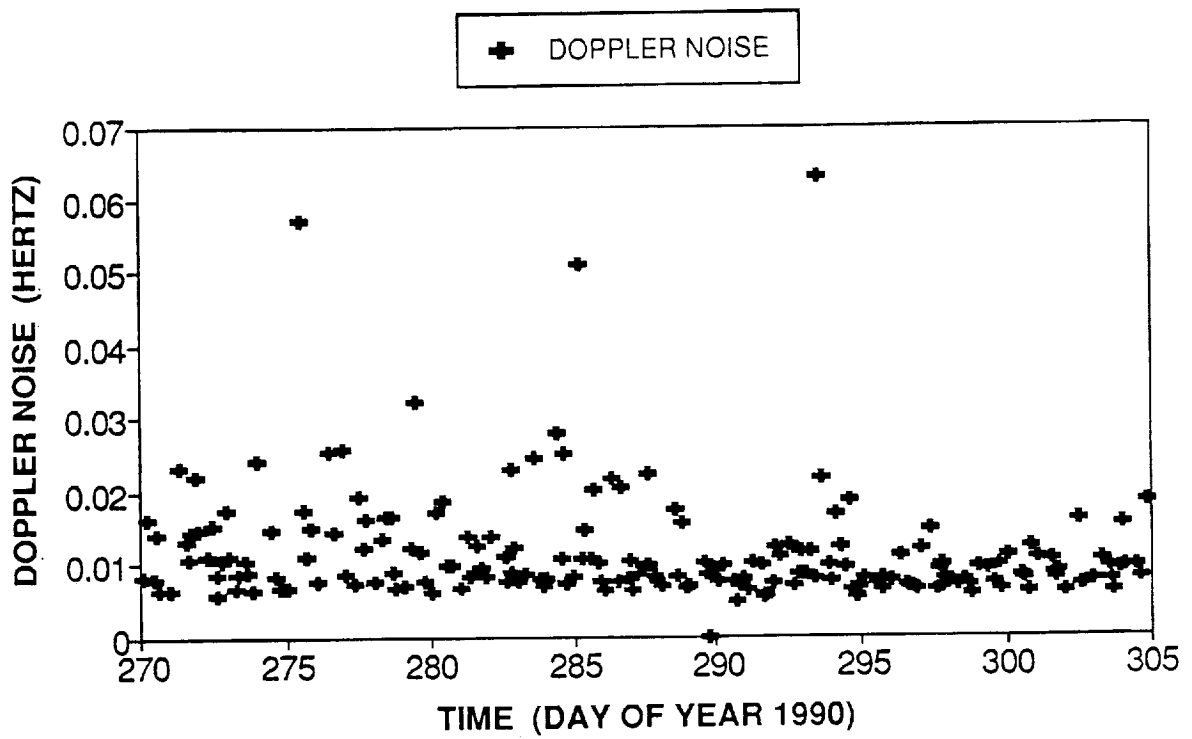


Figure 6. One-Way Doppler Noise for 10-Second Data

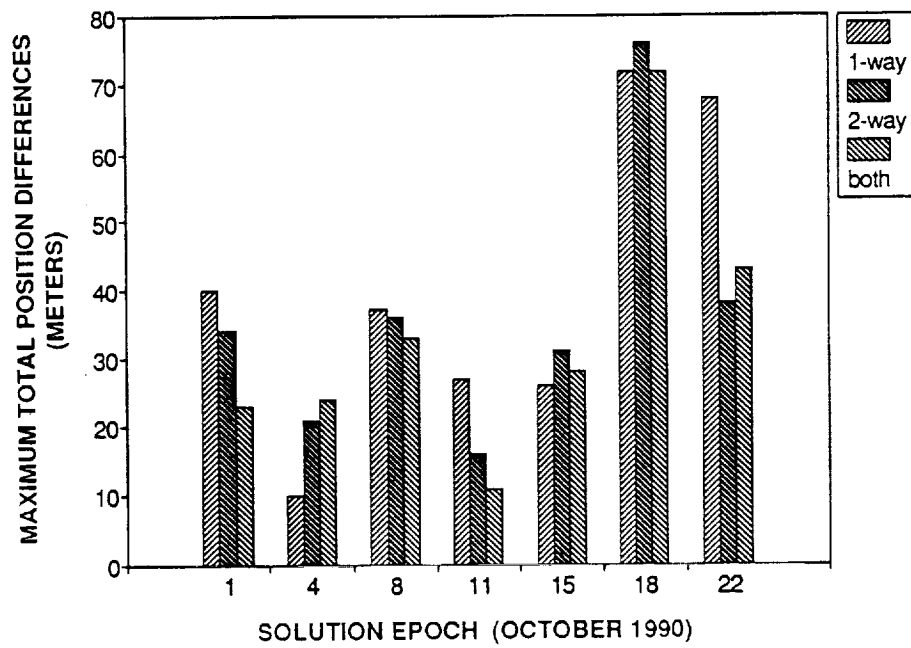


Figure 7. Maximum Position Difference Overlap Comparisons

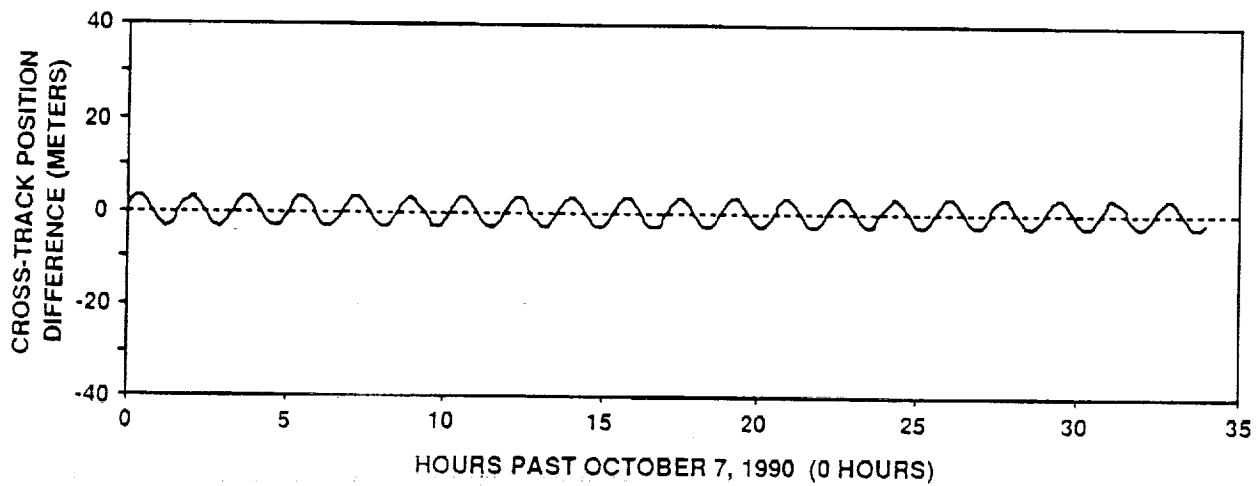
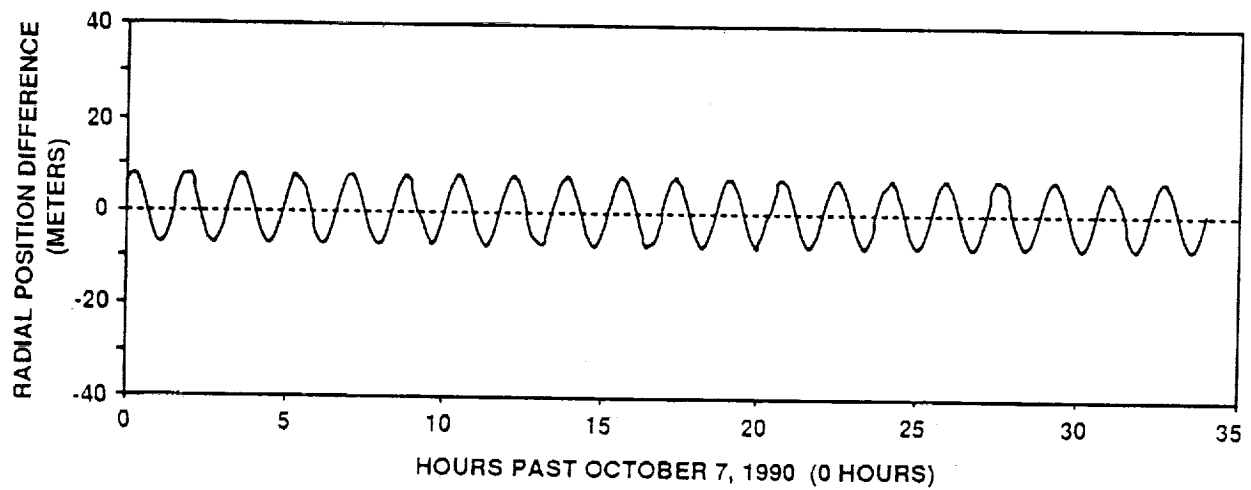
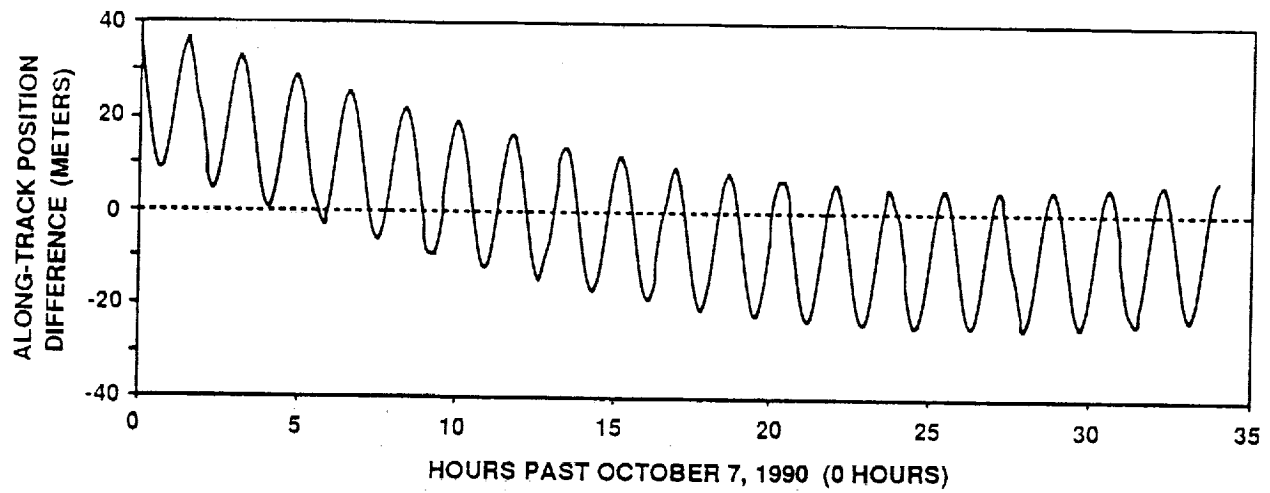


Figure 8. One-Way Overlap Ephemeris Comparison

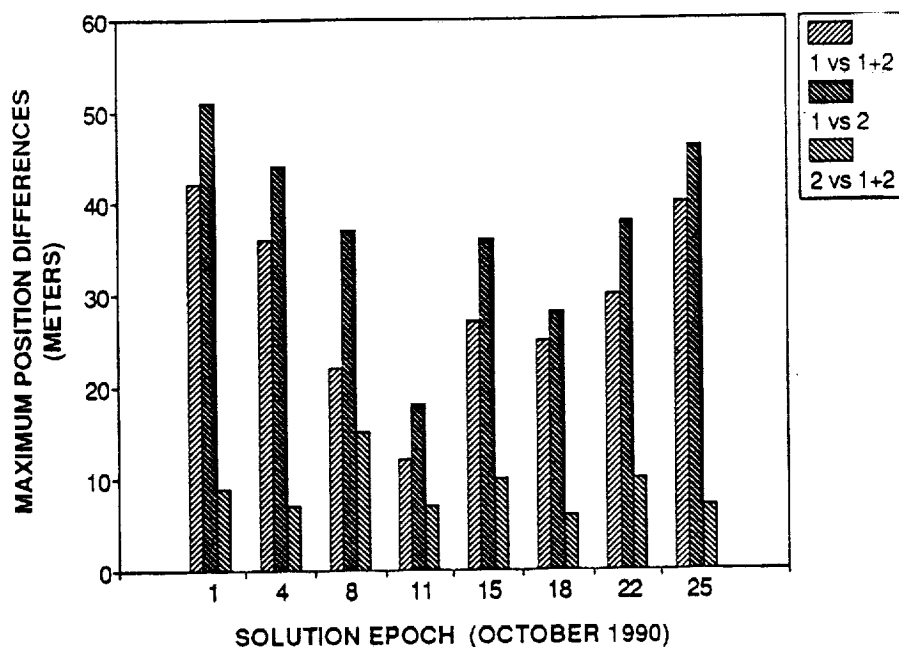


Figure 9. Maximum Position Difference Parallel Comparisons

10-hour definitive arc. Although a parallel comparison can demonstrate concurrent orbit solution quality for two different solutions, it is perhaps more a reflection of the correlation of the two solutions. Thus, Figure 9 reveals best agreement when the two solutions were based on many common tracking measurements (i.e., two-way and combined) and poorest agreement when there were no tracking measurements in common (i.e., one-way and two-way). Furthermore, the poorest parallel comparisons occurred when one-way measurements were the fewest and the best when they were most abundant.

Figures 10 through 12 represents predictive comparison results for 1-week, 2-week, and 3-week predictions, respectively. The prediction interval is measured between the end points of the solution arcs. The maximum position differences within the definitive period occurred usually (but not always) at the end of the later definitive arc. Since the error in the definitive orbit becomes less significant relative to the prediction error as the prediction interval grows, this technique for determining prediction errors works best for long-term predictions. Large variations are seen in the position differences for different solution arcs. This would be explained by the wide fluctuation in atmospheric density during the period under study. An examination of the estimated values of the atmospheric drag variation coefficient, q_1 , given in Table 4, shows excellent agreement among estimates for a given 4-day period but dissimilarity among estimates for distinct 4-day periods. Since the q_1 estimates were used in the propagation, some randomness in the prediction results might be expected (most of the predictive error is in the along-track direction). The important observation is the good consistency in the comparison results among the one-way, two-way, and combined cases for given prediction intervals; this suggests that the one-way and two-way tracking measurements allowed for similar prediction capability.

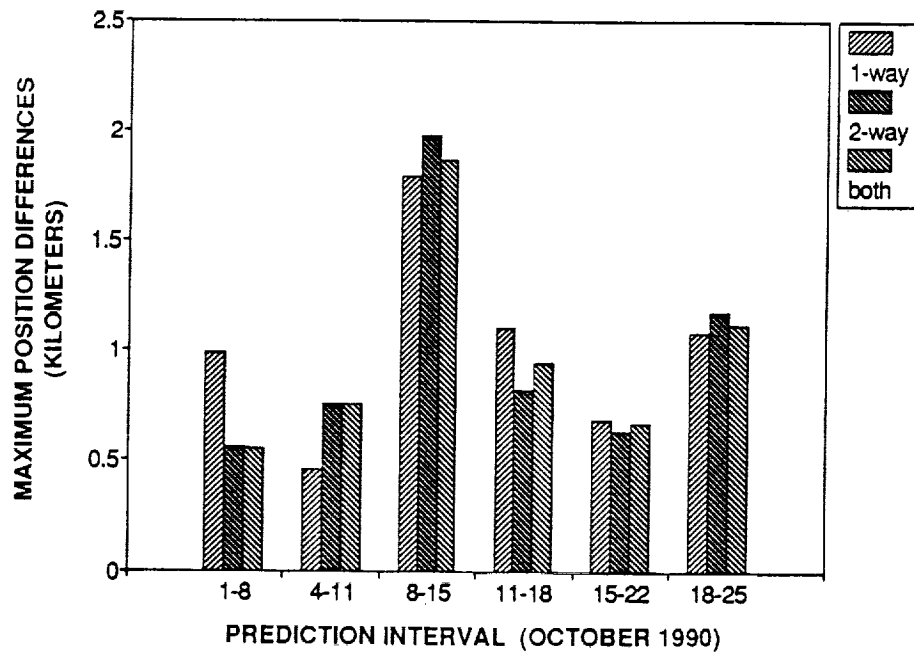


Figure 10. Maximum Position Difference 1-Week Predictions

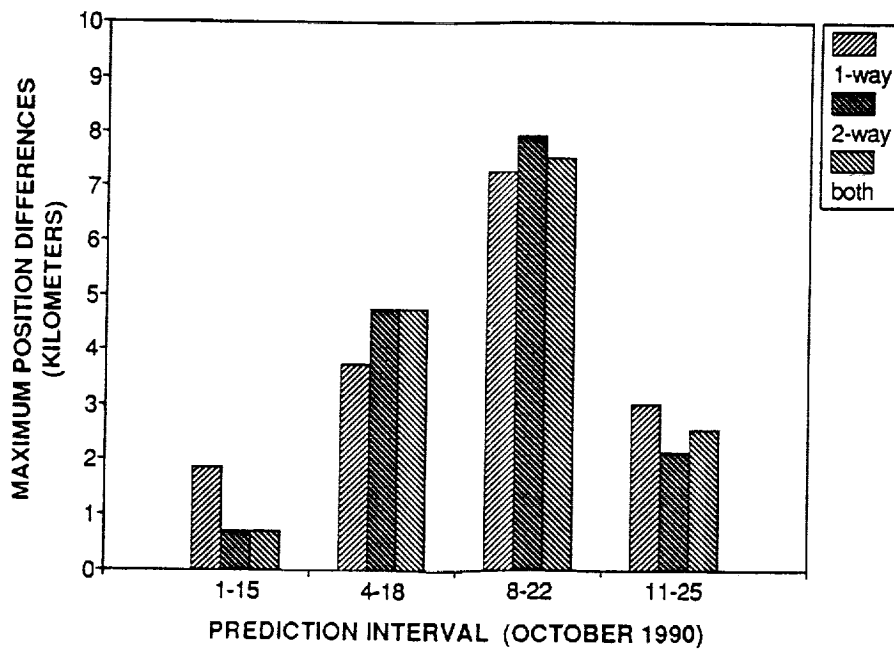


Figure 11. Maximum Position Difference 2-Week Predictions

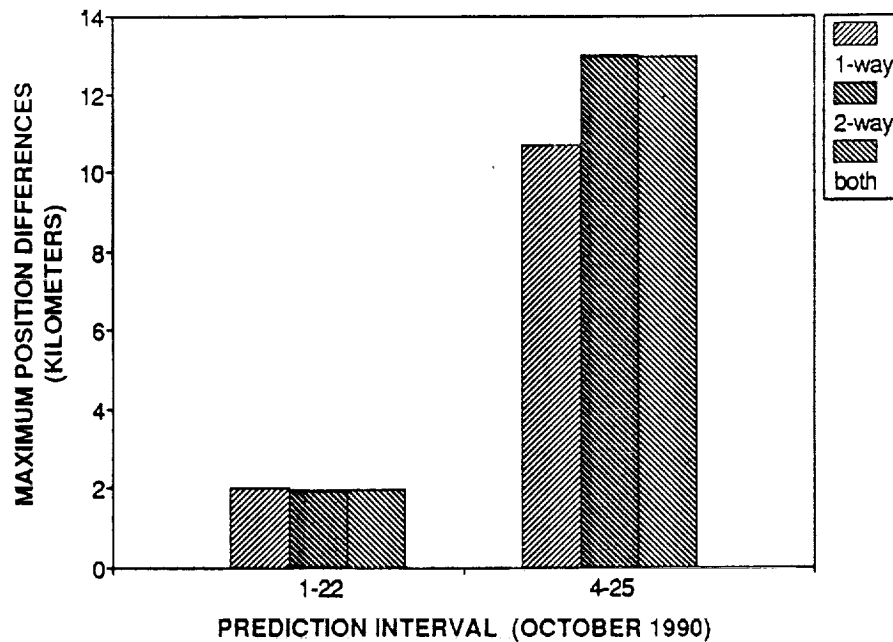


Figure 12. Maximum Position Difference 3-Week Predictions

Table 4. Atmospheric Drag Variation Coefficients (ρ_1) Estimated by One-Way, Two-Way, and Combined Solutions

SOLUTION EPOCH (0 HOURS)	ONE-WAY SOLUTION	TWO-WAY SOLUTION	COMBINED SOLUTION
10/01/90	0.18	0.12	0.12
10/04/90	0.03	-0.004	-0.004
10/08/90	0.03	0.008	0.02
10/11/90	0.34	0.33	0.33
10/15/90	0.21	0.22	0.21
10/18/90	0.20	0.19	0.20
10/22/90	0.36	0.32	0.34
10/25/90	0.18	0.15	0.16

Since the ionosphere tends to increase tracking measurement noise levels, long tracking signal paths through the ionosphere are preferably avoided. Figure 13 shows the accumulated locations of COBE (from the TDRS perspective) at the times TDRS tracking of COBE was occurring for the period under study. The figure shows that most of the tracking (both one-way and two-way) occurred when COBE was outside the Earth's "disk", as viewed from TDRSS. This limited tracking geometry, which resulted largely from the restricted antenna pattern of the TDRSS antenna on COBE (visibility was limited between 65 degrees and 105 degrees of the antenna boresight), allowed little opportunity to avoid long signal path lengths through the ionosphere. Thus, the antenna restriction was a barrier to orbit determination accuracy, whether one-way or two-way data were used. In an attempt to eliminate tracking measurements plagued by heavy ionospheric disturbances, the atmospheric editing criterion discussed earlier was employed. On average, this editing scheme eliminated approximately 30 percent of the available tracking data.

The COBE tracking geometry contributed to accuracy degradation in a second manner. Since COBE is in a near-polar orbit (99-degree inclination), the TDRSs each view the COBE orbit-plane perpendicularly twice a day. For TDRS-East, this occurs at approximately 0300 Greenwich Mean Time (GMT) and 1500 GMT; for TDRS-West, it occurs at approximately 1200 GMT and 0000 GMT. Such a COBE-TDRS orientation permits little Doppler measurement variation. Consequently, the along-track motion of COBE (the largest component of the overall motion) cannot be well determined using only Doppler measurements. Thus, a polar orbit is more favorable to two-way tracking (which involves range measurements) than to one-way Doppler tracking. The deleterious effects of a polar orbit are still further compounded by the exposure of the spacecraft to the electrically stormy polar regions.

SUMMARY AND CONCLUSIONS

The study has shown that, given a USO drift which can be compensated to 10^{-11} parts per day and given equivalent one-way and two-way tracking schedules, TDRSS one-way return-link Doppler tracking of a user spacecraft enables orbit determination accuracy comparable to two-way orbit determination accuracy. Similar ephemeris comparison results were observed for one-way and two-way solutions. Overlap comparisons of 4-day arcs resulted in maximum total position differences of at most 75 meters for both one-way and two-way cases. Parallel 4-day definitive comparisons between one-way and two-way solutions were at most 50 meters. The 1-week through 3-week predictive comparisons produced nearly identical results for the one-way and two-way cases. Post-helium-venting ephemeris comparison results for both the one-way and two-way cases are an order of magnitude improved from the corresponding venting-phase ephemeris comparison results.

Based on the postventing phase analysis, one-way return-link USO frequency-stabilized Doppler tracking is a feasible alternative to two-way range and Doppler tracking for GSFC FDF mission support. Furthermore, a mixture of one-way and two-way tracking measurements is likely to be beneficial because of the improved tracking coverage. Thus, the conclusions reached from the venting phase analysis are affirmed by the postventing phase analysis.

The one-way orbit solution accuracy achieved in this study is not at the limit of one-way accuracy capability, primarily because of poor COBE tracking geometry. Additional analysis

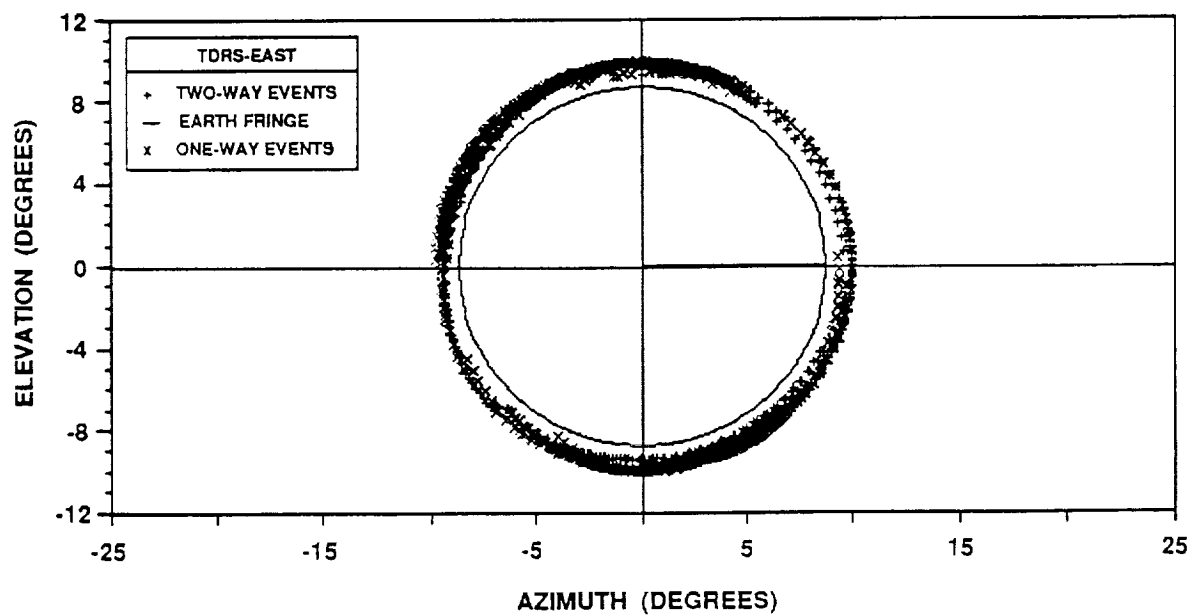
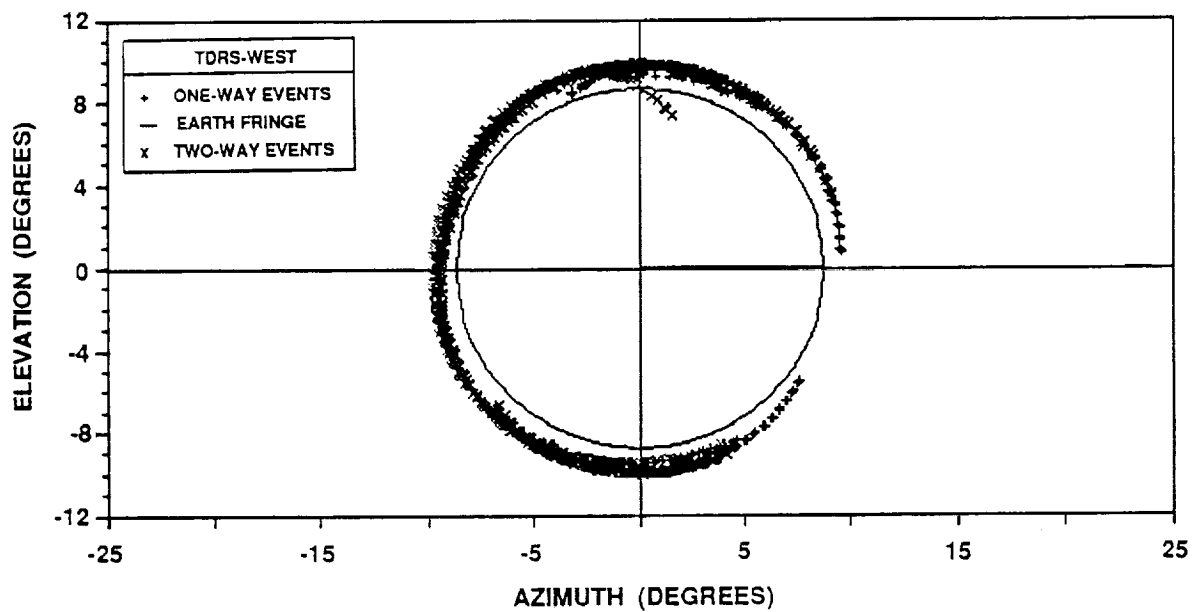


Figure 13. TDRS-East and TDRS-West Views of COBE Based on Radio Frequency (RF) Beam Angles (9/27/90 Through 10/31/90)

involving a more favorable orbit geometry and less restricted TDRS visibility is needed before substantial one-way accuracy improvement can be demonstrated. Such analysis should reexamine the USO frequency stability, since USO limitations to orbit determination accuracy may become more important.

REFERENCES

1. Jet Propulsion Laboratory, 633-711, *TOPEX/POSEIDON Support Instrumentation Requirements Document*, October 1989
2. C. J. Gramling et al., Paper no. 90-3365, *TDRSS Onboard Navigation System (TONS) Experiment for the Explorer Platform (EP)*, presented at the AIAA Guidance, Navigation, and Control Conference, Portland, Oregon, August 20-22, 1990
3. Goddard Space Flight Center, Flight Dynamics Division, FDD/554-90/146, *Cosmic Background Explorer (COBE) Navigation Results Using the Ultra-Stable Oscillator (USO) Doppler Data During the Helium Venting Phase*, December 1990
4. Bendix Field Engineering Company, TR 870110, *Performance Assessment of the COBE Ultra-Stable Oscillator*, May 20, 1987
5. Goddard Space Flight Center, Flight Dynamics Division, FDD/522-89/001, *Goddard Trajectory Determination System (GTDS) Mathematical Theory, Revision 1*, A. C. Long (CSC) et al. (editors), prepared by Computer Sciences Corporation, July 1989
6. Goddard Space Flight Center, NASA TN 100746, *The GEM T2 Gravitational Model*, J. G. Marsh et al. (editors), October 1989
7. Goddard Space Flight Center, Flight Dynamics Division, FDD/554-90/048, *Ionospheric Refraction Effects on TOPEX Orbit Determination Using TDRSS*, M. S. Radomski and K. F. Heuerman (CSC), prepared by Computer Sciences Corporation, June 1990
8. —, FDD/554-90/103, *Effects of Polar Motion and Earth Tides on High-Accuracy Orbit Determination of ERBS*, D. H. Oza and T. Mo (CSC), prepared by Computer Sciences Corporation, May 1990
9. Bendix Field Engineering Company, TDO 79-71, *Variate Difference Noise Analysis*, April 12, 1979
10. Goddard Space Flight Center, Flight Dynamics Division, 554-FDD-91/057, *Cosmic Background Explorer (COBE) Navigation With One-Way Return-Link Doppler in the Post-Helium-Venting Phase*, to be published by Computer Sciences Corporation in the fall of 1991

Preliminary Navigation Accuracy Analysis for the TDRSS Onboard Navigation System (TONS) Experiment on EP/EUVE*

**C. J. Gramling
GODDARD SPACE FLIGHT CENTER (GSFC)**

**A. C. Long, T. Lee, N. A. Ottenstein, and M. V. Samii
COMPUTER SCIENCES CORPORATION (CSC)**

ABSTRACT

A Tracking and Data Relay Satellite System (TDRSS) Onboard Navigation System (TONS) is currently being developed by the National Aeronautics and Space Administration (NASA) to provide a high-accuracy autonomous navigation capability for users of TDRSS and its successor, the Advanced TDRSS (ATDRSS). The fully autonomous user onboard navigation system will support orbit determination, time determination, and frequency determination, based on observation of a continuously available, unscheduled navigation beacon signal. A TONS experiment will be performed in conjunction with the Explorer Platform (EP)/Extreme Ultraviolet Explorer (EUVE) mission to flight qualify TONS Block I.

This paper presents an overview of TONS and a preliminary analysis of the navigation accuracy anticipated for the TONS experiment. Descriptions of the TONS experiment and the associated navigation objectives, as well as a description of the onboard navigation algorithms, are provided. The accuracy of the selected algorithms is evaluated based on the processing of "realistic" simulated TDRSS one-way forward-link Doppler measurements. This paper discusses the analysis process and presents the associated navigation accuracy results.

*This work was supported by the National Aeronautics and Space Administration (NASA)/Goddard Space Flight Center (GSFC), Greenbelt, Maryland, under Contract NAS 5-31500.

1. INTRODUCTION

The Tracking and Data Relay Satellite System (TDRSS) and its successor, the Advanced TDRSS (ATDRSS), will provide future National Aeronautics and Space Administration (NASA) low Earth-orbiting spacecraft with telemetry, command, and tracking services. These user spacecraft require position, time, and frequency data to maintain their operational health and safety and to annotate their science data. Currently, TDRSS supports user spacecraft orbit, time, and frequency determination through ground-based extraction and processing of range and Doppler tracking measurements. TDRSS provides both two-way and one-way return-link scheduled tracking services for equipped users. Proposed enhancements to TDRSS/ATDRSS will provide unscheduled forward-link beacon tracking services.

The capability to support user spacecraft orbit and frequency determination solely by ground-based processing of TDRSS one-way return-link Doppler measurements increases TDRSS availability by reducing scheduled resource requirements and alleviates some operational complexity. This capability is achieved by augmenting the second-generation TDRSS user transponder with an external ultrastable oscillator (USO). This tracking configuration has been flight demonstrated onboard the Cosmic Background Explorer (COBE) mission (Reference 1); and, as a result, the decision was made to use one-way return-link Doppler operationally to support COBE. In 1992, one-way return-link Doppler tracking will also be used to support the Ocean Topography Experiment (TOPEX) mission.

A TDRSS Onboard Navigation System (TONS) is being developed by NASA to provide spacecraft autonomous navigation products for low Earth-orbiting spacecraft via the onboard extraction of highly accurate tracking measurements. TONS will decrease the user's reliance on TDRSS ground operations and scheduled TDRSS resources while at the same time achieving onboard accuracy commensurate with that achievable using the Global Positioning System (GPS). Various levels of upgrades to user spacecraft and TDRSS capabilities will allow corresponding increases in the degree of user autonomy, navigation services, and failure modes. The objective is to develop a fully autonomous user navigation system that supports onboard orbit determination, time determination, and frequency determination, based on observation of a continuously available, unscheduled navigation beacon signal.

TONS is being developed in three stages. The first stage is the TONS experiment, which is being performed in conjunction with the Extreme Ultraviolet Explorer (EUVE) mission, hosted on the Explorer Platform (EP). The EUVE TONS experiment provides an opportunity to flight qualify TONS by processing Doppler data extracted on-orbit and telemetered to the ground in a flight-emulation experiment. On future missions, TONS Block I and TONS Block II will provide onboard user navigation. TONS Block I, the second stage, will use Doppler data derived from scheduled forward-link S-band services to provide onboard orbit and frequency determination. If implemented, TONS Block II, the third stage, will use Doppler and pseudorange data derived from a continuous, unscheduled forward-link S-band beacon service to provide onboard orbit, time, and frequency determination. The TONS Block I and TONS Block II systems are discussed in detail in Reference 2.

Sections 2 and 3 of this paper provide an overview of the TONS experiment and a description of the TONS Flight Software. Section 4 describes the navigation analysis method, and

Section 5 presents the results of a preliminary analysis of the TONS navigation accuracy under the expected operational conditions of the EP/EUVE mission. Remarks and conclusions are provided in Sections 6 and 7, respectively.

2. TONS EXPERIMENT ON EP/EUVE

The TONS experiment requires a forward-link scheduled reference signal from a Tracking and Data Relay Satellite (TDRS), a Doppler extractor (DE) card in the user transponder, a USO, signal acquisition software onboard the user spacecraft, and a ground-based navigation processor. The primary objectives of the TONS experiment follow:

- To flight demonstrate the performance of the Doppler extractor card in the second-generation TDRSS user transponder to extract high-precision Doppler measurements from forward-link S-band signals
- To flight qualify key components of an autonomous navigation processing system that uses the extracted Doppler measurements
- To flight demonstrate onboard Doppler compensation (OBDC) for supporting signal acquisition using onboard software and commands
- To develop and evaluate flight software in a ground-based flight emulation environment

Successful completion of the TONS experiment will demonstrate the flight readiness of the TONS Block I system.

The TONS experiment involves both flight systems onboard EP/EUVE and ground systems for experiment data processing and performance evaluation. Figure 1 provides an overview of the TONS experiment configuration. The flight and ground segments of this configuration are described in detail in References 3 through 6.

2.1 SPACE SEGMENT

To support the experiment, EP/EUVE will accommodate the components to perform the on-board extraction of one-way forward-link TDRSS Doppler measurements and telemeter these data to the ground. The TONS experiment space-based components include an external USO interfaced to the EP second-generation TDRSS user transponder that includes a DE card, Transponder-B. For control purposes and telemetry data collection, the USO and transponder are also interfaced to the onboard computer system (OBC), a NASA Standard Spacecraft Computer (NSSC)-I, through a remote interface unit (RIU). The USO provides a stable frequency reference to Transponder-B. A numerically controlled oscillator (NCO) in the transponder's carrier tracking loop generates internal frequency control words (FCWs) to maintain lock with the received TDRSS forward-link signal. The DE accumulates these internal FCWs. A Doppler count measurement is obtained by sampling the DE 40-bit accumulator every 10.24 seconds. This Doppler extraction capability is discussed in detail in Reference 7.

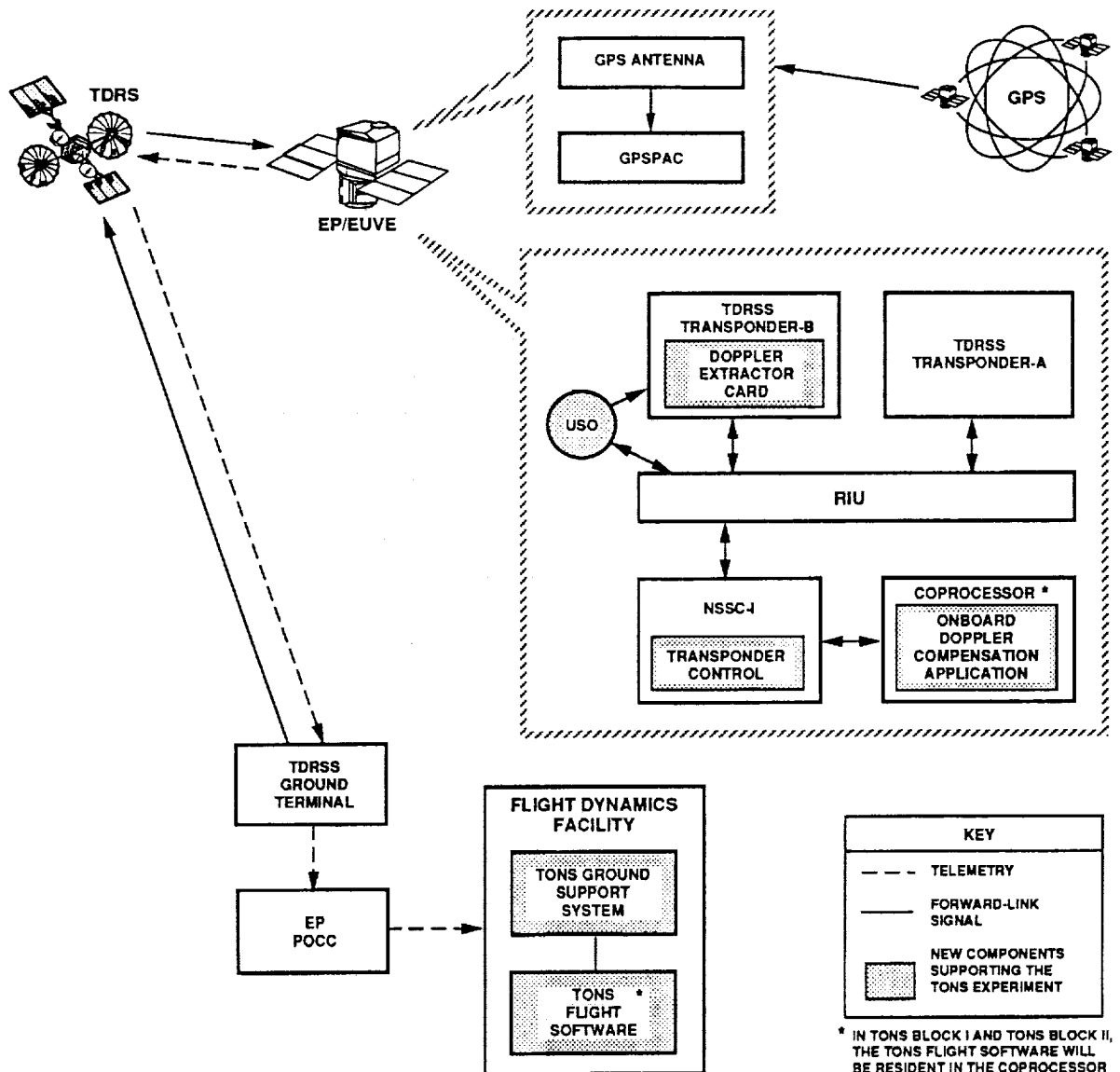


Figure 1. TONS Experiment Overview

Instead of processing the Doppler measurements onboard the EP, the Doppler count data are downlinked via the telemetry stream for ground processing. In addition, EP/EUVE will host a Global Positioning System (GPS) receiver/processor assembly unit as a secondary experiment. The downlink telemetry will also include the GPS-determined EP position, velocity, and time and other GPS engineering data.

EP/EUVE will also demonstrate OBDC and control of TDRSS forward-link signal acquisition using an OBDC application resident in the OBC coprocessor (a MIL STD 1750A architecture microprocessor) and stored commands. This process replaces the current method of signal acquisition, which requires the ground terminal to dynamically compensate the forward-link signal to eliminate the Doppler shift and requires the spacecraft control center to

request that this frequency variation be inhibited when acquisition is verified before a tracking service can be initiated.

2.2 GROUND SEGMENT

To support the TONS experiment, the Goddard Space Flight Center (GSFC) Flight Dynamics Division (FDD) is developing the TONS Ground Support System (TGSS) and the operational TONS Flight Software. The TGSS will extract embedded TONS data from the EP telemetry, simulate the realtime onboard processing environment, assess the quality of Doppler data downlinked from the EP, and compare EP orbit estimates derived via TONS processing with GSFC Flight Dynamics Facility (FDF) definitive (two-way) processing and with the GPS-derived EP ephemeris. The design for the TGSS is presented in Reference 5. The TGSS executes in the multiprocessor environment shown in Figure 2. The institutional FDF National Advanced Systems (NAS) and Digital Equipment Corporation (DEC) VAX processors are used to perform all TGSS support functions except for onboard environment simulation. The onboard environment simulation preparation and control functions are being developed in FORTRAN on a MicroVAX 3100. The realtime interface between the spacecraft's NSSC-I computer and the TDRSS user transponder is simulated using software developed in FORTRAN on a DEC 80286 personal computer (PC), which interfaces with the onboard computer via a MIL STD 1553B communications link.

3. FLIGHT SOFTWARE DESCRIPTION

The TONS Flight Software schedules and executes navigation processing tasks, which consist of state vector estimation and propagation, covariance computation, and Doppler compensation prediction. State vector estimation is performed once for each Doppler measurement that is processed, with the option to sample the data and process less frequently. Doppler compensation prediction is performed prior to the tracking contact to generate input FCWs based on the predicted EP state vectors. The operational TONS Flight Software is being developed for execution in the MIL STD 1750A onboard coprocessor and operates under the coprocessor flight executive software being flown on EP/EUVE.

The navigation algorithms selected for implementation in TONS are based on the following goals:

- Accuracy sufficient to provide a definitive ephemeris accuracy of 10 meters (1σ), with continuous tracking of low Earth-orbiting spacecraft
- A maximum of 256K bytes for the navigation processing
- Efficiency, consuming no more than 20 percent of the available central processing unit (CPU) of a 15 megahertz MIL STD 1750A microprocessor
- Operational simplicity
- Ease of adaptability to the continuous beacon tracking environment
- Enhanced autonomy in the continuous beacon tracking environment

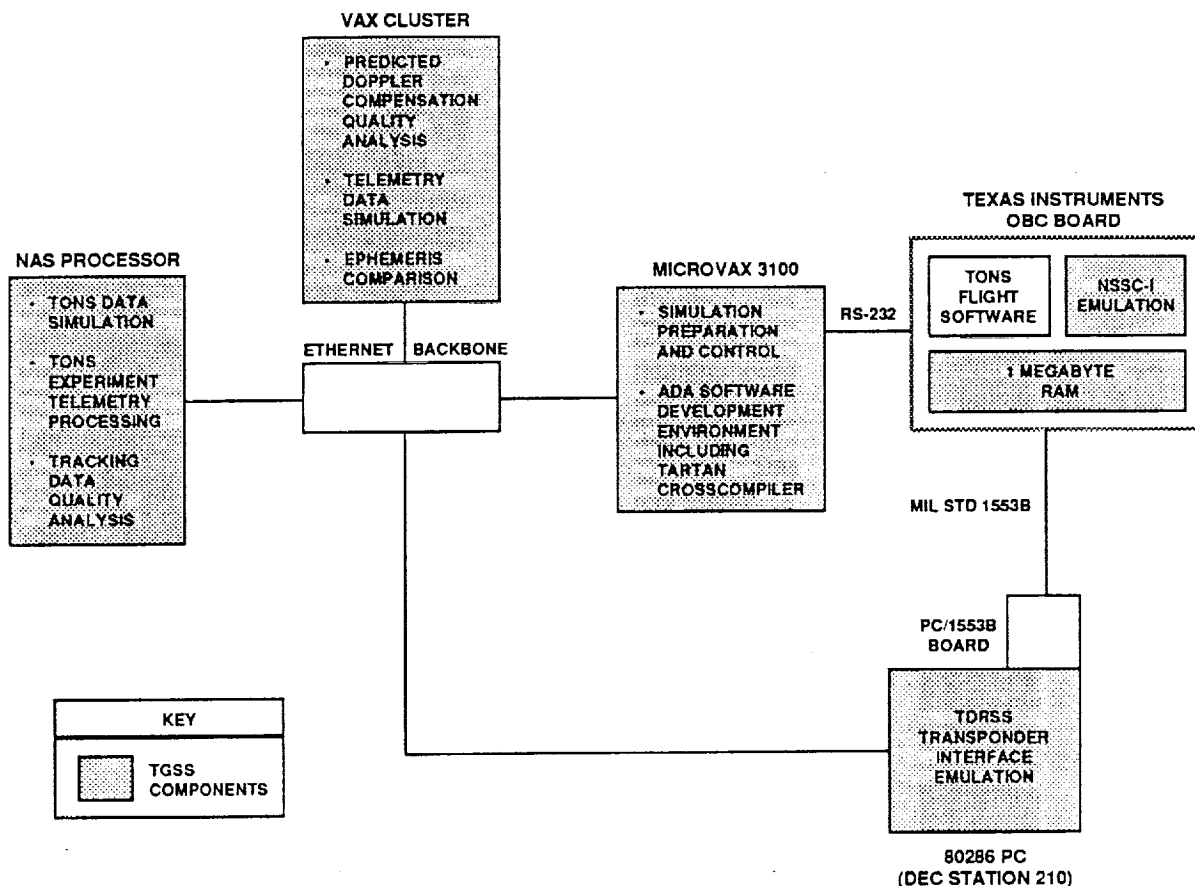


Figure 2. TGSS/Flight Software Configuration

A sequential estimation algorithm was selected over a batch least-squares algorithm because of its computational efficiency, high accuracy, lower memory requirements, and ease of adaptability to the beacon tracking environment. To enhance the performance of the estimator, a physically connected gravity process noise model, which has been adapted from the models given in References 8 and 9, is used in the user state covariance prediction; Gauss-Markov noise models are used for the other estimated parameters, which include corrections to the atmospheric drag coefficient and reference USO frequency bias and drift. Lunar and solar ephemerides, coordinate transformation matrices, and atmospheric density are computed analytically (References 10, 11, and 12). The TDRS ephemerides are computed on the ground and provided as input to the navigation processor. In a TDRSS beacon tracking environment, this information will be included in the beacon signal navigation message.

Table 1 lists the baseline set of TONS Block I navigation algorithms. These algorithms are defined in detail in Reference 13.

Table 1. Summary of TONS Block I Algorithms

ALGORITHM TYPE	ALGORITHM
PRIMARY COORDINATE SYSTEM	MEAN EQUATOR AND EQUINOX OF J2000.0 WITH ANALYTIC COORDINATE TRANSFORMATIONS
PRIMARY TIME SYSTEM	COORDINATED UNIVERSAL TIME (UTC) WITH POLYNOMIAL COEFFICIENTS UPLINKED FOR UTC-TO-UT1 COMPUTATION (UT1 = UNIVERSAL TIME CORRECTED FOR POLAR MOTION)
NUMERICAL INTEGRATOR	RUNGE-KUTTA 3(4+) FOR EP AND THE TDRS STATES AND VARIATIONAL EQUATIONS
EP ACCELERATION MODEL	<ul style="list-style-type: none"> • 30 x 30 NONSPHERICAL GEOPOTENTIAL [GODDARD EARTH MODEL-10B (GEM-10B)] • EARTH, SOLAR, AND LUNAR POINT-MASSSES, WITH ANALYTIC EPHEMERIS • ANALYTIC REPRESENTATION OF THE HARRIS-PRIESTER ATMOSPHERIC DENSITY FOR DRAG
TDRS ACCELERATION MODEL	<ul style="list-style-type: none"> • 8 x 8 NONSPHERICAL GEOPOTENTIAL • EARTH, SOLAR, AND LUNAR POINT-MASSSES, WITH ANALYTIC EPHEMERIS • SOLAR RADIATION PRESSURE
EP PARTIAL DERIVATIVES	NUMERICAL INTEGRATION OF VARIATIONAL EQUATIONS, INCLUDING J_2 , J_3 , J_4 , AND ATMOSPHERIC DRAG
ESTIMATOR	EXTENDED KALMAN FILTER WITH PHYSICALLY CONNECTED PROCESS NOISE MODELS
ESTIMATION STATE	EP POSITION AND VELOCITY VECTORS; ATMOSPHERIC DRAG COEFFICIENT CORRECTION, CLOCK BIAS CORRECTION, AND FREQUENCY OFFSET AND DRIFT CORRECTIONS
MEASUREMENT MODEL	TDRSS ONE-WAY DOPPLER WITH ITERATED LIGHT-TIME SOLUTION, RELATIVISTIC CORRECTION, AND OPTIONAL FREQUENCY OFFSET AND DRIFT CORRECTIONS

6130-2

4. NAVIGATION ANALYSIS METHOD

In parallel with the development of the TONS Flight Software, a preliminary navigation accuracy analysis is being performed. This analysis has three major objectives: (1) assessment of the expected accuracy under nominal operational conditions for the TONS experiment; (2) evaluation of the sensitivity of the navigation accuracy to tracking schedule variations, dynamic modeling errors, and measurement errors; and (3) optimization of the estimation algorithm to reduce the associated error contributions. When the TONS Flight Software is available on the target platform, its operational accuracy and throughput characteristics will be determined, and optimization of the estimation algorithms to improve performance will be performed, if required.

The analysis process consists of the processing of "realistic" simulated tracking data using a sequential estimation algorithm. Accuracy is determined by comparing estimated parameters against the "truth" parameters from which the tracking data are derived.

Truth ephemerides are generated for EP/EUVE and two TDRSs using the force modeling parameters listed in Table 2. The nominal EP/EUVE orbit is circular, with an inclination of

28.5 degrees and a mean altitude of 525 kilometers. The TDRS-East and TDRS-West orbits are circular, geosynchronous, and near-equatorial, located at 41 degrees and 171 degrees west longitude, respectively.

Table 2. Truth Ephemeris Model Parameters

PARAMETER	EP/EUVE	TDRS-EAST	TDRS-WEST
ATMOSPHERIC DRAG COEFFICIENT	2.0	N/A	N/A
SOLAR RADIATION PRESSURE COEFFICIENT	1.2	1.5	1.5
GRAVITY MODEL	GEM-10B (36 x 36)	GEM-10B (12 x 12)	GEM-10B (12 x 12)
ATMOSPHERIC DRAG MODEL (F10.7 SOLAR FLUX*, POWER OF COSINE)	HARRIS-PRIESTER (250, 2)	N/A	N/A
SOLAR, LUNAR EPHEMERIDES	JPL DE-118	JPL DE-118	JPL DE-118

NOTE: GEM = GODDARD EARTH MODEL
JPL = JET PROPULSION LABORATORY
DE = DEVELOPMENT EPHEMERIS

6130-2

*UNITS = 10^{-22} WATTS/METER²/HERTZ

These truth ephemerides are input to the Tracking Data Simulation Program of the Navigation Processing System (NPS) to simulate "realistic" one-way forward-link Doppler tracking measurements. NPS is a version of the Research and Development version of the Goddard Trajectory Determination System (R&DGTDS) upgraded by Stanford Telecommunications, Incorporated, to include the capability to simulate one-way forward-link Doppler measurements using a linear model for the USO frequency (Reference 14). Table 3 lists the preliminary operational USO frequency and tracking model error parameters used in the tracking data simulation. The USO frequency model parameters are based on the performance of the USO as determined in the COBE navigational experiment discussed in Reference 1.

Table 3. Preliminary Operational Tracking Data Simulation Parameters

PARAMETER	VALUE
USO FREQUENCY BIAS	-240 HERTZ
USO FREQUENCY DRIFT	-0.09603 HERTZ PER DAY
DOPPLER NOISE (1σ)	7 MILLIHERTZ
DOPPLER COUNT INTERVAL	10.24 SECONDS
TIMETAG OFFSET	0.0

6130-2

The TDRS-East and TDRS-West ephemerides that are used in the filter processing are created so as to produce predicted ephemerides that are representative of 1-day predictions generated based on operationally determined TDRS orbit solutions. The amplitude of the ephemeris errors is based on an analysis using the operationally determined TDRS vectors. The TDRS-East ephemeris has a maximum error of 42 meters, and the TDRS-West ephemeris has a maximum error of 64 meters. Figure 3 is an example of a 2-day comparison between these 1-day predicted ephemerides and the truth ephemerides. This comparison shows that there is a discontinuity at the day boundary, resulting from the fact that the 1-day predicted ephemerides are based on independent daily operational TDRS orbit solutions which are not constrained to be continuous at the day boundary.

The simulated tracking data are processed in the NPS Filter Program. The NPS Filter Program is used in this preliminary navigation analysis because the TONS Flight Software will not be available earlier than September 1991. The NPS Filter Program includes the majority of the TONS Flight Software algorithms (e.g., physically connected gravity state process noise model, 30 x 30 geopotential model, estimation of USO frequency bias and drift corrections) but does not currently include the Gauss-Markov noise models, the analytic solar/lunar ephemerides, and the analytic atmospheric drag model. Table 4 lists the nominal values for the a priori offsets in the parameters to be estimated; Table 5 lists the nominal TONS force model, a priori variances, and filter parameters.

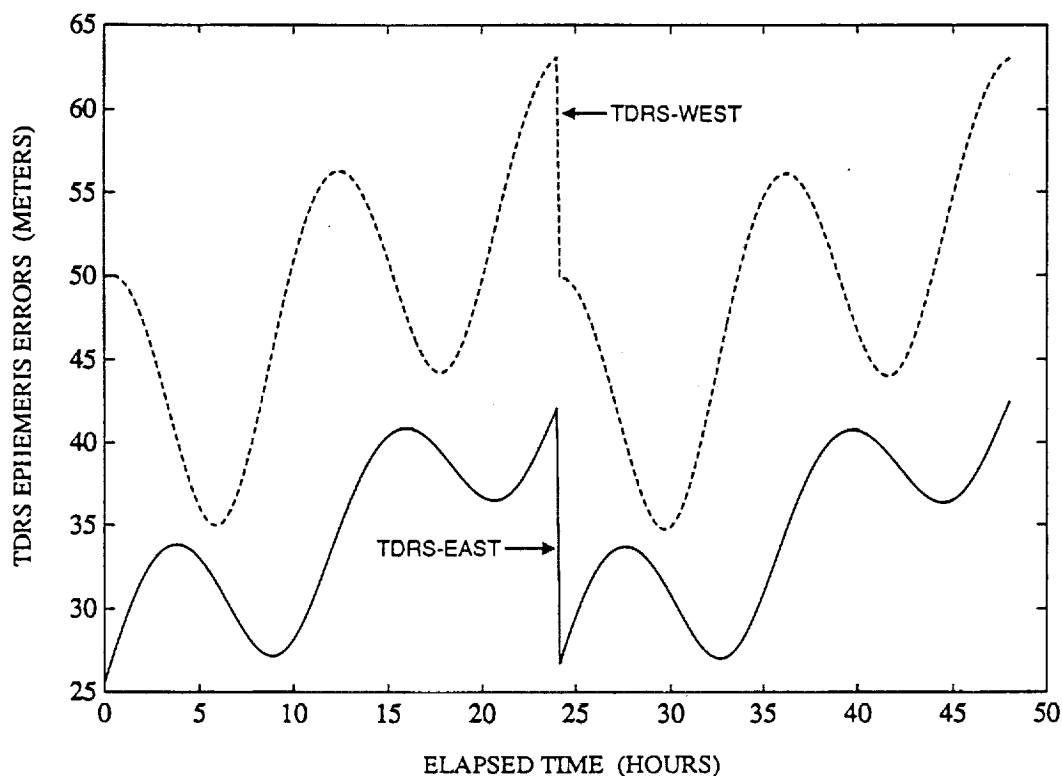


Figure 3. TDRS Ephemeris Errors

Table 4. A Priori Offsets in Parameters

ESTIMATED PARAMETER	A PRIORI OFFSET FROM TRUTH
EP POSITION VECTOR	500 METERS (RSS)
EP VELOCITY VECTOR	0.1 METERS/SECOND (RSS)
ATMOSPHERIC DRAG COEFFICIENT	10 PERCENT
USO FREQUENCY BIAS	8.3 HERTZ
USO FREQUENCY DRIFT	0.0093 HERTZ/DAY

NOTE: RSS = ROOT SUM SQUARE

6130-2

Table 5. TONS Nominal Force Model and Filter Parameters

PARAMETER	VALUE
EP GRAVITY MODEL	GEM-10B (30 x 30)
ATMOSPHERIC DRAG MODEL (F10.7 SOLAR FLUX, POWER OF COSINE)	HARRIS-PRIESTER (250, 2)
INITIAL EP POSITION VARIANCE (KILOMETERS ²)	10, 10, 10
INITIAL EP VELOCITY VARIANCE (METERS ² /SECOND)	9, 9, 9
DOPPLER MEASUREMENT STANDARD DEVIATION (MILLIHERTZ)	50
USO FREQUENCY BIAS INITIAL STANDARD DEVIATION (HERTZ)	252.77
USO FREQUENCY DRIFT INITIAL STANDARD DEVIATION (HERTZ/DAY)	0.1053
DRAG CORRECTION VARIANCE	1.0
CONSTANT RATE VELOCITY PROCESS NOISE (KILOMETERS ² /SECOND ² /SECOND)	10 ⁻¹⁶
USO FREQUENCY BIAS PROCESS NOISE RATE	0.0
USO FREQUENCY DRIFT PROCESS NOISE RATE (HERTZ ² /DAY ² /SECOND)	3.3 x 10 ⁻⁸
DRAG CORRECTION PROCESS NOISE RATE (SECONDS ⁻¹)	10 ⁻⁵

6130-2

There are three different spacecraft state process noise models available in the NPS. A symbol Q is commonly used to denote the process noise covariance matrix. The constant rate model assumes that the process noise matrix is diagonal, with elements that grow linearly with time. When this model is used, a set of constant growth rate parameters, one for each diagonal element, must be specified. The adaptive rate model is similar to the constant rate model, except that the growth rate parameters are adaptively adjusted during the filter processing according to an algorithm that monitors the behavior of the system model against that of the measurement residuals at each measurement point (Reference 14). The third model is based on the formulation known as the physically connected gravity process noise model (References 8 and 9). In the subsequent discussion, these three process noise models will be referred to as the constant rate (CQ), adaptive rate (AQ), and the physically connected gravity (GQ) process noise models, respectively. In applying the CQ and AQ models to the current analysis, only the velocity variances are assumed to be nonzero. Table 5 lists the nominal values for the CQ velocity, USO frequency bias, USO frequency drift, and drag coefficient correction process noise rates. The AQ algorithm requires two growth rate parameters. The AQ results presented below were obtained using the same values as those given in Table 5 for the velocity process noise rates for both parameters, such that the AQ model is nearly identical to the CQ model.

When the TONS Flight Software is available, the major conclusions of this analysis will be verified using the operational software. In addition, further analysis will be performed to investigate the expected accuracy of the TONS estimation algorithms as a function of the additional algorithm tuning parameters (e.g., Gauss-Markov process noise parameters) and to investigate the throughput characteristics of the Flight Software.

5. NAVIGATION ACCURACY ANALYSIS

The navigation accuracy analysis was performed using the simulated tracking data and sequential orbit determination procedures described above. An orbit determination process requires two basic sets of input data: a set of tracking measurements and a set of parameters for the filter processing. The navigation accuracy results presented in this section were obtained using a number of different input data sets. To study the sensitivity of the filter solutions to various error sources and different tracking scenarios, both the tracking measurement set and filter processing control parameters were varied. In particular, these input data sets were prepared to examine the sensitivity of the orbit determination accuracies to the following:

- Tracking scenarios
- Dynamic and local errors, including
 - Geopotential modeling errors
 - TDRS ephemeris errors
 - Atmospheric drag modeling errors
 - Measurement noise
 - USO frequency bias and drift

5.1 SENSITIVITY TO TRACKING SCENARIOS

The sensitivity of navigation accuracy to different tracking scenarios was studied using nominal simulated tracking data (Table 3) and nominal filter processing control parameter values (Tables 4 and 5 and Figure 3). The minimum tracking schedule for the EP/EUVE mission consists of one 5-minute pass of one-way forward-link tracking per orbit; however, in the TONS Block II beacon tracking mode, near-continuous forward-link tracking may be obtained. Tracking data were simulated for the following three scenarios:

- Two-day nominal tracking with an even distribution: one 5-minute tracking contact every EP/EUVE orbit from alternating TDRSs, with a relatively even spacing between contacts (approximately 100 minutes), one measurement every 10.24 seconds
- Two-day nominal tracking with an uneven distribution: one 5-minute tracking contact every EP/EUVE orbit from alternating TDRSs, with several large gaps between contacts (up to 185 minutes), one measurement every 10.24 seconds
- Two-day near-continuous tracking: tracking from each TDRS whenever it is visible, one measurement every 30.72 seconds

Figures 4 and 5 show the total root-sum-square (RSS) position differences between the truth ephemeris and the filter solutions obtained incorporating the TDRS ephemeris errors previously defined and using the GQ process noise model for the nominal and near-continuous tracking scenarios, respectively. After a transient period, each solution appears to reach a steady state. The length of this transient period decreases from approximately 16 hours for the nominal tracking scenarios to 1 hour for the near-continuous tracking scenario.

The accuracy of the steady-state solution obtained using the nominal tracking scenarios is seen to be below 50 and 70 meters in total position for the even and uneven distributions, respectively. This accuracy improves to approximately 12 meters for the near-continuous scenario.

Similar solutions were obtained using the CQ and AQ process noise model options. Figure 6 shows the total EP position error in the solution computed using the CQ and AQ process noise models for the nominal tracking scenario, with the even data distribution. However, the magnitude of the steady-state filter covariance in the two cases is significantly different, particularly for the nominal tracking scenario. The RSS position standard deviation associated with the covariance computed using the GQ process noise model varies between 15 and 200 meters, whereas the corresponding standard deviation associated with the covariance computed using the AQ process noise model varies between 15 and 60 meters. The maximum standard deviation obtained using the GQ process noise model is significantly larger than the observed solution error; the maximum value occurs at the end of the propagation period between tracking contacts and is proportional to the length of the propagation. The effective variance growth rate of the GQ model appears to be significantly larger than the process noise rate used in the CQ and AQ models. Further analysis indicates that the behavior of the covariance computed using the GQ model is consistent with that computed using a constant velocity rate of 10^{-14} [(kilometers/second)²/second]. This overestimate of the covariance may arise

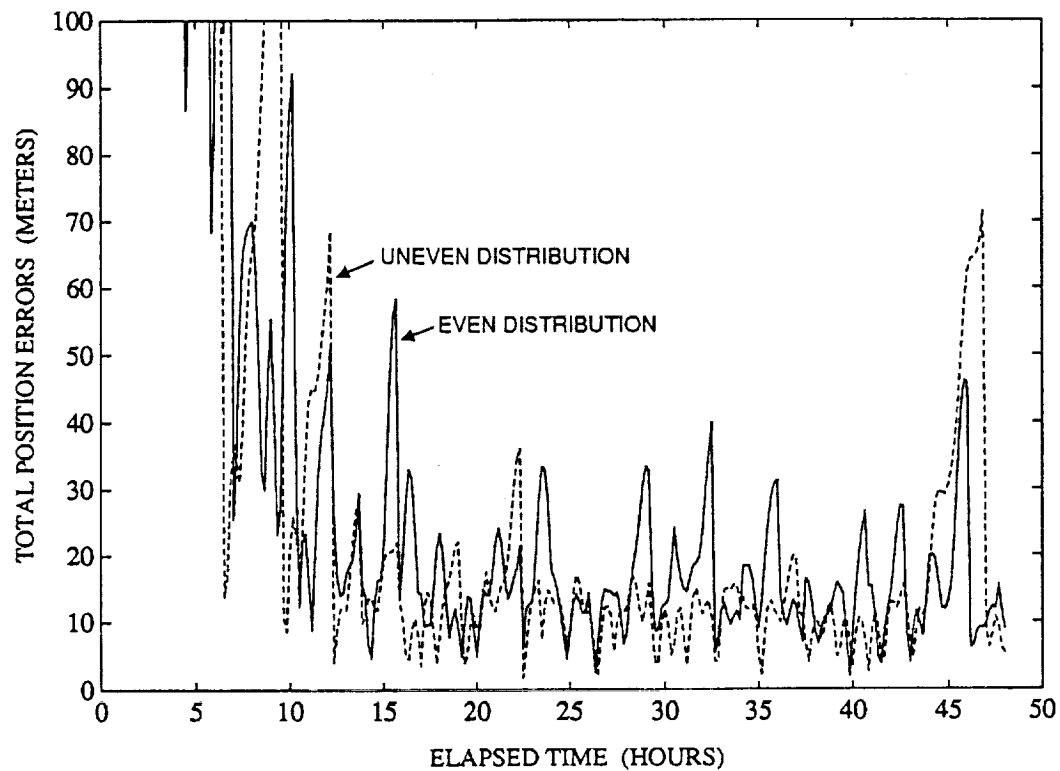


Figure 4. Total EP Position Error Using the Nominal Tracking Scenario With GQ Process Noise

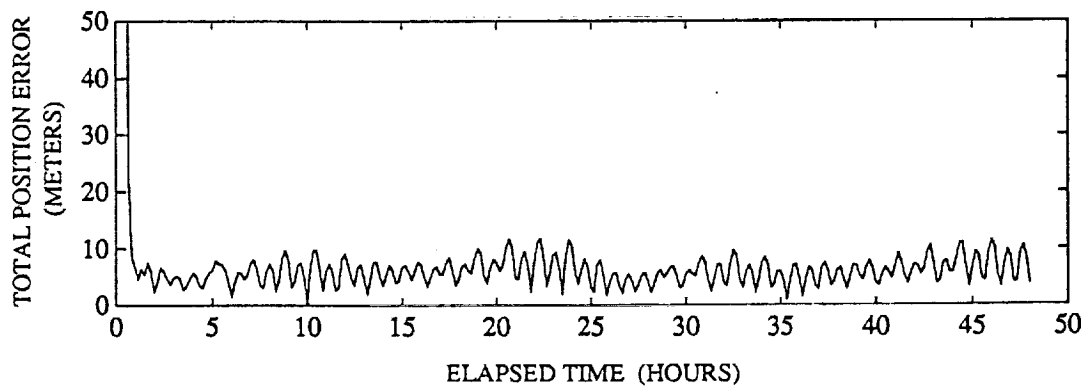


Figure 5. Total EP Position Error Using the Near-Continuous Tracking Scenario With GQ Process Noise

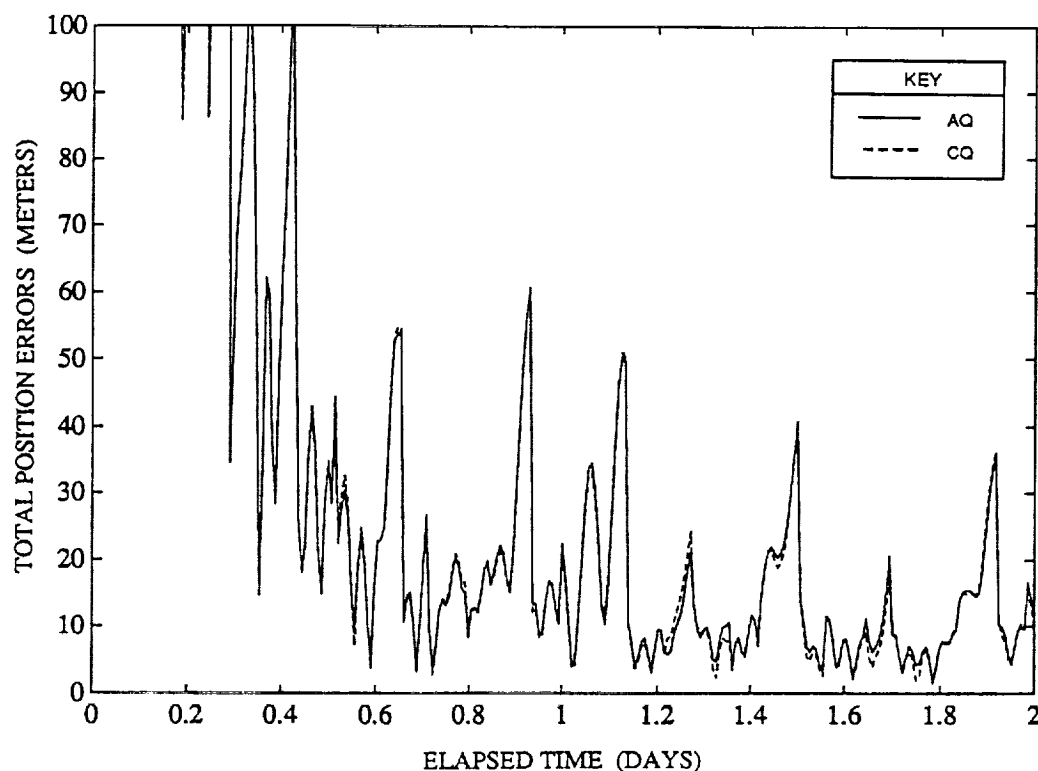


Figure 6. Total EP Position Error Using the Nominal Tracking Scenario With CQ and AQ Process Noise Models

from the fact that the GQ model computes the gravity process noise associated with omission of the gravitational harmonics between orders 30 and 50, whereas the tracking data are simulated using a geopotential model of order 36. The reason for this difference remains under study.

To study the stability of the filter performance over an extended period of time, 18-day solutions were generated using the nominal tracking scenario with an even data distribution. The 18-day TDRS error models were constructed by repeating 2-day error models. These 2-day models represent the 2-day prediction errors for the TDRS ephemerides and are similar in structure to those shown in Figure 3, which model the expected daily upload of 1-day predictions. Thus the predicted TDRS-East and TDRS-West ephemerides used for the 18-day filter solutions have a piece-wise continuous structure with 9 continuous sections, each 2 days long. All other input parameters for the filter processing were the same as those used in the 2-day solutions discussed above. Figures 7 and 8 show the resultant errors in the filter solutions using the GQ and AQ process noise models, respectively. The solution error for the GQ case remains at a maximum of 50 meters after 18 days of processing, and the solution error for the AQ case remains at a 45-meter level, with mean errors of 11.08 and 11.17 meters, respectively.

In the case of nonstate estimated parameters [drag coefficient correction parameter, USO frequency bias (b_0), and USO frequency drift (b_1)], the steady-state solutions fluctuate about

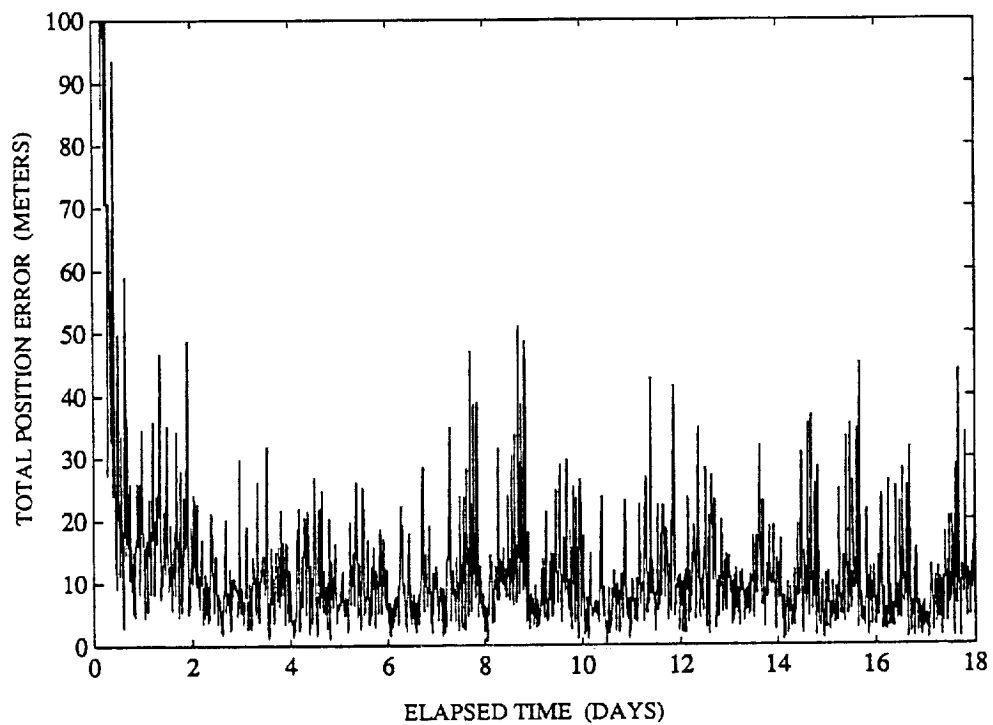


Figure 7. Total EP Position Error Using the GQ Process Noise Model

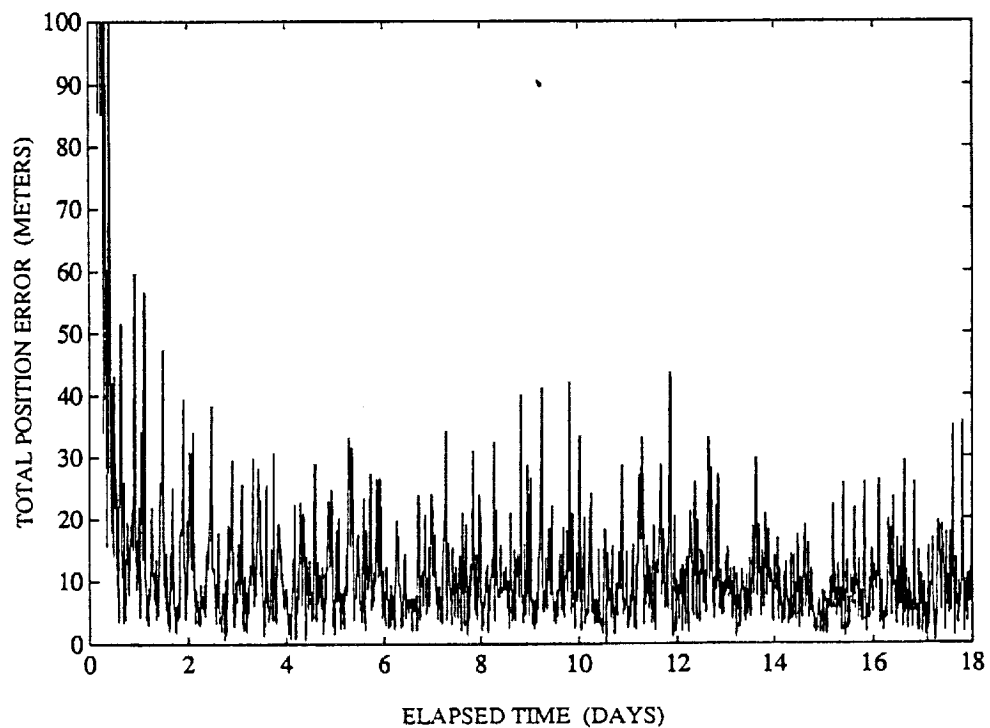


Figure 8. Total EP Position Error Using the AQ Process Noise Model

the true values. In the case of the drag correction coefficient, the mean and standard deviation of the steady state solutions are -0.02 and 0.05 for the nominal tracking scenario and -0.005 and 0.05 for the near-continuous tracking scenario, where the true value is 0.0 , since the nominal and truth drag models were identical except for an initial scale factor offset. The instantaneous USO frequency bias estimates also follow the truth total bias. Figure 9 shows that the estimated USO frequency bias for the continuous case nearly reproduces the true total bias with a maximum error of 0.0107 hertz (5 parts in 10^{12}) and a mean error of 0.001 hertz after 1 hour of processing. The estimated bias for the nominal tracking case shown in Figure 10 exhibits an initial deviation from the truth but eventually converges to the correct value with a maximum steady-state error of 0.077 hertz (4 parts in 10^{11}) and a mean error of 0.004 hertz.

5.2 SENSITIVITY TO DYNAMIC AND LOCAL ERRORS

Dynamic and local error sources that commonly degrade orbit estimation accuracy are the following:

- USO frequency bias and drift
- Atmospheric drag modeling errors
- Geopotential modeling errors
- TDRS ephemeris errors
- Doppler measurement noise
- Measurement timetag errors

Corrections to the atmospheric drag coefficient, USO frequency bias, and USO frequency drift can be estimated in the orbit determination process to reduce the magnitude of the associated errors. Therefore, it is important to examine the accuracy with which the proposed estimation algorithm can determine these parameters for a given tracking scenario. Accurate estimation of the USO frequency corrections was already addressed. However, in the case of the atmospheric drag coefficient correction, the same Harris-Priester atmospheric density table [solar flux level ($F_{10.7}$) = 250] and model [power of the cosine term (N) = 2] was used in both the truth and filter processing, with only a small initial offset impacting the filter processing.

To provide a more realistic test, different atmospheric models were used in the truth and filter processing for the nominal tracking scenario. Figure 11 shows the variation in the estimated drag coefficient corrections obtained using the Harris-Priester models associated with (1) $F_{10.7} = 250$, $N = 6$; (2) $F_{10.7} = 225$, $N = 2$; and (3) $F_{10.7} = 225$, $N = 6$ in the filter processing as compared with the nominal case using $F_{10.7} = 250$, $N = 2$. These results illustrate that the filter was able to readjust the correction values to reflect the changes in the atmospheric densities brought about by modeling errors. The position accuracy associated with these cases was found to be comparable to that obtained in the nominal case discussed earlier.

Table 6 lists the maximum contributions to the steady-state orbit determination errors over a 2-day arc from the remaining error sources that were studied. The impact of measurement timetag errors remains under study.

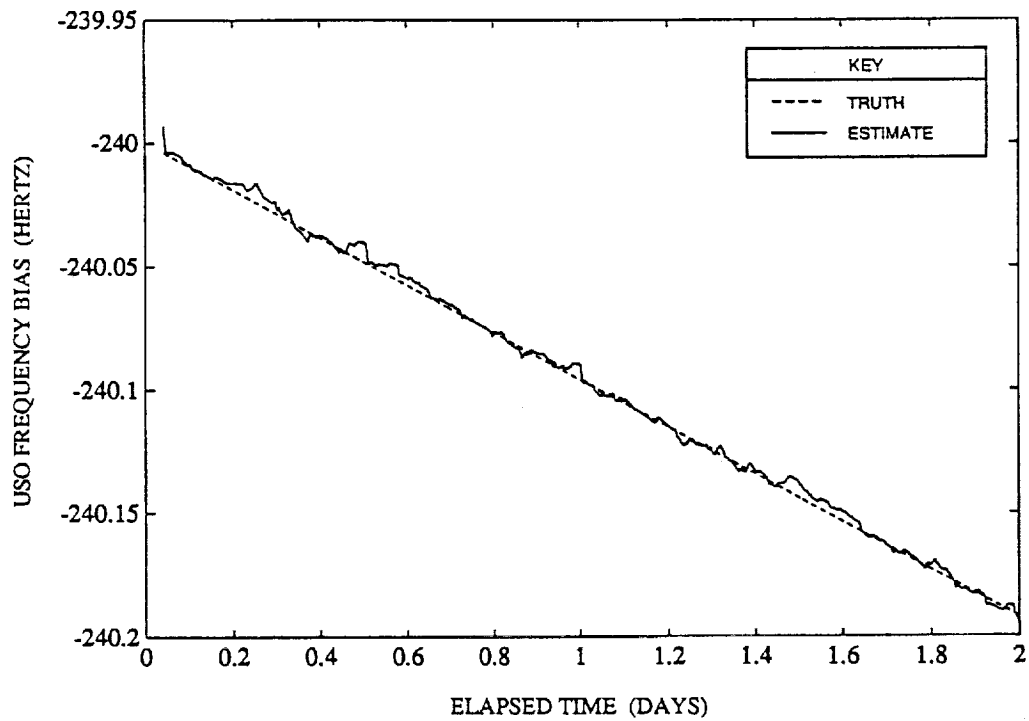


Figure 9. USO Frequency Bias Estimate for the Near-Continuous Tracking Scenario

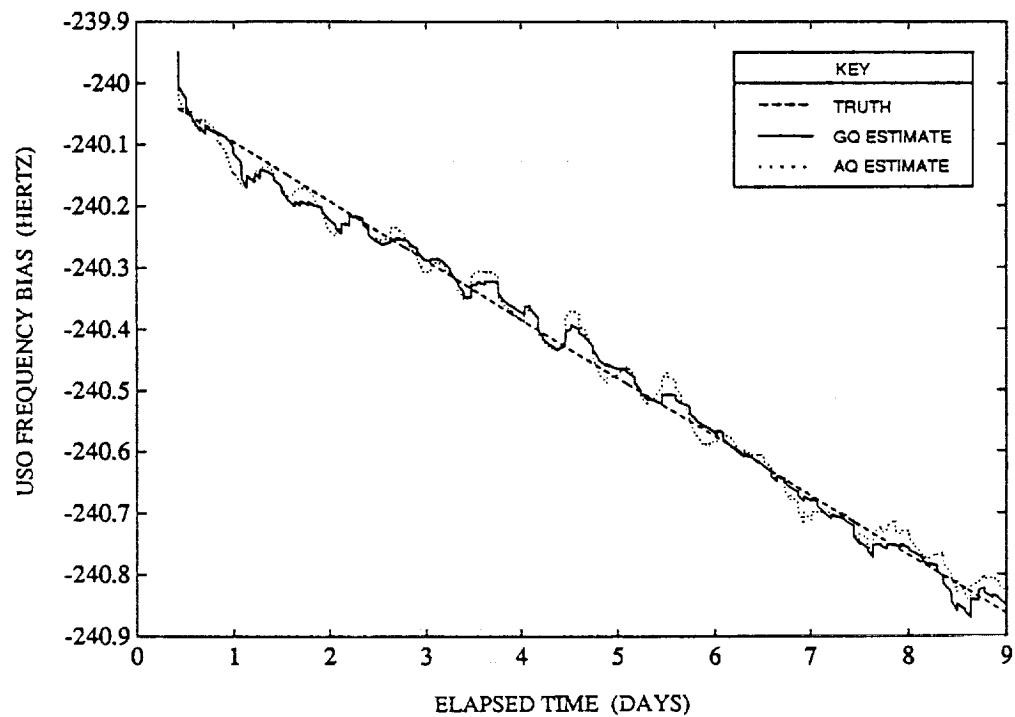


Figure 10. USO Frequency Bias Estimate for the Nominal Tracking Scenario

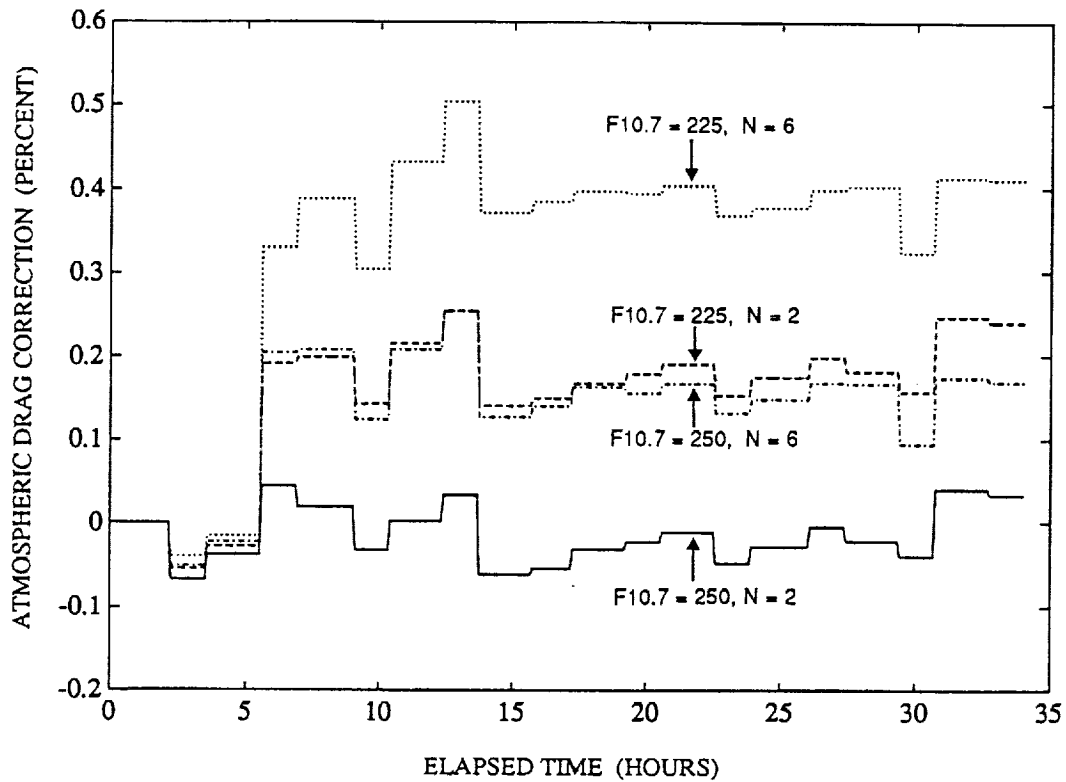


Figure 11. Variation in the Estimated Atmospheric Drag Correction

Table 6. Maximum Contributions to Steady-State Orbit Determination Errors

ERROR SOURCE	MAXIMUM RSS POSITION ERROR CONTRIBUTION (METERS)	
	NOMINAL TRACKING	NEAR-CONTINUOUS TRACKING
GEM-10B (30 x 30)	20	5
GEM-10B (15 x 15)	120	20
TDRS EPHEMERIS (\approx 50 METERS)	10	10
DOPPLER NOISE (7 MILLIHERTZ)	20	< 1
DOPPLER NOISE (35 MILLIHERTZ)	30	< 1

6130-2

Among these error sources, the nonspherical gravity errors were found to have the strongest influence on the orbit determination accuracy. The orbit determination errors due to the gravity model errors depend on the model and its size used in the filter solutions. Figure 12 shows the total EP position error for the nominal tracking scenario using a 15 x 15 geopotential in place of the baseline GEM-10B 30 x 30 model. Because the tracking data were generated using a GEM-10B 36 x 36 geopotential model, the true contribution from geopotential modeling errors is expected to be larger than that shown in Table 6. The magnitude of the geopotential error contribution remains under study.

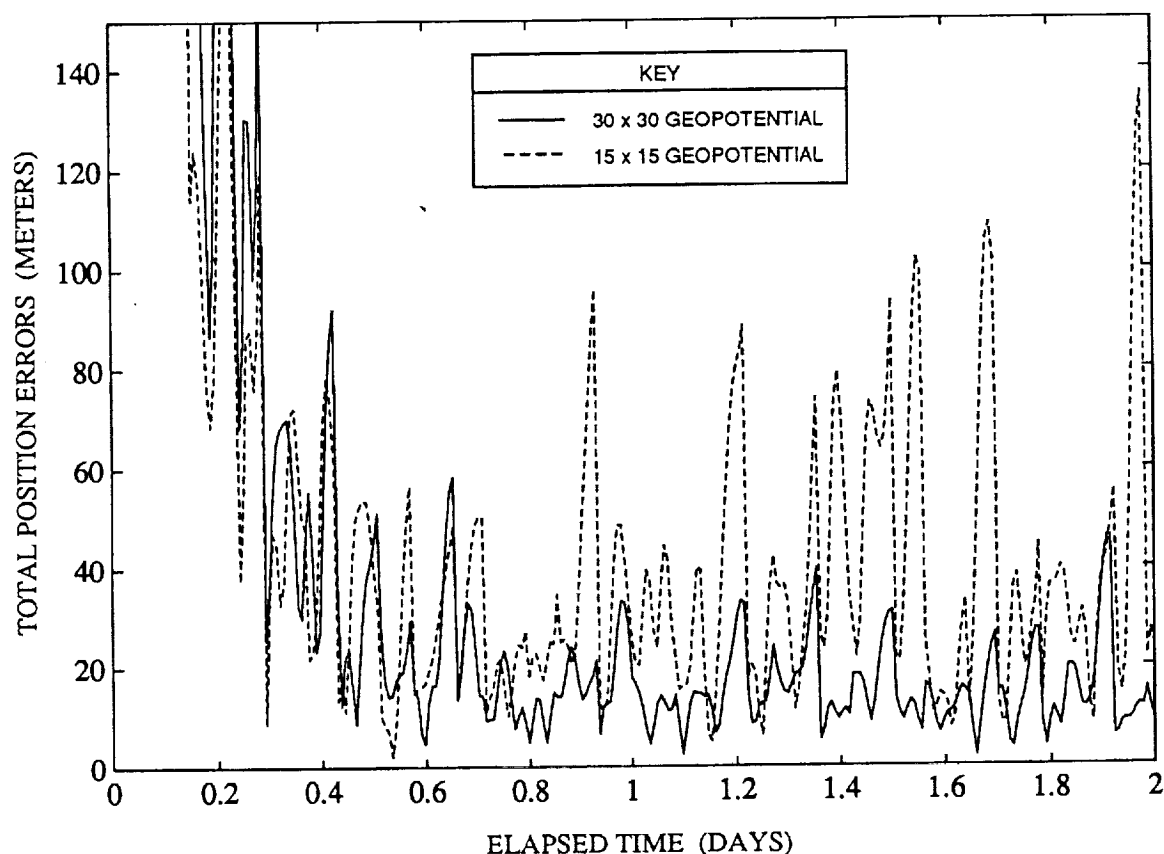


Figure 12. Comparison of Total EP Position Error Using the Nominal Tracking Scenario With GQ Process Noise Using a 15 x 15 Geopotential Model Versus a 30 x 30 Geopotential Model

The error contribution from TDRS ephemeris errors was determined by processing nominal tracking data using TDRS ephemerides with and without ephemeris errors in the filter processing. The impact of TDRS ephemeris errors associated with 1-day predictions based on operational solutions is not very significant.

The error contribution from measurement noise was evaluated by processing tracking data simulated with and without Doppler measurement noise. The values for the observation standard deviation used in the filter processing were approximately 7 times the noise standard

deviation used in tracking data simulation. The measurement noise contribution is significant for the nominal tracking scenario but is insignificant in the near-continuous tracking scenario.

6. REMARKS

The navigation analysis results presented in the previous section are based on a preliminary operational error model and are limited by the data simulation and sequential estimation capabilities available at the time of the study. Further analysis is planned using a more refined operational error model as additional data simulation and sequential estimation capabilities become available.

The impact of Doppler measurement timetag errors on the TONS experiment navigation accuracy are being evaluated. Data simulation using realistic timetag offsets has begun, and a thorough analysis is in progress. If the errors due to poorly known timetag offsets are found to be significant, their impact can be reduced by estimating a timetag offset parameter modeled as a Gauss-Markov process. This approach will be studied using a VAX-based version of the Flight Software. The expected frequency determination accuracy will also be further investigated using the Gauss-Markov process modeling option available in the VAX-based version of the Flight Software.

The preliminary operational error model used a GEM-10B 36 x 36 geopotential model to generate the EP truth ephemeris because it was the most precise model available in NPS at the time. As soon as the capability to use the 50 x 50 GEM-T2 geopotential model is available in NPS, tracking data will be simulated using a truth ephemeris based on this model, and the impact of geopotential model errors will be reassessed. In addition, the covariance predictions obtained using the GQ process noise model will be reevaluated to determine if they are consistent with this more realistic geopotential modeling error. Additional planned navigation analysis includes a more thorough analysis of the impact on performance of the tuning parameters associated with the GQ and AQ process noise models.

7. CONCLUSIONS

The following are the major conclusions resulting from this preliminary navigation analysis for EP/EUVE:

- An orbital position accuracy of better than 50 meters (3σ) and a frequency determination accuracy of better than 0.08 hertz (4 parts in 10^{11}) (3σ) can be achieved for a nominal tracking schedule of one 5-minute contact per orbit after 16 hours of processing using the preliminary operational error models.
- An orbital position accuracy of better than 12 meters (3σ) and a frequency determination accuracy of better than 0.01 hertz (5 parts in 10^{12}) (3σ) can be achieved for a near-continuous tracking schedule after 1 hour of processing using the preliminary operational error models.

- The orbital position accuracy was found to be most sensitive to (1) reduction in the degree of the geopotential model from 30 to 15 and (2) periodic versus near-continuous tracking.
- Comparable navigation accuracy was obtained using either the physically connected gravity process noise model or properly tuned adaptive and constant rate process noise models.

Based on these results, a 30 x 30 geopotential model will be used in the TONS Flight Software, and tracking contacts longer than 5-minutes are recommended whenever possible. In addition, further study will be performed to characterize the expected Doppler measurement timetag errors as part of the EP/EUVE prelaunch testing and to evaluate their impact on the navigation accuracy.

REFERENCES

1. Goddard Space Flight Center, Flight Dynamics Division, FDD/554-90/146, *Cosmic Background Explorer (COBE) Navigation Results Using the Ultra-Stable Oscillator (USO) Doppler Data During the Helium Venting Phase*, J. Dunham, M. Maher, and M. Nemesure (CSC), prepared by Computer Sciences Corporation, December 1990
2. C. Engel, J. Teles, and B. Elrod, *Autonomous Onboard Navigation Using Tracking and Data Relay Satellite System (TDRSS) Signals*, Paper No. AAS 89-175-15, presented at the AAS/GSFC International Symposium on Orbital Mechanics and Mission Design, Goddard Space Flight Center, April 24-27, 1989
3. Stanford Telecommunications, Incorporated, TR 890104, *TDRSS Onboard Navigation System (TONS) Experiment Plan*, R. Daly et al., July 1989
4. Goddard Space Flight Center, Flight Dynamics Division, FDD/554-90/022, *Tracking and Data Relay Satellite System (TDRSS) Onboard Navigation System (TONS) Experiment Ground Support and Flight Software Requirements and Functional Specification, Revision 2*, A. C. Long et al. (CSC), prepared by Computer Sciences Corporation, April 1990
5. Goddard Space Flight Center, Flight Dynamics Division, 552-FDD-91/003, *TDRSS Onboard Navigation System (TONS) Ground Support System System Description*, W. Steger et al.(CSC), prepared by Computer Sciences Corporation, May 1991
6. C. J. Gramling et al., *TDRSS Onboard Navigation System (TONS) Experiment for the Explorer Platform (EP)*, Paper No. AIAA 90-3365, presented at the AIAA Guidance, Navigation, and Control Conference, Portland, Oregon, August 20-22, 1990
7. Motorola Inc., Government Electronics Group, Aerospace Electronics Office; *User's Guide for the NASA Standard TDRSS User Transponder (The Second Generation)*, Issue A; November 4, 1987; and March 1, 1988, update
8. J. Wright, "Sequential Orbit Determination With Auto-Correlated Gravity Modeling Errors," *Journal of Guidance and Control*, vol. 4, 1981, p. 304

9. R. H. Gersten et al., "Statistical Properties of Orbit Perturbations Induced by the Earth's Anomalous Gravity," *Journal of Spacecraft*, vol. 4, 1967, p. 1150
10. Nautical Almanac Office, U. S. Naval Observatory and H. M. Nautical Almanac Office, *The Astronomical Almanac for 1984*. Washington D. C.: U. S. Government Printing Office, and London: Her Majesty's Stationary Office, 1983
11. T. C. Van Flandern and K. F. Pulkkinen, "Low-Precision Formulae for Planetary Positions," *The Astrophysical Journal Supplement Series*, no. 41, November 1979, pp. 391-411
12. Computer Sciences Corporation, CSC/TM-84/6865, *Analytic Representation of the Harris-Priester Atmospheric Density Model in the 110- to 2000-Kilometers Region*, T. Mo and T. Lee, October 1984
13. Goddard Space Flight Center, Flight Dynamics Division, FDD/554-90/104, *Tracking and Data Relay Satellite System (TDRSS) Onboard Navigation System (TONS) Flight Software Mathematical Specifications, Revision 1*, A. C. Long, D. H. Oza, and M. A. Edwards (CSC), prepared by Computer Sciences Corporation, May 1990
14. Stanford Telecommunications, Inc., TR 890112, *COBE Navigation Processing System Volume I—System Description*, B. D. Elrod, D. F. Eggert, and A. K. Kapoor, June 1989

ANALYSIS OF NAVIGATION PERFORMANCE FOR THE EARTH OBSERVING SYSTEM (EOS) USING THE TDRSS ONBOARD NAVIGATION SYSTEM (TONS)*

B. Elrod and A. Kapoor
Stanford Telecom

D. Folta
Flight Dynamics Analysis Branch
Goddard Space Flight Center

K. Liu
Computer Sciences Corporation (CSC)

ABSTRACT

Use of the Tracking and Data Relay Satellite System (TDRSS) Onboard Navigation System (TONS) has been proposed as an alternative to the Global Positioning System (GPS) for supporting the Earth Observing System (EOS) mission. This paper presents the results of EOS navigation performance evaluations with respect to TONS-based orbit, time, and frequency determination (OD/TD/FD). Two TONS modes are considered: one uses scheduled TDRSS forward link service to derive one-way Doppler tracking data for OD/FD support (TONS-I); the other employs an unscheduled navigation beacon service (proposed for Advanced TDRSS (ATDRSS)) to obtain pseudorange and Doppler data for OD/TD/FD support (TONS-II). Key objectives of the analysis were to evaluate nominal performance and potential sensitivities, such as suboptimal tracking geometry, tracking contact scheduling, and modeling parameter selection. OD/TD/FD performance predictions are presented based on covariance and simulation analyses. EOS navigation scenarios and the contributions of principal error sources impacting performance are also described. The results indicate that a TONS mode can be configured to meet current and proposed EOS position accuracy requirements of 100 and 50 meters (3σ), respectively, as well as support onboard time maintenance to an accuracy of 1-2 μ sec or better.

* This work was performed for the National Aeronautics and Space Administration (NASA)/Goddard Space Flight Center (GSFC), Greenbelt, MD, under contract NAS 5-31500.

1.0 INTRODUCTION

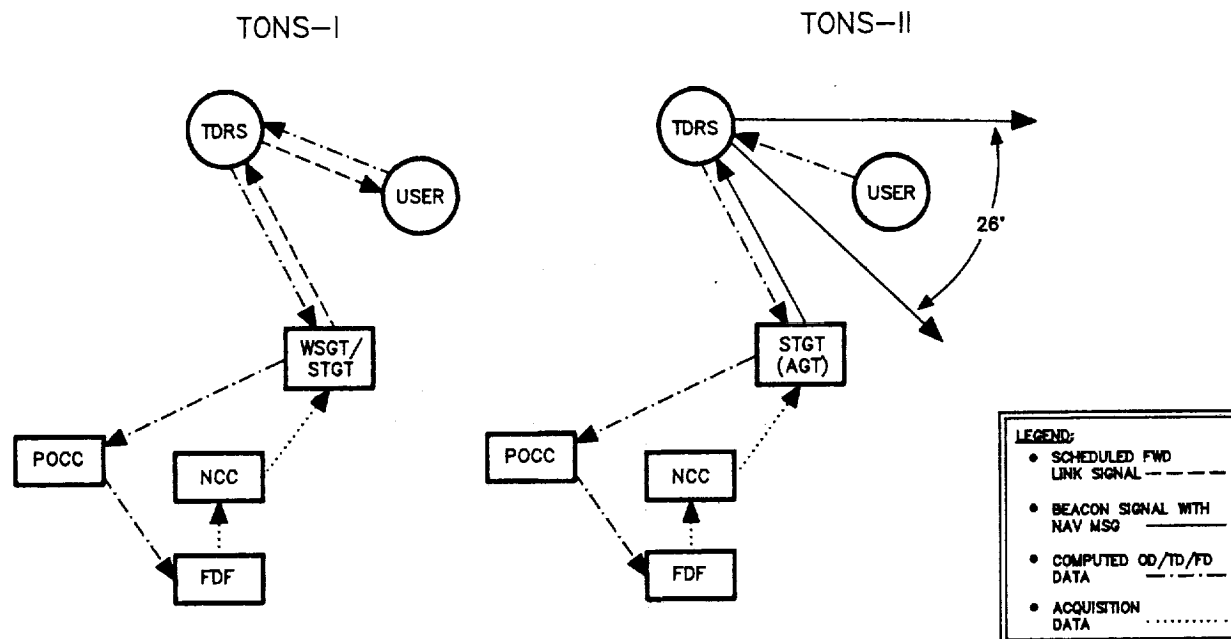
The Earth Observing System (EOS) mission will support a multitude of science instruments on polar orbiting platforms over a 15-year period. In the current baseline program the approved set of EOS instruments will be distributed between two large platforms, each planned for a nominal 5-year design life. To achieve the required 15-year mission lifetime a total of six spacecraft would be launched into Sun-synchronous, high inclination orbits at 30-month intervals via expendable launch vehicles (TITAN-IV class).[1]

To support EOS navigation, science data annotation and other requirements the platforms are specified to have the capability for onboard estimation of orbit data and to provide an accurate time reference. The most stringent orbit determination accuracy requirement for operational phase mission support is 100m (3σ) with a goal of 50m (3σ).[2] This is a derived requirement for support of navigation base attitude determination (36° per axis).[2] The EOS platform time reference is specified to be accurate within 10 μ sec relative to UTC.[2] Use of the Global Positioning System (GPS) signals for orbit and time determination (OD/TD) is the current baseline for providing primary EOS navigation support.[3]

As a backup to GPS navigation, the EOS platform is also specified to have the capability to accept ground-derived orbit data based on TDRSS coherent tracking (2-way range and Doppler-based solutions) or noncoherent tracking (1-way return link Doppler-based solutions). A TDRSS Onboard Navigation System (TONS) under development by the Goddard Space Flight Center (GSFC) has also been proposed as an alternative to GPS for primary EOS navigation support in either of two configurations, TONS-I or TONS-II.

TONS-I can be implemented with the present TDRSS configuration by using one-way Doppler data derived from scheduled forward link S-band Single Access (SSA) or Multiple Access (MA) services to support onboard orbit and frequency determination (OD/FD). The Extreme Ultraviolet Explorer/Explorer Platform (EUVE/EP) mission (1991) will provide the initial TONS-I demonstration.[4,5] A TONS-I user requires a Doppler extractor in the second generation TDRSS user transponder, a stable reference frequency source, such as the Ultrastable Oscillator (USO) on EUVE/EP [4], and navigation processing software. Figure 1 describes the tracking configuration for supporting EOS platforms via TONS-I. Although TONS-I does not support user time determination (TD), the TDRSS-based User Spacecraft Clock Calibration System (USCCS) to be used for the Gamma Ray Observatory (GRO) mission can provide a time update capability of $\sim 1 \mu$ sec.[6] In addition, precise FD available via TONS-I could support the estimation of clock drift corrections to preserve the time accuracy and significantly extend the interval between required USCCS operations.

TONS-II is a proposed future capability which would enable onboard orbit, time and frequency determination (OD/TD/FD) by processing one-way Doppler and pseudorange data derived from unscheduled forward link beacon signals transmitted continuously (see Figure 1). This requires some enhancements to TDRSS to generate the beacon signal and some user enhancements over TONS-I capability to process it (pseudonoise (PN) code agility and pseudorange extractor in the transponder and associated navigation software for pseudorange processing). A demonstration capability may be available with activation of the Second TDRSS Ground Terminal (STGT) [7], launch of additional TDRS satellites, and dedicated use of one or two MA forward links for the beacon signal. A TONS-II operational capability is being considered for implementation with the advent of Advanced TDRSS (ATDRSS) in the late 1990's.[8]



TONS Modes	Key Functions
TONS-I	<p>A. GROUND SEGMENT (WSGT/STGT/POCC/FDF):</p> <ol style="list-style-type: none"> 1. Support Scheduled FWD Link Service (MA, SSA or KSA) to Enable Onboard Doppler Data Acquisition 2. Supply TDRS Ephemeris Data on CMD Channel 3. Receive EOS NAV Data in RTN Link TLM For QC Processing, ACQ/Orbit Support & Ancillary Functions <p>B. USER SEGMENT:</p> <ol style="list-style-type: none"> 1. Acquire FWD Link Signal (Using OBDC) and Extract Doppler Observations 2. Perform OB NAV Processing for OD/FD 3. Supply Computed NAV Data to Onboard Functions and Ground in Standard TLM Format
TONS-II	<p>C. GROUND SEGMENT (STGT(AGT*)/POCC/FDF):</p> <ol style="list-style-type: none"> 1. Generate Continuous (Unscheduled) NAV Beacon Signals For Relay VIA Two TDRSs (ATDRSs)* 2. Supply Beacon NAV Message Data (TDRS Ephem, Timing etc.) 3. Same as A3 <p>D. USER SEGMENT:</p> <ol style="list-style-type: none"> 1. Acquire Beacon Signal (Using OBDC) and Extract Both Doppler and Pseudorange Observations 2. Perform Onboard NAV Processing For OD/TD/FD. 3. Same as B3

* ATDRSS Elements

Figure 1: Overview of User Navigation Via TONS

Previous predictions of navigation performance for future TDRSS/ATDRSS users (e.g., space station and polar platform) indicate that OD/TD accuracies in the range of 20-55 m (3σ) and a 0.3-0.5 μ sec (3σ) may be achieved.[9] Because of this potential navigation performance capability and the weight/cost benefits of a TONS implementation, the EOS Project initiated a GPS/TONS Trade Study to support a possible recommendation relative to EOS onboard navigation alternatives. This paper presents the results of EOS navigation performance evaluations based on TONS which were developed as inputs to the Trade Study.[10] The analysis of TONS-I and TONS-II capabilities to support EOS navigation requirements also addresses potential performance sensitivities such as: suboptimal tracking geometry, contact scheduling/selection, drag solution capability, and selected modeling/navigation algorithm parameters. The following sections present the performance evaluation approach OD accuracy results, TD/FD performance using TONS and the analysis conclusions.

2.0 EOS NAVIGATION PERFORMANCE EVALUATION

The EOS navigation task is to estimate optimal values of the spacecraft trajectory parameters and other selected parameters used in modeling the spacecraft dynamics (e.g., drag) and TDRSS/ATDRSS tracking measurements (e.g., USO bias). With TONS-I, the navigation subsystem would estimate a minimum of seven parameters: three position, three velocity and reference oscillator (USO) bias. With TONS-II at least one additional parameter, user clock bias, would be estimated. Due to inherent inaccuracies in the dynamic and measurement models employed, uncertainties in assumed parameters, and measurement noise, errors will arise in the estimated set of parameters.

To evaluate EOS navigation performance in both TONS modes, covariance analysis techniques were used, and additionally, simulation runs were made for particular cases. Covariance analysis provides a statistical measure (1σ estimate) of the accuracy in orbit, time, and/or frequency determination computed as a function of assumed error contributor statistics, the tracking geometry and contact distribution, and time from a given epoch. Simulation analysis provides a time profile of EOS navigation errors computed by differencing parameters calculated from appropriate truth models with corresponding estimated parameters based on simulated TDRSS tracking data and a suitable emulation of user navigation processing software. The following two subsections describe the specific tracking configurations and scenarios assumed for the covariance and simulation analyses.

2.1 TRACKING CONFIGURATION

The assumed TDRSS/ATDRSS tracking configuration includes two active spacecraft located in circular, 2° inclined geosynchronous orbits stationed nominally at 41° W and 171° W. The EOS platform is assumed to be in a 705 km, 98.2° (Sun-synchronous) orbit with ascending node passage set at 1:30 PM (GMT) on the epoch date: 1 December 1997. Onboard tracking data is assumed to be acquired from TDRS forward link transmissions via scheduled service (one-way Doppler with TONS-I) or continuously broadcast navigation beacon signals (pseudorange and one-way Doppler with TONS-II).

2.2 TRACKING SCENARIOS

If no constraints on EOS antenna pointing or other mission operations are assumed, tracking contacts could be selected within time intervals defined by TDRS/ATDRS line-of-sight visibility and geometrical considerations. The

latter implies satellite selection (41°W or 171°W) to achieve the highest change in Doppler during a tracking pass. This corresponds to choosing the TDRS/ATDRS with the highest angle (θ) between its radius and the EOS orbit normal. (The maximum Doppler rate occurs when $\theta = 90^\circ$.) Two tracking scenarios based on a "best TDRS/ATDRS" criterion are shown in Figure 2.

During normal mission operations, TDRSS/ATDRSS will support the EOS mission with a minimum of one equivalent single access (SA) channel for communication services. Since there may be as many as three spacecraft in orbit simultaneously, time sharing of SA resources is likely. Consequently, for TONS-I EOS tracking, during communication contacts may not necessarily satisfy the "best TDRS/ATDRS" and placement criteria shown in Figure 2.

To assess the potential sensitivity to occasional missed (lost/unavailable) contacts or nonoptimal (poor geometry) contacts, several alternative "degraded" scenarios were considered. On the other hand, the option to schedule occasional TDRSS/ATDRSS multiple access forward link (MAF) tracking contacts to supplement inopportune or unavailable SA contacts is feasible for EOS. Consequently, other scenarios with a combination of degraded contacts and supplemental (5-minute) contacts, where appropriate, were also considered. Table 1 lists the assumed set of scenarios used for analysis.

3.0 COVARIANCE ANALYSIS OF EOS NAVIGATION PERFORMANCE

To evaluate the potential navigation performance for EOS using TONS, an upgraded version of the Sequential Error Analysis (SEA) program [11,12] was used. The program assumes Extended Kalman Filter (EKF) processing of the tracking data and computes the uncertainty in an EOS platform's orbit, time and/or frequency determination as a function of various error sources, and time from a specified epoch. The following subsections discuss the assumed tracking model inputs to the SEA program (see Figure 3) and the OD/TD/FD performance results corresponding to the tracking scenarios defined in Table 1.

3.1 TRACKING MODEL PARAMETERS

Table 2 lists the a priori uncertainties in the basic parameters assumed to be estimated for EOS navigation: three position, three velocity, clock bias and clock drift (or frequency bias in TONS-I). Uncertainties in various systematic and random error sources contribute to the overall covariance of the estimated parameters. The 1σ values of all error sources included in the analysis for TONS-I are listed in Table 2. Changes or additions pertinent to TONS-II are listed in an adjacent column. Since the error analysis is linear, the results for any particular systematic contributor may be scaled up or down to note the impact of values other than those stated here.

3.1.1 Dynamic Model Errors

Errors in force modeling (gravitational harmonics, GM , C_D , C_R) introduce orbit propagation errors in the interval between tracking passes. Values in Table 2 for the gravitational harmonics are based on the GEM-T1 model [13,14]. Their contributions were evaluated individually and the composite effect determined based on the root-sum-square (rss) of errors due to individual harmonics.

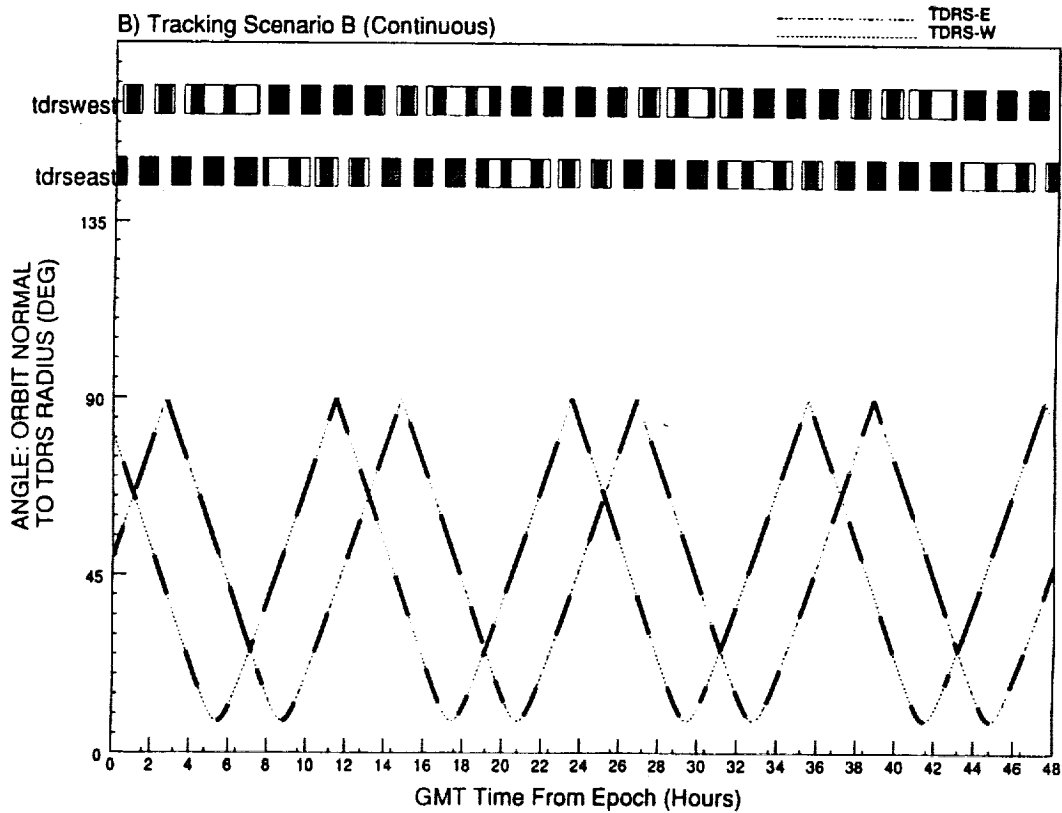
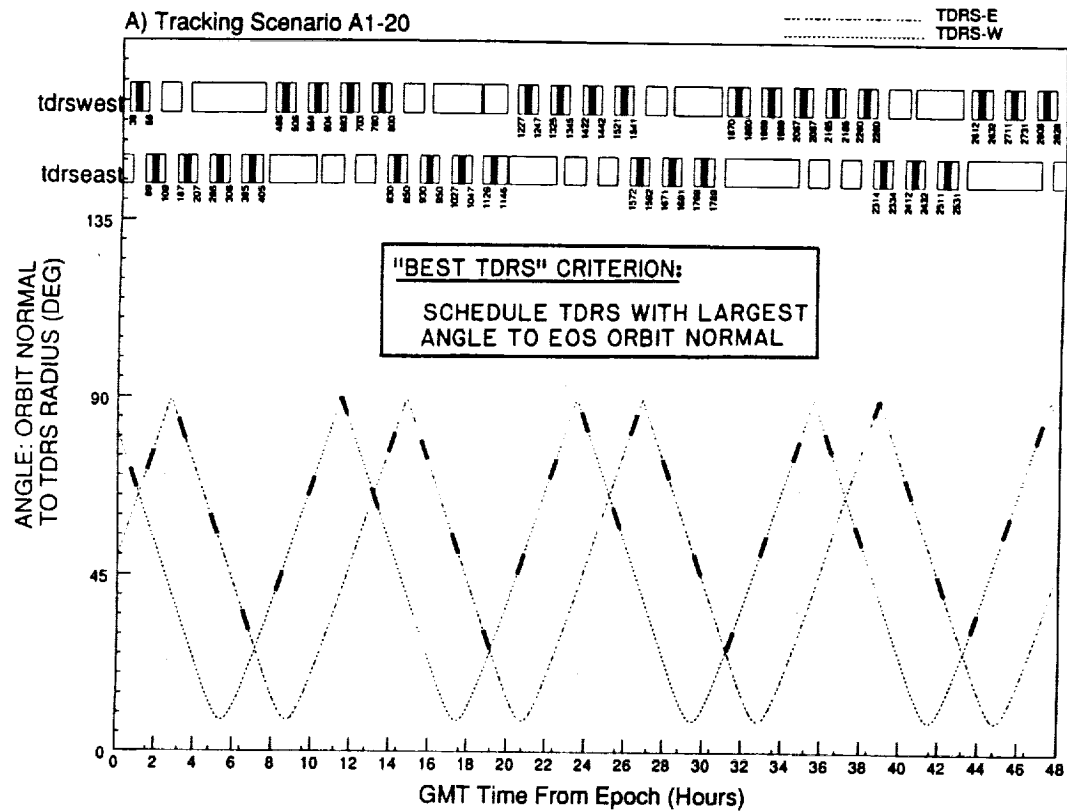


Figure 2: Sample Tracking Scenarios and Angle Between EOS Orbit Normal and TDRS Radius

Table 1
EOS Tracking Scenarios With TONS

TONS Mode	Tracking Scenario	Tracking Contacts	TDRS Scheduling Criteria
TONS-I	A1-20	One Pass/Orbit (20 Mins)	Best Geometry
	A1-10	" (10 Mins)	" "
	A1-5	" (5 Mins)	" "
	C1-20	One Pass/Orbit (20 Mins)	Arbitrary Geometry
	C2-20	Same Except Two Omitted Each Day	" "
	C3-20	One Pass/Orbit (20 Mins)	Arbitrary Geometry, East Only
TONS-II	B1	" "	Arbitrary Geometry, West Only
		C1-20+	One Pass/Orbit (20 Mins)+ Selected 5 Min Contacts
		C2-20+	Same Except Two 20 Min Contacts Omitted Each Day
			Same
TONS-II	B1	Continuous Tracking (Except in ZOE)	Best Geometry

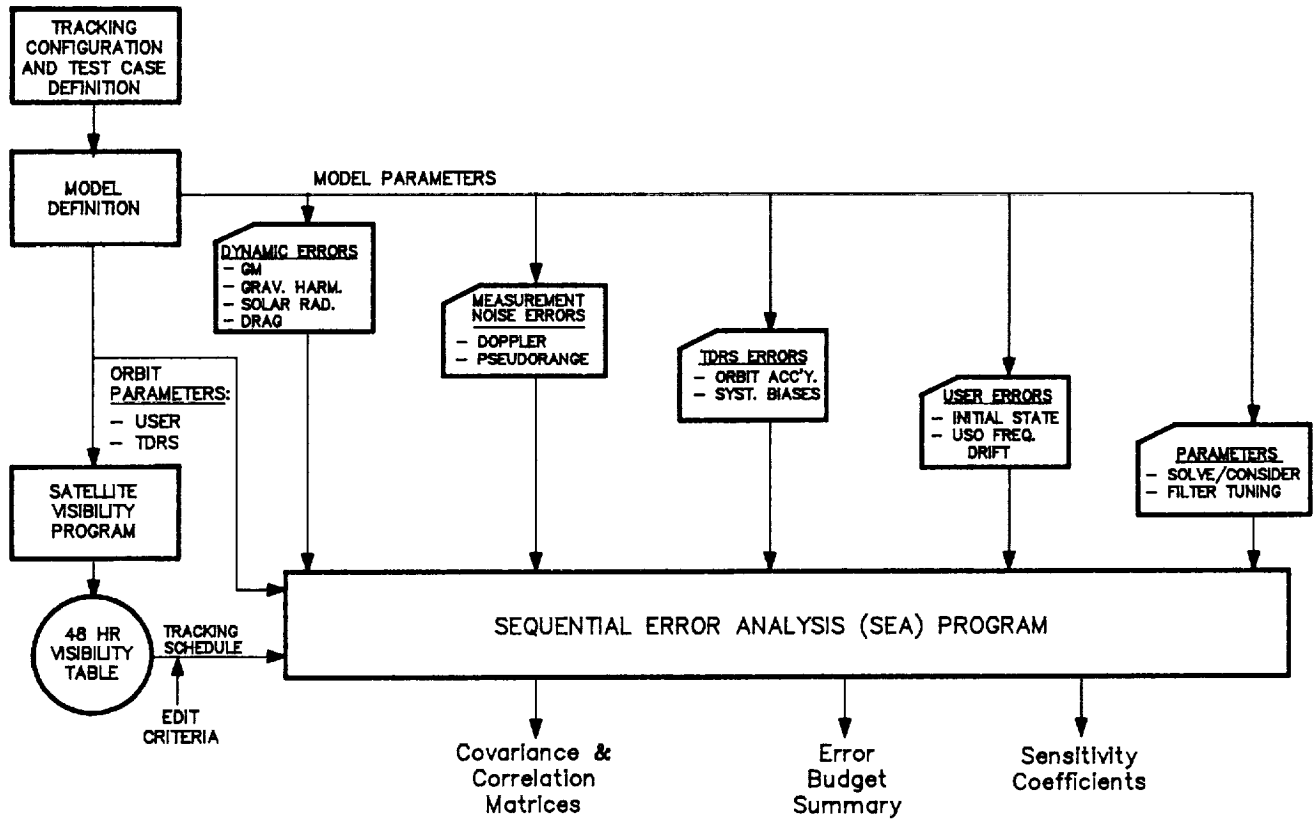


Figure 3: Navigation Performance Evaluation – Overview

The error due to atmospheric drag is modeled as an uncertainty in the drag coefficient, C_D . Although C_D would likely be an estimated parameter, a residual effect is assumed to remain and is treated as a consider parameter with 1σ uncertainty equal to 10% of the assumed nominal value ($C_{D_0} = 2.2$). (While this is extremely conservative, further scrutiny would not be needed unless drag becomes dominant) The impact of this error is directly proportional to the atmospheric density (ρ) and spacecraft area-to-mass ratio (A/m). Computations for ρ were based on a Harris-Priester atmospheric density model and elevated solar flux levels in the range of $225\text{-}325 \times 10^{-22}$ watts/ M^2 /Hz to assess worst case conditions. The A/m algorithm listed in Table 2 was provided by the EOS Project.

Assumed uncertainties in the gravitational constant (GM) and solar pressure coefficient (C_R) are conservative (i.e., high). Since their impact tends to be relatively small, more refined values are unnecessary.

3.1.2 Measurement Processing Errors

Errors in updating the estimated parameters with each new measurement arise from errors in the tracking data and errors in modeling the measurements.

Errors in the tracking data were characterized in terms of equivalent range and range-rate noise uncertainties and system biases. Random measurement error values listed in Table 2 are representative of scheduled (SSA/MA) services using the EOS high gain antenna for TONS-I and the proposed ATDRSS S-band navigation beacon service using an omni-antenna for TONS-II. Although lower random errors would apply if the HGA is available for TONS-II, the more conservative assumption was made for analysis.

The 1σ pseudorange bias values represent the composite of a residual, uniformly distributed $\pm 10\text{m}$ bias attributed to the ground stations, ATDRS and user components. This is also a conservative assumption based on ATDRSS specifications, [9] although it is not particularly significant for OD accuracy, since it primarily affects TD accuracy. The range-rate bias error of 0.1 mm/sec (1σ) was included primarily to observe potential sensitivity, but in any case, it should be absorbed in the reference oscillator bias estimate.

Frequency drift in the EOS reference oscillator appears as a range-rate error which affects Doppler measurement accuracy and as a clock bias acceleration error \ddot{B} which affects pseudoranging accuracy. Oscillator drift was defined as a systematic error with a 1σ uncertainty of 10^{-10} parts per day, a level which is consistent with USO performance specified for the TONS and COBE navigation experiments.[4,15] This value is also conservative, since \ddot{B} can be calibrated to a few parts in 10^{11} per day or better and virtually modeled out based on long-term trending of the frequency bias estimates and/or observation residuals analysis.

Uncertainties in the TDRS orbit contribute directly to the measurement modeling error. The 1σ orbit error assumed in Table 2 for TONS-I is representative of current TDRS tracking accuracy. The 1σ error for TONS-II is consistent with the ATDRS tracking goals [8] and the results of recent studies on tracking improvements.[16,17]

Table 2
Key Tracking Model Parameters for EOS Covariance Analysis

Parameter		1 σ Errors	
		TONS I	TONS II
Estimated	EOS $\left\{ \begin{array}{l} H, C, L \\ \dot{H}, \dot{C}, \dot{L} \end{array} \right.$ (A Priori)	1000 m	1000 m
	Orbit	1 m/sec	1 m/sec
	EOS $\left\{ \begin{array}{l} B \\ \dot{B} \end{array} \right.$ (A Priori)	N/A	1 msec
	Clock	2×10^{-7} parts	2×10^{-7} parts
Unestimated Systematic Errors (Consider Parameters)	Atomospheric Drag (ΔC_D) *	10%	10%
	Grav. Constant (GM)	0.1 ppm	0.1 ppm
	Grav. Harmonics (30 x 30)	GEM-T1 Uncertainties	GEM-T1 Uncertainties
	Solar Radiation (C_R)	10%	10%
	Systems Biases $\left\{ \begin{array}{l} R \\ \dot{R} \end{array} \right.$	N/A 0.1 mm/sec	10 M 0.1 mm/sec
	TDRS Orbit	50 m	25 m
	USO Drift \ddot{B}	10^{-10} ppd	10^{-10} ppd
Random Measurement Errors	Range σ_R	N/A	5 m
	Range Rate $\sigma_{\dot{R}}$	2 mm/sec	5 mm/sec
Other Tracking Parameters	Parameter	Value	
	- Filter Tuning:		
	--User Vel. Process Noise	$10^{-9} \text{ m}^2/\text{sec}^3$	
	--Clock Rate Process Noise	$10^{-6} \text{ nsec}^2/\text{sec}^3$	
	- Tracking Contacts	See Scenarios in Table 1	
	- Data Rate	One/10 sec	
* Drag Coefficient (C_D) is assumed to be estimated (by the user navigation algorithm) with a residual error (ΔC_D) treated here as a consider parameter. (Nominal $C_D = 2.2$, Area/Mass = $.001 + .0163 \sin \theta $, (in m^2/Kg) where θ = spacecraft true anomaly from descending node)			

4/8/91 MIS97X\BE5242

3.1.3 Filter Tuning Parameters

Filter tuning refers to adjustment of the Kalman filter gains to control the weight given to prior estimates. The objective is to achieve some balance between uncertainties introduced by new measurements and those caused by propagating prior estimates with an imperfect dynamical model. The filter process noise variance rates listed in Table 2 were used throughout the analysis and found to give reasonable results. No attempt was made to evaluate the use of dynamic tuning techniques which attempt to continually optimize parameters (e.g., in response to measurement residual levels or modeled phenomena).

3.2 OD PERFORMANCE RESULTS

EOS navigation performance based on TONS-I or TONS-II capabilities was evaluated for each of the tracking scenarios defined in Table 1 and for both moderate and high atmospheric density levels. Altogether, 20 cases were considered (see Table 3), and for each the errors in an EOS platform's position, clock bias, and clock drift (or frequency bias for TONS-I) were computed over 48 hours. A sample of the position error profiles for two cases provided in Figure 4 shows the 1σ errors due to individual error contributors and the 1σ total (RSS) error.

A summary of the OD performance is given for each case in Table 3 in terms of 1σ errors (peak total and mean total).^{*} Mean errors in all cases and even peak errors in all but three cases are within the current EOS position accuracy requirement of 33 meters (1σ).^{**} Results for tracking scenario B indicate that TONS-II could also support the EOS position accuracy goal of 17 meters (1σ). With respect to error sources, the sample plots in Figure 4 show that gravity modeling error is the predominant contributor. Effects of drag model uncertainty are not as significant but do increase during intervals with missed or poor geometry contacts. However, this sensitivity (as indicated by the results for tracking scenarios C1-20 and C2-20) is readily mitigated with a few supplemental (5-minute) tracking contacts (as indicated by the results for scenarios C1-20+ and C2-20+).

3.3 TD/FD PERFORMANCE RESULTS

In addition to EOS orbit determination both TONS-I and II will enable transponder reference frequency determination (FD) by estimating the USO frequency bias. With the availability of pseudorange data via ATDRSS beacon tracking, TONS-II could support EOS time determination by estimating the onboard clock bias. The covariance analysis also provided an evaluation of EOS time and frequency determination (TD/FD) performance. Table 3 lists the mean 1σ FD errors over 48 hours for each case considered (after settling of initial transients). These results are clearly well below the current operational requirements for transponder reference frequency uncertainty (± 700 Hz). Evaluation of potential TD performance with TONS-II (tracking scenario B) indicates 1σ clock bias errors of 100 - 120 nsec (after settling of initial transients).

* The errors listed in Table 3 are the maximum and average over 48 hours (after settling of initial transients) of the 1σ total position errors.

** The current EOS position accuracy requirement of 100m (3σ) and the goal of 50m (3σ) have each been divided by 3 for performance comparison purposes.

Table 3

04/11/91 MIS87X\BF4344

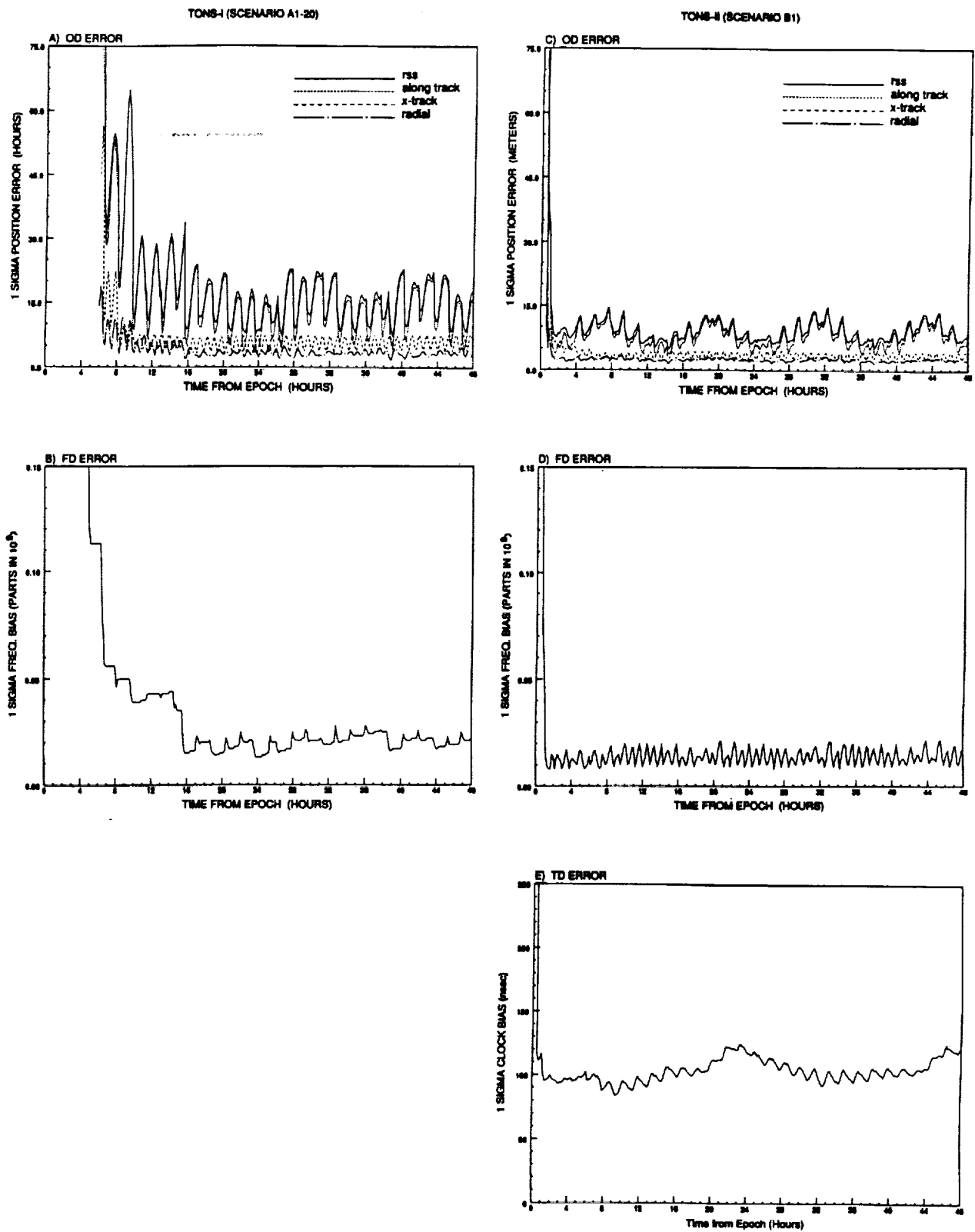


Figure 4: Sample EOS OD/FD/TD Errors for TONS-I & TONS-II (from Covariance Analysis)

Prior to the availability of a TONS-II capability for autonomous onboard updating of the EOS time reference, conventional TDRSS two-way ranging operations utilizing the USCCS could be employed. Clock corrections would be determined and uplinked to the EOS time management system at a rate dependent upon the time maintenance requirement (T_{MAX}), the USCCS accuracy ($\sim 1 \mu\text{sec}$), and the time reference oscillator (TRO) stability. For example, with a TRO long-term stability of 10^{-10} parts per day clock updates would be required about every two days for $T_{MAX} = 10 \mu\text{sec}$ (or ~ 22 days for $T_{MAX} = 100 \mu\text{sec}$). Current EOS specifications [2] relax the time maintenance requirement to $100 \mu\text{sec}$ when updated by ground-based operations, a sacrifice in capability to reduce the ground support impact.

Although a tradeoff between TRO stability and T_{MAX} relaxation might be considered, another alternative is to utilize TONS-I FD capabilities to reduce the frequency of USCCS operations. This approach is based on calibrating the clock drift, assuming that the TRO and transponder reference (USO) frequencies can be derived from a common source. Future TDRSS transponders will likely be configured to accept a standard external reference frequency (e.g., 5 or 10 MHz vs the current 19.056392 MHz). Figure 5a indicates the relevant onboard elements and data interfaces.

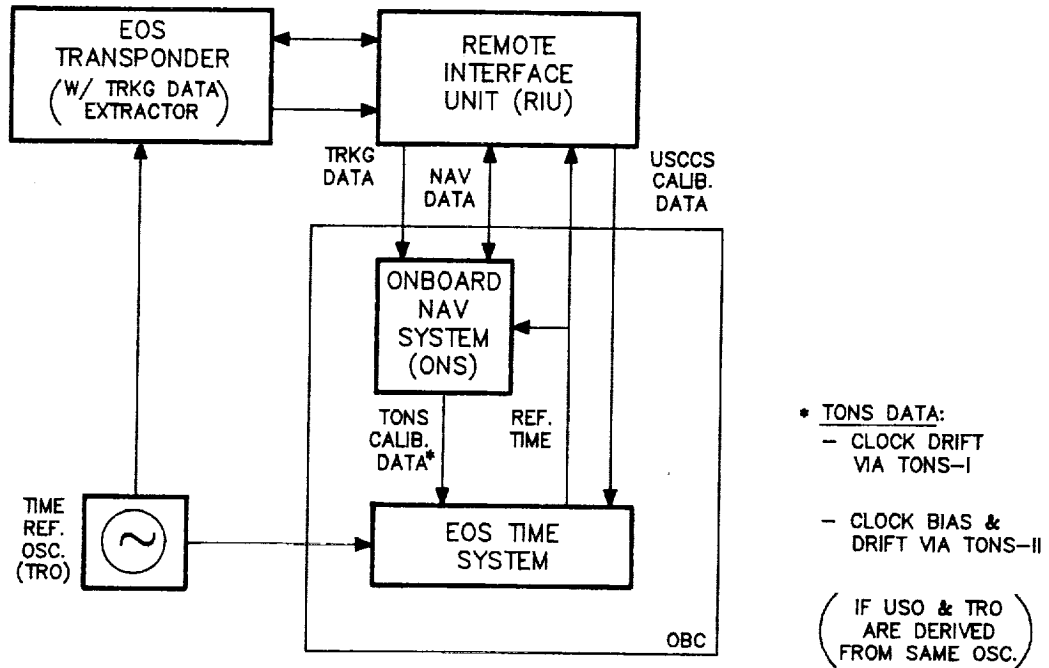
The Onboard Navigation System (ONS) would provide a mean offset ($\overline{\Delta f}$) in the reference oscillator frequency (f_o) over an appropriate averaging interval (T_{AVG}), and the time management system would compute a corresponding incremental clock correction, $(\overline{\Delta f}/f_o)T_{AVG}$. Figure 5b illustrates hypothetical clock drift profiles with and without FD correction data twice per day. Given the FD performance stated in Table 3 and $T_{AVG} = 0.5$ day, the corresponding 1σ uncertainty in the clock updates would be $\leq 1.5 \mu\text{sec}$. This level of incremental correction accuracy would be sufficient to support the $10 \mu\text{sec}$ maintenance requirement with occasional USCCS updates for absolute recalibration. Alternatively, clock corrections derived from long-term ground-based modeling (similar to the COBE/USO characterization [18]) could provide even tighter time maintenance accuracy and longer intervals between USCCS updates. With the eventual availability of TONS-II, however, continuous estimation of both clock bias and drift would enable time maintenance at the sub-microsecond level.

4.0 SIMULATION ANALYSIS OF EOS NAVIGATION PERFORMANCE

To complement the covariance analysis approach in evaluating TONS for supporting EOS navigation it was decided to assess particular performance sensitivity concerns through simulation and to compare estimated parameters against reference or truth data. An upgraded version of GSFC's R&D GTDS program, known as the Navigation Processing System (NPS) [19, 20] was used for all major simulation functions: ephemeris generation, data simulation, (Kalman) filter processing, and ephemeris comparisons. An overview of the simulation elements used for EOS OD/FD performance evaluation is shown in Figure 6. Truth orbits for an EOS platform and two TDRSSs were generated and used in conjunction with a USO model and particular tracking scenarios (as defined in Table 1) to produce simulated TDRSS one-way forward Doppler data.*

* Pseudorange tracking data generation and processing capabilities were not available in the current NPS program, but OD/FD performance evaluations for TONS-II were not significantly affected, since Doppler tracking data is the most effective aid to OD/FD. The need for pseudorange data is primarily for the time-determination function (which was not simulated).

A) ONBOARD CONFIGURATION



B) EXAMPLE OF EOS CLOCK DRIFT COMPENSATION VIA TONS-I

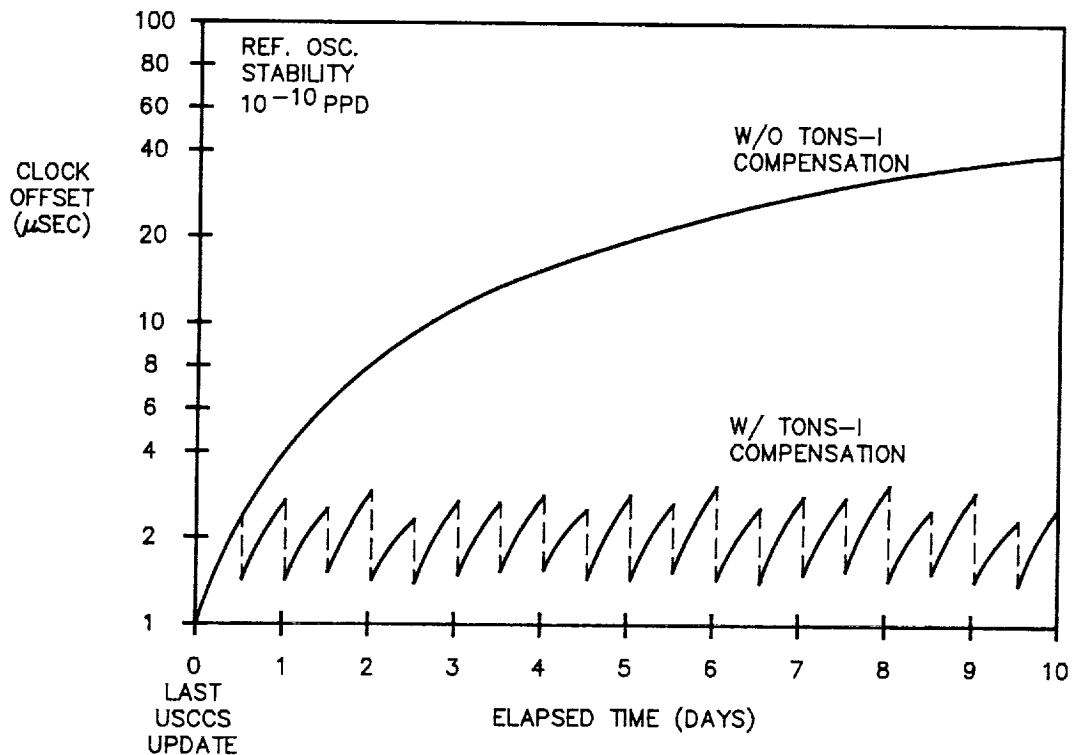


Figure 5: TONS Utilization for EOS Time Maintenance Support

Table 4
Key Tracking Model Parameters for Simulation Analysis

Parameters	Truth (DATASIM)	Model (FILTER)
USO Bias (parts)	1×10^{-12}	$1 \times 10^{-7}^*$
" Drift (ppd)	1×10^{-10}	$3 \times 10^{-10}^*$
Drag Model (ρ_1) **	0	50% *
Grav. Harmonics	GEM-T2 (50 x 50)	GEM-T1 (21 x 21)
TDRS Ephemeris {	41° W	GEM-9 + PRIORI (2 x 0) offset +
	171° W	GEM-9 + PRIORI (4 x 4) offset +

* A Priori Values at Epoch

** Drag error modeled in terms of Scalar offset to drag coefficient $C_D = C_{D0} (1 + \rho_1)$.
(See footnote to Table 2 for other related parameters).

+ To produce nominal (≤ 50 m) or 3 X nominal (≤ 150 m) TDRS ephemeris errors

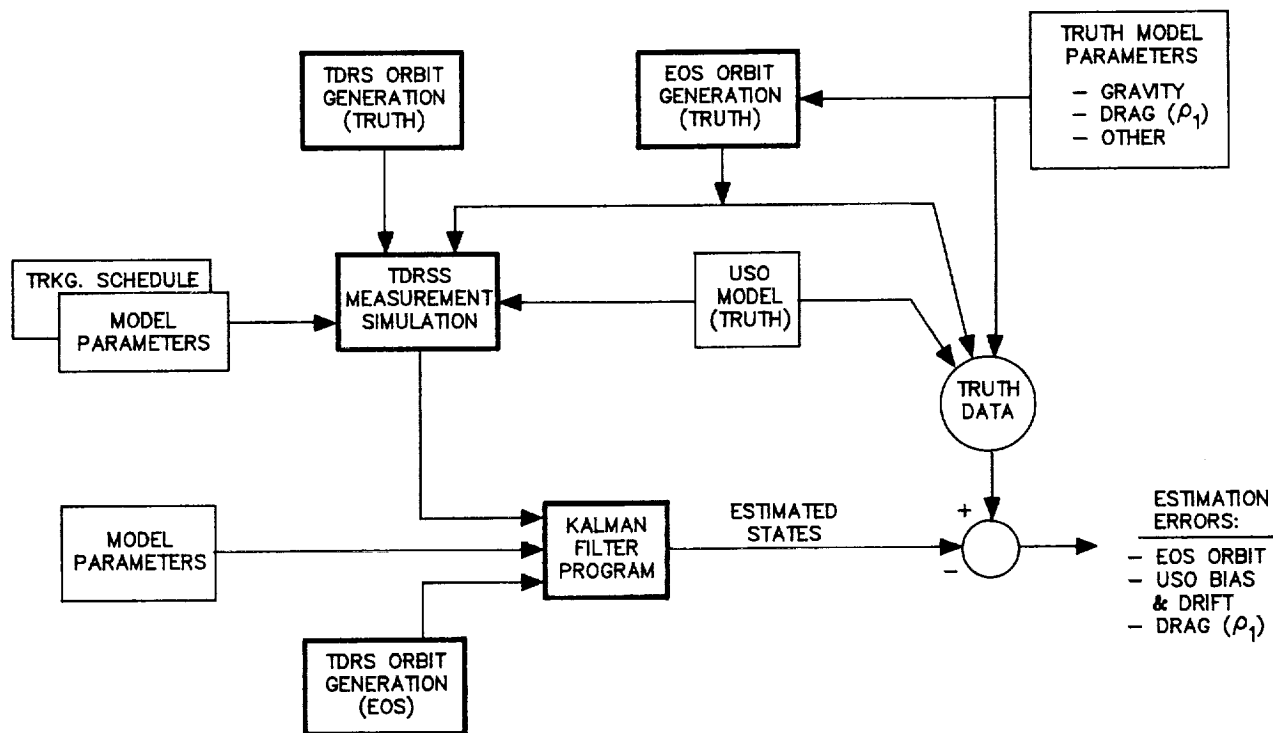


Figure 6: Overview of Navigation Performance Simulation

Processing of the simulated tracking data is performed by an EKF program which, analogous to user navigation software, is provided with TDRS orbit data (nontruth) and various tracking model parameters. The estimated parameters comprise EOS position and velocity states, USO bias and drift states and a drag model parameter (p_1). Error profiles for performance evaluations were derived by comparing truth and estimated parameter data over a specified time interval.

Three particular issues (missed or poor geometry tracking contacts, TDRSS/ATDRSS ephemeris uncertainty, and drag estimation capability) were selected for analysis. The following subsections discuss the assumed tracking model parameters and the performance results.

4.1 TRACKING MODEL PARAMETERS

Initial errors in the EOS orbit were set at the same levels assumed in Table 2 for the covariance analysis. Table 4 lists the a priori offsets in the USO bias and drift parameters assumed to be estimated. The initial offset for p_1 was set arbitrarily at 0.5° with the objective of observing estimation convergence characteristics relative to the 10% residual error assumption made for C_D as a consider parameter in the covariance analysis (see Table 2).

For this analysis, only errors in significant unestimated parameters were assumed, specifically errors in gravity harmonics modeling and user (EOS) knowledge of TDRS orbits. For TDRS orbit error modeling, a non-truth orbit was derived by reducing the assumed gravity model (4x4 to 2x0) and/or offsetting the epoch state vector as noted in Table 4. These model parameters were selected to reflect expected TDRS (or ATDRS) tracking performance for TONS-I (or II) assuming upgraded BRTS (or APLS) capabilities ($\leq 75\text{m} - 3\sigma$).^[17] An off-nominal error model with degraded TDRS accuracy ($\leq 150\text{m} - 3\sigma$) was used to assess sensitivity in a TONS-I application prior to a BRTS upgrade or APLS implementation.

Numerical values for other modeled parameters, measurement noise and bias, and drag model parameters (platform A/m, solar flux level, etc.) were set at the same levels used in the covariance analysis. Filter tuning was adjusted (via velocity state noise level) to accommodate cases with degraded TDRS ephemeris accuracy.

4.2 PERFORMANCE RESULTS

EOS navigation processing was simulated for four tracking scenarios assuming the nominal modeling parameters stated in Table 4. These were repeated for off-nominal TDRS/ATDRS tracking errors to assess performance sensitivities. Altogether, eight cases were considered (see Table 5) and for each case the errors in platform position, velocity, and USO frequency bias were computed over 48 hours. Sample plots of the position error profiles (truth-estimated position vs time) are provided in Figure 7.

A summary of the OD performance results is given in Table 5 in terms of the peak and RMS errors (after settling of initial transients). The data indicate reasonable overall agreement between the OD errors computed for corresponding covariance and simulation analysis cases based on TONS-I and TONS-II. However, the contributions of TDRS ephemeris error at the levels assumed for simulation are clearly dominant over those due to the gravity modeling error. Determining potential sensitivity to missed or poor geometry tracking contacts and/or degraded TDRS orbit information was the intent in comparing performance between the selected TONS-I scenarios: A1-20, C1-20 and C1-20+. As indicated by the results in Table 5, however, there is no clear distinction since each

* This equates to an initial offset of 50% from the truth model where $p_1 = 0$ (i.e., $C_D = (C_{D_0})$). See footnote in Table 5 for parameter definitions.

Table 5
EOS OD Performance Using TONS (Simulation Analysis)

TONS Mode	Tracking Scenario	TDRS/ATDRS Ephem Error	OD Error (m)		RMS Drag (ρ_1) Error
			RMS	Peak	
I	A1-20	Nominal*	16	56	.11
	C1-20		14	45	.13
	C1-20 ⁺		14	47	.10
	A1-20	3x Nominal	19	65	.11
	C1-20		17	74	.15
	C1-20 ⁺		19	63	.08
II	B1	Nominal**	8	24	.09
	"	3x Nominal	12	29	.11

*Nominal Position Error ≤ 50 m (1σ) **Nominal Position Error ≤ 25 m (1σ)

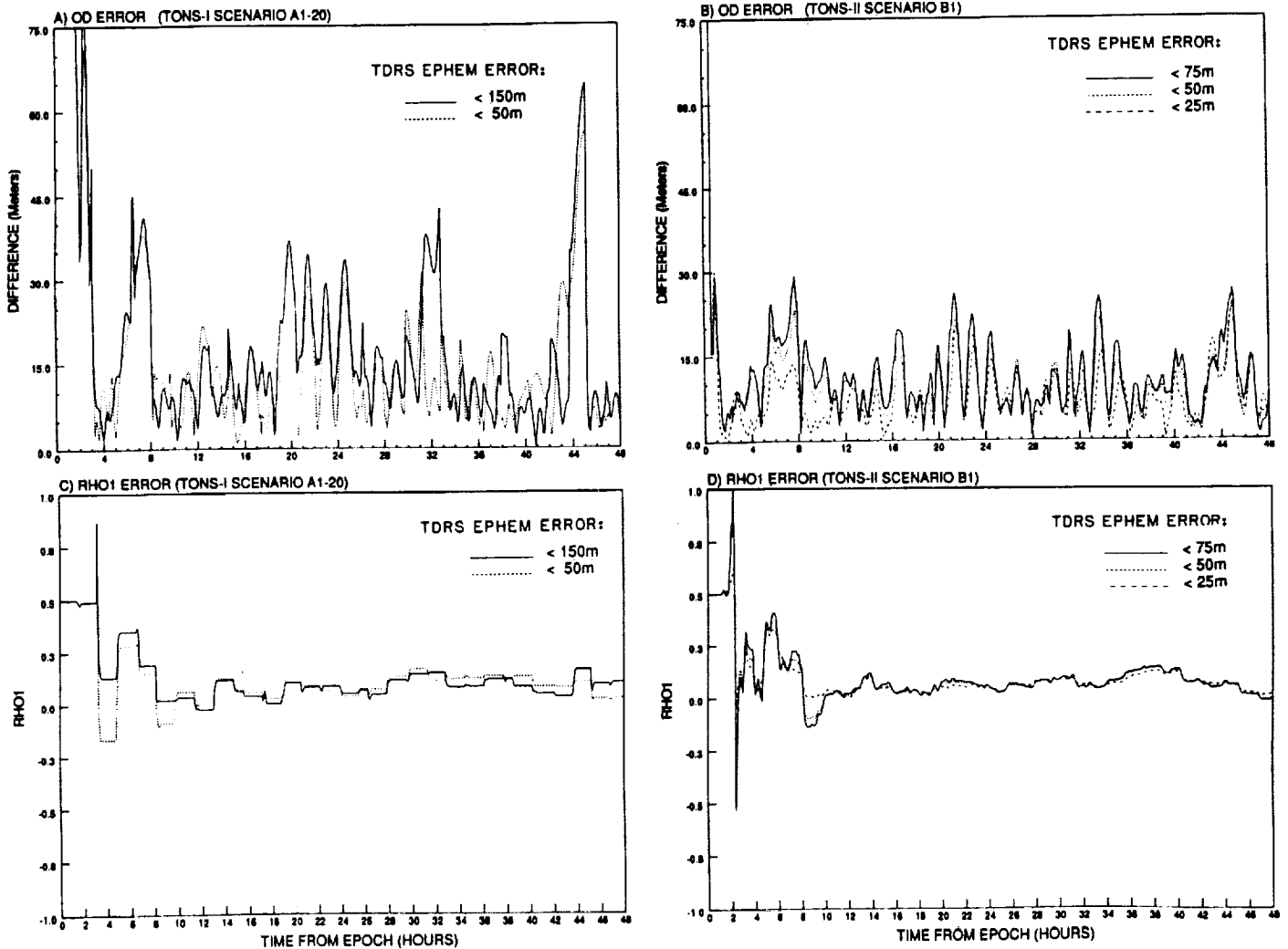


Figure 7: Sample EOS Position and Drag (ρ_1) Estimation Error Profiles

is subject to occasional peak errors under the postulated circumstances. Although the baseline OD requirement (100 m) can be supported, less sensitivity is achievable with more distributed tracking which also alternates between TDRSs (or ATDRSs) as in scenario B1.

With respect to atmospheric drag estimation capability, sample plots of the solutions for drag coefficient offset (ρ_1) from an initial value of 50% are given in Figure 7 for scenarios A1 and B1. Solutions are shown for nominal and above nominal TDRS ephemeris modeling errors. As the results in Table 5 indicate, solutions for ρ_1 indicate generally good convergence toward the assumed truth value of zero. Offsets are typically on the order of 0.1 or less (which is consistent with the 10% C_D error assumption used in the covariance analysis). Further analysis of the OD performance indicates that the peaks in ephemeris errors are also correlated with intervals requiring extended orbit propagation when the drag model was degraded (i.e., ρ_1 not converged). In practice, ρ_1 typically would not converge to zero, because of mismodeling in other drag model parameters and aliasing effects in the estimation process due to other mismodeling (e.g., TDRS/ATDRS ephemeris).

5.0 CONCLUSIONS

The covariance and simulation results for EOS navigation based on TONS indicate that:

- EOS position accuracy is within 25m (1σ) using TONS-I with a nominal scheduled tracking contact of 20 minutes/orbit and 14m (1σ) using TONS-II with unscheduled, near continuous beacon tracking.
 - The current EOS position accuracy requirement, 33m (1σ), could be met by both TONS-I and TONS-II.*
 - The proposed EOS position accuracy goal, 17m (1σ), could also be met by TONS-II (and by TONS-I if more intensive scheduled tracking is provided).
- TONS-I with scheduled service (e.g., 20 min/orbit) is more sensitive to occasional missed, unavailable, or poor geometry contacts than is TONS-II with unscheduled beacon service (near continuous).
- The TONS-II TD capability, 0.1 μ sec (1σ), could easily support EOS time reference maintenance requirements ($\pm 10 \mu$ sec relative to UTC).
- Both TONS-I and TONS-II provide a transponder reference frequency determination (USO FD) capability of better than 0.35×10^{-10} parts (1σ), equivalent to 0.1 Hz (1σ) at S-band.
- TONS-I FD capabilities could support maintenance of the EOS time standard if its frequency reference (TRO) and the transponder reference (USO) are derived from a common source. (Incremental corrections to the time standard based on USO FD would lengthen the time between required timing calibrations with the USCCS.

* The current EOS position accuracy requirement of 100m (3σ) and the goal of 50m (3σ) have each been divided by 3 for direct comparison with covariance analysis results.

REFERENCES

- [1] "Earth Observing System (EOS) Mission-Platform Sizing Study," NASA/GSFC EOS Project Office, EOS-TR-420-03-08, May 1990.
- [2] "EOS-A Platform Control End Item (CEI) Specification," SEP-101, Prepared by GE/ASTRO-Space Division, 26 April 1990.
- [3] "Project Element Requirements Document (PERD) for Platforms," SS-GSFC-0050 (Rev. B), NASA/GSFC EOS Platforms Project, 5 January 1990.
- [4] "TDRSS Onboard Navigation System (TONS) Experiment Plan," Stanford Telecom, TR890104, Report to NASA/GSFC under NAS 5-31500, July 1989.
- [5] C. J. Gramling et al., "TDRSS Onboard Navigation System (TONS) Experiment for the Explorer Platform," Paper No. 90-3365, AIAA Guidance, Navigation and Control Conference, Portland, OR, 21-23 August 1990.
- [6] M. E. Ambrose, "User Spacecraft Clock Calibration System (USCCS) - Characterization Test Results," NASA/GSFC Code 533 Memorandum, 16 November 1988.
- [7] "Phase II Requirements Specification for the Second TDRSS Ground Terminal (STGT) - MA Beacon Demonstration Capability," CCR # 530/439, NASA/GSFC, 7 November 1989.
- [8] "Phase B Advanced Tracking and Data Relay Satellite System (ATDRSS) Service Requirements Specification," S-500-1, NASA/GSFC, 20 November 1989.
- [9] C. Engel, et.al, "Autonomous Onboard Navigation Using TDRSS Signals," Orbital Mechanics and Mission Design, Vol. 69, Advances in the Astronautical Sciences, AAS Publication, 1989.
- [10] B. D. Elrod and A. K. Kapoor, "Earth Observing System (EOS) - Analysis of Navigation Performance Using TONS," FDD/554-90/175, Prepared for NASA/GSFC by Stanford Telecom, November 1990.
- [11] "Sequential Orbit Determination Error Analysis Program (SEA) Programmer's Reference and User's Guide, Vols. I and II (Rev. 1), Computer Sciences Corp., CSC/SD-84/6057, December 1984.
- [12] "Enhancement and Upgrade Supplement to Sequential Orbit Determination Error Analysis Program (SEA) Programmer's Reference and User's Guide," Computer Sciences Corp., CSC/SD-86/6728 UD1, December 1986.
- [13] J. G. Marsh et al., "An Improved Model of the Earth's Gravitational Field: GEM-T1," NASA Technical Memorandum 4019, March 1988.

- [14] F. J. Lerch et al., "An Improved Error Assessment for the GEM-T1 Gravitational Model," NASA/GSFC Technical Memorandum 100713, November 1988.
- [15] "COBE Navigation Experiment Plan," Stanford Telecommunications, Inc., TR850109, Report to NASA/GSFC under NAS 5-27732, October 1985.
- [16] "Error Analysis for the Advanced Tracking and Data Relay System Using a K-band TT&C Station With Remote Bilateral Ranging Transponders," CSC/TM-89/6131, Computer Sciences Corp. Report to NASA/GSFC under NAS 5-31500, September 1989.
- [17] "Assessment of Candidate ATDRS Tracking Techniques," Stanford Telecom, TR91002, Report to NASA/GSFC under NAS 5-30030, April 1991.
- [18] J. B. Dunham et al., "One-Way Return Link Doppler Navigation with TDRSS: The Ultra-Stable Oscillator (USO) Experiment on the Cosmic Background Explorer (COBE)," Paper No. 90-2902, AIAA Guidance, Navigation and Control Conference, Portland, OR, 21-23 August 1990.
- [19] D. F. Eggert, "Navigation Processing System (NPS) for TONS Analysis Support," Stanford Telecom, TR90027, July 1990.
- [20] "TDRSS Onboard Navigation System (TONS) Experiment - Navigation Processing System (NPS) User's Reference," (1st draft), Prepared by Computer Sciences Corp. for NASA/GSFC under NAS 5-31500, August 1990.

Flight Dynamics Facility Operational Orbit Determination Support for the Ocean Topography Experiment*

**D. T. Bolvin, A. F. Schanzle, and M. V. Samii
COMPUTER SCIENCES CORPORATION (CSC)**

**C. E. Doll
GODDARD SPACE FLIGHT CENTER (GSFC)**

ABSTRACT

The Ocean Topography Experiment (TOPEX/POSEIDON) mission is designed to determine the topography of Earth's sea surface across a 3-year period, beginning with launch in June 1992. TOPEX/POSEIDON is a joint venture between the French Centre Nationale d'Etudes Spatiales (CNES) and the United States National Aeronautics and Space Administration (NASA). The Jet Propulsion Laboratory (JPL) has been designated as NASA's TOPEX project center. However, the Goddard Space Flight Center (GSFC) Dynamics Facility (FDF) has the capability to operationally receive and process Tracking and Data Relay Satellite System (TDRSS) tracking data. Because these data will nominally be used to support the day-to-day orbit determination (OD) aspects of the TOPEX mission, the GSFC FDF has been designated to perform TOPEX operational OD.

The scientific data, by their nature, require stringent OD accuracy in navigating the TOPEX spacecraft. The OD accuracy requirements fall into two categories: (1) on-orbit free-flight and (2) maneuver. The maneuver OD accuracy requirements are of two types: (a) premaneuver planning and (b) postmaneuver evaluation. Analysis using the Orbit Determination Error Analysis System (ODEAS) covariance software has shown that, during the first postlaunch mission phase (Assessment Phase) of the TOPEX mission, some postmaneuver evaluation OD accuracy requirements cannot be met.

ODEAS results also show that the most difficult requirements to meet are those that determine the change in the components of velocity for postmaneuver evaluation. Additional ODEAS analysis is currently in progress to determine whether the postmaneuver evaluation requirements can be met by considering only those changes in velocity caused by changes in orbital elements that will result from a maneuver.

* This work was performed for the National Aeronautics and Space Administration (NASA)/Goddard Space Flight Center (GSFC), Greenbelt, Maryland, Contract NAS 5-31500.

1. INTRODUCTION

1.1 MISSION OVERVIEW

The Ocean Topography Experiment (TOPEX)/POSEIDON mission is a collaborative research effort of the United States National Aeronautics and Space Administration (NASA) and the French Centre Nationale d'Etudes Spatiales (CNES) and is designed to study the topography of the Earth's oceans over a period of 3 years. The information in this paper was derived primarily from Reference 1. Exceptions are noted throughout the paper.

Although, technically speaking, TOPEX refers to the NASA payload and POSEIDON refers to the CNES payload, use of the term TOPEX throughout this paper will imply both the TOPEX and POSEIDON payloads, unless otherwise stated. The TOPEX satellite, which is being built by Fairchild Space Systems Division (FSSD), is scheduled for a June 1992 launch by an Ariane 42P expendable launch vehicle from Kourou, French Guyana.

The overall goal of the TOPEX mission is to measure the height of the Earth's oceans, using radar altimetry, to increase knowledge of oceanic circulation and provide for improved models of ocean dynamics. Detailed mission goals include the following (see Reference 2 for more details):

- Measure the sea level to allow the study of ocean dynamics, including the calculation of the mean and variable surface geostrophic currents and the tides of the world's oceans
- Process and verify the scientific data and distribute them in a timely manner, together with other geophysical data, to the principal investigators
- Lay the foundation for a continuing program to provide long-term observations of the oceanic circulation and its variability

The TOPEX spacecraft will not be launched directly into its operational orbit; rather, it will be injected into a biased orbit and then, through a series of maneuvers, placed into operational orbit. The currently planned operational orbit requires a 10-day repeatable ground track to an accuracy of ± 1 kilometer (km), with a 66.018 degree (deg) inclination, a semimajor axis of 7,714.408 km and an eccentricity of 0.00008.

The TOPEX spacecraft attitude is three-axis stabilized, Earth-pointing, and it rotates one revolution per orbit. In addition, the single solar array panel pitches to maintain its position with respect to the Sun.

During normal operations, the Tracking and Data Relay Satellite System (TDRSS) will be used for commanding, telemetry, and tracking functions. The Deep Space Network (DSN) 26-meter subnet will be used to support these functions during the TOPEX launch and during spacecraft emergency or contingency situations. A spacecraft emergency is an event in which the loss of the mission or spacecraft is possible. A spacecraft contingency is an event in which the mission cannot be successfully completed using TDRSS services.

The mission is scheduled to last 3 years after launch, with a possible extension of 2 additional years. The mission's phases are launch, assessment, initial verification, observational, and extended observational. The definitions and activities of each phase are summarized in Table 1.

Table 1. Mission Phases and Activities

Phase/Definition	Activities
Launch Phase From shipment of spacecraft (S/C) to launch site to injection of S/C into biased orbit	Prelaunch testing at Kourou Injection into biased orbit Orientation of S/C and deployment of the solar panel
Assessment Phase First 30-35 days after injection into biased orbit, or until the S/C is placed in operational orbit	Check out S/C functions Turn on and check out sensors Move S/C to operational orbit Complete assessment within 35 days
Initial Verification Phase From end of assessment phase to 6 months after launch	Direct overflights of NASA and CNES verification sites Intensive analysis of sensor performance Verification within 6 months; finalized with a verification report Development of TOPEX geopotential model [by Precision Orbit Determination (POD) group, Code 600]
Observational Phase From end of initial verification phase to 3 years after launch	Continuous, routine collection of sensor data Process data with verified algorithms and precision orbits to end of mission Ground track maintenance maneuvers Distribution of sensor data to principal investigators
Extended Observational Phase From end of observational phase to 5 years after launch	Same as in the observational phase

6130G(24)-9

Because the orbit determination (OD) requirements for the three post-assessment phases—initial verification, observational, and extended observational—are the same, the term “observational phases” will be used to characterize the requirements for all mission phases beyond the assessment phase.

1.2 SPACECRAFT DESCRIPTION

Figure 1 illustrates the TOPEX/POSEIDON spacecraft's deployed configuration, showing the approximate location of some of the scientific instruments and support systems. The spacecraft consists of two modules: the TOPEX/POSEIDON Instrument Module (IM), which

contains the scientific instruments, and the Multimission Modular Spacecraft (MMS) bus, which includes the onboard attitude determination and control, communications, propulsion, and power subsystems. The spacecraft bus has a mass of about 2,650 kilograms (kg), an overall length of about 5.4 meters (m), and a diameter less than 3.8 m.

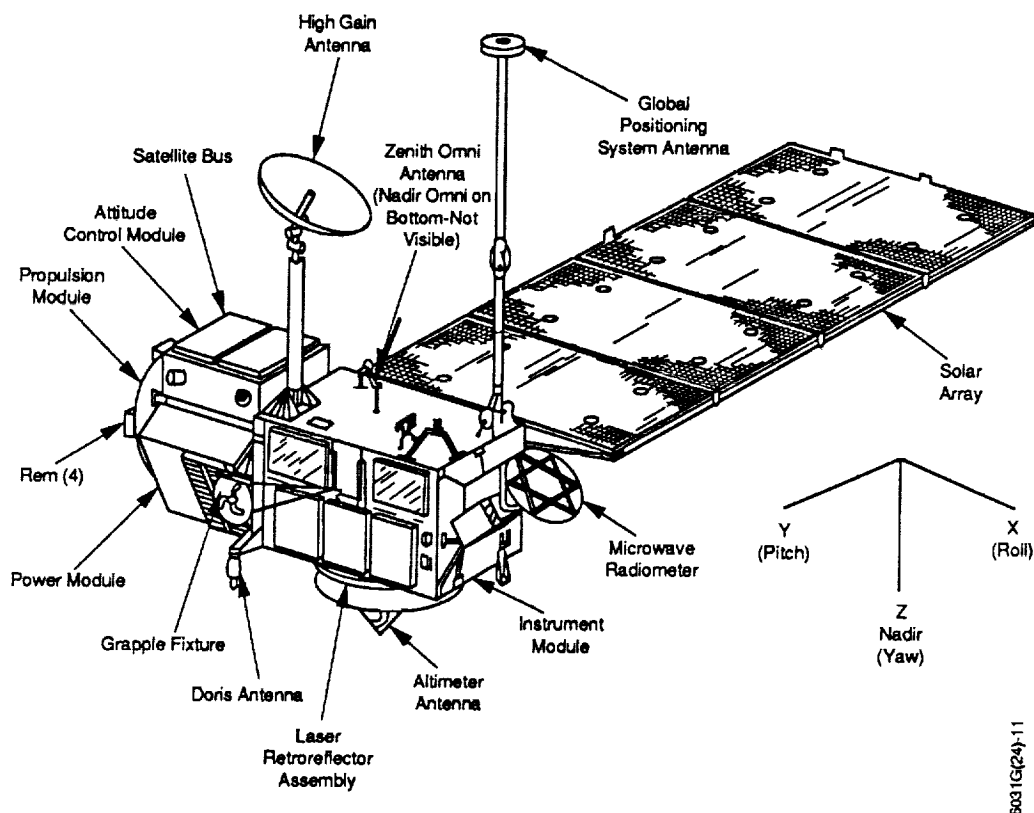


Figure 1. TOPEX Satellite Deployed Configuration

The IM is made up of the TOPEX (NASA) payload and the POSEIDON (CNES) payload. Table 2 describes the instruments in the TOPEX payload; Table 3 describes the instruments in the POSEIDON payload; and Table 4 describes each subsystem of the MMS bus.

2. OPERATIONAL SUPPORT OVERVIEW

2.1 JPL RESPONSIBILITIES

The Jet Propulsion Laboratory (JPL) has been designated as the NASA TOPEX project center and will be responsible for

- Mission operations planning, including maneuver planning
- Flight operations control, which will be performed by the TOPEX Project Operations Control Center (POCC)
- Processing and distribution of the scientific data.

Table 2. TOPEX Payload Description

Instrument	Purpose
Dual-frequency radar altimeter	Provide altimeter measurements (Ku-band) Provide ionospheric correction to the altimeter measurements (C-band)
Three-channel microwave radiometer	Provide wet tropospheric correction to the altimeter measurements
Laser Retroreflector Array (LRA)	Provide laser ranging data for height calibration and precision tracking
Global Positioning System Demonstration Receiver (GPSDR)	Provide experimental POD data
Frequency Reference Unit (FRU)	Provide a timing source for the GPSDR, TDRSS, and DSN

6130G(24)-7

Table 3. POSEIDON Payload Description

Instrument	Purpose
Solid-state experimental radar altimeter	Provide altimeter measurements (Ku-band)
Determination of Orbit Radiopositioning Integrated from Satellite (DORIS) dual-frequency Doppler tracking system receiver	Provide Doppler-based POD data

6031G(24)-8

Table 4. MMS Bus Description

Subsystem	Purpose
Radio frequency communications subsystem (RFCS)	Handles spacecraft radio frequency (RF) communications as well as ranging and Doppler functions
Command and data handling subsystem (CDHS)	Processes spacecraft commands and telemetry, including data recording and playback functions
Attitude determination and control subsystem (ADCS)	Maintains spacecraft attitude
Propulsion subsystem (PS)	Provides fuel and thrusters for attitude and orbit control
Signal conditioning and control unit (SC&CU)	Provides command/telemetry, heater control, and pyrotechnic control interface functions
Electrical power subsystem (EPS)	Derives raw power from the solar array mounted on the IM
Thermal control subsystem (TCS)	Monitors and controls the thermal properties of the spacecraft

6130G(24)-6

The TOPEX POCC will be the interface with the FDF for operationally navigating the TOPEX spacecraft.

2.2 GSFC/FDF RESPONSIBILITIES

The GSFC/FDF is a TOPEX support center whose primary responsibility will be to perform operational OD for TOPEX. This designation was made because the FDF has the capability to operationally receive and process TDRSS tracking data, which will nominally be used to support the TOPEX mission. TOPEX OD support includes performing definitive OD and performing orbit predictions for quality assurance, acquisition data generation, and scheduling purposes. The JPL POCC support will consist of using the FDF's OD solution to perform operational orbit predictions for mission planning. According to the current plan, JPL will perform all attitude-related support and all mission analysis and maneuver support (exclusive of OD).

FDF support activities for the various mission phases are described below:

- *Prelaunch:* Support during this period will consist of requirements analysis, system definition and specification, software development, software testing, interface testing, and mission simulation activities.
- *Launch:* The FDF support will consist of monitoring the Launch Trajectory Acquisition System (LTAS) data from the Ariane launch vehicle.

- *Assessment:* During this period, the FDF will provide pre- and postmaneuver OD support to move the spacecraft from the biased orbit to the operational orbit; it will also provide orbit product support.
- *Initial Verification:* During this period, the FDF will provide routine OD, generate orbit products, and support pre- and postmaneuver OD for periodic ground-track maneuvers necessary to maintain the operational orbit.
- *Observational and Extended Observational:* The FDF will support the same activities described in the initial verification phase.

3. ORBIT DETERMINATION ACCURACY REQUIREMENTS

3.1 MANEUVER SUPPORT REQUIREMENTS

Orbit maneuvers will take place in the assessment and the observational phases; however, the purpose of the maneuvers will be different. In the assessment phase, the TOPEX spacecraft will be moved from its biased orbit into its operational orbit through a series of maneuvers, spaced roughly 3 days apart, over a period of approximately 20 days. In the observational phases, maneuvers will be performed approximately every 30 days to maintain the 10-day repeat groundtrack cycle for the operational orbit.

Three different types of maneuvers—coarse, calibration, and precision—will support the TOPEX mission. Coarse maneuvers are high-thrust, performed only in the assessment phase and used to move the spacecraft from the biased orbit into the operational orbit. Here, high thrust means the change in the velocity resulting from the maneuver will be greater than 100 millimeters/second. Calibration maneuvers are equivalent to coarse maneuvers, except they will be used to calibrate the thrusters. Precision maneuvers are low-thrust maneuvers and will be performed in the last stages of the assessment phase to achieve the operational orbit. Low thrust means the change in the velocity resulting from the maneuver will be less than 100 millimeters/second. Precision maneuvers will also be performed in the observational phases to maintain the spacecraft groundtrack.

For each maneuver type, the TOPEX project has defined a set of premaneuver planning requirements and a set of postmaneuver evaluation requirements. Requirements for premaneuver planning OD define constraints on the accuracy of the osculating orbital parameters at the maneuver ignition. It should be noted that these requirements need to be met 24 hours prior to maneuver ignition. Therefore, an OD solution must be obtained 24 hours prior to maneuver ignition, and then propagated up to the maneuver ignition. Postmaneuver evaluation OD requirements involve constraints on osculating orbital parameter changes that may arise from velocity increments at the maneuver time. These requirements must be met 24 hours after the maneuver burnout. Tables 5 and 6 give the operational OD requirements for maneuver planning and maneuver evaluation (Reference 3), respectively. Note that the requirements for the precision maneuver are independent of mission phase.

3.2 ON-ORBIT SUPPORT REQUIREMENT

In addition to maneuver OD support, on-orbit free-flight OD will also be performed during the observational phases. This on-orbit, or routine, support consists of performing OD on a

Table 5. TOPEX OD Requirements on Predicted Osculating Elements Used in Premaneuver Planning

Parameter	Calibration Maneuver	Coarse Maneuver	Precision Maneuver
Semimajor axis (m)	None	None	1
Period (msec)	4	4	None
Eccentricity	1×10^{-5}	1×10^{-5}	5×10^{-6}
Inclination (deg)	1×10^{-3}	1×10^{-3}	1×10^{-4}
Argument of latitude equivalent along track error (m)	670	None	None

6130G(24)-3

Table 6. TOPEX OD Requirements on Postmaneuver Evaluation of Changes in Osculating Parameters

Parameter	Calibration Maneuver	Coarse Maneuver	Precision Maneuver
Radial velocity (mm/sec) 5.0 lbf thruster 0.2 lbf thruster	10 2	10 N/A	N/A 2
Cross-track velocity (mm/sec) 5.0 lbf thruster 0.2 lbf thruster	20 10	20 N/A	N/A 10
Along-track velocity (mm/sec) 5.0 lbf thruster 0.2 lbf thruster	4 0.1	4 N/A	N/A 0.1
Inclination (deg)	None	5×10^{-4}	1×10^{-4}
Semimajor axis (m)	None	None	0.2

6130G(24)-4

weekly basis using maneuver-free tracking data. The solution resulting from this 7-day OD arc will be used by JPL to perform long-term (30-day) predictions for mission planning purposes. Table 7 presents the single routine support requirement.

Table 7. TOPEX Requirement on Long-Term Predictions for the Observational Phases

Parameter	On-orbit requirement
Equator longitude crossing (m)	225 m after 30 days of prediction past end of data span assuming no errors in solar flux in the predicted interval

6031G(24)-5

4. ERROR ANALYSIS RESULTS

The Orbit Determination Error Analysis System (ODEAS) was used to estimate the OD capabilities corresponding to the requirements given in Section 3.0. These capabilities are a result of simulations using a weighted Bayesian least squares process.

Two 3-sigma error models have been used in this analysis. The first, referred to as the nominal error model (Table 8), represents the 1990 capabilities of the GTDS program to support the TOPEX mission. The second model, called the optimistic error model, assumes zero errors in the Earth mass constant (GM) and geopotential field. It also assumes station location component uncertainties of 1 meter. These two models give bounds on the expected OD capabilities.

Table 9 presents the requirements and the corresponding maneuver planning OD capabilities using a 3-day definitive period and a 24-hour prediction. The only requirement that is not met involves the semi-major axis in conjunction with the nominal error model. Failure to meet this constraint is a result of the uncertainty in the gravitational field of the Earth, which uses the GEM 9 model. The a priori sigma for this error source will be reduced substantially with the use of the GEM T2 gravity field representation, which is currently available and is expected to be incorporated into GTDS by the time of launch. It is therefore reasonable to assume that all requirements on osculating elements for maneuver planning will be achieved.

Before discussing the postmaneuver evaluation OD analysis results, it is important to note that the JPL perceived the need for a math process corresponding to that used for maneuver evaluation of deep space trajectories. This process assumes a data span that includes tracking data before and after a maneuver and solves for the epoch state vector at the beginning of the data span and velocity increments at the time of the maneuver. Currently, the ODEAS covariance program does not have the capability to model maneuvers in this manner.

These ODEAS limitations have introduced the need for a mathematical technique that approximates, as closely as possible, the desired procedure. The selected process assumes

Table 8. Error Sources and Associated 3-Sigma Uncertainties for the Nominal Error Model

Parameter	3-Sigma Uncertainty		
GM	GM x (3 x 10 ⁻⁷)		
Gravity Field	135%(GEM9 - GEM7) _(1,1) THROUGH (21,21) PLUS 100%(GEM9) _(22,22) THROUGH (30,30)		
C _D	30% when not solved for		
Solar Flux (watts/m ² /Hz)	Nominal = 225		
C _R TOPEX TDRS-E TDRS-W	30% 2% 2%		
Station Positions Ascension BRTS Alice Springs BRTS White Sands BRTS White Sands GRND Local X Local Y Local Z	15 m 15 m 30 m		
Troposphere	45%		
Ionosphere From Stations From TDRS-E From TDRS-W	100% 100% 100%		
Measurements	Noise	Weight Sigma	Bias
BRTS Range (m)	1.5	3.0 x 10 ⁻⁴	7.0
TDRSS Range (m)	1.5	90.0	7.0
TDRSS R/R (mm/sec) 2-Way	2.82	100.0	0.0
1-Way	4.00	4.0	0.0

6130-4

Table 9. OD Requirements and Capabilities on Predicted Osculating Parameters Used in Maneuver Planning

Definitive period = 3 days
Solar flux = 225

Parameter	Maximum 3-Sigma Error		
	Most Stringent Requirement	Capability	
		Nominal	Optimistic
Semimajor axis (m)	1	3.0	0.1
Period (msec)	4	3.9	0.1
Eccentricity	5×10^{-6}	0.7×10^{-6}	0.4×10^{-6}
Inclination (deg)	1×10^{-4}	0.6×10^{-4}	0.2×10^{-4}
Along track (m)	670	29	16

6130G(24)-1

instantaneous maneuvers and involves the differencing, parameter-by-parameter, of two error budgets at the time of the maneuver. The first error budget is obtained from tracking data covering only the postmaneuver time interval. The second error budget is obtained from tracking data covering only the premaneuver time interval.

Table 10 summarizes the requirements and OD capabilities for postmaneuver evaluation of the errors in the changes of parameters. The results indicate that the nominal error model produces change-of-parameter errors that are larger than the requirements for all parameters except the inclination. The optimistic error model produces errors in the changes of parameters that exceed the requirements for only the radial and along-track components of velocity. All results are based on 3 days of premaneuver tracking data and 24 hours of postmaneuver tracking data.

Additional analysis is currently in progress to determine the error in the components of velocity assuming the errors were limited to those associated with the orbit elements. Preliminary results show that the errors in the along-track component noted in Table 10 are reduced from 2.8 and 2.4 millimeters/second for the nominal and optimistic models to 0.18 and 0.06, respectively. These latter values meet, or only slightly exceed, the requirement of 0.1 millimeters/second noted in Table 10. Additional simulations, which assume a lower mean value of solar flux, indicate a corresponding reduction in the errors of all parameters.

Table 11 presents the requirement and orbit prediction capability for the error in the equator longitude crossing. As can be seen, the requirement is easily met. For a complete description of the analysis procedures, see References 4 and 5.

Table 10. OD Requirements and Capabilities on Postmaneuver Evaluation of Changes in Osculating Parameters

Premaneuver orbit = 3 days
Solar flux = 225

Parameter	Maximum 3-Sigma Error		
	Most Stringent Requirement	Capability	
		Nominal	Optimistic
Velocity (mm/sec)			
Radial	2.0	13.0	8.9
Cross track	10.0	14.0	7.1
Along track	0.1	2.8	2.4
Inclination (deg)	1.0×10^{-4}	0.6×10^{-4}	0.3×10^{-4}
Semimajor axis (m)	0.2	0.39	0.12

6130G(24)-2

Table 11. Orbit Prediction Requirement and Capability for the Error in the Longitude of the Equator Crossing

Parameter	Maximum 3-Sigma Error		
	Requirement	Capability	
		Nominal	Optimistic
Equator longitude crossing after 30 days prediction past the data span (m)	225	40	30

6130G(24)-10

5. CONCLUSIONS

The error analysis results using the ODEAS program supports the following conclusions:

- All premaneuver planning OD requirements on the predicted osculating elements can be met using a 3-day OD arc with a 24-hour prediction.
- Some postmaneuver evaluation OD requirements cannot be met using a 3-day premaneuver OD arc and a 24-hour postmaneuver arc.
- The long-term (30-day) prediction requirement for the equator longitude crossing can be met.

The above conclusions are based on the results using the optimistic error model, which assumes zero errors in the geopotential model and station location position errors of 1 m. In truth, the errors associated with the GEM T2 geopotential model, to be used for TOPEX operational support, lie somewhere between the nominal and the optimistic model errors. However, based on preliminary analysis results, the GEM T2 geopotential errors are closer to the optimistic model errors than to the nominal model errors.

6. ACKNOWLEDGMENTS

The authors wish to acknowledge the contributions of Taesul Lee (CSC) and Paul Arnold (CSC) in the preparation of this paper.

7. REFERENCES

1. Jet Propulsion Laboratory, 633-711, *TOPEX/Poseidon Support Instrumentation Requirements Document* (Approval Copy), September 6, 1990
2. —, 633-201, *TOPEX/Poseidon Project Mission Plan* (Approval Copy), H. M. Harris, September 1989
3. —, D-7362, *Presentation Materials From Navigation Development Review #3*, R. Bhat, May 16, 1990
4. Goddard Space Flight Center, Flight Dynamics Facility, FDD/554-90/131, *Ocean Topography Experiment (TOPEX) Satellite 1990 Flight Dynamics Analysis Report 1: Pre-launch Orbital Error Analysis*, A. F. Schanzle and J. Rovnak, prepared by Computer Sciences Corporation, August 1990
5. —, FDD/554-91/018, *Ocean Topography Experiment (TOPEX) Satellite 1990 Flight Dynamics Analysis Report 4: Orbital Error Analysis for Maneuver Planning and Maneuver Evaluation in the Observational Phases*, A. F. Schanzle and J. Rovnak, prepared by Computer Sciences Corporation, February 1991

Comparison of ERBS Orbit Determination Accuracy Using Batch Least-Squares and Sequential Methods*

D. H. Oza, T. L. Jones, and S. M. Fabien
COMPUTER SCIENCES CORPORATION (CSC)

G. D. Mistretta, R. C. Hart, and C. E. Doll
GODDARD SPACE FLIGHT CENTER (GSFC)

ABSTRACT

The Flight Dynamics Division (FDD) at the Goddard Space Flight Center (GSFC) commissioned Applied Technology Associates, Incorporated, to develop the Real-Time Orbit Determination/Enhanced (RTOD/E) system as a prototype system for sequential orbit determination of spacecraft on a DOS-based personal computer (PC). This paper presents an overview of RTOD/E capabilities and presents the results of a study to compare the orbit determination accuracy for a Tracking and Data Relay Satellite System (TDRSS) user spacecraft obtained using RTOD/E on a PC with the accuracy of an established batch least-squares system, the Goddard Trajectory Determination System (GTDS), operating on a mainframe computer.

RTOD/E was used to perform sequential orbit determination for the Earth Radiation Budget Satellite (ERBS), and the Goddard Trajectory Determination System (GTDS) was used to perform the batch least-squares orbit determination. The estimated ERBS ephemerides were obtained for the August 16-22, 1989, timeframe, during which intensive TDRSS tracking data for ERBS were available. Independent assessments were made to examine the consistencies (overlap comparisons for the batch case and covariances and the first measurement residuals for the sequential case) of results obtained by the batch and sequential methods. Comparisons were made between the forward filtered RTOD/E orbit solutions and definitive GTDS orbit solutions for ERBS; the solution differences were less than 40 meters after the filter had reached steady state.

* This work was supported by the National Aeronautics and Space Administration (NASA)/Goddard Space Flight Center (GSFC), Greenbelt, Maryland, under Contract NAS 5-31500.

1. INTRODUCTION

This paper describes a prototype of a sequential orbit determination system and compares the orbit determination accuracy for a Tracking and Data Relay Satellite (TDRS) System (TDRSS) user spacecraft using this prototype system with that achieved using an established batch least-squares system.

The National Aeronautics and Space Administration (NASA) has completed a transition from tracking and communications support of low Earth-orbiting satellites with a ground-based station network, the Ground Spaceflight Tracking and Data Network (GSTDN), to the geosynchronous relay satellite network, the TDRSS. TDRSS currently consists of three operational geosynchronous spacecraft (TDRS-East, TDRS-West, and TDRS-Spare) and the White Sands Ground Terminal (WSGT) at White Sands, New Mexico. TDRS-East, TDRS-West, and TDRS-Spare are located at 41, 174, and 171 degrees west longitude, respectively. The ground network provided only about 15-percent visibility coverage, while TDRSS has the operational capability to provide 85-percent to 100-percent coverage.

The Bilateral Ranging Transponder System (BRTS) is used to provide range and Doppler measurements for each TDRS. The ground-based BRTS transponders are tracked as if they were TDRSS user spacecraft. Since the positions of the BRTS transponders are known, their ranging data can be used to precisely determine the trajectory of the TDRS spacecraft.

To meet stringent accuracy requirements for definitive and predicted ephemerides in a timely manner for future low Earth-orbiting missions, there is an ongoing effort at Goddard Space Flight Center (GSFC) to improve the orbit determination methods and the analysis of them in such areas as force modeling, geophysical modeling, observation corrections, estimation methods, propagation methods, and numerical methods. Assessment of the relative orbit determination accuracy of the sequential and batch least-squares estimation methods is the focus of this paper.

The orbit determination methods used in this study are the batch least-squares method used for current operational orbit determination support and a sequential method implemented in a prototype system used for analysis at the GSFC Flight Dynamics Facility (FDF). The batch weighted least-squares algorithm implemented in the Goddard Trajectory Determination System (GTDS) estimates the set of orbital elements, force modeling parameters, and measurement-related parameters that minimize the squared difference between observed and calculated values of selected tracking data over a solution arc. GTDS resides and operates on the mainframe computer system at the FDF. The sequential estimation algorithm implemented in a prototype system, the Real-Time Orbit Determination/Enhanced (RTOD/E), simultaneously estimates the TDRSS user and relay spacecraft orbital elements and other parameters in the force and observation models at each measurement time. RTOD/E performs forward filtering of tracking measurements using an extended Kalman filter with a process noise model to account for geopotential-induced errors, as well as Gauss-Markov processes for drag, solar radiation pressure, and measurement biases. The main features of RTOD/E are described in Section 2.

RTOD/E and GTDS are used in this study to perform orbit determination for the Earth Radiation Budget Satellite (ERBS) and the TDRSSs. The estimated ERBS ephemerides were

obtained for the August 16–22, 1989, timeframe, during which intensive TDRSS tracking data for ERBS were available. This particular timeframe was chosen because detailed orbit determination analysis was previously performed using GTDS (Reference 1). Comparisons were made between the RTOD/E and GTDS results. Independent assessments were made to examine the consistencies (overlap comparisons for the batch case and state error covariances for the sequential case) of results obtained by the batch and sequential methods.

Section 3 of this paper describes the orbit determination and evaluation procedures used in this study, and Section 4 gives the results obtained by the batch least-squares and sequential estimation methods and provides the resulting consistency and cross comparisons. Section 5 presents the conclusions of this study.

2. DESCRIPTION OF RTOD/E

RTOD/E was recently developed by Applied Technology Associates, Incorporated (ATA) for the GSFC Flight Dynamics Division (FDD) to respond to the need for a real-time estimation capability, to address future increased TDRSS-navigation accuracy requirements, and to provide automation of some routine orbit determination operations. The goal for future orbit determination accuracy is 10 meters (1σ) total position error for the user and 25 meters (1σ) total position error for the TDRSSs. RTOD/E provides a proof of concept for the use of sequential estimation techniques for orbit determination with TDRSS tracking data and offers the potential for enhanced accuracy navigation with real-time responsiveness. RTOD/E is a research tool for assessment of sequential estimation for FDF navigation applications in realistic operational situations.

RTOD/E uses an extended Kalman filter for sequential orbit estimation. With the sequential estimation method, each tracking measurement can be processed immediately upon receipt to produce an update of a spacecraft's state vector and auxiliary state parameters. This fact makes it well-suited for real-time or near-real-time operation. Sequential estimation is particularly well-suited to the development of systems to perform orbit determination autonomously on the spacecraft's onboard computer (Reference 2). Spacecraft orbit determination during and just after a maneuver is a critical support function for which orbit determination is needed in near-real-time. Therefore, sequential estimation is also well-suited for such an application. In addition, the forward filter can be augmented with a backward smoothing filter to further improve the overall accuracy, especially during periods without tracking data.

RTOD/E employs a sequential estimation algorithm with a process noise model to stochastically account for gravity model errors (References 3 and 4). In addition to the state vectors, the filter estimates free parameters of the force model and the measurement model, treating these parameters as random variables whose behavior is governed by a Gauss-Markov stochastic process. The primary capabilities of RTOD/E are the following:

- Simultaneously determine orbits for a TDRSS user and two TDRS spacecraft using TDRSS with/without BRTS tracking measurements.
- Separately determine the TDRS orbit using BRTS tracking measurements.

- Perform near-real-time orbit determination when supplied with near-real-time tracking data through NPI.
- Perform orbit determination using archived tracking data.
- Process TDRSS and BRTS range and two-way Doppler tracking measurements.
- Perform predictions for spacecraft orbits.
- Generate graphical displays of the spacecraft covariance estimates, measurement residuals, and ground-track while concurrently processing data.
- For each tracking configuration, estimate the spacecraft state vector, drag parameter, and solar reflectivity coefficient for the user spacecraft; the solar reflectivity coefficients for the TDRSSs; and the range and range-rate bias. The estimated parameters are obtained sequentially after processing each measurement.

The NAS-to-PC Interface (NPI) is used for the near-real-time extraction and transfer of TDRSS and BRTS tracking data from a tracking data base on the NAS 8063 mainframe computer to the RTOD/E PCs (Reference 5).

3. ORBIT DETERMINATION AND EVALUATION PROCEDURE

This section describes the analysis procedures used in this study. The TDRSS and BRTS tracking data characteristics are presented in Section 3.1, and the orbit determination evaluation methodology and options used are described in Section 3.2.

3.1 TRACKING MEASUREMENTS

The user spacecraft chosen for this study was the Earth Radiation Budget Satellite (ERBS), which was deployed by the Space Transportation System (STS)-41G in October 1984. ERBS has a nearly circular orbit, with an altitude of approximately 600 kilometers, an inclination of 57 degrees, and a period of approximately 96 minutes. The time period chosen for this study was from 0 hours Greenwich mean time (GMT) on August 16, 1989, through 10 hours GMT on August 23, 1989. During this interval, an unusually dense TDRSS tracking of the ERBS satellite was made available. Another significant component of the tracking characteristics is that the tracking was scheduled by alternately using both relay spacecraft on a pass-by-pass basis. The tracking consisted of an average of 25 15-minute passes of two-way TDRSS range and Doppler observations each day. A timeline plot of the TDRSS tracking data distribution is given in Figure 1.

The typical scenario for BRTS tracking of the TDRSSs during the period of study included approximately 4 minutes of range and two-way Doppler measurements from two ground transponders for each relay every 2 to 3 hours. BRTS stations for TDRS-East are located at White Sands and Ascension Island. BRTS stations for TDRS-West are located at White Sands, American Samoa, and Alice Springs, Australia. The Alice Springs station was inoperative during August 1989, the period of this study.

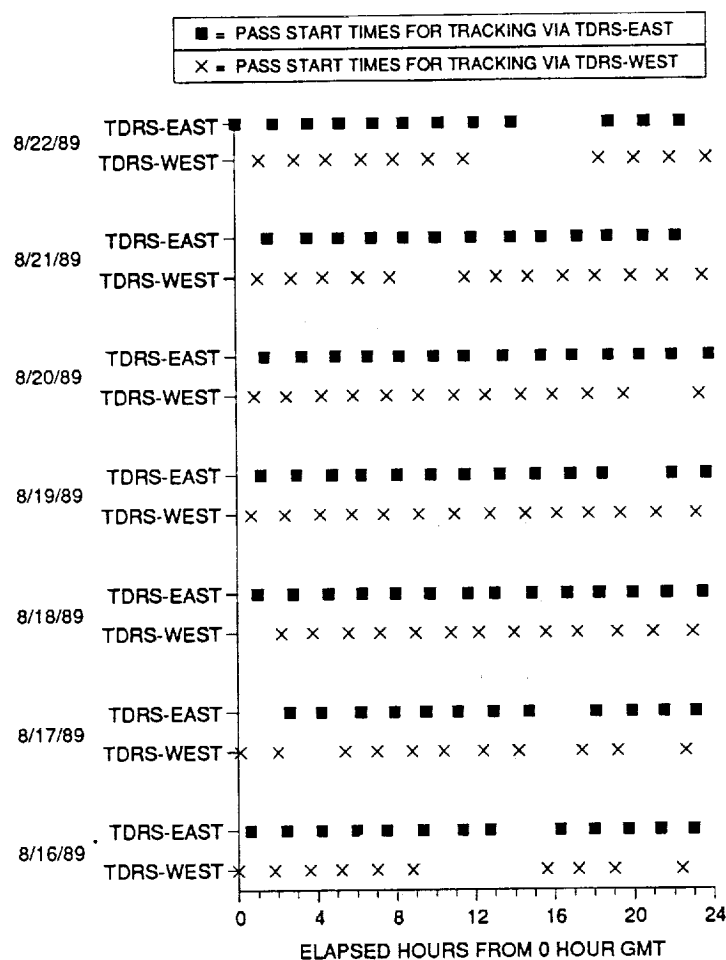


Figure 1. Tracking Data for ERBS

3.2 EVALUATION METHODOLOGY

The evaluation methodologies for the batch least-squares and sequential estimation methods are described below. Table 1 gives the parameters and options for the simultaneous solutions of the user and relay spacecraft. Table 2 gives the force and measurement model specifications. Since there are some known differences between the GTDS and RTOD/E force models and since the RTOD/E TDRSS and BRTS measurement models were implemented independently from GTDS, the two systems are not expected to provide identical results. Therefore, this study assumes that each system is used in its optimal configuration.

Batch Least-Squares Method

Except for the variations noted, the computational procedures and mathematical methods used in this study are those used for routine operational orbit determination at the GSFC FDF. The batch weighted least-squares algorithm implemented in GTDS (Reference 6) solves for the set of orbital elements and other parameters that minimizes the squared difference between observed and calculated values of selected tracking data over a solution arc.

Table 1. Parameters and Options for the Simultaneous Solutions of User and Relay Spacecraft

ORBIT DETERMINATION PARAMETER OR OPTION	GTDS VALUES		RTOD/E VALUES	
	USER (ERBS)	RELAY (TDRS-EAST & TDRS-WEST)	USER (ERBS)	RELAY (TDRS-EAST & TDRS-WEST)
ESTIMATED PARAMETERS	STATE, DRAG SCALING PARAMETER (θ_1), RANGE AND DOPPLER MEASUREMENT BIASES FOR TRACK- ING VIA EACH TDRS	STATE, TRANSPONDER DELAYS FOR EACH BRTS TRANSPONDER	STATE, COEFFICIENT OF DRAG, RANGE AND DOPPLER MEASURE- MENT BIASES FOR TRACKING VIA EACH TDRS	STATE, SOLAR REFLEC- TIVITY COEFFICIENT (C_R), RANGE AND DOPPLER MEASUREMENT BIASES FOR TRACKING VIA EACH TRANSPONDER
INTEGRATION TYPE	FIXED-STEP COWELL	FIXED-STEP COWELL	VARIATION OF PARAMETERS	VARIATION OF PARAMETERS
COORDINATE SYSTEM OF INTEGRATION	MEAN OF 1950.0	MEAN OF 1950.0	MEAN OF 1950.0	MEAN OF 1950.0
INTEGRATION STEP SIZE (SECONDS)	30.0	600.0	60.0	600.0
TRACKING DATA	TDRSS	BRTS	TDRSS	BRTS
DATA RATE	1 PER 10 SECONDS	1 PER 10 SECONDS	1 PER 60 SECONDS	1 PER 60 SECONDS
DC CONVERGENCE PARAMETER	0.005	0.005	N/A	N/A
EDITING CRITERION	3 σ	3 σ	3 σ	3 σ
MEASUREMENT σ 's: RANGE DOPPLER	30.0 METERS 0.25 HERTZ	10.0 METERS 0.003 HERTZ	0.4 METER 0.004 HERTZ	0.25 METER 0.002 HERTZ
GAUSS-MARKOV PARAMETERS: DRAG HALF-LIFE DRAG SIGMA C_R HALF-LIFE C_R SIGMA RANGE BIAS HALF-LIFE RANGE BIAS SIGMA DOPPLER BIAS HALF-LIFE DOPPLER BIAS SIGMA	N/A	N/A	720 MINUTES 0.5 N/A N/A 60 MINUTES 6 METERS 60 MINUTES 0.034 HERTZ	N/A N/A 11520 MINUTES 0.2 60 MINUTES 4.5 METERS 60 MINUTES 0.02 HERTZ
SATELLITE DIAMETER	2.45 METERS	9.42 METERS	2.45 METERS	9.42 METERS
SATELLITE MASS	2116 KILOGRAMS	2068 KILOGRAMS	2116 KILOGRAMS	2068 KILOGRAMS

N/A = NOT APPLICABLE

6130-5

Table 2. Force and Measurement Model Specifications

ORBIT DETERMINATION PARAMETER OR OPTION	GTDS VALUES		RTOD/E VALUES	
	USER (ERBS)	RELAY (TDRS-EAST & TDRS-WEST)	USER (ERBS)	RELAY (TDRS-EAST & TDRS-WEST)
GEOPOTENTIAL MODEL	GEM-T2 (50 x 50)	GEM-T2 (8 x 8)	GEM-10B (30 x 30)	GEM-10B (8 x 8)
ATMOSPHERIC DENSITY MODEL	HARRIS-PRIESTER FOR SOLAR FLUX 225	N/A	JACCHIA-WALKER DAILY SOLAR FLUX VALUES (253, 258, 258, 243, 231, 220, 200)	N/A
SOLAR AND LUNAR EPHEMERIDES	JPL DE-118	JPL DE-118	ANALYTICAL	ANALYTICAL
SOLAR REFLECTIVITY COEFFICIENT (C_R)	1.2	SEE TEXT	1.2	ESTIMATED
COEFFICIENT OF DRAG (C_D)	ESTIMATED	N/A	ESTIMATED	N/A
IONOSPHERIC REFRACTION CORRECTION	BENT MODEL	BENT MODEL	NO	NO
GROUND-TO-SPACECRAFT SPACECRAFT-TO-SPACECRAFT	NO YES	YES N/A		
TROPOSPHERIC REFRACTION CORRECTION	YES	YES	YES	YES
ANTENNA MOUNT CORRECTION	NO	NO	NO	NO
POLAR MOTION CORRECTION	YES	YES	NO	NO
EARTH TIDES	YES	NO	NO	NO

GEM = GODDARD EARTH MODEL
JPL = JET PROPULSION LABORATORY
N/A = NOT APPLICABLE

6130-5

Parameters solved for, other than the spacecraft state at epoch, include free parameters of the force model and/or the observation model. The options used for the study described in this paper are summarized in columns 2 and 3 of Tables 1 and 2.

The solar reflectivity coefficients (C_R) for TDRS-East and TDRS-West were not estimated in the simultaneous solutions of ERBS, TDRS-East, and TDRS-West but were applied. The values of C_R applied in the present calculations were obtained from separate solutions of TDRS-East and TDRS-West from a previous study where C_R values were estimated (Series C and D of Reference 1).

To evaluate the orbit determination consistency achievable with a particular choice of options using least-squares estimation, a series of seven 34-hour definitive solutions was performed with 10-hour overlaps between neighboring arcs. The GTDS Ephemeris Comparison Program was used to determine the root-mean-square (RMS) position differences between the definitive ephemerides for neighboring solutions in the 10-hour overlap time period. These "overlap" comparisons measure the adjacent solution consistency, not the absolute accuracy.

Sequential Estimation Method

RTOD/E uses a forward-processing extended Kalman filter for sequential orbit estimation. The mathematical algorithms and computational procedures are described in References 3

and 4. The specific options used in RTOD/E for this study are listed in the last two columns of Tables 1 and 2.

A good indicator of the consistency of the sequential estimation results is the state error covariance function generated during the estimation process (Reference 7). In addition, the relationship of the first predicted measurement residual of each tracking pass to the associated predicted residual variance provides an indication of the physical integrity of the state error covariance of the filtered orbits. These parameters were monitored during the sequential estimation process.

4. RESULTS AND DISCUSSION

The results of this study for the ERBS and relay spacecraft are presented in this section, along with an analysis of the results. Greater emphasis is placed on the ERBS results, since the primary objective is to study TDRSS user orbit determination. The orbit determination results using batch least-squares calculations and sequential estimation are given in Sections 4.1 and 4.2, respectively; the comparisons are presented in Section 4.3.

4.1 BATCH LEAST-SQUARES RESULTS

An extensive analysis of the batch least-squares orbit determination of ERBS and the TDRSSs in terms of variations in the force models, measurement models, and solution modes was reported in Reference 1. The results reported here do not significantly differ from those of Reference 1. The only difference between the calculations of series M in Reference 1 and the present calculations is that in the present calculations the biases on TDRSS range and two-way Doppler measurements and the transponder delays for BRTS measurements were also estimated. (The options used for calculations of series M of Reference 1 are the same as those given in columns 2 and 3 of Tables 1 and 2, with the exception of the parameter set.) The choice to expand the state space of the least-squares solutions was motivated by the fact that the RTOD/E orbit determination algorithm estimates an equivalent set of bias parameters. The resulting differences are discussed below.

The RMS values of six ERBS overlap comparisons are summarized in Figure 2. The overlap values vary from about 4 to 17 meters. The mean and sample standard deviation of this distribution, in the form of *mean* \pm *standard deviation*, is 13.3 ± 5.9 meters. The maximum total position differences over the same distribution vary between 6 and 46 meters, with mean and standard deviation of 29.7 ± 14.8 meters. The maximum position difference values for ERBS are typically a factor of 2 larger than the RMS values.

The RMS values of six TDRS-East and TDRS-West overlap comparisons are summarized in Figure 3. The overlap values for TDRS-East vary from about 14 to 45 meters. The mean and sample standard deviation of this distribution is 25.0 ± 10.7 meters. The maximum total position differences over the same distribution vary between 17 and 58 meters, with mean and standard deviation of 33.9 ± 13.5 meters. The overlap values for TDRS-West vary from about 19 to 42 meters. The mean and the sample standard deviation of this distribution is 25.2 ± 9.0 meters. The maximum total position differences over the same distribution vary between 25 and 63 meters, with mean and standard deviation of 35.4 ± 14.2 meters. The

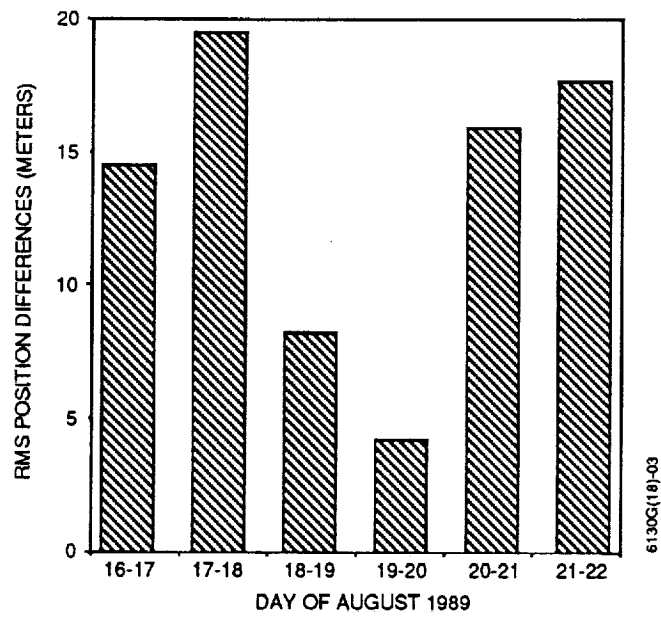


Figure 2. ERBS Overlap Comparisons

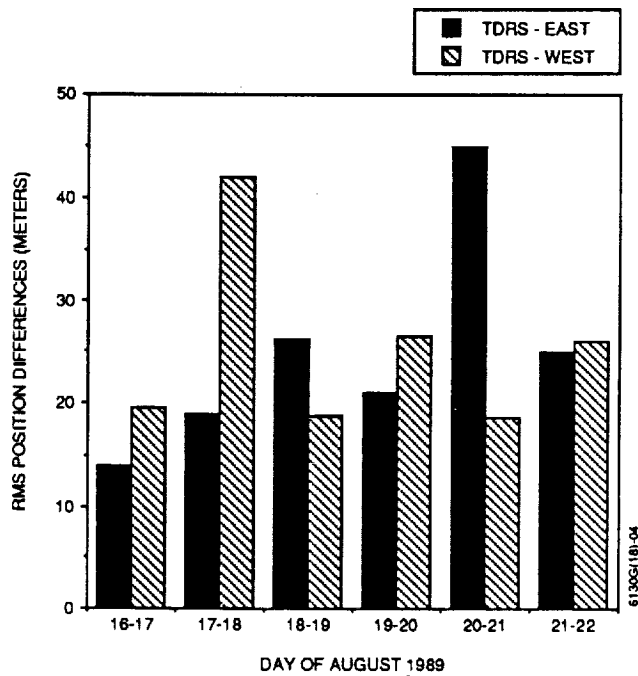


Figure 3. TDRS-East and TDRS-West Overlap Comparisons

maximum position difference values for the TDRSs are typically a factor of 1.2 larger than the RMS values.

The possible advantage of estimating a set of bias parameters (as was done in this study) versus not estimating the set (as was done in the series M calculation of Reference 1) was evaluated. The mean values of the range and Doppler measurement residuals (i.e., the observed-minus-computed values for each solution) as calculated in Reference 1 indicated the existence of a systematic error. The mean range measurement residuals varied between 6.3 ± 4.7 meters and 7.6 ± 4.6 meters for the seven solution arcs. The mean Doppler measurement residuals varied between -12.7 ± 91.1 millihertz and -17.5 ± 83.6 millihertz. The estimation of a set of bias parameters in the calculations in this study effectively removed the systematic error, thereby significantly reducing the mean range and mean Doppler measurement values, as expected. The standard deviations of the residuals were also somewhat reduced. However, although the removal of a bias may improve accuracy, it was not expected to improve consistency. As a matter of fact, the mean RMS overlap value without estimating for a set of bias parameters (series M of Reference 1) was comparable for ERBS (13.1 ± 6.1 meters) and somewhat smaller for TDRS-East (21.6 ± 7.9 meters) and TDRS-West (18.0 ± 9.2 meters).

4.2 SEQUENTIAL ESTIMATION RESULTS

During sequential processing of the TDRSS and BRTS measurements using RTOD/E, the state error covariance function (2σ) was closely monitored. The filter was started with high initial diagonal values in the covariance matrix. In the initial phases of filtering, the covariance values for ERBS were as high as 1200 meters and those for the TDRSs were 800 meters. However, this is not unusual before the filter has reached steady-state performance. After an initial filter settling period (about 24 hours), the covariance values varied from about 15 to 30 meters in the RMS position for ERBS and 40 to 60 meters for the TDRSs. The covariance values dropped to their lowest levels during a tracking pass and then gradually rose to the maximum values during the time update phase (propagation phase).

The first predicted range residuals of ERBS tracking passes after the filter processed the tracking data for 5 days are shown in Figure 4. The tracking passes via TDRS-East and TDRS-West are plotted separately. The value of the residual varied from nearly -5 meters to about 8 meters for passes via TDRS-East and from -8 meters to about 20 meters for passes via TDRS-West. The largest value (19.4 meters) occurred after about 1 hour of the prediction period following the previous tracking pass. The larger scatter for passes via TDRS-West is most likely attributable to the absence of BRTS tracking of TDRS-West by the Alice Springs station. The postmeasurement-update range residuals were negligibly small, typically of the order of 0.3 meter or less.

The estimated force model parameters varied as a function of time and were updated after each measurement processed. The time variation of the atmospheric drag coefficient for ERBS is shown in Figure 5. It varied from a low value of 1.6 to a high value of 3.0. The time variations of the solar radiation pressure coefficient for TDRS-East and TDRS-West are given in Figures 6 and 7, respectively. After the filter has reached steady state, the coefficient varied between 1.4 and 1.55.

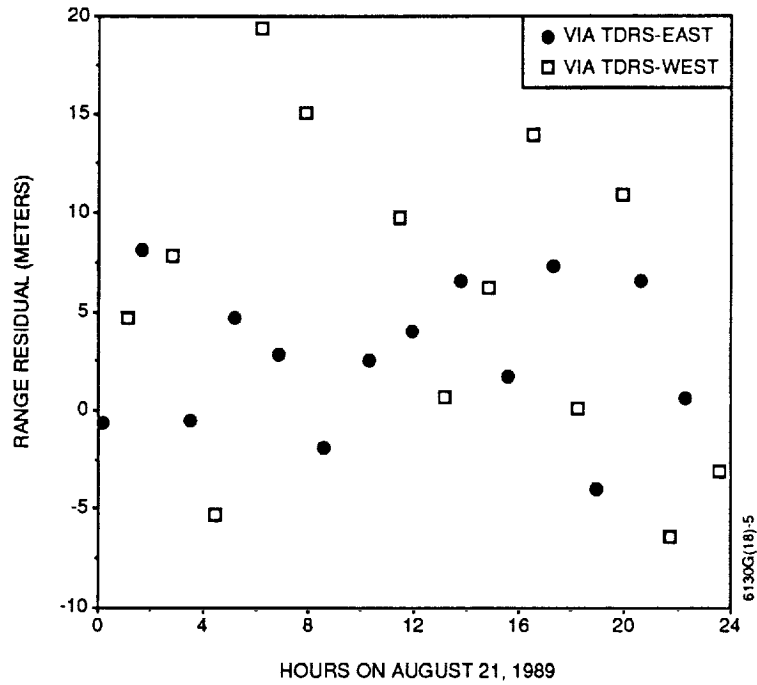


Figure 4. First Predicted Range Residual of TDRSS Tracking Passes for ERBS

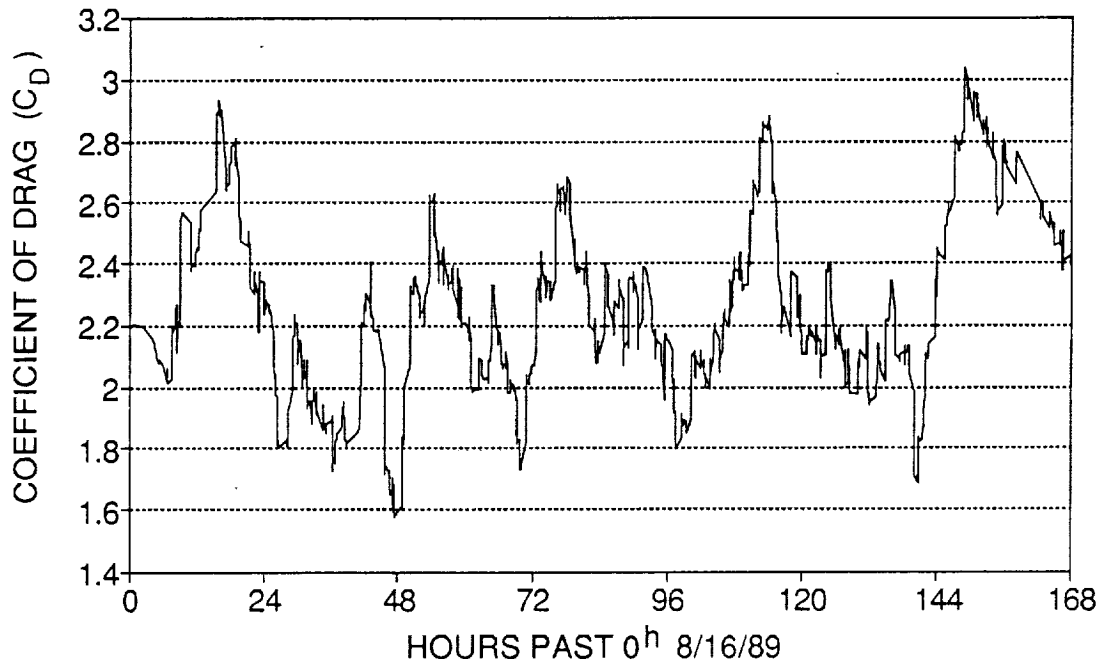


Figure 5. Coefficient of Atmospheric Drag (C_D) for ERBS

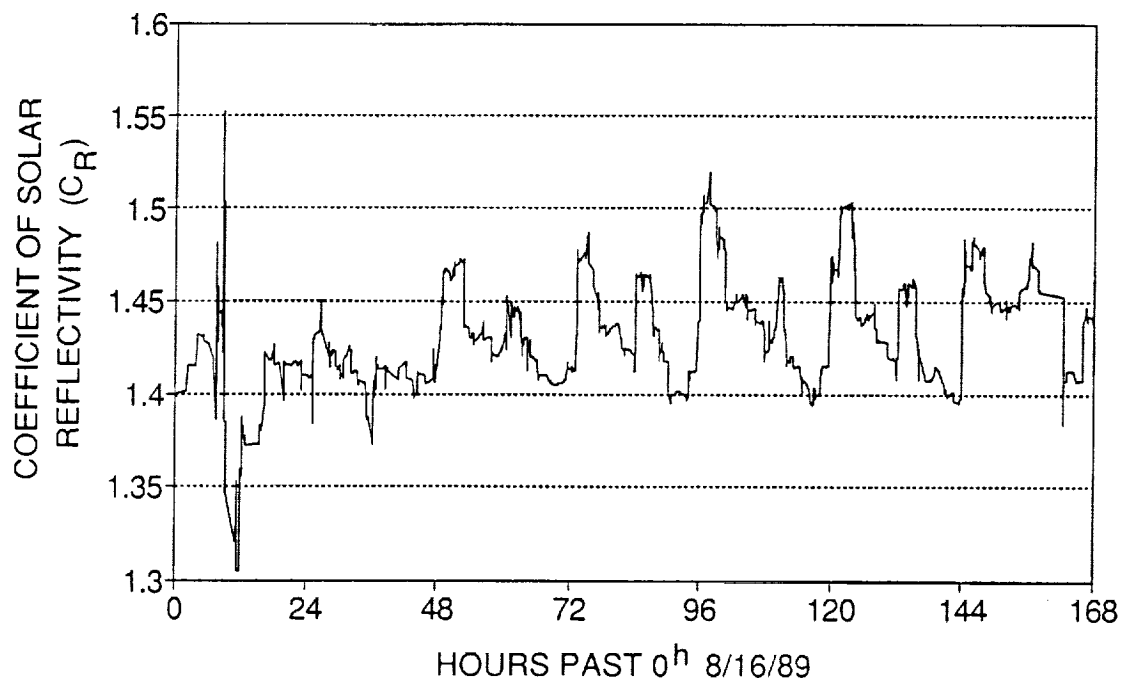


Figure 6. Coefficient of Solar Radiation Pressure (C_R) for TDRS-East

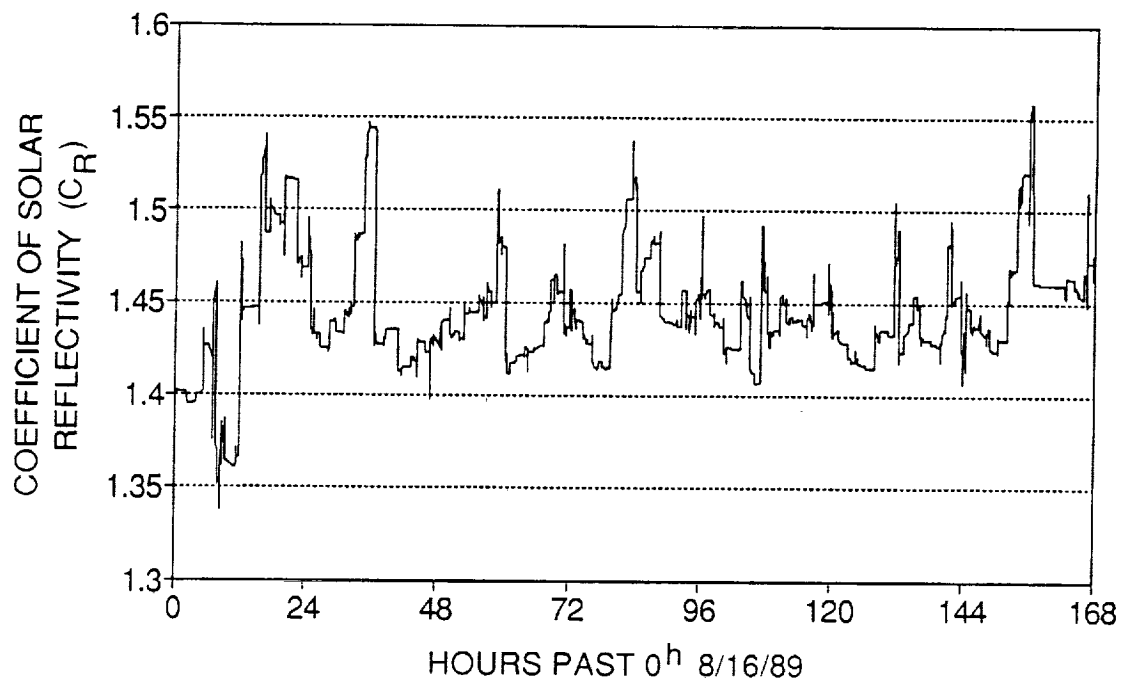


Figure 7. Coefficient of Solar Radiation Pressure (C_R) for TDRS-West

The solar flux values are input to RTOD/E on a daily basis. The time variation of the flux value over the 24-hour period is not input. Therefore, the atmospheric drag coefficient has to adjust itself for the variation (Figure 5). RTOD/E models the area of the TDRS to be a constant throughout the day, whereas in actuality the TDRS area exposed to the solar flux varies with a 24-hour period. The C_R estimated values for TDRS-East, shown in Figure 6, display an approximately repeated variation over 24-hours for the last 5 days during steady-state performance. Such a clear signature of variation is not evident in the C_R values for TDRS-West shown in Figure 7.

The time variation of the estimated range bias values for ERBS via TDRS-East and TDRS-West are shown in Figures 8 and 9, respectively. The bias values varied from approximately -3 meters to approximately 20 meters, with an average value of approximately 4 meters. There are some known physical phenomena and considerations that are absorbed in the estimation of the range bias. The variation in the offset of the ERBS antenna position from the center of mass is not modeled in RTOD/E. The time-varying tropospheric refraction delay and ionospheric refraction delay, which are not modeled in the measurement model, are absorbed in the range bias estimates.

4.3 COMPARISON OF BATCH AND SEQUENTIAL ESTIMATION RESULTS

Comparisons of the estimated ERBS orbits between GTDS solutions and RTOD/E forward-filtered solutions are presented in Figures 10 and 11. Figure 10 shows the differences during the first day of the filtered solution. Since the filter had not reached steady state during the early phases of this period, the position difference was as large as about 600 meters. However, this difference is not larger than the corresponding state error covariance values of the filter, an indicator of the internal consistency of the filtered solution. After the filter had reached steady state, the differences between the GTDS and RTOD/E solutions were much smaller than on the first day. Therefore, these results were plotted in Figure 11 with a different vertical scale; the position differences shown in this figure are all less than 40 meters. The maximum difference did not increase or decrease toward the end of the 7-day comparison period. The maximum difference of less than 40 meters is consistent within the cumulative consistencies of batch and sequential solutions.

A significant part of the difference between the batch and sequential orbit determination results in Figure 11 can be attributed to the differences in the force and measurement models used for GTDS and RTOD/E. Quantitative estimates for some of these model difference effects are available from previous studies using GTDS. It was reported in Reference 1 that the maximum position difference for definitive ERBS orbits using the GEM-T2 (50 x 50) and GEM-10B (36 x 36) geopotential models can be as high as 30.1 ± 5.2 meters. RTOD/E uses the GEM-10B geopotential model with order and degree 30. Due to the inclusion of a process noise model for geopotential errors in RTOD/E and its absence in GTDS, the impact differences in the models used would be different in the two systems. Estimates of the effects of differences in the Harris-Priester and Jacchia-Walker atmospheric density models are not available but may be significant. The maximum position differences in the definitive ERBS orbits due to the presence and absence of ionospheric refraction correction in the measurement model for the spacecraft-to-spacecraft leg can be 2.6 ± 0.9 meters (Reference 1). The maximum position difference due to polar motion and solid Earth tide effects are about

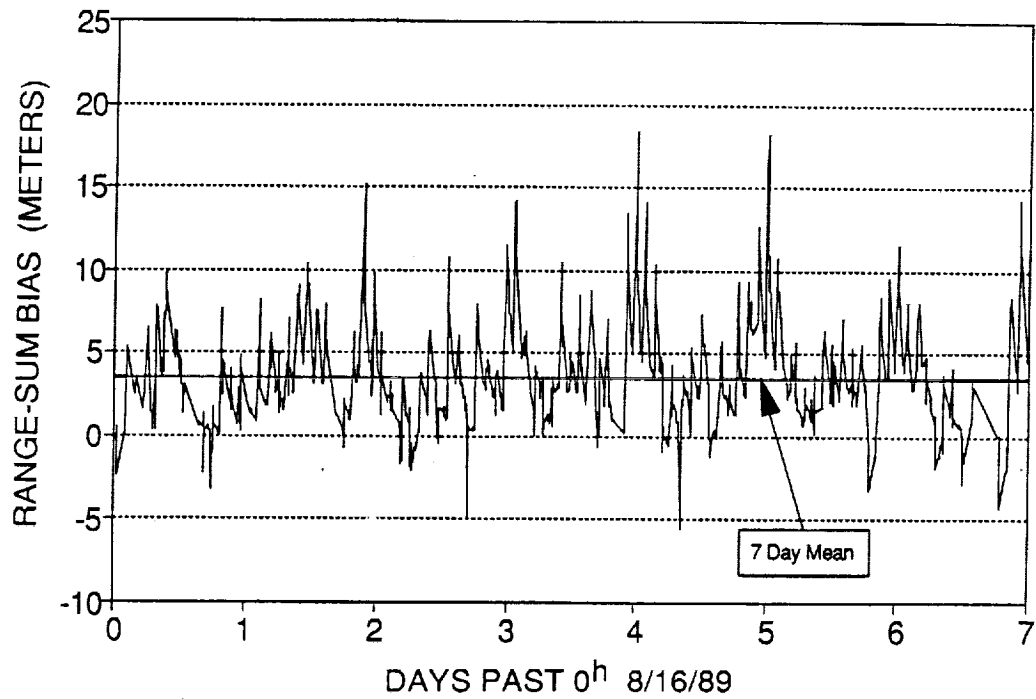


Figure 8. ERBS Range Bias via TDRS-East

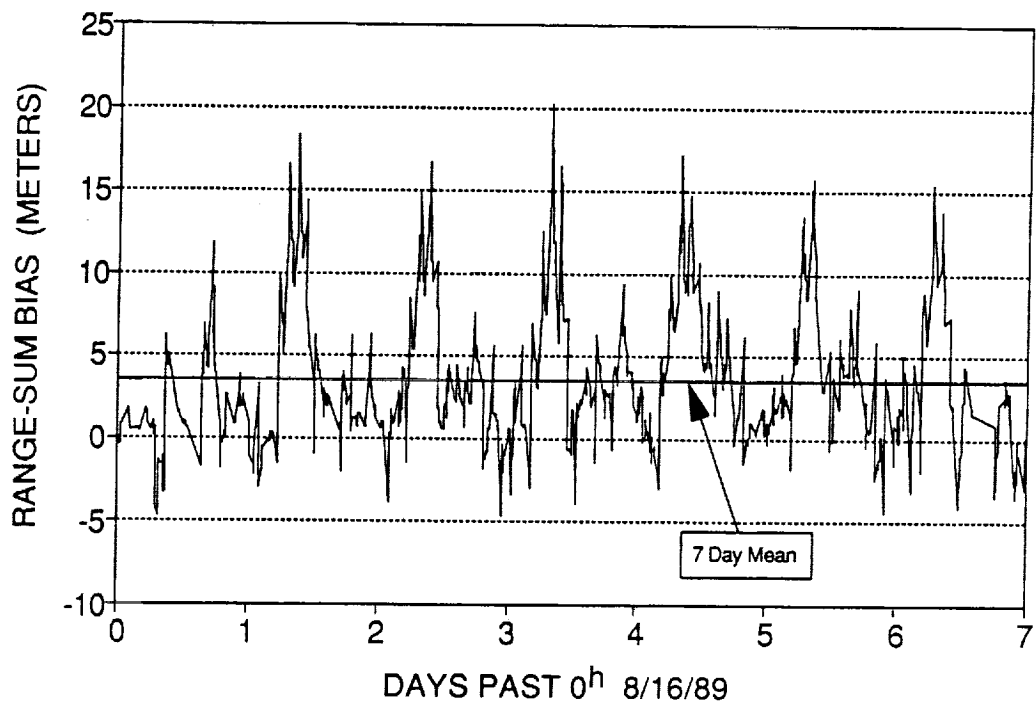


Figure 9. ERBS Range Bias via TDRS-West

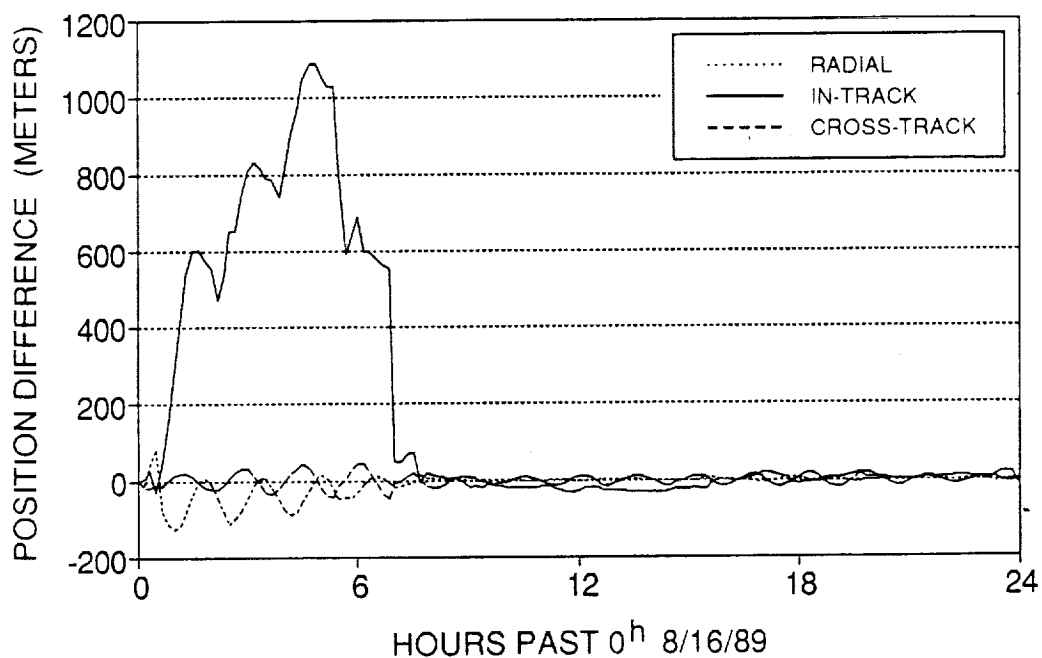


Figure 10. Comparison of Estimated GTDS and RTOD/E Ephemerides for ERBS (Radial, In-Track, and Cross-Track Components)

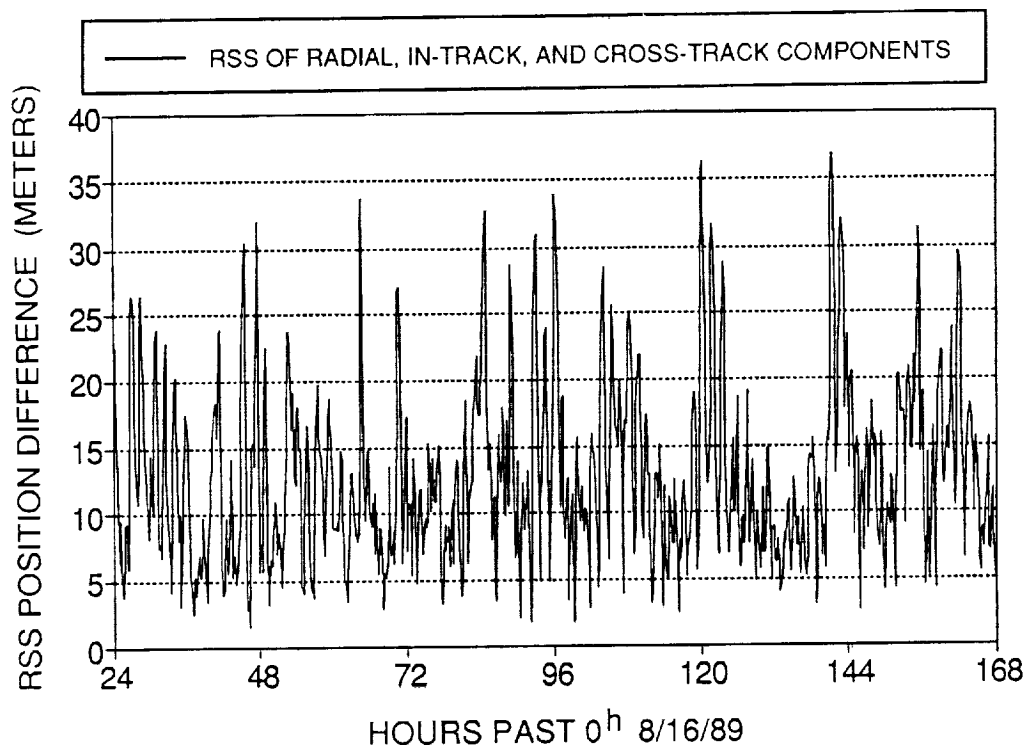


Figure 11. Comparison of Estimated GTDS and RTOD/E Ephemerides for ERBS (RSS of Components)

8.3 \pm 1.0 meters and 7.0 \pm 3.2 meters, respectively. A more detailed analysis of the influence of polar motion and solid Earth tides on ERBS orbits is given in Reference 8.

Another source of the difference between the GTDS and RTOD/E estimated ephemerides is due to the fundamental difference in the way the estimated parameters are obtained in the batch least-squares and sequential estimation techniques. In the batch least-squares method, a single set of parameter values is estimated over an entire arc. In the sequential estimation process, the set of estimated parameter values is updated at each measurement time. The time variations in selected estimated parameters were shown in Figures 5 through 9.

Based on the magnitude of these differences and the differences in the estimation techniques, the maximum position difference of about 40 meters between the GTDS and RTOD/E results is not large.

5. REMARKS

The results presented in this paper were obtained using dense-tracking TDRSS measurements for ERBS. A previous study of ERBS with single-relay (TDRS-East only) TDRSS tracking has shown that to achieve the highest precision orbit determination using the batch least-square method, the tracking coverage should not fall below 10 minutes every two orbits (Reference 9). The tracking coverage used in the present study, as shown in Figure 2, was well above this criterion. The impact of tracking coverage on accuracy using sequential estimation techniques will be pursued in future studies. In theory, the filter is expected to be more sensitive to large gaps in tracking data than the batch least-squares method; but, on the other hand, it would benefit more from more continuous tracking than would the batch least-squares method.

An investigation to assess the prediction accuracy measured by comparing propagated solutions with the definitive solutions using GTDS and RTOD/E is in progress.

6. CONCLUSIONS

This study presented an analysis of TDRSS user orbit determination using a batch least-squares method and a sequential estimation method. Independent assessments were performed of the orbit determination consistency within each method, and the estimated orbits obtained by the two methods were also compared. This assessment is applicable to the dense-tracking measurement scenario for tracking ERBS.

In batch least-squares method analysis, the orbit determination consistency for ERBS, which was heavily tracked by TDRSS during August 1989, was found to be about 15 meters in the RMS overlap comparisons and about 30 meters in the maximum position differences in overlap comparisons. In sequential method analysis, the consistency was found to be about 15 to 30 meters in the 2σ state error covariance function.

After the filter had reached steady state, the differences between the definitive batch least-squares ephemerides and the forward filtered sequentially estimated ephemerides were

no larger than 40 meters, which is approximately the limit of the consistency for each separate method. Since the two methods of determining orbits are algorithmically and computationally independent, an accuracy level of about 40 meters (3σ) may be assigned to the orbits determined by either method from the present analysis, barring any tracking-system-related systematic error. Further studies will investigate the relative qualities of the two methods within this difference.

ACKNOWLEDGMENTS

The authors want to recognize the achievement of J. Wright and W. Chuba of ATA for their successful development of the RTOD/E prototype system. The authors also express their gratitude to J. Teles of GSFC; to A. Long, P. Rennert, and D. Niklewski of Computer Sciences Corporation (CSC) for valuable discussions; and to E. J. Smith of CSC for assistance with preparation of this paper.

REFERENCES

1. D. H. Oza, M. Hodjatzadeh, M. S. Radomski, C. E. Doll, and C. J. Gramling, "Evaluation of Orbit Determination Using Dual-TDRS Tracking," Paper No. AIAA-90-2925-CP in *A Collection of Technical Papers Part 1*, page 410, published by AIAA; presented at the AIAA/AAS Astrodynamics Conference, Portland, Oregon, August 20-22, 1990
2. Goddard Space Flight Center, Flight Dynamics Division, FDD/554-90/104, *Tracking and Data Relay Satellite System (TDRSS) Onboard Navigation System (TONS) Flight Software Mathematical Specifications, Revision 1*, A. C. Long, D. H. Oza, and M. A. Edwards (CSC), prepared by Computer Sciences Corporation, May 1990
3. Goddard Space Flight Center, Flight Dynamics Division, FDD/554-91/064, *Enhanced RTOD Demonstration System*, W. Chubba, prepared by Applied Technology Associates, Inc., March 1991
4. J. R. Wright, "Sequential Orbit Determination with Auto-Correlated Gravity Modeling Errors," *Journal of Guidance and Control*, vol. 4, 1981, page 304
5. Goddard Space Flight Center, Flight Dynamics Division, 554-FDD-91/068, *NAS 8063 - RTOD/E System Interface, Systems Description and User's Guide*, M. Madden, B. Gianni, and D. Panitz (CSC), to be published by Computer Sciences Corporation in June 1991
6. —, FDD/552-89/001, *Goddard Trajectory Determination System (GTDS) Mathematical Theory, Revision 1*, A. C. Long, and J. O. Cappellari, Jr. (CSC) and C. E. Valez and A. J. Fuchs (GSFC) (editors), prepared by Computer Sciences Corporation, July 1989
7. A. Gelb (editor), *Applied Optimal Estimation*. Cambridge, Massachusetts: M.I.T. Press, 1974

8. Goddard Space Flight Center, Flight Dynamics Division, FDD/554-90/103, "Effects of Polar Motion and Earth Tides on High-Accuracy Orbit Determination of the Earth Radiation Budget Satellite (ERBS)," *Operational Orbit Techniques, 1990 Flight Dynamics Analysis Report 1*, D. H. Oza and T. Mo (CSC), prepared by Computer Sciences Corporation, May 1990
9. C. E. Doll, C. J. Gramling, D. H. Oza, and M. S. Radomski, "Sensitivity of High-Accuracy Tracking and Data Relay Satellite System (TDRSS) User Spacecraft Orbit Determination to Tracking Schedules," Paper No. CNES 89/143, presented at the CNES International Symposium on Space Dynamics, Toulouse, France, November 6-10, 1989

N 9 2 - 1 4 0 7 6

NAVIGATION OF THE TSS - 1 MISSION

by

Timothy C. Jackson
John G. Pido
Patrick L. Zimmerman

Rockwell Space Operation Company
600 Gemini
Houston, Texas 77058

**FLIGHT MECHANICS / ESTIMATION THEORY
SYMPOSIUM**

GODDARD SPACE FLIGHT CENTER
GREENBELT, MARYLAND 20271

NAVIGATION OF THE TSS-1 MISSION

The Tethered Satellite System Mission was analyzed to determine its impacts on the Mission Control Center (MCC) Navigation section's ability to maintain an accurate state vector for the Space Shuttle during nominal and off-nominal flight operations. Tether dynamics expected on the Shuttle introduces new phenomena when determining the best estimation of its position and velocity. In the following analysis, emphasis was placed on determining the navigation state vectors accuracies resulting when the tether induced forces were and were not modeled as an additional acceleration upon processing tracking measurements around a TSS-1 trajectory. Results of the analyses show that when the forces are not modeled in the state vector generation process, the resulting solution state reflects a solution about the center gravity (c.g.) of the tethered system and not that of the orbiter. The Navigation team's ability to provide accurate state vector estimates necessary for trajectory planning are significantly impeded. In addition to this consequent is an impact to Onboard Navigation state vector accuracies. These analyses will show that in order to preserve an accurate state onboard the orbiter a new operational procedure would have to be adopted. Previous Shuttle missions have shown that an accurate state could be maintained onboard when periodic updates are made utilizing the most accurate solution state vector computed by ground tracking data processing. However, the forces acting on the orbiter are much larger than those which have been modeled during previous mission and must be included in the Onboard Navigation state vector update process. The following analyses will show that significant improvements to state vector accuracies on both the ground and onboard can be achieved when the forces are modeled throughout the TSS-1 mission profile.

Introduction

The introduction of a Tethered Satellite System is new to the MCC Navigation section. The dynamics imposed on the orbiter are much larger than any which have been experienced during previously flown Space Transportation System (STS) missions. Consequently, many pre-mission analyses have been performed to better understand the behavior of a tethered system on the navigation process thereby assuring crew safety and mission success.

The TSS-1 mission is currently scheduled for launch in February 1992. Its design includes a 500 kg satellite which will be deployed upward and away from the earth with the aid of a tether to a maximum length of 20 km. The tether will be electrically conductive. The satellite, on the other hand, will be electrically positive and is designed to collect electrons from the ionosphere. The electrons will be passed through the tether to the orbiter and emitted with an electron emitter.

The following sections provide the results of several analyses performed in order to satisfy the above mentioned objectives.

MCC Ground Navigation Overview

The MCC Ground Navigation section is responsible for maintaining accurate knowledge of the Shuttle's position and velocity. This task is accomplished by utilizing the tracking

measurements which are provided by space and ground based tracking facilities strategically located throughout the world to compute the orbiter's state.

The analyses discussed in the following sections utilized tracking measurements which were computed around the TSS-1 trajectories using the Spacecraft Tracking Data Simulation (STDS) program. The measurements computed included those from selected C-band stations and both Tracking Data Relay Satellites (TDRSE, TDRSW). C-band stations with a maximum elevation below 3 degrees were not included in the analyses due to their likelihood of inherently introducing erroneous measurements caused by atmospheric refraction.

The Ground Navigation team processes these measurements using trajectory applications inherent in the Mission Operations computer (MOC). Tracking measurements may be processed in both a homogeneous or heterogeneous fashion. The homogeneous method is referred to as the Batch-to-Batch (BB) mode. Measurements from a single tracker are processed to determine the orbiter's state. The heterogeneous technique on the other hand, acknowledges measurements from several trackers for which the orbiter was visible over some orbital timeframe and is referred to as the Superbatch (SB) mode.

The two techniques utilize a weighted least squares processor which computes the state of the orbiter upon satisfying a set of convergence criteria for the measurements, (e.g., Doppler, range, elevation, azimuth), considered in the computation of the state. The quality of the state vector can be determined by minimization the measurement residuals resulting upon execution of the weighted least squares process.

Analysis Overview

The analyses were performed for trajectories defined by the TSS-1 Design Reference Mission (DRM), baselined March 18, 1990. The trajectories included all of the effects of tether dynamics on the orbiter as computed by the Shuttle Tethered Object Control Simulation (STOCS). The tether community at the Johnson Spacecraft Center (JSC) have relied heavily on STOCS to determine the behavior of tethers during Shuttle operations. Current flow expected during the mission were briefly analyzed but did not provide a significant orbital perturbation. Table (1) provides a detailed mission timeline for the DRM.

The analyses were performed to assess whether the MCC Ground Navigation section could successfully support TSS-1 under both nominal and off-nominal flight conditions. The off-nominal scenario which will be discussed is that of the impacts of a tether cut on Shuttle navigation. Also included is an assessment of the frequency at which the Onboard navigation state vector would needed to be updated to preserve flight rules which protect for a safe deorbit in the event of a loss of communication between the ground and crew is experienced.

The primary objective of the Navigation team during STS mission is to provide accurate state vectors to the Flight Dynamics Officer (FDO) to assist in trajectory planning (e.g., translational maneuvers, deorbit burns, contingency operations, etc.). The configuration of the tethered system introduces larger external forces on the orbiter than have been experienced in previous missions. There also exist the phenomenon which in given two orbiting bodies of different masses, attached by a tether, a center of gravity (c.g.) point is defined along the tether. Experience has shown that when processing tracking measurements around a trajectory influenced by tethered dynamics, resulting solution state vectors may be biased to reflect solutions about the c.g. of the system and not that of the orbiter. The following analyses will show that successful navigation of the TSS-1 mission

can only be achieved by modeling the tether forces as an additional acceleration when computing the orbiter's state.

Table 1
ATTITUDE TIMELINE

ATTITUDE	TIME (YY:MM:SS)	MODE	P/Y/R (DEG)	TETHER LENGTH (KM)	PHASE
1	1:00:00:00	LVLH	30.0 180.0 0.0	0.00	DEPLOY
2	1:00:45:00	LVLH	40.0 180.0 0.0	0.00	
3	1:01:46:00	LVLH	30.0 180.0 0.0	2.40	
4	1:01:57:00	LVLH	15.0 180.0 0.0	3.00	
5	1:02:07:30	LVLH	5.5 180.0 0.0	4.50	
6	1:02:38:30	LVLH	-22.0 180.0 0.0	5.80	
7	1:04:55:30	LVLH	-25.5 180.0 0.0	18.30	
8	1:07:16:00	LVLH	43.7 -51.4 37.6	20.00	ON- STATION 1
9	1:07:46:00	LVLH	43.7 51.4 -37.6	20.00	
10	1:08:21:00	LVLH	-25.5 180.0 0.0	20.00	
11	1:10:16:00	LVLH	43.7 -51.4 37.6	20.00	
12	1:10:46:00	LVLH	43.7 51.4 -37.6	20.00	
13	1:11:24:30	LVLH	-25.5 180.0 0.0	20.00	
14	1:13:16:00	LVLH	43.7 -51.4 37.6	20.00	
15	1:13:46:00	LVLH	43.7 51.4 -37.6	20.00	
16	1:14:20:00	LVLH	-25.5 180.0 0.0	20.00	
17	1:14:46:00	LVLH	43.7 -51.4 37.6	20.00	
18	1:15:06:00	LVLH	25.5 0.0 0.0	20.00	
19	1:19:26:00	LVLH	23.0 0.0 0.0	11.30	RETRIEVAL 1
20	1:21:27:00	LVLH	25.0 0.0 0.0	3.40	
21	1:21:46:00	LVLH	29.0 0.0 0.0	2.80	
22	1:21:50:00	LVLH	33.0 0.0 0.0	2.70	
23	1:22:04:00	LVLH	37.5 0.0 0.0	2.50	
24	1:23:13:00	LVLH	123.1 43.4 -133.5	2.40	ON- STATION 2
25	1:23:13:00	LVLH	-37.5 180.0 0.0	2.40	
26	1:23:33:00	LVLH	123.1 -43.4 0.0	2.40	
27	2:01:23:00	LVLH	37.5 0.0 0.0	2.40	
28	2:01:43:00	LVLH	0.0 0.0 0.0	2.40	
29	2:02:03:00	LVLH	-10.0 0.0 0.0	2.10	RETRIEVAL 2
30	2:03:51:00	LVLH	-20.0 0.0 0.0	1.81	
31	2:03:53:30	LVLH	-30.0 0.0 0.0	1.60	

Tether Vent Computation

The ability to maintain an accurate state vector during TSS-1 operations depends upon accurately modeling the external forces acting on the orbiter. An analytical approach for determining the magnitude of the forces acting on the orbiter was formulated. The technique utilizes characteristics of the tethered system and in brief, can be viewed as the sum of the earth's gravitational force and the centrifugal force on the orbiter due to a rotating system and can be computed by ;

$$F = 3 \times M \omega^2$$

where

F = tether force in the radial direction

X = distance between the orbiter's center of mass and
the tether system center of mass

M = mass of the orbiter

ω = angular velocity of the tether system center of mass

A set of mass properties were assumed for the orbiter and the satellite. The orbiter's mass and area were 6670.11 slugs and 2690 sq.ft., respectively. The satellite's mass was assumed as 37.69 slugs. The tether was assumed to have length of 20 km when fully deployed, its density was roughly 0.0001744 lb/ft. Given these initial conditions the tethered system's center of mass (c.m.) is roughly 424 feet radially above the orbiter's when the satellite is fully deployed. Using the analytical algorithm the magnitude of the force acting on the orbiter was computed as,

$$F_{\text{TETHER}} = 11.37 \text{ lbf}$$

Inherent in the MCC Trajectory applications exist the capability to solve for all of the external forces acting on the orbiter as reflected in the tracking measurements. The forces are computed in Shuttle body reference coordinates and utilizes the SB technique. Selecting an arc of tracking measurements during the onstation phase of the mission, the MCC solve-for force function computed the following forces,

$$F_x = 4.43 \text{ lbs} \quad \& \quad F_z = -9.90 \text{ lbs}$$

A limitation however, exist in the solve-for force tool. This important tool tries to solve for a constant force which is not the case during satellite deployment and retrieval. These phases of the TSS-1 profile are very dynamic with significant changes in the magnitude of the tether forces coupled with excessive pulses from the Reaction Control System (RCS) required to maintain prescribed attitudes. The RCS profile for the nominal mission profile is shown in Figure (1). It is not recommended that the solve for force technique be used during these dynamic periods, but instead utilize the analytical technique.

Navigation Results (Nominal Flight Profile)

The following section highlights the results of an analysis which determines the impacts to state vector accuracies when processing tracking measurements about the nominal TSS-1 mission profile. Of emphasis will be noted the impacts to navigation state vector accuracies when the tether forces were and were not modeled. Table (2) provides the tether force timeline used in the analysis.

Table 2
TETHER FORCE TIMELINE (Nominal Profile)

VENT	START TIME	END TIME	FX_LBS	FY_LBS	FZ_LBS
1	01:00:00:00	01:00:35:59	-0.50	0.00	0.00
2	01:00:36:00	01:01:45:59	0.10	0.00	-0.60
3	01:01:46:00	01:02:38:29	0.00	0.00	-1.60
4	01:02:38:30	01:03:44:59	2.00	0.00	-3.90
5	01:03:45:00	01:04:55:29	3.60	0.00	-7.40
6	01:04:55:30	01:16:29:59	4.30	0.00	-8.90
7	01:16:30:00	01:18:29:59	3.60	0.00	-7.40
8	01:18:30:00	01:20:14:59	2.80	0.00	-5.60
9	01:20:15:00	01:22:03:59	1.40	0.00	-2.50
10	01:22:04:00	02:02:02:59	0.70	0.00	-0.80
11	02:02:03:00	02:03:44:29	0.00	0.00	-1.00
12	02:03:44:30	02:05:30:00	0.00	0.00	-0.50

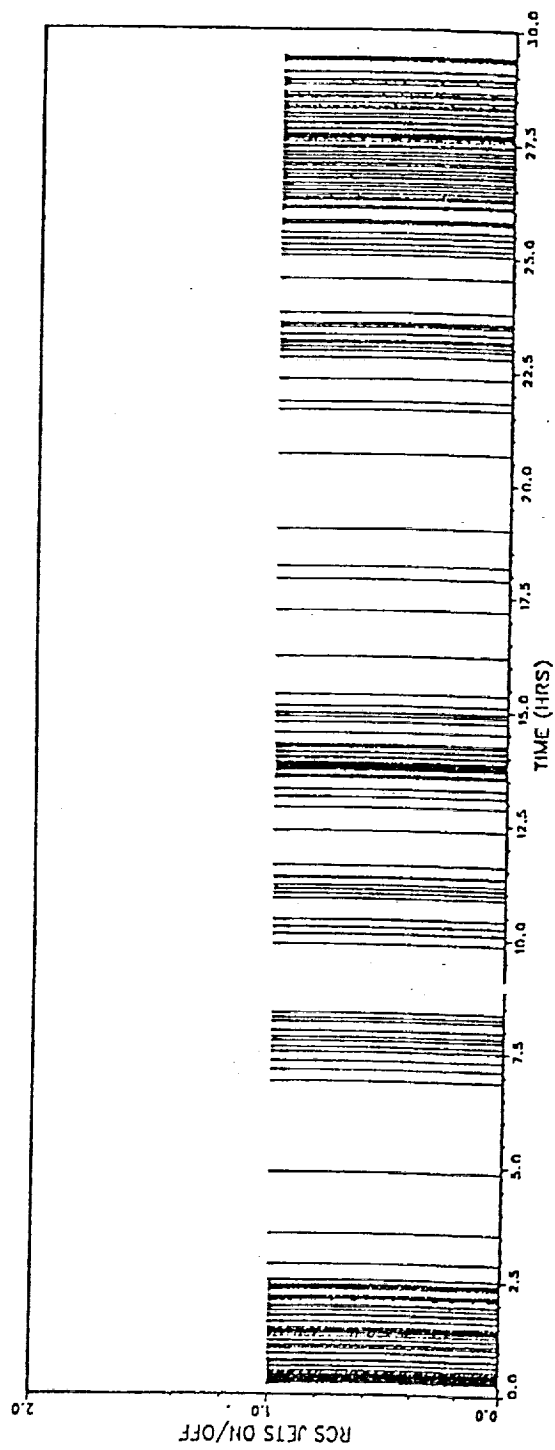


Fig. 1 RSC Profile (Nominal Mission)

Experience has shown that confidence in the knowledge of the orbiter's trajectory is determined by the stability observed in the changes in semimajor axis. Figures (2) and (3) provide plots of the magnitude of the change in semimajor axis denoted for each BB solution considered in the set of tracking measurement when the tether forces were not and were modeled, respectively. Taking note of the erratic signature displayed in Figure (2), the changes in semimajor axis appear very unstable with magnitudes that vary between 0 ft to 375 ft. Figure (3), on the other hand, shows that the magnitude of the changes in semimajor axis can be reduced by modeling the tether forces. Changes in semimajor axis observed in both plots during satellite deployment and retrieval are attributed to the occurrence of high amounts of RCS activity and the many attitude maneuvers seen over these periods.

To determine the error in each of the BB solution state vectors which were computed, a comparison was made with the reference ephemeris defined by STOCs. The set of ephemerides chosen for the compares were selected such that their timetags were within 30 seconds of the associating solution state vector.

A correlation between tether length, tension, attitude maneuvers, and the computed error in semimajor axis is noted in Figure (4). The magnitude of the error in general was roughly three to four times that of the center of gravity offset. This reinforces the fact that the BB solution state vectors were those computed to reflect a state about the c.g. of the system. Figure (5) shows the magnitudes of the error in semimajor axis resulting when the tether forces were modeled. As can be readily noticed, a significant reduction is made in the magnitudes of these errors.

Figure (6) through (11) show plots of the errors in the instantaneous position components resulting when the tether forces were and were not modeled. Of important note that should be mentioned when viewing these particular plots is that the c.g. offset manifests itself as an error in radial position when the forces are not modeled. The average error in radial position as shown in Figure (6) was roughly 471 ft, the c.g. offset at satellite full deployment is 424 ft. Further, when the forces are not modeled an extreme degradation in the knowledge of downtrack position is evident see (Figure (8)) and consequently, the ability to comfortably support contingency operations suffer. Figures (12) and (13) show the error seen in total position.

Ground State Vector Propagation Analysis

The MCC Ground Navigation section plays a very important role during the deorbit timeframe. Flight rules which govern the navigation accuracies required for a safe deorbit are strictly followed to assure crew safety. Current criteria dictates that the downtrack position error seen in the onboard navigation state will not exceed 20 nautical miles at the time of the deorbit burn. Acknowledging the fact that the TSS-1 mission is extremely complex, contingency plans and navigation accuracies which support them were analyzed.

The deorbit preparation timeframe starts approximately four revolutions prior to the deorbit burn. A preliminary state vector is provided to the FDO for computations necessary for the deorbit burn. A final state vector is delivered during the deorbit revolution. Given the nature and complexity of the TSS-1 mission, Ground Navigation flight controllers should be prepared at all times to support a contingency deorbit.

To satisfy the requirements levied by the flight rule which is mentioned above, validity tests were performed using the BB solution state vectors computed for each of the BB chains.

For the test, a selected set of solution state vectors from each BB chain were propagated for four revolutions and then compared to a corresponding state vector at the end of the propagation interval as defined by STOCS. Modeling of the tether forces were performed in the propagation interval for those vectors computed using the forces shown in Table (2).

Figure (14) provides plots of the magnitude of the error in semimajor axis resulting after the propagation of the solution state vectors computed for the two chains. The anchor time for the vectors used in this study are noted in Table (3). The plot readily shows the significant reduction in the magnitude of the error in semimajor axis when the tether forces are modeled. The magnitude of the error in semimajor axis remains about four times the c.g. offset for those vectors selected during satellite deploy and onstation operations when the forces are not modeled. The ground Navigation section strives to minimize the error in semimajor axis when tasked to provide state vectors to assist in trajectory planning.

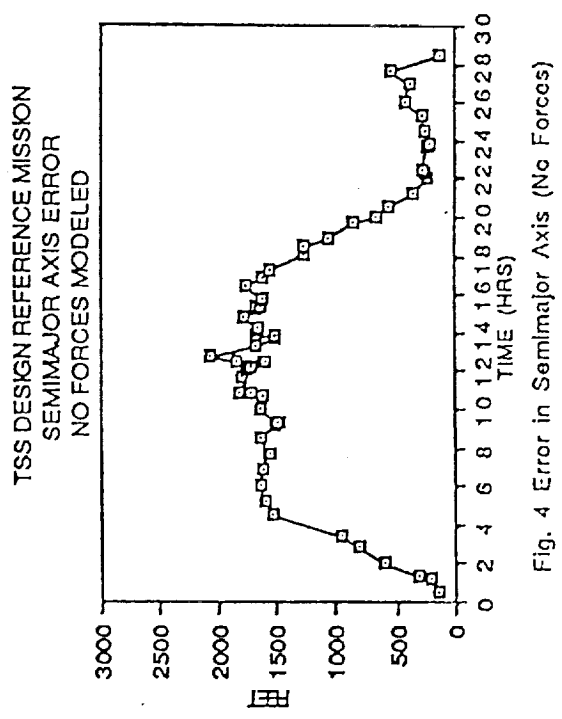
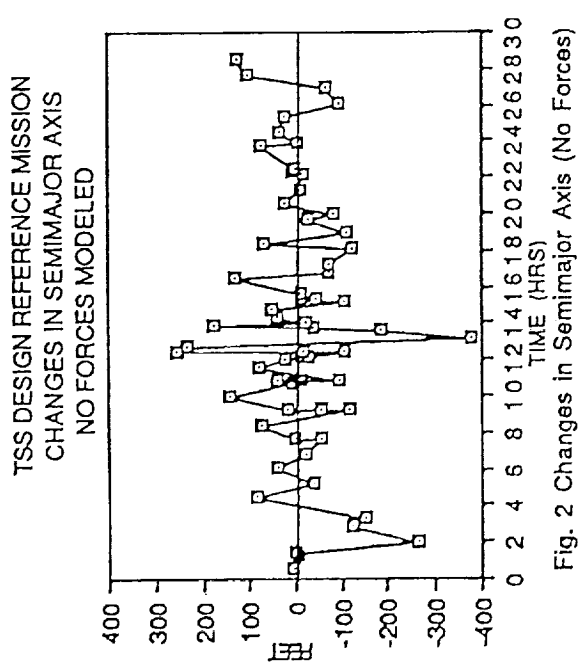
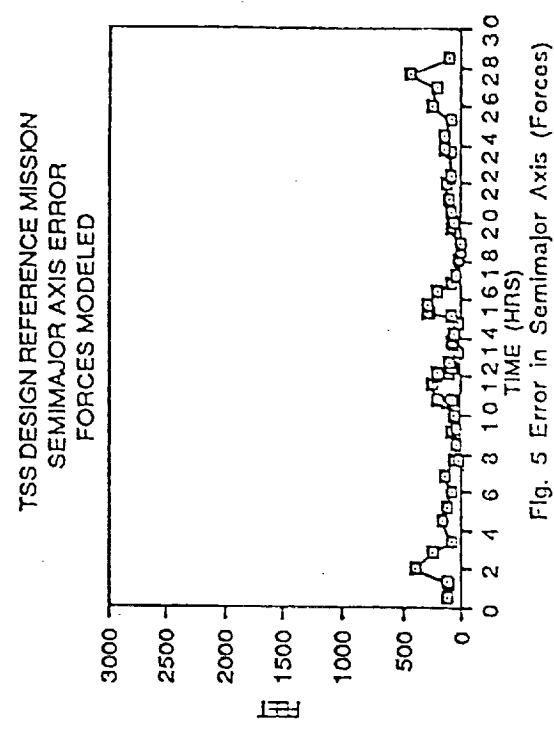
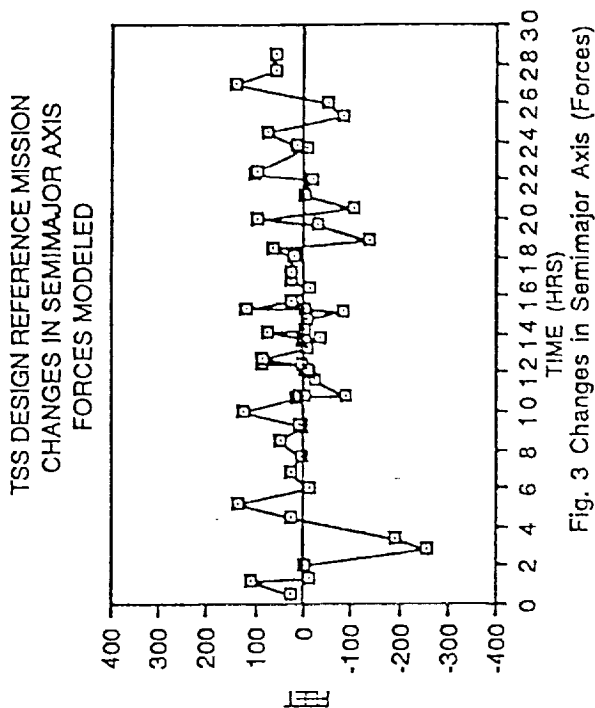
Figure (15) shows the magnitude of the error in downtrack position resulting after each state vector propagations. As is expected, a correlation is seen between the error in semimajor axis and the downtrack position error for the two chains. Although the 20 nautical mile downtrack error criteria is not violated for either case, the case in which the tether forces were modeled provides the accuracies in both semimajor axis and downtrack position and thus may be confidently used for trajectory planning.

Table (3)
VECTOR PROPAGATION TIMES

PROP NO.	MET
1	00:33:00
2	02:01:00
3	03:37:00
4	05:14:20
5	06:51:00
6	08:27:40
7	10:03:40
8	11:39:00
9	13:15:00
10	15:15:28
11	18:05:00
12	19:41:40
13	22:07:40

Tether Cut Analysis

Given the complexity and technical unknowns associated with the TSS-1 mission, off-nominal mission scenarios needed to be analyzed. The scenario which will be discussed in this section addresses the ability of the Navigation section to successfully provide accurate solution state vectors in the event the tethered is cut voluntarily or involuntarily. The physical properties of the tethered system concludes that when the tether is cut, a decrease in orbital energy results in the Shuttle's trajectory. The following analysis addresses the



TSS DESIGN REFERENCE MISSION
RADIAL POSITION ERROR
NO FORCES MODELED

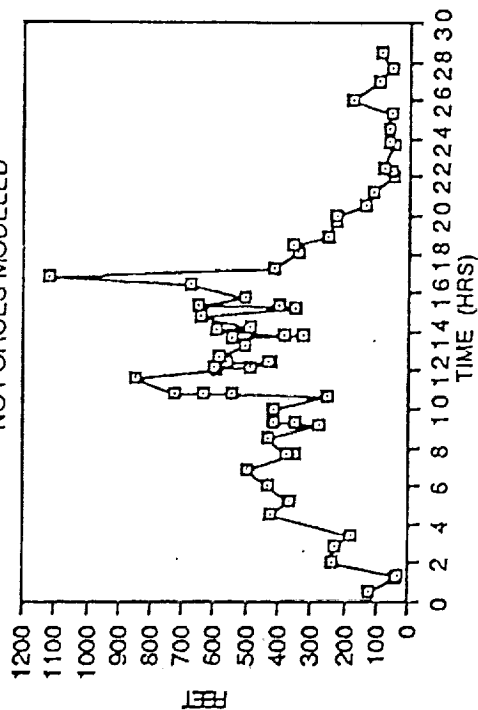


Fig. 6 Radial Position Error (No Forces)

TSS DESIGN REFERENCE MISSION
DOWNTRACK POSITION ERROR
NO FORCES MODELED

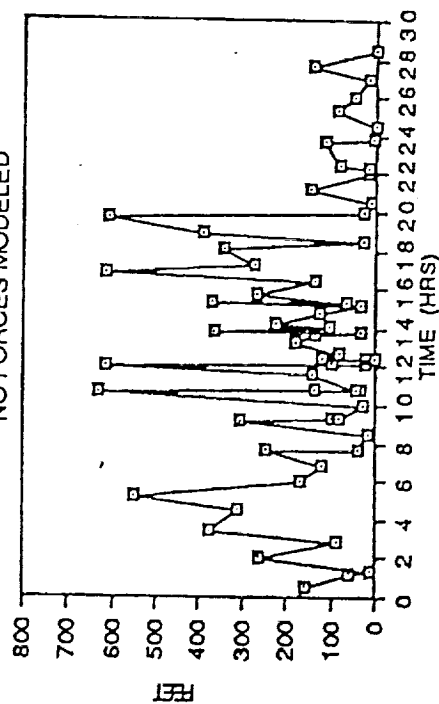


Fig. 8 Downtrack Position Error (No Forces)

TSS DESIGN REFERENCE MISSION
RADIAL POSITION ERROR
FORCES MODELED

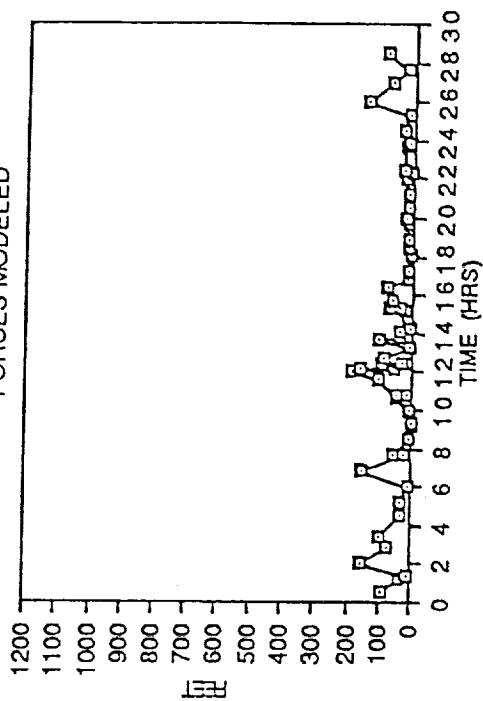


Fig. 7 Radial Position Error (Forces)

TSS DESIGN REFERENCE MISSION
DOWNTRACK POSITION ERROR
FORCES MODELED

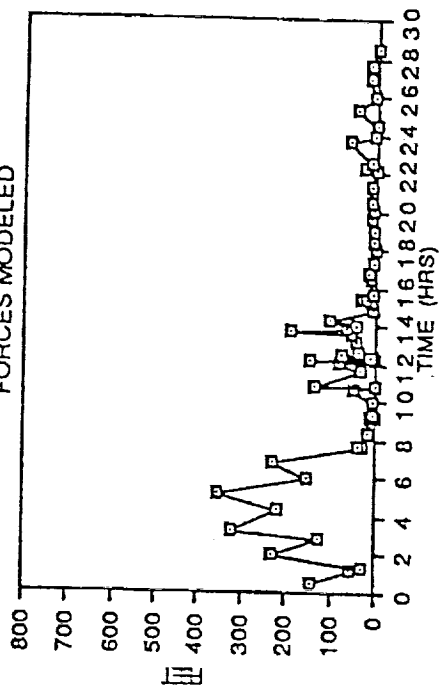


Fig. 9 Downtrack Position Error (Forces)

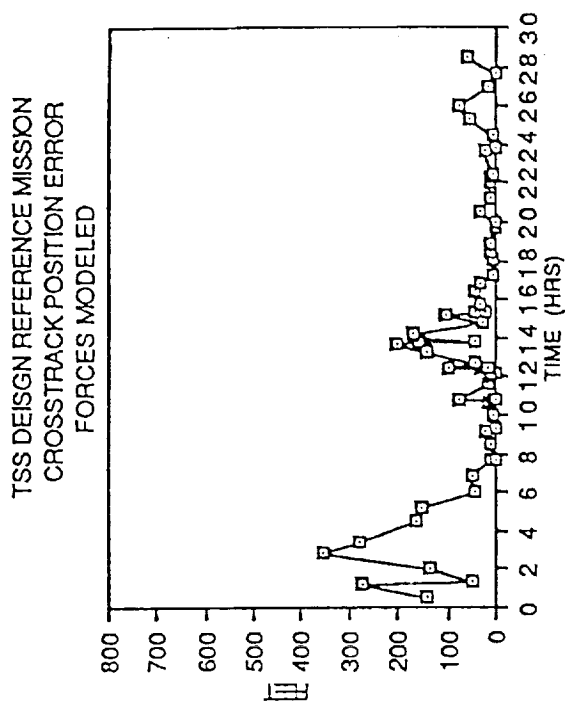


Fig. 11 Crosstrack Position Error (Forces)

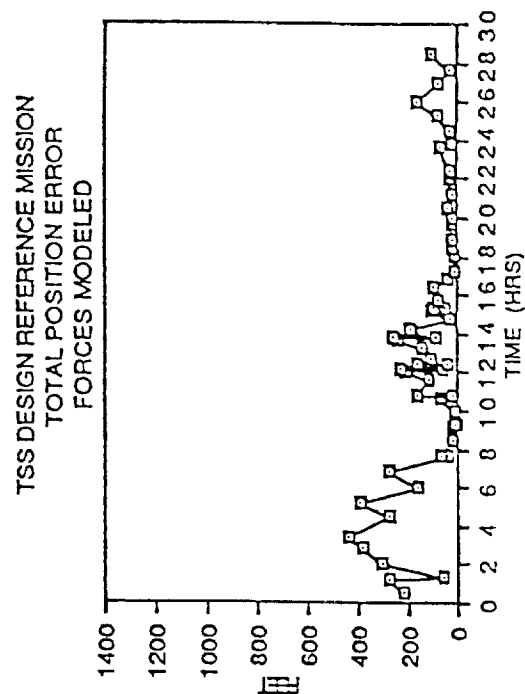


Fig. 13. Total Position Error (Forces)

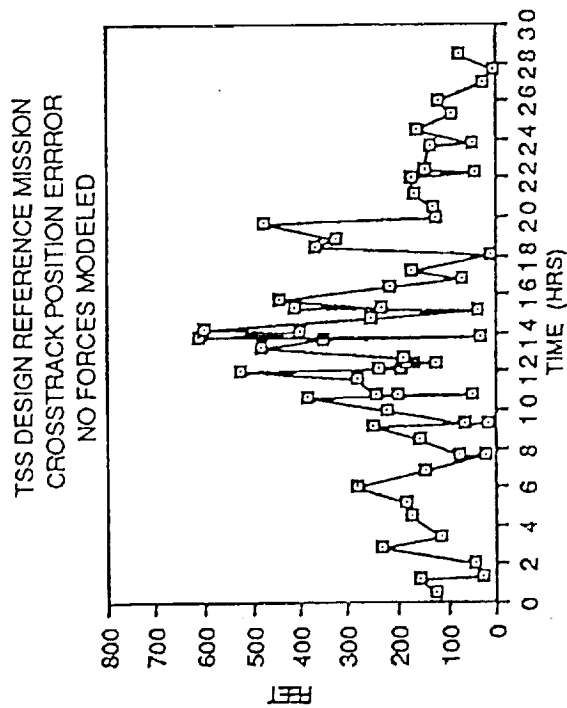


Fig. 10 Crosstrack Position Error (No Forces)

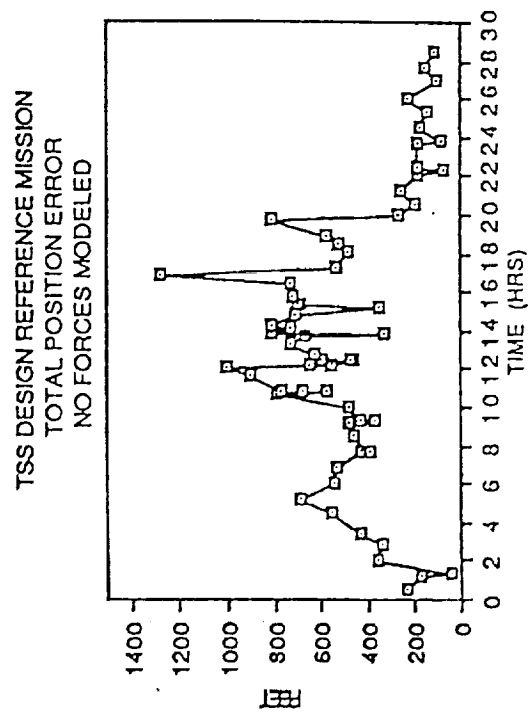


Fig. 12 Total Position Error (No Forces)

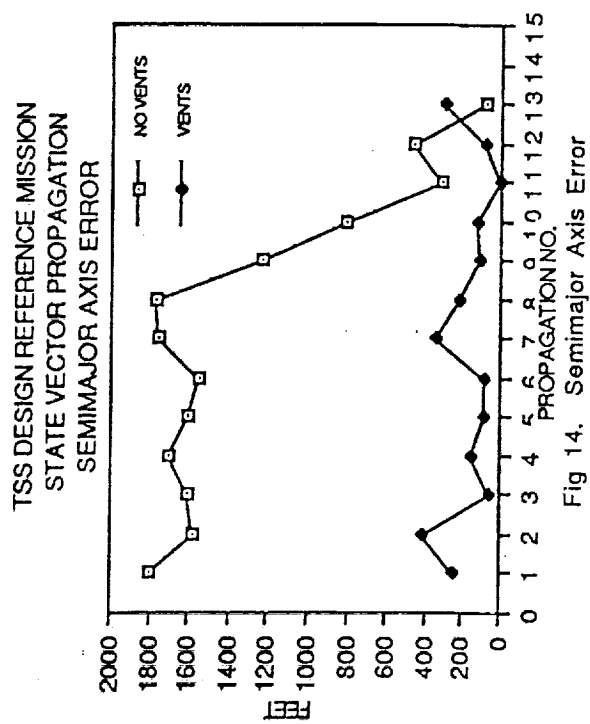


Fig 14. Semimajor Axis Error

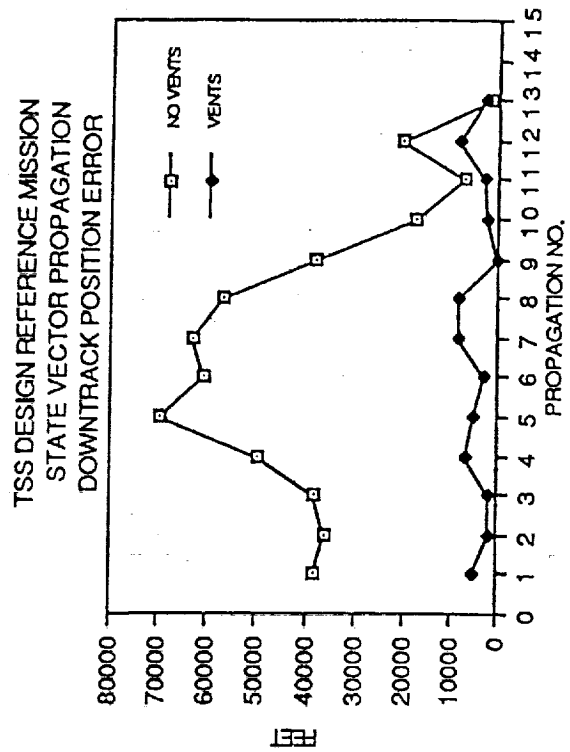


Fig 15. Downtrack Position Error

amount of time required to determine the new trajectory as reflected in the tracking measurements. The analysis includes discussions of the results of a tether cut at 5, 10, 15, and 20 km. The occurrence of the tether cuts are depicted in Figure (16).

The analysis was performed with the aid of tracking measurements computed using both STDS and the Houston Operations Predictor Estimator (HOPE) programs. STDS was used for the creation of the tracking measurements which included tether induced perturbations prior to the tether cut. HOPE was used to create the tracking measurements after the tether cut and utilized a state vector as defined by STOCs which coincided with the time of the tether cut. The tracking measurements were merged to create one master tracking data file and were processed in the BB mode with and without the tether forces being modeled.

In each of the cases analyzed, the stop time of the modeled tether force coincided with the time of the tether cut. The assumption used in this scenario was that the tether forces' stop time modeled in the Ground Navigation software could be readily modified to reflect the actual time of the cut during real-time operations. This assumption was also adopted when assessing the Onboard Navigation system performance. However, the onboard tether force will not likely be zeroed at the exact time of the tether cut due a combination of ground flight controller and crew interventions necessary in accomplishing this task. Each case was therefore analyzed to determine what were the net effects if the tether forces were never zeroed out and represents a three sigma procedural scenario.

Basic orbit mechanics dictates that the position at which the tether cut occurs will become the new apogee for the Shuttle's orbit. The perigee will be defined 180 degrees away from the tether cut, see Figure (17). The tether cut introduces an instantaneous removal of the tether tension. This analysis will show that when the tether forces are not modeled in the navigation software, the instantaneous removal of tether tension appears as a semimajor axis change in the solution state equal to roughly four times the c.g. offset distance. The analysis will also show that when the tether forces are modeled in the timeframe prior to the tether cut and properly zeroed out that a smooth transition to the new orbit can be achieved.

Trajectory Analysis (Tether Cut)

The results of BB processing for the error in semimajor axis are shown in Figure (18) through (21). The error is computed when a comparison is made between each BB solution and a chosen ephemeris vector. For the case in which tether forces were modeled, the forces were modeled only at the times prior to the tether cut. The plots readily show that a smooth transition to the new orbit is achieved upon accurately modeling the tether forces prior to the cut. For the cases in which the forces were not modeled the resulting error in semimajor axis is directly proportional to the length at which the tether is cut. As is shown when the tether length is 20 km, a large error results for the case in which the forces were modeled. The error can be attributed not only to the inaccuracies in the BB solution state vectors computed, but also the impact of high RCS activity as is shown in Figure (1).

In determining whether the Flight Rule which governs the navigation state vector accuracies in the event of a Loss of Communication between the ground and the Shuttle, a two revolution navigation accuracy analysis was performed. Each case was analyzed to determine when the 20,000 ft predicted downtrack position error criteria was violated.

For the chains in which the tether forces were not modeled the criteria was violated in a very short time. In the case at which the cut occurred at 20 km, the violation occurred within one orbital revolution. Whereas for the 5 km case, the violation was delayed for just over two revolutions. When however, the tether forces were modeled the magnitude of the

downtrack error prediction in two revolution resulting after the cut was minimized. In these cases, no update would be required to the reference ground ephemeris following the tether cut given the smooth transition to the new orbit as displayed in Figure (22) through (25).

Each of the BB chains for the tether length analyzed were compared against truth vectors as defined by STOCS and HOPE during pre-and post tether cut phases, respectively. Figures (26) through (29) show the error in semimajor axis resulting after each vector compare. The statistics show the magnitude of the the error in each solution when compared to the orbiter's true position and also the time required to recover a ground solution of the quality necessary to support trajectory planning. For the cases in which the tether forces were not modeled prior to the cut, the solution converged within a rev after the cut. For the four cases which acknowledged the tether forces, the solution remains very close to the truth and no recovery time is necessary. The error in total position for the the chains are shown in Figures (30) through (33).

Conclusions

The TSS-1 mission will indeed be a challenging undertaking for the STS program. The dynamics which are expected during tethered operations will require that new real-time navigation flight procedures be developed to meet all mission objectives and to assure crew safety. The results have shown that with proper modeling of the tether forces acting on the orbiter, accurate prediction of the true state of the orbiter can be maintained under both nominal and off-nominal flight conditions. This will not be a trivial task and will require that pertinent systems information be made readily available to the navigation team during TSS-1 operations. Precise coordination between ground flight controllers and the crew must be maintained to properly monitor the true state of the orbiter. This can only be accomplished through extensive training in an integrated MCC simulation environment.

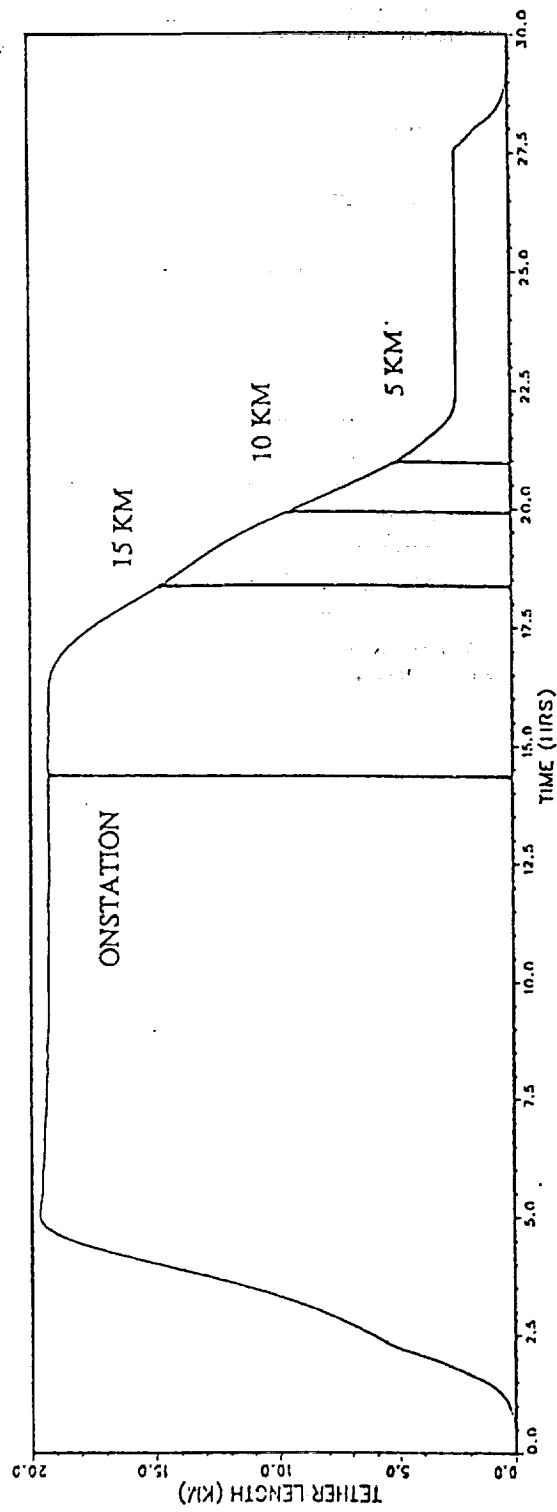


Fig 16. Tether Length VS. Time

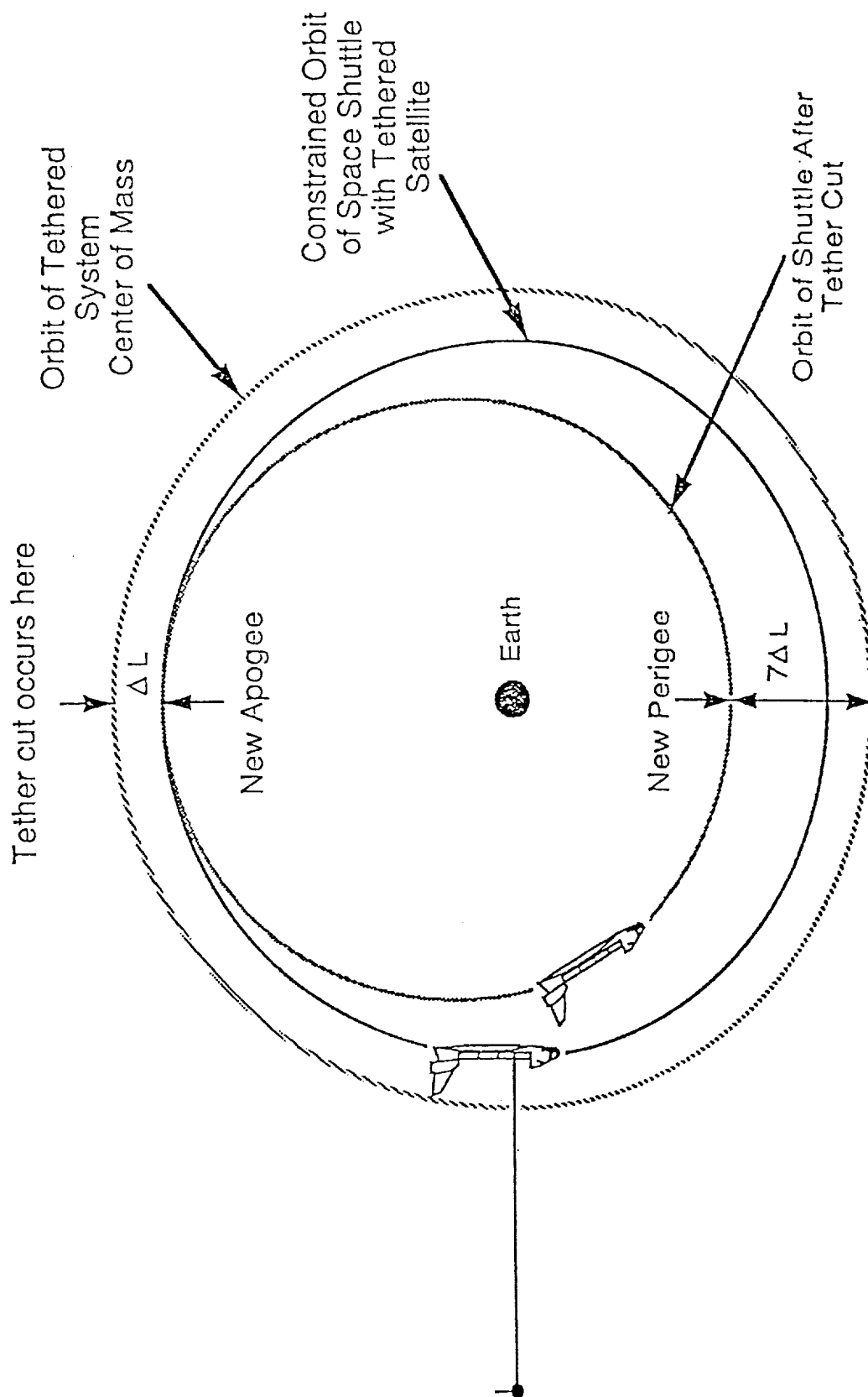


Fig 17. Orbits Defined After Tether Cut

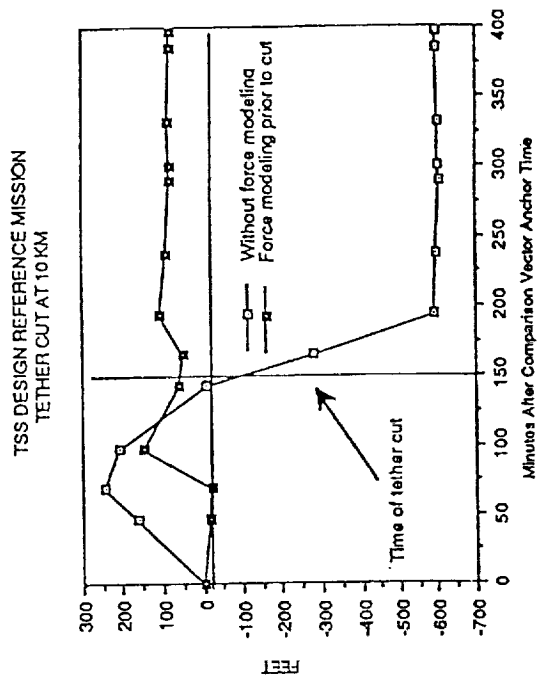


Fig 19. Semimajor Axis Error (Length - 10 km)

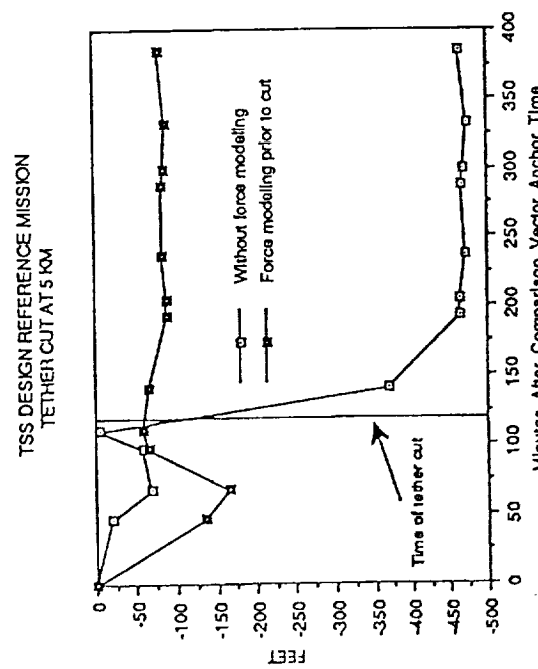


Fig 18. Semimajor Axis Error (Length - 5 km)

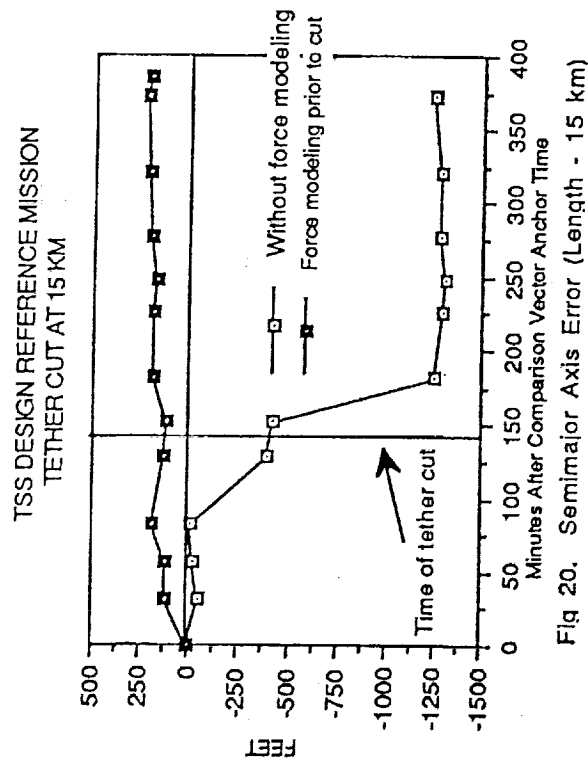


Fig 20. Semimajor Axis Error (Length - 15 km)

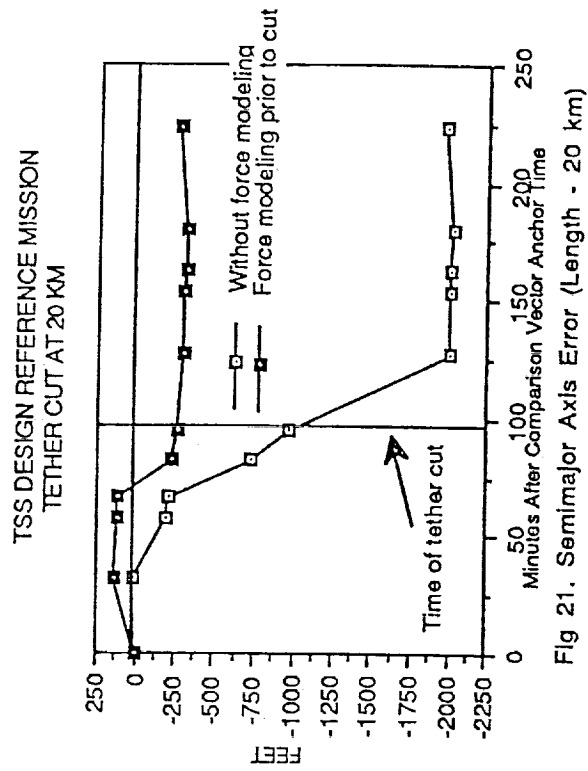


Fig 21. Semimajor Axis Error (Length - 20 km)

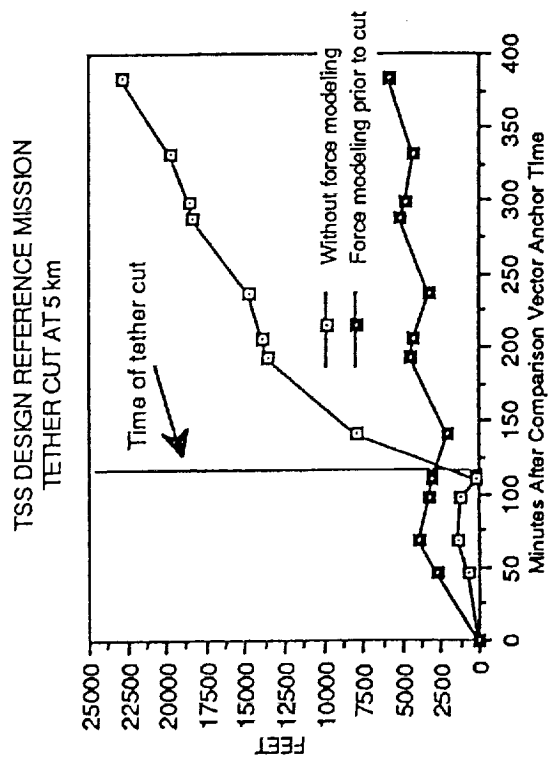


Fig. 22 Downtrack Error 2 Rev's (Length - 5 km)

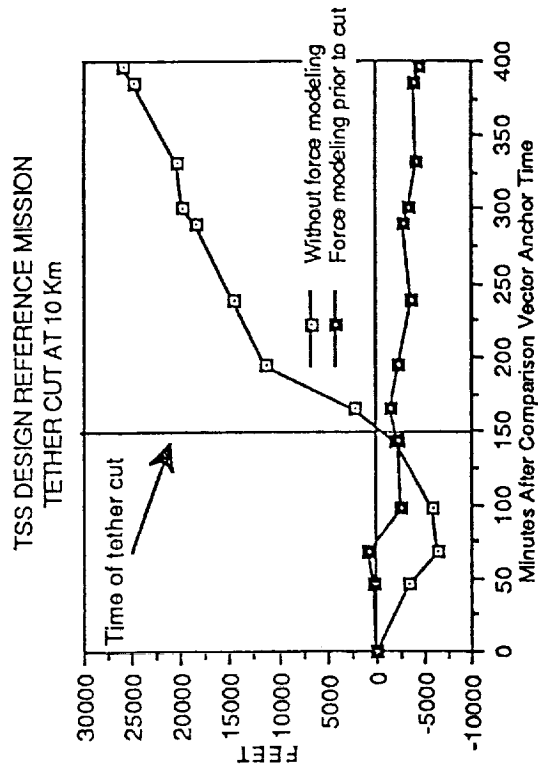


Fig 23. Downtrack Error 2 Rev's (Length - 10 km)

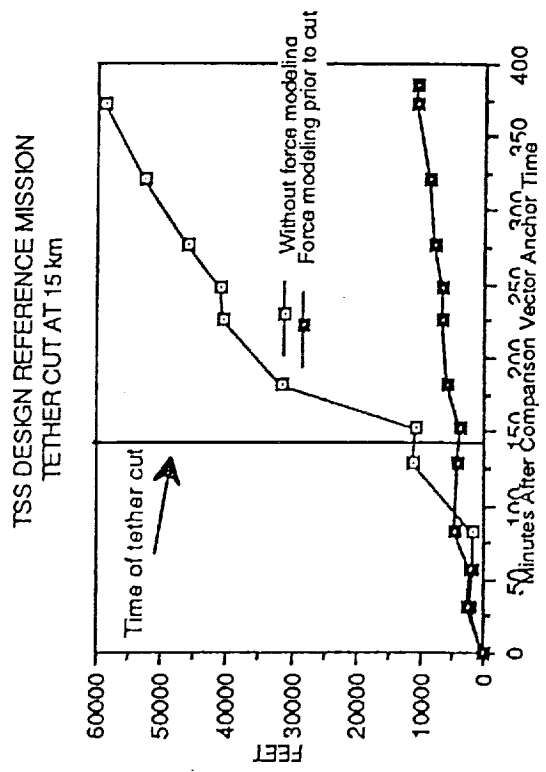


Fig. 24 Downtrack Error 2 Rev's (Length - 15 km)

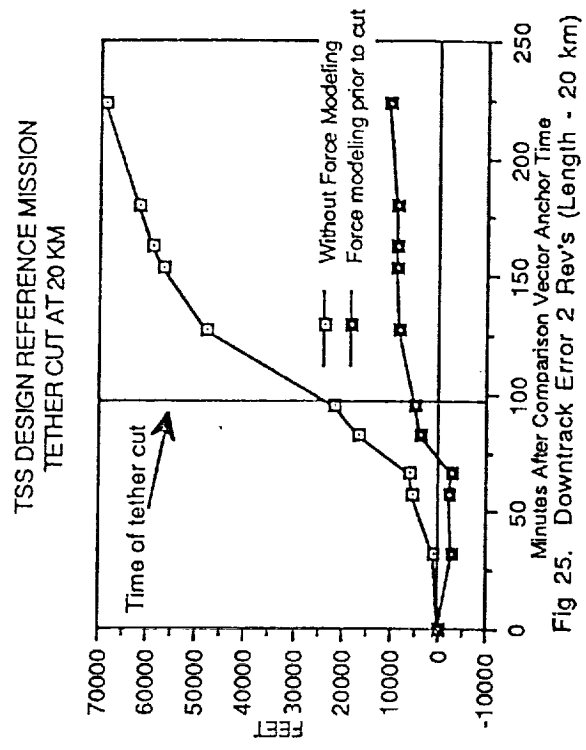


Fig 25. Downtrack Error 2 Rev's (Length - 20 km)

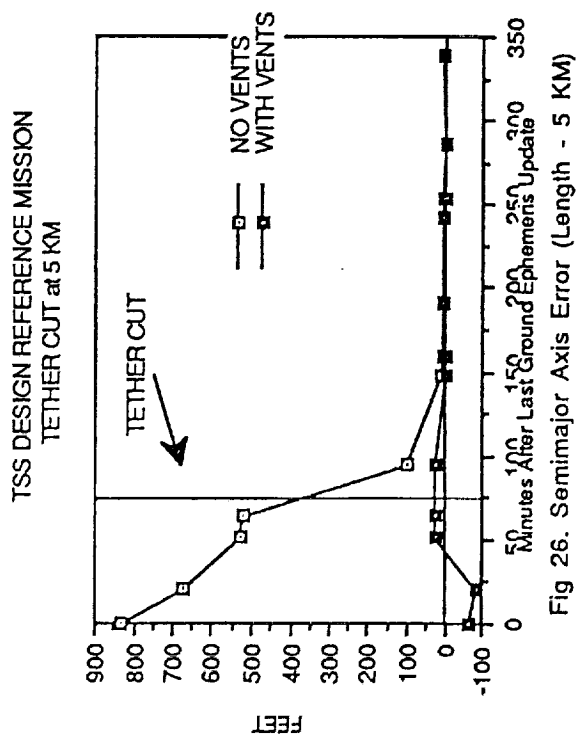


Fig 26. Semimajor Axis Error (Length - 5 KM)

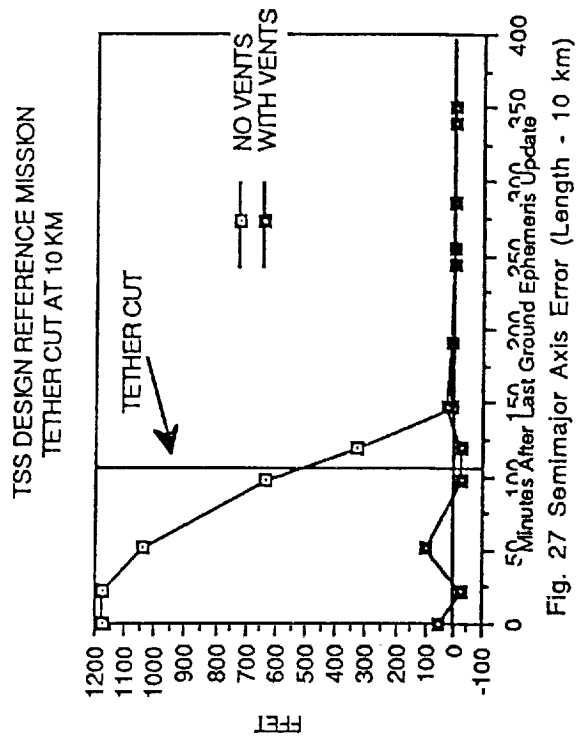


Fig. 27 Semimajor Axis Error (Length - 10 km)

TSS DESIGN REFERENCE MISSION
TETHER CUT AT 15 KM

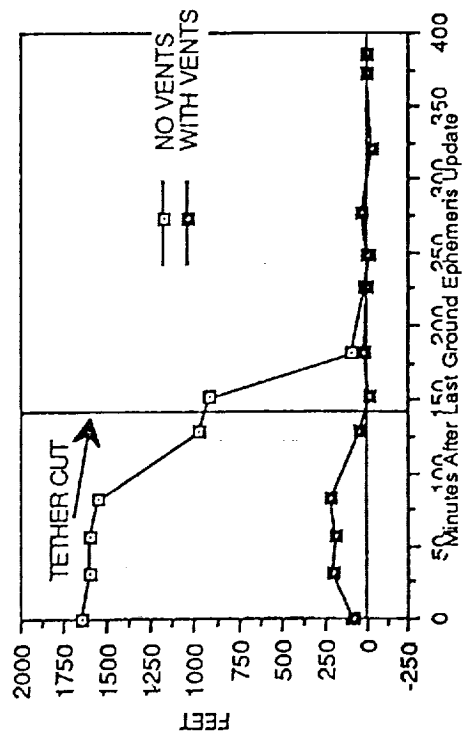


Fig. 28 Semimajor Axis Error (Length - 15 km)

TSS DESIGN REFERENCE MISSION
TETHER CUT AT 20 KM

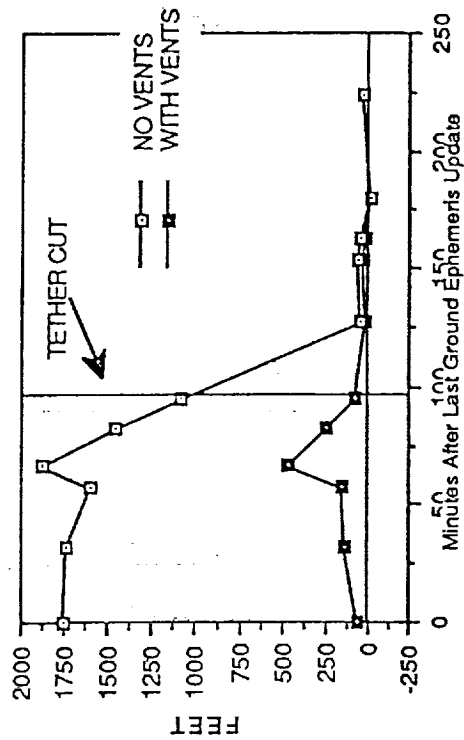


Fig. 29. Semimajor Axis Error (Length - 20 km)

TSS DESIGN REFERENCE MISSION
TETHER CUT AT 5 KM

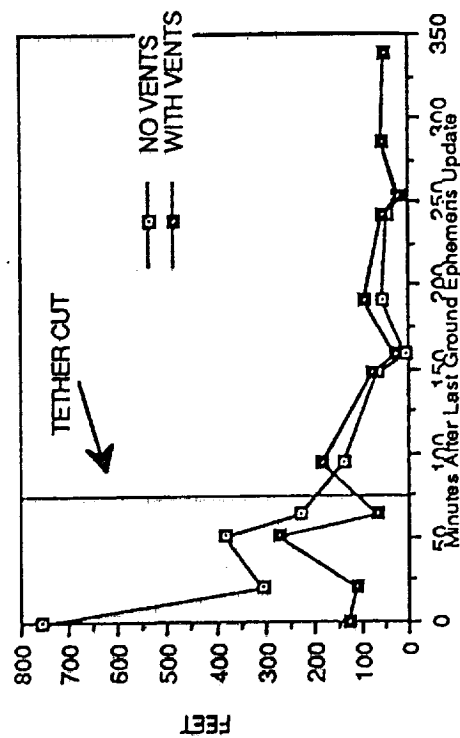


Fig. 30 Total Position Error (Length - 5 km)

TSS DESIGN REFERENCE MISSION
TETHER CUT AT 10 KM

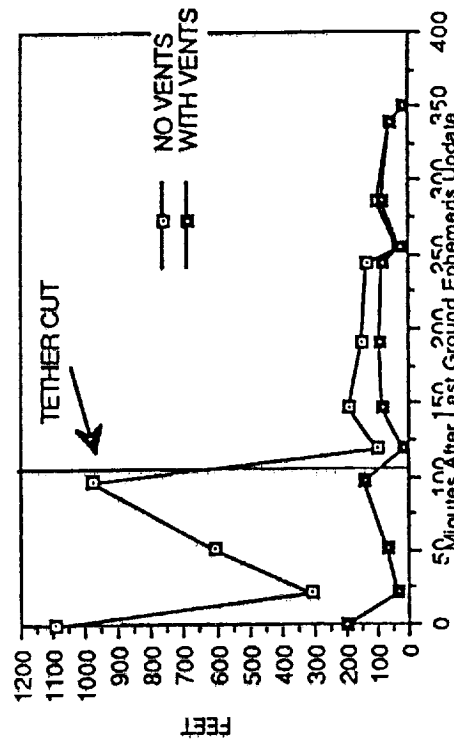


Fig. 31 Total Position Error (Length - 10 km)

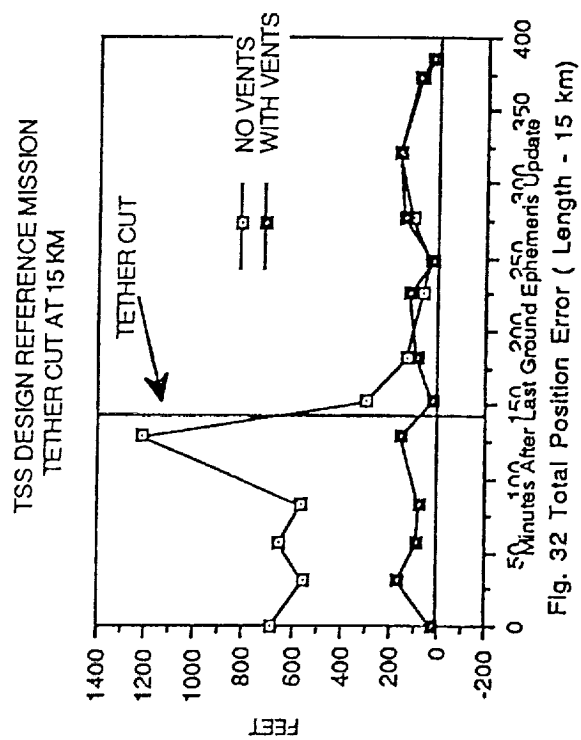


Fig. 32 Total Position Error (Length - 15 km)

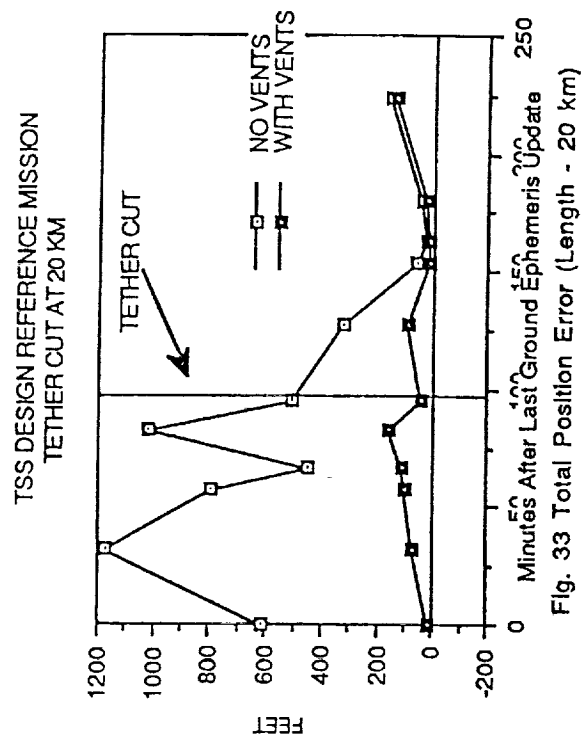


Fig. 33 Total Position Error (Length - 20 km)

References

1. Zimmerman, P.L., "Impacts of Tether Cutting on Ground Navigation", August 22, 1990, STSOC Transmittal Form #FDD-NAV-640-90-041.
2. National Aeronautics and Space Administration, "STS Operational Flight Rules", January 20, 1989, Document No. JSC-12820.
3. Zimmerman, P., "Generation of Tether Cut Tracking Data Files for use with SONAV", May 10, 1990, STSOC Transmittal Form #FDD-NAV-640-90-024.
4. Hass, L., "Ground Navigation Vent Modeling of the Tethered Satellite System", April 25, 1990, STSOC Transmittal Form #FDD-NAV-620-90-018.
5. Jackson, T.C., "Ground Navigation Analysis of TSS-1", July 19, 1990, STSOC Transmittal Form #FDD-NAV-640-90-053.

FLIGHT MECHANICS/ESTIMATION THEORY SYMPOSIUM

MAY 21-23, 1991

SESSION 2

NEW QUESTS FOR BETTER ATTITUDES

Malcolm D. Shuster

The Johns Hopkins University, Applied Physics Laboratory,
Laurel, Maryland 20723-6099

ABSTRACT

During the past few years considerable insight has been gained into the QUEST algorithm both as a maximum-likelihood estimator and as a Kalman filter/smoothen for systems devoid of dynamical noise. This conference contribution describes the new algorithms and software and makes analytic comparisons with the more conventional attitude Kalman filter. We also describe how they may be accommodated to noisy dynamical systems.

Introduction: the QUEST Algorithm

The QUEST algorithm is based on a least-square problem first proposed in 1965 by Grace Wahba, then a graduate student in Statistics at George Washington University and working during that summer for IBM in Gaithersburg, Maryland. The problem, which appeared in *SIAM Review* [1], was, in fact, Wahba's first publication. In it she posed the problem of finding the attitude which minimizes the loss function

$$L(A) = \frac{1}{2} \sum_{i=1}^n a_i |\hat{\mathbf{W}}_i - A \hat{\mathbf{V}}_i|^2, \quad (1)$$

where $\hat{\mathbf{W}}_i, i = 1, \dots, n$, are a set of unit-vector observations in the spacecraft-fixed reference frame, and $\hat{\mathbf{V}}_i, i = 1, \dots, n$, are the representations of the same unit vectors with respect to the primary reference frame (the frame to which the attitude is referred). The a_i are a set of non-negative weights. Provided that at least two of the observation vectors are not parallel (or anti-parallel) and the corresponding weights are positive, a unique minimizing attitude matrix will always exist. Dozens of solutions have been proposed to find this attitude matrix, of which the fastest currently and most frequently used is the QUEST algorithm [2], based on the q -algorithm of Davenport [3].

To solve for the optimal attitude we first write equation (1) in the form

$$L(A) = \sum_{i=1}^n a_i - \sum_{i=1}^n a_i \hat{\mathbf{W}}_i \cdot A \hat{\mathbf{V}}_i, \quad (2)$$

$$= \sum_{i=1}^n a_i - g(A). \quad (3)$$

The gain function, $g(A)$, may be further manipulated to give

$$g(A) = \text{tr}(B^T A), \quad (4)$$

where B , the attitude profile matrix, is given by

$$B = \sum_{i=1}^n a_i \hat{\mathbf{W}}_i \hat{\mathbf{V}}_i^T. \quad (5)$$

The minimization of $L(A)$ is equivalent to the maximization of $g(A)$.

We now note that $g(A)$ is linear in A . Nonetheless, the minimization of $g(A)$ is not simple because the 3×3 matrix A is subject to six nonlinear constraints. Thus, the minimization of $g(A)$ over A is not necessarily simple.¹ The attitude matrix, however, can be written as a quadratic function of the quaternion,

$$\bar{\mathbf{q}} = [q_1, q_2, q_3, q_4]^T = \begin{bmatrix} \mathbf{q} \\ q_4 \end{bmatrix}, \quad (6)$$

namely,

$$A(\bar{\mathbf{q}}) = (q_4^2 - \mathbf{q} \cdot \mathbf{q}) I_{3 \times 3} + 2\mathbf{q}\mathbf{q}^T + 2q_4 [[\mathbf{q}]], \quad (7)$$

where

$$[[\mathbf{q}]] \equiv \begin{bmatrix} 0 & q_3 & -q_2 \\ -q_3 & 0 & q_1 \\ q_2 & -q_1 & 0 \end{bmatrix}. \quad (8)$$

Defining further the quantities

$$S = B + B^T, \quad s = \text{tr } B, \quad [[\mathbf{Z}]] = B - B^T, \quad (9)$$

the gain function may be rewritten in terms of the quaternion as

$$g(\bar{\mathbf{q}}) \equiv g(A(\bar{\mathbf{q}})) = \bar{\mathbf{q}}^T K \bar{\mathbf{q}}, \quad (10)$$

where

$$K = \begin{bmatrix} S - s I_{3 \times 3} & \mathbf{Z} \\ \mathbf{Z}^T & s \end{bmatrix}. \quad (11)$$

¹Not all students of the Wahba problem will agree, as shown by Markley [4].

The maximization of this gain function, subject to the constraint that the quaternion have unit norm, leads to an eigenvalue equation for \bar{q}^* , the optimal quaternion, which is [2, 3]

$$K \bar{q}^* = \lambda_{\max} \bar{q}^*, \quad (12)$$

where λ_{\max} is the largest eigenvalue of K . Thus, the optimal quaternion may be found by solving this 4×4 eigenvalue problem and choosing the eigenvector with the largest eigenvalue. This is Davenport's q -method, which was applied in this form to the HEAO mission [5].

The QUEST algorithm, a very fast implementation of Davenport's q -method which avoids the complete solution of the eigenvalue problem, is formulated in terms of the Gibbs vector, \mathbf{Y} ,

$$\mathbf{Y} \equiv \mathbf{q}/q_4. \quad (13)$$

In terms of the Gibbs vector the optimal attitude may be written as

$$\mathbf{Y}^* = [(\lambda_{\max} + s) I_{3 \times 3} - S]^{-1} \mathbf{Z}, \quad (14)$$

and the optimal quaternion then reconstructed as

$$\bar{q}^* = \frac{1}{\sqrt{1 + |\mathbf{Y}^*|^2}} \begin{bmatrix} \mathbf{Y}^* \\ 1 \end{bmatrix}. \quad (15)$$

Key to the QUEST algorithm is the fact that a very good first approximation of the optimal attitude (accurate to $O(\sigma^4)$, where σ is the standard deviation of a typical sensor error) may be obtained by substituting $\lambda_{\max}^{(o)}$ for λ_{\max} , with

$$\lambda_{\max}^{(o)} \equiv \sum_{i=1}^n a_i. \quad (16)$$

It is easy to show that

$$\lambda_{\max} = \lambda_{\max}^{(o)} (1 + O(\sigma^2)). \quad (17)$$

The further refinement of λ_{\max} is described in detail in [2]. This amounts to solving the equation

$$\lambda_{\max} = s + \mathbf{Z}^T [(\lambda_{\max} + s) I_{3 \times 3} - S]^{-1} \mathbf{Z}, \quad (18)$$

by the Newton-Raphson method using $\lambda_{\max}^{(o)}$ as a starting value.

If the measurements are assumed to be corrupted solely by Gaussian random errors of the form,

$$\hat{\mathbf{W}}_i = A \hat{\mathbf{V}}_i + \Delta \hat{\mathbf{W}}_i, \quad (19)$$

where the sensor error $\Delta \hat{\mathbf{W}}_i$ satisfies

$$E\{\Delta \hat{\mathbf{W}}_i\} = \mathbf{0}, \quad (20)$$

$$E\{\Delta \hat{\mathbf{W}}_i \Delta \hat{\mathbf{W}}_i^T\} = \sigma_i^2 [I_{3 \times 3} - (A \hat{\mathbf{V}}_i)(A \hat{\mathbf{V}}_i)^T], \quad (21)$$

and the weights a_i , $i = 1, \dots, n$, are chosen so that

$$a_i = \frac{c}{\sigma_i^2} \quad (22)$$

for some constant c , then Reference [2] shows that the attitude covariance matrix is given by

$$P_{\theta\theta} = \left[\sum_{i=1}^n \frac{1}{\sigma_i^2} \left(I_{3 \times 3} - (\hat{\mathbf{W}}_i)_{\text{true}} (\hat{\mathbf{W}}_i)_{\text{true}}^T \right) \right]^{-1}, \quad (23)$$

where

$$(\hat{\mathbf{W}}_i)_{\text{true}} \equiv A_{\text{true}} \hat{\mathbf{V}}_i. \quad (24)$$

In actual computation we generally substitute $\hat{\mathbf{W}}_i$ for $(\hat{\mathbf{W}}_i)_{\text{true}}$, since the latter value is not known, in general. The attitude covariance matrix is defined here as

$$P_{\theta\theta} = \text{Cov}(\Delta\theta), \quad (25)$$

where $\Delta\theta$, the attitude error, is given by

$$A^* A_{\text{true}}^T \approx I_{3 \times 3} + [[\Delta\theta]], \quad (26)$$

and Cov denotes the covariance. Thus, the QUEST algorithm gives a fast direct method for constructing the optimal attitude. The algorithm has other valuable properties as well, which are discussed in [2].

The Attitude Kalman Filter for the QUEST Model

QUEST is a batch estimator taking as input a collection of *simultaneously* measured unit vectors. When the data is not simultaneous and we wish to use data at widely different times, the algorithm of choice has been the Kalman filter. In the present section we present the Kalman filter for the measurement model of equations (19)–(21).

Since the QUEST algorithm does not treat dynamical noise (the measurements being all simultaneous, this would hardly be relevant), we examine the Kalman filter for a system without dynamical noise, that is, a system for which the temporal development of the attitude is described by

$$A_k = \Phi_{k-1} A_{k-1}, \quad (27)$$

where the transition matrices, Φ_k , $k = 0, \dots, N-1$, is known perfectly. In general, the subscript k will indicate the time, and the subscript i will indicate the sensor. For such a system the prediction of the attitude matrix must have the form

$$A_{k|k-1}^* = \Phi_{k-1} A_{k-1|k-1}^*, \quad (28)$$

where $A_{k-1|k-1}^*$ is the estimate of the attitude matrix at time t_{k-1} based on all the measurements up to that time inclusively, and $A_{k|k-1}^*$ is the estimate of the attitude matrix at time t_k based on the same data. Since dynamical noise is absent, the prediction of the attitude covariance matrix is given by

$$P_{k|k-1} = \Phi_{k-1} P_{k-1|k-1} \Phi_{k-1}^T. \quad (29)$$

and, since no confusion can result, we have dropped the subscript $\theta\theta$ to make the notation less cumbersome.

For updates the calculation is more involved. Since the attitude has only three free parameters while the attitude matrix has nine, we do not update the attitude matrix directly but compute instead the updated value of ξ_k , the incremental rotation vector, which is defined by

$$A_k = e^{[[\xi_k]]} A_{k|k-1}^*, \quad (30)$$

$$\approx A_{k|k-1}^* + [[\xi_k]] A_{k|k-1}^*, \quad (31)$$

so that by definition

$$\xi_{k|k-1}^* = \mathbf{0}. \quad (32)$$

Then we can write the linearized measurement as

$$\zeta_k \equiv \hat{\mathbf{W}}_k - \hat{\mathbf{W}}_{k|k-1}, \quad (33)$$

where

$$\hat{\mathbf{W}}_{k|k-1} = A_{k|k-1}^* \hat{\mathbf{V}}_k. \quad (34)$$

Combining equations (31)–(34) yields

$$\zeta_k = H_k \xi_k + \mathbf{v}_k, \quad (35)$$

where

$$H_k = -[[\hat{\mathbf{W}}_{k|k-1}]]. \quad (36)$$

The measurement noise of our linearized measurement, \mathbf{v}_k , is assumed to be Gaussian and zero-mean. Its covariance matrix can have only rank 2 since unit-vector measurements have only two degrees of freedom. However, it can be shown that the true covariance matrix of \mathbf{v}_k can be replaced by

$$R_k = \sigma_k I_{3 \times 3}, \quad (37)$$

which is obviously of rank 3. This substitution leads to the same estimates and covariance matrices as the form given by equation (21) [6]. The reason for this is that the additional noise which makes the covariance matrix of rank 3 is along the direction of $\hat{\mathbf{W}}_k$, to which the attitude is not sensitive. It can be seen from equation (36) that H_k annihilates that component from $\hat{\mathbf{W}}_k$.

The Kalman filter update equations now become

$$\mathcal{B}_k = H_k^T P_{k|k-1} H_k + R_k, \quad (38)$$

$$K_k = P_{k|k-1} H_k^T \mathcal{B}_k^{-1} \quad (39)$$

$$\xi_{k|k}^* = K_k \hat{\mathbf{W}}_k, \quad (40)$$

$$P_{k|k} = (I_{3 \times 3} - K_k H_k) P_{k|k-1} \quad (41)$$

$$= (I_{3 \times 3} - K_k H_k) P_{k|k-1} (I_{3 \times 3} - K_k H_k)^T + K_k R_k H_k. \quad (42)$$

The Kalman filter equations, (28) through (42), can treat non-simultaneous data but are considerably more complicated than the QUEST algorithm for simultaneous data. It is natural

ask, therefore, whether the QUEST equations can be manipulated to remove the restriction to simultaneous data. The answer is affirmative. In fact, the Wahba problem was applied to non-simultaneous quite some time ago [5] but in a batch framework, not in a sequential framework like the Kalman filter.

The Sequentialization of QUEST: Filter QUEST

Suppose that we have a set of simultaneous measurements at time t_{k-1} which we can denote by $\hat{\mathbf{W}}_{i,k-1}$, $i = 1, \dots, n$, and let us denote the optimal attitude at time t_{k-1} computed using the QUEST algorithm by $A_{k-1|k-1}^*$. Recalling equation (27), the optimal value of A_k based on the data at time t_{k-1} is obtained by minimizing

$$L_{k-1}(A_k) = \frac{1}{2} \sum_{i=1}^{n_{k-1}} a_{i,k-1} |\hat{\mathbf{W}}_{i,k-1} - \Phi_{k-1}^{-1} A_k \hat{\mathbf{V}}_{i,k-1}|^2, \quad (43)$$

where the additional subscript on $L(A)$ indicates the time of the data. Since Φ_k is orthogonal, this is clearly the same as finding the value of A_k which minimizes

$$L_{k-1}(A_k) = \frac{1}{2} \sum_{i=1}^{n_{k-1}} a_{i,k-1} |\Phi_{k-1} \hat{\mathbf{W}}_{i,k-1} - A_k \hat{\mathbf{V}}_{i,k-1}|^2, \quad (44)$$

that is, by replacing $\hat{\mathbf{W}}_{i,k-1}$ by $\Phi_{k-1} \hat{\mathbf{W}}_{i,k-1}$, or equivalently, noting equation (5), by replacing

$$B_{k-1|k-1} \equiv \sum_{i=1}^{n_{k-1}} a_{i,k-1} \hat{\mathbf{W}}_{i,k-1} \hat{\mathbf{V}}_{i,k-1}^T \quad (45)$$

by

$$B_{k|k-1} \equiv \sum_{i=1}^{n_{k-1}} a_{i,k-1} \Phi_{k-1} \hat{\mathbf{W}}_{i,k-1} \hat{\mathbf{V}}_{i,k-1}^T \quad (46)$$

Thus, for the filter version of QUEST, the prediction step becomes simply [7]

$$B_{k|k-1} = \Phi_{k-1} B_{k-1|k-1}. \quad (47)$$

We may, in fact, drop the distinction between the indices i and k and treat each unit vector as having a distinct time t_k , reference vector $\hat{\mathbf{V}}_k$ and weight a_k associated with it. If two vector measurements $\hat{\mathbf{W}}_{k+1}$ and $\hat{\mathbf{W}}_k$ are simultaneous, then $t_{k+1} = t_k$ and $\Phi_k = I_{3 \times 3}$.

For the update step of Filter QUEST, we note that when we increase the number of measurements in the measurement set of equation (5) we simply add a term, $a_k \hat{\mathbf{W}}_k \hat{\mathbf{V}}_k^T$, to B . Thus, the update step in terms of the attitude profile matrix is

$$B_{k|k} = B_{k|k-1} + a_k \hat{\mathbf{W}}_k \hat{\mathbf{V}}_k^T. \quad (48)$$

The QUEST algorithm requires also that we know the value of $\lambda_{\max k}^{(o)}$ separately. This is given by

$$\lambda_{\max k}^{(o)} = \lambda_{\max k-1}^{(o)} + a_k. \quad (49)$$

Equations (47)–(49) are clearly much simpler than the corresponding Kalman filter equations (28)–(42).

The covariance matrix can be computed sequentially also by first computing the attitude information matrix, $F \equiv P^{-1}$. The relevant equations are

$$F_{k|k-1} = \Phi_{k-1} F_{k-1|k-1} \Phi_{k-1}^T \quad (50)$$

$$F_{k|k} = F_{k|k-1} + \frac{1}{\sigma_k^2} \left(I_{3 \times 3} - \hat{W}_k \hat{W}_k^T \right). \quad (51)$$

These can be computed likewise [7, 8] from

$$F = \text{tr}(A^* B^T) I_{3 \times 3} - A^* B^T, \quad (52)$$

without the need to have a separate recursion relation for F . Equation (52), in fact, is very important because it can be solved for B to yield

$$B = \left(\frac{1}{2} \text{tr}(F) I_{3 \times 3} - F \right) A^*. \quad (53)$$

Thus, given initial values, $A_{o|o}^*$ and $P_{o|o}$, the initial value of the attitude profile matrix, $B_{o|o}$ can be computed from equation (53). This last fact makes the analogy of Filter QUEST with the Kalman filter complete. In fact, since it can be shown that QUEST is a maximum-likelihood estimator for Gaussian errors [7], the Kalman filter and Filter QUEST will yield identical attitude estimates for the attitude system considered above.

It is well to note that the Filter QUEST is an information filter rather than a covariance filter. This is made clear by the fact that $B_{1|1}$ is a meaningful quantity even though the attitude cannot be calculated from a single measurement.

While the prediction and update equations of Filter QUEST are simple, it is also true that the need to apply the part of QUEST which computes the optimal attitude and covariance matrix from the attitude profile matrix is an additional computational burden. The real advantage of Filter QUEST comes when one does not require an attitude solution at every measurement update. In this case, the efficiency of Filter QUEST relative to the Kalman filter is greatly enhanced.

The Treatment of Noisy Processes

In general, attitude systems are subject to random torques, or the dynamical equations are replaced by the gyro equations [9] so that the gyro measurement noise becomes process noise. In the Kalman filter formulation, this extra complication results in the prediction equation for the attitude being replaced by

$$P_{k|k-1} = \Phi_{k-1} P_{k-1|k-1} \Phi_{k-1}^T + Q_{k-1}. \quad (54)$$

where Q_{k-1} is the covariance of the accumulated process noise from time t_{k-1} to time t_k . Possibly also, the state vector must be augmented to include the state of the Markov process driving the gyro errors [9].

Such an enhancement is not possible in Filter QUEST since there is no simple way of adding process noise to B . One could, of course, compute $P_{k|k-1}$ after every prediction step of Filter QUEST, add the process noise covariance to $P_{k|k-1}$, and then use equation (53) to compute a new $B_{k|k-1}$. This would be extremely burdensome and destroy whatever computational advantage Filter QUEST offered.

An approximate way to simulate the treatment of process noise is to modify Filter QUEST so that it becomes a fading memory filter. Thus, we replace the prediction step in QUEST by

$$B_{k|k-1} = \alpha_k \Phi_{k-1} B_{k-1|k-1}, \quad (55)$$

where α_k is a number between zero and one, and which is also a function of k . Clearly, if α is chosen to be zero, then Filter QUEST will have no memory at all. If the data consists of a sequence of frames each containing several simultaneous vector measurements, then choosing $\alpha_k = 0$ at the end of each frame and $\alpha_k = 1$ otherwise will produce a sequence of single-frame QUEST estimates. Choosing $\alpha_k = 1$ for all k corresponds to infinite memory, which would be appropriate for a genuinely noiseless system.

How should one choose α ? Clearly, if the accumulated process noise between measurements is generally much smaller than the measurement noise, then it should be expected that Filter QUEST properly adjusted will average several measurements and obtain a much more accurate result than the single-frame estimate. If α_k is adjusted to be too small, then Filter QUEST will take insufficient advantage of the data and the result will be less accurate. Likewise, if α_k is too large, then the Filter will overweight data which has become less accurate due to the accumulation of process noise, and the solution will be less accurate again. Thus, there is generally an optimal choice for α_k .

Let us consider the case where the process noise is equivalent to

$$A_k = e^{[w_{k-1}]} \Phi_{k-1} A_{k-1}, \quad (56)$$

where w_k is a white sequence with covariance $qI_{3 \times 3}$. Such a model is characteristic of an idealized laser gyro and would be appropriate if the dynamical information were coming from laser-gyro measurements. Let us consider also that the spacecraft is equipped with three attitude sensors which at each time t_k sense simultaneously unit vectors along each of the coordinate axes, each with an accuracy of σ . In such a case, clearly, we would choose $\alpha_k = 1$ between the unit-vector measurements in each frame and $\alpha_k = \alpha$ after the last measurement in each frame. In this case, an analytical solution is possible for the covariance matrix of the QUEST filter, which in the limit that an infinite number of measurements have been processed turns out to be

$$P_{k|k}^{QF} = p_{k|k}^{QF} I_{3 \times 3}, \quad (57)$$

with

$$p_{k|k}^{QF} = \frac{\sigma^2}{2} \left[\frac{1-\alpha}{1+\alpha} + \frac{2}{x} \frac{\alpha^2}{1-\alpha^2} \right], \quad (58)$$

and

$$x \equiv \sigma^2/q. \quad (59)$$

This function is a minimum for

$$\alpha_{\text{opt}} = \frac{x+1-\sqrt{1+2x}}{x}. \quad (60)$$

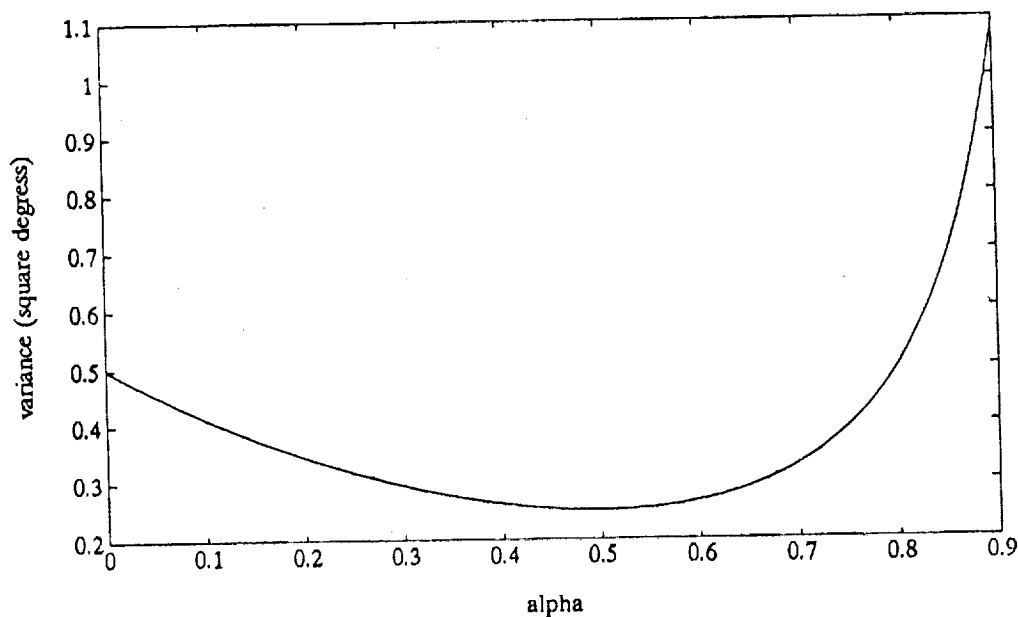


Figure 1. Filter QUEST Covariance as a Function of the Fading Memory Factor for $\sigma^2 \approx q$

If we choose values such as

$$\sigma = 1 \text{ deg}, \quad q = (.5 \text{ deg})^2, \quad (61)$$

then a plot of $p_{k|k}^{\text{QF}}$ will look like Figure 1, which shows a broad minimum at $\alpha = 0.5$ and a minimum variance of $p_{k|k}^{\text{QF}} = (.5 \text{ deg})^2$. This should be compared with the single-frame result which is

$$p^{\text{single-frame}} = \frac{\sigma^2}{2} = (.707 \text{ deg})^2. \quad (62)$$

The Filter QUEST solution is not a very large improvement over the single frame solution but not inconsistent with the relatively large gyro noise we have chosen compared to the vector-sensor noise.

The general formula for the minimum Filter QUEST variance for this example as a function of σ and q is

$$p_{\min}^{\text{QF}}(+) = \frac{\sigma^2}{2} \frac{-1 + \sqrt{1 + 2x}}{x}. \quad (63)$$

Thus,

$$p_{\min k|k}^{\text{QF}} \rightarrow \frac{\sigma^2}{2} = p^{\text{single-frame}} \quad \text{as } x \rightarrow 0, \quad (64)$$

as expected, and

$$p_{\min k|k}^{\text{QF}} \rightarrow \frac{\sigma^2}{2} \sqrt{\frac{2}{x}} \quad \text{as } x \rightarrow \infty. \quad (65)$$

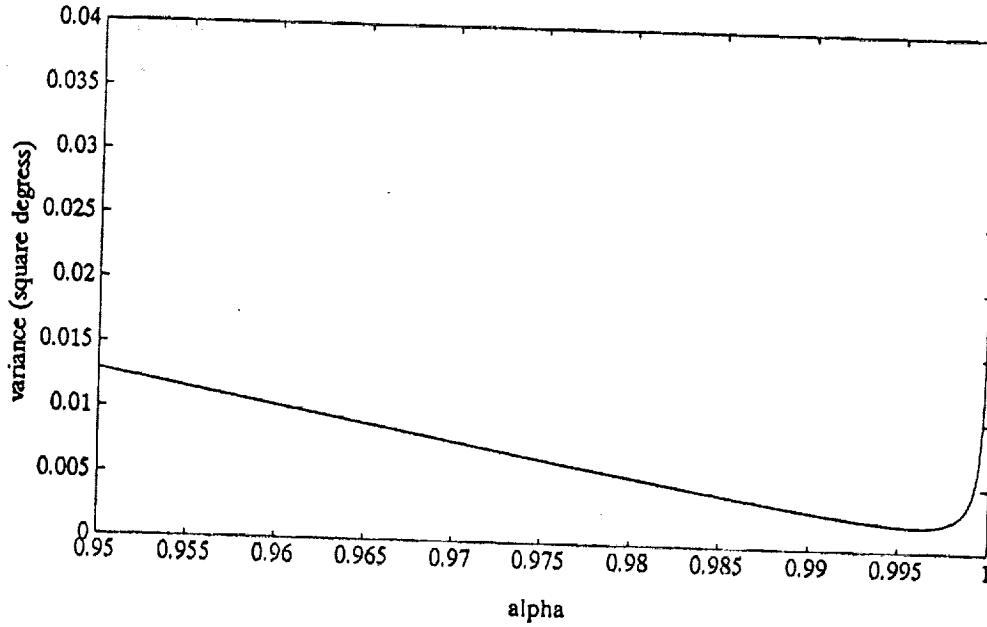


Figure 2. Filter QUEST Covariance as a Function of the Fading Memory Factor for $\sigma^2 \gg q$

Equation (65) shows that for x very large, the effective number of previous measurements which Filter QUEST is averaging to reduce the error is

$$N_{\text{eff}} = x/2. \quad (66)$$

Note that the dependence of α_{opt} on the measurements is in the limiting cases

$$\alpha_{\text{opt}} \rightarrow x \quad \text{as} \quad x \rightarrow 0, \quad (67)$$

and

$$\alpha_{\text{opt}} \rightarrow 1 - \sqrt{\frac{2}{x}} \quad \text{as} \quad x \rightarrow \infty. \quad (68)$$

Thus, α_{opt} will generally be extremely close to unity for cases where we would generally want to use a filter. For example, if we choose instead of the previous case more physical values such as $\sigma = 1 \text{ deg}$, $q = (1 \text{ arc min})^2$, then $\alpha_{\text{opt}} = .976$ and $p_{k|k}^{\text{QF}} = (.11 \text{ deg})^2$. The standard deviation is, thus, almost seven times smaller than the single-frame value. The dependence of the variance on the fading-memory parameter for this case is shown in Figure 2.

Smoother QUEST

The Kalman filter has the disadvantage that only anterior data is used in the estimate. Thus, posterior data, which is equally accurate, is not considered, thereby increasing the covariance by at least a factor of 2 over its achievable value. Also, for early estimates, less data is used leading to a less accurate result than for later estimates.

A Kalman filter/smoothing uses both the data which precedes the time of the estimate and the data which follows the time of the estimate. While such an estimator is more accurate, it has the disadvantage that it cannot function in real-time. Thus, a smoother is generally more applicable to background processing on the ground rather than real-time processing on the spacecraft.

The QUEST algorithm also admits a smoother implementation. Suppose we are given measurements $\hat{\mathbf{W}}_k$, $k = 1, \dots, N$. Then the smoothed attitude profile matrix $B_{k|N}$ at time t_k , $k = 0, \dots, N$, is given by

$$\begin{aligned}
 B_{k|N} = & \alpha^k \left(\prod_{i=0}^{k-1} \Phi_i \right) B_{o|o} \\
 & + \sum_{i=1}^{k-1} \alpha^{|k-i|} \Phi_{k-1} \dots \Phi_i a_i \hat{\mathbf{W}}_i \hat{\mathbf{V}}_i^T \\
 & + a_k \hat{\mathbf{W}}_k \hat{\mathbf{V}}_k^T \\
 & + \sum_{i=k+1}^N \alpha^{|k-i|} \Phi_k^{-1} \dots \Phi_{i-1}^{-1} a_i \hat{\mathbf{W}}_i \hat{\mathbf{V}}_i^T.
 \end{aligned} \tag{69}$$

The first term in this equation is the contribution of the *a priori* estimate of the attitude. If the smoother were implemented in segments, $B_{o|o}$ would be the attitude profile matrix for the final estimate of the previous segment. The second term gives the predicted contributions of the measurements preceding the current measurement. The third term is the current measurement. The first three terms thus constitute the usual Filter QUEST expression for the attitude profile matrix. The fourth term gives the contribution from the measurements which come after the time of the estimate. The factors of the transition matrices transform the measurements to the body frame at time t_k and the factors of $\alpha^{|k-i|}$ downgrade the data to reflect the ravages of process noise. Equation (70) may be rewritten as

$$B_{k|N} = B_{k|k} + D_k, \quad k = 0, \dots, N, \tag{70}$$

where $B_{k|k}$ is the "filtered" attitude profile matrix, which satisfies the previous Filter QUEST (forward) recursion relations, and is given by the first three lines of equation (69). D_k is the contribution of the posterior measurements, which is given by the last line of equation (68). By inspection, we see that D_k satisfies a backward recursion relation,

$$D_N = 0, \tag{71}$$

$$D_{k-1} = \alpha \Phi_{k-1}^{-1} \left[D_k + a_k \hat{\mathbf{W}}_k \hat{\mathbf{V}}_k^T \right], \tag{72}$$

in complete analogy to the usual Rauch-Tung-Striebel Kalman filter/smoothing [10]. The information matrix again is given by equation (52) but with $B_{k|N}$ replacing $B_{k|k}$. Since Φ_k in

the present application is orthogonal, the inverse is given by the transpose. Thus, the set of smoothed attitude estimates for an interval of data is obtained with only twice the computational burden of the calculation of the filtered estimates. An obvious drawback, however, is that all of the data, filtered attitude profiles matrices, and attitude transition matrices must be stored. Thus, it is beneficial to process overlapping segments (but whose data length is much greater than N_{eff}) in order to keep storage requirements for the processing within reason.

Discussion

Despite its simplicity and obvious power in the above example, Filter QUEST has its drawbacks. First, it only estimates attitude. Thus, in a system in which angular velocity or gyro biases must also be estimated, Filter QUEST will not be sufficient. Also, for systems with poor geometries, say only a single measurement, Filter QUEST's approximation of a single fading-memory factor may be inadequate. Also, Filter QUEST suffers from the short-comings of QUEST, which, if viewed as a maximum-likelihood estimator, effectively assumes the measurement error model given by equations (19)–(21). This is not always the case. However, it is frequently so, and for the most part this model is reasonable, and Filter QUEST offers a useful if limited alternative to the full Kalman filter. In one recent example Filter QUEST has been applied to the COBE mission with encouraging, if not spectacular, results [11].

Acknowledgment

The author is grateful to F Landis Markley for many interesting discussions and criticisms on this topic and to Orville Filla and Donald Chu for sharing their experience in integrating the algorithm in the COBE software.

References

- [1] WAHBA, G., "A Least-Squares Estimate of Satellite Attitude," Problem 65-1, *Siam Review*, Vol. 7, No. 3, July 1965, p. 409.
- [2] SHUSTER, M. D., and OH, S. D., "Three-Axis Attitude Determination from Vector Observations," *Journal of Guidance, Control and Dynamics*, Vol. 4, No. 1, Jan.–Feb. 1981 pp. 70–77.
- [3] J. KEAT, "Analysis of Least Squares Attitude Determination Routine, DOAOP," Computer Sciences Corporation, CSC/TM-77/6034, February 1977.
- [4] MARKLEY, F. L., "Attitude Determination Using Vector Measurements and the Singular Value Decomposition," *Journal of the Astronautical Sciences*, Vol. 36, No. 3, January–March 1989, pp. 245–258.
- [5] FALLON, L. III, HARROP, I. H., and STURCH, C. R., "Ground Attitude Determination and Gyro Calibration Procedures for the HEAO Mission," *Proceedings, ALAA 17th Aerospace Sciences Meeting*, New Orleans, Louisiana, 1979.

- [6] SHUSTER, M. D., "Kalman Filtering of Spacecraft Attitude and the QUEST Model," *Journal of the Astronautical Sciences*, Vol. 38, No. 3, July-September, 1990, pp. 377-393.
- [7] SHUSTER, M. D., "Maximum Likelihood Estimation of Spacecraft Attitude," *Journal of the Astronautical Sciences*, Vol. 37, No. 1, January-March 1989, pp. 79-88.
- [8] SHUSTER, M. D., "A Simple Kalman Filter and Smoother for Spacecraft Attitude," *Journal of the Astronautical Sciences*, Vol. 37, No. 1, January-March 1989, pp. 89-106.
- [9] LEFFERTS, E. J., MARKLEY, F. L., and SHUSTER, M. D., "Kalman Filtering for Spacecraft Attitude Estimation," *Journal of Guidance, Control and Dynamics*, Vol. 5, No. 5, Sept.-Oct. 1982, pp. 417-429.
- [10] RAUCH, H. E., TUNG, F., and STRIEBEL, C. T., "Maximum Likelihood Estimation of Linear Dynamic Systems," *AIAA Journal*, Vol. 3, No. 8, pp. 1445-1450, 1965.
- [11] FILLA, O., KEAT, J., and CHU, D., "COBE Experience with Filter QUEST," *Proceedings, Flight Mechanics/Estimation Theory Symposium*, NASA Goddard Space Flight Center, Greenbelt, Maryland, May 21-23, 1991.

COBE Experience With Filter QUEST*

O. Filla, J. Keat, and D. Chu
COMPUTER SCIENCES CORPORATION (CSC)

ABSTRACT

A gyro-based filter variation on the standard QUEST attitude determination algorithm is applied to the Cosmic Background Explorer (COBE). Filter QUEST is found to be three times as fast as the batch estimator and slightly more accurate than regular QUEST. Perhaps more important than its speed or accuracy is the fact that Filter QUEST can provide real-time attitude solutions when regular QUEST cannot due to lack of observability. Filter QUEST is also easy to use and adjust for the proper memory length. Suitable applications for Filter QUEST include coarse and real-time attitude determination.

* This work was supported by the National Aeronautics and Space Administration (NASA)/Goddard Space Flight Center (GSFC), Greenbelt, Maryland, Contract NAS 5-31500.

1. INTRODUCTION

Filter QUEST is a new version of the familiar QUEST attitude determination software. Because it makes use of gyro data, it promises to combine the speed of QUEST with the accuracy of gyro-based estimators. Just how fast and how accurate is seen from experience with Cosmic Background Explorer (COBE) data.

2. BACKGROUND ON QUEST

QUEST is Shuster's implementation of the Davenport q-algorithm for attitude determination (Reference 1). Since its introduction in 1978, it has been a standard part of the attitude ground support systems built for three-axis spacecraft at the NASA Goddard Space Flight Center Flight Dynamics Facility. Explanations of the algorithm and its implementation are available elsewhere (References 2, 3, and 4), but a few remarks about QUEST that are relevant to the following discussion are included for convenience.

First, QUEST uses only unit vector observations expressed in body coordinates. These are denoted here by \hat{w}_i , where i indicates the particular observation. The corresponding reference vectors in inertial coordinates are \hat{v}_i . Each observation is also given a scalar weight a_i , which is normalized so that the sum over all observations equals one.

$$\sum_{i=1}^N a_i = 1 \quad (1)$$

Second, an intermediate quantity called the attitude profile, or "B-matrix," is computed as follows:

$$B = \sum_{i=1}^N a_i \hat{v}_i \hat{w}_i^T \quad (2)$$

Several secondary quantities are also defined:

$$z \equiv \begin{vmatrix} B_{23} - B_{32} \\ B_{31} - B_{13} \\ B_{12} - B_{21} \end{vmatrix} \quad (3)$$

$$S \equiv B + B^T \quad (4)$$

$$\sigma \equiv \text{trace}[B] \quad (5)$$

Third, the attitude quaternion q is then the solution to the eigenvalue equation

$$Kq = \lambda q \quad (6)$$

where the matrix is constructed from those secondary quantities:

$$K = \begin{bmatrix} (S - \sigma I) & z \\ z^T & \sigma \end{bmatrix} \quad (7)$$

3. FILTER QUEST

Filter QUEST is a natural generalization of the QUEST attitude determination algorithm (References 5 and 6). QUEST is limited to using "single-frame" observations from the same time or a constant attitude. Filter QUEST, however, can accept observations from different times or attitudes so long as it has the incremental rotation angle between those times. This information typically comes from gyros. In the past, systems have been built that propagate the unit vector observations to a common time before providing them to QUEST for "batch" processing. Filter QUEST differs in that it handles that preprocessing internally. Filter QUEST also differs in that it is a sequential estimator with a simple "fading" memory rather than a batch estimator. In Filter QUEST, the B-matrix is corrected for spacecraft rotation between observation times t_i and t_{i-1} . Here $B_{i/j}$ denotes the value of the B-matrix at time t_i based on observations up to and including those at time t_j :

$$B_{i/i-1} = \alpha \Phi(t_i, t_{i-1}) B_{i-1/i-1} \quad (8)$$

The memory length parameter α is a number between zero and one. α equal to one implies infinite memory, and α equal to zero produces the standard QUEST algorithm. Φ is the attitude propagation matrix computed from the angular increment vector $\vec{\theta}$ for the time interval (t_i, t_{i-1}) . It is given by the expression

$$\Phi(t_i, t_{i-1}) = \cos \theta I + (1 - \cos \theta) \hat{\theta} \hat{\theta}^T - \sin \theta [\hat{\theta}_x] \quad (9)$$

where θ is the magnitude and $\hat{\theta}$ is the direction of $\vec{\theta}$

$$\vec{\theta} = \theta \hat{\theta}$$

and

$$[\hat{\theta}_x] = \begin{bmatrix} 0 & -\hat{\theta}_3 & \hat{\theta}_2 \\ \hat{\theta}_3 & 0 & -\hat{\theta}_1 \\ -\hat{\theta}_2 & \hat{\theta}_1 & 0 \end{bmatrix}$$

At each observation time, the B-matrix is updated using the new pair of vectors \hat{v}_i and \hat{w}_i

$$B_{i/i} = B_{i/i-1} + a_i \hat{v}_i \hat{w}_i^T \quad (10)$$

Attitude is computed at selected times using the standard QUEST algorithm.

There are three reasons for interest in Filter QUEST. First, because it uses gyro data, it can provide more accurate real-time attitude solutions than regular QUEST. It can also extend observability into periods such as orbit night, when single-frame methods may be useless. Second, because QUEST is fast, it is hoped that Filter QUEST will provide accuracies approaching those of the batch estimator with less CPU time. This is useful for producing 24-hour attitude histories, as in definitive processing. Third, the simplicity and familiarity of Filter QUEST make it a suitable "training" filter. Tuning is accomplished by adjusting the single parameter a , which can always be set equal to zero to return to the original QUEST. Because QUEST is so well known, any improvement is also likely to be accepted.

To evaluate its performance with real data, Filter QUEST was built into the Coarse Attitude Determination Subsystem (CADS) of the Cosmic Background Explorer (COBE) Flight Dynamics Support System (FDSS), where it replaced regular QUEST. Tests were then made to see how much attitude error could be eliminated by increasing a and to determine an optimal value for a that would minimize error while avoiding long-term divergence. For these tests, the Fine Attitude Determination Subsystem (FADS) solution computed using Diffuse Infrared Background Experiment (DIRBE) star observations was used as a reference. FADS is a batch estimator that uses gyro data to provide the most accurate COBE attitude solutions. The Filter QUEST and these DIRBE batch solutions were then compared in the Quality Assurance (QA) subsystem, where the plots and statistics on their differences were computed. Finally, timing comparisons were made for the batch, regular QUEST, and Filter QUEST estimators.

4. THE EFFECT OF MEMORY LENGTH

The length of the fading memory is controlled by the parameter a , which determines the effect of the current observation on the current attitude estimate. Although a is constant, the

“effective” weight, which is the ratio of the current observation weight to the total weight, is not. If all observation types have the same weight ∂ , the sum of these weights at time t_i is

$$W_i = a \sum_{j=0}^{i-1} a^j = \frac{a(i - a^i)}{1 - a} \quad (11)$$

The ratio of the current weight to the total weight is

$$1 \geq \frac{a}{W_i} = \frac{1 - a}{(1 - a^i)} \rightarrow 1 - a \quad (12)$$

This number decreases from one and converges to $(1 - a)$. Thus, the fading memory filter is more responsive to early observations than later ones. This is particularly so a is set high and there is no a priori solution. In this case, the solution can lock up quickly based on a few inaccurate measurements and then take a very long time to converge to the correct attitude.

The error in a Filter QUEST solution is taken to be the difference between that solution and a DIRBE batch solution. For the short timespan shown in Figure 1, the error is random with amplitude consistent with the 0.5 degree Sun sensor resolution. The size of the error corresponds to the spread of the difference curve or the root of the mean squared (rms) difference.

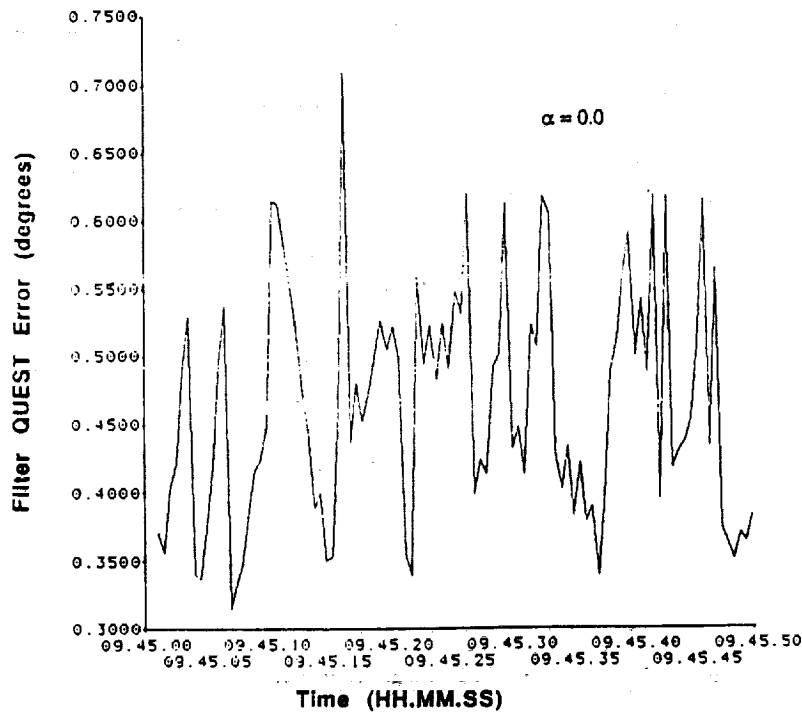


Figure 1. Filter QUEST Solution Error

As the memory length parameter α increases from zero to one, the rms difference decreases, as shown in Figure 2. The rms difference does not go to zero because the observation errors are not completely random.

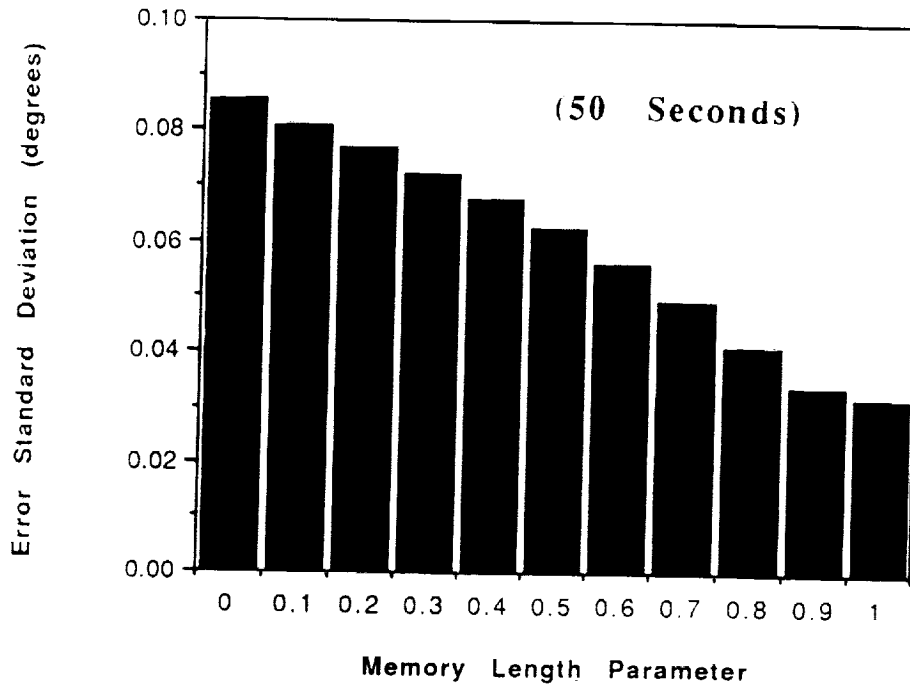


Figure 2. Error Standard Deviation as a Function of Memory Length

It would seem then that the memory length should be made as large as possible. The adverse effect of doing so becomes apparent over longer timespans. As shown in Figure 3, the difference can increase with time and exceed the one degree (3σ) COBE accuracy goal. Figure 4 gives a plot of the rms differences for full-orbit (100-minute) solutions as a function of α . There is no sharply defined value of α that minimizes the error. Any value between 0.90 and 0.99 is suitable. The determination of this value is sometimes called "tuning." In practice, the true attitude is not apt to be known, and tuning must be done by examining how well the observations are fit by the attitude solution. QUEST and Filter QUEST provide such a figure of merit in the output "RESIDU" ρ , which equals one minus the "overlap eigenvalue" λ (Reference 7). When all the observations fit the attitude solution, RESIDU equals zero.

$$\rho = 1 - \lambda \quad (13)$$

RESIDU is plotted in Figure 5 for the solution of Figure 3. Just as the growing difference curve indicates that α is set too high, the growth of RESIDU says the same thing without the need for an absolute attitude reference. Figure 6 gives a plot of the maximum RESIDU values for full-orbit solutions as a function of α corresponding to the rms differences provided by Figure 4. Again, there is no clearly optimal value for α . Any value between 0.90 and 0.99 will do. Alternatively, α can be chosen such that RESIDU is as large as possible but does not grow over time.

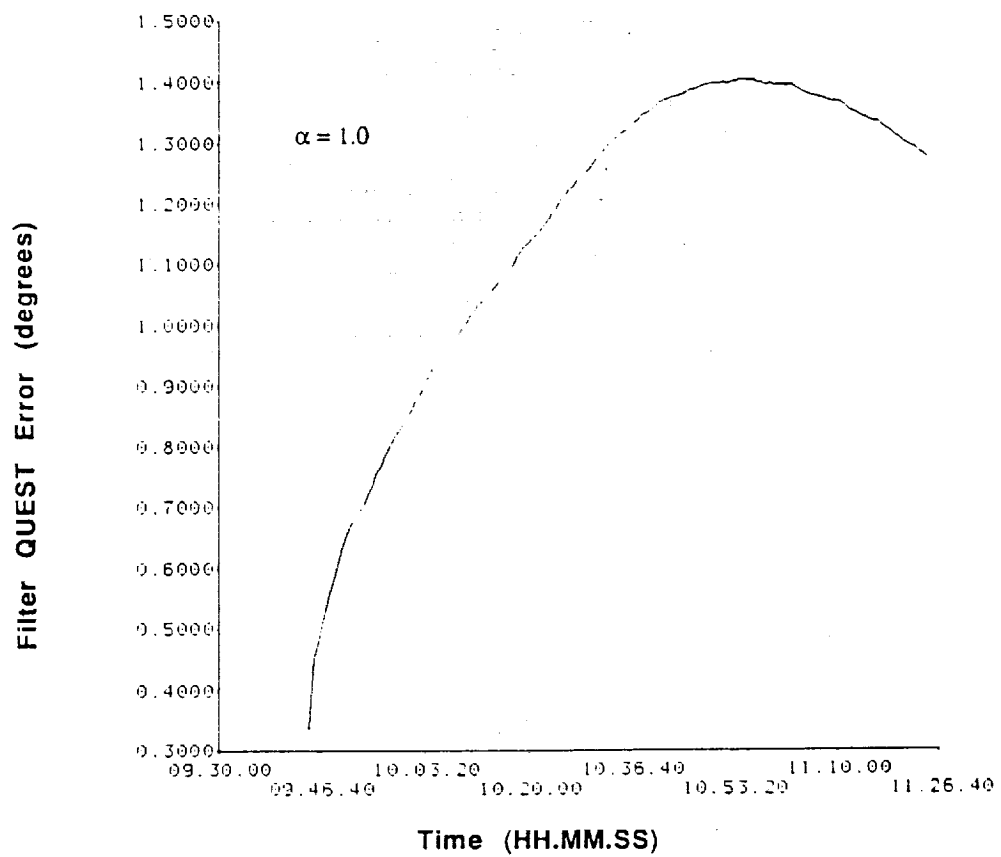


Figure 3. Divergence of Filter QUEST Solution Over a Full Orbit

ORIGINAL PAGE IS
OF POOR QUALITY

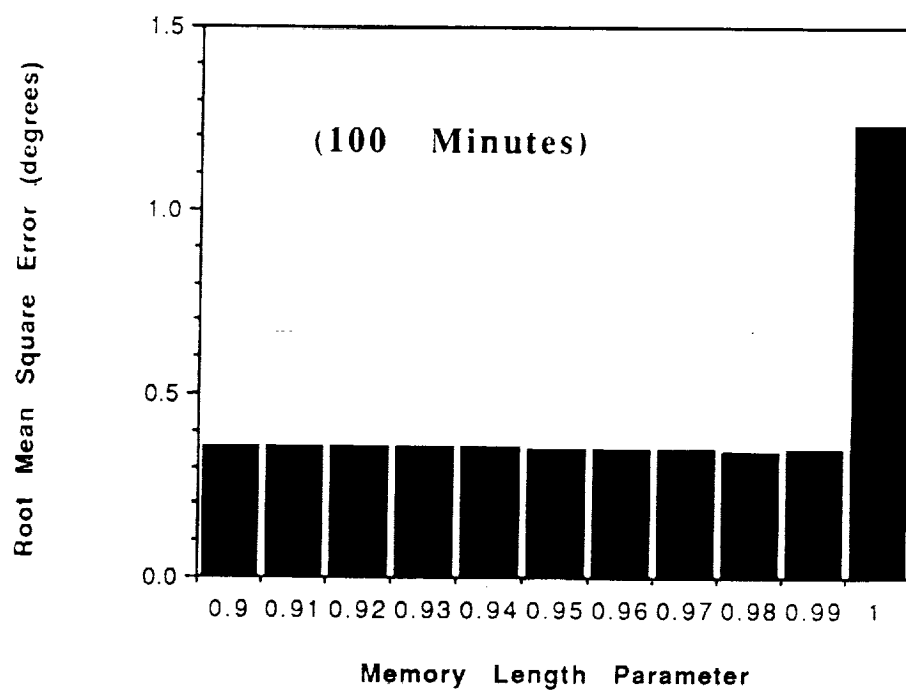


Figure 4. Root Mean Square Error as a Function of Memory Length

ADDITIONAL INFORMATION: This figure is a bar chart showing the Root Mean Square Error (RMSE) in degrees as a function of the Memory Length Parameter. The x-axis represents the Memory Length Parameter, ranging from 0.9 to 1.0. The y-axis represents the RMSE in degrees, ranging from 0.0 to 1.5. The chart shows that the RMSE is relatively low (around 0.35 degrees) for parameters 0.9 through 0.99, but it increases significantly to approximately 1.25 degrees at parameter 1.0. The text "(100 Minutes)" is displayed within the plot area.

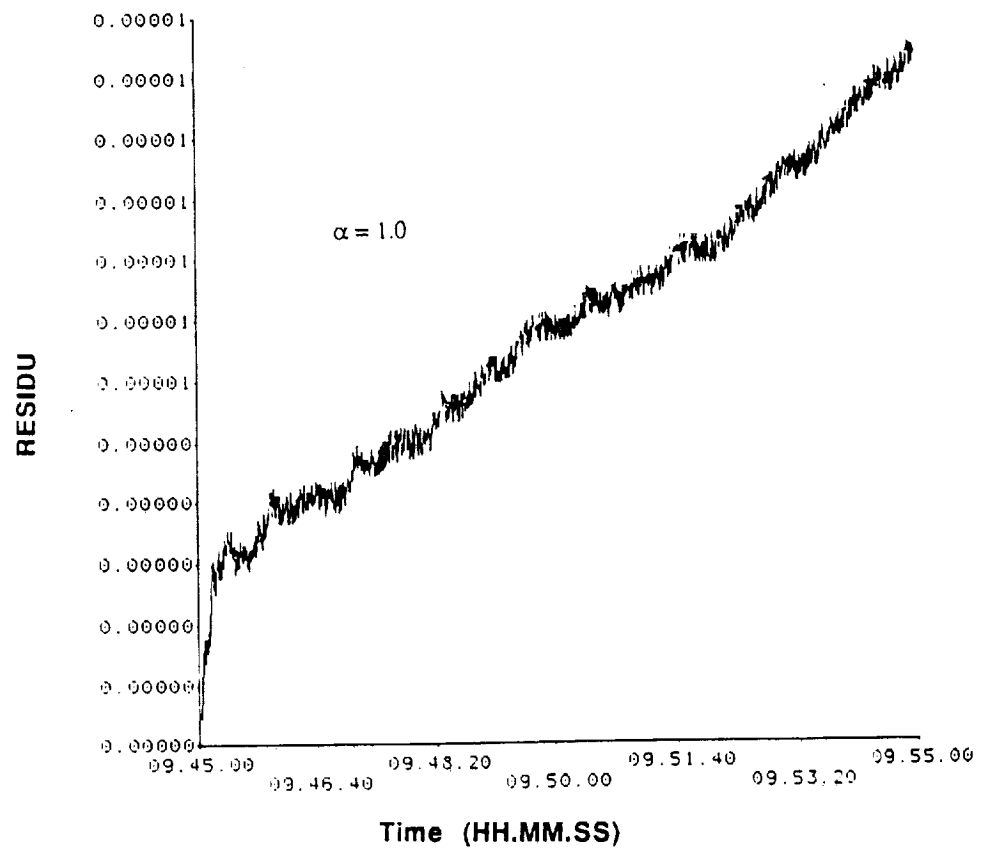


Figure 5. RESIDU as an Indicator of Divergence

ORIGINAL PAGE IS
OF POOR QUALITY

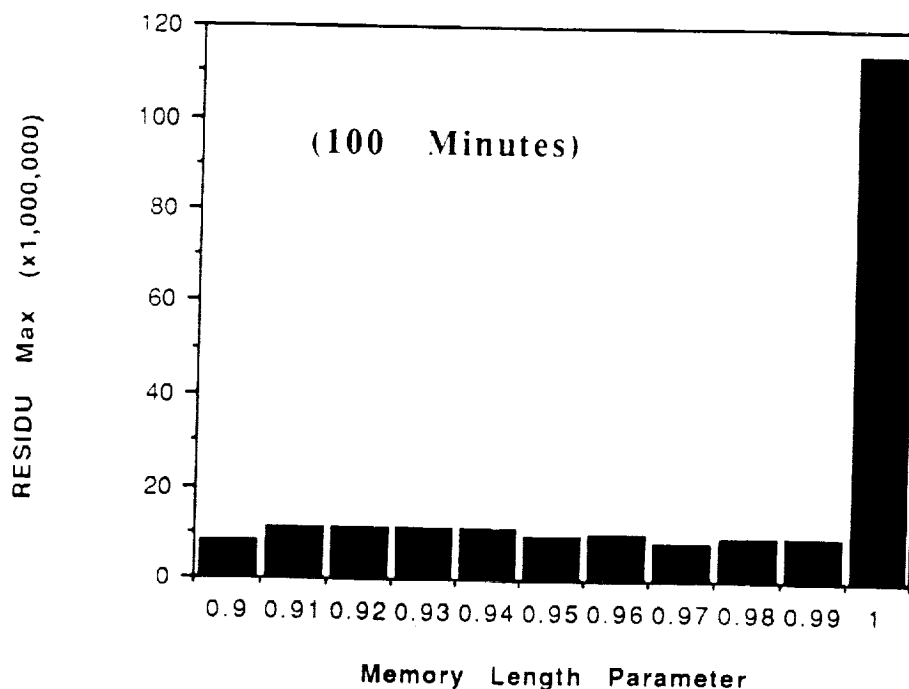


Figure 6. RESIDU as a Function of Memory Length

5. SPEED AND ACCURACY COMPARISONS

Since the batch estimator and QUEST represent the current COBE capabilities, they are used as standards against which Filter QUEST is measured. For comparison, all three estimators are applied to a full orbit (100 minutes) of data. The memory length parameter α is set to 0.98 to keep the attitude from diverging over this timespan. As before, the reference is a batch solution computed using DIRBE star data. The batch error plotted here is the difference between this reference and a batch solution obtained from Sun and Earth sensor data alone.

The rms errors of the three solutions are shown in Figure 7. For this comparison, gyro biases were first solved for in the batch estimator, and the corrections were made in the Data Adjuster (DA) subsystem. This improved the Filter QUEST solution accuracy as well as that of the batch estimator. In spite of having gyro data, Filter QUEST had an rms error only 14 percent smaller than that of regular QUEST, and still far greater than that of the batch solution. The reason for this small improvement is that like any sequential estimator, Filter QUEST cannot look ahead of the current solution time. While the batch estimator effectively has infinite memory and thus can average out orbital and higher frequency errors, Filter QUEST cannot set α to one without diverging. Unless observation errors are really random, or are much smaller than the propagation error, no filter compares favorably with a batch estimator in accuracy. Unfortunately, all nonrandom errors seem not to have been eliminated from the COBE observations.

The speed of each estimator in producing these solutions is plotted in Figure 8. These numbers are for the Flight Dynamics Facility Hitachi NAS 8063 computers and come from

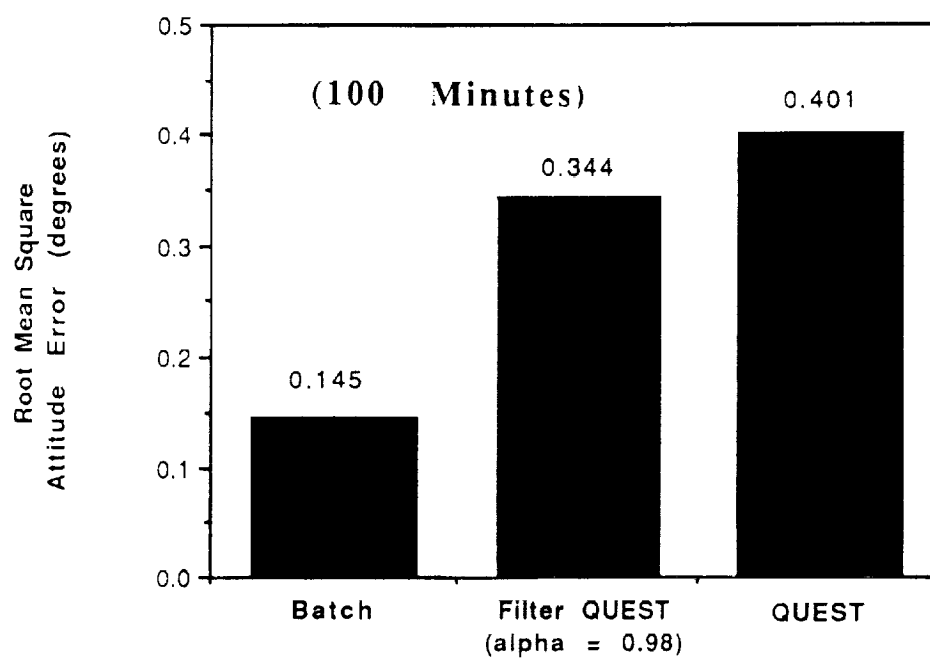


Figure 7. Estimator Error

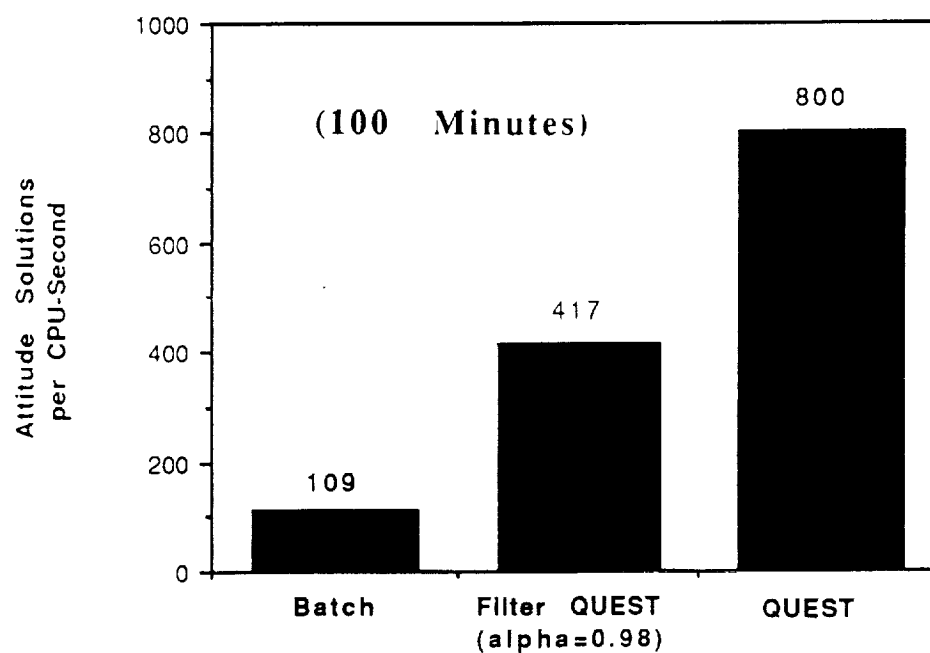


Figure 8. Estimator Speed

running only the estimators. The conversion of telemetry, correction for known calibration errors, and generation reference data are not included. These speeds are for running interactively rather than in background mode. Background execution can be much faster, but the relative speeds should be similar. As expected, regular QUEST is the fastest. Addition of propagation to Filter QUEST cuts its speed in half. It is still, however, more than three times as fast as the batch estimator, the speed of which has been greatly increased since it was originally coded.

6. CONCLUSIONS

In conclusion, this study suggests that Filter QUEST pays in speed for what can be a small increase in accuracy. For this reason, it seems more suited for use as an upgrade from regular QUEST than as a replacement for the batch estimator. For spacecraft with only limited periods of complete attitude observability, however, this can mean the difference between knowing and not knowing the attitude in real time. Because the Filter QUEST algorithm reduces to regular QUEST when the memory length parameter α is zero, there is no risk in substituting it in all current and future applications of QUEST.

7. ACKNOWLEDGMENTS

The authors thank Dr. Malcolm D. Shuster of the Johns Hopkins University Applied Physics Laboratory for sharing Filter QUEST and Gerald Klitsch of the Computer Sciences Corporation System Sciences Division for helping to integrate Filter QUEST with the COBE Flight Dynamics Support System.

REFERENCES

1. M. D. Shuster and S. D. Oh, "Three-Axis Attitude Determination from Vector Observations," *Journal of Guidance*, January–February 1981, vol. 4, no. 1, pp. 70–77
2. Computer Sciences Corporation, CSC/TM-77/6034, *Analysis of the Least Squares Attitude Determination Routine DOAOP*, J. Keat, February 1977
3. —, CSC/TM-78/6056, *Algorithms for Determining Optimal Attitude Solutions*, M. D. Shuster, April 1978
4. J. R. Wertz, ed., *Spacecraft Attitude Determination and Control*, D. Reidel Publishing Co., 1980, pp. 426–428
5. M. D. Shuster, "A Simple Kalman Filter and Smoother for Spacecraft Attitude," *Journal of the Astronautical Sciences*, January–February 1989, vol. 37, no. 1
6. M. D. Shuster, "New QUESTs for Better Attitudes," to appear in the Proceedings of the NASA/GSFC Flight Mechanics/Estimation Theory Symposium, 1991
7. Computer Sciences Corporation, *Quaternion Estimator (QUEST) Program Description*, B. Fang, December 1982

COBE GROUND SEGMENT ATTITUDE DETERMINATION

V. K. Kumar, I. Freedman (ST Systems Corporation, Lanham, MD 20706)

E. L. Wright (UCLA, Los Angeles, CA 90024)

F. S. Patt (GSC, Laurel, MD 20707)

ABSTRACT

The COsmic Background Explorer (COBE) spacecraft was launched in November 1989 by NASA to survey the sky for primordial radiation left from the "Big Bang" explosion. The success of the mission requires an accurate determination of the spacecraft attitude. While the accuracy of the attitude obtained from the attitude sensors is adequate for two of the experiments, the higher-accuracy attitude required by the Diffuse InfraRed Background Experiment (DIRBE) is obtained by using the DIRBE instrument as a special type of star sensor. This paper presents an overview of the attitude processing algorithms used at the Cosmology Data Analysis Center (CDAC) and discusses some of the results obtained from the flight data.

1.0 INTRODUCTION

The COsmic Background Explorer (COBE) spacecraft was launched by NASA in November 1989 to survey the sky for primordial radiation left from the Big Bang. The spacecraft carried three very sensitive instruments: (1) the Diffuse InfraRed Background Experiment (DIRBE) to survey the sky in the 1 to 300 micrometers wavelength in ten bands; (2) the Far InfraRed Absolute Spectrophotometer (FIRAS) to survey the sky in the 0.1 to 10 millimeter wavelength bands; and (3) the Differential Microwave Radiometer (DMR) to determine whether the primordial explosion was equally bright in all directions. The FIRAS and DIRBE are enclosed in a liquid helium cryostat to provide a stable low-temperature environment. These three instruments, along with the cryostat and the shield to protect the instruments from illumination by the Sun and Earth, form the upper half of the spacecraft (instrument module) (Figure 1). The lower half of the spacecraft (spacecraft module) includes the mechanical support structure, the attitude control system, the instrument and spacecraft electronics, and the solar cell arrays.

The COBE was placed into a circular Sun-synchronous orbit 900 km above the surface of the Earth. The spacecraft crosses the equator from north to south at approximately 6 a.m. local time. The orbit of the spacecraft is inclined 99 degrees to the equator and precesses to follow the apparent motion of the Sun relative to the Earth.

The COBE spacecraft rotates about the spacecraft X-axis at approximately 0.815 rpm. The COBE attitude control system points the spin axis (FIRAS line of sight) at approximately 94 degrees away from the Sun and in a generally outward direction from the Earth. The spacecraft rotation allows DIRBE and DMR to observe half the sky every orbit, as their lines of sight are 30 degrees away from the spin axis.

The COBE attitude control system is composed of: (1) attitude sensors: two-axis Digital Sun Sensors (DSS), infrared Earth-horizon Scanner Assemblies (ESA), rate integrating gyros, and Three-Axis Magnetometers (TAM); (2) attitude controllers: reaction wheels, electromagnets (torquer bars), and a pair of large rotating momentum wheels; and (3) a set of control electronics. Figure 2 shows the COBE attitude sensor and control system geometric configuration. The three control axes lie in a plane perpendicular to the spacecraft spin axis and are labeled A, B, and C. The reaction wheels control the spacecraft spin axis orientation by applying controlled torques along these axes. The large momentum wheels are used to control the spacecraft spin rate and to maintain approximately zero net angular momentum about the X-axis. The electromagnets provide control torques from the Earth's magnetic field to discharge the angular momentum build-up in the reaction and momentum wheels. The electronics and data handling systems on the spacecraft collect the data from the instruments and attitude sensors and transmits these data to the ground. The complete data stream is recorded on two on-board tape recorders and played back to the ground-receiving station at Wallops Flight Facility once (or twice) per day. In addition, the spacecraft is monitored periodically in realtime and commands are sent to it through the Tracking and Data Relay Satellite System (TDRSS).

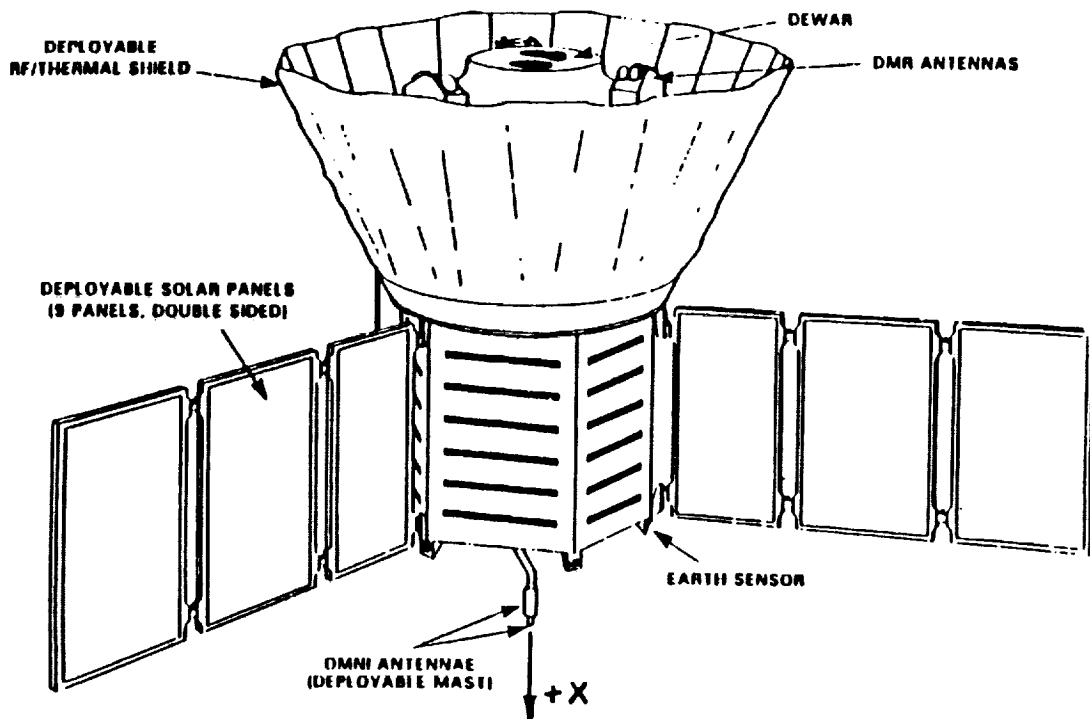


Figure 1. COBE Observatory Deployed

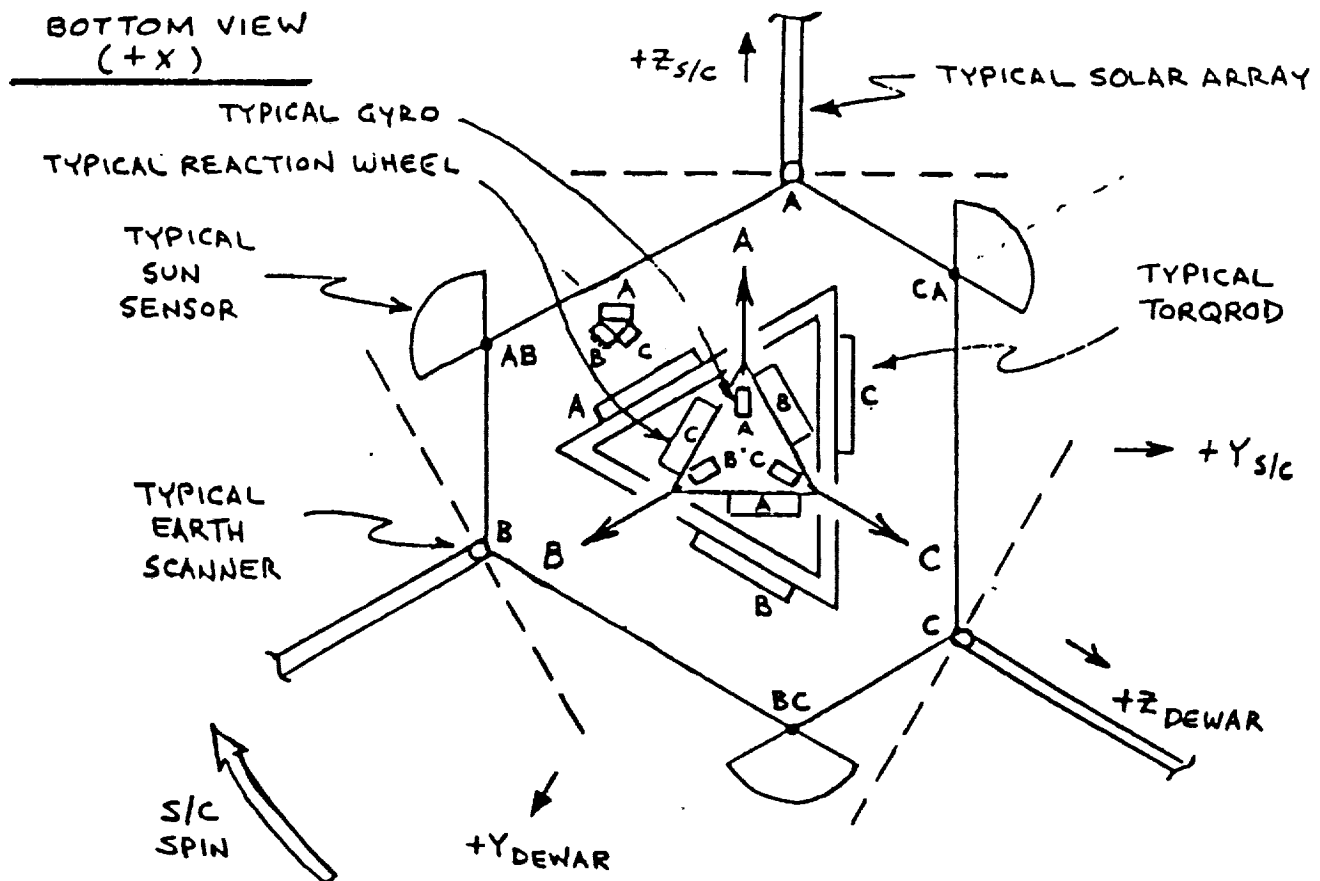


Figure 2. COBE Attitude Control System (ACS) Configuration

The ground reconstruction of the spacecraft attitude for instrument data interpretation is performed at the NASA Cosmology Data Analysis Center (CDAC). This paper presents an overview of the CDAC attitude processing algorithms and discusses some of the results obtained from flight data.

2.0 PROCESSING ALGORITHMS

The initial estimate of the spacecraft attitude is obtained by processing the attitude sensor data. The initial attitude estimate is also called the "coarse aspect". The accuracy of the coarse aspect is further improved using the DIRBE instrument payload data in the telemetry. This refined attitude is called the "DIRBE fine aspect".

2.1 Coarse Aspect

The coarse aspect is derived from the Sun sensor, Earth scanner, and gyro measurements. Observation vectors required in the attitude computation are constructed from the sensor measurements. The inertial reference vectors are constructed using analytical methods. The Q-method (QUEST) (References 1, 9) is used to obtain an epoch attitude from observation vectors and reference vectors. The attitude at other times is obtained by propagating the epoch attitude to the observation times using the body angular velocity derived from the gyro measurements.

2.1.1 Observation Vectors Computation

There are six two-axis digital Sun sensors (DSS) on the COBE spacecraft. Three of the DSS's serve as primary sensors, and the other three serve as backups. The alignment of the sensor axes with respect to the spacecraft reference frame is shown in Figure 3.

Each DSS has a 128x128 degree square field-of-view (FOV). They measure the projection angles of the Sun vector in the DSS sensor reference frame. A detailed description and operation of the DSS used on COBE, as well as the procedure for obtaining the Sun vector in the spacecraft coordinate frame, are also described in Reference 1.

The spacecraft-to-Sun vector in the inertial frame is obtained by the analytical procedure described in Reference 2. The distance between the spacecraft and the Earth is neglected in computing this vector.

The COBE spacecraft has three infrared Earth-horizon Scanner Assemblies (ESA) for tracking the spacecraft nadir. A brief description and operation of the sensor can be found in Reference 3. The ESA sensor reference axes orientation in the spacecraft reference frame is as shown in Figure 4. The ESA's measure the angle between the spacecraft +X axis and the nadir vector in the sensor scan plane (split-to-index angle), which is normal to the sensor Z axis.

The ESA split-to-index angle measurement, along with the Sun observation vector computed earlier, is used to compute the spacecraft nadir angle, η (Figure 5). By using techniques of spherical trigonometry one can derive the following relation for η :

$$\cos(\eta) = \frac{cB \times cP + sB \times cF \times \sqrt{(sB^2 \times cF^2) + cB^2 - cP^2}}{(sB^2 \times cF^2) + cB^2} \quad (1)$$

$s() = \sin()$; $c() = \cos()$; B, P, F are the angles defined in Figure 5.

The nadir vector direction in the ESA sensor reference frame is then given by

$$\hat{N}_{ESA} = [s\eta \times cA, s\eta \times sA, c\eta]^T. \quad (2)$$

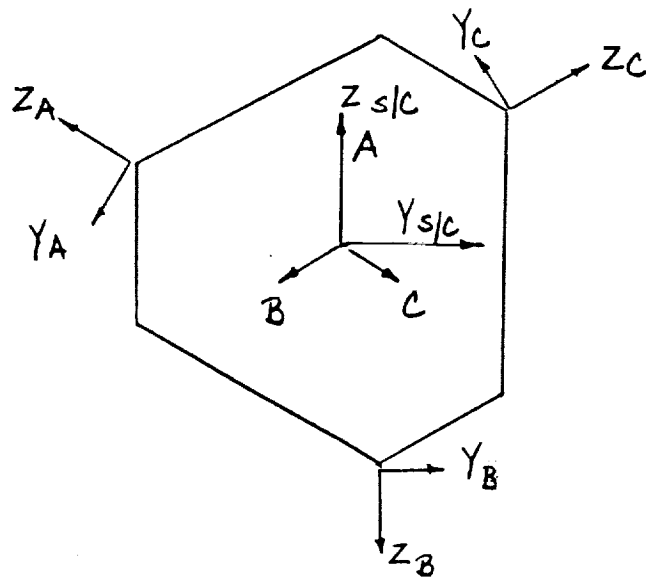


Figure 3. DSS Axes Orientation

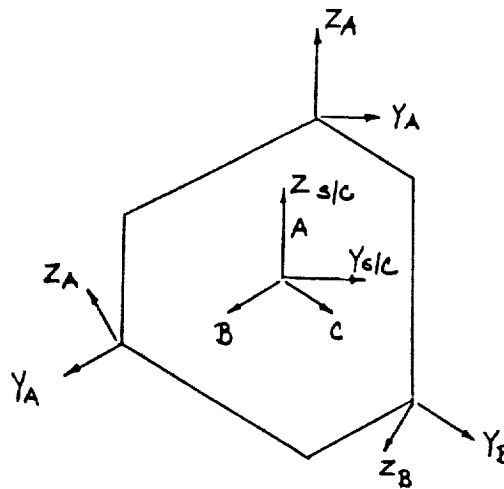


Figure 4. ESA Axes Orientation

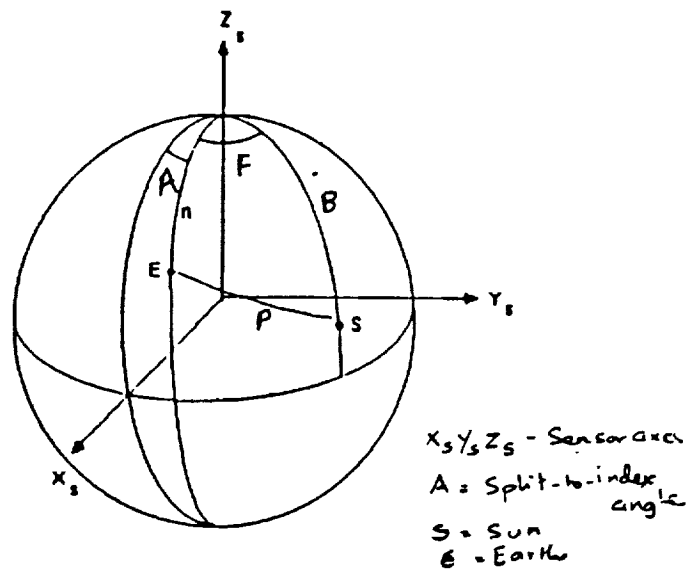


Figure 5. Geometry for Nadir Vector Computation

The nadir vector in the spacecraft reference frame is obtained by premultiplying N by the sensor-to-spacecraft alignment matrix. It can be noted that two solution vectors exist for each split-to-index angle measurement (one for each value of η). The correct nadir solution vectors cluster very closely in the spacecraft reference frame. The effective nadir vector is taken as the average of all the correct solution vectors.

The spacecraft nadir vector in the inertial frame is obtained from the spacecraft orbit data computed by the Goddard Space Flight Center's Flight Dynamics Facility (FDF) (Reference 4).

2.1.2 Spacecraft Body Angular Velocity

The COBE spacecraft has six single-axis rate integrating gyros for spacecraft body angular velocity measurements. The gyro input axes are oriented in the spacecraft frame as shown in Figure 6. For ground processing, measurements from only one of the three X-axis gyros is telemetered to the ground. The X-axis gyro selected for the telemetry is commanded from the ground. Currently, of the three control axis gyros, only A- and C-axis gyros are active. The B-axis gyro failed in flight a few days after the launch.

The spacecraft angular velocity component in the direction of the gyro input axis is related to the gyro measurement of this quantity, W_i , by

$$W_i = (1 + K_i) \dot{U}_i \bar{W}_i + N_i + B_i \quad (i = A, C, X) \quad (3)$$

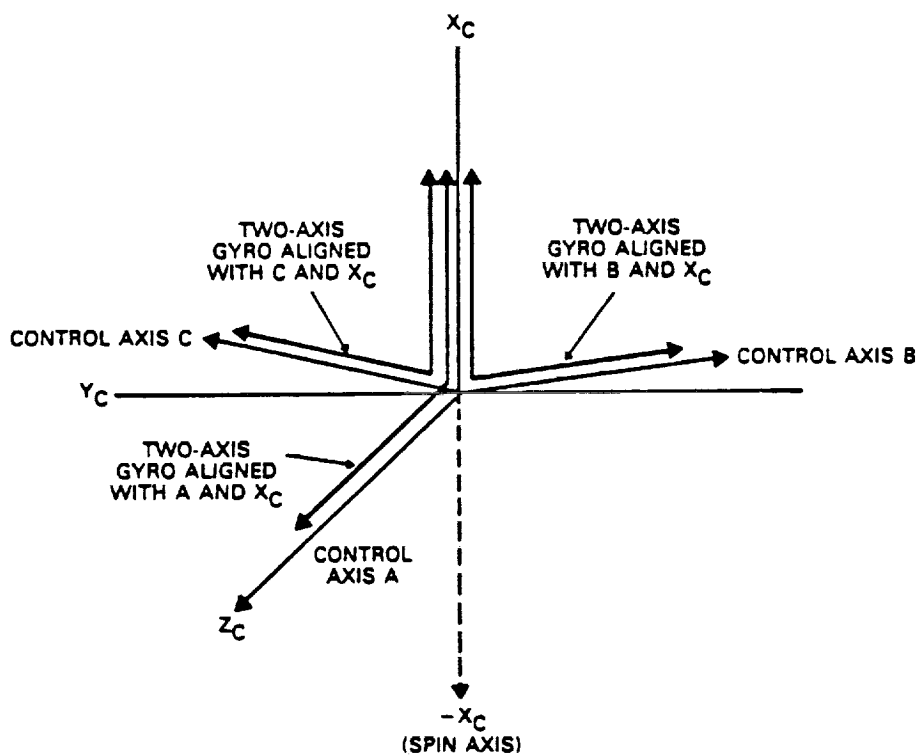


Figure 6. Gyro Input Axes Orientation

where U 's are unit vectors in the direction of the gyro input axes in the spacecraft body frame; W is the true body angular velocity vector; B designates the gyro rate biases; K represents the gyro scale factors; and N specifies the gyro output noise terms, which are assumed to be negligible. The direction vectors of the gyro input axes are obtained from the pre-launch alignment measurements of the gyro input axes. Given the values of gyro drift rate biases and the scale factors, the above set of linear equations can be solved for the components of the spacecraft angular velocity in the spacecraft body frame. Estimation of COBE gyro drift rate biases and scale factors are discussed in Reference 5.

2.1.3 Attitude Computation

The coarse aspect determination procedure is based on the key assumption that the error in the modeling of the spacecraft motion using gyro data is smaller than the error in the sensor data. The procedure uses all the Sun and nadir vectors in a batch process to determine the spacecraft attitude at an epoch time and uses spacecraft body angular velocities to propagate the epoch attitude to other times. This method has been used successfully in other spacecraft missions (see Reference 7).

Assume that we have a set of vector observations resolved in the body frame: W_1, W_2, \dots, W_n at times T_1, T_2, \dots etc., as well as the corresponding reference vectors in the inertial frame (e.g., GCI). Assume also that we have gyro data synchronized to the observation times, and that the calibrations of the gyros (scale factors, alignments, and drift rates) are reasonably well known. We wish to compute an attitude at some epoch time (assume T_1 for convenience, but it could be any time in the interval).

Take some initial attitude estimate at time T_1 ; this could be the result of a single-frame attitude algorithm or could be completely arbitrary, since the QUEST algorithm is linear and, therefore, does not depend on the initial estimate. Express the estimate as a quaternion Q_1 (see Reference 1 for quaternion definition). Use the gyro data to compute rotation quaternions between the observation times: Q_{12}, Q_{23} , etc. Propagate the initial estimate to the observation times

$$\begin{aligned} Q_2 &= Q_1 \times Q_{12}, \\ Q_3 &= Q_1 \times Q_{12} \times Q_{23}, \text{ etc.} \end{aligned} \quad (4)$$

The propagated quaternions are used to rotate the observation vectors to the inertial frame at T_1 . This can be done by calculating the rotation matrix $[A]$ corresponding to each Q and multiplying the observation vectors by the inverse of the matrix; i.e.,

$$W_k' = \text{Inv}[A(Q_k)] W_k, \quad (k=1,2,\dots). \quad (5)$$

All of the transformed observation vectors and the reference vectors are used as input to the QUEST algorithm and a correction quaternion DQ is computed. The initial estimate is then corrected by quaternion multiplication

$$Q_1' = DQ \times Q_1. \quad (6)$$

Any of the other propagated quaternions can be corrected in the same sense to provide attitude estimates at other observation times.

2.2 DIRBE Fine Aspect

The DIRBE fine aspect determination system uses the DIRBE experiment as a star tracker to improve the accuracy of the coarse aspect solutions. The DIRBE field-of-view (FOV) traces a helical scan path in the sky. The fine aspect determination procedure consists of identifying stars that pass through the DIRBE FOV and then correcting the coarse attitude using these identified stars as attitude reference points.

2.2.1 DIRBE Star Identification

The DIRBE data in the short wavelength (1.25-5.0 micron) bands contain a large number of peaks due to star passages across the instruments' FOV, as well as sharp spikes due to cosmic rays and broader peaks due to the galactic plane and extended sources. Of the three short wavelength DIRBE bands, one has the greatest a priori knowledge of the sky in the K-band (2.2 micron) because of the Two Micron Sky Survey (TMSS) (Reference 8). Hence, the DIRBE data from the K-band channels was chosen for star identification.

In order to separate DIRBE star peaks from the broader peaks due to galactic plane and extended sources, DIRBE data is passed through a non-recursive filter ("matched filter") of the form

$$Y_k = \sum_{i=1}^L W_{k-i} \times \frac{X_{k-i}}{G_k}, \quad (k=1,2,\dots), \quad (7)$$

where Y is the filter output; X represents the DIRBE measurements; W represents the filter weights; G_k is the filter output normalizing gain and L is the filter length.

The filter length, L, is determined by the width of the DIRBE star passage given by (DIRBE FOV size)*(DIRBE sampling rate)/(DIRBE scan speed). The DIRBE instrument has a 0.7 x 0.7 degree square FOV. The DIRBE samples are telemetered at the rate of eight samples per second. Since the DIRBE optical axis is inclined at 30 degrees to the spacecraft X-axis, the DIRBE scan speed on the sky is half the spacecraft spin rate. At the spacecraft nominal spin rate of 0.815 rpm, the DIRBE star peak is 2-3 samples wide. In the present work, the filter length is chosen to be eight samples with the following set of filter weights: $W=(-1,-1,3/4,5/4,5/4,3/4,-1,-1)$. Note that the filter output is zero for constant input signals as well as input ramps. Also, with the filter length of 8 samples, the confusing sources more than 2 degrees away will be outside the filter window.

The filter output normalizing gain function, G_k is chosen as

$$\begin{aligned} G_k &= \text{Min}[32767, 1.1G_{k-1} + 1] && \text{if } 100|Y_k| > G_{k-1} \\ &= \text{Max}\left[1.5, \frac{G_{k-1}}{1.1}\right] && \text{otherwise.} \end{aligned} \quad (8)$$

The value of $G(0)$ is arbitrary. In between star peaks, the matched filter output tracks the background noise in the DIRBE data. The gain algorithm then dampens the response to the filter output, thereby normalizing the star peak intensity to the current estimated noise level.

The filtered DIRBE signal from all the selected channels is scanned for candidate star peaks using the following selection criteria:

- 1) The peak flux should be greater than a specified minimum.
- 2) The signal should peak in all the selected DIRBE channels simultaneously. This ensures rejection of spikes due to charged particles.

The time of the star observation at a candidate star peak is computed as

$$T_p = T(k) - \frac{[(L-1)/2 - N(k)]}{8} \quad (9)$$

where $N(k)$ is the star position (in number of DIRBE samples) within the last L data points (centroid). The centroid in each of the DIRBE channels is computed as

$$C_k = \sum_{i=1}^L f_{k-1} * X_{k-1} / \sum_{i=1}^L g_{k-1} * X_{k-1}. \quad (10)$$

for $L=8$, $f=(5/12, 5/12, -3/2, -1/2, 1/2, 3/2, -5/12, -5/12)$ and $g=(-1, -1, 1, 1, 1, 1, -1, -1)$. The effective centroid is taken as the average centroid of all the selected DIRBE channels.

The approximate DIRBE line-of-sight (LOS) direction (in the inertial frame) at the star observation time, T_p , is defined by the unit vector

$$\hat{U}_p = A_B \times A_{BD} \times \hat{U}_D \quad (11)$$

where: \hat{U}_D is the DIRBE LOS in the DIRBE reference frame.

A_{BD} = rotation matrix to go from the DIRBE frame to the spacecraft body frame (derived from the DIRBE alignment data).

A_{IB} = rotation matrix to go from spacecraft body frame to inertial frame (derived from the coarse attitude).

The DIRBE fine aspect star catalog is searched for a star that lies very close (within a predefined search radius) to \hat{U}_p . The fine aspect star catalog contains 1207 bright stars selected from TMSS, Smithsonian Astrophysical Observatory (SAO), and IRAS point source catalogs. The selection was based on the following three criteria (Reference 6):

- 1) the K-magnitude < 3.0. This ensures that a measured 2.2 micron flux exist for most sources.
- 2) RMS centroiding error less than 1.5 arc-min, as determined from the effects of other stars near the bright star.
- 3) No brighter neighbors within a 1.75 degree radius. Because the nearest star to the coarse attitude position is assumed to be the identified star, stars with brighter neighbors should be avoided.

If the catalog search fails to find a star to associate with a candidate star peak, then that peak is dropped and is labeled as "false peak".

2.2.2 DIRBE Differential Correction

The differential correction consists of finding small corrections to the coarse attitude using the DIRBE identified known stars as attitude references. The attitude error can be represented as an inertial vector (Reference 7). If we assume that the error due to the imperfect modeling of the spacecraft motion by the gyros is negligible, then the coarse attitude error can be represented by constant rotation in the inertial frame. The following differential correction procedure is based on this key assumption.

Let dA denote the constant rotation matrix which takes the coarse attitude predicted body frame to the true body frame. Assuming that this rotation is small, one can write

$$dA = \begin{bmatrix} 1 & c & -b \\ -c & 1 & a \\ b & -a & 1 \end{bmatrix} \quad (12)$$

where a, b, and c are small angle rotations about the body x, y, and z axes, respectively. Thus, the differential correction problem is reduced to finding the three small rotation angles a, b, and c.

If we define a vector, $\bar{P} = \text{transpose } [a, b, c]$, then the change in any unit vector, \hat{V} , under the action of dA is given by

$$d\hat{V} = \bar{P} \times \hat{V} \quad (13)$$

Assume that N DIRBE star sightings have been identified after processing the DIRBE raw data. Then

$$\hat{O}_k - \hat{D}_k = \bar{P} \times \hat{D}_k, \quad (k=1, \dots, N), \quad (14)$$

where \hat{O} is the unit vector to the k^{th} DIRBE sighted star, and \hat{D} is the unit vector along the DIRBE LOS predicted by the coarse attitude at the k^{th} star observation time.

It is also true that

$$\langle \hat{O}_k - \hat{D}_k, \bar{W}_k \times \hat{D}_k \rangle = \langle \bar{P} \times \hat{D}_k, \bar{W}_k \times \hat{D}_k \rangle, \quad (15)$$

where \bar{W} is the body angular velocity at the k^{th} star observation time and $\langle \cdot \rangle$ denotes the scalar product of two vectors. The left-hand side of the above equation is the along scan component of the vector representing the deviation of the coarse attitude-predicted DIRBE LOS vector from the vector pointing to the DIRBE sighted star.

Using techniques of vector algebra, the right-hand side of Equation (15) can be written as

$$\langle \bar{P} \times \hat{D}_k, \bar{W}_k \times \hat{D}_k \rangle = \langle \bar{P}, \bar{E}_k \rangle \quad (16)$$

where $\bar{E}_k = \bar{W}_k - \hat{D}_k \langle \hat{D}_k, \bar{W}_k \rangle$ denotes a vector perpendicular to \hat{D}_k in the plane formed by \bar{W}_k and \hat{D}_k .

One can set up the following N-linear equations, one corresponding to each DIRBE-sighted star, for the three unknowns a, b, and c:

$$\langle \bar{P}, \bar{E}_k \rangle = \langle \hat{O}_k - \hat{D}_k, \bar{W}_k \times \hat{D}_k \rangle, \quad (k=1, \dots, N). \quad (17)$$

For $N > 3$, this will be an over-determined system which can be easily solved for a, b, and c in a least-squares sense.

The quaternion representing the differential correction rotation is given by (first order approximation)

$$dQ = \left[\frac{a}{2}, \frac{b}{2}, \frac{c}{2}, 1 \right] \quad (18)$$

3.0 ANALYSIS AND PROCESSING PIPELINE PERFORMANCE USING FLIGHT DATA

A number of significant improvements to the COBE Attitude processing pipeline have resulted directly from analysis of the flight data. The most important of these are:

- 1) Earth scanner acquisition-of-signal (AOS) timing adjustments

- 2) Gyro calibration and temperature correction
- 3) DIRBE boresight alignment

Each of these is discussed below, followed by a summary of the overall system performance.

3.1 Earth Scanner AOS Timing Adjustment

During the first several months of the mission, the coarse aspect solutions contained significant periodic pitch errors. The errors could readily be seen by projecting the fine aspect differential corrections onto the roll, pitch, and spin axes. These errors had an orbital frequency and the magnitude varied according to the time of year. The errors were not symmetric about the orbit but appeared to depend on the angle between the spin axis and the orbit plane. The maximum error was approximately 0.4 degrees at the winter solstice; the errors were small in early March 1990, but then increased to approximately 0.6 degree at the summer solstice.

It was proposed by one of us (E. Wright) that this was consistent with an average timing error of 0.25 degree (one telemetry minor frame) in the Earth-horizon scanner data, at the COBE spin rate. This prompted a detailed analysis of the Earth-horizon Scanner Assembly (ESA) data timing and, in particular, the ESA Acquisition-of-Signal (AOS) data in the ESA telemetry.

The AOS is meant to indicate the delay between the computation of each ESA Split-to-Index (SI) value and the time at which the ESA is read by the spacecraft telemetry unit. The ESA rotates at approximately 4 hz, the same as the minor frame (mF) period, so the SI data can be up to 1 mF old by the time it is sampled. In principle, the SI time tag can be corrected by the AOS to get the true sample time.

The flight data showed that the telemetered AOS seemed to contain no useful information about the SI sample times. The AOS values for all three ESA's cycled continuously through the total range of 0.0 to 0.25 seconds with a period of about 11 seconds, producing a "saw-tooth" pattern. The SI values showed no behavior which correlated with the AOS cycles; in fact, correcting the SI data using the AOS resulted in obvious discontinuities in the SI data first derivatives at the AOS roll-over points. Thus the AOS data were determined to be not useful and were ignored for data processing.

Additional analysis was performed to determine if the true AOS could be derived from the data. Simulated ESA SI data were generated using the Aspect solutions and compared with the telemetered values. Figure 7 is a plot of the differences between the telemetered and simulated values for one ESA over a 20-minute period. The oscillation in the data is produced by the spacecraft rotation period of approximately 73 seconds. The pattern in the plot is consistent with a true AOS which "rolls over" from 0.25 to zero seconds about every 10 minutes. The differences resulting from the AOS are out-of-phase with the SI data and are proportional in amplitude to the magnitude of the AOS and the amplitude of the SI data.

The difficulty with this conclusion is that there is no direct method to determine the AOS from telemetry alone. The simplest scheme from an operational standpoint was to simply average the AOS by including a constant correction of 1/2 mF (0.125 second) to the time tags. This average correction produces reasonable results if the attitude propagation intervals are longer than the AOS rollover period. Fortunately this period was shorter (about 10 minutes) than the typical solution interval (20 to 45 minutes). This average correction has produced very satisfactory results.

Figure 8 (a) shows the pitch corrections applied to the coarse aspect by the fine aspect solutions for the prelaunch definition of the AOS, while Figure 8(b) shows the corrections for the same time period using the 1/2 mF average AOS value. The pitch errors are now typically less than 0.1 degree. This has had the added benefit of allowing the star identification tolerance for the fine aspect system to be reduced, resulting in fewer misidentifications.

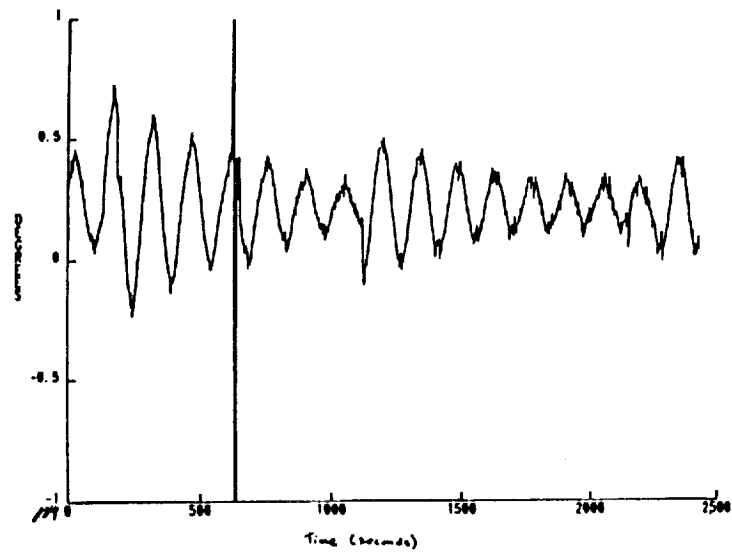


Figure 7. Difference Between Raw and Simulated ESA-A SI Data

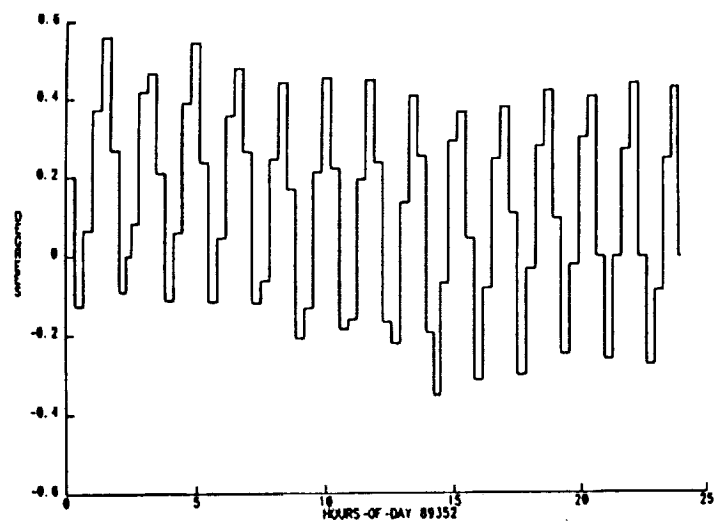


Figure 8(a). Coarse Aspect Pitch Errors (AOS From Telemetry)

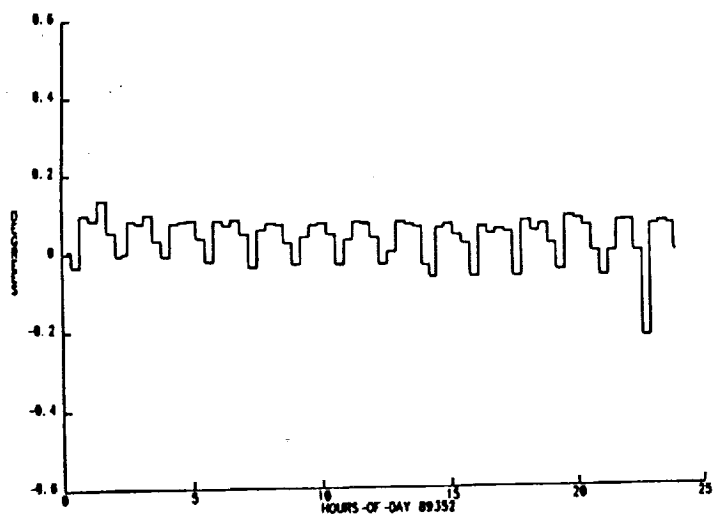


Figure 8(b). Coarse Aspect Pitch Errors (AOS=-0.125)

3.2 Gyro Calibration and Temperature Correction

This topic is discussed in considerable detail in Reference 5. Only the analysis and performance results will be summarized here.

For much of the first year of the mission the ground segment calibration facility was still in the development and testing stages. The attitude processing for quick-look analysis relied mainly on manual estimation of the spin axis scale factor to minimize the attitude propagation errors. While this was adequate to support the coarse requirement (1 degree 3 sigma), it was time-consuming, did not allow quick response to calibration changes, and did not support calibration of the control axis gyros. The problem was aggravated by the apparent drift in the spin axis gyro calibration, especially at the start and end of the eclipse season. At various times calibration parameters were obtained from the COBE FDF, but this was only an interim solution. The fine aspect processing from this period clearly showed the effects of the gyro propagation errors, and only in rare instances was the 3 arc-minute requirement met.

It was not until late summer 1990 that serious attention could be devoted to the attitude propagation problem. At this time the gyro calibration facility testing schedule was accelerated. At the same time, analysis was undertaken of other possible sources of propagation error, since these errors showed periodic behavior which did not seem to reflect calibration errors. This analysis culminated in the demonstration of the AX gyro scale factor/baseplate temperature correlation in August 1990, an effect that explained not only the short-term variations but also the seasonal drift. A correction for the temperature effect was included in the Attitude pipeline shortly thereafter.

With the temperature correction in place, the testing of the calibration facility was rapidly completed. The algorithm was shown to converge rapidly for two test cases: the early-mission spin-up of the spacecraft from 0.23 to 0.82 rpm, and the normal mission phase with nearly constant spin rate. The early mission results provided useful visibility on the important gyro calibration parameters (X gyro scale factor and bias and control axis gyro scale factors). This parameter set was used to initiate the normal mission calibration activities.

The results of the gyro calibration and temperature correction can be clearly seen in the observation residuals for the fine aspect solutions. As previously stated, the fine aspect solution residuals did not consistently meet the 3 arc-minute specification prior to the resolution of the gyro propagation errors. With current capabilities, the residuals Figure 9 are typically 1.5 arc-minutes (includes some error from the star centroids in the star catalog, where the criterion was 1.5 arc-minutes), half of the specification. (Note that this is after the boresight alignment adjustment, discussed in the following section.) The fine aspect residuals are also much more consistent, without the large variations in solution quality that were previously evident. Finally, the improvements in gyro propagation have also allowed the solution arcs to be increased from 20 to 45 minutes. This has allowed more DIRBE star observations to be included in each solution, improving the outlier rejection capability, and has allowed solutions to span intervals of no observation that result from DIRBE calibration activities and South Atlantic Anomaly crossings.

3.3 DIRBE Boresight Alignment

The errors of the DIRBE boresight alignment components (azimuth and elevation) were evaluated at different stages of the Attitude Pipeline analysis. The elevation (i.e., cross-scan) error became apparent soon after regular fine aspect processing was initiated. Plots of star observations in the DIRBE FOV showed that the cross-scan pattern was of approximately the width of the beam (0.7 degrees), but the average was offset from zero by about 4 arc-minutes. This offset was consistently observed in all of the fine aspect processing, so a correction of the elevation angle was approved early on for both the attitude and the DIRBE processing. This change had no effect on the fine aspect observation measurements (as only along-scan residuals are used in the fine aspect correction), and hence did not affect the solution results.

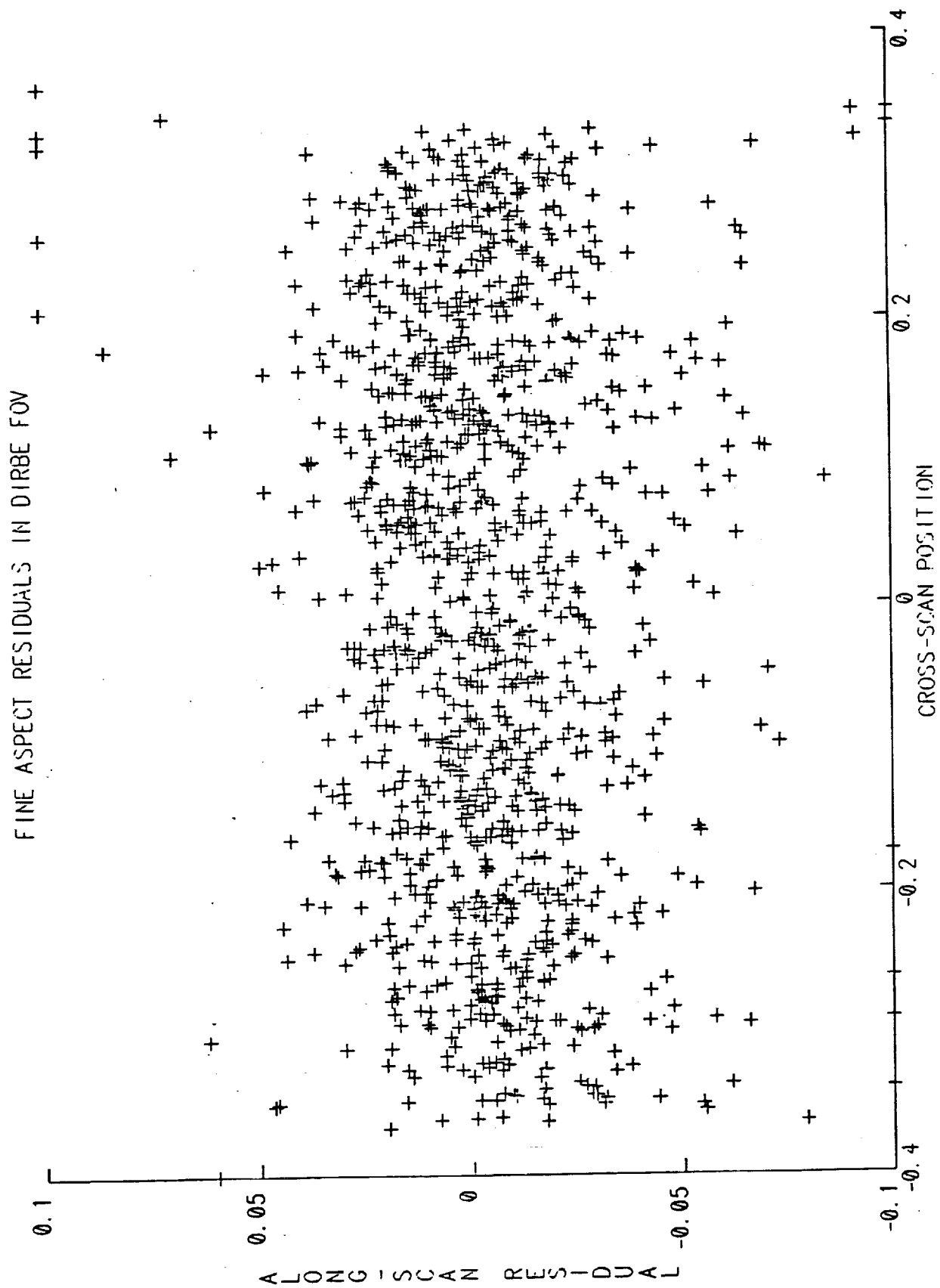


Figure 9. Fine Aspect Residuals in DIRBE FOV

The azimuth (along-scan) error is much more difficult to observe, since the fine aspect differential corrector is performing a least-squares minimization of the along-scan deviations. For short solution intervals, in which the total spin axis precession is not significantly greater than the size of the DIRBE scan cone, the minimization process tends to absorb most of the azimuth alignment as a component of the computed aspect correction. Since the gyro propagations remained short (20 minutes or less) and the observation residual noise was relatively large, the azimuth alignment error was not observable.

As discussed above, following the incorporation of the gyro calibration and the temperature correction, the propagation intervals were increased and the fine aspect observation noise was reduced. Under these circumstances, a consistent mean residual was observed of a magnitude of approximately 1 arc-minute. For longer propagation intervals, the rotation required to remove the mean residual introduced by an azimuth alignment error changes too much to be computed as a single rotation; in fact, for the 45-minute propagation intervals (almost half of the orbit period), the required rotation is almost completely reversed from the start to the end of the interval. Thus a significant mean residual remains even after the minimization process.

Initial experiments to nullify the mean residual used adjustments of the DIRBE data sample timing rather than the boresight azimuth; for a constant spin rate, the effects of these two changes are indistinguishable, and the design of the Attitude Pipeline made it easier to use the timing adjustment for testing purposes. It was readily found that a sample timing delay of 15 milliseconds was sufficient to reduce the mean residual to negligible values for several test intervals. This change also reduced the RMS observation residuals by about 25 percent, indicating that the retiming of the data also improved the overall fit to the error model. Note that this timing change represents along-scan boresight motion of approximately 0.036 degrees, more than twice the observed mean residual, indicating that a large part of the mean residual was still being absorbed by the least-squares fit even with 45-minute propagation intervals.

For implementation of this correction it was decided, in consultation with the DIRBE science team and the software developers, to use a correction to the azimuth alignment rather than the sample timing, as this form of the change was more easily accommodated by the system as a whole. The correction was computed to be 0.0738 degrees, equivalent to 15 milliseconds of spacecraft rotation at the average spin rate of 4.92 degrees per second. This correction was shown, as expected, to have precisely the same effect as the timing change.

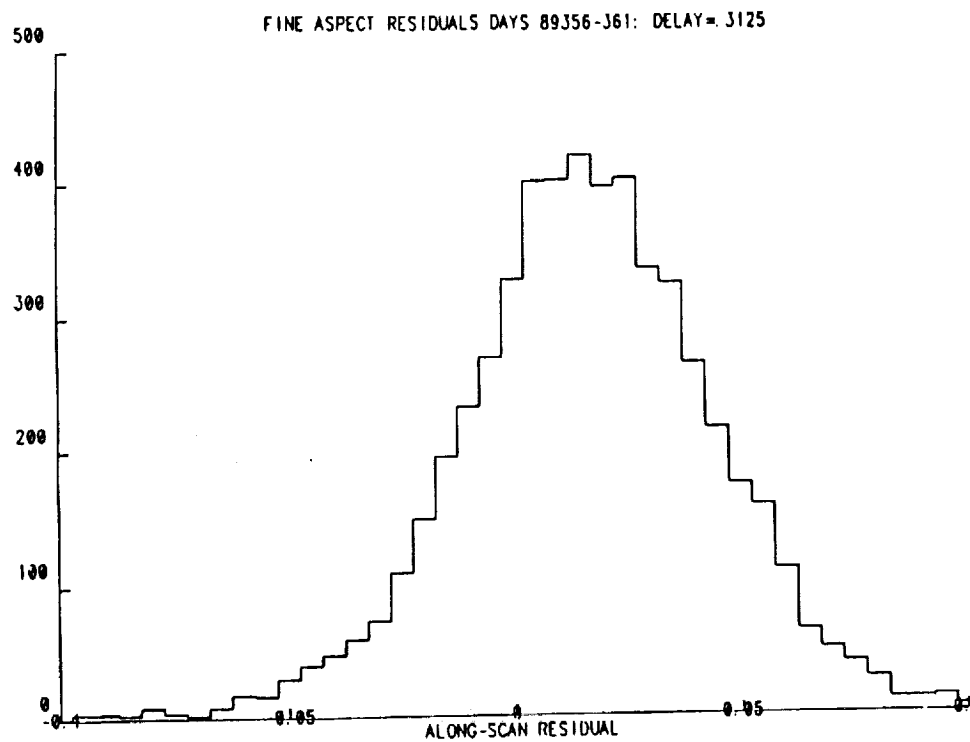
The effect of the boresight azimuth correction is illustrated in Figure 10. The first figure shows a histogram of the fine aspect observation residuals for a 5-day period with 5,710 star observations, using the prelaunch-measured boresight azimuth. The second plot shows the same data with the updated azimuth. The latest gyro calibrations were used for both cases. The plots illustrate the reduction in both the mean and the spread of the residuals. In the second case, the RMS residual is 1.2 arc-minutes, less than half of the fine aspect specification.

In retrospect, it might have seemed reasonable to include in the ground segment software a capability to determine the azimuth alignment directly, since it clearly impacts the fine aspect solution quality. However, the experience with the flight data shows that the observability of this parameter would have remained poor until the gyro propagation problems were resolved. At that point, determination of the correction became trivial; the most significant part of the effort was to verify the value over the duration of the mission.

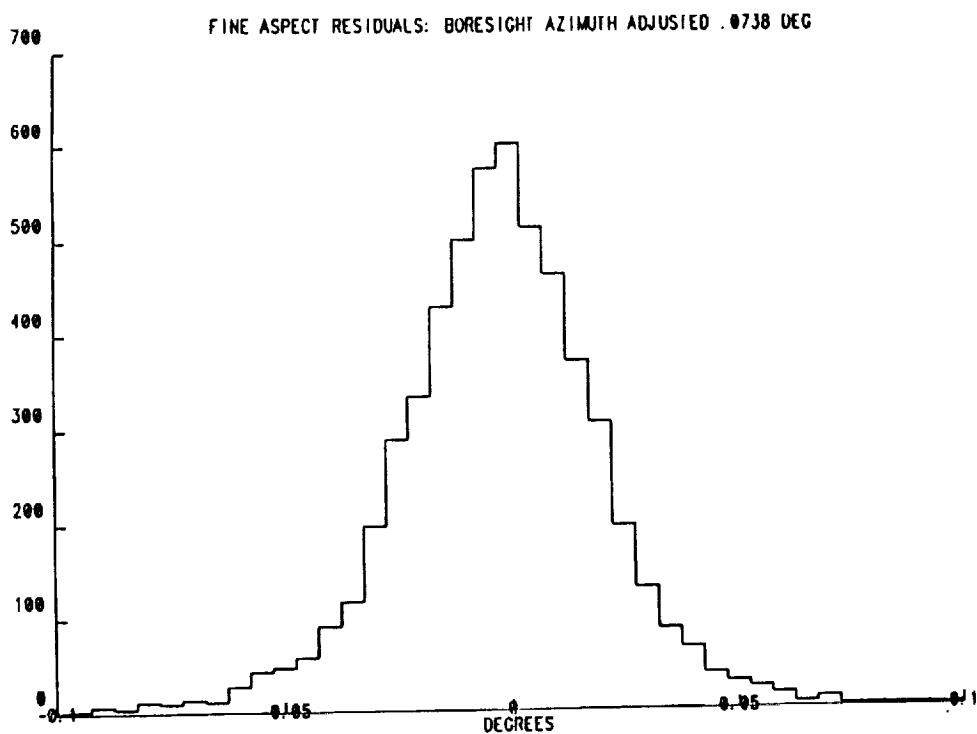
3.4 System Performance

The CDAC attitude processing software is designed to operate in an automated production processing environment. Typically, the system (a shared VAX 8820 computer) generates the attitude for a 24-hour data segment in about 1 hour. With the current system, the accuracy of the fine aspect is typically in the range of 1.5–2.0 arc-minutes for the 1989 and 1990 mission data.

At the beginning of 1991, the quality of the attitude solutions degraded because of the poor quality X-axis gyro data resulting from the degradation in the A_x gyro hardware performance. In March 1990 the X-axis gyros on the spacecraft were reconfigured to feed B_x gyro data into the telemetry for ground processing. At this time, the tuning of system parameters for data from B_x gyro is still in progress.



(a) Before DIRBE Boresight Alignment Adjustment



(b) After DIRBE Boresight Alignment Adjustment

Figure 10. DIRBE Along Scan Residual Histogram

References

1. "Spacecraft Attitude Determination and Control", Wertz, J.R., et al, D. Reidel Publishing Co., 1986
2. "Low-precision Formulae for Planetary Positions", Van Flandern, T.C., and Pulkkinen, K. F., *The Astrophysical Journal*, November 1979
3. "Cosmic Background Explorer (COBE) Attitude Ground Support Requirement Analysis", Computer Sciences Corporation report CSC/TM-84/6142, dtd. December 1984
4. "Interface Control Document between FDF and the COBE Science Data Room (CSDR)", March 1990
5. "COBE Ground Segment Gyro Calibration", Freedman, I., et al, *Proceedings of Flight Mechanics and Estimation Theory Symposium*, May 1991
6. "COBE Attitude Determination System", Wright, E. L., et al, a poster paper presented at the AAS meeting in New Mexico, 1990
7. "High Energy Astronomy Observatory-B (HEAO-B) Attitude Ground Support System (AGSS) Minor Frame Processor", Computer Sciences Corporation report CSC/TM-78/6006, dtd. January 1973
8. "Two Micron Sky Survey", Neugebauer, G., and Leighton, R.B., NASA SP-3047, Washington, DC, 1969.
9. "Three-Axis Attitude Determination from Vector Observations", *J. of Guidance, Control, and Dynamics*, Vol. 4, No. 1, January-February 1981, pp. 70-77.

COBE GROUND SEGMENT GYRO CALIBRATION

I. Freedman, V.K. Kumar, A. Rae, R. Venkataraman (ST Systems Corporation [STX], Lanham, MD 20706),
F.S. Patt (General Sciences Corporation [GSC], Laurel, MD 20707),
E.L. Wright (UCLA, Los Angeles, CA 90024-1562)

ABSTRACT

This paper discusses calibration of the scale factors and rate biases for the Cosmic Background Explorer (COBE) spacecraft gyroscopes, with emphasis on the adaptation for COBE of an algorithm previously developed for the Solar Maximum Mission (SMM). Detailed choice of parameters, convergence, verification, and use of the algorithm in an environment where the reference attitudes are determined from the Sun, Earth, and star observations (via the Diffuse Infrared Background Experiment [DIRBE]) are considered. Results of some recent experiments will be shown. These include tests where the gyro rate data are corrected for the effect of the gyro baseplate temperature on the spacecraft electronics.

1. INTRODUCTION

This paper presents the results of a successful implementation of a gyro calibration system for support of the ongoing Cosmic Background Explorer (COBE) mission. The algorithm has been previously implemented successfully in the High-Energy Astrophysical Observatory (HEAO), SMM, and (most recently) Hubble Space Telescope (HST) projects. The application for COBE is in support of final aspect determination for the production of the Project Data Sets in the Cosmology Data Analysis Center (CDAC). The COBE attitude profile is unique and thus imposes constraints and demands on the calibration algorithm that have not been encountered in prior applications.

The scope of this paper is somewhat unusual in that it combines the implementation and theoretical verification of the calibration system with the analysis of results and practical limitations based on the flight data. A coauthor (Freedman) performed substantial verification of the algorithm based purely on mathematical analysis and verified these conclusions using simulated data following implementation. Another (Patt) relied upon hands-on experience with past calibration applications to explore the practical limitations of the algorithm using the flight data and to thoroughly exercise the system in a variety of on-orbit situations. In doing so, we discovered the surprisingly dynamic behavior of the gyro temperature and the substantial impact that it has on the calibration stability.

The paper has been organized as follows: Section 1 summarizes the need for gyro calibration in the aspect determination and the choice of the algorithm. Section 2 presents the implementation details and the preflight verification. Section 3 discusses the results of the actual calibration using the flight data. Section 4 summarizes the results and discusses the human interface.

1.1 THE NEED FOR GYRO CALIBRATION IN THE COBE GROUND SEGMENT

The final aspect determination for the COBE mission depends critically on the accuracy of the gyro-propagated attitude. This is especially true for the DIRBE Fine Aspect determination; because the DIRBE star sightings occur on the average once per minute, the gyro propagation is the critical link that spans the time between observations and allows a number of observations to be incorporated into a single solution. Even for the Coarse Attitude determination, which has much less stringent requirements, the gyro propagation provides substantial smoothing of the solutions and minimizes the effects of sensor quantization errors, misalignments, and unmodeled systematic errors. Although at some point the gyro attitude propagation will inevitably degrade because of gyro noise and digitization errors, the accuracy of propagation depends to a large degree on the quality of the gyro calibration.

1.2 THE CHOICE OF THE CALIBRATION ALGORITHM

The SMM gyro calibration algorithm (Ref. 1) was chosen over in-line (i.e., integral to the attitude determination process) algorithms based on the following factors:

- This algorithm, which was originally developed at Goddard Space Flight Center (GSFC) by Mr. P. Davenport, has been thoroughly flight-tested on previous Center projects. It is well known to one coauthor (Patt), who has used it successfully on the SMM and previous missions.
- Input to the algorithm consists of attitude quaternions and angular velocities so it is independent of sensor data type and may be used with Fine Aspect solutions.
- It is compatible with the use of the Quest algorithm and with batch-least-squares attitude algorithms, which had already been designed into the COBE ground segment.
- The algorithm is linear in the complete set of gyro calibration parameters: scale factor corrections, misalignments, and biases. It readily supports user selection of the solve-for parameter subset, and it allows for analytical determination of parameter visibility.
- It has no inherent limitations on the number of attitude solutions that can be incorporated into the calibration and therefore can use an arbitrary time span of data.
- It can be fully automated using the existing file structure in the COBE Attitude software system. Its design as an adjunct to the software rather than an integral part is consistent with the philosophy of automated pipeline processing and supports its use as a quality assurance tool.

2.1 ALGORITHM DESCRIPTION

Following the presentation in Ref. 1 (which contains more detail), we note that any rate gyro assembly (RGA) must be composed of at least three gyroscopes whose axis directions taken together completely span the space of possible rotations.

An RGA consisting of three gyros will produce as a response a "vector" \bar{R} of responses of individual gyros whose sensitive axes are \hat{u}_i ($i=1,2,3$) in the spacecraft body frame. This response vector is translated into a measured angular velocity \bar{W}_M in the body frame via the relation

$$\bar{W}_M = \bar{G}_0 \bar{R} - \bar{D}_0 \quad [1]$$

where \bar{G}_0 is the RGA 3 x 3 scale-factor/alignment matrix and \bar{D}_0 is the drift rate bias.

\bar{G}_0 is related to the scale factors k_i and gyro alignments \hat{u}_i by the equation

$$\bar{G}_0 = (1 + k_i) \hat{u}_i, \quad (i=1,2,3). \quad [2]$$

If \bar{G}_0 and \bar{D}_0 deviate from their true values, either because of poor initial calibration or because of temporal changes in the RGA, \bar{W}_M will differ from the true angular rate \bar{W} . The goal of the algorithm is to determine correction matrices \bar{M} and \bar{d} that may be applied to \bar{G}_0 and \bar{D}_0 so that a modified equation [1] will yield the true angular rate:

$$\bar{G} = \bar{M} \bar{G}_0; \quad \bar{D} = \bar{M} \bar{D}_0 + \bar{d}; \quad \bar{W} = \bar{G} \bar{R} - \bar{D} = \bar{M} \bar{W}_M - \bar{d} \quad [3]$$

The angular rate deviation $\bar{\omega}$ between the measured and true rates is given by

$$\bar{\omega} = \bar{W}_M - \bar{W} = -\bar{m}\bar{W}_M + \bar{d} \quad [4]$$

where $\bar{m} = \bar{M} - \bar{I}$ and \bar{I} is the identity matrix. The algorithm will solve for \bar{m} and \bar{d} , separately or together. Because the RGA we are considering contains exactly three gyros, \bar{m} and \bar{d} contain sufficient information to allow separate calibration updates of scale factor alignment and drift for the individual gyros.

The rotation from the RGA-determined end-of-interval attitude to the true end-of-interval attitude transformed to the start-of-interval reference frame may be determined. The vector part of this rotation quaternion, \bar{Z}_n for the nth calibration interval is given by equation [13] of Ref. 1 under the approximations that the rotation determined from the RGA is in agreement with the true rotation to the first order in the error and that the error rotation angle is sufficiently small that the cosine may be approximated by 1 (i.e., the fourth component of error quaternion is 1).

$$\bar{Z}_n = -1/2 [\bar{T}_n (\bar{m}\bar{W}_M - \bar{d})], n = 1, 2, \dots, N. \quad [5]$$

Here \bar{T}_n is the matrix for transforming vectors to start-of-interval spacecraft body coordinates.

Equation [2.1-5] is linear in the unknowns \bar{m} and \bar{d} and lends itself naturally to standard least-squares techniques.

Following equation (4-182) of Ref. 2, this rotation may also be written as

$$\bar{Z}_n = \text{vector portion of } \{q_0 \dot{q}_0^* q_{1K} \dot{q}_{1K}^* - \dot{I}_n \quad [6]$$

where q_0 and q_K are the propagated attitudes at the start and end of the calibration interval, and q_{0K} and q_{1K} are the reference attitudes, respectively. The $*$ denotes a quaternion conjugate.

The matrix equation that represents this equation applied to N calibration intervals is written as

$$\bar{Z} = \bar{H} \bar{x} \quad [7]$$

where \bar{Z} and the state vector \bar{x} are defined as

$$\begin{aligned} \bar{Z} &= \{Z_1^T, Z_2^T, \dots, Z_N^T\}^T, \\ \bar{x} &= 1/2 (m_{11}, m_{12}, m_{13}, m_{21}, m_{22}, m_{23}, m_{31}, m_{32}, m_{33}, d_1, d_2, d_3) \end{aligned}$$

and H is a $3N \times 12$ matrix determined by equation [5] above.

The linear "Bayesian" weighted least-squares loss function J may be used to place appropriate relative emphasis on a priori known calibration values and the updated values as

$$J = 1/2 [E^T \bar{W} E + (\bar{x} - \bar{x}_0)^T \bar{S}_0 (\bar{x} - \bar{x}_0)] \quad [8]$$

$$\text{where } E = \bar{Z} - \bar{H} \bar{x}_0$$

\bar{W} and \bar{S}_0 are symmetric nonnegative definite weighting matrices and \bar{x}_0 is an a priori estimate of \bar{x} .

The gradient minimization approach applied to equation [7] yields the following equations for the state-vector x of corrections to the drift rates and biases:

$$[A]_{12 \times 12} \quad x_{12 \times 1} = y \quad [9]$$

$$A = \bar{S}_a + \bar{H} \bar{W} \bar{H}^T; \bar{y} = \bar{H} \bar{W} \bar{Z}^T + \bar{S}_a x_a$$

The A matrix above may be partitioned into submatrices as below:

$$A = \begin{bmatrix} A_{11} & A_{12} \\ A_{21} & A_{22} \end{bmatrix} \quad \text{where } A \text{ is a } 9 \times 9 \text{ matrix, and } A_{12}, A_{21}, \text{ and } A_{22} \text{ are } 3 \times 3.$$

For scale-factor calculation alone, A_{12} and A_{21} are zero. Thus, scale-factor and bias may be separately computed.

The solved-for scale-factors are related to the solved-for \tilde{G} matrix by

$$(1+k)_i \tilde{u}_i = |G_i| \text{ where } G_i \text{ is the } i^{\text{th}} \text{ row-vector of } \tilde{G}. \quad [10]$$

Application of this algorithm to COBE demands consideration of the following:

COBE has three 2-axis gyro packages, each of which contains one gyro closely aligned to the A, B, or C control axes 120° apart in a plane, and one loosely aligned to the (orthogonal) spacecraft X axis. At any one time, data from one X-axis gyro only are included in the processing. The B control-axis gyro failed early in the mission, leaving the A and C control-axis gyros to support the mission. Because we do not have observability on all the gyro misalignments, the sensitive axis unit vectors were fixed at the prelaunch values throughout the mission.

The input to this algorithm consists of the gyro sample rate $T = 1$ second, the reference attitude quaternions q_R and q_{IK} at the beginning and end of a calibration interval respectively, the measured angular velocities, and the duration of a calibration interval, which consists of n equally spaced samples. The entire data set consists of N calibration intervals. At least four calibration intervals are required to compute a scale-factor. One interval is sufficient to compute a bias. Our implementation accepts only calibration intervals for which all gyro samples are present. A robust matrix inversion technique (Singular Value Decomposition) was used to solve the calibration equations.

Requirements of better than 3 arcminutes RMS residuals with up to 45-min smoothing intervals demanded the use of 1-sec gyro samples to compute the propagated attitudes multiplicatively in double precision arithmetic. COBE rotates through approximately 4.8° per second about the X axis, and it proved to be insufficiently accurate to interpolate the 4-sec sampling rate attitude solutions to obtain adequate angular velocities. Gyro noise effects were not significant in batches as long as 45 minutes.

Previous missions to which this algorithm has been applied carry an independent attitude sensor that yields reference attitudes at commanded times considerably more accurate than is required of the overall solution, often as commanded maneuvers.

The only formal attitude maneuvers in the early mission useful for calibration were the spin-up/roll-slew data, which are discussed in Section 3.

COBE has no star-tracker, but data from the ongoing DIRBE star observations may be used to differentially correct QUEST solutions obtained from batch estimates of the attitude from Earth and Sun sensors (see Ref. 3).

Comparison of the single-frame with gyro-smoothed attitude solutions demonstrated the attitude propagation discontinuities at the smoothing interval boundaries. Numerical experiments showed that the QUEST solutions were appropriate for reference attitudes and should be determined without interpolation. The QUEST solutions themselves

depend on the accuracy of sensor observation propagation for synchronization (Ref. 3), so an iterative approach, "calibrate—determine QUEST solutions—recalibrate," was applied.

A null initial parameter set led to very slow or nonconvergence with oscillation over many iterations. Convergence required a starting approximation so that the correction was small. An initial parameter set was therefore obtained from the manual adjustment of the X-axis gyro scale factors and rate biases as described in Section 3.

The integrated difference rotation between reference and propagated attitudes was $\ll 180^\circ$ over the calibration interval; thus, ambiguities and aliasing problems were avoided.

The attitude accuracy is isotropic (given several star-sightings), so the observation weights (\bar{W}) were chosen to be identity matrices.

An "optimal" choice for the state vector weight matrix (\bar{S}_0) is the inverse of the normalized solution covariance matrix. These weights are updated at each iteration.

This weighting scheme—in terms of the inverse of covariance matrices—is proportional to the inverse of the A matrix described above; an order of magnitude estimate of A_{11}^{-1} will be made in Section 2.3.

2.2 SIMULATED DATA TESTS

Simulated sinusoidal 3-axis attitudes with constant scale factor and alignment matrices and rate biases at constant vector angular velocity were used to verify the implementation.

Table 1 shows that the input and recovered scale-factors and biases agree to several significant figures.

A sensitivity study performed with kinematically simulated data showed the expected proportional sensitivity to scale-factor errors.

2.3 IMPLEMENTATION CHECK

Analytic expressions for every quantity of the algorithm were derived for detailed checks in the special case where the reference attitudes are the transformation at the interval endpoints, combined with constant uniaxial angular velocity and scale-factor-and-alignment matrix. The observation weights were chosen to be identity matrices, and no a priori knowledge of the parameters was assumed.

This study led to order of magnitude estimates for the calibration equations in the notation of Ref. 1.

$$A_{11}(1,1) = 1 + N(Wn)^2$$

$$A_{11}(2,2) = 1$$

$$A_{11}(3,3) = 1$$

$$A_{12}(1,1) = -(Wn^2)$$

[11]

$$A_{22}(2,2) = n^2$$

$$y_1(1) = (NWn) \sin(WnT/2)$$

$$y_2(1) = (NWn) \sin(WnT/2)$$

Table 1. Tests of Gyro Calibration Algorithm Using Simulated Data

Test #	Description	Result
Tests using simulator		
In each case - 800 second smoothing interval, 4 smoothing intervals of data sampled at 4 second intervals		
NULL TEST		
1.	No gyro calibration errors in input attitudes	Successful - the scale factor and biases were computed as zeroes
SCALE-FACTOR DETERMINATION		
- X-AXIS SPIN ONLY		
2.	-4.8 deg/sec spin about X axis; X scale-factor error = $1.2e-3$; state vector was weighted to determine X scale-factor only	Successful - the computed X scale-factor = $1.2e-3$
3.	Similar to case-2; X scale-factor error was set to $1.0e-3$	Successful - the computed X scale-factor = $1.0e-3$
4.	Similar to case-2; X scale-factor error was set to 0.2 (a large value)	Successful - the computed X scale-factor = $-1.5e-2$ (aliased as more than 360 deg rotation between reference attitudes)
- SWITCH X-AXIS GYRO IN SOFTWARE		
5.	As case-3, but using BX or CX gyros	Successful - we were able to switch X axis gyros in software.
- TRANSVERSE AXIS SPIN PROJECTION		
6.	-4.8 deg/sec spin about Z-axis; scale-factor error was set to $1.2e-3$ on Z-axis; A, C, AX gyros.	Successful - the computed A-axis scale-factor = $1.2e-3$; - the computed C-axis scale-factor = $3.0e-4$; (correct projection on C-axis)
7.	-4.8 deg/sec spin about C-axis; scale factor error set to $1.0e-3$ on C-axis; A, C, AX gyros.	Successful - the computed C-axis scale-factor = $1.0e-3$; - the computed A-axis scale-factor = $4.0e-4$; (correct projection on A-axis)
BIAS DETERMINATION		
8.	-4.8 deg/sec spin about X-axis; bias set to $5.0e-4$ deg/sec on X-axis; state-vector weighting permitted only bias determination; A, C, AX gyros.	Successful - the computed X-axis bias = $5.0e-4$
- PROJECTION ON TRANSVERSE AXES		
9.	No spin; bias set to $0.0e-4$ deg/sec about Y-axis; AX gyro only.	Successful - null result
10.	As case-9 but bias set to $0.0e-4$ deg/sec about Z-axis; AX gyro only.	Successful - null result
11.	As case-9 but bias set to $0.0e-4$ deg/sec about Z-axis; A, C, AX gyros.	Successful - computed A-axis bias = $5.0e-4$; - computed C-axis bias = $-3.0e-4$; (correct projection on C-axis)

all other terms being zero, where N is the number of calibration intervals and n is the number of attitude samples per interval. W represents the observed angular velocity. T represents the duration of a calibration interval.

If we start with zero initial corrections, the calibration equations become:

$$A_m = A_{11} - A_{12} A_{22}^{-1} A_{12}^T = [1 + N(Wn)^2] + Wn^2 (1 + n^2)^{-1} (-Wn^2), \quad [12]$$

$$y_m = y_1 - A_{12} A_{22}^{-1} y_2 \text{ as above } (m=1,2,\dots,n),$$

where A_{22}^{-1} denotes the pseudo-inverse of the A_{22} submatrix.

These results were checked against the simulated values.

Note that the relative accuracy of propagation must be better than n^{-2} for adequate estimate of the calibration equations, and an "optimal" relative weighting of n^{-2} on the sensitive axis is indicated.

3.1 CHOICE OF PARAMETERS AND STATE VECTOR CONVERGENCE (FLIGHT DATA)

The choice of the state vector elements to be included in the solve-for parameter set was based on a combination of prelaunch analysis, simulation, and on-orbit verification of the calibration algorithm. The on-orbit results were obtained for two cases: the initial spin-up of the spacecraft, and the constant-spin, standard operational mode. The following subsections discuss the factors that limit state vector observability, followed by the methods and results for the two cases.

Limitations on State Vector Observability

The COBE attitude control configuration (spin about one axis at 0.8 RPM combined with precession about the Sun vector once per orbit) severely limits the observability of some gyro parameters and results in significant correlations among others. The details of these limitations are best explored via the detailed methods of analysis, simulation, and algorithm verification mentioned above; however, in a qualitative sense these results can be inferred intuitively, which provides a convenient means for summarizing the observability problem.

The COBE gyro configuration has one gyro aligned with the spin axis (there is onboard redundancy in this area, but only one spin axis gyro output can be telemetered) and two working gyros in the spin-normal plane, the redundant gyro in this plane having failed soon after launch. (The spacecraft axes in this plane are referred to as the control axes because they are used to control the spacecraft precession, or pitch, rate.) The control axis gyros are not orthogonal but are 120° apart. In the standard gyro calibration parameter set, each gyro is subject to a scale factor error, misalignments (measured as azimuth, or rotation about the spin axis, and elevation, or angle relative to the spin axis), and a constant rate error, or bias.

For the spin axis gyro, if the spin rate variations are small, the scale factor and bias are almost completely correlated; thus, one of these can be held constant. The effect of misalignments of this gyro is small, for two reasons: the effect of any misalignment is a small fraction of the orbit precession rate, which is itself smaller than the spin rate by a factor of 80, and the effect is cyclic and tends to integrate to zero each spin. Thus, for most of the mission only one term need be considered for this gyro. The exception, of course, was during the spin-up, when both the bias and scale factor could be evaluated.

The control axis gyro biases have an effect that is similar to the spin axis gyro misalignments: at the mission spin rate they contribute a small cyclic error that integrates to effectively zero over one spin. The elevation components of the misalignments result in an error that is a small fraction of the spin rate; in the mission mode this also amounts to a constant rate error, which, like the biases, is essentially unobservable. The biases and the elevation errors are thus highly correlated. (These parameters may be more visible at the lower spin rates from the early mission, and

this possibility had not been explored as of this writing.) The scale factors have reasonable observability because the control axis gyro output is essentially a sinusoidal modulation of the spacecraft pitch rate; in other words, errors in these scale factors would result in a pitch error that accumulates linearly. On the other hand, for an ideal (wobble-free) control system, the control axis scale factors are completely correlated; the extent to which these are individually observable depends on the nonuniformity of the pitch rate, the spin axis wobble, and the spin rate. The azimuth alignment errors in these gyros have observability and correlation characteristics that are essentially identical to those of the scale factors because they contribute to an accumulation of error about an axis perpendicular to the pitch axis.

Weighting Scheme and Convergence Criteria

The algorithm allows for the observation and state vectors each to be independently weighted. For the COBE calibrations we chose to use observation weights of unity and to use relative values for the state weights; in fact, based on the estimated solution accuracy, the true observation weights would have been approximately $1.E+6$ for the Coarse attitudes and $4.E+6$ for the Fine Aspect. Therefore, the state weights were reduced by about $1.E+6$ from values based on the estimated uncertainties, and evaluations of the state vector observability using the calibration algorithm were performed by reducing the variances by the same factor. Thus, for example, a bias correction of $1.E-6$ was considered significant only if the square root of the variance was $1.E-3$ or less.

The state weights for the solve-for parameters were typically set at unity in the first iteration, equivalent to uncertainties of about $1.E-3$. The weight for the spin-axis gyro bias was generally left at this value, although the uncertainty was usually much smaller because the observability of this parameter was very good. The weights for the other parameters would typically be increased after each iteration, depending on the magnitude of the correction and its estimated effect on the attitude propagation errors. The best example of this is given in the following section.

As stated previously, the calibration algorithm is very linear, but only to the extent that the calibration errors in the current iteration did not affect the accuracy of the attitude solutions used for the next iteration. For the COBE attitude profile the propagation errors do not accumulate linearly with time; thus, even the attitudes at the midpoints of the gyro propagation intervals were affected by the calibration errors. Therefore, it was necessary to iterate on the calibration if the errors in the a priori state vector were not small. The convergence criteria were selected for each parameter based on its effect on the overall propagation accuracy relative to the Fine Aspect specification; the criteria were $1.E-6$ for the spin axis scale factor, $1.E-5$ for the spin axis bias, and $1.E-4$ for the control axis scale factors.

Gyro Calibration During the Spacecraft Spin-Up

The COBE spin rate was increased from its initial value of 0.23 RPM to the mission mode rate of 0.82 RPM in three roughly equal steps, at 1-day intervals (November 25, 26, and 27, 1989). This activity provided the only opportunity to separately calibrate the spin axis gyro scale factor and bias; it also provided excellent visibility on the individual control axis scale factors.

The following table illustrates the convergence of the state vector. The a priori values were chosen to be $1.E-3$ for the spin axis scale factor correction (based on the experience with manual adjustments to the scale factor) and zero for all other parameters.

<u>Iteration</u>	<u>X Scale Factor</u>	<u>X Bias (deg/sec)</u>	<u>A Scale Factor</u>	<u>C Scale Factor</u>
A Priori	1.0E-3	0.0	0.0	0.0
1	1.060E-3	4.7E-4	1.96E-3	0.0
2	1.066E-3	5.2E-4	1.96E-3	-0.34E-3
3	1.066E-3	5.2E-4	1.96E-3	-0.46E-3

The initial weights were chosen to be unity for the solve-for parameters (for the control axis gyros this included the scale factors and azimuth misalignments; because of the nonorthogonal transformation between the control gyro and

the spacecraft axes, the scale factor and azimuth corrections are coupled in the calibration; the misalignments corrections were insignificant) and $1.E+4$ for all other parameters. At each iteration, the weights for the updated parameters were increased by a factor of 100, except for the spin (X) axis bias, which was allowed to "float." The convergence was very rapid for the spin (X) axis parameters, with about 90% of the residual error being removed at each step. The A gyro scale factor also converged rapidly. The correction to the C gyro was small in the first iteration and was intentionally omitted to ensure that it was not affected by the much larger errors contributed by the A and X scale factors.

It is interesting to note that during the spin-up calibration, the A and C gyro scale factors were not highly correlated. This was most likely due to the combined effects of lower spin rates and increased spin axis wobble at the lower rates, both of which increase the observability of the individual contributions of these gyros to the propagation errors. These initial values provided an excellent starting point for the subsequent calibrations to be performed, for which the correlation of these scale factors is expected to be much higher because only differential corrections should be required for the remainder of the mission.

The effect of the control axis scale factor calibration is illustrated in Figures 1a, 1b, and 2. Figures 1a and 1b show a histogram of Fine Aspect observation residuals before and after the full calibration for 1,170 stars observations on December 18, 1989, with the temperature effect discussed in Section 3.2 included for both runs. For Figure 1a, the X-axis scale factor was adjusted by hand to minimize the average drift rate, and nominal control axis scale factors were used; the full calibration parameter set was used for Figure 1b. The overall reduction in the residuals is clear, with the RMS reduced from 0.031° to 0.020° . Perhaps more importantly, the full calibration dramatically reduced the number of observations with residuals greater than 0.05° (the Fine Aspect requirement), and the overall distribution is much more Gaussian.

In addition to the Fine Aspect residuals, another sensitive measure of the gyro propagation accuracy is the continuity of the attitude at the boundaries between propagation intervals. Figure 2 shows the discontinuities between attitude intervals before and after the calibration; the average discontinuity was reduced by more than half, from 0.16° to 0.07° .

The independent determination of the spin axis and scale factor is useful in that there is enough variation in the spin rate (from 0.80 to 0.83 RPM) to set a minimum accuracy level for the scale factor itself. This parameter can then be fixed for the remainder of the mission, and any residual spin axis rate errors can be absorbed by the bias term.

Gyro Calibration During Normal Operations

As discussed in the previous section, the requirement for the ground segment gyro calibration activities during the COBE mission phase is twofold: to null the average azimuth drift rate by computing the spin axis bias to high accuracy and to compute differential corrections to the control axis gyros to minimize any pitch rate propagation errors. The spin axis gyro temperature correction is expected to account for most of the drift rate errors observed during the first year of the mission, so the bias corrections are also expected to be small.

As of this writing, the ground segment gyro calibration had not yet been performed for the entire first year of the mission, so only a few test cases have been performed. An illustration of the mission calibration procedure was provided by processing a segment of data from December 1989, a few weeks after the spin-up. The a priori values for this calibration were the final results of the spin-up calibration, and the weights for the solve-for parameters were once again set at unity. The convergence for this calibration was very rapid, using the same convergence criteria as before, so there was no need to adjust the state weights. The results were as follows:

	<u>X Bias</u> <u>(deg/sec)</u>	<u>A Scale</u> <u>Factor</u>	<u>C Scale</u> <u>Factor</u>
Initial	5.2E-4	1.96E-3	-0.46E-3
Final	3.2E-4	1.68E-3	-0.78E-3

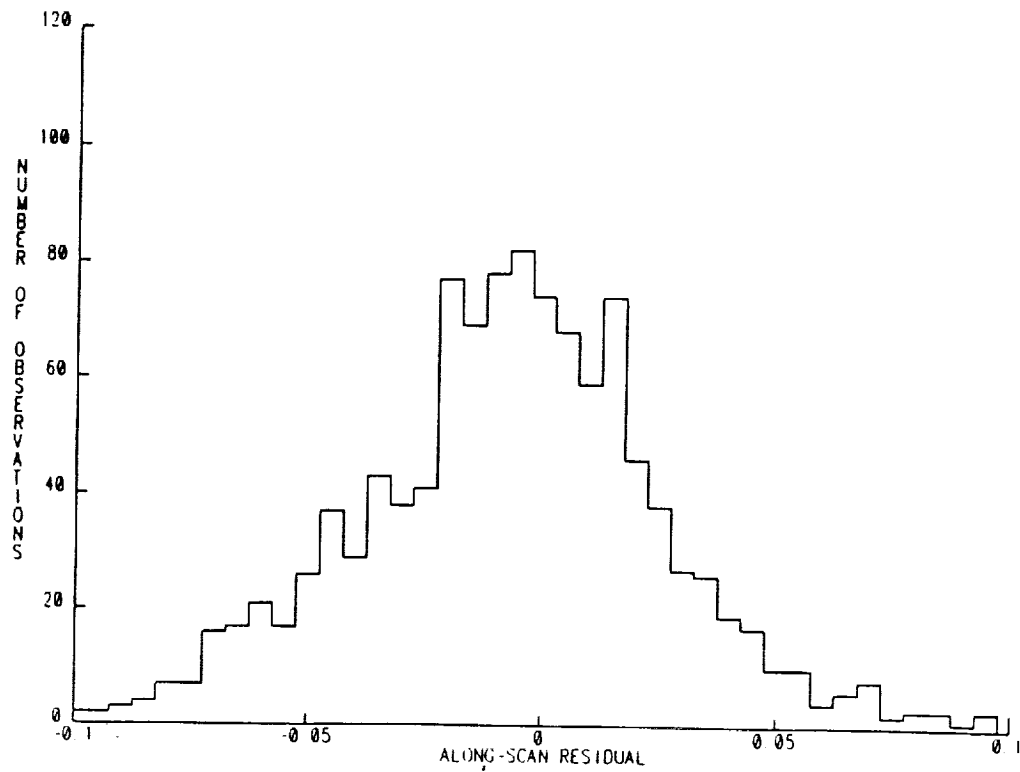


Figure 1a. Fine Aspect Residuals With X-Axis Calibration Only

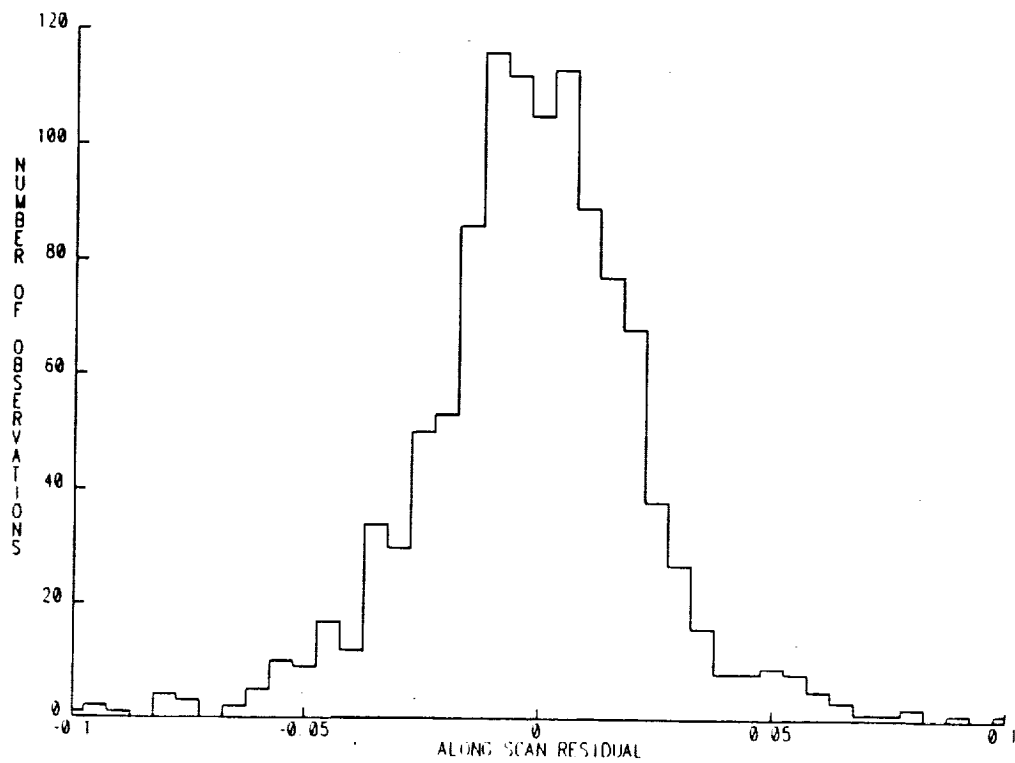


Figure 1b. Fine Aspect Residuals with Full Gyro Calibration

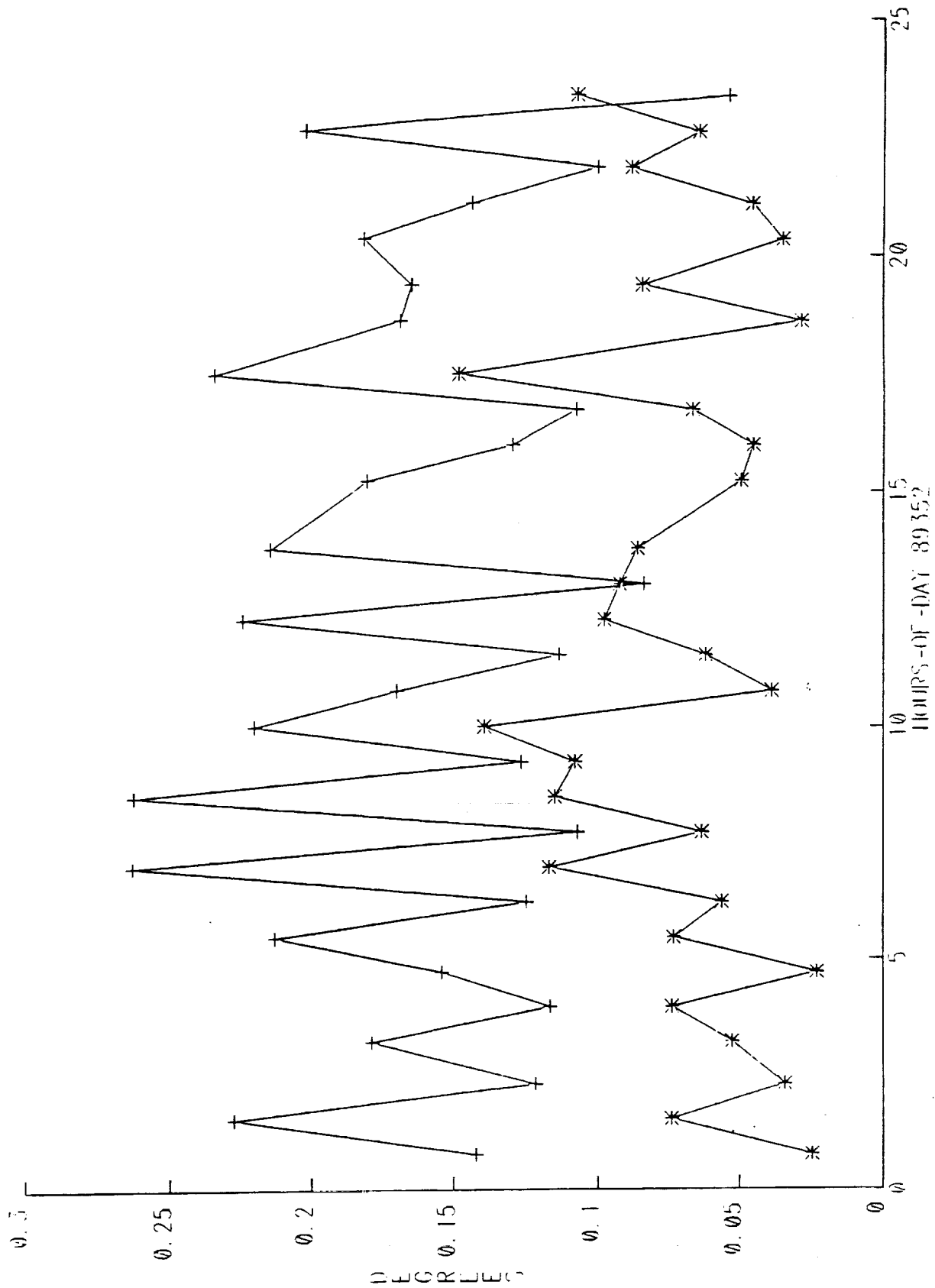


Figure 2. Attitude Discontinuities Before and After Calibration

These results illustrate the correlation of the control gyro scale factors because the corrections to each were nearly the same. Nonetheless, the corrections succeeded in minimizing the pitch component of the propagation errors. The success of this calibration can be judged by the fact that the Fine Aspect solution for this time period produced RMS observation residuals of 1.2 arcminutes, vs. a 3-arcmin accuracy requirement. Thus we conclude that this approach will be very effective for the entire COBE mission, barring any gyro anomalies.

3.2 TEMPERATURE CORRECTION

For most of the first year of the COBE mission, the gyro-propagated attitudes demonstrated cyclic drift rate errors about the spacecraft X axis. The cycle had an orbital and a diurnal component and varied with the spacecraft-commanded roll attitude. The orbital peak-to-peak drift rate errors were typically 1° per hour. This effect could not be attributed to an error in any of the gyro calibration terms and was large enough at times to affect the ability of the DIRBE Fine Aspect system to meet the 3-arcmin requirement.

In addition to this short-term effect, the spin axis drift rates showed considerable variation over the course of the mission. For operational processing these were corrected by manual adjustments of the X-axis gyro scale factor, as discussed in Section 2.1. The scale factor corrections ranged from approximately $0.8\text{E-}3$ to $1.34\text{E-}3$, corresponding to variations in drift rate of over 20° per hour.

The effect can be most clearly seen by comparison of the gyro-smoothed coarse attitude with the single-frame coarse attitude. The single-frame attitudes are noisy but reasonably free of long-term systematic errors; the gyro-smoothed attitudes are smooth but show the effects of propagation errors.

To illustrate the various effects of orbital frequency and spacecraft attitude, we have chosen a day that included spacecraft roll slews (December 18, 1989, which included slews from the nominal 4° to 8° and 2° at intervals of a few orbits). The X-axis calibration was chosen to minimize the average drift rate. The gyro-smoothed attitudes were integrated for 45 minutes. Figures 3a through 3c show the azimuth (X-axis), roll, and pitch components of the gyro-smoothed vs. single-frame comparison on this day. The azimuth and roll plots clearly show the variations in the gyro propagation errors over the course of the day.

The cause of this effect was discovered during a test run on the December 18 data. The observed drift variations prompted an investigation of possible external causes for the drift rate variations. A cursory examination of the gyro baseplate temperatures, available from the spacecraft telemetry data base, revealed that they also had an orbital cycle and varied according to the spacecraft roll angle. The effect of the roll slews was to increase the temperature range to about 4° . It was a simple matter to show that the azimuth drift rate errors correlated extremely well with the baseplate temperatures. The temperature variations are shown in Figure 4a, and the correlation of drift rate with temperature on this day is shown in Figure 4b.

After extensive analysis of correlation between the baseplate temperature and the drift rate, the following conclusions were reached: the effect was consistent throughout the mission, it was linear over the observed range of temperatures ($15\text{--}25^\circ\text{C}$), the temperature appeared to affect the gyro scale factor rather than the bias term (at the level of 76 PPM per $^\circ\text{C}$), and there was a time lag of roughly 10 telemetry major frames (320 seconds) between the temperature and drift rate variations.

The CDAC Attitude pipeline software was modified to include a linear temperature correction to the gyro rates, with the linear coefficients and the time delay specified as input parameters. One implementation issue was that the temperature telemetry digitization was fairly coarse (about 0.38°C); this was resolved by including polynomial smoothing in the correction algorithm. Figure 4a shows both the raw (plotted points) and smoothed (continuous line) temperatures.

This correction, in conjunction with the overall gyro calibration, reduced the typical gyro azimuth propagation error rates to 0.1° per hour. Figures 5a, 5b, and 5c show the single-frame vs. gyro-propagated differences with the temperature correction applied. The correction reduced the typical propagation error to less than the noise in the single-frame solutions in azimuth and roll. The Fine Aspect observation residuals with all corrections applied were

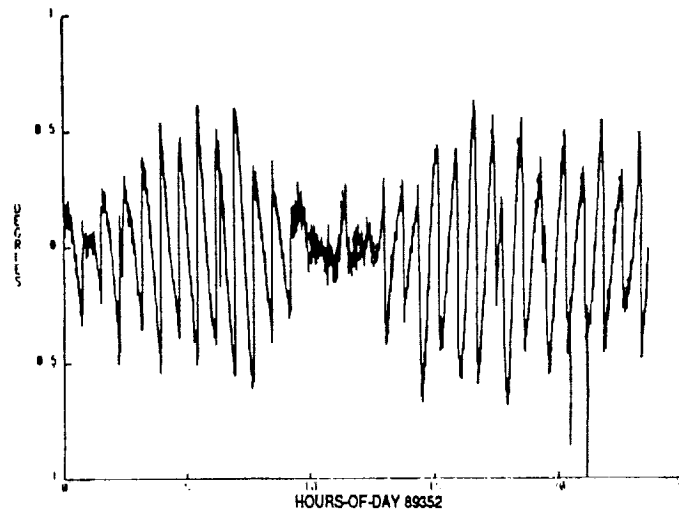


Figure 3a. Gyro Propagation Errors Without Temperature Correction: Azimuth

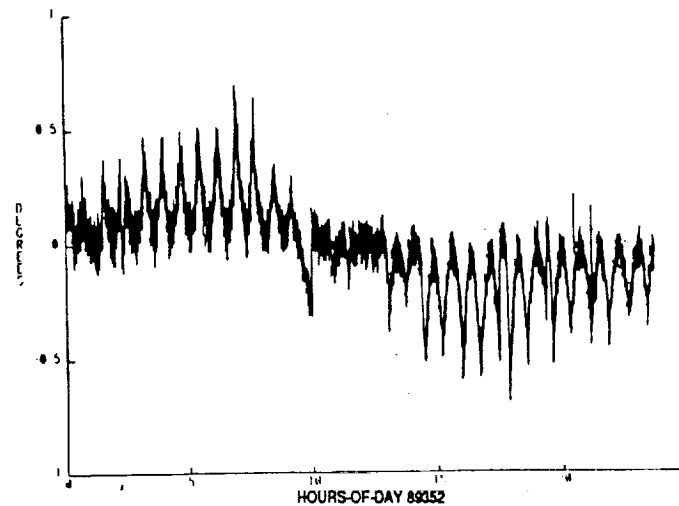


Figure 3b. Gyro Propagation Errors Without Temperature Correction: Roll

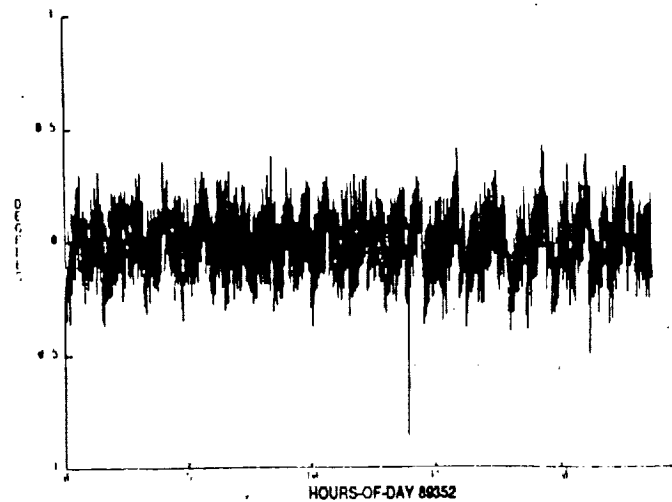


Figure 3c. Gyro Propagation Errors Without Temperature Correction: Pitch

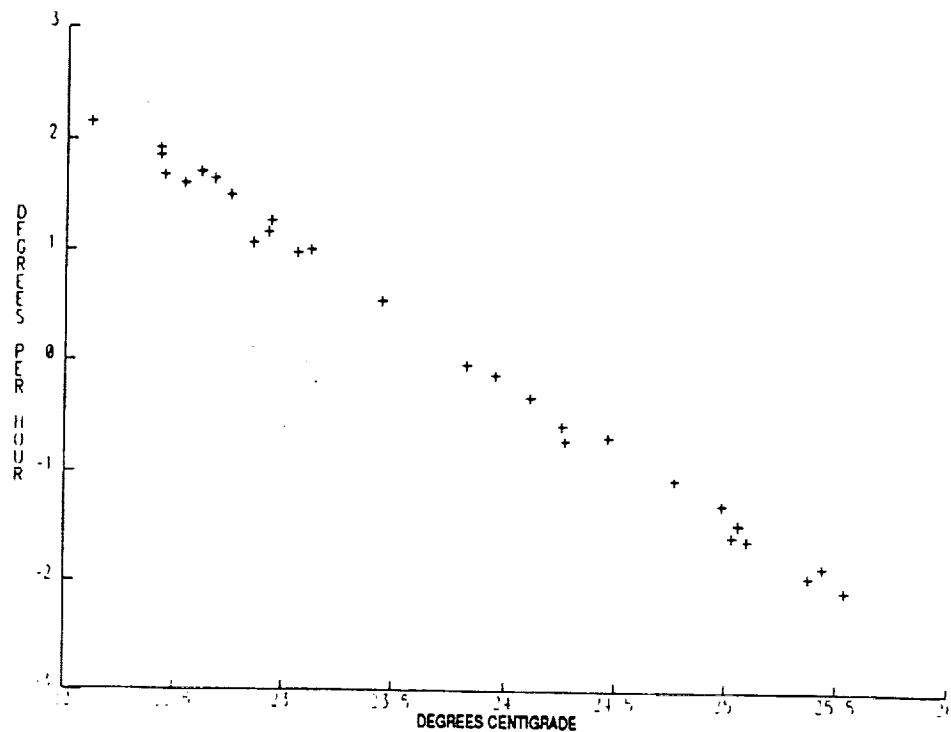


Figure 4a. Azimuth Drift Rate Vs. Gyro Temperature

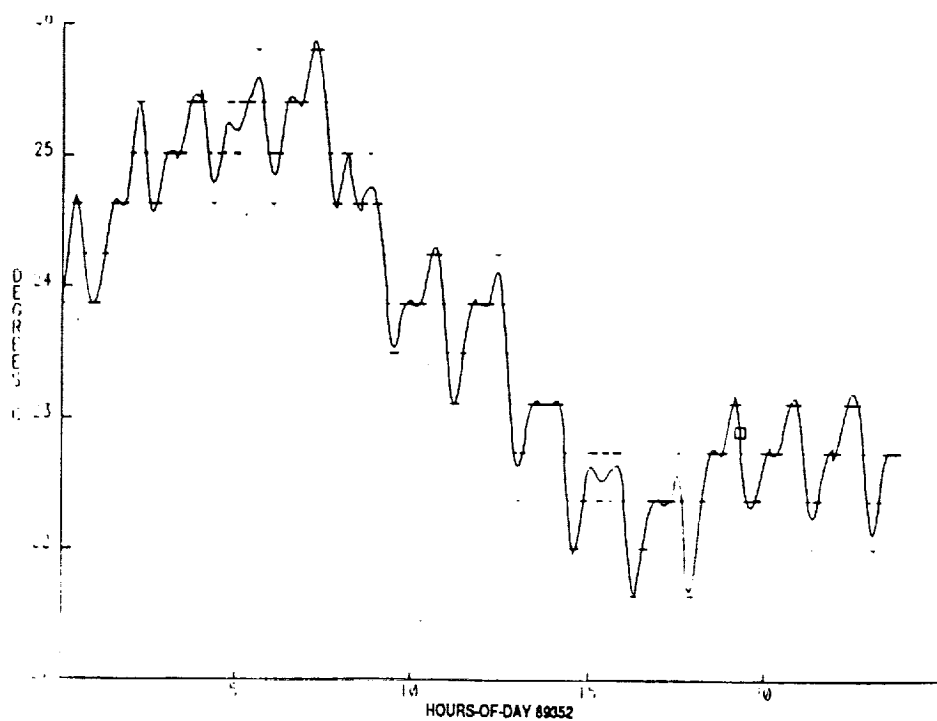


Figure 4b. Raw and Smoothed Gyro Baseplate Temperature

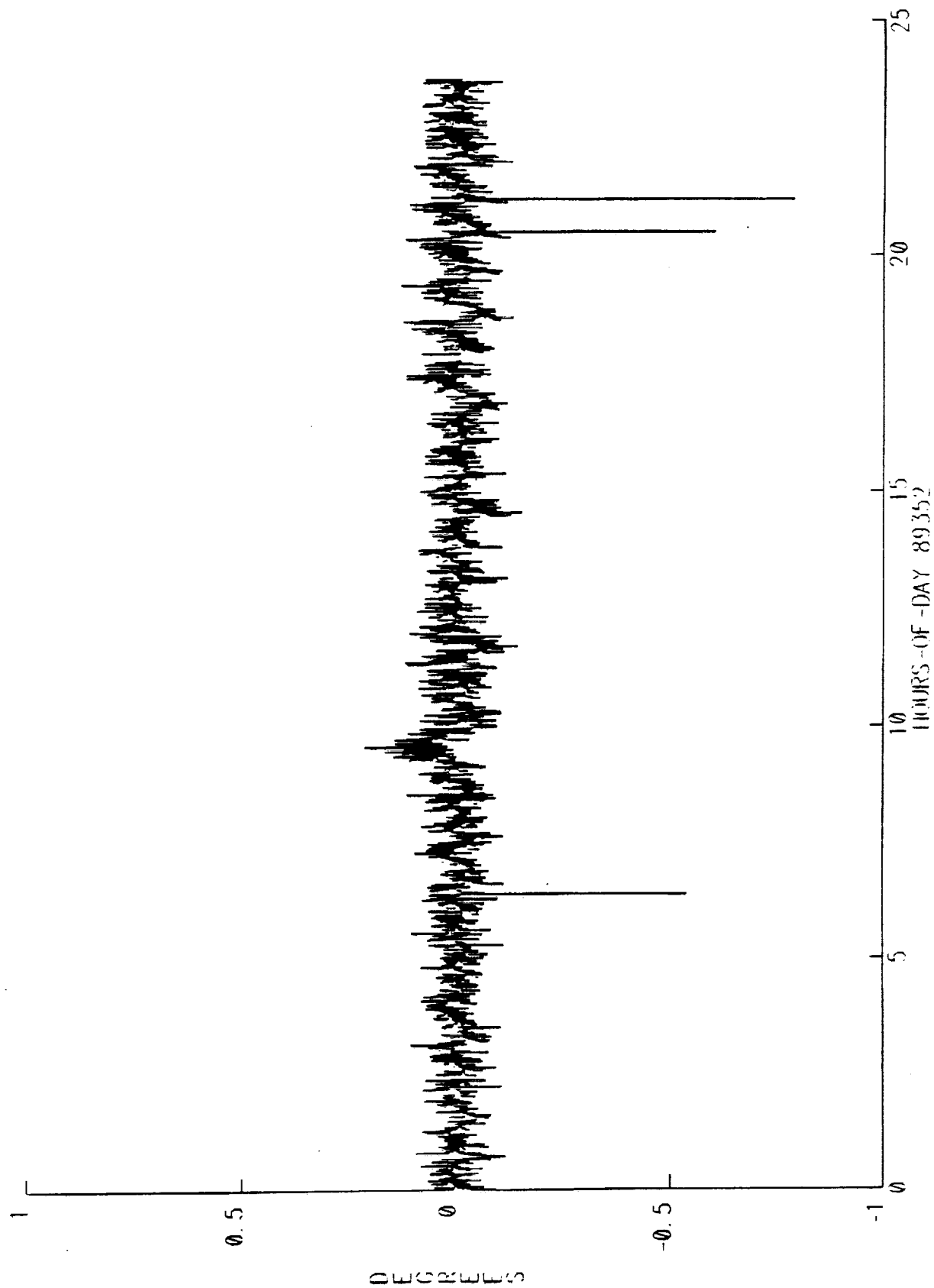


Figure 5a. Gyro Propagation Errors With Temperature Correction: Azimuth

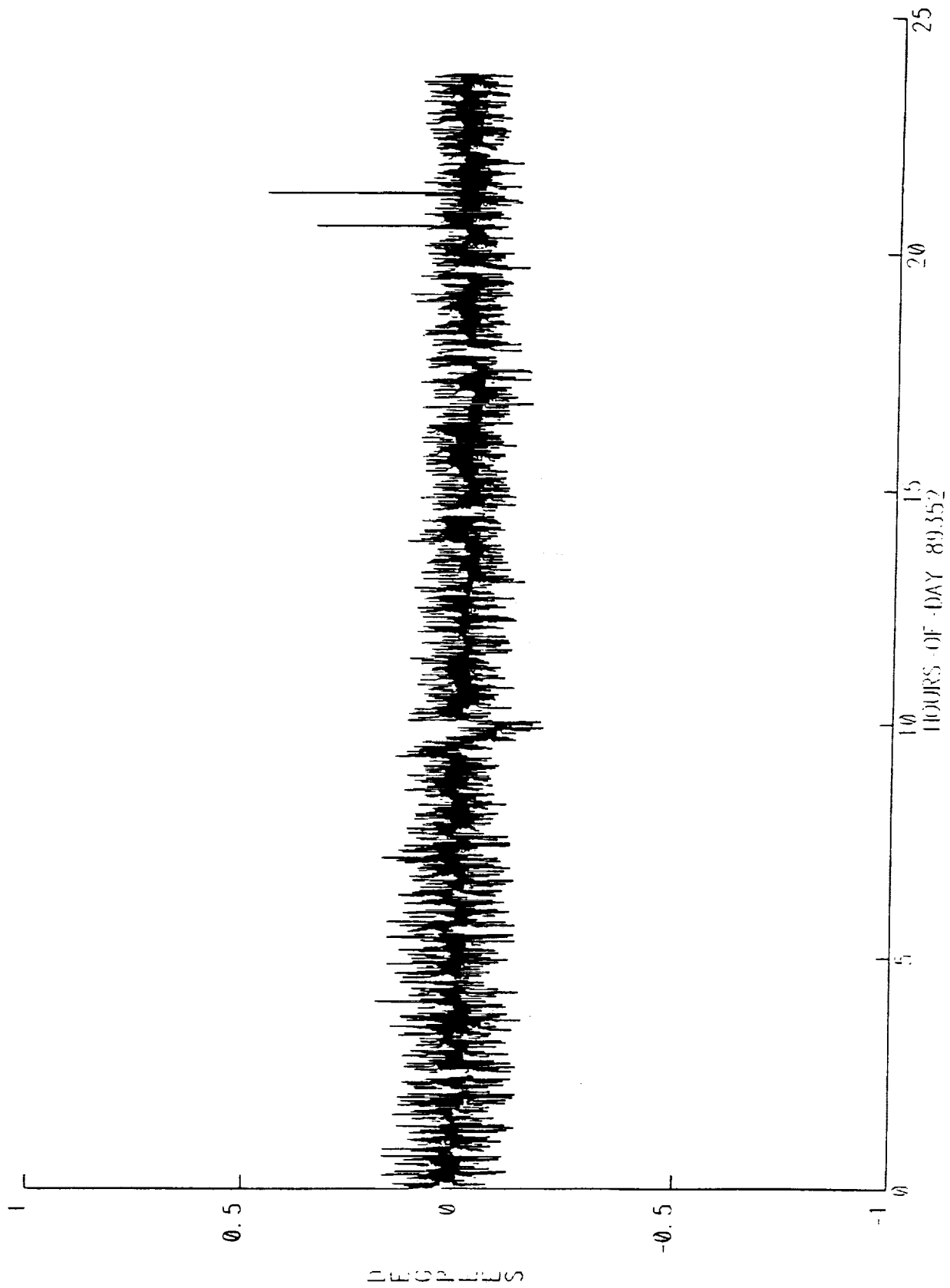


Figure 5b. Gyro Propagation Errors With Temperature Correction: Roll

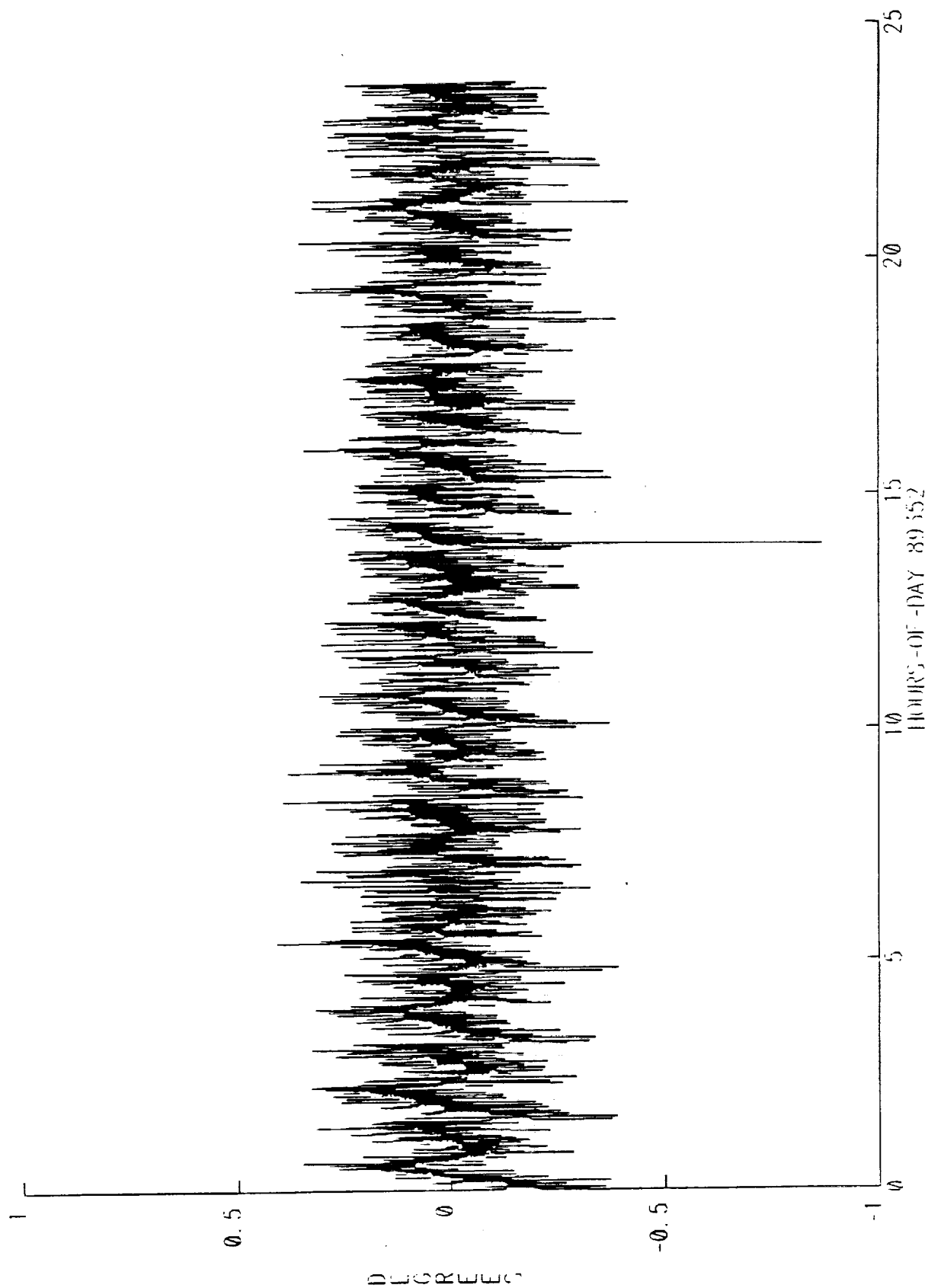


Figure 5c. Gyro Propagation Errors With Temperature Correction: Pitch

reduced from 3 arcminutes RMS using 20-min propagations to less than 1.5 arcminutes using 45-min propagations. After the correction was incorporated into the COBE Science Data Room (CSDR) Attitude operational procedures, the apparent X-axis gyro calibration remained stable for approximately 3 months.

In summary, the characterization of the X-axis gyro temperature effect unlocked the full performance potential of the COBE ground segment gyro calibration and the Fine Aspect system.

4.1 QUALITY ASSURANCE

The operational scenario includes a human intervention step so that the quality of the calibration may be checked before use in the Attitude Pipeline. The quality assurance procedures rely on the plots as shown in the figures to verify the improvement in the aspect solution quality:

- Figure 1 shows the Fine Aspect residual distribution with X-axis calibration only and with full calibration, which includes the control axis gyros.
- Figure 2 shows the attitude discontinuities before and after full calibration.
- Figures 3 and 5 show the single-frame vs. gyro-propagated attitude differences in azimuth, roll, and pitch errors, before and after the temperature correction.

In addition to its support of aspect determination in the production environment, the gyro calibration is an effective diagnostic tool. The best example of this is its recent use to document an instability in the spin-axis gyro for 20 days from Day 16 of 1991. This gyro had been replaced by a backup unit at the time of writing.

4.2 PERFORMANCE RESULTS

Typical results are 120 CPU seconds and 280 I/O operations on a moderately loaded VAX 8800 to process 8 hours of attitude data with 12-min calibration intervals containing attitude samples at 1-sec intervals.

The performance was optimized by storing each full interval of propagated attitude solutions in memory and minimizing the I/O operations.

This implementation is fast enough for closed loop calibration to become possible—the Gyro Calibrator may write a file of partial results per interval that the Pipeline Gyro Propagator may read, especially if a gyro is unstable on the scale of a calibration interval.

SUMMARY AND CONCLUSIONS

This algorithm has been adapted for use on a mission with a unique attitude profile and in an environment where the reference attitudes result from the same system as the propagated attitudes. The gyro calibration results have enabled the overall aspect system to consistently exceed specifications by a comfortable margin, and the implementation has produced an efficient and flexible calibration capability.

ACKNOWLEDGEMENTS

The National Aeronautics and Space Administration/Goddard Space Flight Center (NASA/GSFC) is responsible for the design, development, and operation of the Cosmic Background Explorer (COBE) under the guidance of the COBE Science Working Group. GSFC is also responsible for the development of the analysis software and for the production of the mission data sets.

Special thanks are due to the scientists and engineers who designed and built the DIRBE and to the staff in the attitude control systems branch at GSFC.

REFERENCES

1. "Algorithm for In-Flight Gyroscope Calibration," P.B. Davenport and G.L. Welter, NASA Goddard Space Flight Center Flight Mechanics and Estimation Theory Symposium, 1988.
2. "Solar Maximum Mission Attitude System Functional Specifications and Requirements," Computer Sciences Corporation, CSC/SD-68/6082.
3. "COBE Ground Segment Attitude Determination," V.K. Kumar et al., NASA Goddard Space Flight Center Flight Mechanics and Estimation Theory Symposium, 1991.

FLIGHT MECHANICS/ESTIMATION THEORY SYMPOSIUM

MAY 21-23, 1991

SESSION 3

Evidence of Chaotic Pattern in Solar Flux Through a Reproducible Sequence of Period-Doubling-Type Bifurcations

S. Ashrafi and L. Roszman
COMPUTER SCIENCES CORPORATION (CSC)

ABSTRACT

This paper presents a preliminary study of the limits to solar flux intensity prediction, and of whether the general lack of predictability in the solar flux arises from the nonlinear chaotic nature of the Sun's physical activity. Statistical analysis of a chaotic signal can extract only its most gross features, and detailed physical models fail, since even the simplest equations of motion for a nonlinear system can exhibit chaotic behavior.

A recent theory by Feigenbaum suggests that nonlinear systems that can be led into chaotic behavior through a sequence of period-doubling bifurcations will exhibit a universal behavior. As the control parameter is increased, the bifurcation points occur in such a way that a proper ratio of these will approach the universal Feigenbaum number. Experimental evidence supporting the applicability of the Feigenbaum scenario to solar flux data is sparse. However, given the hypothesis that the Sun's convection zones are similar to a Rayleigh-Benard mechanism, we can learn a great deal from the remarkable agreement observed between the prediction by theory (period doubling — a universal route to chaos) and the amplitude decrease of the signal's regular subharmonics.

This paper will show that period-doubling-type bifurcation is a possible route to a chaotic pattern of solar flux that is distinguishable from the logarithm of its power spectral density. This conclusion is the first positive step toward a reformulation of solar flux by a nonlinear chaotic approach.

The ultimate goal of this research is to be able to predict an estimate of the upper and lower bounds for solar flux within its predictable zones. Naturally, it is an important task to identify the time horizons beyond which predictability becomes incompatible with computability.

1. INTRODUCTION

An accurate forecast of the intensity of solar flux is a prerequisite to accurate orbit and lifetime prediction for spacecraft. The orbit lifetime is a function of the atmospheric drag force. The drag depends on the atmospheric density, which is influenced by the solar flux. Solar ultraviolet and X-ray emissions that directly affect the Earth's atmosphere are highly correlated with solar flux F10.7 observed on the surface of the Earth. Present density models, such as Jacchia-Roberts (J-R), Harris-Priester (H-P), and mass spectrometer incoherent scatter (MSIS), use F10.7 solar flux intensity as the indicator of the potential strength of ionizing radiation (References 1, 2, 3, and 4).

Current forecasting methods use statistical models to predict solar flux; for example, the Schatten method used by Goddard Space Flight Center (GSFC), Marshall Space Flight Center (MSFC), and National Oceanic and Atmospheric Administration (NOAA) (Reference 5). These models use traditional stochastic analysis (usually based on structurally random data) to predict solar flux. However, as shown below, the patterns exhibited by the solar flux data indicate that the dynamical system creating the solar flux signal is inherently chaotic rather than completely stochastic. Starting with the postulate that solar flux is a chaotic time series, a chaotic model is developed to reproduce essential features of the solar flux signal.

The solar flux signal is classified in Section 2 through analysis of a few basic descriptive properties. Section 3 presents a possible model for the solar flux signal based upon recently developed nonlinear dynamics concepts of period-doubling bifurcations and upon the results shown in References 5, 6, 7, and 8.

2. CLASSIFICATION OF SOLAR FLUX SIGNAL

Signals such as the solar flux have been categorized historically as either deterministic (meaning that a model of the physical system can be constructed and used to predict the particular signal that will occur at a given time from a signal(s) at a another time) or random (meaning that no model of the physical system can be constructed, but, rather, that a method can be found to predict the probability that any particular signal will occur at a given time, based on the history of the signal). These general categories can be divided further, as shown in Figure 1. For deterministic signals, predictability is achieved by deriving for the model of the system equations of motion for the signal. For random signals, a statistical analysis of the signal history must be performed and either an existing statistical theory applied or a new statistical theory constructed.

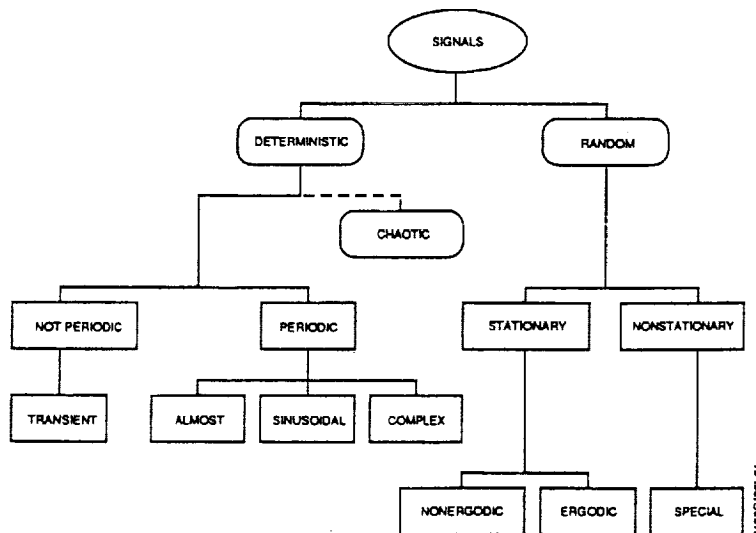


Figure 1. Categories of Signals in Data Analysis

Recent research on dynamic systems indicates that the cascade of categorizations shown in Figure 1 is incomplete and that signals can exist for a system that has a detailed physical model (the system is deterministic), but that the derived equations of motion cannot be used to predict the signal. Such signals and their systems of origin are categorized as chaotic. While the lack of predictability in a deterministic system may seem inconsistent, mathematical precision must be separated from the precision of physical observation. When a model is mathematically deterministic, only one solution to its equations of motion exists for the given initial conditions (Reference 9). To predict a signal to some specified accuracy, the observer must know the initial conditions of the system to some related accuracy; however, one well-defined class of models has equations of motion for which variations beyond the precision of the observer's knowledge of the initial conditions prevent predictions to a specified accuracy. Terrestrial weather (to which solar activity is perfectly analogous) is an example of such a chaotic system.

Several statistical functions can be used to analyze the possible extent of the chaotic nature of the solar flux signal. Sections 2.1 and 2.2 present the application of these functions, and Section 2.3 presents some conclusions.

2.1 AUTOVARIANCE AND AUTOCORRELATION OF THE SOLAR FLUX

The solar flux data shown in Figure 2 present an example of a statistical time series. By plotting a scatter diagram using pairs of values $(f_i, f_{i+\ell})$ of a time series, we can visualize the joint probability distribution $P(f_i, f_j)$. For the solar flux data from Figure 2(a), we obtain the scatter diagram in Figure 3 for lags of $\ell = 0$ and $\ell = 27$. By plotting f_{i+27} versus f_i (Reference 10), this plot shows that the correlation between f_{i+27} and f_i is positive.

Figure 4 shows the plots of autocovariances, autocorrelations, and autocorrelation errors for 600 shifts. These plots were generated from more than 4,000 points of the solar flux time series shown in Figure 2(b).

Figures 5(a) and 5(b) show the plots of the power spectra for the solar flux data from Figures 2(a) and 2(b), respectively. Figure 6 has the plot of the power spectra of data from Figure 2(a), scaled to have the same horizontal axis as in Figure 5(b). This plot was scaled to show a global symmetry of the power spectra under time extension.

2.2 FOURIER FILTERING

In the low-pass Fourier filter method, we Fourier-transform the signal and then take the inverse Fourier-transform, omitting frequencies greater than a specified limit. Using this technique, we can determine what frequencies to disregard for construction of a simple iterative map. Figure 7 contains the solar flux time series for the period November 1977 to November 1980, and a plot for 27-point rectangular averaging. Figure 8 has plots from 7- and 27-point triangular averaging. Figure 9 shows a plot of Fourier-filtered solar flux time series with 20 and 50 harmonics retained.

2.3 CONCLUSIONS FROM STATISTICAL ANALYSIS

Looking at the solar flux time series shown in Figure 2(a), it is difficult to see any pattern or structure in the solar flux data. However, the scatter diagram of Figure 3(b) shows regions where points are clustered together. This clustering is an indication of correlation between f_i and f_{i+27} . Figure 4 has a plot of the autocovariance and autocorrelation function with its standard error, and shows the small peaks that are separated by exactly 27-day solar rotations. Additionally, we can see that every 183 days, an anomaly occurs in the autocorrelation function. This anomaly is probably due to a change of the magnetic latitude of the Earth every 6 months ($\frac{1}{2}$ year ≈ 183 days). To determine if this is a numerical or computational artifact, we also have plotted the standard error of autocorrelation function. At the particular location of these anomalies, no considerable change in standard error of autocorrelation function was observed; therefore, these anomalies are dynamical in character and are not produced by computational artifacts. The autocorrelation plots show that the autocorrelation of the solar flux decreases with increasing time shifts, a characteristic common to chaotic time series.

Comparing Figure 8(a) to Figure 9(b), and Figure 8(b) to Figure 9(c), we can see that 27-point triangular averaging is equivalent to retaining 20 harmonics in a Fourier low-pass filtered solar flux signal; 7-point triangular averaging is equivalent to retaining 50 harmonics. This information is useful for constructing an iterative

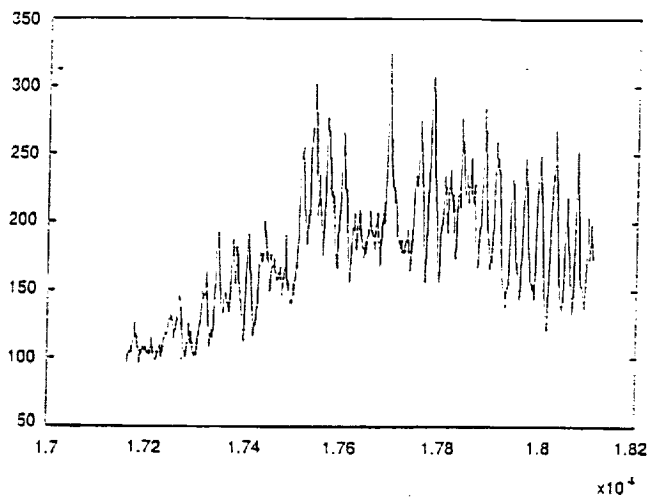


Figure 2(a). Short-Duration Solar Flux F10.7 (10^{-22} watt/m².Hz) Plotted Versus Modified Julian Date (MJD)

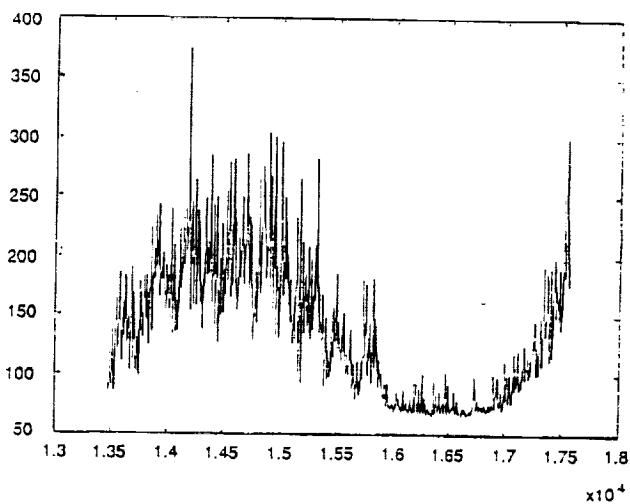


Figure 2(b). Long-Duration Solar Flux F10.7 Plotted Versus Modified Julian Date (MJD)

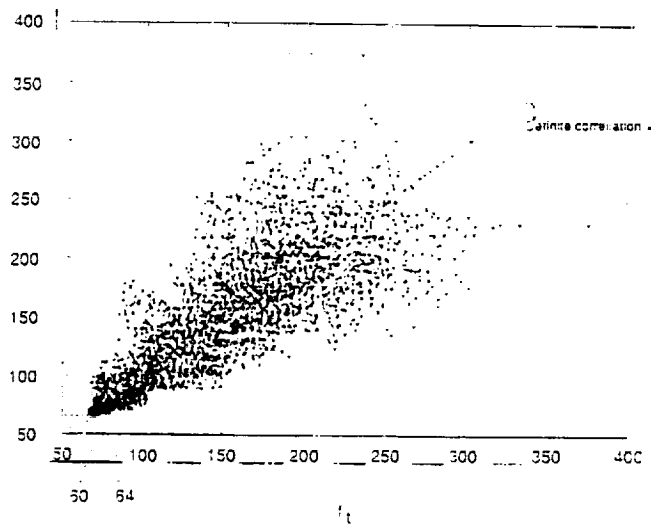
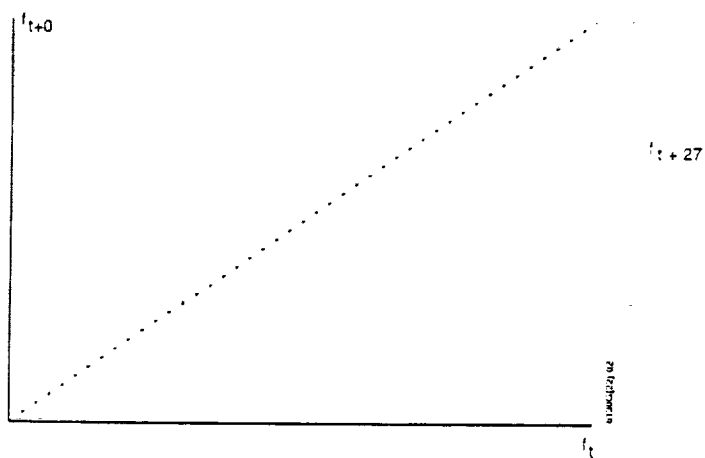
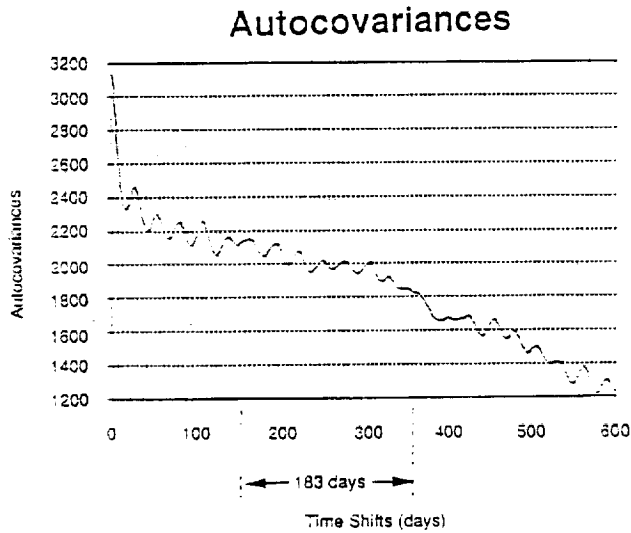


Figure 3. Scatter Diagram at Lags (a) $\ell = 0$ and (b) $\ell = 27$



A time series could be checked to determine whether ϕ_k is zero after a lag ℓ . A check is necessary to identify a model for a time series. The approximate form of the variance of the estimated autocorrelation coefficient is given by

$$\text{var}[r_\ell] \approx \frac{1}{n} \sum_{j=-\infty}^{\infty} (\phi_j^2 + \phi_{j+\ell} \phi_{j-\ell} - 4\phi_j \phi_{j+\ell} + 2\phi_j^2 \phi_\ell^2)$$

If autocorrelation damps out exponentially ($\phi_\ell = \psi^{|\ell|}$, $(-1 < \psi < 1)$), then

$$\text{var}[r_\ell] \approx \frac{1}{n} \left[\frac{(1 + \psi^2)(1 - \psi^{2\ell})}{1 - \psi^2} - 2\ell\psi^{2\ell} \right]$$

Figure 4(a). Plot of Autocovariances for Solar Flux Time Series of Figure 2(b) (600 Shifts)

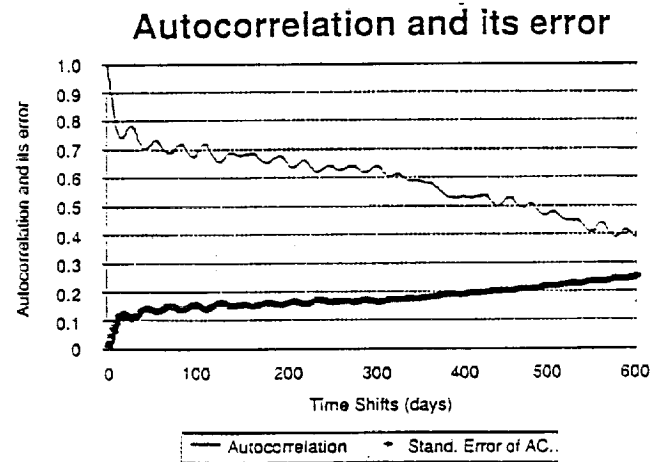


Figure 4(b). Plot of Autocorrelation and Standard Error of Autocorrelation for Solar Flux Time Series of Figure 2(b) (600 Shifts)

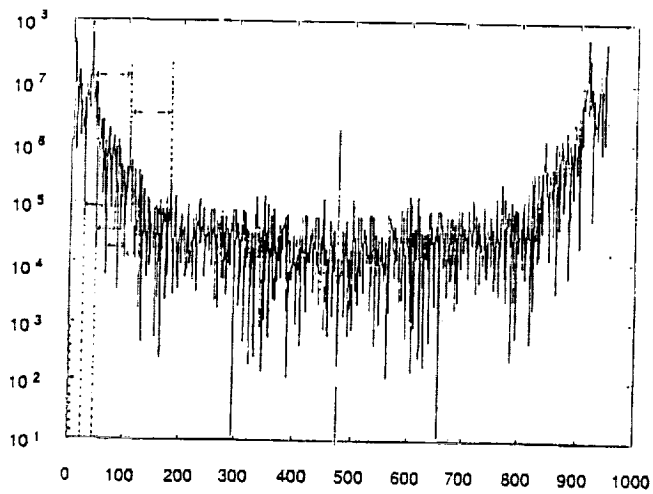


Figure 5(a). Logarithm of Power Spectrum for Solar Flux Time Series of Figure 2(a)

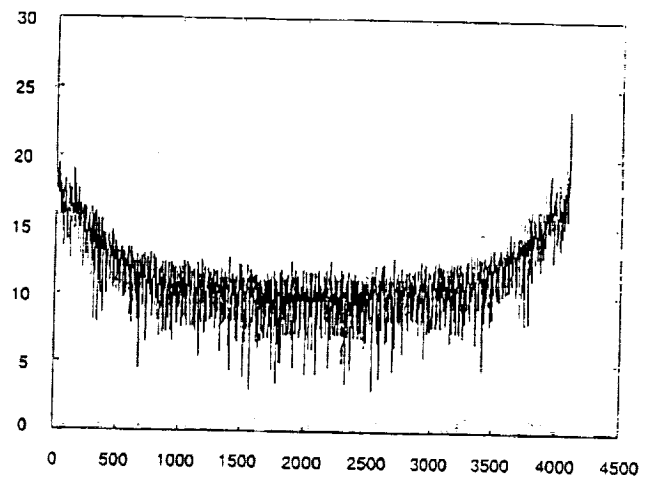


Figure 5(b). Logarithm of Power Spectrum for Solar Flux Time Series of Figure 2(b)

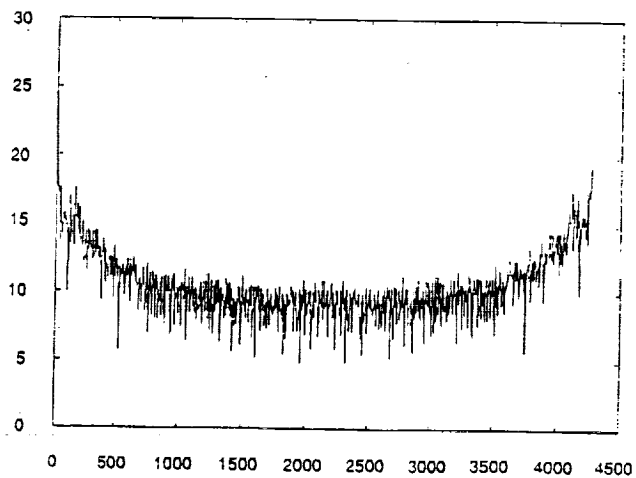


Figure 6. Logarithm of Power Spectrum for Solar Flux Time Series of Figure 2(a), Scaled to the Timespan of Figure 2(b)

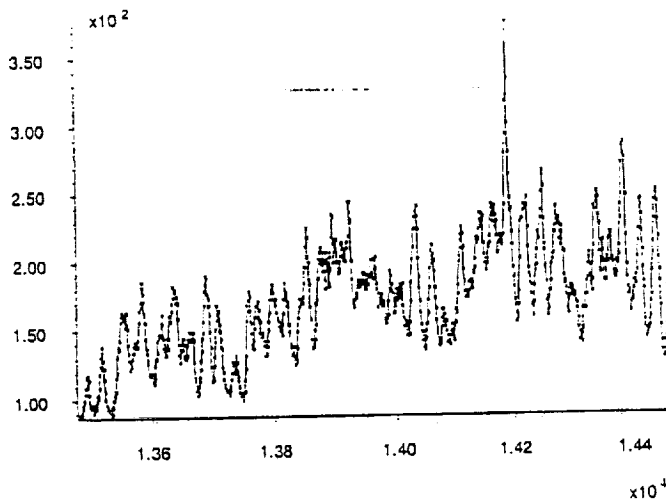
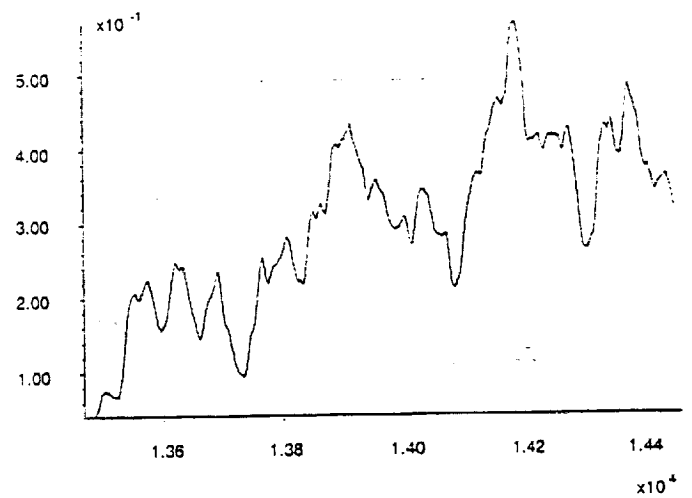


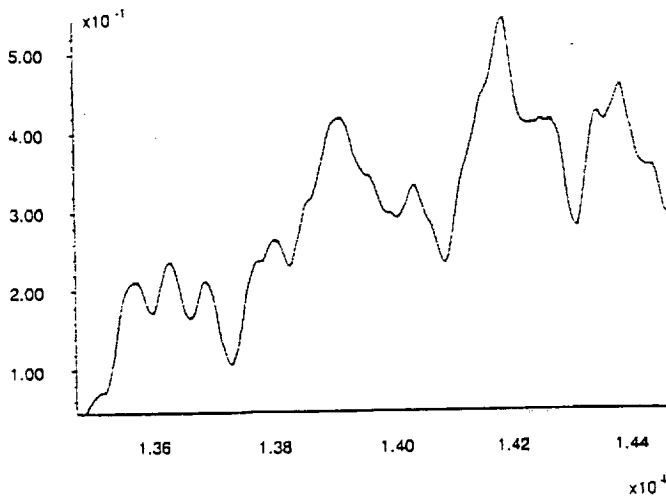
Figure 7(a). Solar Flux Time Series Versus Modified Julian Dates; The Dots Indicate Solar Flux Values Measured at That Specific Day



$$\bar{f}_i = \frac{f_{i-3} + f_{i-2} + f_{i-1} + f_i + f_{i+1} + f_{i+2} + f_{i+3}}{7}$$

for $i = 4$ to 7

Figure 7(b). 27-Point Rectangular Average From Figure 7(a)



$$\bar{f}_i = \frac{f_{i-3} + 2f_{i-2} + 3f_{i-1} + 4f_i + 3f_{i+1} + 2f_{i+2} + f_{i+3}}{16}$$

for $i = 4$ to 7

Figure 8(a). 27-Point Triangular Average of Solar Flux Time Series of Figure 7(a)

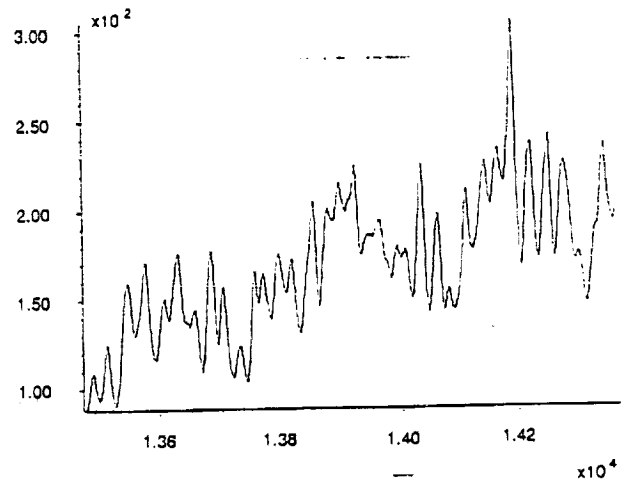


Figure 8(b). 7-Point Triangular Average of Solar Flux Time Series of Figure 7(a)

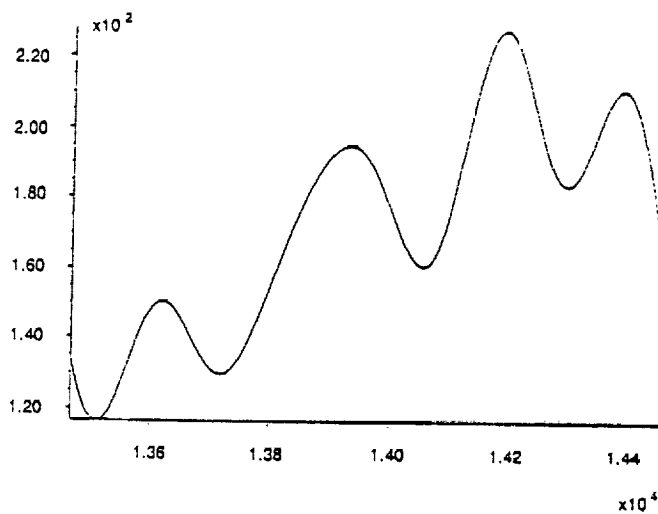


Figure 9(a). Fourier-Filtered (5 Harmonics Retained) Signal From Solar Flux Time Series of Figure 7(a)

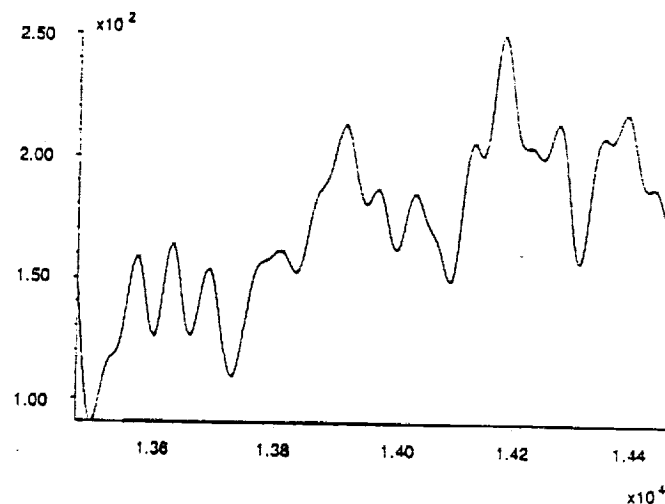


Figure 9(b). Fourier-Filtered (20 Harmonics Retained) Signal From Solar Flux Time Series of Figure 7(a)

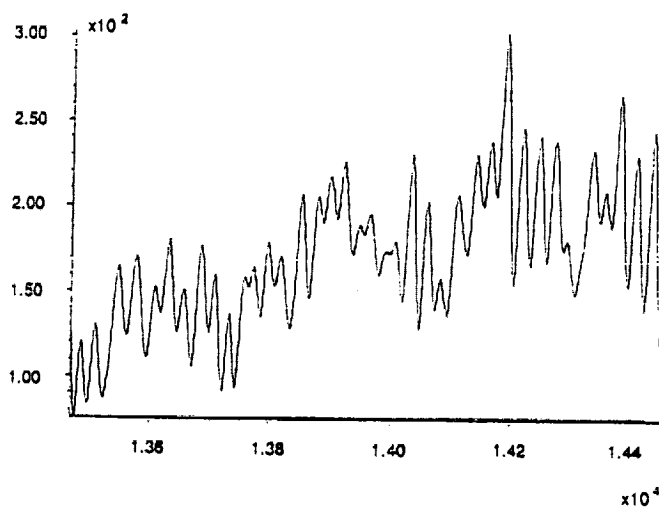


Figure 9(c). Fourier-Filtered (50 Harmonics Retained) Signal From Solar Flux Time Series of Figure 7(a)

manifold (see Section 3) that can reproduce our time series. Figure 10 shows the Fourier spectrum of the autocorrelation of the time series shown in Figure 8(a), which clearly shows the particular patterns such as the 27-day periodicity, the 183-day anomaly, and other periodic anomalies.

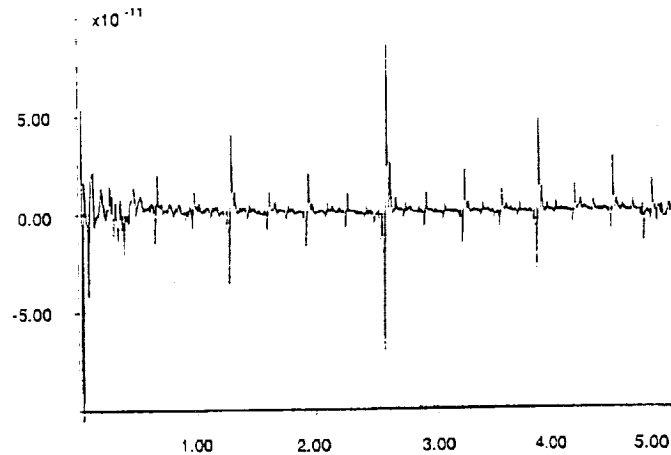


Figure 10. Fourier-Transform of the Autocorrelation of the Solar Flux Time Series From Figure 7(a), Showing the Periodicity Pattern in the Autocorrelation Function

Figure 6 shows the plot of a power spectrum for a timespan that was scaled for another time space. This plot was done to observe the global symmetry of the power spectra under time extension (a fractal characteristic). Fractal structures are common to chaotic time series.

Figures 5(a) and 5(b) show the plots of the power spectra for the solar flux data presented in Figures 2(a) and 2(b), respectively. Many obvious patterns are evident in the power spectra of Figure 5(a); for example, we can clearly see the peaks for 27-day solar rotation periodicity. One interesting feature of this figure is that, starting from the midpoint of the spectra (the "glitch" close to the 480 Fourier component), we can find the first largest glitch to the left at about the 295 Fourier component. If we divide the distance from 295 to 480 by 2, we see the next-largest downward glitch near the 390 Fourier component. Furthermore, if we divide the distance from the 295 glitch to the 390 glitch, we will once again find the next-largest glitch. The regular appearance of these glitches demonstrates successive frequency halving or period doubling for the solar flux signal. In laboratory experiments, period doubling was observed in several chaotic systems (Reference 11). As with the solar flux signal, noise limited the number of observed period doublings to only a few. Based upon laboratory experiments, we conclude that period doubling is a possible route to chaos in the solar flux signal. (Currently, three established routes to chaos have been found: the Grossmann-Feigenbaum period-doubling route, the Manneville-Pomeau route, and the Ruelle-Takens-Newhouse route.)

3. INTRODUCTION TO CHAOS IN DYNAMICAL SYSTEMS

This section presents some examples of the various states of chaos.

3.1 EXAMPLES OF CHAOTIC SYSTEMS

Two examples are introduced here. The first one (Rayleigh-Benard) is very similar to the dynamical behavior of the Sun. The second one (dripping faucet) is a model system for studying the strange attractor of solar flux; because it exhibits period doubling, it is a good candidate for studying solar flux.

Most scientists know the dynamical behavior of systems in which systems eventually settle into either periodic motion (limit cycle) or into a steady state (system ceases its motion). However, another important class is called the chaotic system. This system cannot be represented using standard analytical functions (Reference 12).

Our first example considers the dripping faucet model (see Figures 11, 12, 13, and 14). In this model, water drops fall from the faucet at a steady rate, the drops pass a detector, and the pattern is seen to be periodic. When the rate of flow is small, the time difference between the drops ($\Delta t = t_{i+1} - t_i$) is constant. As the rate is increased, two drops fall together over a longer period. Therefore, two periods are associated with this system: one is short, Δt_s , and the other is long, Δt_L . The sequence of time intervals, then, is $\dots \Delta t_s, \Delta t_L, \Delta t_s, \Delta t_L$. This interval is called period-two sequence. Longer periodic sequences are possible at a specific flow rate. This sequence can become irregular and therefore chaotic (Reference 13).

Our second example considers the experiment of Libchaber and Maurer (Reference 11). In this experiment, a liquid contained in a small box is heated from the bottom. The important points are as follows:

- The experiment has a controllable parameter, the Rayleigh number, which is proportional to the temperature difference between the bottom and the top of the cell. The Rayleigh number describes the stability of a convective flow.
- The system is dissipative. Whenever the Rayleigh number is increased, the transients begin to die out. For small temperature gradients, heat flows across the cell, but the liquid is static. At a critical temperature, a convective flow sets in. The hot liquid rises in the middle, the cool liquid flows down at the sides, and the two convective rolls appear (see Figure 15).

As the temperature difference is increased further, the rolls become unstable in a very specific way—a wave starts running along the roll, as shown in Figure 16(a). As the warm liquid rises on one side of the roll and cool liquid descends down the other side, the position and the sideways velocity of the ridge can be measured with a thermometer, as shown in Figure 16(b). A sinusoid is then observed, as shown in Figure 17(a); two other ways of displaying the measurement are suggested by the graphs in Figure 17(b).

The temperature difference is now increased. After the stabilization of the phase-space trajectory, a new wave is observed superimposed on the original sinusoidal instability. The three ways of looking at it (real time, phase-space, and frequency spectrum) are illustrated in Figure 18.

At first it appears that T_0 is the periodicity; however, a closer look reveals that the phase-space trajectory misses the starting point at T_0 and closes on itself only after $2T_0$. A new band has appeared at half the original frequency on the frequency spectrum. Its amplitude is small because the phase-space trajectory is still approximately a circle with periodicity T_0 .

As the temperature increases slightly, a fascinating thing happens. The phase-space trajectory undergoes the very fine splitting seen in Figure 19(a).

Three scales are involved here: casual observation reveals a circle with period T_0 ; closer scrutiny shows ∞ with period $2T_0$; and very close examination shows that the trajectory closes on itself only after $4T_0$. The same information can be read off the frequency spectrum; the dominant frequency is f_0 (the circle), then $f_0/2$, and finally, much weaker $f_0/4$ and $3f_0/4$.

The experiment now becomes very difficult. A tiny increase in the temperature gradient causes the phase-space trajectory to split on an even finer scale, with the periodicity 2^3T_0 . If the noise were not too loud to continue, it would be expected that these splittings would continue, yielding a trajectory with finer and finer detail and the frequency spectrum seen in Figure 19(b) with families of weaker frequency components. For a critical value of the Rayleigh number, the periodicity of the system is $2^n T_0$, and the convective rolls have become turbulent. The ripples that are running along them show no periodicity, and the spectrum of idealized noise-free experiment contains infinitely many subharmonics. If increases are made to the temperature gradient beyond this critical value, further surprises occur. The following section provides a numerical simulation of a simple nonlinear oscillator to provide an understanding of why the phase-space trajectory splits in this peculiar fashion.

In an externally driven pendulum, one can see that for a wide range of initial points, the phase-space trajectory converges to a limit cycle (trajectory loops onto itself), which for some $k = k_0$ is as shown in Figure 20(a). If not for the external driving force, the oscillator would have simply come to a stop; as it is, it is executing a motion

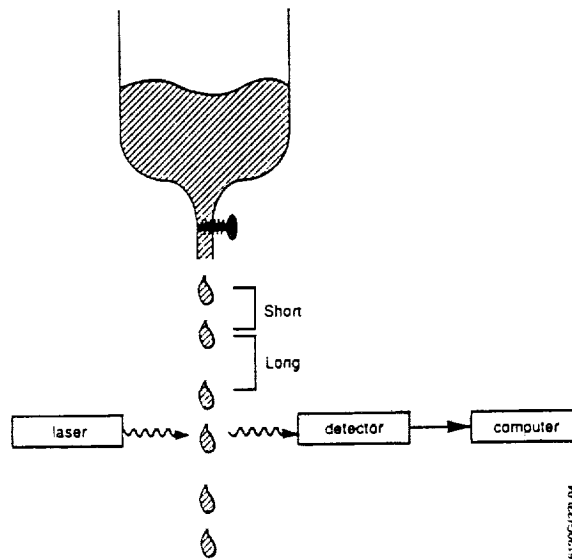


Figure 11. Dripping Faucet Experiment

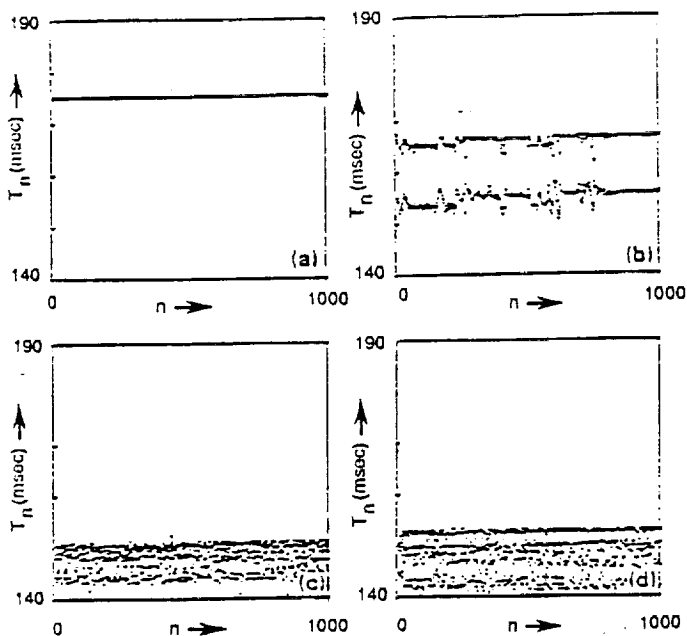


Figure 12. Time Interval Versus Drop Number at Four Low Drip Rates (Reference 10): (a) Periodic Dripping, (b) Biperiodic Dripping, (c) Chaos With an Average Interval, and (d) Chaos With a Different Average Interval

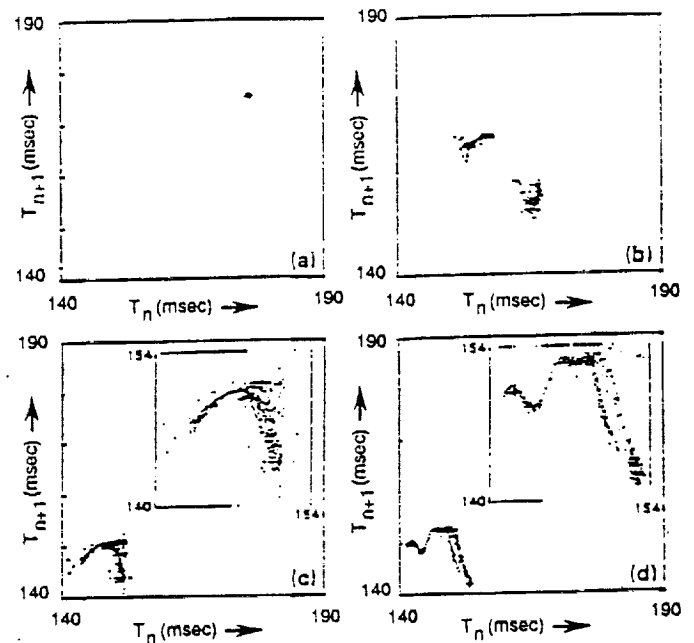


Figure 13. Time Interval Versus Next Time Interval, (T_n, T_{n+1}) , From Data of Figure 12: (a) Periodic Case, (b) Biperiodic Case, (c) The "Parabola" Formed by the Random-Looking Data of Figure 12(c), and (d) The "Camel" Formed by the Random-Looking Data of Figure 12(d)

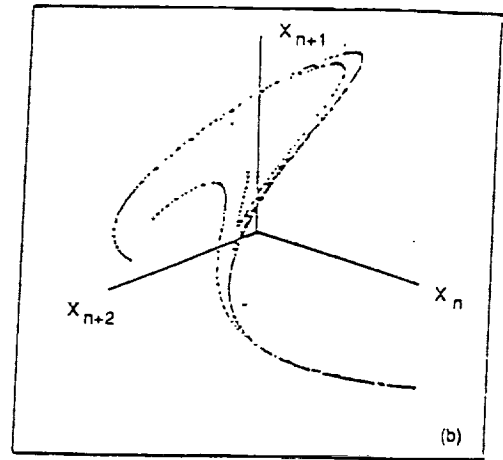
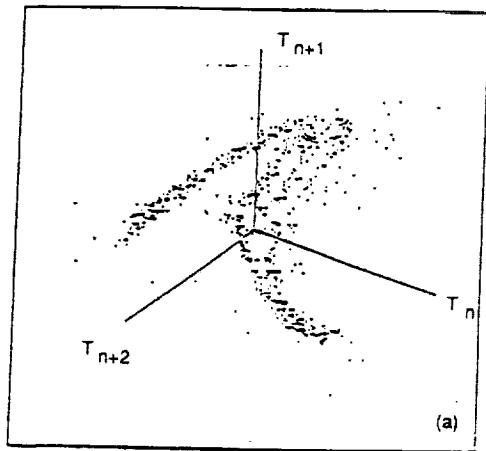


Figure 14. Sample Plots: (a) 3-Dimensional Plot (T_n, T_{n+1}, T_{n+2}) From Data of Figure 12(c), (b) The Hénon Attractor Displayed in the Same 3-Dimensional Coordinates as the Water Drop Data of Figure 14(a).

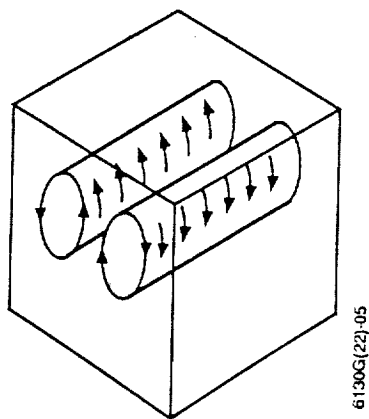
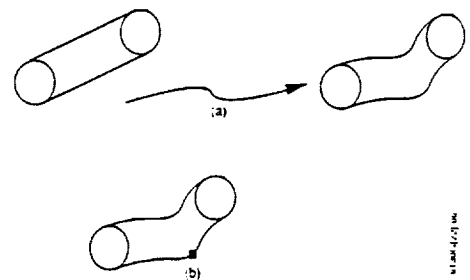
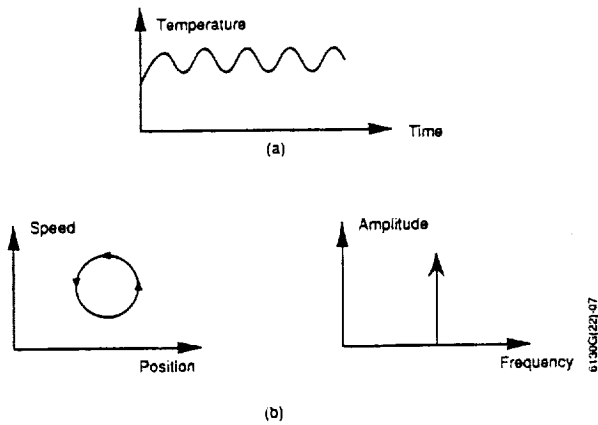


Figure 15. Rayleigh-Benard Convection Rolls



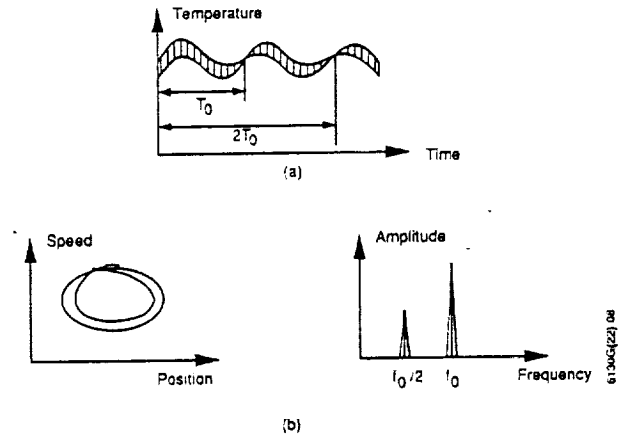
(a) A Wave Starts Running Along the Roll as the Temperature is Increased.
(b) The Position and the Sideways Velocity of the Ridge can be measured With a Thermometer

Figure 16. Convection Rolls Affected by Temperature



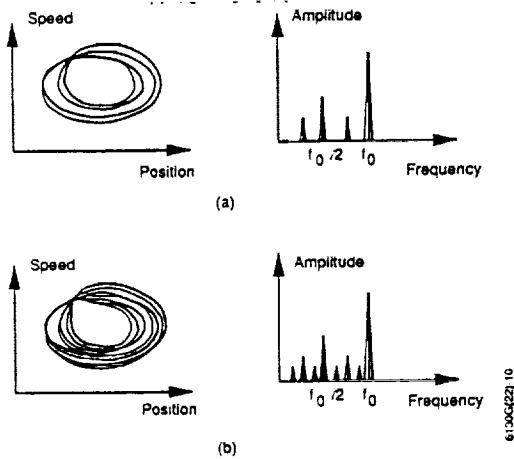
(a) Thermometer Reading, Indicating Position and Sideways Velocity of the Ridge.
(b) Two Different Representations of This Dynamical System: Phase-Space and Frequency Representations

Figure 17. Additional Ways to Display the Measurements



(a) Time domain representation.
(b) Phase space and frequency representation.

Figure 18. Phases-Space Trajectory Misses the Starting Point at T_0 and Closes on Itself Only After $2T_0$



(a) As the Temperature Gradient is Increased, the Phase-Space Trajectory Undergoes a Very Fine Splitting: Phase-Space and Frequency Representations.
(b) A Tiny Increase in the Temperature Gradient Causes the Phase-space Trajectory to Split on an Even Finer Scale with Periodicity $2^3 T_0$.

Figure 19. Phase-Space Trajectories

forced on it externally, independent of the initial displacement and velocity. It is easy to visualize this nonlinear pendulum executing little backward jerks as it swings back and forth. Starting at the point marked 1, the pendulum returns to it after the unit period T_0 . However, as the friction is decreased, the same phenomenon is observed as in the turbulence experiment where the limit cycle undergoes a series of period doubling as illustrated in Figure 20(b).

The trajectory continues to nearly miss the starting point, until it hits after $2^n T_0$. The phase-space trajectory is getting increasingly hard to draw. However, the sequence of points 1, 2, ..., 2^n , which corresponds to the state of the oscillator at times $T_0, 2T_0, \dots, 2^n T_0$, sits in a small region of the phase space, and it can be enlarged for a closer look, as seen in Figure 21(a). Globally, the phase-space trajectories of the turbulence experiment and of the nonlinear oscillator numerical experiment look very different. However, the sequence of near misses is local and looks roughly the same for both systems, as illustrated in Figure 21(b). This method of reducing the dimensionality of the phase-space is often called a Poincaré map. Instead of starting at the entire phase-space trajectory, we find its points of intersection with a given surface. The Poincaré map contains all the needed information and enables the scientist to read off where an instability occurs and how large it is. By continuously varying the nonlinearity parameter (such as friction and Rayleigh number) and plotting the location of the intersection points (in the present case, the Poincaré surface is a line), the result is the bifurcation tree seen in Figure 22(b). A computer-generated example of a real bifurcation tree for a simple chaotic system is shown in Figure 22(a). The phase-space trajectories that have been drawn are localized so the tree has a finite span. Bifurcation occurs simultaneously because it is cutting a single trajectory; when it splits, it does so everywhere along its length. Finer and finer scales characterize both the branch separations and the branch lengths.

Feigenbaum's discovery consists of the following quantitative observations:

- The parameter convergence is universal (independent of the particular physical system), as shown in Figure 22(c).
- The relative scale of successive branch splittings is universal (independent of the particular physical system), as seen in Figure 22(d).

The beauty of this discovery is that if turbulence (chaos) is arrived at through an infinite sequence of bifurcations, the following two predictions result:

$$\delta = \lim_{i \rightarrow \text{large}} \frac{\Delta_i}{\Delta_{i+1}} = 4.6692 \qquad \alpha = \lim_{i \rightarrow \text{large}} \frac{\epsilon_i}{\epsilon_{i+1}} = 2.5029$$

3.2 SENSITIVITY TO INITIAL CONDITIONS (ATTRACTORS)

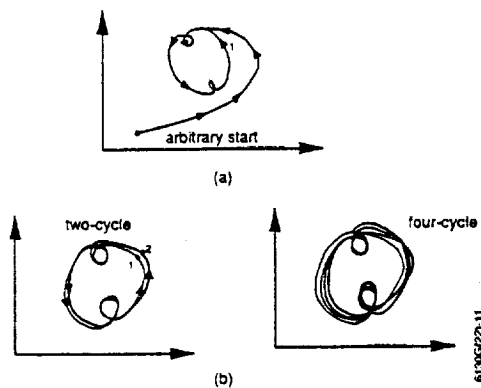
Here we intend to show that a time horizon exists above which predictions are impossible. To demonstrate this, we use the dripping faucet attractor (the Hénon attractor), which contains multiple periodicities in its dynamics.

One of the most important concepts in dynamics of dissipative systems is the presence of attracting sets, or attractors, in phase space. These are bounded sets where regions of initial conditions asymptote as time increases; that is, dynamical systems that are conservative do not have attractors. Two examples of attractors are shown in Figure 23 (Reference 14).

NOTE: The dimensionality of a point attractor is 0 and the dimensionality of a limit-cycle attractor is 1 (it is a line rather than a point). In general, the dimension of an attractor can be a noninteger fraction or a fractal attractor; such attractors are called strange attractors. An example of a strange attractor is shown in Figure 24 and is generated from the Hénon map (10^4 successive iterations).

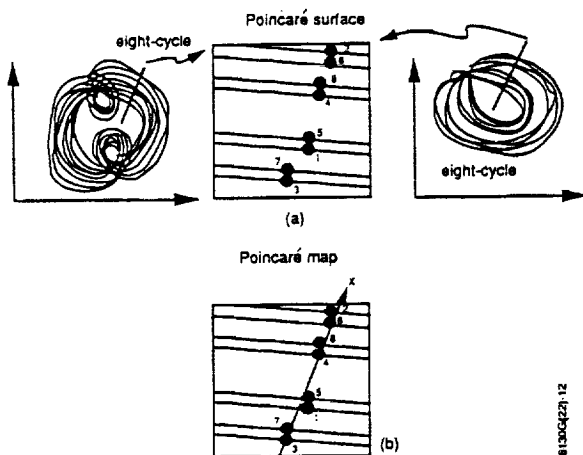
$$\begin{aligned} x_{n+1} &= A - x_n^2 + B y_n \\ y_{n+1} &= x_n \end{aligned}$$

After a small number of iterates of two trajectories, one computed using single precision, the other computed using double precision, and both originating from the same initial condition, they are still far apart. This approach was recently proposed by C. Grebogi.



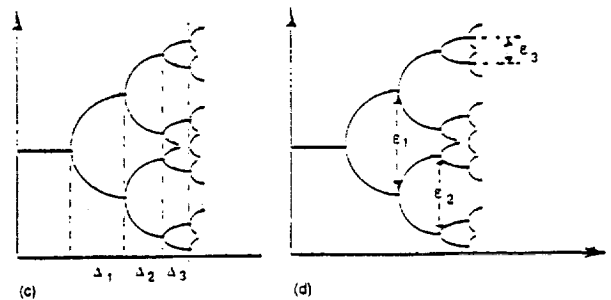
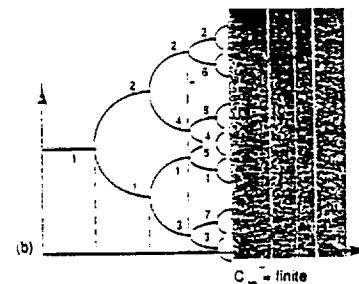
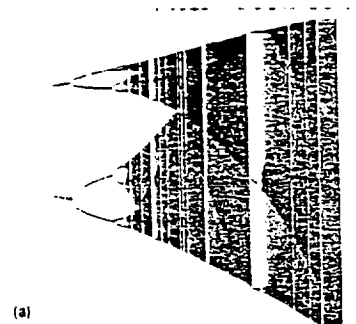
- (a) The Phase-Space Trajectory Converges to a Limit Cycle
- (b) In a Pendulum, Starting at the Point Marked 1, the Pendulum Returns to it After the Unit Period To. However as the friction is decreased, the Same Phenomenon is Observed as in the Turbulence Experiment Where the Limit Cycle Undergoes a Series of Period-Doublings

Figure 20. Phase-Space Phenomena



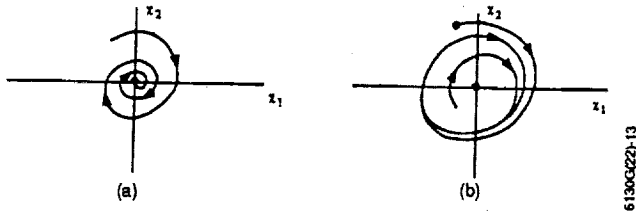
- (a) The Trajectory Continues to Nearly Miss the Starting Point Until it Hits After 2^n To Here We Have Two Different Dynamical Systems: a Pendulum and a Rayleigh-Bernard System, but They are Both Led to Chaotic Behavior Through the Same Universal Route (Period-Doublings). The Poincaré Surface Reveals This Universality.
- (b) The Segments of Near Misses is Local and Looks Roughly the Same for Both the Pendulum System and the Rayleigh-Bernard System.

Figure 21. Comparison of Trajectory Systems



- (a) Computer-Generated version of a Real Bifurcation for a Chaotic System.
- (b) Location of Intersection Points in the Present Mechanisms: the Poincaré Surface is a Line and the Result is a Bifurcation Tree.
- (c) The Parameter Convergence is Universal (Independent of the Particular Physical System).
- (d) The Relative Scale of Successive Branch Splittings is Universal (Independent of the Particular Physical System).

Figure 22. Examples of Bifurcation Trees



(a) Point Attractor: A Damped Harmonic Oscillator-model of a Pendulum.
(b) Limit-cycle Attractor: A Van der Pol Oscillator-model of a circuit Oscillator.

Figure 23. Examples of Attractors

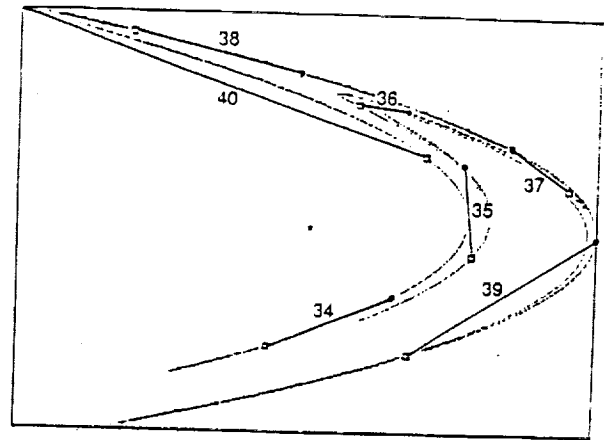


Figure 24. Example of a Strange Attractor

Attractors that can show chaotic behavior represent exponential sensitivity to initial conditions. Consider two initial conditions $|f_1>_0$ and $|f_2>_0 = |f_1>_0 + |\epsilon>_0$. The dynamical evolution gives a final state $|f_1>_t$ and $|f_2>_t$, as shown in Figure 25.

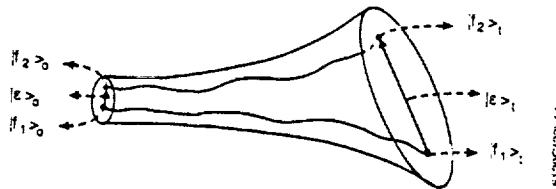


Figure 25. Exponential Evolution of Two Near Orbits in Phase Space

After time t , the distance between the two orbits is $|\epsilon>_t = |f_2>_t - |f_1>_t$. In the limit $|\epsilon>_0 \rightarrow 0$ and $t \rightarrow \text{large}$, orbits remain bounded and the difference between the solutions $|\epsilon>_t$ evolve exponentially for a

given direction of $|\epsilon>_0$. That is, $\left| \frac{|\epsilon>_t}{|\epsilon>_0} \right| \sim e^{\lambda t}$, $\lambda > 0$. Therefore, the system is very sensitive to initial conditions and is chaotic.

This means that small errors in the prediction can evolve rapidly with time. Thus, there is a time horizon at which noise and computer roundoff can totally change the dynamics. To illustrate this computational limit, a computer experiment is performed on a simple attractor of Figure 24, with $A = 1.4$ and $B = 0.3$.

As shown in Figure 24, we have generated 34 to 40 iterates of an orbit starting from an identical initial condition $|f_1>_0 = 0$, $|f_2>_0 = 0$. The computations are identical except that one uses single precision and the other double precision. Single-precision round-off error is 10^{-14} . Single precision is indicated by squares and double precision by circles. For every iterate connected with a vector, we see that at the 40th iteration, the magnitude of this vector is as large as the variables themselves. Consequently, if using a computer that has 10^{-14} round-off error, prediction after the 40th iteration is nothing but a guess if the dynamics we are working with are indeed chaotic and have a Hénon attractor. This was just an example. In practice, the chaotic attractor of a solar flux time series should be identified before any meaningful prediction procedure is implemented, which is the goal of such an approach to solar flux prediction.

Returning to the Hénon map example, we see that after the first iterate, $|\epsilon >_1$ and $|\epsilon >_0$ are different by an order of 10^{-14} (round off). If in the next iteration, the error doubles ($e^{\ln 2} = 2^1$), then the $|\epsilon >_1$ and $|\epsilon >_0$ are different by an order of attractor size in $t - 45$ ($2^1 10^{-14} - 1$). That is, if the error doubles, it is impossible to improve prediction. If we want to predict the evolution past $t - 45$ to $t - 90$, which is twice as long a prediction; then we should have an accuracy of 10^{-28} , which is 14 orders of magnitude more accurate. Therefore, improving prediction by a factor of two is impossible.

In other words, structural stability (Topological Orbital Equivalence [TOE]) breaks over a time horizon, making prediction impossible. Therefore, structural stability and computability are inherently incompatible. This is precisely why weather prediction over a time horizon is impossible. Lorenz' conclusion for weather-generating mechanisms was that thermally driven convections could make the atmosphere chaotic.

Now, returning to our problem, we have many reasons to believe that multiple interactions in the Sun introduce nuclear, chemical, electrodynamic, hydrodynamic, and other nonlinearities. It is easy to visualize chaotic behavior in solar flux because the Sun is like a rotating fluid that introduces turbulence, and its sunspots are similar to convection rolls. These behaviors introduce chaos just as does the Rayleigh-Benard mechanism. Furthermore, all atmospheres are really chaotic—even those ionized gases in solar atmosphere that chaotically modulate solar radio emission.

4. CONCLUSIONS

In May of 1990, we postulated that solar flux is a chaotic time series. This postulation was apparent from many physical features of the Sun. For example, the Sun is a rotating fluid that introduces turbulence, and most of the interactions, whether chemical, nuclear, or other, are nonlinear. We have also argued that the pattern in the logarithm of the power spectrum and the autocorrelation function is a concrete example that solar flux is a pattern-structured, time series. Therefore, an approach to study solar flux should be through nonlinear chaotic dynamics.

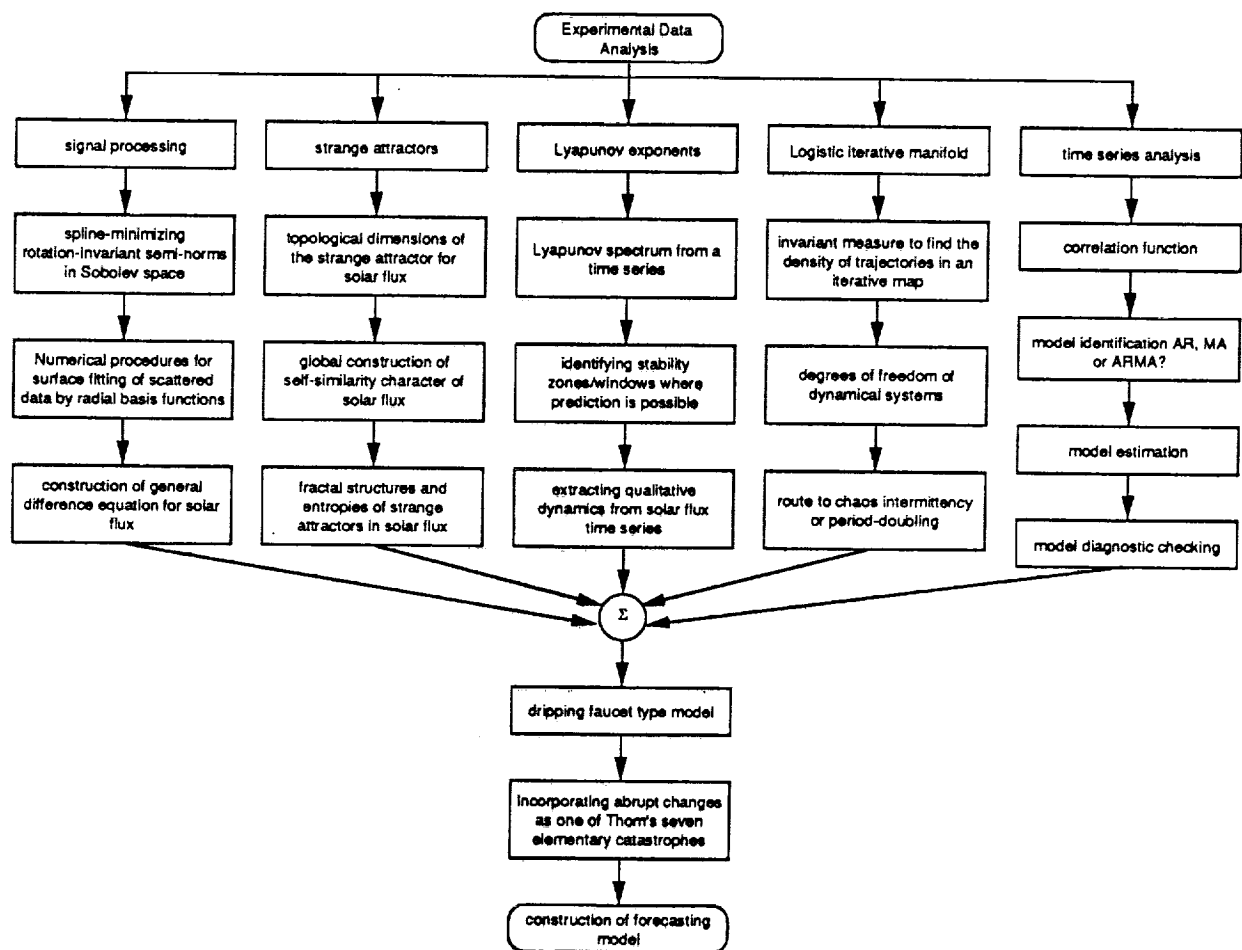
We have further claimed that a time horizon exists above which predictions are computationally impossible. To demonstrate this claim, we used the dripping faucet attractor, which roughly resembles the multiple periodicities observed in the dynamics of the solar flux. We also suggested that the Hénon-type attractors provide good candidates for study, although in the absence of a detailed demonstration that strange attractors or ensembles of strange attractors are really Hénon types, this theory remains in the realm of speculation.

Convection rolls were also introduced as models of sunspots that are products of nonlinear interaction (like solitons). These convection rolls could be produced in the ionized gases of solar atmosphere, further modulating (chaotically) the solar flux signal.

We also discovered evidence of a period-doubling type of route to chaos in the behavior of solar flux. In this case, we observed less power at frequencies that follow the well-known period-doubling bifurcations. This was further recognized as a new form of order that could be a new route to chaos. We also found evidence of fractal (self-similarity invariance, under contraction and dilation) structure in solar flux that deserves a separate investigation (see Figure 26).

ACKNOWLEDGMENTS

Thanks to D. Ashrafi, C. Schiff, M. Rokni, and In-Hwan Oh for valuable discussions, suggestions, and support. It is also a pleasure to thank J. Yorke for his suggestion to use cascaded linear maps to reconstruct our time series; C. Grebogi for proper directions; and E. Ott for teaching the fundamental concepts of chaos.



6130G(22)-09

Figure 26. Future Investigation Possibilities

REFERENCES

1. P. McIntosh, "Did Sunspot Maximum Occur in 1989?" *Sky & Telescope*, 1991
2. In-Hwan Oh, "The Average Solar Flux (F10.7 cm) Model For an 11-Year Solar Cycle," prepared for NASA GSFC (contract # NAS-11933 mod 13) by Wolf Research and Development Corp., September 1974
3. J. C. Brandt, *Introduction to Solar Wind*, W. Freeman & Company, 1970
4. J. Cappellari, A. Long, C. Velez, and A. Fuchs, *Goddard Trajectory Determination System (GTDS)*, CSC/TR-89/6021, prepared for NASA GSFC (Contract NAS 5-31500) by Computer Sciences Corporation, July 1989
5. S. Ashrafi, *Future Mission Studies on Preliminary Comparisons of Solar Flux Models*, FDD/554-91/004, prepared for NASA GSFC (contract NAS 5-31500), by Computer Sciences Corporation, December 1990
6. S. Ashrafi, *Future Mission Studies on Solar Flux Analysis*, FDD/554-91/006, prepared for NASA GSFC (contract NAS 5-31500) by Computer Sciences Corporation, December 1990
7. S. Ashrafi, "Existence of a Time Horizon for 'Structural Stability' and 'Computability' to Become Formally Incompatible in Prediction of Solar Flux," (In Preparation)
8. S. Ashrafi, "Toward Modeling the Formation of Abrupt Changes in Solar Flux by Thom's Catastrophe Theory," (In Preparation)
9. E. A. Jackson, *Perspectives of Nonlinear Dynamics*, Cambridge University Press, 1989
10. G. Box and G. Jenkins, *Time Series Analysis*, Holden-Day, 1976
11. P. Cvitanovic', *Universality in Chaos*, Bristol, England: Adam Higler, 1984
12. "Predictability in Science and Society," *Proceedings of a Joint Symposium of the Royal Society and the British Academy*, 1986
13. R. Cahalan, H. Leidecker, and G. Cahalan, "Chaotic Rhythms of a Dripping Faucet," *Computers in Physics*, August 1990
14. E. Ott, "Chaos in Dynamical Systems," (preprint) 1991

Ionospheric Refraction Effects on TOPEX Orbit Determination Accuracy Using the Tracking and Data Relay Satellite System (TDRSS)*

**M. S. Radomski
COMPUTER SCIENCES CORPORATION (CSC)**

**C. E. Doll
GODDARD SPACE FLIGHT CENTER (GSFC)**

ABSTRACT

This investigation concerns the effects on Ocean Topography Experiment (TOPEX) spacecraft operational orbit determination of ionospheric refraction error affecting tracking measurements from the Tracking and Data Relay Satellite System (TDRSS). Although tracking error from this source is mitigated by the high frequencies (K-band) used for the space-to-ground links and by the high altitudes for the space-to-space links, these effects are of concern for the relatively high-altitude (1334 kilometers) TOPEX mission. This concern is due to the accuracy required for operational orbit-determination by GSFC and to the expectation that solar activity will still be relatively high at TOPEX launch in mid-1992.

The ionospheric refraction error on S-band space-to-space links was calculated by a prototype observation-correction algorithm using the Bent model of ionospheric electron densities implemented in the context of the Goddard Trajectory Determination System (GTDS). Orbit determination error was evaluated by comparing parallel TOPEX orbit solutions, applying and omitting the correction, using the same simulated TDRSS tracking observations. The tracking scenarios simulated those planned for the observation phase of the TOPEX mission, with a preponderance of one-way return-link Doppler measurements.

The results of the analysis showed most TOPEX operational accuracy requirements to be little affected by space-to-space ionospheric error. The determination of along-track velocity changes after ground-track adjustment maneuvers, however, is significantly affected when compared with the stringent 0.1-millimeter-per-second accuracy requirement, assuming uncoupled pre-maneuver and postmaneuver orbit determination. Space-to-space ionospheric refraction on the 24-hour postmaneuver arc alone causes 0.2 millimeter-per-second errors in along-track delta-v determination using uncoupled solutions. Coupling the premaneuver and postmaneuver solutions, however, appears likely to reduce this figure substantially. Plans and recommendations for response to these findings are presented.

* This work was supported by the National Aeronautics and Space Administration (NASA)/Goddard Space Flight Center (GSFC), Greenbelt, Maryland, under Contract NAS 5-31500.

1. INTRODUCTION

Continuing improvement of the physical models and mathematical methods of orbit determination is necessary to meet stringent accuracy requirements for missions such as the Ocean Topography Experiment (TOPEX). One area for possible improvement is the methods used to correct the Tracking and Data Relay Satellite System (TDRSS) metric tracking data for the effects of atmospheric refraction. The Goddard Trajectory Determination System (GTDS) currently omits correction for such effects on spacecraft-to-spacecraft (S/C-to-S/C) tracking links.

Goddard Space Flight Center (GSFC) is to provide operational orbit determination support for TOPEX maneuver planning and evaluation. This is not to be confused with the definitive orbit determination that will be performed in support of the scientific data analysis. Some operational orbit-determination accuracy requirements for TOPEX appear to challenge the current capabilities of GTDS and the TDRSS. This report presents the results of a study conducted to determine whether inclusion of an atmospheric correction for S/C-to-S/C links is necessary to satisfy TOPEX requirements.

1.1 MOTIVATION AND OBJECTIVES OF ANALYSIS

The main effect of the atmosphere on S/C-to-S/C relay legs is caused by the free electrons of the ionosphere, which extend to altitudes above 3000 kilometers (km). To evaluate this effect, it is necessary to integrate the free electron density along the S/C-to-S/C relay communication path. An electron density model (the Bent Ionospheric Model, Reference 1) is already implemented in GTDS (Reference 2), but some expense would be involved in coding the required numerical integration and in documenting, testing, and certifying the code and the algorithm for operational use. Because the electron density model is expensive to compute, use of such a correction would also impose an additional burden on Flight Dynamics Facility (FDF) computer resources. Therefore, before implementing the correction, it is prudent to study the size of the orbit-determination effects to see whether accuracy requirements for current or future missions are seriously affected.

Two aspects of the TOPEX mission combine to make it perhaps the only one that, in the near term, requires the S/C-to-S/C ionospheric refraction correction. First is the stringency of the orbit-determination accuracy requirements. Second is that the early mission will occur during the later stages of the current solar maximum period. High solar activity causes the ionospheric electron-density distribution to increase and to extend to higher altitudes. The relatively high altitude of TOPEX will not render it completely immune to ionospheric refraction effects under these circumstances. The effects will be much smaller than the effects on lower altitude missions, but they must be judged relative to the stringent TOPEX accuracy requirements.

The two operational orbit-determination regimes in the TOPEX mission scenario (Reference 3) are distinguished by the tracking coverage and the orbit-determination accuracy requirements. The first regime coincides with the TOPEX mission Assessment Phase. The second regime combines the Initial Verification and Observation phases of the TOPEX mission plan. In this paper, the second regime will be referred to as the Observation Phase.

In the Assessment Phase, TDRSS tracking is planned to consist of 40 minutes (min) per revolution of two-way coherent S-band range and Doppler tracking plus nearly continuous one-way return link Doppler coverage during the remaining time. Stated accuracy requirements (References 3 and 4) for this regime consist of premaneuver requirements and postmaneuver requirements. The former are applicable to orbital quantities determined using tracking available over arcs of up to several days immediately before each orbit-adjust maneuver. The latter apply to the determination of changes in the orbit caused by the maneuver, not necessarily to the accuracy of postmaneuver orbit determination. This important distinction is drawn because of the possibility that some sources of orbit-determination error may cancel in the subtraction of premaneuver from postmaneuver determinations. Postmaneuver accuracy requirements must be satisfied using tracking extending no more than 24 hours after the maneuver. Both types of requirements depend on the type of orbit maneuver; that is, "calibration," "coarse," or "precision."

TDRSS tracking in the Observation Phase is to consist of 40 min per revolution of one-way Doppler tracking and one 10-min two-way range and Doppler pass per day. Precision maneuvers will continue, at reduced frequency, and the two-way coverage will be enhanced to 40 min per revolution for three revolutions after each such maneuver. The associated premaneuver and postmaneuver accuracy requirements are the same as in the Assessment Phase. An additional requirement for the Observation Phase applies to orbit determination that will be performed on several-day arcs between the maneuvers. This solution process is required to contribute less than 225 meters (m) to the prediction of the longitude of equator crossing 30 days after the end of the solution arc.

Table 1 quantifies the accuracy requirements. The accuracies for calibration maneuvers are those required for calibrations of the 1-Newton thrusters; requirements for calibrations of the 22-Newton thrusters are less stringent. Each number in the "Combined" column (Table 1) is the minimum of all required accuracies for each quantity; that is, the accuracy that the orbit-determination system must be able to achieve. All stated requirements are three-standard-deviation error limits. All orbital quantities involved in these requirements are osculating quantities.

Of the three sets of accuracy requirements for orbit determination associated with maneuvers, the precision requirements pose the greatest challenge to system capabilities. Attaining these accuracies will be no more difficult in the Assessment Phase than in the Observation Phase because tracking coverage will be more extensive. The study was therefore performed using tracking scenarios corresponding to the Observation Phase.

1.2 DESIGN AND DESCRIPTION OF THE STUDY

TOPEX orbit determination using simulated TDRSS tracking data was performed both with and without an ionospheric refraction correction. The two sets of results were compared, with particular attention to the differences in orbital quantities for which there are specific accuracy requirements. If these differences are not found to be small compared to the corresponding accuracy requirements, the ionospheric effects will be significant to the mission orbit-determination accuracy and presumably should be corrected.

This study is based on the assumption that the postmaneuver change determination is to be performed by subtracting quantities determined using separate premaneuver and

Table 1. TOPEX Operational Orbit-Determination Accuracy Requirements

SOLUTION TYPE	ORBIT PROPERTY	CALIBRATION (1 nt)	COARSE	PRECISION	COMBINED
PREMANEUVER STATUS	PERIOD, T (ms)	4	4		4
	SEMIMAJOR AXIS, a (cm)			100	100
	ECCENTRICITY, e (10 ⁻⁶)	10	10	5	5
	INCLINATION, I (10 ⁻⁶ deg)	1000	1000	100	100
	ARGUMENT OF LATITUDE (10 ⁻⁶ deg)	5000	5000		5000
POSTMANEUVER CHANGE	PERIOD, δT (MS)		2		2
	SEMIMAJOR AXIS, δa (cm)			20	20
	INCLINATION, δI (10 ⁻⁶ deg)		500	100	100
	VELOCITY CHANGE ALONG-TRACK δV_a (mm/s)	0.1	4.0	0.1	0.1
	VELOCITY CHANGE CROSS-TRACK δV_c (mm/s)	10	20	10	10
	VELOCITY CHANGE RADIAL δV_r (mm/s)	2	10	2	2
BETWEEN MANEUVERS (OBSERVATION PHASE)	30-DAY PREDICTION OF E-W POSITION AT EQUATOR CROSSING (m)	N/A	N/A	N/A	225

6130-14

postmaneuver tracking arcs. This is a standard procedure at the Flight Dynamics Facility of GSFC, but it does not make use of the fact that the spacecraft position is continuous through the maneuver.

An alternate orbit determination scenario for postmaneuver requirements involves solving for maneuver thrusting parameters in a unified solution arc, including both premaneuver and postmaneuver tracking. The results of this study are not directly applicable to this unified orbit determination scenario. Plausible arguments will nevertheless be made to estimate ionospheric error bounds on along-track velocity change error for this scenario.

A further assumption in the design and analysis of this study is that the effects of ionospheric refraction on the separate premaneuver and postmaneuver orbit determination solutions are

not highly correlated under random variations of the tracking schedule and the solar activity. The ionospheric error in the differences between premaneuver and postmaneuver solutions is not expected to be systematically less than the ionospheric error in either separate solution. Because errors in the relatively short postmaneuver arc are expected, in general, to exceed those in the premaneuver arc, the assumption relieves us of the burden of analyzing a long premaneuver arc preceding each of our several postmaneuver arcs. This assumption is inapplicable to other error sources in TOPEX orbit determination (such as gravitational constant error); this implies that overall TOPEX error analysis must be performed with coordinated premaneuver and postmaneuver arcs (References 5 and 6).

Effects of ionospheric refraction on postmaneuver accuracy requirements were studied using four 24-hour postmaneuver arcs with simulated tracking data scheduled according to the Observation Phase postmaneuver tracking requirements. Four arcs were used to attempt to sample over relevant variables, such as season and orbital orientation. The impact on the premaneuver accuracy requirements was studied using a single 7-day arc of routine Observation Phase simulated tracking.

While this analysis may prove that implementation of a full ionospheric correction is necessary for the satisfaction of the TOPEX accuracy requirements, it cannot show it to be sufficient. There are two reasons for this. First, the actual accuracy attainable by an ionospheric refraction correction model, and thus the fraction of ionospheric error that may remain after correction, is unknown. Second, the current analysis only treats the ionospheric refraction contribution to the orbit-determination error. A full orbit-determination error analysis for TOPEX is beyond the scope of this work.

1.3 PREVIOUS STUDIES

References 7 and 8 describe previous studies of the orbit-determination effects of the S/C-to-S/C refraction correction. Using real and simulated tracking data for the Earth Radiation Budget Satellite, Solar Maximum Mission, and Solar Mesosphere Explorer at both high and low solar activities, these studies investigated the effects of uncorrected ionospheric refraction on orbit determination for spacecraft in the 500- to 600-km altitude range. For the lower end of this altitude range, this effect was shown to produce ephemeris differences of 30 to 100 m over 34-hour definitive arcs at maximum solar activity. Effects of this size significantly hinder the continuing effort to improve orbit-determination precision and accuracy. There are, however, no near-term missions in this altitude range whose accuracy requirements are threatened by this level of error. References 7 and 8 do not establish an operational need to correct for the S/C-to-S/C ionospheric refraction.

A somewhat fuller discussion of the methods of the current study may be found in Reference 9.

1.4 ORGANIZATION OF THE PAPER

The remainder of this paper comprises three sections. Section 2 describes the methods of analysis, including tracking data simulation. Section 3 describes and discusses the results. Section 4 describes the conclusions and makes recommendations for implementing the ionospheric refraction correction and for TOPEX orbit-determination techniques.

2. ANALYTICAL METHODS

2.1 ORBIT AND TRACKING DATA SIMULATION METHODS

The data simulation methods comprise the orbital initial conditions, the orbit propagation methods, the measurement simulation methods, and the choice of tracking data distribution.

Orbital initial conditions at several epochs were based on the reference set of Brouwer mean elements given in Table 2. These elements were adapted from Reference 10 and, according to that source, represent a frozen orbital shape (i. e., there is no secular change in eccentricity and mean anomaly). The goal of TOPEX orbit adjustment maneuvering will be to keep the groundtrack on a 10-day, 127-orbit repeat cycle. To provide initial conditions for orbit simulations at epochs other than June 6, 1992, therefore, only the Brouwer mean longitude of ascending node and the mean anomaly needed to be changed. The former was regressed by 2.2005 deg/day. The latter was advanced exactly 12.7 revolutions per rotation of the Earth, relative to the regressing TOPEX orbital plane.

Table 2. Brouwer Mean Orbital Elements in the TOD Coordinate System at 0000 UTC of Epoch Date

ORBITAL ELEMENT	VALUE
EPOCH, t_0	6/21/1992
SEMIMAJOR AXIS, a_0 (km)	7713.3869
ECCENTRICITY, e_0	0.0011399
INCLINATION, i_0 (deg)	64.606
RIGHT ASCENSION OF NODE, Ω_0 (deg)	139.552
ARGUMENT OF PERIGEE, ω_0 (deg)	270
MEAN ANOMALY, M_0 (deg)	0

6130-14

Four 24-hour sets of tracking data were simulated. The epochs were chosen so that the four data sets would sample over the first quadrant of the angle between the Sun and the orbit normal and provide some relevant seasonal variation as well. The simulation epochs and Sun angles are given in Table 3. The orbit simulation for the 7-day arc also used the October 27, 1992, epoch. Note that monthly ionospheric maps (Reference 11) at fixed solar activity show generally high ionospheric densities in October and low densities in June. All orbit simulations were initialized at 0000 UTC of the dates shown in Table 3.

The optional methods and models used in the orbit and tracking simulations are presented in the "TOPEX Simulation" and "Relay Orbit" columns of Table 4. Observation simulation used the TDRSS version of the Research and Development (R&D) GTDS Data Simulation program. The measurement noise amplitudes were chosen to resemble the actual high-frequency noise observed in TDRSS measurements. It was not possible to include either ionospheric or tropospheric refraction effects in the data simulation because of R&D GTDS

Table 3. Simulation Epoch Dates, Sun-to-Orbit-Normal Angles, and Tracking Intervals

EPOCH DATE (0000 UTC)	SUN ANGLE (deg)	TRACKING PERIOD (UTC)
JUNE 9, 1992	2.8	00 ^h 11 ^m 38 ^s –24 ^h 11 ^m 37 ^s
OCTOBER 3, 1992	30.5	01 ^h 01 ^m 33 ^s –24 ^h 19 ^m 48 ^s
OCTOBER 17, 1992	61.5	00 ^h 23 ^m 08 ^s –24 ^h 13 ^m 07 ^s
OCTOBER 27, 1992	89.9	01 ^h 27 ^m 17 ^s –25 ^h 05 ^m 18 ^s
OCTOBER 27, 1992	89.9	00 ^h 59 ^m 50 ^s –NOVEMBER 2, 23 ^h 59 ^m 40 ^s

6130-14

software limitations. These and other sources of orbit error were included by choosing different options for the GTDS solution process than were used in simulation, as discussed in Section 2.2.

Every effort has been made to simulate tracking schedules representative of the actual tracking scenarios planned for the Observation Phase, as described in Section 1.1. The basic element of simulated tracking coverage per spacecraft revolution is one 35-min pass, through either TDRS-East(E) or TDRS-West(W), of one-way downlink S-band Doppler (TD1S) tracking. The definition of tracking visibility was usually restricted to times when the tracking relay elevation, as seen from the user spacecraft and measured relative to the local horizontal plane, was greater than 5 deg. The mean ionospheric correction is a strong function of this relay elevation (Reference 9), and, to control the effect of ionospheric corrections, atmospheric editing on this variable will be advisable for operational TOPEX orbit determination. Variations on this theme include substitution of 20 min of two-way coherent tracking (TD2S and TR2S) for 35 min of one-way; allowing tracking at relay elevations down to 0 deg; and phasing the tracking pass at the beginning, middle, or end of the visible interval.

Data simulation for the four 24-hour postmaneuver arcs was scheduled according to the following rules:

- The observation interval and the Doppler count interval are both 10 seconds (sec).
- The first three passes consist of 20 min each of two-way range and Doppler tracking.
- One 35-min pass of one-way Doppler tracking occurs in each succeeding revolution.
- Fifty percent of the passes begin at the beginning of the restricted visibility interval, 25 percent end at the end; the remainder are centered in the visible interval.
- TDRS-E and TDRS-W are used at random after the first three revolutions.
- Visibility is generally cut off at 5-deg relay elevation, but one two-way pass and one one-way pass per day extend to zero elevation.

Table 4. Models and Parameters for Data Simulation and Orbit Determination (1 of 2)

MODELS AND PARAMETERS	TOPEX SIMULATION	TOPEX DC	RELAY ORBIT
INTEGRATION TYPE	12TH-ORDER FIXED-STEP COWELL	12TH-ORDER FIXED-STEP COWELL	12TH-ORDER FIXED-STEP COWELL
COORDINATE SYSTEM OF INTEGRATION	TRUE OF REFERENCE	TRUE OF REFERENCE	TRUE OF REFERENCE
INTEGRATION STEP SIZE	60 sec	60 sec	600 sec
GEOPOTENTIAL MODEL	GEM-9 (21 x 21)	GEM-L2A (21 x 21)	GEM-L2A (8 x 8)*
ATMOSPHERIC DENSITY MODEL	N/A	HARRIS-PRIESTER, F = 225, N = 6	N/A
COEFFICIENT OF DRAG (C_D)	0	2.2 (7-DAY ARC) 0.0 (1-DAY ARCS)	N/A
DRAG SCALING ADJUSTMENT PARAMETER (ϕ_1)	N/A	SOLVE-FOR, IN 7-DAY ARC ONLY	N/A
SOLAR/LUNAR EPHEMERIDES	DE-118	DE-118	DE-118
SOLAR/LUNAR GRAVITATION	YES	YES	YES
SOLAR REFLECTIVITY COEFFICIENT (C_R)	1.2	0.8	1.4
SOLAR PRESSURE CONSTANT	0.00457	0.00457	0.00457
POLAR MOTION	NO	NO	NO
SPACECRAFT CROSS-SECTION	17.0 M ²	17.0 M ²	40.0 M ²
SPACECRAFT MASS	2650 kg	2650 kg	2000 kg

* Except GEM-9 (8 x 8) used for October 3 data simulations only.

6130-14

Table 4. Models and Parameters for Data Simulation and Orbit Determination (2 of 2)

MODELS AND PARAMETERS	TOPEX SIMULATION	TOPEX DC	RELAY ORBIT
RELAY INCLINATION ERROR	0	+ 27 x 10 ⁻⁶ deg (TDRS-E) -27 x 10 ⁻⁶ deg (TDRS-W)	N/A
RELAY MEAN ANOMALY ERROR	0	+ 41 x 10 ⁻⁶ deg (TDRS-E) -41 x 10 ⁻⁶ deg (TDRS-W)	N/A
ESTIMATED PARAMETERS	N/A	STATE, LOCAL OSCILLATOR BIAS AND DRIFT, DRAG SCALING (ϕ_1 , 7-DAY ONLY)	N/A
DC CONVERGENCE PARAMETER	N/A	0.0001	N/A
DC EDITING	N/A	3 σ	N/A
IONOSPHERIC CORRECTION	NONE	BENT MODEL OR NONE	N/A
TROPOSPHERIC CORRECTION	NONE	NONE	N/A
ANTENNA MOUNT CORRECTION	NONE	NONE	N/A
ATMOSPHERIC EDITING	BY SCHEDULE (SEE TEXT)	NONE	N/A
TR2S NOISE STANDARD DEVIATION	1 M	30 M	N/A
TD2S NOISE STANDARD DEVIATION	0.01 Hz	0.25 Hz	N/A
TD1S NOISE STANDARD DEVIATION	0.01 Hz	0.25 Hz	N/A

6130-14

- Two passes are scheduled in the first 2 hours, as if to support immediate postmaneuver orbit determination.

On the assumption that orbit adjustment maneuvers will be scheduled to end at times when tracking is possible, the putative maneuver times (no actual thrusting) were taken to coincide with the first simulated observation (see Table 3). These were also the eventual DC solution epochs. The intervals of tracking data collection were ended just 24 hours thereafter.

Data simulation for the 7-day routine orbit-determination arc was scheduled according to the same rules, with the following exceptions:

- Each day, one 20-min two-way pass replaces a regular 35-min one-way pass, not necessarily at the beginning of the day.
- The data interval for one-way passes is 30 sec (although the Doppler count interval was maintained at 10 sec).
- All passes commence at first visibility (because the precise phasing of individual passes within a 7-day arc is unimportant).
- A total of 17 passes (2 or 3 each day) begin at 0-deg relay elevation, and the rest at 5 deg. On days 2, 4, and 6, one of the 0-deg passes is a two-way pass.

The 168-hour interval of tracking data collection was begun at 0000 UTC of October 27, 1992. The putative maneuver was at 0000 UTC, November 3.

2.2 ORBIT-DETERMINATION METHODS

Spacecraft orbit determination for this study used IONPRO/GTDS 2.1. This version differs from GTDS principally in that it has the optional capability to calculate and apply corrections to TDRSS tracking observations for the ionospheric refraction on the S/C-to-S/C legs of the relay communication path. Batch least-squares orbit determination was performed by the Differential Correction (DC) program within IONPRO/GTDS.

The orbit-determination options used in this study are presented in the "TOPEX DC" column of Table 4. For each of the five arcs, DC solutions were generated twice, once with and once without observation correction for ionospheric refraction, but with no other differences in the solution conditions.

In the comparison of orbit solutions generated with and without ionospheric error, the effects of small variations in input measurements cancel to first order. The nonlinearities caused by dynamic editing differences spoil this cancellation. In an attempt to provide a realistic set of background observation residuals influencing the dynamic editing and its variation with ionospheric effects, several sources of background orbit-determination error were built into both the ionospherically corrected and uncorrected DC solutions. Comparison of the "TOPEX Simulation" and "TOPEX DC" columns of Table 4 reveals those error sources. Geopotential modeling error (including central gravitational constant) is represented by the difference between the Goddard Earth Models GEM-L2A and GEM-9, both truncated at order and deg 21. Atmospheric density modeling error and tropospheric refraction error are

not included. Solar radiation force modeling error is represented by a difference in reflectivity of 50 percent. Measurement noise error is discussed in Section 2.1.

Except for the October 3 arc, all TDRSS relay orbits were generated with options identical to those used in data simulation (see the "Relay Orbit" column of Table 4). Relay orbit error is simulated in this study by varying the initial TDRS relay Keplerian elements from those with which the tracking data were simulated. An oscillatory cross-track error of amplitude 19.9 m was obtained by changing the TDRS-E (-W) inclination by $+0.000027$ deg (-0.000027 deg). Approximately constant along-track errors of 30.2 m were obtained by changing the TDRS-E (-W) mean anomaly by $+0.000041$ deg (-0.000041 deg). The data simulations for October 3 were inadvertently performed using GEM-9 rather than GEM-L2A for the relay geopotential. This introduces additional relay orbit error in the solutions for this arc, which is dominated by along-track position error that grows linearly from 0 to 12 m by the end of the arc.

Since available tracking data simulation software lacks the S/C-to-S/C ionospheric refraction capability, ionospheric refraction error was implemented in this study by applying an ionospheric correction to observations that were simulated without the effect. Contrary to the situation that exists during actual orbit determination, the solution obtained here without ionospheric refraction correction is the closest to the true orbit, and the solutions obtained with ionospheric refraction correction are degraded in accuracy. The sign of the orbit-determination error may be opposite to that caused, in reality, by failing to correct real observations, but there is no reason to expect the magnitude to differ.

The observation standard deviations appearing in the "TOPEX DC" column of Table 4 are those whose inverse squares define the weight factors for least-squares estimation. These values are currently used for operational orbit determination. The value used for the one-way measurements (TD1S) has been used for Cosmic Background Explorer (COBE) operational support using an onboard ultra-stable oscillator, as planned for TOPEX.

The convergence tolerance used, 0.0001, is only 2 percent of the standard usage for operational orbit determination. This value was used to minimize the effects of differences in degree of convergence between ionospherically corrected and uncorrected solutions.

2.3 REFRACTION CORRECTION METHODS

The current method of GTDS atmospheric correction of TDRSS tracking observations is to correct all ground-to-space legs for both the ionosphere and the troposphere, except that the ionospheric correction is justifiably ignored for K-band legs because of the inverse-square dependence on frequency. Ionospheric correction is thus applied to the TDRS-to-transponder legs of Bilateral Ranging Transponder System (BRTS) data and not at all to user tracking data. This neglect of refraction correction for the S/C-to-S/C legs is justifiable for the troposphere, which extends only to tens of kilometers, but not, in general, for the ionosphere. IONPRO/GTDS, in contrast, uses one of two algorithms described in Reference 12 to evaluate the electron-density line integrals along the S/C-to-S/C communication paths. The electron-density function, n_e , for the integrals is provided by the existing GTDS implementation of the Bent Ionospheric Model (Reference 2).

In the current study, numerical integration of the electron density is performed using Gaussian integration (Method I of Reference 2). The integral is divided at 3000-km altitude

into two segments. The lower altitude segment is evaluated using 20-point Gaussian integration in the path variable, s . The segment above 3000-km altitude is extended to infinity in the direction beyond the relay spacecraft and evaluated by three-point Gaussian integration in the variable

$$u = \exp(-k_5 s) \quad (1)$$

where k_5 is the inverse scale height of the top layer of the segmented Bent model profile.

2.4 SOLAR ACTIVITY SIMULATIONS

The electron-density distribution in the ionosphere is highly dependent on the level of solar activity. As described by the Bent model, it depends primarily on the monthly value of 12-month smoothed solar flux, F_{12} , on the daily solar flux, F , and, to a lesser degree, on the 12-month smoothed sunspot number, R . Values of these parameters were carefully chosen for use in the ionospherically corrected DCs to provide a moderately pessimistic estimate of an extreme ionospheric state in the early TOPEX mission time frame.

A recent prediction (Reference 13) for the two-standard-deviation upper limit of F_{12} for June 1992 (that is, 169), was used for all five DC arcs. With this value of F_{12} , the sunspot number (Reference 14) was derived by solving

$$F_{12} = 63.75 + 0.728 R + 0.00089 R^2 \quad (2)$$

Solar flux values around the peak of cycle 19, the previous cycle that most closely resembles the rising portion of the current cycle 22, were studied. In August, 1960, 4 months after cycle 19 had decayed to F_{12} of 169, an apparent solar storm produced a peak daily solar flux of 250 (Reference 15). That daily solar flux value was used for each of the four 24-hour postmaneuver arcs. The daily flux values for August 17-23, 1960, were used for October 27 to November 2, 1992, in the 7-day routine orbit-determination arc. Those F -values, specified in Table 5, have a mean of 215.9.

2.5 EVALUATION METHODS

As stated in Section 1, the basic method of determining the orbit-determination effects of ionospheric refraction was by comparing orbit-determination results obtained without an ionospheric refraction correction to similar results obtained with exactly the same tracking data, but now applying the ionospheric refraction correction. Osculating Keplerian period, semimajor axis, eccentricity, and inclination were calculated from the ephemeris file output of definitive solution trajectories; differences were calculated as functions of time within the definitive arc. The radial, cross-track, and along-track components of velocity differences were obtained from the GTDS ephemeris comparison (COMPARE) program.

Since the TOPEX premaneuver and postmaneuver accuracy requirements apply only to the maneuver time, it would seem necessary only to calculate the ephemeris comparisons at a

Table 5. Solar Activity Simulations

	F12	F	R
24-HOUR ORBIT DETERMINATION ARCS			
JUNE 6, 1992	169.0	250.0	125.4
OCTOBER 3, 1992	169.0	250.0	125.4
OCTOBER 17, 1992	169.0	250.0	125.4
OCTOBER 27, 1992	169.0	250.0	125.4
7-DAY ORBIT DETERMINATION ARC			
OCTOBER 27, 1992	169.0	247.0	125.4
OCTOBER 28, 1992	169.0	250.0	125.4
OCTOBER 29, 1992	169.0	234.0	125.4
OCTOBER 30, 1992	169.0	219.0	125.4
OCTOBER 31, 1992	169.0	201.0	125.4
NOVEMBER 1, 1992	169.0	189.0	125.4
NOVEMBER 2, 1992	169.0	171.0	125.4
MEAN	169.0	215.9	125.4
STANDARD DEVIATION	0.0	30.1	0.0

6130-14

solution epoch coincident with this time. Velocity differences, however, vary sinusoidally on the orbital period, while eccentricity and semimajor axis differences have been found to vary more rapidly. If the maneuver is taken to be at some random time before the beginning of the postmaneuver tracking arc, these variations will be sampled over. A single-point comparison may produce values less than the sample averages. To guard against this possibility, Keplerian and velocity comparisons of ephemerides need to be sampled over at least an orbital revolution near epoch. Since the character of the tracking data in the postmaneuver scenarios differs systematically between the initial revolutions of the arc and the later ones, it is unnecessary, and potentially misleading, to extend this sampling over the entire definitive arc. Analytical emphasis was therefore placed on root-mean-squares (rms) over one-orbit samples of ephemeris comparisons; that is, the first 112 min of the postmaneuver arcs and the last 112 min of the premaneuver arc. Single-point samples at epoch and full definitive samples were, however, also calculated for comparison purposes. One-orbit samples were taken at 1-min sampling intervals, whereas longer samples were taken at 10-min sampling intervals.

Detailed analysis of the accuracy requirement for premaneuver determination of the osculating argument of latitude was not performed. The results strongly indicate that this requirement is not in any way challenged by ionospheric refraction error. Analysis (see Reference 9) of the 30-day equator crossing prediction requirement, using orbit determination results for the 7-day arc of simulated tracking data, shows that ionospheric refraction has a negligible impact. Because of space limitations, that analysis will not be discussed in this paper.

3. RESULTS AND DISCUSSION

Table 6 summarizes the corrected and uncorrected DC solutions for each of the five orbit-determination arcs. The first four pairs of solutions represent the four 24-hour postmaneuver arcs, with epochs at the beginnings of the arcs specified in Table 3. The last pair of solutions represents the 7-day arc with DC epoch at the end of the arc, 0000 UTC, November 3, 1992. The results of definitive parallel ephemeris comparison between the corresponding corrected and uncorrected solutions are listed in Table 6 under the "Maximum Compare Position Differences" column.

The numbers of accepted observations shown in Table 6 reflect the absence of DC editing of two-way observations in the 24-hour arcs, except for 44 Doppler observations edited in only the corrected solution for October 27. Although editing of a single one-way observation did occur on October 3, the same rejection was made in both corrected and uncorrected solutions. Thus, October 27 is the only 24-hour solution to partake of the nonlinear effect of a DC editing difference. There is also a difference in the selection of two-way Doppler observations in the 7-day arc.

In keeping with the fact that the refraction correction is applied to unrefracted simulated observations, the corrected solutions generally show inferior fit to the tracking data, as revealed by larger weighted rms residuals and residual standard deviations.

The definitive maximum along-track position differences at the far right of Table 6 do not exceed 2.1 m for the long arc (and are still less for the premaneuver arcs). Thus, the ionospheric effect on determination of argument of latitude is in the neighborhood of 16×10^{-6} deg. The requirement for determination of this quantity will, therefore, not be impacted by ionospheric refraction error and will not be considered further.

Table 7 summarizes the differences between corrected and uncorrected solutions in the quantities related to the remaining TOPEX orbit-determination accuracy requirements. Shown are the actual differences at epoch for each solution and the rms values over one-orbit and full definitive samples as described in Section 2.5. The ionospheric refraction effects on period and eccentricity are smaller by two orders of magnitude than any accuracy requirement. The inclination discrepancies are less than 4 percent of the minimum postmaneuver requirement, except for the October 27 result (13 percent of the requirement) associated with the 10-percent TD2S editing difference. The inclination error for the 7-day arc is only 3 percent of the precision premaneuver inclination accuracy requirement. The rms of the four one-orbit postmaneuver samples of discrepancy in semimajor axis, 1.13 centimeters (cm), barely exceeds 5 percent of the 20-cm accuracy requirement. Premaneuver semimajor axis discrepancies are smaller than that, and also less than 0.3 percent of the corresponding premaneuver accuracy requirement.

The situation revealed by Table 7, with regard to determination of postmaneuver velocity changes, contrasts with that seen for Keplerian elements. The RMS postmaneuver effect on cross-track velocity change determination is only 7 percent of the accuracy requirement, while the premaneuver effect on the same determination is smaller. The RMS postmaneuver effect on radial velocity change determination, however, is 30 percent of the accuracy requirement, and the single premaneuver sample is 45 percent thereof. The along-track

Table 6. DC Summaries for Corrected and Uncorrected Solutions

EPOCH DATE	IONOSPHERIC CORRECTION	NUMBER OF OBSERVATIONS			WEIGHTED RMS	STANDARD DEVIATIONS			ρ_1	LOCAL OSCILLATOR		MAXIMUM COMPARE-POSITION DIFFERENCES (m)			
		TR2S	TD2S	TD1S		TR2S (m)	TD2S (mHz)	TD1S (mHz)		BIAS (mHz)	DRIIFT (10^{-9} Hz/sec)	RADIAL	CROSS-TRACK	ALONG-TRACK	TOTAL
6/8	NO	362	362	2072	0.1525	3.14	54.6	32.1	-1	-25.0	807	0.205	0.059	0.592	0.595
	YES	362	362	2072	0.1572	3.35	58.5	32.2	-1	-25.4	822				
10/3	NO	363	363	2108	0.1411	1.75	58.1	28.0	-1	-3.9	67	0.233	0.608	1.614	1.665
	YES	363	363	2108	0.1430	1.90	60.8	20.2	-1	-1.8	-22				
10/17	NO	363	363	2110	0.1115	2.57	23.9	28.8	-1	+18.4	-581	0.295	0.404	1.479	1.507
	YES	363	363	2110	0.1138	2.61	22.7	29.4	-1	+19.8	-598				
10/27	NO	363	363	2110	0.1060	1.92	29.1	28.3	-1	20.0	-715	0.182	1.859	1.405	2.201
	YES	363	319	2110	0.1125	1.42	33.6	28.9	-1	15.3	-623				
11/3	NO	847	791	5358	0.1437	2.75	44.8	35.4	-0.9853	38.4	79	0.451	0.573	2.052	2.055
	YES	847	835	5358	0.1485	2.70	49.3	35.8	-0.9886	30.2	71				

6130-14

Table 7. RMS Values of Definitive Solution Ephemeris Differences (Corrected Solution Minus Uncorrected Solution)

EPOCH DATE	SAMPLED INTERVAL	PERIOD, ΔT (MSEC)	SEMAJOR AXIS, Δa (CM)	ECCENTRICITY, Δe (10^{-6})	INCLINATION, Δi (10^{-6} DEG)	ΔV_r (MM/SEC)	ΔV_c (MM/SEC)	ΔV_t (MM/SEC)	$\Delta a/2144$ SEC (MM/SEC)
INDIVIDUAL POSTMANEUVER ARCS									
06/09	EPOCH 1 ORBIT DEF. ARC	0.002 0.002 0.002	0.12 0.11 0.11	0.021 0.017 0.017	-0.42 0.42 0.42	0.09 0.16 0.19	0.03 0.04 0.04	-0.19 0.14 0.13	0.0006 0.0005 0.0005
10/03	EPOCH 1 ORBIT DEF. ARC	0.021 0.021 0.021	1.64 1.59 1.59	0.011 0.025 0.025	-3.76 3.76 3.76	-0.62 0.52 0.58	-0.17 0.39 0.39	0.19 0.14 0.14	0.0076 0.0074 0.0074
10/17	EPOCH 1 ORBIT DEF. ARC	0.016 0.015 0.015	1.25 1.12 1.12	0.037 0.024 0.024	-2.98 2.98 2.98	-0.55 0.32 0.49	0.20 0.27 0.27	0.06 0.19 0.19	0.0058 0.0052 0.0052
10/27	EPOCH 1 ORBIT DEF. ARC	-0.016 0.015 0.015	-1.23 1.13 1.12	-0.017 0.019 0.019	-13.45 13.46 13.46	0.91 1.01 0.55	-1.65 1.23 1.21	0.03 0.11 0.11	-0.0057 0.0053 0.0052
RMS OF FOUR POSTMANEUVER ARCS									
	1 ORBIT	0.015	1.13	0.022	7.15	0.60	0.66	0.15	0.0053
PREMANEUVER ARC									
11/03	EPOCH 1 ORBIT DEF. ARC	-0.002 0.002 0.005	-0.14 0.18 0.35	-0.051 0.047 0.047	-3.17 3.17 3.17	0.59 0.89 0.88	-0.17 0.38 0.34	0.34 0.29 0.29	-0.0007 0.0008 0.0016

6130-14

velocity errors exceed the accuracy requirement by 50 to 200 percent, including the pre-maneuver result.

The last column of Table 7 represents the first term on the right side of the equation

$$\Delta V_a = \frac{\Delta a}{2144 \text{ sec}} - \frac{\Delta r}{1072 \text{ sec}} \quad (3)$$

where Δr is the error in radial position. This equation is the differential form of the *vis viva* equation for the osculating semimajor axis, specialized to TOPEX in the circular orbit approximation. The results for ΔV_a in Table 7 are clearly dominated by the second term. If, however, Equation (3) is applied to changes in quantities computed just before and just after a maneuver, while using the unified orbit determination scenario that does not permit a position discontinuity, the second term exactly cancels (Reference 5), so that

$$\delta \Delta V_a' = \frac{\delta \Delta a'}{2144 \text{ sec}} \quad (4)$$

where δ signifies the postmaneuver-premaneuver difference and the primes remind us that the subtracted quantities are not those of the independent orbit determination scenario. Unless the unified orbit determination scenario actually increases the ionospheric effect on determination of semimajor axis changes, $\delta \Delta V_a'$ will be of the order of the first term in Equation (3) from the original orbit determination scenario. In Table 7, this term averages, for the 24-hour arcs, about 5 percent of the accuracy requirement.

The central processing unit (CPU) time for the corrected 7-day DC was 53.3 min, compared with 13.8 min without ionospheric correction. This difference can easily be cut by a factor of 3 or 4, by changing IONPRO/GTDS so as not to recalculate corrections every DC iteration. It is nevertheless clear that operational use of this correction for TOPEX orbit determination may pose a significant computational burden.

4. CONCLUSIONS AND RECOMMENDATIONS

4.1 CONCLUSIONS

The analysis of the orbit-determination effects of the S/C-to-S/C ionospheric refraction correction shows that, although the effects are small in an absolute sense, they are in some cases comparable with the stringent TOPEX accuracy requirements. Most notably, ionospheric refraction effects cause along-track velocity change errors of up to triple the postmaneuver accuracy requirement. They also cause radial velocity change errors of 20 to 45 percent of the accuracy requirement. On the other hand, ionospheric refraction effects are at the 10 percent

level, or less, relative to Keplerian element premaneuver and postmaneuver accuracy requirements. These conclusions are only strictly applicable to the independent postmaneuver orbit determination scenario and to the Observation Phase.

Conclusions about the unified premaneuver and postmaneuver orbit determination scenario are somewhat conjectural. A very strong conjecture is that the semimajor axis change determination in this scenario is no more sensitive to the ionosphere than in the other scenario. In that case, along-track velocity change errors from ionospheric refraction will be reduced to 5 percent of the accuracy requirement. Therefore, the radial velocity change errors may be the most significant.

This analysis does not determine how well the ionospheric error can be reduced by a correction algorithm using the Bent model. A reduction to the 30 percent level is a reasonable guess. At that level, residual ionospheric error may still account for 50 to 100 percent of the allowable error in along-track velocity change.

4.2 RECOMMENDATIONS

This analysis shows that the effects of neglected ionospheric refraction error on TOPEX orbit determination accuracy using a serious candidate solution scheme are very significant relative to that mission's stringent requirements. It certainly implies that this error source is a significant one for orbit determination using the TDRSS in the new decade, and must not be slighted in error analysis.

By employing an alternate orbit determination scenario, it may be possible to avoid immediate implementation of a spacecraft-to-spacecraft ionospheric correction algorithm for GTDS use in TOPEX orbit support. Reliable proof of this remains to be established and should be pursued urgently. It is certainly not possible to meet the current TOPEX accuracy requirements using the FDF standard maneuver support scenario (with separate premaneuver and postmaneuver arcs) lacking such a correction. Unfortunately, global error analysis (References 5 and 6) seems to indicate this goal to be out of reach even with accurate ionospheric correction.

Research into methods of ionospheric correction and into its orbit determination effects should be pursued so that an accurate, efficient correction may be employed, at the latest, during the next solar activity maximum. The errors in candidate ionospheric correction algorithms must be analyzed to establish the level of residual ionospheric error. Orbit determination analysis using real tracking data from COBE, now that it has ceased to vent helium gas, will be useful in this last endeavor. Not only does that mission provide one-way downlink Doppler measurements with the onboard ultrastable oscillator, but its relatively high altitude mitigates the impact of orbit determination error on the evaluation of observation corrections. TOPEX tracking data and precision orbit determination results will eventually be of use in this evaluation, as well.

It is desirable to have the accuracy of the ionospheric correction approach 20 percent. The inherent unpredictability of the ionosphere probably precludes a more accurate correction. The computational burden of ionospheric correction is significant, approximately a factor of 2 in CPU usage, with most of the increase coming from evaluating the Bent model. These two

considerations argue in favor of modernizing the ionospheric model, a not inconsiderable effort.

REFERENCES

1. Atlantic Science Corporation, Final Report No. 76 W 110 F4, *Evaluation, Modification, and Improvement of the Ionospheric Refraction Algorithm in the GTDS*, G. Nesterczuk et al., August 1976
2. Goddard Space Flight Center, Flight Dynamics Division, FDD/552-89/001, *Goddard Trajectory Determination System (GTDS) Mathematical Theory, Revision 1*, A. C. Long et al., prepared by Computer Sciences Corporation, July 1989
3. Jet Propulsion Laboratory, 633-711, *TOPEX/Poseidon Support Instrumentation Requirements Document (SIRD)*, September 6, 1990
4. —, JPL D-7362, *TOPEX/Poseidon Navigation Development Review 3*, May 16, 1990
5. Goddard Space Flight Center, Flight Dynamics Division, FDD/554-90/131, *Ocean Topography Experiment (TOPEX) Satellite, 1990 Flight Dynamics Analysis Report 1: Pre-launch Orbital Error Analysis*, A. Schanzle and J. Rovnak, prepared by Computer Sciences Corporation, September 1990
6. —, FDD/554-91/018 *Ocean Topography Experiment (TOPEX) Satellite, 1990 Flight Dynamics Analysis Report 4: Orbital Error Analysis for Maneuver Planning and Maneuver Evaluation in the Operational Phase*, J. Rovnak and A. Schanzle, prepared by Computer Sciences Corporation, February 1991
7. Computer Sciences Corporation, CSC/TM-88/6052, Analysis Report 88001, *Operational Orbit Techniques Compendium of Analysis Reports: Effects of Ionospheric Refraction on Tracking and Data Relay Satellite System (TDRSS) User Orbit Determination*, M. Radomski, and A. Binebrink, July 1988
8. —, CSC/TM-89/6037, Analysis Report 89002, *Operational Orbit Techniques Compendium of Analysis Reports: TDRSS User Orbit-Determination Error Due to Ionospheric Refraction*, M. Radomski and A. Binebrink, September 1989
9. Goddard Space Flight Center, Flight Dynamics Division, FDD/554-90/048, *Ionospheric Refraction Effects on Ocean Topography Experiment (TOPEX) Orbit Determination Accuracy Using the Tracking and Data Relay Satellite System (TDRSS)*, M. Radomski and K. Heuerman, prepared by Computer Sciences Corporation, August 1990
10. R. S. Bhat, R. B. Frauenholz, and Patrick E. Cannell, "TOPEX/Poseidon Orbit Maintenance Maneuver Design" (paper AAS 89-408 presented at American Astronautical Society/American Institute of Aeronautics and Astronautics Astrodynamics Specialist Conference, Stowe, Vermont, August 7-10, 1989)
11. International Radio Consultative Committee, Report 340-4, *CCIR Atlas of Ionospheric Characteristics*, 1982

12. Computer Sciences Corporation, CSC/TM-88/6052, Analysis Report 88003, *Operational Orbit Techniques Compendium of Analysis Reports: Refraction Correction Algorithms for Tracking and Data Relay Satellite System (TDRSS) Tracking Observations*, M. Radomski, October 1988
13. K. H. Schatten, "November 1989 Solar and Geomagnetic Prediction Data," Goddard Space Flight Center, Memorandum, November 1989
14. Goddard Space Flight Center, X-591-73-281, *NASA-GSFC Ionospheric Corrections to Satellite Tracking Data*, P. E. Schmid et al., December 1973
15. National Bureau of Standards, CRPL-F 161, *Part B, Solar-Geophysical Data*, Boulder, Colorado: Central Radio Propagation Laboratory, January 1958

Study of Geopotential Error Models Used in Orbit Determination Error Analysis*

C. Yee, D. Kelbel, T. Lee, and M. Samii
COMPUTER SCIENCES CORPORATION (CSC)

G. Mistretta and R. Hart
GODDARD SPACE FLIGHT CENTER (GSFC)

ABSTRACT

The uncertainty in the geopotential model is currently one of the major error sources in the orbit determination of low-altitude Earth-orbiting spacecraft. This paper presents the results of an investigation of different geopotential error models and modeling approaches currently used for operational orbit error analysis support at the Goddard Space Flight Center (GSFC), with emphasis placed on sequential orbit error analysis using a Kalman filtering algorithm.

Several geopotential models, known as the Goddard Earth Models (GEMs), have been developed and used at GSFC for orbit determination. The errors in the geopotential models arise from the truncation errors that result from the omission of higher order terms (omission errors) and the errors in the spherical harmonic coefficients themselves (commission errors). At GSFC, two error modeling approaches have been operationally used to analyze the effects of geopotential uncertainties on the accuracy of spacecraft orbit determination — the *lumped error modeling* and *uncorrelated error modeling*.

The lumped error modeling approach computes the orbit determination errors on the basis of either the calibrated standard deviations of a geopotential model's coefficients or the weighted difference between two independently derived geopotential models. The uncorrelated error modeling approach treats the errors in the individual spherical harmonic components as uncorrelated error sources and computes the aggregate effect using a combination of individual coefficient effects.

The study presented in this paper assesses the reasonableness of the two error modeling approaches in terms of global error distribution characteristics and orbit error analysis results. Specifically, this study presents the global distribution of geopotential acceleration errors for several gravity error models and assesses the orbit determination errors resulting from these error models for three types of spacecraft — the Gamma Ray Observatory, the Ocean Topography Experiment, and the Cosmic Background Explorer.

* This work was performed for the National Aeronautics and Space Administration (NASA)/Goddard Space Flight Center (GSFC) under Contract NAS 5-31500.

1. INTRODUCTION

The Earth's geopotential field, V , is commonly represented by the following spherical harmonic equation:

$$V = \frac{\mu}{r} \left[1 + \sum_{n=2}^{\infty} \sum_{m=0}^n (R_e/r)^n P_n^m(\sin \phi) [S_n^m \sin m\lambda + C_n^m \cos m\lambda] \right] \quad (1)$$

- where μ = gravitational constant times mass of the Earth
 r = spacecraft orbital radius
 R_e = radius of the Earth (usually taken as the equatorial radius)
 P_n^m = associated Legendre function
 S_n^m, C_n^m = harmonic coefficients of degree n and order m
 ϕ, λ = geocentric latitude and east longitude

Of computational necessity, the geopotential field represented by Equation (1) is truncated at some finite degree and order. Over the years, several progressively more accurate geopotential models, known as the Goddard Earth Models (GEMs), have been developed and used at Goddard Space Flight Center (GSFC) for satellite orbit determination. Although the geopotential modeling accuracy has improved, it remains one of the major error sources in the orbit determination of low-altitude Earth-orbiting spacecraft. The errors in the geopotential force models arise from the truncation errors resulting from the omission of higher order terms (omission errors) and the errors in the spherical harmonic coefficients (commission errors).

In deriving each GEM, a covariance matrix associated with the spherical harmonic coefficients (or the calibrated form of this matrix) can generally be used to analyze the effects of commission errors on spacecraft orbit determination. However, because of the large size of the matrix, it is computationally expensive and, thus, is impractical for operational use.

As an alternative, a computationally simpler modeling approach, known as the *lumped error model* (Reference 1), has been used at GSFC for orbit error analysis using the batch-weighted least-squares estimation method. A second approach currently being used in sequential error analysis, the *uncorrelated error model*, treats each spherical harmonic component as uncorrelated and considers each to be an independent error source.

1.1 LUMPED ERROR MODEL

In the lumped error modeling approach (LEMA), the orbit determination errors that result from the geopotential model errors are computed by summing algebraically the contributions of the individual spherical harmonic coefficient errors. The algebraic summation assumes that the individual harmonic coefficient errors are fully correlated. This approach also results

in better computational efficiency by having to evaluate only one variational equation to account for the geopotential errors contributed from all harmonic coefficient error sources (Reference 2). The error models used for this approach commonly belong to two categories: *gravity difference* and *standard deviations*.

In the first category, an error model is constructed by taking the weighted difference between two independently derived geopotential model coefficients—the gravity difference error models. The rationale for such an approach is that, if two geopotential models are independently derived, then the weighted average of the two model coefficients may be closer to the “truth,” and the weighted difference between the two models can be regarded as a measure of the error for one of the models. However, operationally, the gravity difference models have been usually generated based on differencing two somewhat correlated geopotential models, for example, GEM9-GEM7 gravity difference model.

In the second category, the estimated errors of the geopotential coefficients—the calibrated standard deviations—are used as the error model. These standard deviation values are obtained from the corresponding calibrated error covariance matrix obtained for each geopotential model (References 3, 4, and 5). However, it was demonstrated in References 6 and 7 that the use of GEM9 standard deviations as a lumped error model can be faulty, because of the anomalous global distribution of acceleration errors that is greater in the northern hemisphere with a singularity near zero degree longitude and 60 degrees latitude. Such anomalous distribution is not supported, however, by other evidence (References 3 and 8).

1.2 UNCORRELATED ERROR MODEL

The uncorrelated error modeling approach (UEMA) is generally used with the standard deviations models and assumes that each spherical harmonic coefficient can be treated as an independent error source. The orbital error caused by the geopotential error is then computed as the root sum square (RSS) of the independent error contributions from all the harmonic coefficients. This approach still requires a substantial amount of computational resources when compared with the LEMA because it requires evaluating one variational equation for each of the spherical harmonic coefficient error sources (Reference 2). For example, for the GEMT1 model with degree and order of 36, UEMA will require evaluating 1363 variational equations. Although some of the coefficients are known to be correlated (Reference 8), this approach may be reasonable (short of having to consider the correlations by including the entire covariance matrix).

It was demonstrated in Reference 6, using the GEM9 standard deviations model, that this approach produced more uniform global error distribution and more “realistic” orbital error distribution, and has, thus, been used previously in sequential error analyses performed for GSFC.

The study presented in this paper investigates the LEMA and UEMA in terms of global error distribution characteristics and reasonableness of error magnitudes predicted for a variety of spacecraft orbital scenarios. The reasonableness of a geopotential error model is assessed in terms of global error distribution characteristics and orbit error analysis results. The geopotential error models studied are listed in Table 1. The study results are presented in two parts.

In the first part, the global error distribution characteristics are analyzed for each of the geopotential models described in Table 1. In the second part of the study, the orbit determination

Table 1. Geopotential Error Models and Modeling Approaches Investigated in This Study

Geopotential Model	Corresponding Error Models		Approach
	Model	Size (Deg. Order)	
GEM 9	GEM9 Standard Deviations GEM9 Standard Deviations GEM9 - GEM7 Gravity Difference ^a	30, 30	LEMA UEMA LEMA
GEM T1	GEMT1 Standard Deviations GEMT1 Standard Deviations GEMT1 - Clone ^b	36, 36	LEMA UEMA LEMA
GEM T2	GEMT2 Standard Deviations GEMT2 Standard Deviations GEMT2 - Clone ^b	50, 50	LEMA UEMA LEMA

6130G(22)-16

Notes:

LEMA: Lumped error modeling approach

UEMA: Uncorrelated error modeling approach

- a. GEM9 - GEM7 difference model is the geopotential error model currently used for operational error analysis support to represent the 3 σ values of GEM9 force model error. This model is derived by taking the 135% of GEM9 - GEM7 differences up to degree and order of 21 to represent commission errors of the terms used in operational orbit determination and 100% of GEM9 coefficients from degree and order of 22 up to 30 to represent omission errors.
- b. The clone models (References 9 and 10) are constructed such that the gravity errors computed using the difference between the original models (GEMT1 and GEMT2) and the respective GEMT1 and GEMT2 clone models give similar results obtained using the full calibrated error covariance matrices. A multiplication factor of 3 can be applied to represent 3σ error values.

errors resulting from the geopotential errors are assessed by performing linear error analysis using the Orbit Determination Error Analysis System (ODEAS) (Reference 2) for a variety of spacecraft mission scenarios. Specifically, analyses were performed for the Gamma Ray Observatory (GRO), the Cosmic Background Explorer (COBE), and the Ocean Topography Experiment (TOPEX) types of missions, primarily in a sequential Kalman filtering mode.

2. RESULTS

The results of this study are presented in two parts. Section 2.1 discusses the global distribution of geopotential acceleration errors for each of the error models listed in Table 1. Section 2.2 discusses the orbit determination errors resulting from geopotential errors predicted by different geopotential models and modeling approaches for GRO, COBE, and TOPEX spacecraft missions.

2.1 GLOBAL DISTRIBUTION OF GEOPOTENTIAL ACCELERATION ERRORS

Errors in the spherical harmonic coefficients will cause errors in computing the geopotential accelerations (forces) acting on an orbiting spacecraft. These acceleration errors vary as a function of geocentric latitude and longitude, and the error magnitude decreases with the increase in orbital height for a fixed latitude and longitude grid point in space. Figures 1

through 9 show the acceleration error magnitudes (1σ values) as a function of geocentric latitude and east longitude at an altitude of 200 kilometers above the surface of the Earth for different geopotential error models and modeling approaches. The acceleration errors shown are in the units of mgal (10^{-5} m/sec²), rounded to the nearest integer.

For the LEMA, the acceleration errors at each of the latitude and longitude grid points are computed by algebraically summing the contributions from each of the sine and cosine harmonic coefficients at that particular location, using Equation (2).

$$\Delta \bar{a}_{\text{LEMA}} = \sum_{n=2}^{n_{\max}} \sum_{m=0}^n \left(\frac{\partial \bar{a}}{\partial C_n^m} \Delta C_n^m + \frac{\partial \bar{a}}{\partial S_n^m} \Delta S_n^m \right) \quad (2)$$

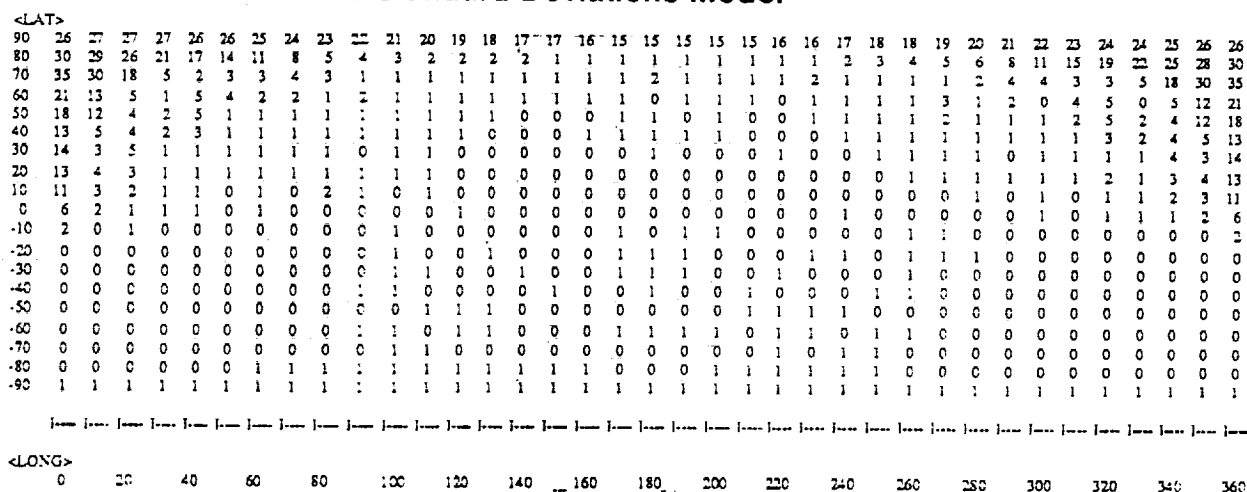
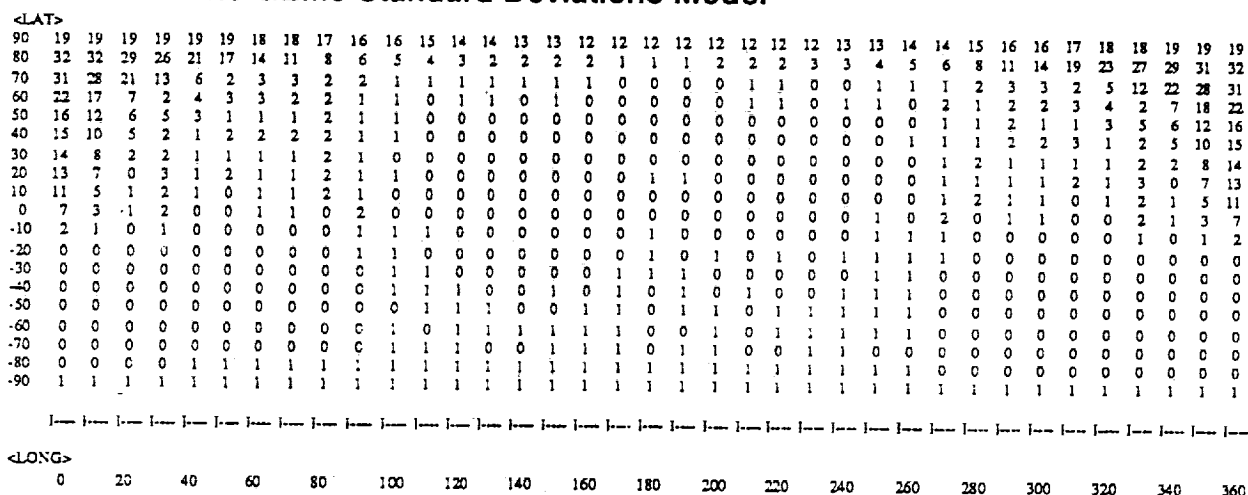
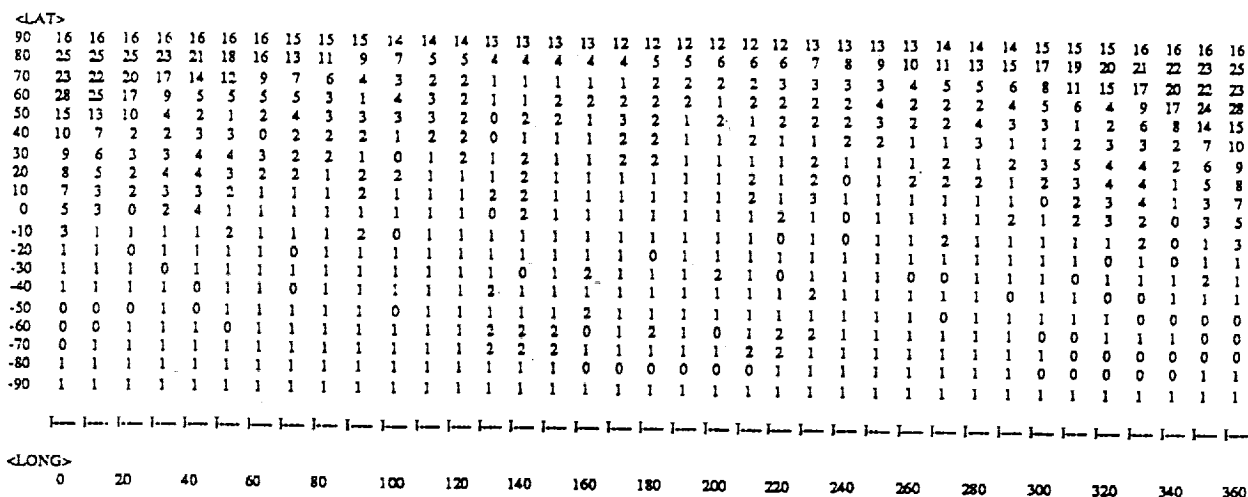
where n_{\max} represents maximum degree of the geopotential error model, and $\Delta \bar{a}_{\text{LEMA}}$ represents an instantaneous geopotential acceleration error a spacecraft would experience due to errors in the spherical harmonic coefficients C_n^m and S_n^m , which are represented by ΔC_n^m and ΔS_n^m in Equation (2). The acceleration error maps obtained using this modeling approach are shown in Figures 1 through 6. In orbit error analysis computation using the LEMA, the spacecraft position and velocity errors are obtained by integrating the effect of $\Delta \bar{a}_{\text{LEMA}}$ given by Equation (2) in one variational equation.

For the UEMA, the acceleration errors are obtained by computing the RSS of the contributions from each of the sine and cosine harmonic coefficients rather than summing them algebraically. This approach is shown mathematically in Equation (3) where Δa_{UEMA} represents the acceleration error magnitude obtained using the UEMA. The acceleration error maps obtained using this modeling approach are shown in Figures 7 through 9.

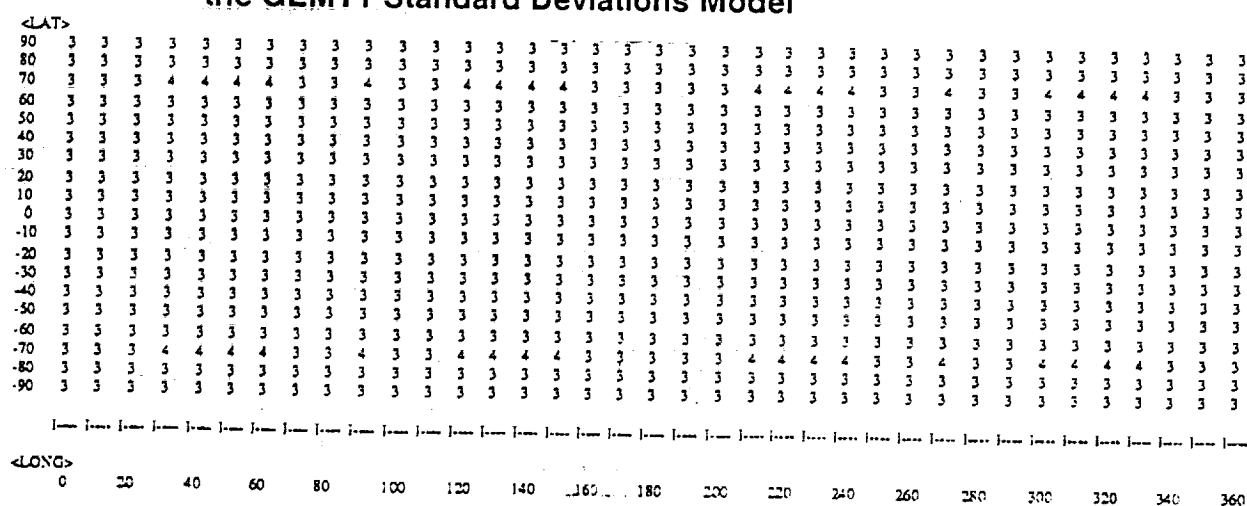
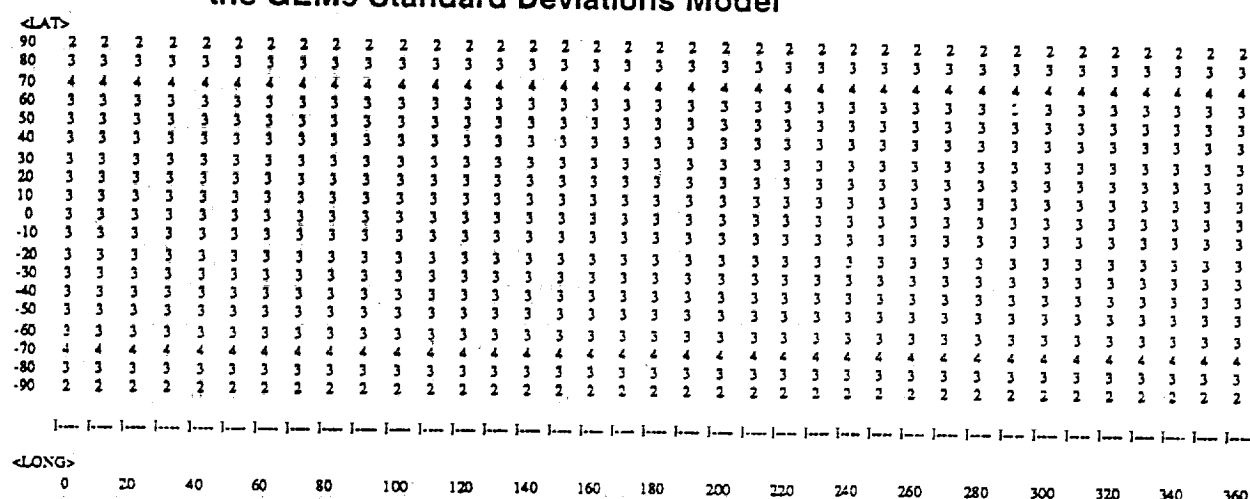
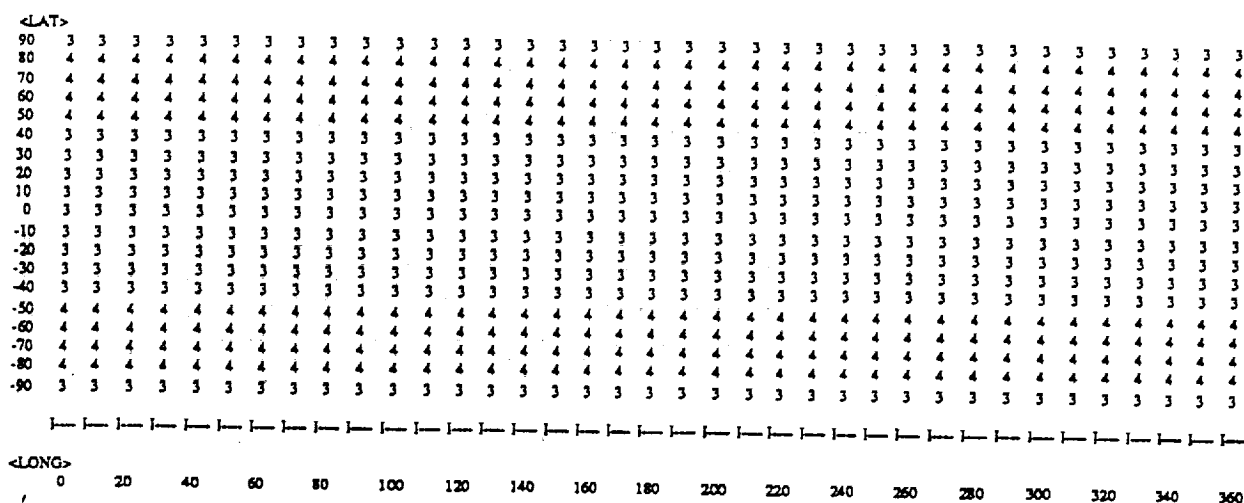
$$\Delta a_{\text{UEMA}} = \sqrt{\sum_{n=2}^{n_{\max}} \sum_{m=0}^n \left[\left(\frac{\partial \bar{a}}{\partial C_n^m} \Delta C_n^m \right)^2 + \left(\frac{\partial \bar{a}}{\partial S_n^m} \Delta S_n^m \right)^2 \right]} \quad (3)$$

It should be noted that in orbit error analysis computation using the UEMA, the spacecraft position and velocity errors are obtained by integrating the individual vectors in the summation (i.e., $\frac{\partial \bar{a}}{\partial C_n^m} \Delta C_n^m$ and $\frac{\partial \bar{a}}{\partial S_n^m} \Delta S_n^m$) in separate variational equations and computing the RSS of all individual error contributions.

It is interesting to see from Figures 1 through 3 that all acceleration error maps obtained for the LEMA using the GEM9, GEMT1, and GEMT2 standard deviations models tend to show the same anomalous error distribution (i.e., a high concentration of large errors localized in a particular region around zero degree longitude in the northern hemisphere and the rest of the globe relatively error-free). The world map of gravity anomalies computed from GEM9 and GEM10 models (Reference 3), the gravity anomalies computed from GEM7 and GEM8, and the gravimetry data (Reference 8) do not support such anomalous distribution. This implies that the orbit determination errors predicted by using such error models will also be anomalous.







On the other hand, the acceleration error distributions obtained for the UEMA seem to be too uniform and symmetric to be realistic. (See Figures 7 through 9.) Comparisons between GEM models and surface gravity measurement data (References 3 and 8) show that a more realistic error distribution may be somewhere between these two cases.

It is also interesting to see that the LEMA based on the gravity difference models (i.e., GEM9-GEM7, GEMT1-Clone, and GEMT2-Clone models) give rise to error maps showing random distributions in error magnitudes. (See Figures 4 through 6.) In the absence of the absolute standard, the gravity difference models appear to be more realistic in terms of global acceleration errors distribution.

2.2 ORBIT DETERMINATION ERRORS RESULTING FROM GEOPOTENTIAL MODELING ERRORS

To assess the orbit determination errors that result from the geopotential modeling errors, linear error analyses were performed using ODEAS for a variety of spacecraft missions with different altitudes and inclinations. Specifically, error analyses were performed for GRO, COBE, and TOPEX missions assuming an orbit determination mode using a sequential Kalman filter. Batch-weighted least-squares results are also shown for COBE spacecraft.

The orbital elements at epoch for GRO, COBE, and TOPEX, their respective spacecraft parameters, force models, and the integration parameters used in the study are shown in Table 2. Tracking simulations were performed for each spacecraft assuming a Tracking and Data Relay Satellite System (TDRSS) tracking scenario, whereby the user spacecraft (GRO, COBE, or TOPEX) is tracked for 2 days via TDRS-East (41 degrees west longitude) and TDRS-West (171 degrees west longitude) with tracking pass lengths of 20 minutes per user spacecraft revolution. Measurements include one range and one range rate every 10 seconds.

Error analyses were performed by estimating the orbital elements of the user spacecraft and the atmospheric drag scaling parameter. Because the primary interest of this study is in orbital errors resulting from the geopotential error sources, only the characteristics of geopotential errors on orbit determination accuracy are presented. The orbital errors presented below are based on 3σ errors.

Figures 10a through 10c illustrate the GRO (altitude: 450 km) spacecraft orbit determination errors resulting from the GEM9, GEMT1, and GEMT2 geopotential model errors, respectively. Figures 11 and 12 illustrate similar plots of orbit determination errors for COBE (altitude: 900 km) and TOPEX (altitude: 1340 km) spacecraft, respectively. Table 3 shows the root mean square (RMS) values, standard deviations, and maximum values of the orbital errors after the initial transient period (taken to be 6 hours past epoch).

The RMS and maximum errors resulting from a given geopotential error model are expected to decrease with increasing orbital altitudes from GRO to TOPEX. The orbital errors for a given spacecraft are also expected to decrease from GEM9 to the more refined models—GEMT1 and GEMT2. The observations made for each of the geopotential modeling approaches are summarized below.

1. *UEMA results using the standard deviations models* generally produce rather uniform error distributions at the expense of substantially higher computer processing times

Table 2. Spacecraft Orbital Elements and Parameters

	GRO	COBE	TOPEX
EPOCH: (YYMMDD) (HHMMSS)	920201 000000	921109 000000	920901 000000
ORBITAL ELEMENTS AT EPOCH			
Semi-major axis (km)	6828.15	7278.047	7718.756
Eccentricity	0.0001	0.0003238	0.00112783
Inclination (deg)	28.5	99.0296	63.14283
R. A. of ascending node (deg)	0.0	86.8450	0.0
Argument of perigee (deg)	0.0	94.9595	0.0
Mean anomaly (deg)	0.0	270.8221	0.0
Orbital Period (minutes)	93.59	102.99	112.48
SPACECRAFT PARAMETERS			
Drag coefficient (C_D)	2.2	2.3	2.3
Spacecraft area to mass (m^2/kg)	0.003347	0.006487	0.006487
Solar reflectivity (C_R)	1.5	1.3	1.3
FORCE MODELING			
GEM9 30 X 30 for reference trajectory computation			
Solar radiation pressure			
Solid Earth tide			
Atmospheric drag force using Harris-Priester density model			
(Mean $F_{10.7}$ solar flux level = 175×10^{-22} watts/ m^2/Hz)			
ORBIT INTEGRATION			
Integrator: Fourth-order Runge-Kutta Integrator			
Step size: 60 seconds			
TRACKING SCENARIO			
20 min/user spacecraft orbit from TDRS-East or TDRS-West			
Range noise = 3.0 m			
Range-rate noise = 0.00282 m/sec			
Date rate = 1 range and range rate per 10 seconds			
For batch-weighted least-squares method, the data weights are set to be the same as for data noise			

6130G(22)-17

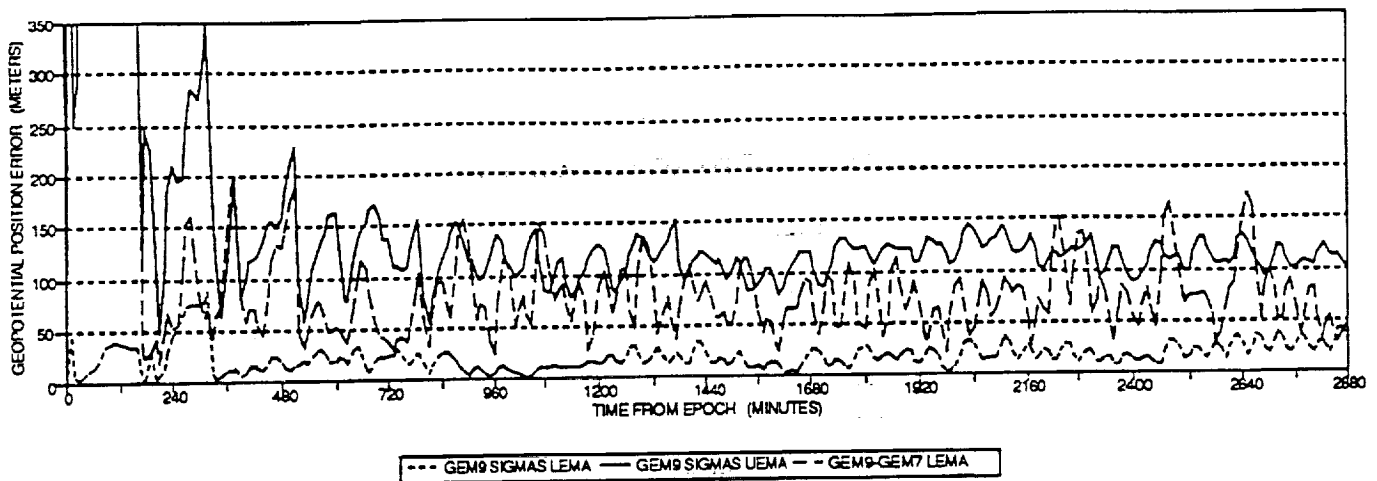


Figure 10a. GEM9 Geopotential Errors for GRO Processed in Sequential Mode

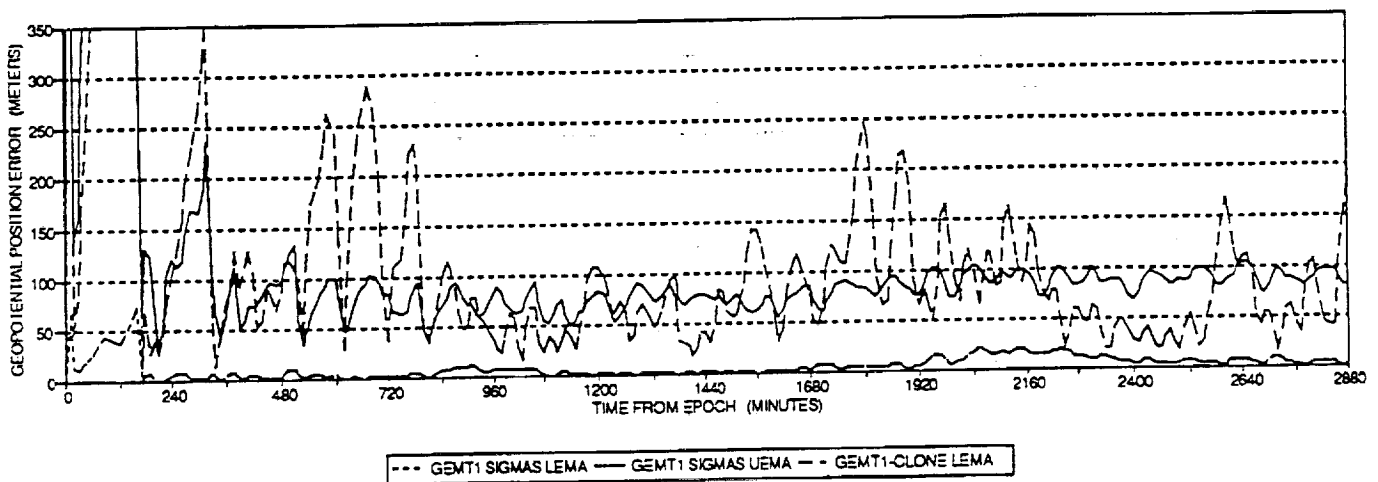


Figure 10b. GEMT1 Geopotential Errors for GRO Processed in Sequential Mode

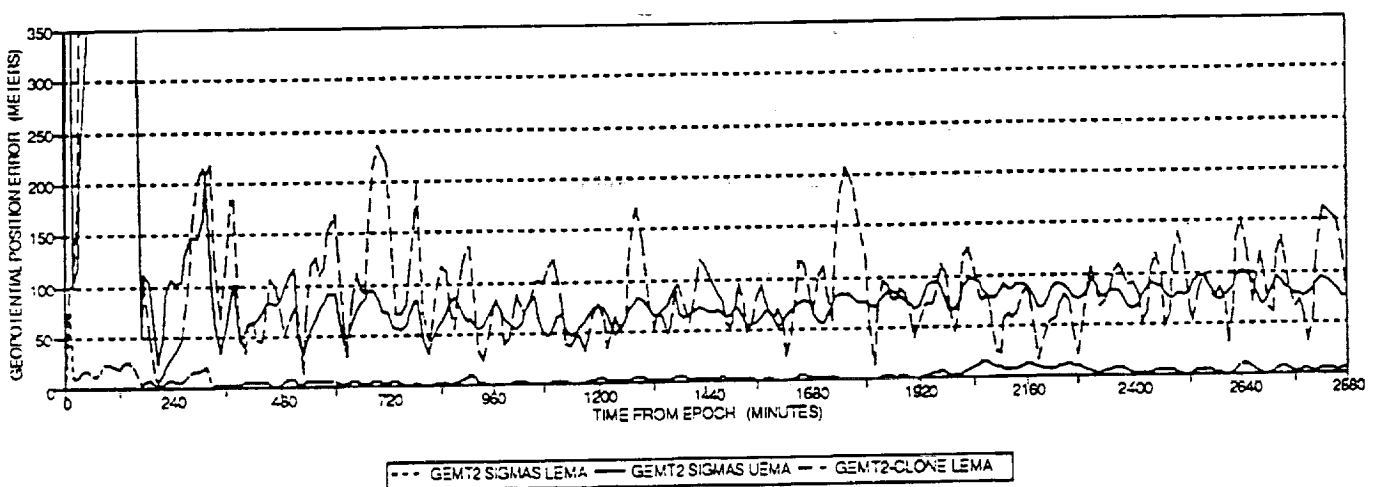


Figure 10c. GEMT2 Geopotential Errors for GRO Processed in Sequential Mode

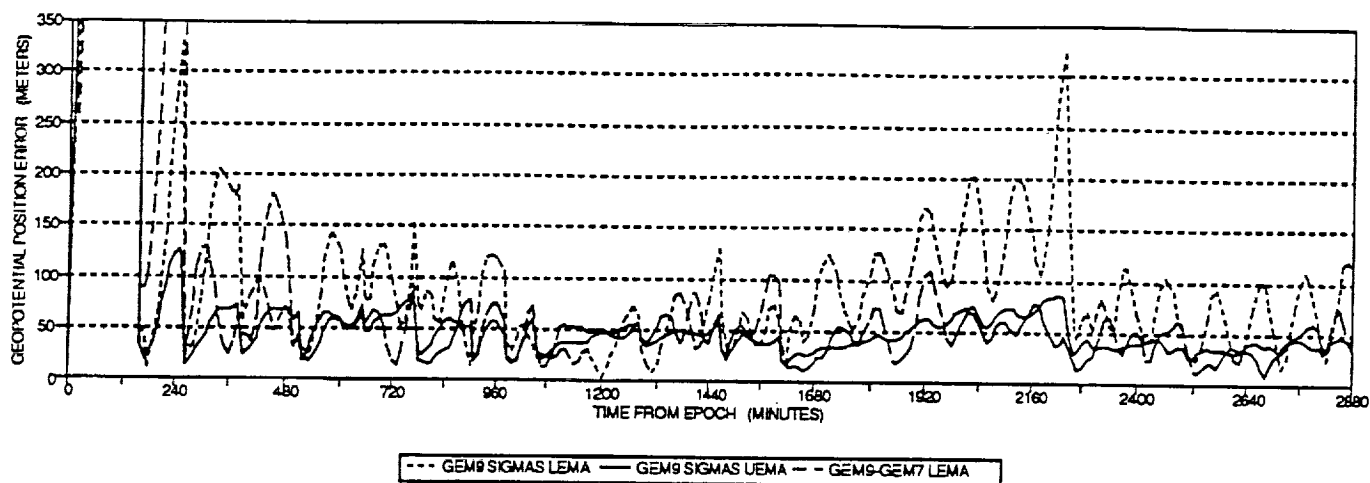


Figure 11a. GEM9 Geopotential Errors for COBE Processed in Sequential Mode

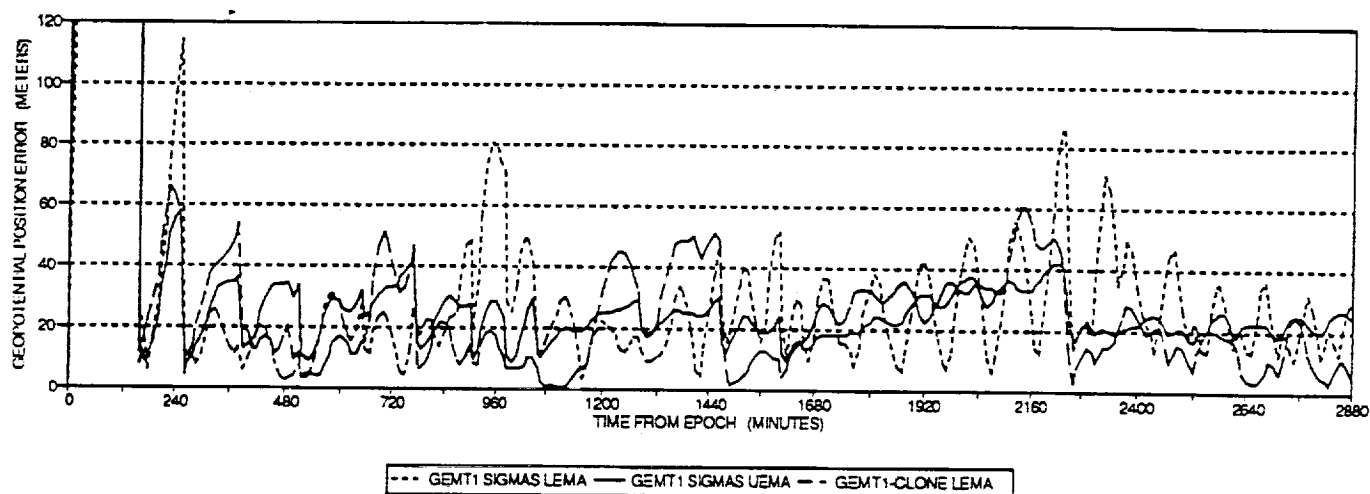


Figure 11b. GEMT1 Geopotential Errors for COBE Processed in Sequential Mode

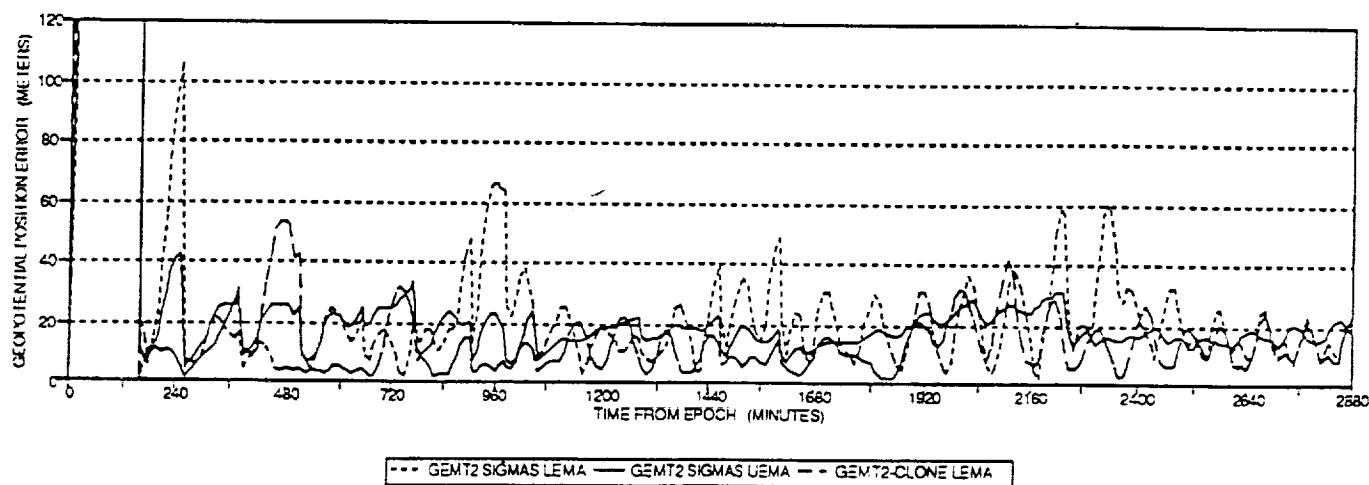


Figure 11c. GEMT2 Geopotential Errors for COBE Processed in Sequential Mode

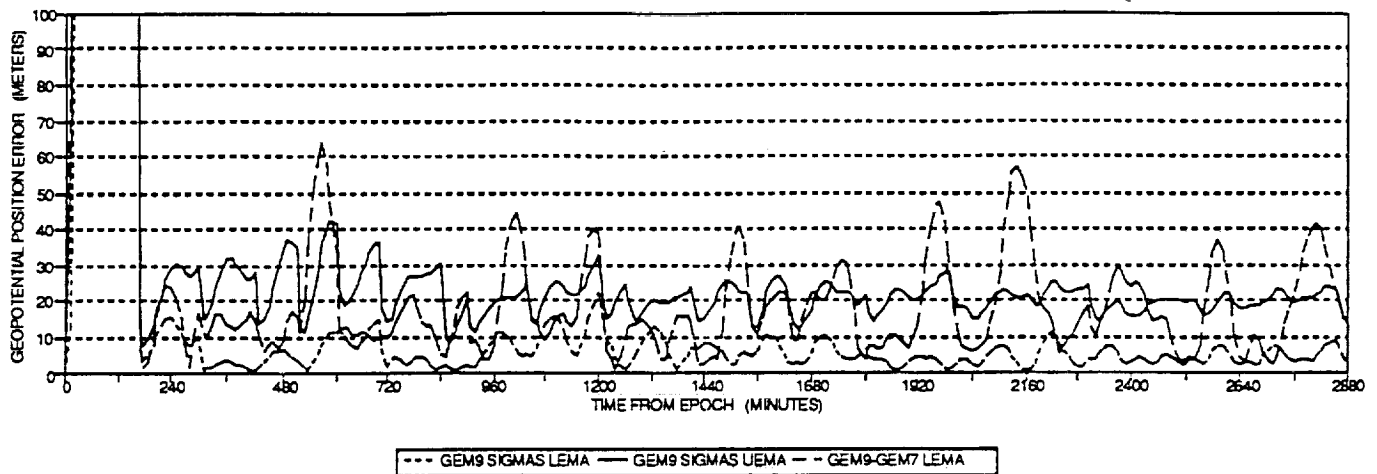


Figure 12a. GEM9 Geopotential Errors for TOPEX Processed in Sequential Mode

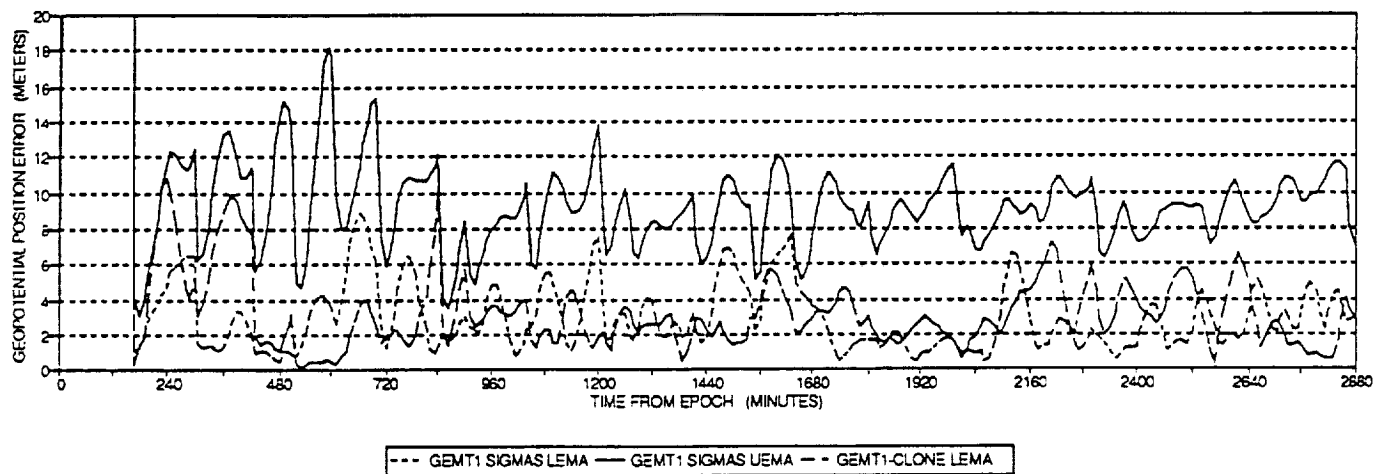


Figure 12b. GEMT1 Geopotential Errors for TOPEX Processed in Sequential Mode

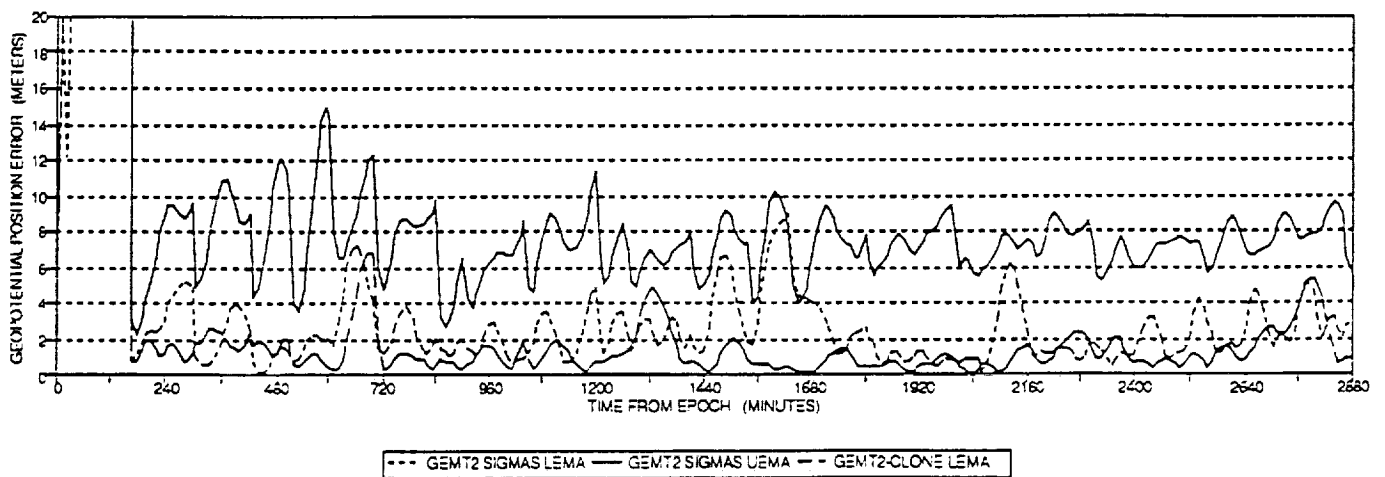


Figure 12c. GEMT2 Geopotential Errors for TOPEX Processed in Sequential Mode

Table 3. Steady-State RMSs, Maximums, and Standard Deviations of Orbital Errors in Sequential Filtering Mode

	LEMA USING STANDARD DEVIATIONS			LEMA USING GRAVITY DIFFERENCES			UEMA USING STANDARD DEVIATIONS		
	GEM9	GEMT1	GEMT2	GEM9 ^a	GEMT1 ^b	GEMT2 ^c	GEM9	GEMT1	GEMT2
RMS									
GRO	20.462	8.578	5.693	85.155	105.188	96.495	119.717	83.700	76.112
COBE	96.004	30.581	23.799	56.067	26.588	16.786	48.529	25.288	19.211
TOPEX	6.598	3.463	3.027	22.459	3.527	1.813	22.111	9.500	7.689
Maximum									
GRO	42.344	23.146	15.784	200.430	288.670	235.400	227.350	135.420	117.960
COBE	323.620	86.041	66.670	181.480	60.767	53.962	85.404	43.749	34.032
TOPEX	22.229	8.848	9.052	63.587	10.399	6.866	42.564	18.198	15.028
Standard Deviation									
GRO	8.462	4.894	3.148	33.998	56.350	40.462	22.190	14.929	14.059
COBE	50.265	16.092	12.824	26.493	14.655	9.964	15.127	7.129	5.356
TOPEX	3.498	1.841	1.702	12.737	1.848	1.199	5.498	2.274	1.881

Units are in meters

Notes:

- a. GEM9-GEM7 difference model is used to represent GEM9 errors
- b. GEMT1-Clone difference model is used to represent GEMT1 errors
- c. GEMT2-Clone difference model is used to represent GEMT2 errors

(generally requiring three to seven times as much central processing unit (CPU) time as the corresponding LEMA results). The uniformity is characterized by the relatively small standard deviation values when compared with the corresponding RMS values for all the spacecraft studied. Table 3 also indicates that the orbital errors predicted by the UEMA follow the expected trends.

2. *LEMA results using standard deviations models* produce either large error spikes (as in the case of COBE) or relatively small errors (as in the case of GRO) when compared with the corresponding UEMA results. These results are expected because of the anomalous distributions of geopotential acceleration errors as illustrated in Figures 1 through 3. The effect of such distribution is that the orbital errors predicted for spacecraft with high orbital inclination, such as COBE (99 degrees), will result in large local error spikes. In contrast, the orbital errors predicted for spacecraft with lower orbital inclinations, such as GRO (28.5 degrees), can be unrealistically small. Such error characteristics are not supported by operational experience.

3. *LEMA results using the gravity difference models* are found to exhibit different behaviors for different spacecraft orbital scenarios. From Table 3, it can be determined that the RMS and the maximum errors resulting from a given geopotential error model decrease, as expected, when going from a low-altitude orbit of GRO to a high-altitude orbit of TOPEX.

However, the orbital errors do not follow the expected decreasing trend from GEM9 to the more refined GEMT1 and GEMT2 error models for GRO, where the orbital errors resulting from the GEMT1-Clone and GEMT2-Clone error models are larger than those of GEM9-GEM7 error model. The error analysis results specific to each of the gravity difference models are summarized below:

- GEM9-GEM7 difference model produces reasonably close agreement with the GEM9 UEMA results for GRO and COBE spacecraft. For TOPEX spacecraft, while GEM9-GEM7 produces RMS orbital errors close to the UEMA results (Table 3), relatively large and spiky errors are observed in orbital error distributions. (See Figures 10a, 11a, and 12a.)
- GEMT1-Clone model produces results comparable with the GEMT1 UEMA results for COBE but produces comparatively higher errors in GRO and comparatively lower errors in TOPEX. (See Figures 10b, 11b, and 12b.)
- GEMT2-Clone model produces results comparable with the GEMT2 UEMA results for COBE but also produces comparatively higher errors in GRO and lower errors in TOPEX. (See Figures 10c, 11c, and 12c.)

To assess the reasonableness of the error magnitudes predicted by each error modeling approach, the orbital errors must be compared with independent results. Reference 5 provides independent error analysis results for TOPEX-type spacecraft for GEMT1 and GEMT2 models. These results were obtained using the first-order analytical perturbation theory of Kaula (Reference 11) and fully calibrated covariance matrices of GEMT1 and GEMT2 solutions, assuming a 10-day TOPEX arc.

Because such analyses do not account for the effect of imperfect tracking scenarios, the orbital errors thus obtained can be regarded as errors due entirely to the geopotential model under a perfect tracking condition. According to Reference 5, the projected orbital errors resulting from GEMT1 and GEMT2 model errors for a 10-day TOPEX arc are 1.9 and 0.9 meters (1σ), respectively. This translates to 5.7 and 2.7 meters (3σ) as shown in Table 4.

For comparison purposes, additional TOPEX error analysis was performed using the ODEAS sequential processing mode assuming a continuous tracking of TOPEX from TDRS-East and TDRS-West for 2 days using range and range-rate data. Continuous tracking was used to minimize the effect of imperfect tracking conditions on orbital errors. Table 4 lists the RMS orbital errors obtained after the initial transient period using different GEMT1 and GEMT2 error models.

The results indicate that, for TOPEX-type spacecraft, the projected orbital errors quoted in Reference 5 lie in between the UEMA and the LEMA results with UEMA results being on the high side.

Figures 13a through 13c show the batch-weighted least-squares orbit determination errors for COBE spacecraft resulting from GEM9, GEMT1, and GEMT2 error models, respectively. Error analysis results are presented assuming a 2-day definitive data for all cases. Again, it can be observed that the LEMA using standard deviations models produces very

Table 4. Comparison of TOPEX Orbital Errors (3σ values) Using Different Geopotential Error Modeling Approaches

Geopotential Model	Projected orbital errors for 10-day arc (meters) (Reference 5)	Steady-state RMS orbital errors for a 2-day continuous tracking (meters)	
		UEMA	LEMA ^a
GEMT1	5.7	7.4	3.2
GEMT2	2.7	6.1	1.3

6130G(22)-19

Notes:

- a. GEMT1-Clone and GEMT2-Clone gravity difference models are used to represent geopotential errors due to GEMT1 and GEMT2 models, respectively.

large spikes in orbit errors. However, the LEMA using the gravity difference models produces results similar to the corresponding UEMA results. This was also found to be the case for COBE spacecraft in sequential processing mode. (See Figures 11a through 11c.)

Figures 14a through 14c compare COBE orbit determination errors processed in sequential Kalman filtering with batch-weighted least-squares modes using identical tracking schedules in both modes. As expected, the effects of local error spikes are less severe in the batch-weighted least-squares mode than in the sequential Kalman filtering mode, and the batch solutions agree with the corresponding sequential solutions at the end of the data arc.

3. CONCLUSIONS AND RECOMMENDATIONS

From the observation of geopotential acceleration error maps, two primary conclusions can be drawn.

1. The LEMA using standard deviations models produces an anomalous trend having a high concentration of large acceleration errors that are localized in a particular region around zero degree longitude in the northern hemisphere and the rest of the globe remains relatively error-free. Such an error distribution can give rise to spurious local error spikes for high-inclination spacecraft (such as COBE) and unrealistically small errors for low-inclination spacecraft (such as GRO). It can, therefore, be concluded that the standard deviations models should not be used in conjunction with the LEMA.

2. However, the UEMA using standard deviations models is found to produce uniform acceleration error bands symmetric in northern and southern hemispheres. This may, again, be unrealistic. On the other hand, the LEMA using gravity difference models gives error maps showing random distributions in error magnitudes. In the absence of the absolute

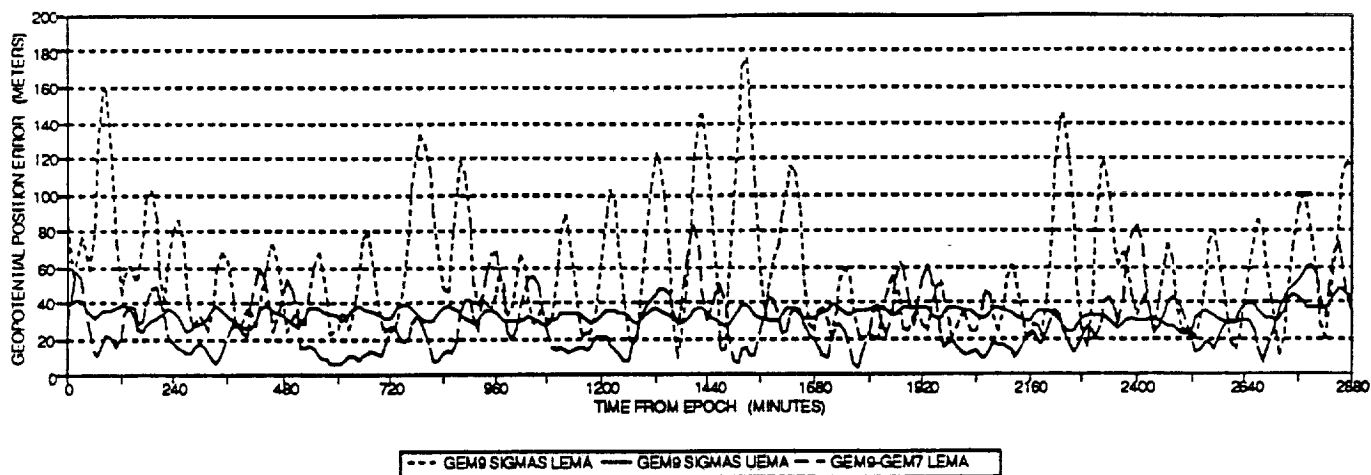


Figure 13a. GEM9 Geopotential Errors for COBE Processed in Batch Mode

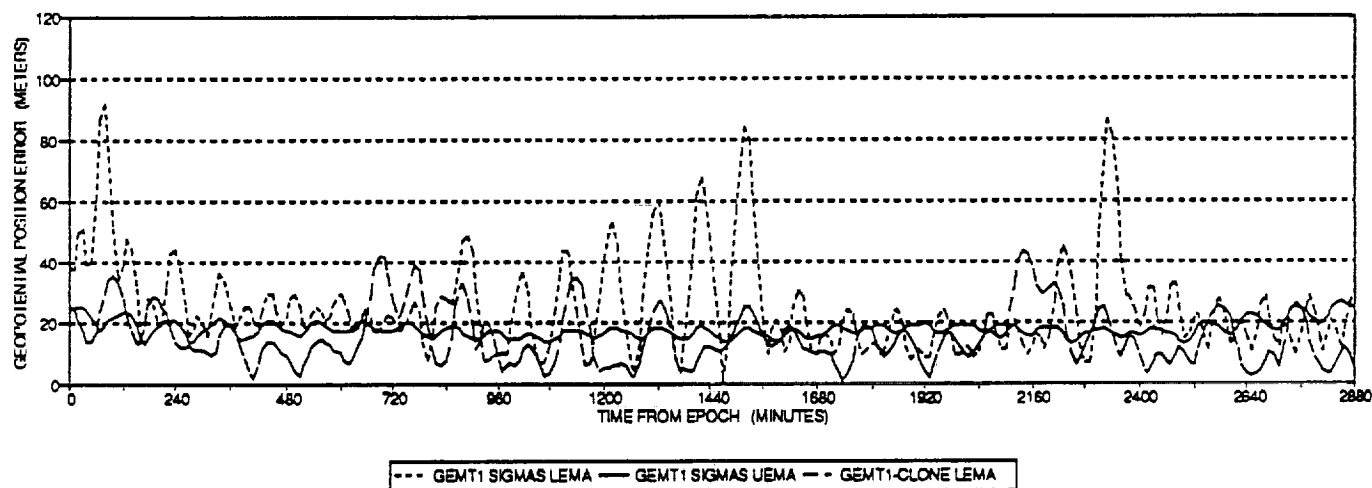


Figure 13b. GEMT1 Geopotential Errors for COBE Processed in Batch Mode

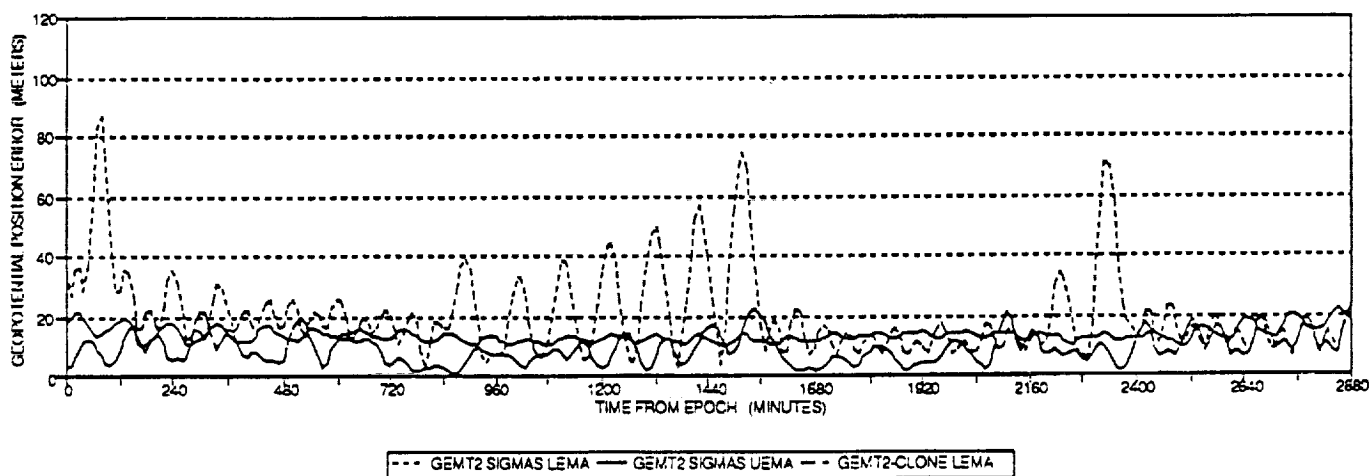


Figure 13c. GEMT2 Geopotential Errors for COBE Processed in Batch Mode

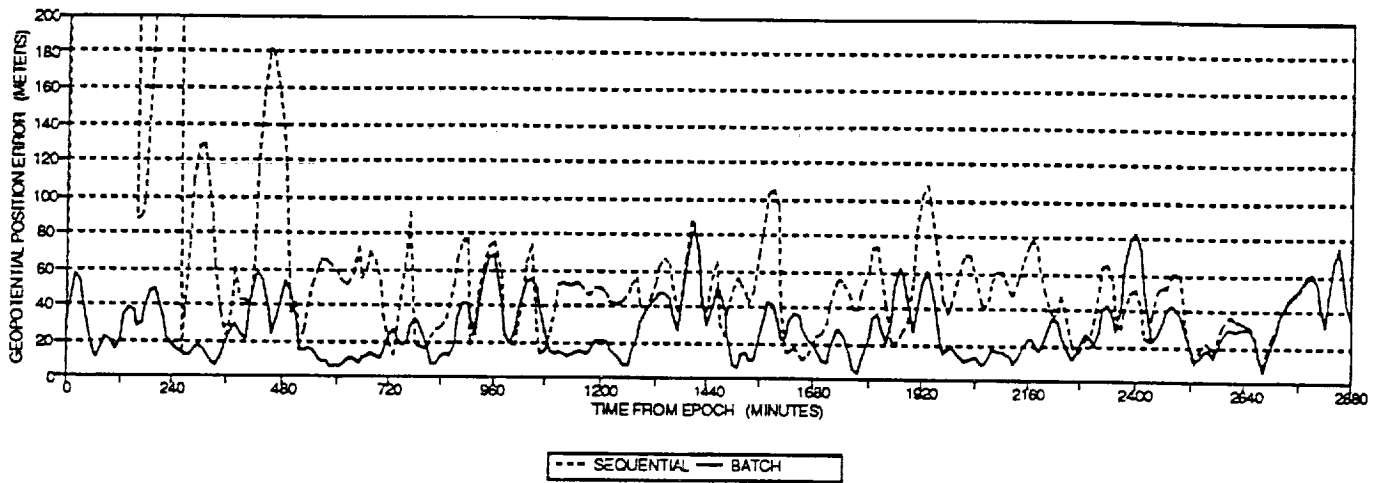


Figure 14a. Geopotential Errors for COBE Using GEM9-GEM7 Model

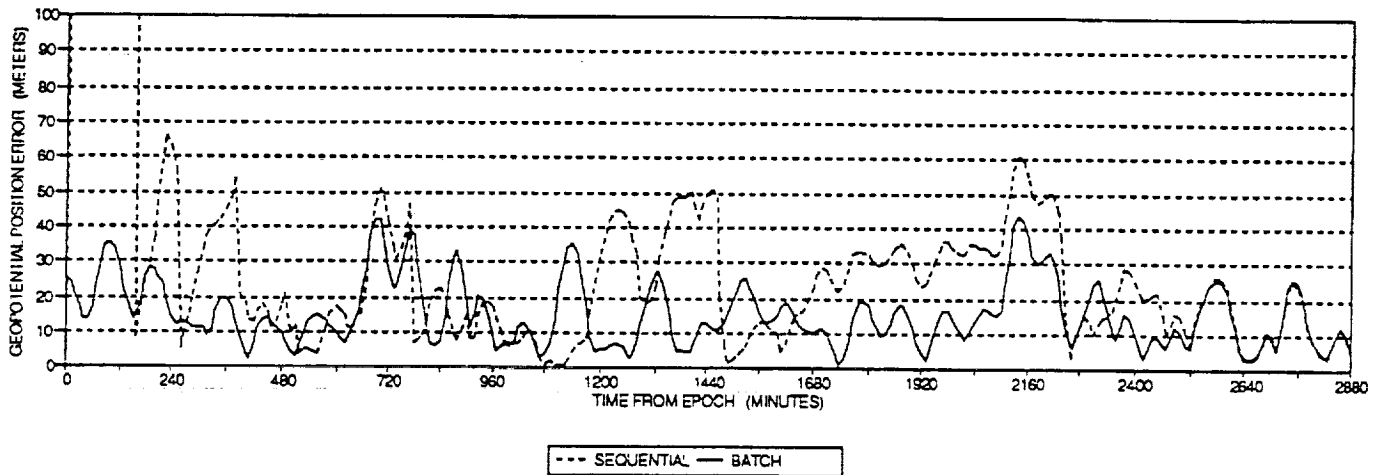


Figure 14b. Geopotential Errors for COBE Using GEMT1-Clone Model

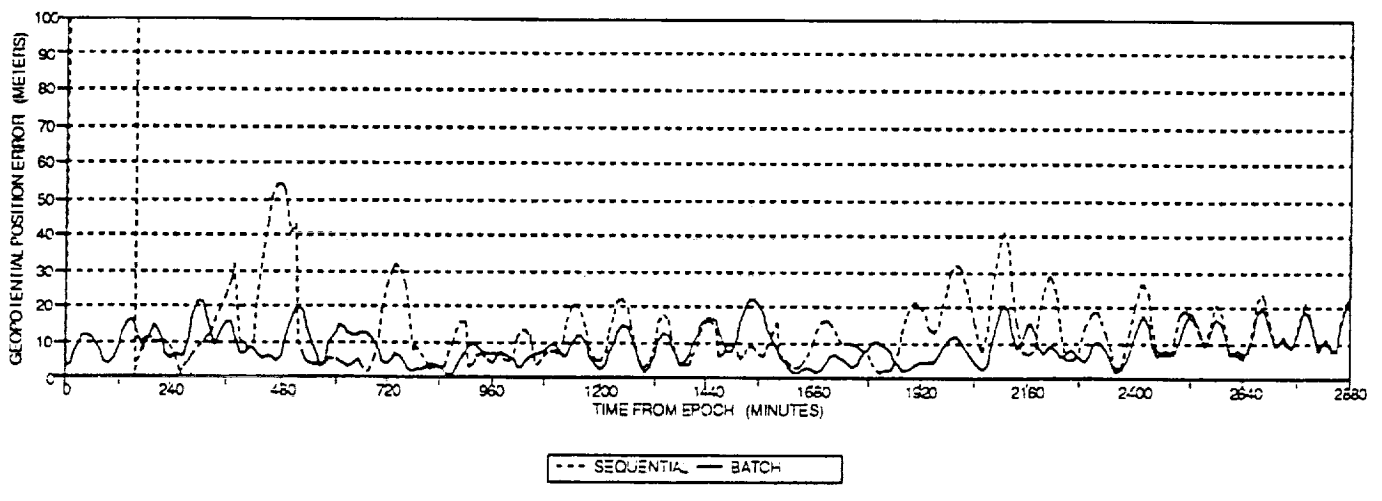


Figure 14c. Geopotential Errors for COBE Using GEMT2-Clone Model

standard, the error characteristics shown in the gravity difference models appear to be the more reasonable representation of geopotential errors.

From the error analysis results, three additional conclusions can be drawn.

1. The geopotential error models that are based on the UEMA generally produce fairly uniform error distributions usually free from unrealistic error spikes at the expense of substantially higher computer processing times (generally requiring three to seven times as much CPU as the LEMA). The uniformity is characterized by relatively small standard deviation values when compared with the corresponding RMS values. This was found to be the case in both sequential and batch processing modes. Also, the orbital errors predicted by this modeling approach generally follow the expected trends—meaning that, for a given geopotential error model, the RMS and the maximum orbital errors decrease with increasing orbital altitudes from GRO to TOPEX; and for a given spacecraft, the orbital errors decrease from GEM9 to the more refined models (GEMT1 and GEMT2).

2. The difference error models in LEMA generally produce higher fluctuation in errors than the UEMA. This is characterized by relatively large standard deviation values when compared with the corresponding RMS values.

3. Generally, the error characteristics produced by different geopotential error modeling approaches are not sensitive to orbit error estimation mode. For COBE spacecraft, the error signatures produced by the batch-weighted least-squares mode are similar to those of sequential Kalman filtering mode, except that the error magnitudes and the error fluctuations are smaller in batch mode. This is expected because of the data-smoothing effect realized in the batch estimation mode.

It is difficult to suggest a general error modeling approach that can be used for all spacecraft scenarios. As discussed earlier, if central processing unit (CPU) and computing resources are not of a concern, error analysis should be performed using the entire covariance matrix of spherical harmonic coefficients, to account correctly for the correlations that exist among these coefficients. In the absence of this, the UEMA may be a reasonable error modeling approach for most spacecraft scenarios because the orbital errors predicted by UEMA are mostly free from unrealistic error spikes and follow the expected trends as discussed earlier. The disadvantage of this approach is still the substantially higher CPU requirement over the LEMA for operational error analysis support.

The LEMA using difference models, while computationally efficient, is found to exhibit different characteristics for different spacecraft. GEM9-GEM7 seems to be a good error model to represent GEM9 modeling errors for GRO and COBE spacecraft, but it is not very reasonable for TOPEX because of some sporadic, large error spikes. GEMT1-Clone and GEMT2-Clone models seem to be good error models for representing GEMT1 and GEMT2 errors, respectively, for TOPEX and COBE spacecraft, but tend to produce large error spikes in GRO spacecraft.

As discussed previously, geopotential error models based on either the LEMA or the UEMA do not properly take into account the correlations that exist among the harmonic coefficients. If computer resources permit, future studies should include orbital error analyses using the

entire covariance matrix of spherical harmonic coefficients to take proper account of the correlations. This will also provide a reference point for calibrating other geopotential error modeling approaches. Future study should also include the development of an improved error modeling approach feasible for operational use. Such a modeling approach will be based on a certain combination of LEMA and UEMA with proper correlation information obtained from the calibrated error covariance. To augment the error analysis results, the authors also recommend performing sequential and batch orbit determination studies using real tracking data.

ACKNOWLEDGMENTS

The authors wish to thank F. Lerch (GSFC) for providing reference materials and useful discussions and A. Schanzle (CSC) for his thoughtful comments during the preparation of this paper.

REFERENCES

1. Martin, C. F., and Roy, N. A., "Error Model for the SAO Standard Earth," *The Uses of Artificial Satellite for Geodesy*, AGU Monograph 15, Washington, D.C., 1970
2. Goddard Space Flight Center, Flight Dynamics Division, FDD/554-90/029, *Orbit Determination Error Analysis System (ODEAS) Mathematical Specifications, Revision 1*, C. P. Yee and T. Lee, prepared by Computer Sciences Corporation, January 1990
3. Goddard Space Flight Center, X-921-77-246, *Gravity Model Improvement Using GEOS-3 (GEM 9 & 10)*, F. J. Lerch, S. M. Klosko, R. E. Laubscher, C. A. Wagner, September 1977
4. Goddard Space Flight Center, NASA TM-4019, *An Improved Model of the Earth's Gravitational Field: GEM-T1*, J. G. Marsh, et al., July 1987
5. Goddard Space Flight Center, NASA TM-10076, *The GEM-T2 Gravitational Model*, J. G. Marsh et al., October 1989
6. Stanford Telecommunications, Inc., STI/E-TR-25066, *Tracking and Data Acquisition System (TDAS) for the 1990's*, Volume VI, TDAS Navigation System Architecture, B. D. Elrod et al., May 1983
7. Computer Sciences Corporation, CSC/TM-53-6119, *Navigation Study for Low-Altitude Earth Satellite*, P. R. Pastor, B. T. Fang, and C. P. Yee, December 1985
8. Goddard Space Flight Center, X-921-76-187, *The Accuracy of Goddard Earth Models*, C. A. Wagner, June 1976
9. Private communications with F. Lerch (GSFC)
10. Memorandum from S. Klosko (ST Systems Corporation) to E. Christensen (Jet Propulsion Laboratory) dated November 7, 1990
11. W. M. Kaula, *Theory of Satellite Geodesy*, Balisdell Publishing Co.: Waltham, Mass., 1966

INCREASED EPHEMERIS ACCURACY USING
ATTITUDE-DEPENDENT AERODYNAMIC FORCE COEFFICIENTS
FOR INERTIALLY STABILIZED SPACECRAFT

by

David C. Folta & David F. Baker

NASA - Goddard Space Flight Center
Flight Dynamics Analysis Branch
Greenbelt, MD 20771

ABSTRACT

Current techniques for generating spacecraft ephemerides typically use a constant value of the ballistic coefficient during orbit propagation. This is due in part to the added complexity of calculating attitude-dependent aerodynamic forces and in part to the great inaccuracy in the prediction of the atmospheric density, which would result in substantial orbital position errors even if the ballistic coefficient were to be determined exactly at all times. Assuming a constant ballistic coefficient, however, introduces errors that may be as large as those caused by the density uncertainty. For inertially-stabilized spacecraft, these errors may be reduced either by calculating orbit-averaged ballistic coefficients for each viewing attitude, or by calculating aerodynamic force coefficients for the appropriate geometry at each integration step.

This report describes briefly the FREEMAC program used to generate the aerodynamic coefficients, as well as associated routines that allow the results to be used in other software. These capabilities are applied in two numerical examples to the short-term orbit prediction of the GRO and HST spacecraft. Predictions using attitude-dependent aerodynamic coefficients were made on a modified version of the PC-based Ephemeris Generation Program (EPHGEN) and were compared to definitive orbit solutions obtained from actual tracking data. The numerical results show improvement in the predicted semi-major axis and along-track positions that would seem to be worth the added computational effort.

Finally, other orbit and attitude analysis applications are noted that could profit from using FREEMAC-calculated aerodynamic coefficients, including orbital lifetime studies, orbit determination methods, attitude dynamics simulators, and spacecraft control system component sizing.

1.0 INTRODUCTION

In the course of planning and supporting a low-Earth-orbit satellite mission, both long- and short-term orbit predictions are required. Long-term predictions (over months or years) are used to plan orbit reboost maneuvers and to estimate time of atmospheric reentry, while short-term predictions (over days or weeks) are used to schedule tracking resources and scientific data collection. Since the position of a satellite in low Earth orbit is highly dependent on aerodynamic drag, this effect must be modeled as well as possible for accurate orbit predictions.

Aerodynamic drag is given by:

$$D = \frac{1}{2} \rho |V_r| C_d A V_r$$

where

- ρ = atmospheric density
- V_r = relative velocity of spacecraft and atmosphere
- C_d = coefficient of drag
- A = satellite cross-sectional area

The predominant error source in the drag calculation is due to density modeling inaccuracies. Substantial errors may also be introduced through the C_d and A terms, however; these terms vary with attitude and orbit position, and can be difficult to calculate. The benefits of calculating attitude-dependent $C_d A$ values have generally been considered in the past to be not worth the computational effort required, especially given large errors due to density modeling which would still cause errors in the drag estimate even if values for $C_d A$ were to be calculated perfectly at each instant. The $C_d A$ term in the drag equation is therefore typically held constant over the period of prediction, often for the spacecraft's entire operational lifetime.

As might be imagined, using such a constant $C_d A$ introduces substantial errors in addition to those due to the density uncertainty. These errors may be quite large, especially for spacecraft with large appendages, and may approach in magnitude the errors due to density mismodeling.

This report presents recent work done in Goddard's Flight Dynamics Analysis Branch that enables attitude-dependent drag coefficients and areas to be calculated. In particular, software tools are described that calculate these coefficients and permit them to be accessed easily in a variety of orbit and attitude applications. These routines are applied to the case of short-term orbit determination of inertially stabilized spacecraft through numerical examples using real data from the Hubble Space

Telescope (HST) and the Gamma Ray Observatory (GRO). Finally, suggestions are made for other uses of FREEMAC-determined attitude-dependent aerodynamic coefficients in the orbit and attitude analysis fields.

2.0 CURRENT ORBIT DETERMINATION AND PREDICTION TECHNIQUES

Orbit determination and short-term prediction for Earth-orbiting satellites are currently performed in NASA/Goddard's Flight Dynamics Division (FDD) with the Goddard Trajectory Determination System (GTDS). GTDS uses the following equation for drag when in orbit prediction mode:

$$D = \frac{1}{2} \rho_0 (1 + \beta_1) |\mathbf{v}_r| C_d A |\mathbf{v}_r|$$

where

- ρ_0 = atmospheric density taken from Harris-Priester table
- β_1 = corrective density term
- \mathbf{v}_r = relative velocity of spacecraft and atmosphere
- C_d = coefficient of drag
- A = satellite cross-sectional area

Parameter β_1 in this equation is generally solved for in the orbit determination process, then used subsequently in the prediction; it accounts for differences between the actual density and the assumed atmospheric density.

Because any $C_d A$ mismodeling is compensated for in β_1 , there is a tendency not to calculate the most accurate $C_d A$ for use in GTDS, since any errors in $C_d A$ will be removed in solving for β_1 . Moreover, lumping the $C_d A$ and density errors together into the term hides the fact that the $C_d A$ product can be fairly accurately calculated if the effort is expended to do so, while the density calculation will have substantial errors in any case due to the random nature of the solar flux, which drives atmospheric density.

In practice, the drag coefficient is usually taken as 2.2 or 2.0, while the cross-sectional area is approximated from the views on the blueprint.

3.0 ATTITUDE-DEPENDENT AERODYNAMIC COEFFICIENTS

Constant $C_d A$ values have been used in the past probably because the complexity of calculating a changing values for different mission geometries was deemed not worth the effort. In recent years, however, software tools have been developed that

make the use of more accurate attitude-dependent aerodynamic coefficients easy to implement in a variety of applications. These routines, based on the FREEMAC program described in Fredo [1], are described in some detail in the Appendix and are summarized below.

FREEMAC calculates the spacecraft aerodynamic force, moment, and drag coefficients as a function of body frame velocity direction using a user-input geometrical model of the spacecraft, a shadowing technique, and free molecular flow theory. The coefficients are written to a file for velocity vectors spaced every 10° in azimuth and elevation in the body frame. A subroutine has been written that interpolates quadratically between these values to obtain accurate coefficients for any given input body frame velocity vector. Because this interpolation can be performed quickly on a digital computer, this subroutine can be used to return aerodynamic coefficients at the same frequency that other environmental perturbations (e.g., third body accelerations, gravity gradient torques, etc.) are calculated in orbit and attitude integrators.

3.1 CONSTANT COEFFICIENTS: OVERALL & ORBIT-AVERAGED

FREEMAC-determined drag coefficients (or, alternatively, C_dA values) can be applied to the orbit prediction problem at several levels of complexity and computational effort. First, constant attitude-independent C_dA values can be used for lifetime predictions and other situations where the velocity vector is known to take on essentially a random directional distribution in the body frame during the prediction period, as is the case, for example, for an inertially-stabilized spacecraft changing its attitude frequently. In these situations, a FREEMAC-calculated C_dA values averaged over all possible body frame velocity directions could be applied. These average C_dAs can be used in all the current software. They have the advantage of being detailed calculations based on a model of the spacecraft, rather than being just the "eyeball" estimates of the spacecraft area currently used times a drag coefficient value of 2.2.

For spacecraft stabilized in a constant orbit-based reference frame in which the velocity vector remains fixed in the body frame, a FREEMAC-determined C_dA can be interpolated from the coefficient file and can be used for the remainder of the mission, without further recourse to FREEMAC. For inertially stabilized spacecraft, however, the velocity vector rotates 360° in the body frame, causing the C_dA to change sinusoidally around the orbit. The effect of this varying C_dA on orbit decay can be approximated by an orbit-averaged C_dA for time spans of less than

a week or so (for periods in which the orbit orientation does not change too much). Section A.3 of the Appendix describes a subroutine that has been developed to calculate these orbit-averaged coefficients.

3.2 CONSTANT COEFFICIENTS FOR EACH INERTIAL ATTITUDE

The next level of complexity is to calculate drag using C_d s held constant over various spans of the prediction period. This segmentation technique can be used for inertially-stabilized spacecraft that change viewing attitudes regularly, for example. It has the advantage of being applicable to current software, with the constant C_d s being precalculated from the FREEMAC results. This method does lose some accuracy, however, if the orientation of the orbit plane changes significantly over the prediction span.

3.3 COEFFICIENTS DETERMINED EACH INTEGRATION STEP

The third and most accurate approach is also the most rigorous computationally: as with other perturbing forces (third body, Earth asphericity, etc.) a FREEMAC-determined drag force is calculated at each orbit integration step. The complete aerodynamic force coefficient vector $[C_x, C_y, C_z]^T$ is interpolated from the FREEMAC coefficient file at each time step; this allows for the determination of the aerodynamic effect on not only the in-plane elements, but on inclination and node as well.

The third approach above was implemented on EPHGEN, a PC-based orbit generator using the GTDS 12th order Cowell integrator. Test runs have shown that this approach increases run time by approximately 45%, an increase which, though it seems large, is roughly equivalent to increasing the order of the Earth gravitational potential model from 16x16 to 21x21.

4.0 NUMERICAL EXAMPLES

To assess the accuracy benefits to be gained by using the above FREEMAC-based approaches, two numerical prediction cases were run and are presented below, the first using GRO data, the second using HST data. For all the predictions, the 12th order Cowell integrator in EPHGEN was used with a 60 second step size. Both solar and lunar gravitation perturbations were applied, and a 16x16 geopotential model was used with a cosine power of 2 and a bulge angle of 30°. The mass of GRO was taken as 15700 kg, and that of HST as 11328 kg.

4.1 NUMERICAL EXAMPLE: GRO DATA

Tracking data for the GRO spacecraft were obtained for an approximately four week period spanning 910418.00 to 910515.21. The spacecraft assumed seven different inertial attitudes during this period, as given in Table 1. Predictions were made for the 4 week span using the current operational approach and the latter two methods above, based on epoch elements obtained from a GTDS solution using the real tracking data. The three predictions at the end time were then compared to another GTDS solution at the end of the span which again used the real tracking data.

TABLE 1 -- GRO ATTITUDES

Times	1-2-3 Euler Angles [deg]			Solar array angles [deg]	Average $C_d A$ [m ²]
414.05-419.03	-96.86	-18.00	-10.24	2.	93.9
419.03-428.15	-67.88	3.01	-0.51	37.	82.5
428.15-501.17	-74.76	0.22	-49.90	48.	80.2
501.17-504.16	-74.76	0.22	40.20	52.	96.8
504.16-507.16	-67.86	6.00	-0.90	51.	94.8
507.16-510.17	-10.98	-31.04	64.20	.6	91.5
510.17-515.22	-144.93	-30.05	-81.55	-11.	92.7

The three prediction methods were:

- #1 -- Current operational approach: a C_d of 2.2 and an average area of 47 m² were used for the whole 4 week period. (Note that this area is actually the FREEMAC area averaged over all body frame velocity vector directions.)
- #2 -- Average $C_d A$ s used for each attitude. Orbit-averaged $C_d A$ values were calculated from the FREEMAC coefficients for each of the seven attitudes and were applied as constants over the respective time spans. Mid-span orbital elements were used in the orbital averaging, with the ascending node drift rate approximated beforehand.
- #3 -- Force coefficient vector $[C_x, C_y, C_z]^T$ extracted and applied at each integration time step.

Note in Table 1 that the solar array angles changed with each attitude. Since each FREEMAC coefficient file is only valid for a single geometric configuration, some approximation was required here. For three of the attitudes, a file created with a 0° array angle was used, while one for 45° was used for the other four.

Atmospheric density is modeled in EPHGEN using Harris-Priester tables corresponding to flux levels at increments of 25. The table for a flux level of 225 was used in the predictions, this level being the one closest to the 90-day average flux of 236 at the beginning of the four weeks (see Figure 1).

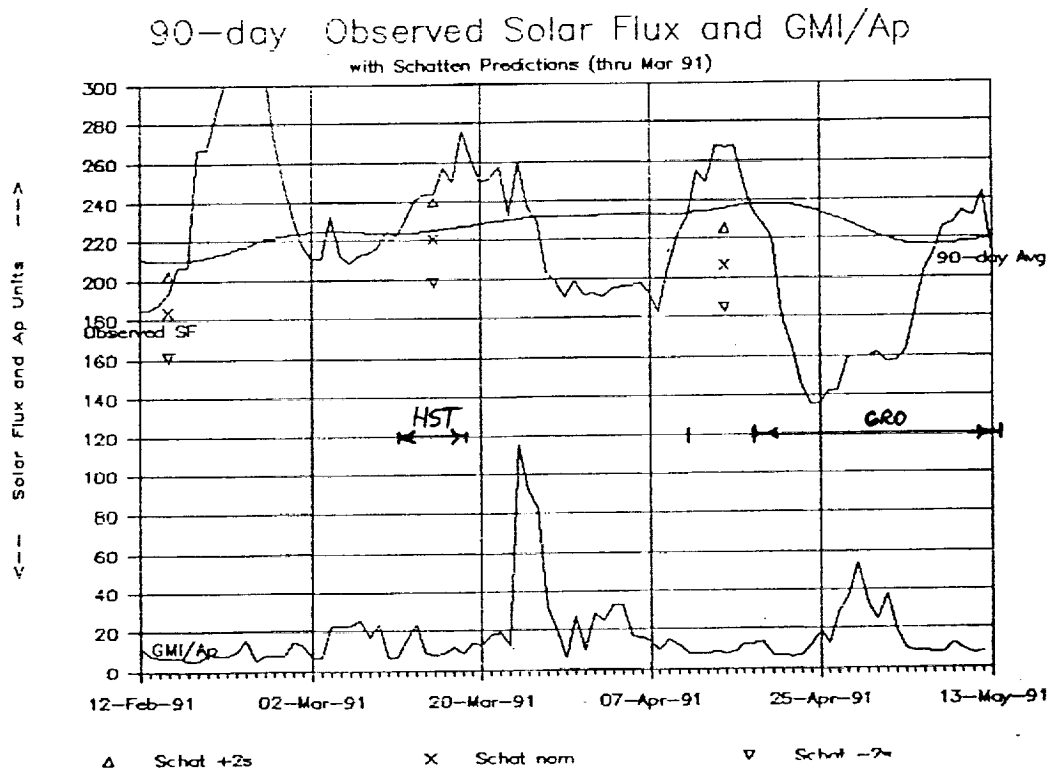


Figure 1.

Table 2 shows the predicted end-of-span Keplerian elements for these three methods, as well as the GTDS solution. The table shows the prediction errors for the three methods, as well; the semi-major axis errors and along-track position errors indicate that Methods #2 and #3 both predicted the spacecraft position more accurately than Method #1.

TABLE 2 -- GRO ORBIT PREDICTION RESULTS

	Epoch Elements:		End-of-Span Elements:		
	GTDS	GTDS	Method #1	Method #2	Method #3
Time	910418.00	910515.21	910515.21	910515.21	910515.21
SMA	6831.8933	6827.6276	6826.7265	6827.2884	6827.6931
ECC	.00202200	.00169399	.00164543	.00169023	.00170903
INC	28.438234	28.298850	28.427451	28.427224	28.427381
LAN	153.22101	319.90855	320.20086	320.24621	320.26151
ARP	84.043841	51.170140	52.747475	50.810026	50.458236
MAN	40.158192	32.337343	43.780799	34.814229	31.085599
Argument of latitude:		83.507483	96.528274	85.624255	81.543835
<u>Prediction Errors:</u>			<u>Method #1</u>	<u>Method #2</u>	<u>Method #3</u>
Semi-major axis [km]:			-.9011	-.3392	+.0655
Eccentricity:			-.00004856	-.00000376	+.00001504
Inclination [deg]:			+.128601	+.128374	+.128531
RA ascend. node [deg]:			+.29231	+.33766	+.35296
Arg. of perigee [deg]:			+1.577335	-.360114	-.711904
Mean anomaly [deg]:			+11.443456	+2.476886	-1.251744
Arg. latitude [deg]:			+13.020791	+2.116772	-1.963648
Along-track position error (approx.) [km]:			+1551.5	+252.2	-234.0

The most notable result is the accuracy to which Method #3 predicted the semi-major axis (to within 70 m over the 4 weeks, as compared to an error of over 700 m for Method #1). The improvement in along-track error is also impressive: Methods #1 & #2 gave errors of only about 250 km, as opposed to 1500 km for Method #1.

4.2 NUMERICAL EXAMPLE: HST DATA

Tracking data for the HST spacecraft were obtained for an approximately one week period spanning 910311.0415 to 910317.2215. Since the spacecraft changed its attitude 36 times during this span, using the orbit-averaged C_d method and the force-coefficient-every-integration-step method was deemed impractical with the software currently available. Instead, the following constant C_dA cases were used for the predictions:

- #1 -- Average C_dA value used operationally: $C_d = 2.47$,
Area = 74 m^2 . Corresponds to $C_dA = 182.78 \text{ m}^2$.
- #2 -- FREEMAC C_dA averaged over all body frame velocity
directions: $C_d = 1.873$, Area = 78.3 m^2 . $C_dA = 146.7 \text{ m}^2$.
- #3 -- Best FREEMAC C_dA estimate. Using the facts that HST
points its solar arrays at the sun and that the sun
vector lies in the orbit plane at this time, the average
 C_dA in method #2 was adjusted upward to account for the
greater area swept out by the solar arrays in this
geometry as compared to the average over all body frame
velocity directions. This readjustment was given by:

$$A_3 = A_2 + A_{S/a} * (2/\pi - 1/2)$$

where $2/\pi$ and $1/2$ are the proportions of the solar array seen on average in an orbit with the orbit normal parallel to the solar array, and on average from all directions, respectively. The resulting calculation gives: Area = 86 m^2 . Using a similar C_d of 1.873 gives $C_dA = 161 \text{ m}^2$. These numbers represent then the best guess C_dA for the given orbit/attitude geometry and the FREEMAC coefficients.

Again, actual tracking data was used in GTDS to obtain the initial elements and the end-of-span elements to which the predicted end-of-span elements were compared. The Harris-Priester density table for a flux level of 225 was again used in the predictions, this level being the one closest to the 90-day average flux of 224 at the beginning of the span (see Figure 1).

Table 3 shows the predicted end-of-span Keplerian elements for the three predictions and the GTDS solution, as well giving the prediction errors for the three cases. The prediction errors indicate that the FREEMAC best-estimate of the average C_dA (Case #3) predicted the semi-major axis surprisingly well (to within about 3m, as compared to about 40m with the standard numbers of Case #1). This makes the lack of improvement in the along-track position somewhat perplexing, since one might suppose the two quantities would be correlated somewhat.

TABLE 3 -- HST ORBIT PREDICTION RESULTS

Epoch Elements:		End-of-Span Elements:			
GTDS	GTDS	Method #1	Method #2	Method #3	
Time	910311.0415	910317.2215			
SMA	6988.7524	6989.0337	6988.9920	6989.0567	6989.0310
ECC	.00064063	.00179858	.00179714	.00179976	.00179872
INC	28.409823	28.272128	28.414024	28.413882	28.413938
LAN	348.53786	305.25818	305.40857	305.40973	305.40927
ARP	3.944306	95.843055	95.999651	95.851540	95.910008
MAN	275.07443	20.102278	20.044183	19.866536	19.937082
Argument					
of latitude:	115.94533	116.04383	115.71807	115.84709	
<u>Prediction Errors:</u>		<u>Method #1</u>	<u>Method #2</u>	<u>Method #3</u>	
Semi-major axis [km]:	-.0417	+.0230	-.0027		
Eccentricity:	-.00000144	+.00000118	+.00000014		
Inclination [deg]:	+.141896	+.141754	+.141810		
RA ascend. node [deg]:	+.15039	+.15155	+.15109		
Arg. of perigee [deg]:	+.156596	+.008485	+.066953		
Mean anomaly [deg]:	-.058095	-.235742	-.165196		
Arg. latitude [deg]:	+.098500	-.227260	-.098240		
Along-track position					
error (approx.) [km]:	+12.0	-27.7	-12.0		

4.3 COMMENT ON RESULTS

Because atmospheric density and the $C_d A$ term are so difficult to distinguish between, the accuracy of the results above is highly dependent on the density over the spans in question. Fortunately, for the runs presented above, the 90-day average solar flux across the spans averaged almost exactly 225 in both cases (see Figure 1), suggesting that the actual densities in these runs may have been close to the table values. This in turn suggests that the improvements in ephemeris accuracy noted above are real, rather than just happy coincidence.

Further experimentation with the FREEMAC coefficients is needed in any case to validate the improvement in ephemeris accuracy. Possibly a large number of runs could be made to statistically reduce the effect of the density variation.

5.0 OTHER POTENTIAL USES OF FREEMAC COEFFICIENTS

In addition to the improvement in the short-term predictions noted above, using FREEMAC-determined average ballistic coefficients (or C_dA values) should greatly improve lifetime studies and long-term decay studies, especially if the target attitudes are known beforehand. Orbit-averaged C_dA s or ballistic coefficients for each attitude could then be determined and used in the propagator. Alternatively, the FREEMAC coefficients obtained by averaging over all wind directions (see Section 3.1) could be used to get more accurate constant C_dA values.

Orbit determination (OD) from tracking measurements could also benefit from FREEMAC-determined coefficients. If GTDS could be modified to accept a varying value for the C_dA term in the drag equation, the effect of C_dA and density variations could be decoupled somewhat, with the effect of the C_dA variation being removed, thus leading to potentially lower residuals and greater orbit determination accuracy. The sinusoidal variation in C_dA cannot be modeled accurately by the fifth order polynomial for ρ_{h1} currently used in GTDS.

GTDS should be modified to accept a Fourier series representation of the varying C_dA , or at least a general sine curve, with the independent variable being the mean or true anomaly. The coefficients for these curves could then be calculated in the same program that calculates the orbit-averaged FREEMAC coefficients (see Section A.3).

The attitude analysis field could use FREEMAC aerodynamic torque coefficients to possible an even greater extent than the orbit field could use the force coefficients. By inserting a subroutine described in the Appendix (Section A.2) into any host program, the user can obtain the FREEMAC torque coefficients for a given body frame wind direction. Used in attitude dynamics simulators, these coefficients would result in more realistic and accurate aerodynamic torques. These coefficients could be used, for example, to predict the effect of aerodynamic torques on the drift rates of spinning spacecraft spin axis attitude. Orbit-averaged torque coefficients (see Appendix A.3) could be used to size control system components, or to determine at what torque levels (and thus altitudes) the control systems will fail.

Another potential application of FREEMAC pertains to spacecraft in higher Earth orbits. Because the FREEMAC shadowing routine is based on a shadow projection technique, the program could be modified to calculate solar radiation pressure coefficients. FREEMAC would then provide coefficients for the largest environmental torques on spacecraft in both the lowest and highest Earth orbits.

6.0 CONCLUSION

New techniques for calculating attitude-dependent aerodynamic coefficients have been described here, along with suggestions for their use in various areas of orbit and attitude analysis. These techniques have been applied to the short-term orbit prediction of the GRO and HST spacecraft in two numerical examples. The use of attitude-dependent drag coefficients resulted in improved ephemeris accuracy, particularly when these coefficients were determined at each orbit integration step. Further work is required to validate the improvements suggested by these results, and to calibrate the FREEMAC-determined coefficients, if necessary.

REFERENCES

- [1] Boring, J.W. and R.R. Humphries, Drag Coefficients for Free Molecular Flow in the Velocity Range 7-37 km/sec, AIAA Journal, Vol.8, No.9, September 1970, pp. 1658-1662.
- [2] Folta, D.C., Hubble Space Telescope (HST) Deployment Altitude and Atmosphere Density Profiles, Memorandum to Flight Dynamics Analysis Branch, January 1990.
- [3] Fredo, F.M., A Numerical Procedure for Calculating the Aerodynamic Coefficients for Complex Spacecraft Configurations in Free-Molecular Flow, Pennsylvania State University, Dept. of Aerospace Engineering, August 1980.
- [4] Herrero, F.A., Satellite Drag Coefficients and Upper Atmosphere Densities: Present Status and Future Directions, AAS Paper 87-551.
- [5] Knechtel, E.D., and W.C. Pitts, Normal and Tangential Momentum Accommodation Coefficients for Earth Satellite Conditions, Astronautica Acta, Vol. 18, pp. 171-184.

APPENDIX

The FREEMAC software referenced in the paper was presented originally in Fredo [1]. Through additions and modifications due to one of the authors (Baker) and others, the capabilities and results of FREEMAC have been enhanced and made more accessible for a variety of mission analysis and operations applications. This appendix summarizes present FREEMAC capabilities, giving some details on recent program enhancements.

A.1 FREEMAC CAPABILITIES

The original FREEMAC software presented in Fredo [1] calculated the aerodynamic force and moment coefficients of a spacecraft modeled on the computer with certain basic geometrical shapes (flat plates, spheres, cylinders, etc.). These basic shapes were subdivided into smaller planar elements, which were checked using a shadow projection technique to determine whether they were exposed to the flow or shielded by other elements. The forces and torques due to each exposed element were summed to obtain those values for the whole spacecraft, and the nondimensional coefficients were calculated by dividing the forces and torques by certain dimensioned quantities, including a reference area and length. Experimentally-determined momentum accommodation coefficients from Knechtel and Pitts [5] were used in determining the force on each exposed element.

The force and moment coefficients were determined in this manner for each direction that the wind could approach the spacecraft, as represented by different wind vector directions in the body frame. The quantities calculated for each wind vector direction were:

C_x, C_y, C_z	-- Aerodynamic force coefficients
M_x, M_y, M_z	-- Aerodynamic moment coefficients
C_d	-- Aerodynamic drag coefficient
A	-- The exposed cross-sectional area of the spacecraft as viewed down the wind vector direction

The program has been modified slightly to output the last quantity, as well as to calculate weighted averages of the above coefficients and areas over all the various wind vector locations. Such an overall average area or C_d could be used, for example, in analyzing the lifetime of spacecraft in low Earth orbit if the wind could be assumed to approach the spacecraft from all directions with roughly equal probability over the course of a mission, as might be the case for an inertially-stabilized satellite changing attitudes fairly regularly.

A.2 USING FREEMAC OUTPUT

In order to access the results of FREEMAC with other computer programs, a coefficient file was output from FREEMAC, and an interpolation subroutine was written to return the FREEMAC-determined coefficients for any given body frame velocity vector direction input to it. In particular, the eight coefficients listed above were calculated and output to the file for velocity vector directions spaced every 10° in body frame right ascension and declination. The output accessing subroutine obtains the coefficient values for any arbitrary velocity direction using a quadratic interpolation scheme using 16 data points from the FREEMAC coefficient file. This subroutine allows quick access to FREEMAC results, and can be inserted into a wide variety of mission analysis and operations programs (see Section 5.0) to improve the modeling of aerodynamic forces and torques.

A.3 ORBIT-AVERAGED COEFFICIENTS DETERMINATION

For inertially stabilized spacecraft, the velocity vector slews through 360° in the body coordinate frame over the course of an orbit, with the value of $C_d A$ changing as it moves. Because of this, it is often necessary to calculate orbit-averaged aerodynamic coefficients. An auxiliary program has been coded that calculates these by stepping through the orbit and averaging the FREEMAC coefficients obtained at each point using the interpolation subroutine mentioned above. Steps of constant true anomaly are used, concentrating the samples at perigee, where the greatest drag occurs. The orbit averaged coefficients are obtained by:

$$C = \frac{\sum_i \rho_i V_i^2 C_i}{\sum_i \rho_i V_i^2} \quad C = C_x, C_y, C_z, M_x, M_y, M_z, C_d$$

Calculating the coefficients in this way accounts for the greater aerodynamic effects at perigee, especially for highly eccentric orbits. Harris-Priester tables are used for the densities.

A.4 VALIDATION OF SPACECRAFT MODEL WITH GRAPHICS PACKAGE

One impediment to the use of FREEMAC in the past has been the difficulty in determining whether or not the geometric model of the spacecraft is correct, due to the somewhat non-user-friendly input format used. This problem has been alleviated somewhat by a new capability allowing the geometric model to be

displayed on with a CAD graphics package. By viewing the model with the CAD package, the user can quickly determine whether the constituent basic shapes are of the right size and are oriented correctly. Figure 2 and 3 show CAD displays of the GRO and HST models used in the numerical examples presented in the report.

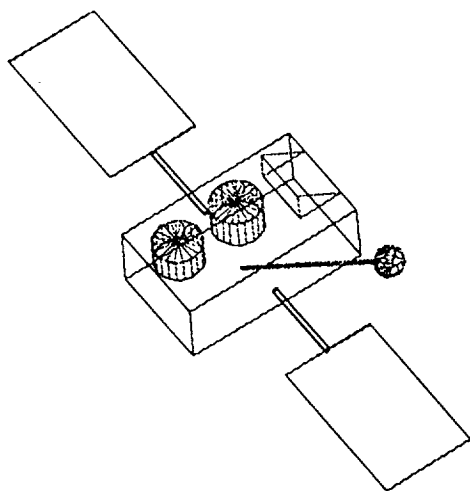


Figure 2.
GRO

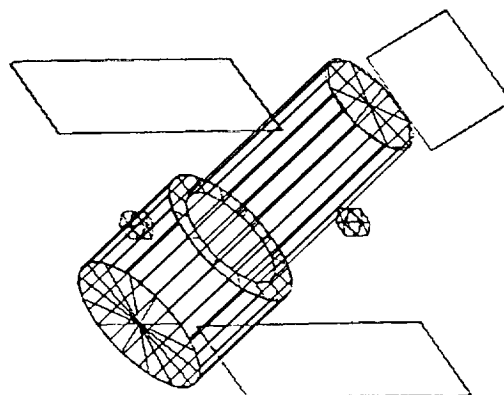


Figure 3.
HST

A.5 VALIDATION OF FREEMAC RESULTS

Another reason for hesitation in using FREEMAC in the past was the concern that the program had not been rigorously tested. Over the past few years, confidence in the program has increased as hand-calculations of such easily-calculable quantities as area has agreed with the program results. Validating the aerodynamic coefficients has been more complicated, however, and has been done only partially by comparing FREEMAC C_d s for HST to those used at Marshall Space Flight Center (MSFC) and at Johns Hopkins' Applied Physics Laboratory (APL). The FREEMAC numbers agree well with the others, as Figure 4 shows for a sample attitude/orbit configuration.

A.6 A CAUTIONARY NOTE REGARDING FREEMAC COEFFICIENTS

It should be noted that FREEMAC cannot account for the drag due to inflow behind shielding elements. This additional drag source is due to the atmospheric particles having an intrinsic velocity due to their thermal motion; this velocity, when added vectorially to the spacecraft's, can particles to flow in behind

shielding elements and hit the spacecraft in a region FREEMAC considers in shadow, causing an additional unmodeled force. Thus, the actual C_d may be somewhat greater than the FREEMAC value; this effect will be greater for long, thin spacecraft and for spacecraft with long shielding appendages.

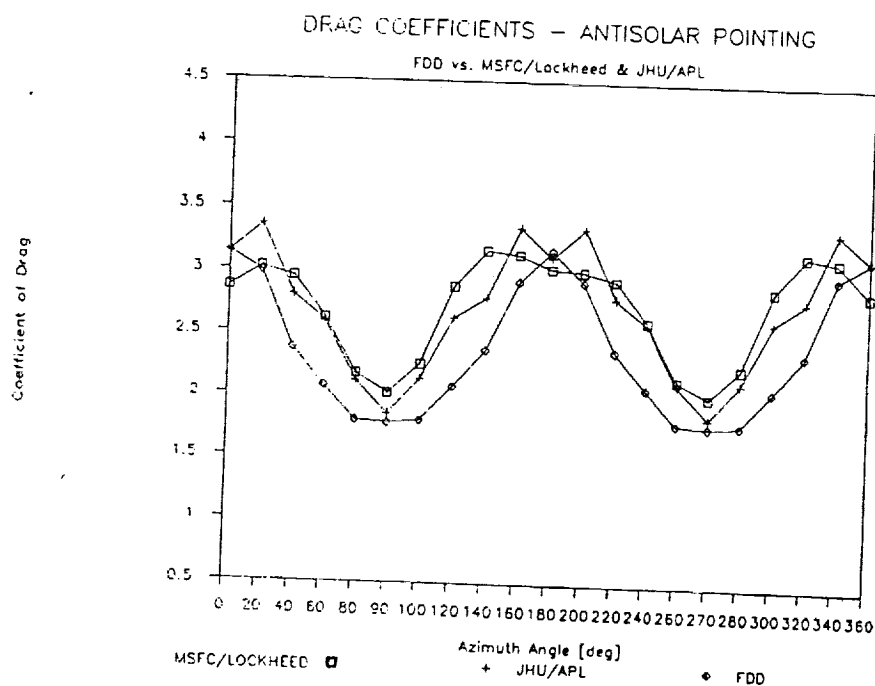


Figure 4.

Elimination Of Secular Terms From The Differential Equations For The Elements of Perturbed Two-Body Motion

Victor R. Bond
and
Michael F. Fraietta

McDonnell Douglas Space Systems Company
Engineering Services Division
Houston, Texas

ABSTRACT

In 1961, Sperling linearized and regularized the differential equations of motion of the two-body problem by changing the independent variable from time to fictitious time by Sundman's transformation ($r = \frac{dt}{ds}$) and by embedding the two-body energy integral and the Laplace vector. In 1968, Burdet developed a perturbation theory which was uniformly valid for all types of orbits using a variation of parameters approach on the elements which appeared in Sperling's equations for the two-body solution. In 1973, Bond and Hanssen improved Burdet's set of differential equations by embedding the total energy (which is a constant when the potential function is explicitly dependent upon time.) The Jacobian constant was used as an element to replace the total energy in a reformulation of the differential equations of motion. In the process, another element which is proportional to a component of the angular momentum was introduced.

Recently trajectories computed during numerical studies of atmospheric entry from circular orbits and low thrust beginning in near-circular orbits exhibited numerical instability when solved by the method of Bond and Gottlieb (1989) for long time intervals. It was found that this instability was due to secular terms which appear on the right-hand sides of the differential equations of some of the elements. In this paper, this instability is removed by the introduction of another vector integral called the delta integral (which replaces the Laplace Vector) and another scalar integral which remove the secular terms. The introduction of these integrals requires a new derivation of the differential equations for most of the elements. For this rederivation, the Lagrange method of variation of parameters is used making the development more concise. Numerical examples of this improvement will be presented.

This work was performed for NASA-JSC Houston, Texas under Contract No. NAS9-17885.

1.0 Summary

In 1961 Sperling linearized and regularized the differential equations of motion of the two-body problem by changing the independent variable from time to fictitious time by Sundman's transformation ($r = \frac{dt}{ds}$) and by embedding the two-body energy integral and the Laplace vector which is also an integral of the motion into the Newtonian form of the differential equations of motion. The solution of Sperling's differential equations was uniformly valid for all types of orbits. In 1968, Burdet developed a perturbation theory using a variation of parameters approach on the 14 elements which appeared in the two-body solution. In 1973, Bond and Hanssen improved Burdet's set of differential equations by using the total energy of the perturbed system as a parameter instead of the two-body energy and by reducing the number of elements to 13. In 1989 Bond and Gottlieb embedded the Jacobian integral, which is a constant when the potential function is explicitly dependent upon time as well as position in the Newtonian equations. The Jacobian constant was used as an element to replace the total energy in a reformulation of the differential equations of motion. In this process, another element which is proportional to a component of the angular momentum is introduced. This brought the total number of elements back to 14. In this paper the Laplace vector is replaced by another vector integral as well as another scalar integral which remove small secular terms which appear in the differential equations for some of the elements.

2.0 Introduction

The non-linear differential equations of motion for the cartesian coordinates of the two-body problem can be regularized and linearized by the three-step procedure of changing the independent variable from time (t) to fictitious time (s) by the application of the Sundman transformation, embedding the Laplace integral and embedding the Jacobian integral.

By regularization we mean the removal of all singularities, and by linearization we mean that the differential equations for the cartesian coordinates are transformed to harmonic oscillators. Previously, regularization and linearization were done by Burdet (1968) by embedding the two-body energy which is constant only for the two-body problem and by Bond and Hanssen (1973) by embedding the total energy which is a constant when the two-body system is perturbed by a conservative potential (function of position only). In Bond and Gottlieb (1989), the Jacobian integral, which is a constant for the case of the two-body system perturbed by a potential function that is explicitly dependent on time as well as position, was embedded in the Newtonian equations. All three of these approaches reduce to the same system of equations in the absence of perturbations.

Recent numerical studies on atmospheric entry from near circular orbits and on low thrust in near circular orbits exhibit numerical instability when solved by the method of Bond and Gottlieb (1989) for long time intervals. These two cases are similar since both have persistent, tangential, non-conservative perturbations. It was found that this instability was due to secular terms which appear on the right hand sides of the differential equations of some of the elements. In this paper this instability is removed by the introduction of another vector integral of the motion and another scalar integral which remove the secular terms. The introduction of these integrals which were included by Burdet (1968) require a new derivation of the differential equations for most of the elements. For this rederivation the Lagrange method of variation of parameters is used making the development more concise.

2.1 The Differential Equations of Motion in the Fictitious Time

The differential equation for perturbed two-body motion is

$$\ddot{\underline{r}} + \frac{\mu}{r^3} \underline{r} = \underline{F} \quad (2.1)$$

where \underline{r} is the position vector of one of the masses with respect to the other in cartesian coordinates and r is the magnitude of \underline{r} and $(\dot{}) = \frac{d()}{dt}$. Also the gravitational constant is

$$\mu = G(M + m) \quad (2.2)$$

where G is the universal gravitational constant and M and m are the masses of the two bodies. The quantity \underline{F} is the perturbation which can be expressed by,

$$\underline{F} = \underline{P} - \frac{\partial}{\partial \underline{r}} V(\underline{r}, t) \quad (2.3)$$

where $V(\underline{r}, t)$ is the potential due to perturbing masses and \underline{P} is any perturbative acceleration which is not derived from a potential.

Equation (2.1) can be linearized (except for the perturbation) in three steps:

STEP (1) Change the independent variable from time (t) to fictitious time (s) according to the transformation

$$\frac{dt}{ds} = r \quad (2.4)$$

The derivatives of \underline{r} with respect to t become

$$\dot{\underline{r}} = \underline{r}' / r \quad (2.5)$$

where $(\)' = \frac{d(\)}{ds}$, and

$$\ddot{\underline{r}} = \underline{r}'' / r^2 - \underline{r}' r' / r^3 \quad (2.6)$$

where

$$\underline{r}' = \underline{r} \cdot \underline{r}' / r \quad (2.7)$$

STEP (2) Embed the integral called the Laplace vector (a constant when $\underline{F}=0$)

$$\underline{\varepsilon} = \frac{1}{\mu} \left[\left(\dot{\underline{r}} \cdot \dot{\underline{r}} \right) \underline{r} - \left(\underline{r} \cdot \underline{r} \right) \dot{\underline{r}} \right] - \underline{r}/r \quad (2.8)$$

which becomes

$$\underline{\varepsilon} = \frac{1}{\mu r^2} \left[\left(\underline{r}' \cdot \underline{r}' \right) \underline{r} - \left(\underline{r}' \cdot \underline{r} \right) \underline{r}' \right] - \underline{r}/r \quad (2.9)$$

when the new independent variable s is used.

STEP (3) Embed the energy integral (a constant when $\underline{F}=0$)

$$\alpha_k = \frac{2\mu}{r} - \dot{\underline{r}} \cdot \dot{\underline{r}} \quad (2.10)$$

which becomes

$$\alpha_k = \frac{2\mu}{r} - \frac{1}{r^2} \underline{r}' \cdot \underline{r}' \quad (2.11)$$

when the new independent variable is used. Note that

$$\alpha_k = -2 h_k \quad (2.12)$$

where h_k is the two-body or Keplerian energy. Using these three steps in order, equation (2.1) becomes

$$\underline{r}'' + \alpha_k \underline{r} = -\mu \underline{\varepsilon} + r^2 \underline{F} \quad (2.13)$$

which is the differential equation for the position vector \underline{r} . By taking the dot product of equation (2.13) with the position vector \underline{r} we obtain

$$r'' + \alpha_k r = \mu + r \underline{\varepsilon} \cdot \underline{F} \quad (2.14)$$

which is the differential equation for the distance r . We now change from the energy integral α_k to

the Jacobian integral α_J (Bond and Gottlieb (1989)) which is given by

$$\alpha_J = \alpha_k + 2\sigma - 2V(\underline{r}, t) \quad (2.15)$$

where σ is called the axial element and is defined by

$$\sigma = \underline{\omega} \cdot (\underline{r} \times \dot{\underline{r}}) \quad (2.16)$$

The vector $\underline{\omega}$ is the constant rotational rate of the central attracting body or orbital rate of a third body giving rise to the perturbing potential $V(\underline{r}, t)$. In Section 4.0 it will be shown that $\alpha_J = \text{constant}$ when $|\underline{P}| = 0$ and that $\sigma = \text{constant}$ when $|\underline{\omega}| = 0$. Solving equation (2.15) for α_k and substituting into equations (2.13) and (2.14) we obtain

$$\underline{r}'' + \alpha_J \underline{r} = -\mu \underline{e} + r^2 \underline{F} + 2(\sigma - V(\underline{r}, t))\underline{r} = -\mu \underline{e} + \underline{Q} \quad (2.17)$$

and

$$\underline{r}'' + \alpha_J \underline{r} = \mu + r \underline{r} \cdot \underline{F} + 2(\sigma - V(\underline{r}, t))\underline{r} = \mu + \frac{1}{r} \underline{Q} \cdot \underline{r} \quad (2.18)$$

Note that all of the perturbation terms have been moved to the right side in equation (2.17) and (2.18).

Equation (2.17) and (2.18) are coupled only through the perturbation terms. We will refer to equation (2.17) as the spatial differential equation since its solution provides position and velocity. We will refer to equation (2.18) along with equation (2.4) as the temporal differential equations since their solutions provide time. Note that when there are no perturbations (that is $|\underline{F}| = 0$ and $|\underline{\omega}| = 0$) then we have the two-body differential equations

$$\underline{r}'' + \alpha_J \underline{r} = -\mu \underline{e} \quad (2.19)$$

and

$$r'' + \alpha_J r = \mu \quad (2.20)$$

and the Jacobi constant and Keplerian energy become the same

$$\alpha_J = \alpha_k$$

3.0 Two Body Solution

The differential equation of motion for the two-body problem in the fictitious time was shown in the previous section to be

$$\underline{r}'' + \alpha_J \underline{r} = -\mu \underline{e} \quad (3.1)$$

The solution of (3.1) in terms of the Stumpff functions of Appendix B is

$$\underline{r} = \underline{r}_o c_o + \underline{r}_o' s c_1 - \mu \underline{e} s^2 c_2 \quad (3.2)$$

where \underline{r}_o and \underline{r}_o' are the initial values of \underline{r} and \underline{r}' , and the Stumpff functions are $c_i = c_i(\alpha_J s^2)$. This can be verified by direct substitution of (3.2) into (3.1) and using the derivatives of the Stumpff functions

$$\begin{aligned} c_o' &= -\alpha_J s c_1 \\ s c_1' + c_1 &= c_o \\ s c_2' + 2c_2 &= c_1 \end{aligned} \quad (3.3)$$

The first derivative of (3.2) which is the "velocity" in the fictitious time is

$$\underline{r}' = -(\alpha_J \underline{r}_o + \mu \underline{e}) s c_1 + \underline{r}_o' c_o \quad (3.4)$$

In place of $\mu \underline{e}$ which is a constant of the motion we define the constant "delta vector"

$$\underline{\delta} = -\alpha_J \underline{r}_o - \mu \underline{e} \quad (3.5)$$

Now using the Stumpff function identity

$$c_o + \alpha_J s^2 c_2 = 1 \quad (3.6)$$

and equation (3.5) and (3.2) we obtain

$$\underline{r} = \underline{r}_o + \underline{r}_o' s c_1 + \underline{\delta} s^2 c_2 \quad (3.7)$$

similarly equation (3.4) becomes

$$\underline{r}' = \underline{r}_o' c_o + \underline{\delta} s c_1 \quad (3.8)$$

The differential equation of motion for the distance r was shown in the previous section to be

$$r'' + \alpha_J r = \mu \quad (3.9)$$

The solution of equation (3.9) is similar to that for (3.1). In terms of Stumpff functions the distance is

$$r = r_o c_o + r_o' s c_1 + \mu s^2 c_2 \quad (3.10)$$

and its derivative is

$$r' = (\mu - r_o \alpha_J) s c_1 + r_o' c_o \quad (3.11)$$

Now define the constant

$$\gamma = \mu - r_o \alpha_J \quad (3.12)$$

which we substitute for μ in equation (3.10) along with the identity of equation (3.6) to obtain

$$r = r_o + r_o' s c_1 + \gamma s^2 c_2 \quad (3.13)$$

Similarly equation (3.1) becomes

$$r' = r_o' c_o + \gamma s c_1 \quad (3.14)$$

Now substitute equation (3.13) for r in the independent variable transformation, equation (2.4), to obtain

$$dt = r_o ds + r_o' s c_1 ds + \gamma s^2 c_2 ds \quad (3.15)$$

Now use the integration formula

$$\int s^m c_m ds = s^{m+1} c_{m+1}$$

which is from Appendix B to obtain the equation for time (Kepler's equation),

$$t = t_o + r_o s + r_o' s^2 c_2 + \gamma s^3 c_3 \quad (3.16)$$

where t_o is the initial time.

The integration constants which were introduced in this section are \underline{r}_o , \underline{r}_o' , r_o , r_o' , t_o . The new constant $\underline{\delta}$ simply replaces the Laplace vector which is a constant of two-body motion through the definition (3.5). Similarly we note that the constant γ replaces the gravitational constant (equation (3.12)). The introduction of the constants $\underline{\delta}$ and γ was done by Burdet (1968). This fact was noted by Bond and Hanssen (1973). The Jacobian element α_J is the same as the two-body energy parameter α_k in the unperturbed case is also a constant of the motion. In addition we have the axial element σ which is also a constant of the motion (see equation 2.16). This is a total of 15 constants of the motion.

The constants \underline{r}_o , \underline{r}_o' and $\underline{\delta}$ will be treated as orbital elements associated with the spatial differential equation (2.17) and r_o , r_o' , γ , t_o will be treated as orbital elements associated with the temporal differential equations (2.4) and (2.18).

4.0 The Differential Equations For The Elements

When perturbations are present the elements are no longer constant. First we derive the differential equation for the axial element σ . Differentiate equation (2.16) with respect to time and substitute equation (2.1) and (2.3) to obtain

$$\dot{\sigma} = \underline{\omega} \cdot (\underline{r} \times \underline{\dot{r}}) = \underline{\omega} \cdot \underline{r} \times \underline{F} = \underline{\omega} \cdot \underline{r} \times \left[\underline{P} - \frac{\partial}{\partial \underline{r}} V(\underline{r}, t) \right] \quad (4.1)$$

now use equation (2.4) to change to fictitious time

$$\sigma' = r \underline{\omega} \cdot \underline{r} \times \left[\underline{P} - \frac{\partial}{\partial \underline{r}} V(\underline{r}, t) \right] \quad (4.2)$$

Clearly $\sigma = \text{constant}$ when $|\underline{\omega}| = 0$. Now we derive the differential equation for the Jacobian element α_J . Differentiate equation (2.15) with respect to time to obtain

$$\dot{\alpha}_J = \dot{\alpha}_k + 2\dot{\sigma} - 2 \left[\frac{\partial}{\partial t} V(\underline{r}, t) + \underline{\dot{r}} \cdot \frac{\partial}{\partial \underline{r}} V(\underline{r}, t) \right]$$

From equations (2.10) and (2.1)

$$\dot{\alpha}_k = -2\underline{\dot{r}} \cdot \left[\underline{P} - \frac{\partial}{\partial \underline{r}} V(\underline{r}, t) \right]$$

and from Bond and Mulcihy (1988) also Bond and Gottlieb (1989)

$$\frac{\partial}{\partial t} V(\underline{r}, t) = -\underline{\omega} \cdot \underline{r} \times \frac{\partial}{\partial \underline{r}} V(\underline{r}, t)$$

and from equation (4.1) the expression for $\dot{\alpha}_J$ becomes

$$\dot{\alpha}_J = 2(-\underline{\dot{r}} + \underline{\omega} \times \underline{r}) \cdot \underline{P} \quad (4.3)$$

Now use equation (2.4) to change to fictitious time

$$\alpha_J' = 2(-\underline{r}' + r \underline{\omega} \times \underline{r}) \cdot \underline{P} \quad (4.4)$$

Note that $\alpha_J = \text{constant}$ when $|\underline{P}| = 0$. The Jacobian constant α_J will be treated as an orbital element for both the spatial and temporal equations since α_J appears in the two-body equations (2.19) and (2.20). Even though we have already obtained the differential equation for α_J (equation (4.4)) we must include it in the variation of parameters procedures of the spatial and temporal equations. The axial element σ appears only as a perturbation in equations (2.17) and (2.18). We have also obtained the differential equation for σ (equation (4.2)). We will include σ in the variation of parameters procedure for convenience and completeness.

Even though the Laplace vector will be eliminated as an element we will need the derivative of the Laplace vector as a perturbation. This derivative as found by differentiating equation (2.8) will respect to time, then using equation (2.1) to eliminate $\underline{\dot{r}}$, and finally using equation (2.4) to obtain

$$\underline{\mu \dot{E}} = 2(\underline{r}' \cdot \underline{F})\underline{r} - (\underline{r} \cdot \underline{F})\underline{r}' - (\underline{r} \cdot \underline{r}')\underline{F} \quad (4.4a)$$

4.1 Spatial Elements

Now we apply the variation of parameters method of Lagrange to equations (2.17), (4.2) and (4.4). Define

$$\begin{aligned} \underline{x}_1 &= \underline{r} \\ \underline{x}_2 &= \underline{r}' \\ \underline{x}_3 &= -\alpha_J \underline{r} - \underline{\mu E} = -x_5 \underline{x}_1 - \underline{\mu E} \end{aligned} \quad (4.5)$$

$$x_4 = \sigma$$

$$x_5 = \alpha_j$$

Now differentiate equations (4.5) and use (2.17), (4.2) and (4.4) to obtain

$$\begin{aligned}\dot{x}_1 &= x_2 \\ \dot{x}_2 &= x_3 + \underline{Q} = x_3 + \underline{G}_2 \\ \dot{x}_3 &= -x_5 x_2 - (\alpha_j \underline{r} + \mu \underline{\epsilon}) = -x_5 x_2 + \underline{G}_3 \\ \dot{x}_4 &= \sigma' = G_4 \\ \dot{x}_5 &= \alpha_j' = G_5\end{aligned}\tag{4.6}$$

Where $\underline{G}_1 = 0$. Equations (4.6) can be separated into unperturbed (i.e., two-body or Keplerian) and perturbed parts, that is into the form of $\dot{x} = \underline{F} + \underline{G}$, making them suitable for Lagrange's variation of parameters method as given by Appendix A. In this form equation (4.6) becomes

$$\begin{bmatrix} \dot{x}_1 \\ \dot{x}_2 \\ \dot{x}_3 \\ \dot{x}_4 \\ \dot{x}_5 \end{bmatrix} = \begin{bmatrix} x_2 \\ x_3 \\ -x_5 x_2 \\ 0 \\ 0 \end{bmatrix} + \begin{bmatrix} \underline{G}_1 \\ \underline{G}_2 \\ \underline{G}_3 \\ G_4 \\ G_5 \end{bmatrix}\tag{4.7}$$

where $\underline{G}_1, \underline{G}_2, \underline{G}_3, G_4, G_5$ are defined from equations (4.6). The array of constants, which will become the new dependent variables, is defined as

$$\underline{c}^T = (\underline{\alpha}^T, \underline{\beta}^T, \underline{\delta}^T, \sigma, \alpha_j)\tag{4.8}$$

where

$$\begin{aligned}\underline{\alpha} &= \underline{r}_\phi = x_1(0) \\ \underline{\beta} &= \underline{r}'_\phi = x_2(0) \\ \underline{\delta} &= -\alpha_j \underline{\alpha} - \mu \underline{\epsilon} = x_3(0)\end{aligned}\tag{4.9}$$

and of course σ and α_j which have already been established as constants of the motion. The differential equation for \underline{c} , has the form, $\frac{\partial x}{\partial \underline{c}} \dot{\underline{c}} = \underline{G}$ where

$$\frac{\partial x}{\partial \underline{c}} = \begin{bmatrix} \frac{\partial x_1}{\partial \underline{\alpha}} & \frac{\partial x_1}{\partial \underline{\beta}} & \frac{\partial x_1}{\partial \underline{\delta}} & \frac{\partial x_1}{\partial \sigma} & \frac{\partial x_1}{\partial \alpha_j} \\ \frac{\partial x_2}{\partial \underline{\alpha}} & \frac{\partial x_2}{\partial \underline{\beta}} & \frac{\partial x_2}{\partial \underline{\delta}} & \frac{\partial x_2}{\partial \sigma} & \frac{\partial x_2}{\partial \alpha_j} \\ \frac{\partial x_3}{\partial \underline{\alpha}} & \frac{\partial x_3}{\partial \underline{\beta}} & \frac{\partial x_3}{\partial \underline{\delta}} & \frac{\partial x_3}{\partial \sigma} & \frac{\partial x_3}{\partial \alpha_j} \\ \frac{\partial x_4}{\partial \underline{\alpha}} & \frac{\partial x_4}{\partial \underline{\beta}} & \frac{\partial x_4}{\partial \underline{\delta}} & \frac{\partial x_4}{\partial \sigma} & \frac{\partial x_4}{\partial \alpha_j} \\ \frac{\partial x_5}{\partial \underline{\alpha}} & \frac{\partial x_5}{\partial \underline{\beta}} & \frac{\partial x_5}{\partial \underline{\delta}} & \frac{\partial x_5}{\partial \sigma} & \frac{\partial x_5}{\partial \alpha_j} \end{bmatrix}\tag{4.10}$$

Noting from Section (3.0) that

$$\begin{aligned}x_1 &= \underline{r} = \underline{\alpha} + \underline{\beta} s c_1 + \underline{\delta} s^2 c_2 \\ x_2 &= \underline{r}' = \underline{\beta} c_0 + \underline{\delta} s c_1\end{aligned}\tag{4.11}$$

and from equation (3.5), (4.5) and (4.9)

$$\underline{x}_3 = \alpha_J(\underline{\alpha} - \underline{r}) + \underline{\delta}$$

also

$$\begin{aligned} x_4 &= \sigma \\ x_5 &= \alpha_J \end{aligned} \quad (4.12)$$

The differential equations become

$$\begin{bmatrix} I & Isc_1 & Is^2c_2 & 0 & \frac{\partial r}{\partial \alpha_J} \\ [0] & Ic_o & Isc_1 & 0 & \frac{\partial r'}{\partial \alpha_J} \\ [0] & -I\alpha_J sc_1 & Ic_o & 0 & \frac{\partial x_3}{\partial \alpha_J} \\ \underline{0}^T & \underline{0}^T & \underline{0}^T & 1 & 0 \\ \underline{0}^T & \underline{0}^T & \underline{0}^T & 0 & 1 \end{bmatrix} \begin{bmatrix} \underline{\alpha}' \\ \underline{\beta}' \\ \underline{\delta}' \\ \underline{\sigma}' \\ \alpha_J' \end{bmatrix} = \begin{bmatrix} \underline{G}_1 \\ \underline{G}_2 \\ \underline{G}_3 \\ G_4 \\ G_5 \end{bmatrix} \quad (4.13)$$

where we have used the identity from Appendix B

$$c_o = 1 - \alpha_J s^2 c_2$$

also, I is the 3 by 3 identity matrix; $[0]$ is the 3 by 3 null matrix; $\underline{0}$ is a column vector with 3 components; $\underline{0}^T$ is a row vector with 3 components. Equation (4.13) yields the equations

$$\begin{aligned} \underline{\alpha}' + \underline{\beta}' sc_1 + \underline{\delta}' s^2 c_2 + \alpha_J' \frac{\partial r}{\partial \alpha_J} &= 0 \\ \underline{\beta}' c_o + \underline{\delta}' sc_1 + \alpha_J' \frac{\partial r'}{\partial \alpha_J} &= \underline{Q} \\ -\underline{\beta}' \alpha_J sc_1 + \underline{\delta}' c_o + \alpha_J' \frac{\partial x_3}{\partial \alpha_J} &= -\alpha_J' \underline{r} - \mu \underline{\varepsilon}' \\ \underline{\sigma}' &= r \underline{\omega} \cdot \underline{r} \times \underline{F} \\ \alpha_J' &= 2(-\underline{r}' + r \underline{\omega} \times \underline{r}) \cdot \underline{P} \end{aligned} \quad (4.14)$$

where we have restored the original notations for $\underline{G}_1, \underline{G}_2, \underline{G}_3, G_4, G_5$. Now using the partial derivatives,

$$\begin{aligned} \frac{\partial r}{\partial \alpha_J} &= \underline{\beta}' s \frac{\partial c_1}{\partial \alpha_J} + \underline{\delta}' s^2 \frac{\partial c_2}{\partial \alpha_J} \\ \frac{\partial r'}{\partial \alpha_J} &= \underline{\beta}' \frac{\partial c_o}{\partial \alpha_J} + \underline{\delta}' s \frac{\partial c_1}{\partial \alpha_J} \\ \frac{\partial x_3}{\partial \alpha_J} &= \underline{\alpha} - \underline{r} - \alpha_J \frac{\partial r}{\partial \alpha_J} \end{aligned} \quad (4.15)$$

where the Stumpff function derivatives are

$$\begin{aligned} \frac{\partial c_o}{\partial \alpha_J} &= -\frac{1}{2} s^2 c_1 \\ \frac{\partial c_k}{\partial \alpha_J} &= \frac{1}{2\alpha_J} (c_{k-1} - k c_k), \quad k \geq 1 \end{aligned} \quad (4.15a)$$

and other Stumpff function identities from Appendix B equation (4.14) can be solved simultaneously, omitting several algebraic steps to give

$$\begin{aligned}
\underline{\alpha}' &= -\underline{Q}sc_1 - \underline{\mu}\underline{\epsilon}'s^2c_2 - \alpha_j' \left[\underline{\alpha}s^2c_2 + 2\underline{\beta}s^3\tilde{c}_3 + \frac{1}{2}\underline{\delta}s^4c_2^2 \right] \\
\underline{\beta}' &= \underline{Q}c_o + \underline{\mu}\underline{\epsilon}'sc_1 + \alpha_j' \left[\underline{\alpha}sc_1 + \underline{\beta}s^2\tilde{c}_2 - \underline{\delta}s^3(2\tilde{c}_3 - c_1c_2) \right] \\
\underline{\delta}' &= \underline{Q}\alpha_jsc_1 - \underline{\mu}\underline{\epsilon}'c_o + \alpha_j' \left[-\underline{\alpha}c_o + 2\alpha_j\underline{\beta}s^3\tilde{c}_3 + \frac{1}{2}\underline{\delta}\alpha_js^4c_2^2 \right] \\
\underline{\sigma}' &= r\underline{\omega} \cdot \underline{r} \times \underline{F} \\
\underline{\alpha}_j' &= 2(-\underline{r}' + r\underline{\omega} \times \underline{r}) \cdot \underline{P}
\end{aligned} \tag{4.16}$$

where $\tilde{c}_1 = c_1(4\alpha_js^2)$ as discussed in Appendix B. In the reference Bond and Gottlieb (1989) the coefficient of the factor $\alpha_j'\underline{\alpha}$ in the differential equation for $\underline{\beta}$ had a secular term. This term does not appear in equation (4.16). Note that the Laplace vector ($\underline{\mu}\underline{\epsilon}$) has been entirely removed from the formulation. The derivative of the Laplace vector ($\underline{\mu}\underline{\epsilon}'$) remains but only as an abbreviation for the perturbations given in equation (4.4a).

4.2 Temporal Elements

Now we apply Lagrange's variation of parameters method to equations (2.18), (2.4) and (4.4). Define

$$\begin{aligned}
y_1 &= r \\
y_2 &= r' \\
y_3 &= \mu - \alpha_j r \\
y_4 &= t \\
y_5 &= \alpha_j
\end{aligned} \tag{4.17}$$

Note that α_j is the only element which is common to both the spatial and temporal systems. Now differentiate equations (4.17) equation (2.18), (2.4), and (4.4) become

$$\begin{aligned}
y_1' &= y_2 \\
y_2' &= y_3 + \frac{1}{r}\underline{Q} \cdot \underline{r} = y_3 + g_2 \\
y_3' &= -y_5y_2 - \alpha_j'r = -y_5y_2 + g_3 \\
y_4' &= y_1 \\
y_5' &= \alpha_j' = g_5
\end{aligned} \tag{4.18}$$

Where $g_1 = 0$ and $g_4 = 0$. Equation (4.18) can also be expressed in the form $y' = f + g$

$$\begin{pmatrix} y_1' \\ y_2' \\ y_3' \\ y_4' \\ y_5' \end{pmatrix} = \begin{pmatrix} y_2 \\ y_3 \\ -y_5y_2 \\ y_1 \\ 0 \end{pmatrix} + \begin{pmatrix} g_1 \\ g_2 \\ g_3 \\ g_4 \\ g_5 \end{pmatrix} \tag{4.19}$$

where g_1, g_2, g_3, g_4, g_5 are defined by equation (4.18). The array of constants which will become the new dependent variables are

$$\underline{\kappa}^T = (a, b, \gamma, \tau, \alpha_j) \tag{4.20}$$

where

$$a = r_o = y_1(0)$$

$$b = r_o' = y_2(0) \quad (4.21)$$

$$\gamma = \mu - \alpha_J a = y_3(0)$$

$$\tau = t_o = y_4(0)$$

and α_J has already been established as a constant of the motion.

The differential equations for $\underline{\kappa}$ (having the form $\frac{\partial y}{\partial \underline{\kappa}} \underline{\kappa}' = g$) becomes

$$\begin{bmatrix} \frac{\partial y_1}{\partial a} & \frac{\partial y_1}{\partial b} & \frac{\partial y_1}{\partial \gamma} & \frac{\partial y_1}{\partial \tau} & \frac{\partial y_1}{\partial \alpha_J} \\ \frac{\partial y_2}{\partial a} & \frac{\partial y_2}{\partial b} & \frac{\partial y_2}{\partial \gamma} & \frac{\partial y_2}{\partial \tau} & \frac{\partial y_2}{\partial \alpha_J} \\ \frac{\partial y_3}{\partial a} & \frac{\partial y_3}{\partial b} & \frac{\partial y_3}{\partial \gamma} & \frac{\partial y_3}{\partial \tau} & \frac{\partial y_3}{\partial \alpha_J} \\ \frac{\partial y_4}{\partial a} & \frac{\partial y_4}{\partial b} & \frac{\partial y_4}{\partial \gamma} & \frac{\partial y_4}{\partial \tau} & \frac{\partial y_4}{\partial \alpha_J} \\ \frac{\partial y_5}{\partial a} & \frac{\partial y_5}{\partial b} & \frac{\partial y_5}{\partial \gamma} & \frac{\partial y_5}{\partial \tau} & \frac{\partial y_5}{\partial \alpha_J} \end{bmatrix} \begin{bmatrix} a' \\ b' \\ \gamma' \\ \tau' \\ \alpha_J' \end{bmatrix} = \begin{bmatrix} g_1 \\ g_2 \\ g_3 \\ g_4 \\ g_5 \end{bmatrix} \quad (4.22)$$

but from equations (3.12), (3.13), (3.14), (3.15) and (4.21)

$$\begin{aligned} y_1 &= r = a + bsc_1 + \gamma s^2 c_2 \\ y_2 &= r' = bc_o + \gamma sc_1 \\ y_3 &= \mu - \alpha_J r = \gamma + \alpha_J a - \alpha_J r = \gamma + \alpha_J (a - r) \\ y_4 &= t = \tau + as + bs^2 c_2 + \gamma s^3 c_3 \\ y_5 &= \alpha_J \end{aligned} \quad (4.23)$$

So we can evaluate the matrix elements in (4.22) to obtain

$$\begin{bmatrix} 1 & sc_1 & s^2 c_2 & 0 & \frac{\partial r}{\partial \alpha_J} \\ 0 & c_o & sc_1 & 0 & \frac{\partial r'}{\partial \alpha_J} \\ 0 & -\alpha_J sc_1 & c_o & 0 & \frac{\partial y_3}{\partial \alpha_J} \\ s & s^2 c_2 & s^3 c_3 & 1 & \frac{\partial t}{\partial \alpha_J} \\ 0 & 0 & 0 & 0 & 1 \end{bmatrix} \begin{bmatrix} a' \\ b' \\ \gamma' \\ \tau' \\ \alpha_J' \end{bmatrix} = \begin{bmatrix} g_1 \\ g_2 \\ g_3 \\ g_4 \\ g_5 \end{bmatrix} \quad (4.24)$$

Equation (4.24) when expanded yields,

$$\begin{aligned} a' + b' sc_1 + \gamma' s^2 c_2 + \alpha_J' \frac{\partial r}{\partial \alpha_J} &= 0 \\ b' c_o + \gamma' sc_1 + \alpha_J' \frac{\partial r'}{\partial \alpha_J} &= \frac{1}{r} \underline{Q} \cdot \underline{r} \\ -b' \alpha_J sc_1 + \gamma' c_o + \alpha_J' \frac{\partial y_3}{\partial \alpha_J} &= -r \alpha_J' \end{aligned} \quad (4.25)$$

$$a's + b's^2c_2 + \gamma s^3c_3 + \tau' + \alpha_j' \frac{\partial t}{\partial \alpha_j} = 0$$

$$\alpha_j' = 2(-\underline{r}' + r \underline{\omega} \times \underline{r}) \cdot \underline{P}$$

Where we have restored the original notations for g_2 , g_3 and g_5 . We evaluate the partial derivatives in equations (4.25) using equations (4.23)

$$\begin{aligned} \frac{\partial r}{\partial \alpha_j} &= bs \frac{\partial c_1}{\partial \alpha_j} + \gamma s^2 \frac{\partial c_2}{\partial \alpha_j} \\ \frac{\partial r'}{\partial \alpha_j} &= b \frac{\partial c_0}{\partial \alpha_j} + \gamma s \frac{\partial c_1}{\partial \alpha_j} \\ \frac{\partial y_3}{\partial \alpha_j} &= a - r - \alpha_j \frac{\partial r}{\partial \alpha_j} \\ \frac{\partial t}{\partial \alpha_j} &= bs^2 \frac{\partial c_2}{\partial \alpha_j} + \gamma s^3 \frac{\partial c_3}{\partial \alpha_j} \end{aligned} \quad (4.26)$$

where the Stumpff function derivatives are given by equations (4.15a). Equations (4.25) can be solved simultaneously for the derivatives,

$$\begin{aligned} a' &= -\frac{1}{r} \underline{r} \cdot \underline{Q} s c_1 - \alpha_j' \left[as^2c_2 + 2bs^3c_3 + \frac{1}{2} \gamma s^4 c_2^2 \right] \\ b' &= \frac{1}{r} \underline{r} \cdot \underline{Q} c_0 + \alpha_j' \left[asc_1 + bs^2c_2 - \gamma s^3(2c_3 - c_1c_2) \right] \\ \gamma' &= \frac{1}{r} \underline{r} \cdot \underline{Q} \alpha_j s c_1 + \alpha_j' \left[-ac_0 + 2b\alpha_j s^3c_3 + \frac{1}{2} \gamma \alpha_j s^4 c_2^2 \right] \\ \tau' &= \frac{1}{r} \underline{r} \cdot \underline{Q} s^2c_2 + \alpha_j' \left[as^3c_3 + \frac{1}{2} bs^4 c_2^2 - 2\gamma s^5(c_3 - 4c_5) \right] \end{aligned} \quad (4.27)$$

As in the development of equations (4.16) the Stumpff function identities of Appendix B have been used. In the reference Bond and Gottlieb (1989) the coefficient of the factor $\alpha_j a$ in the differential equation for b had a secular term. This term does not appear in equation (4.27).

It is useful to note that

$$\mu = \gamma + \alpha_j a \quad (4.28)$$

is an integral of the system of equations (4.27). From equations (4.27) it is easy to show that

$$\gamma' + a' \alpha_j + a \alpha_j' = 0 \quad (4.29)$$

which can be integrated to give

$$\gamma + a \alpha_j = \text{constant} \quad (4.30)$$

By comparison of equation (4.30) to equation (4.21) the constant of integration is the gravitational constant μ . Therefore it is not necessary to compute γ from its differential equation. We can compute γ from equation (4.28),

$$\gamma = \mu - \alpha_j a \quad (4.31)$$

5.0 Minimization Of Perturbations

The variation of parameters approach is not dependent on the magnitude of the perturbation. No assumption on the size of the perturbation is required in order that the method be rigorous. However,

small perturbations enhance the efficiency, speed, and accuracy of any perturbation method. In the method described in this paper, the embedding of the Jacobi integral has the effect of introducing a perturbation parameter ω that is the rotational speed of the planet, or the mean motion of the perturbing third body. To prevent this perturbation from becoming too large the following modification is offered:

Let,

$$\sigma = \sigma_o + \Delta\sigma \quad (5.1)$$

where σ_o is the initial value of σ and $\Delta\sigma$ is the change in σ . In effect we can let $\Delta\sigma$ replace σ so that the differential equations reflect only changes in σ . Substitute equation (5.1) into equation (2.17) to obtain

$$\underline{r}'' + \alpha_J \underline{r} = -\mu \underline{e} + r^2 \underline{F} + 2(\sigma_o + \Delta\sigma - V(\underline{r}, t))\underline{r}$$

Now since σ_o is constant we can move it to the left side of this differential equation to get

$$\underline{r}'' + (\alpha_J - 2\sigma_o)\underline{r} = -\mu \underline{e} + r^2 \underline{F} + 2(\Delta\sigma - V(\underline{r}, t))\underline{r} \quad (5.2)$$

Similarly equation (2.18) becomes

$$\underline{r}'' + (\alpha_J - 2\sigma_o)\underline{r} = \mu + \underline{r} \cdot \underline{F} + 2(\Delta\sigma - V(\underline{r}, t))\underline{r} \quad (5.3)$$

This change does not affect the outcome of the variation of parameters approach taken here. This change is only a computational convenience and is in effect in the computational procedure of Section 6.1 where the element α_J is actually $\alpha_J - 2\sigma_o$ and σ is actually $\Delta\sigma$. Note that the initial value of $\Delta\sigma$ is

$$\Delta\sigma = 0 \quad (5.4)$$

6.0 Application

In this section the most important equations are collected and listed in a logical order suitable for computation. Also two numerical examples are presented.

6.1 Computational Procedure

Given $\underline{r}_o, \underline{v}_o, t_o$ find $\underline{r}(t)$ and $\underline{v}(t)$.

STEP 1 Initialization

$$s = 0$$

$$r_o = (\underline{r}_o \cdot \underline{r}_o)^{1/2}$$

$$a = r_o$$

$$b = \underline{r}_o \cdot \underline{v}_o$$

$$\tau = t_o$$

$$\underline{\alpha} = \underline{r}_o$$

$$\underline{\beta} = a \underline{v}_o$$

Evaluate Perturbations $V_o, \left[\frac{\partial V}{\partial \underline{r}} \right]_o, \underline{P}_o$.

$$\alpha_J = \frac{2\mu}{r_o} - \underline{v}_o \cdot \underline{v}_o - 2 V_o$$

$$\gamma = \mu - \alpha_J a$$

$$\underline{\delta} = -(\underline{v}_o \cdot \underline{v}_o)\underline{r}_o + (\underline{r}_o \cdot \underline{v}_o)\underline{v}_o + \frac{\mu}{r_o}\underline{r}_o - \alpha_J \underline{r}_o$$

$$\sigma = 0$$

STEP 2 Transform Elements to Coordinates

$$\underline{r} = \underline{\alpha} + \underline{\beta}sc_1 + \underline{\delta}s^2c_2$$

$$\underline{r}' = \underline{\beta}c_o + \underline{\delta}sc_1$$

$$\underline{x}_3 = \alpha_J(\underline{\alpha} - \underline{r}) + \underline{\delta}$$

$$\gamma = \mu - \alpha_J a$$

$$\underline{r} = \underline{a} + \underline{b}sc_1 + \underline{\gamma}s^2c_2$$

$$\underline{v} = \underline{r}'/r$$

$$\underline{r}' = \underline{b}c_o + \underline{\gamma}sc_1$$

$$\underline{t} = \underline{\tau} + \underline{a}s + \underline{b}s^2c_2 + \underline{\gamma}s^3c_3$$

STEP 3 Evaluate Differential Equations For The Elements

$$\underline{F} = \underline{P} - \frac{\partial V}{\partial \underline{r}}$$

$$\underline{Q} = r^2 \underline{F} + 2\underline{r}(-V + \sigma)$$

$$\alpha_J' = 2(-\underline{r}' + r \underline{\omega} \times \underline{r}) \cdot \underline{P}$$

$$\underline{\mu}\underline{g}' = 2(\underline{r}' \cdot \underline{F})\underline{r} - (\underline{r} \cdot \underline{F})\underline{r}' - (\underline{r} \cdot \underline{r}')\underline{F}$$

$$\underline{\alpha}' = -\underline{Q}sc_1 - \underline{\mu}\underline{g}'s^2c_2 - \alpha_J' \left[\underline{\alpha}s^2c_2 + 2\underline{\beta}s^3c_3 + \frac{1}{2}\underline{\delta}s^4c_2^2 \right]$$

$$\underline{\beta}' = \underline{Q}c_o + \underline{\mu}\underline{g}'sc_1 + \alpha_J' \left[\underline{\alpha}sc_1 + \underline{\beta}s^2c_2 - \underline{\delta}s^3(2c_3 - c_1c_2) \right]$$

$$\underline{\delta}' = \underline{Q}\alpha_Jsc_1 - \underline{\mu}\underline{g}'c_o + \alpha_J' \left[-\underline{\alpha}c_o + 2\alpha_J\underline{\beta}s^3c_3 + \frac{1}{2}\underline{\delta}\alpha_Js^4c_2^2 \right]$$

$$\underline{\sigma}' = r \underline{\omega} \cdot \underline{r} \times \underline{F}$$

$$\underline{a}' = -\frac{1}{r}\underline{r} \cdot \underline{Q}sc_1 - \alpha_J' \left[\underline{a}s^2c_2 + 2\underline{b}s^3c_3 + \frac{1}{2}\underline{\gamma}s^4c_2^2 \right]$$

$$\underline{b}' = \frac{1}{r}\underline{r} \cdot \underline{Q}c_o + \alpha_J' \left[\underline{a}sc_1 + \underline{b}s^2c_2 - \underline{\gamma}s^3(2c_3 - c_1c_2) \right]$$

$$\underline{\gamma}' = \frac{1}{r}\underline{r} \cdot \underline{Q}\alpha_Jsc_1 + \alpha_J' \left[-\underline{a}c_o + 2\underline{b}\alpha_Js^3c_3 + \frac{1}{2}\underline{\gamma}\alpha_Js^4c_2^2 \right] \quad (\text{optional})$$

$$\underline{\tau}' = \frac{1}{r}\underline{r} \cdot \underline{Q}s^2c_2 + \alpha_J' \left[\underline{a}s^3c_3 + \frac{1}{2}\underline{b}s^4c_2^2 - 2\underline{\gamma}s^5(c_3 - 4c_5) \right]$$

STEP 4 Numerically Integrate Over Δs To Obtain Elements At $s + \Delta s$

STEP 5

$$s = s + \Delta s$$

Go back to step 2.

6.2 Numerical Applications

The equations of the BG14 δ element method given above in Section 6.1 were programmed as nearly as possible in the same format as the older BG14 ϵ method (Bond and Goutlieb, 1989). The two methods were then compared to reference cases. The RK45 numerical method (Fehlberg, 1969) was used as the numerical integration method in both examples.

6.2.1 Example 1

The first example is that of a highly eccentric ($e \approx 0.95$) orbit about the Earth. The orbit is subject to the J_2 (Earth oblateness) perturbing potential, which is conservative, plus lunar perturbations. This orbit was computed by both BG14 δ and BG14 ϵ methods. This example was also computed by Stiefel and Scheifele (1971) with extremely high precision and will be used as the reference. Table I shows the components of the position vector in Cartesian coordinates as computed by each method after 50 revolutions of the satellite. It is seen that both methods compare very closely with the reference but the new BG14 δ method being slightly closer to the reference.

The problem description for the first example is:

Coordinate system: X and Y fixed in Earth equatorial plane; Z perpendicular to Earth equatorial plane.

Initial conditions:

Initial State Vector				
Position	0.0	-5888.9727	-3400.0	km
Velocity	10.691338	0.0	0.0	km/sec

The time of comparison is at 288.12768941 days, after approximately 50 revolutions.

TABLE I - Comparison of BG14 δ and BG14 ϵ Methods Final Value Of Position Vector				
Method	X (km)	Y (km)	Z (km)	Steps/Rev (Avg)
REFERENCE Stiefel and Scheifele (1971)	-24219.0503	227962.1064	129753.4424	500
BG14 (RK45 Fixed Step) δ Method	-24218.8175	227961.9146	129753.3431	62
BG14 (RK45 Fixed Step) ϵ Method	-24218.8069	227961.9186	129753.3344	62

The Earth oblateness and lunar models used are somewhat idealized and are taken from Stiefel and Scheifele (1971). These models are specified as follows:

The Earth oblateness perturbations were compared from the potential model

$$V = \frac{3}{2} (GE) J_2 \frac{a_e^2}{r^3} \left[\frac{Z^2}{r^2} - \frac{1}{3} \right]$$

where

$$GE = 398601 \text{ km}^3/\text{sec}^2 \text{ (gravitational constant of Earth)}$$

$$a_e = 6371.22 \text{ km (equatorial radius of Earth)}$$

$$J_2 = 1.08265 \times 10^{-3} \text{ (second harmonic of geopotential)}$$

The lunar perturbation was computed from

$$\underline{P} = -GM \left[\frac{\underline{r} - \underline{a}}{|\underline{r} - \underline{a}|^3} + \frac{\underline{a}}{\rho^3} \right]$$

and the lunar ephemeris is approximated by

$$a_x = \rho \sin \Omega t$$

$$a_y = -\frac{\sqrt{3}}{2} \rho \cos \Omega t$$

$$a_z = -\frac{1}{2} \rho \cos \Omega t$$

$$\rho = 384400 \text{ km (the Earth-Moon distance)}$$

$$\Omega = 2.665315780887 \times 10^{-6} \text{ rad/sec (Moon orbital rate)}$$

$$GM = 4902.66 \text{ km}^3/\text{sec}^2 \text{ (gravitational constant of Moon)}$$

6.2.2 Example 2

The second example (Adamo, 1989) is that of a near circular geocentric satellite orbit numerically integrated by the BG14 δ method from an initial altitude of 300 km down to entry interface altitude of 123.278 km (66.565 nautical miles). The perturbations considered were the Jacchia 1970 atmospheric model and the GEM-10 (Lerch, 1979) geopotential restricted to second order and degree. The time of flight was about 29.736111 days and the ballistic number was 78.606675 kg/m². This case failed at an altitude of approximately 135 km (72.894 nautical miles) with the older BG14 ϵ method.

Coordinate System: True Equator and Greenwich Meridian Of Epoch

Initial conditions:

Initial State Vector at UT1 = 0 on 3 September 1991.				
Position	6677832.962	-62810.44513	-27301.63472	m
Velocity	78.98607579	6821.102837	3626.863958	m/sec

TABLE II - Comparison of BG14 δ and BG14 ϵ Methods Final Value Of Position Vector				
Method	X (m)	Y (m)	Z (m)	Steps/Rev (Avg)
BG14 (RK45 Variable Step) δ Method	2664837.2	-5838760.8	1033865.4	29
BG14 (RK45 Variable Step) ϵ Method	FAILED	FAILED	FAILED	-

Additional stress cases (not shown) have been computed in which the solution was propagated down to the surface of the Earth (assuming no change in atmospheric density below 90 km).

7.0 Final Comments

Recent numerical studies on atmospheric entry from near circular orbits and on low thrust in near circular orbits exhibit numerical instability when solved by the method of Bond and Gottlieb (1989) for long time intervals. These two cases are similar since both have persistent, tangential, non-conservative perturbations. It was found that this instability was due to secular terms which appear on the right hand sides of the differential equations of some of the elements. In this paper this instability is removed by the introduction of another vector integral of the motion and another scalar integral which remove the secular terms. The introduction of these new integrals require a new derivation of the differential equations for most of the elements. For this rederivation the Lagrange method of variation of parameters is used making the development more concise.

8.0 References

Adamo, D.: Personal Communication, April 1989.

Bond, Victor R. and Hanssen, Veit.: *The Burdet Formulation of the Perturbed Two-Body Problem with Total Energy as an Element*, NASA Johnson Space Center Publication JSC Internal Note No. 73-FM-86 (JSC-08004), June 1973.

Bond, Victor R. and Mulcihy, David D.: *Computation of Orbits Using Total Energy*, Presented at the Flight Mechanics and Estimation Theory Symposium-1988, Goddard Space Flight Center, Greenbelt, Maryland, May 1988 (NASA CP 3011).

Bond, Victor R. and Gottlieb, Robert G.: *A Perturbed Two-Body Element Method Utilizing The Jacobian Integral*, NASA Johnson Space Center Publication JSC Internal Note No. 89-FM-3 (JSC-23495), May 1989.

Burdet, C.A.: *Theory of Kepler Motion*, Zeitschrift fur Angewandte Mathematic und Physik, Vol. 19 , 1968.

Fehlberg, E.: *Low Order Classical Runge-Kutta Formulas With Step Size Control*. NASA TR-315, 1969.

Jacchia, L.G.: New Static Models of Thermosphere and Exosphere with Empirical Temperature Profiles, Smithsonian Astrophysical Observatory. Special Report No. 313 (1970).

Lerch, F.J.; et al: Gravity Model Improvement Using GEOS3 (GEM9 and 10). J. Geophysical Research, Vol. 84 No. B8 (30 July 1979).

Sperling, Hans.: *Computation of Keplerian Conic Sections*, ARS Journal, May 1961

Stiefel, E. and Scheifele, G., Linear And Regular Celestial Mechanics. Springer-Verlag, 1971.

Szebehely, V., Theory Of Orbits. Academic Press, 1967.

Appendix A - The Variation Of Parameters Method Of Lagrange

Assume that we have a mechanical system given by

$$\dot{\underline{x}} = \underline{f}(\underline{x}, t) \quad (\text{A1})$$

where

$$\begin{aligned} \underline{x}^T &= (x_1, \dots, x_n) \\ \underline{f}^T &= (f_1, \dots, f_n) \end{aligned}$$

and t is the independent variable.

We also assume that the solution of the system of equations (A1) is possible and can be expressed

$$\underline{x} = \underline{x}(\underline{c}, t) \quad (\text{A2})$$

where the integration constants, or parameters, are given by

$$\underline{c}^T = (c_1, \dots, c_n) \quad (\text{A3})$$

Now consider another system similar to the system (A1),

$$\dot{\underline{x}} = \underline{f}(\underline{x}, t) + \underline{g}(\underline{x}, t) \quad (\text{A4})$$

where the new term is called a perturbation and is given by

$$\underline{g}^T(\underline{x}, t) = (g_1, \dots, g_n) \quad (\text{A5})$$

The objective is to make the solution, equation (A2) of the system (A1), valid for the perturbed system (A4) by allowing the parameter \underline{c} to be a function of the independent variable. In other words the solution (A2) still applies but with the constant (\underline{c}) replaced by the function ($\underline{c}(t)$). So we have

$$\underline{x} = \underline{x}(\underline{c}(t), t) \quad (\text{A6})$$

Now take the total derivative of equation (A6)

$$\dot{\underline{x}} = \frac{\partial \underline{x}}{\partial \underline{c}} \dot{\underline{c}} + \frac{\partial \underline{x}}{\partial t} \quad (\text{A7})$$

Also take the total derivative of (A2) and use (A1) to obtain

$$\frac{\partial \underline{x}}{\partial t} = \dot{\underline{x}} = \underline{f}(\underline{x}, t) \quad (\text{A8})$$

Note we have used the fact that for unperturbed case the total and partial derivatives of \underline{x} are the same. Using equation (A8) we can eliminate the partial derivative $\frac{\partial \underline{x}}{\partial t}$ from equation (A7) obtaining,

$$\dot{\underline{x}} = \frac{\partial \underline{x}}{\partial \underline{c}} \dot{\underline{c}} + \underline{f}(\underline{x}, t) \quad (\text{A9})$$

Now compare equation (A9) with equation (A4) to obtain

$$\dot{\underline{x}} = \frac{\partial \underline{x}}{\partial \underline{c}} \dot{\underline{c}} + \underline{f}(\underline{x}, t) = \underline{f}(\underline{x}, t) + \underline{g}(\underline{x}, t)$$

After the obvious cancellation

$$\frac{\partial \underline{x}}{\partial \underline{c}} \dot{\underline{c}} = \underline{g} \quad (\text{A10})$$

where the matrix $\frac{\partial \underline{x}}{\partial \underline{c}}$ is obtained from the solution, equation (A2). The matrix must be invertible. That is

$$DET \left[\frac{\partial x}{\partial \underline{c}} \right] \neq 0$$

The system of differential equations for the parameter \underline{c} is therefore

$$\dot{\underline{c}} = \left[\frac{\partial x}{\partial \underline{c}} \right]^{-1} \underline{g} \quad (\text{A11})$$

Appendix B - The Stumpff Functions

These functions are related to the trigonometric and hyperbolic functions. The general equation for the n th Stumpff function is,

$$c_n(z) = \sum_{k=0}^{\infty} (-1)^k \frac{z^k}{(2k+n)!}, \quad n=0,1,2,\dots \quad (B1)$$

When these series are compared to the series of the trigonometric and hyperbolic functions, the following relations exist:

$$\begin{aligned} c_0(x^2) &= \cos x, \text{ or } c_0(-x^2) = \cosh x \\ c_1(x^2) &= \frac{\sin x}{x}, \text{ or } c_1(-x^2) = \frac{\sinh x}{x} \\ c_2(x^2) &= \frac{1 - \cos x}{x^2}, \text{ or } c_2(-x^2) = \frac{\cosh x - 1}{x^2} \\ c_3(x^2) &= \frac{x - \sin x}{x^3}, \text{ or } c_3(-x^2) = \frac{\sinh x - x}{x^3} \\ c_4(x^2) &= \frac{\cos x - \left[1 - \frac{x^2}{2}\right]}{x^4}, \text{ or } c_4(-x^2) = \frac{\cosh x - \left[1 + \frac{x^2}{2}\right]}{x^4} \end{aligned} \quad (B2)$$

etc.

The following identities may also be easily verified:

$$\begin{aligned} c_0(z)^2 + z c_1(z)^2 &= 1 \\ c_0(z)^2 - z c_1(z)^2 &= c_0(4z) \\ c_0(z)^2 &= 1 - 2z c_2(4z) \\ c_1(z) &= 2c_2(4z) \\ c_0(z) c_1(z) &= c_1(4z) \\ c_2(z) &= c_1(z)^2 - c_2(z) c_0(z) \end{aligned} \quad (B3)$$

The more general identities

$$c_{n+2}(z) = \frac{1}{n} c_{n+1}(z) + \frac{1}{z} \left[-c_n(z) + \frac{1}{n} c_{n-1}(z) \right], \quad n > 0 \quad (B4)$$

and

$$c_n(z) + z c_{n+2}(z) = \frac{1}{n!} \quad (B5)$$

are also valid.

The derivatives of these functions may be expressed as

$$2z \frac{dc_n(z)}{dz} = c_{n-1}(z) - n c_n(z), \quad n > 0 \quad (B6)$$

and

$$\frac{dc_n(z)}{dz} = \frac{1}{2} \left[n c_{n+2}(z) - c_{n+1}(z) \right] \quad (B7)$$

A convenient integration formula is

$$\int s^k c_k(\rho s^2) ds = s^{k+1} c_{k+1}(\rho s^2) \quad (B8)$$

IMPROVED ACCURACIES FOR SATELLITE TRACKING

P. C. Kammeyer, A. D. Fiala, P. K. Seidelmann
Orbital Mechanics Department, U.S. Naval Observatory,
Washington, D.C. 20392

ABSTRACT

A CCD camera on an optical telescope which follows the stars can be used to provide high accuracy comparisons between the line of sight to a satellite, over a large range of satellite altitudes, and lines of sight to nearby stars. The CCD camera can be rotated so the motion of the satellite is down columns of the CCD chip, and charge can be moved from row to row of the chip at a rate which matches the motion of the optical image of the satellite across the chip. Measurement of satellite and star images, together with accurate timing of charge motion, provides accurate comparisons of lines of sight. Given lines of sight to stars near the satellite, the satellite line of sight may be determined. Initial experiments with this technique, using an 18 cm telescope, have produced TDRS-4 observations which have an rms error of 0.5 arc second, 100 m at synchronous altitude.

Use of a mosaic of CCD chips, each having its own rate of charge motion, in the focal plane of a telescope would allow point images of a geosynchronous satellite and of stars to be formed simultaneously in the same telescope. The line of sight of such a satellite could be measured relative to nearby star lines of sight with an accuracy of approximately 0.03 arc second. Development of a star catalog with 0.04 arc second rms accuracy and perhaps ten stars per square degree would allow determination of satellite lines of sight with 0.05 arc second rms absolute accuracy, corresponding to 10 m at synchronous altitude.

Multiple station time transfers through a communications satellite can provide accurate distances from the satellite to the ground stations. Such observations can, if calibrated for delays, determine satellite orbits to an accuracy approaching 10 m rms.

INTRODUCTION

The U.S. Naval Observatory, as part of its primary mission, makes accurate astrometric observations of stars and solar system objects, maintains the Master Clock of the United States, and makes precise time comparisons between that clock and other time standards around the world. As a by-product of these activities, techniques for improved satellite tracking have been developed.

Charge coupled device (CCD) chips are light sensitive integrated circuits used in astronomy for photometric and astrometric observations. Some of the characteristics applicable to artificial satellite observations with a telescope guided to follow the stars are that

- 1) high quantum efficiency permits short exposure times,
- 2) pixel and image sizes permit accurate determination of the centroid of the image,
- 3) variable read-out rates permit accumulating into pointlike charge images photoelectrons from a satellite optical image moving across the chip as well as from star images fixed on the chip,
- 4) observations can be read directly from chip to computer for immediate, automated analysis, and
- 5) mosaics of CCD's can be operated so that one CCD tracks a satellite and others accumulate star images, allowing relative positions to be determined accurately.

The characteristics of the CCD detector mean that a relatively small telescope, of 20-50 centimeter aperture, can be used. The trade-off between field of view, duration of observation, and accuracy of observation is dependent upon the size of the CCD or mosaic, the size of the pixels, and the telescope specifications. Depending on the operational requirements, specific instrument designs and observational procedures can be implemented. With computer control, the entire process of obtaining images and extracting from them satellite line of sight information can be performed autonomously.

Equipment used for time transfer through communications satellites allows measuring accurate ranges from ground stations to a communications satellite. High accuracy orbits can be determined from the range data. Calibration of range biases can be accomplished by high accuracy optical observations.

OBSERVATIONS OF TDRS-4

Observations are made with a Photometrics series 200 CCD camera containing a 1024 by 1024 Thompson CCD chip which has a photosensitive area 2 centimeters on a side. Each pixel of the CCD covers a region of the sky 2.4 seconds of arc on a side, and the CCD chip covers a region 40 arc minutes on a side. The CCD camera is attached by a rotator to a 18-cm-aperture telescope of 168-cm focal length, guided to follow the stars. The rotator allows aligning the columns of the CCD chip with the direction of satellite motion relative to the stars. By controlling the rate of motion of charge along columns of the CCD chip, it is then possible to accumulate photoelectrons from the satellite image.

Observation times and fields are chosen so that the satellite observed, TDRS-4, will be in the same field with two reference stars in a star catalog. The telescope is pointed to the direction of the center of the desired field and the CCD camera is rotated so that the satellite image moves along CCD columns. When the satellite is near the center of the field, the shutter is opened and the CCD controller advances charge from row to row of the CCD at a rate matching the motion of the satellite. This charge transfer is identical to the charge transfer normally accomplished when reading out the CCD chip after an exposure, but is commanded row by row by a specially designed timing circuit. This circuit causes a uniformly spaced sequence of charge advances and allows the times of charge advance to be accurately determined.

After a pre-fixed number of rows is transferred (40 in the present case), depending on the brightness and thus the required exposure time of the satellite (6 seconds in the present case), charge transfer stops and the shutter is closed for a few seconds. At the end of charge transfer, the charge image of the satellite extends over only a few pixels while star images are trails 40 rows long (Figure 1a).

The shutter next opens, for a star exposure with no charge motion, to form the charge image found in Figure 1b. While the shutter is closed before this exposure, there is an interval of charge advance and there is an interval in which charge does not move but the satellite optical image continues its motion downward in the figure. The shutter last opens for a star exposure which forms the charge image shown in Figure 1c. There is again before this exposure an interval of charge advance and an interval with no charge motion. The durations of the star exposures are 2 seconds, sufficient to allow accurate measurement of the centroids of the star images. After the shutter closes for the last time, charge is read out of the CCD chip.

MEASUREMENT OF IMAGES

The satellite charge image at the end of the satellite exposure is the sum of the charge images produced in the intervals between charge advances. The centroid of the distribution, at the end of the satellite exposure, of the photoelectrons produced in a particular interval is the centroid of the optical image of the satellite at the middle of the interval, advanced by an integer number of rows. The centroid of the final satellite charge image is thus the centroid of the optical image of the satellite at the midpoint of the satellite exposure, advanced by the average of the amounts by which the summed images are advanced.

Observed CCD frames are analyzed with an interactive image processing program which displays a CCD frame on a screen and allows adjustment of brightness and contrast for maximum visibility of star and satellite images. Using a mouse-controlled arrow displayed on the screen, the user indicates the point image of the satellite and the two point images of each reference star. The program locates the brightest pixel near each indicated position and forms a smaller, 7-by-7 subimage centered on this brightest pixel. From each pixel brightness in the subimage is subtracted the average of the brightnesses of all pixels in the subimage. The center of the subimage is calculated to be the centroid of the pixels with positive differences, each such pixel weighted by its difference value.

The determined satellite position for a CCD frame corresponds to the position, with respect to the midpoint of the great circle arc connecting the reference stars, of the satellite at the observation time. Displacement components are measured in pixels in the direction of satellite motion and in an orthogonal direction. The distance in pixels between the reference star images is also measured.

COMPARISON OF MEASURED POSITIONS TO DETERMINED ORBITS

Following each night of optical observations of TDRS-4, Goddard Space Flight Center provides satellite positions and velocities at two-hour intervals from an orbit fit to a span, including the time of the optical observations, of radio data. A numerical orbit integrator is used to calculate the position of the satellite at the time of each satellite observation.

An observation simulation program calculates the observed lines of sight of the two reference stars for each CCD frame, and the distance between them, on the basis of positions in the star catalog. Simulated lines of sight are calculated by applying refraction to apparent places which include proper motion, precession, nutation, and that part of aberration due to the motion of the center of mass of the Earth.

Together with the reference star lines of sight, the observation simulation program calculates for each frame the line of sight to the satellite at the observation time. The satellite line of sight includes the effects of refraction, the motion of the satellite in the light time to the observer, polar motion, and the difference between UT1 and UTC. The satellite orbit as provided by Goddard Space Flight Center is with respect to true of date coordinates with the FK4 equinox, while Earth orientation and star positions are given with respect to true of date coordinates with the FK5 equinox. To convert satellite positions to true of date coordinates with the FK5 equinox, the satellite is displaced forward 0.070 second of time in its orbit.

From the lines of sight are calculated the components, in the direction of satellite motion and an orthogonal direction, of the displacement to the satellite line of sight from the midpoint of the great circle arc connecting the reference star lines of sight. That part of aberration due to the rotation of the Earth is included neither in the simulated star nor satellite lines of sight.

The observation simulation program calculates all distances in radians and converts these values to pixels, using an angular pixel size which is constant for a night's observations. The simulation program is run once to determine the angular size of a pixel (the scale of the frame) by comparing the observed sum of distances between reference stars with the sum calculated using an assumed pixel size. A second run of the simulation program uses the angular pixel size calculated in the first run.

We consider the measured position of each image to be the sum of a random position measurement error and a measured image position averaged over all possible variations in atmospheric refraction and over all possible image measurement errors. We further consider that the line of sight of each reference star, calculated from its catalog position and a mean refraction value, differs from the line of sight corresponding to the mean image position by a catalog error with zero mean.

Figure 2 shows, for CCD frames made in observing sessions near 0 hours UT on December 10, 11, and 13, the deviations of measured from calculated distances between reference stars. Each deviation is the sum of the position measurement error and the catalog error along the great circle connecting the stars. The root mean square value of the deviations is 0.49 arc second.

The star catalog used is the Astrogaphic Catalog Reference System (ACRS) catalog developed at the U.S. Naval Observatory by Corbin and Urban (1990) to provide the most accurate high-density reference catalog (325,000 stars) available. The standard deviation in each coordinate is 0.21 arc second for 1990. This error contributes 0.30 arc second to the root mean square difference of calculated and measured distances between two reference stars. Differences of refraction with star color add a further error, since no filter is used in the optical system. Errors in the distance due to variations in atmospheric refraction and those introduced in the process of recording and measuring star images must together have approximately 0.38 arc second standard deviation in order for the sum of the square of this standard deviation and the square of the standard deviation of catalog error to reach the observed $(0.49 \text{ arc second})^2$. Dividing by the square root of 2 gives the value 0.27 arc second, or 0.12 pixel, for the standard deviation of each component of the position measurement error.

Figure 3 shows the displacement of measured from calculated TDRS-4 lines of sight on three nights in December 1990. Different reference stars are used for each observation. The rms value, for all observations on the night of December 10, of the displacement of the measured from the calculated satellite line of sight is 0.25 arc seconds; corresponding values for December 11 and 13 are 0.58 and 0.55 arc second. An angular displacement of 0.5 arc second, 0.21 pixel, corresponds to a linear displacement of 100 meters at synchronous altitude. The mean displacement of measured from calculated lines of sight is within 0.5 arc second of a constant one arc second westward offset for each night. Changes from night to night in the mean displacement are consistent with the accuracy stated for the provided satellite ephemerides. The cause of the one arc second offset is not at present understood. Possible causes of the offset include software errors and misunderstanding of the coordinate system used for the provided orbit.

We also reduced the data using the Smithsonian Astrophysical Observatory (SAO) star catalog. As expected from the known errors in this catalog, rms deviations of measured from calculated satellite lines of sight were twice as large as those in lines of sight measured by comparison with the ACRS catalog stars. The improvement produced by using the ACRS catalog rather than the SAO star catalog points out the importance of using the most accurate star catalog available and the need for high-density star catalogs considerably more accurate than ACRS.

HIGH ACCURACY SATELLITE LINE OF SIGHT DETERMINATION BY OPTICAL OBSERVATIONS

An instrument for high accuracy optical satellite observations might consist (Kammeyer, Fliegel, and Harrington, 1990) of a 0.5-meter aperture telescope of 4-meter focal length with a 2000 by 2000 pixel CCD focal plane assembly having 20 micron pixels (Figure 4). The focal plane assembly could be either a single, specially designed CCD chip, or a mosaic of CCD chips. When observing a satellite, part of the focal plane assembly would form point images of stars and part would form a point image of the satellite (Figure 5). The time required for the optical image of a geosynchronous satellite to cross the focal plane assembly, which corresponds to a 30 by 30 arc minute region of sky, is two minutes. A narrow bandpass filter is shown, which reduces the number of photoelectrons to 8000 per pixel for an image of 3 pixel radius, exposed 40 seconds, of a magnitude 10 star (filter transmission is 50% and CCD efficiency is 40%). Such a narrow bandpass makes refraction differences with color insignificant.

By making several exposures in the crossing time of a geostationary satellite, the line of sight to such a satellite could be located to perhaps 0.03 arc second rms relative to nearby stars. This includes a one-fortieth pixel error due to causes within the CCD (Monet, 1988) and an error of 0.01 arc second due to atmospheric turbulence (Han, 1989). If several stars in the field of the telescope had lines of sight known to an absolute accuracy of 0.04 arc second rms, the line of sight of the satellite could be determined with an absolute accuracy of 0.05 arc second, corresponding to 10 meters at synchronous altitude.

The ideal source of star positions would be a star catalog with 0.04 arc second rms accuracy and approximately ten stars per square degree. An alternative approach, too expensive to apply to more than a small number of ground stations and geostationary satellites, would be to measure relative star positions in small regions along the observed paths of the satellites. Calibration with the U.S. Naval Observatory optical interferometer could be used to convert the relative measurements of star positions in each region to absolute star positions. The optical interferometer will be able to measure star positions with an accuracy better than 0.01 arc second.

Another technique for determining an absolute line of sight for a satellite would not require the use of absolute star positions. In this technique, one would observe passages of a Global Positioning System (GPS) satellite and of the geostationary satellite through the same star field. The rms error in locating the line of sight of a GPS satellite relative to nearby stars with the described instrument is expected to be approximately 0.04 arc second (Kammeyer, et al., 1990). This includes a one-fortieth pixel error due to causes within the CCD (Monet, 1988) and an error of 0.025 arc second due to atmospheric turbulence (Han, 1989). Excluding error in the GPS ephemeris, the line of sight of the geostationary satellite near its crossing of the path of the GPS satellite could be determined to an accuracy of 0.05 arc second. GPS ephemeris error, approximately 0.025 arc second (2.5 meters) for a GPS definitive orbit at present, raises the line of sight error to 0.06 arc second.

SATELLITE TRACKING USING TIME TRANSFER TECHNIQUES

Time transfer at the nanosecond level between widely separated radio transmitters using communications satellites is a new technique currently in its experimental stages. It uses spread spectrum coding techniques developed by Hartl et. al. (1983, 1985). The experiments are being currently conducted by the U.S. Naval Observatory, in collaboration with National Institute of Standards and Technology in Boulder and National Research Council in Ottawa. The experiments involve the SBS-3 communications satellite and ground stations in Washington, DC, Boulder, CO, Ottawa, ONT, and Miami, FL.

This technique has also been used for range measurements from one station. These measurements demonstrate an rms scatter of 1 nanosecond in round-trip time, corresponding to 30 cm in round-trip distance, over 5 minutes (W. Klepczynski, USNO, private communication).

Microwave transmissions are subject to many influences: atmospheric effects, placement of equipment at the ground station, orientation of the spacecraft, etc. However, transmission is independent of clouds and daylight, and the other effects can be brought down to less than 30 cm rms in range. The combined effect of all error sources is to produce a satellite to ground station range error less than 40 cm rms.

By using simultaneous ranging from three ground stations, the position of the satellite can be determined uniquely through triangulation. For three ground stations spread over approximately 2000 km north-south and east-west, 40 cm range errors will produce errors in satellite position of approximately 10 m rms.

Ranging measurements with this technique are limited to communications satellites. However, ground stations installed for time transfer purposes could be used intermittently for tracking. The stations should be selected or established with the widest possible separation in both east-west and north-south coordinates. If optical calibration observations were also applied, then a tracking operation might be inexpensively conducted with 10 m - 20 m rms error.

References

- Corbin, T.E. and Urban, S.E.: 1990, in *Proceedings of IAU Symposium 141, Inertial Coordinate System on the Sky*. Ed. J.H. Lieske and B.K. Abalakin. Dordrecht, Holland: Kluwer Academic Publishers. 433
- Monet, D.G.: 1988, in *Ann. Rev. Astron. Astrophys.* **26**, 413
- Han, I.: 1989, *Astron. J.* **97**, 607
- Kammeyer, P.C., Fliegel, H.F., Harrington, R.S.: 1991, in *Proceedings of IAU Colloquium 127, Reference Systems, held in Virginia Beach, Va., October , 1990*.
- Hartl Ph. et al.: 1983, *Z. Flugwiss. Weltraumforsch.* **7**, 335
- Hartl Ph. et al.: 1985, *Acta Astronomica* **12**, 629

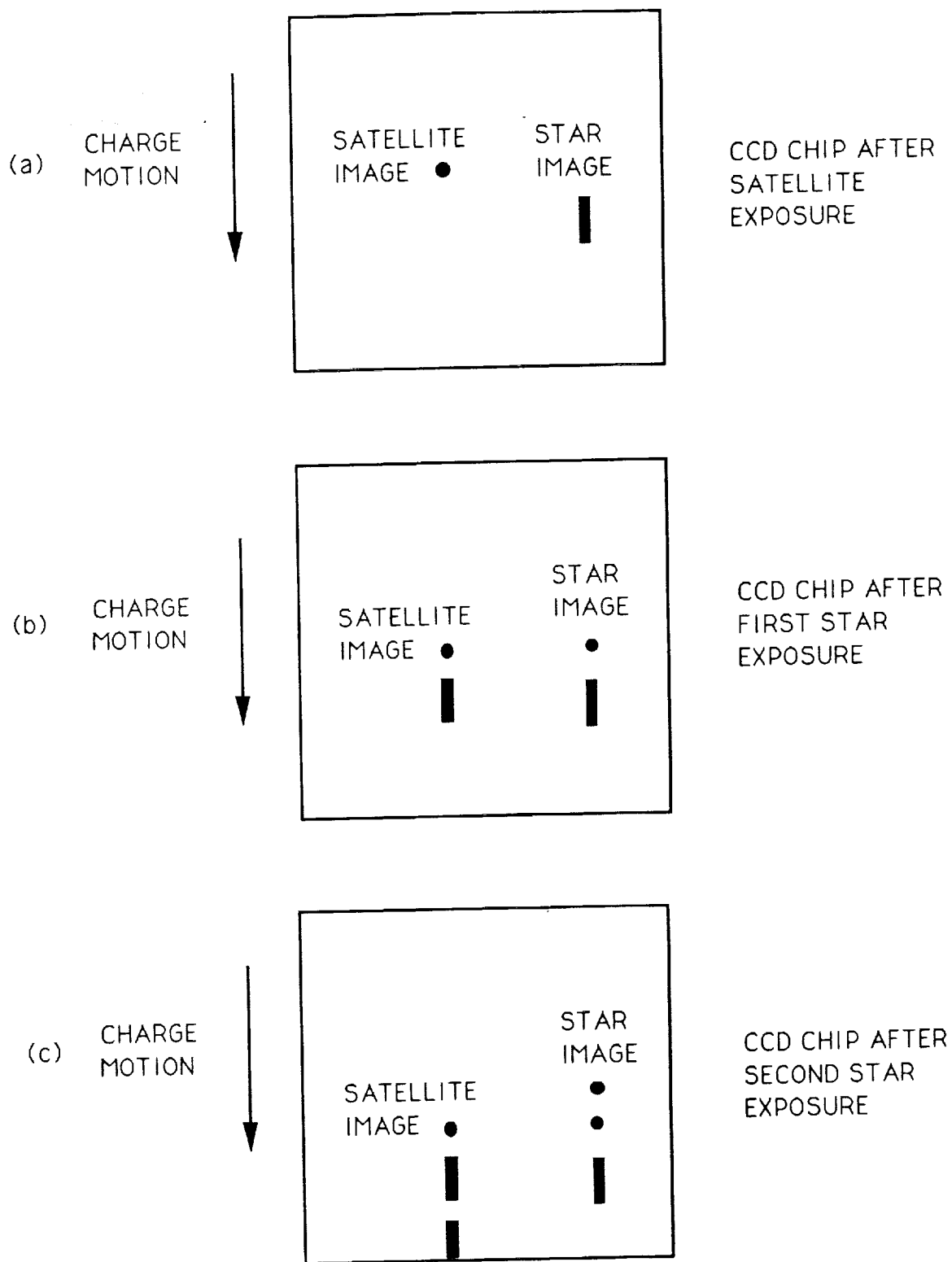


FIGURE 1. FORMATION OF SATELLITE AND STAR CHARGE IMAGES

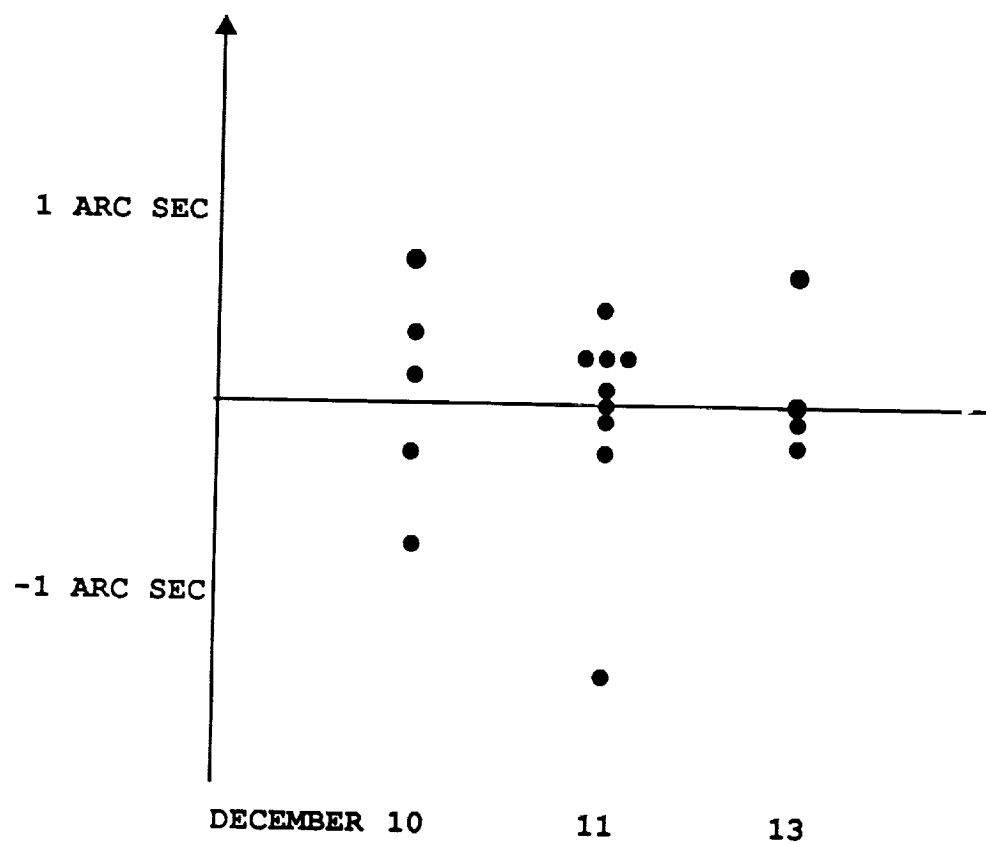


FIGURE 2. DEVIATIONS FROM CALCULATED TO MEASURED DISTANCES BETWEEN REFERENCE STARS

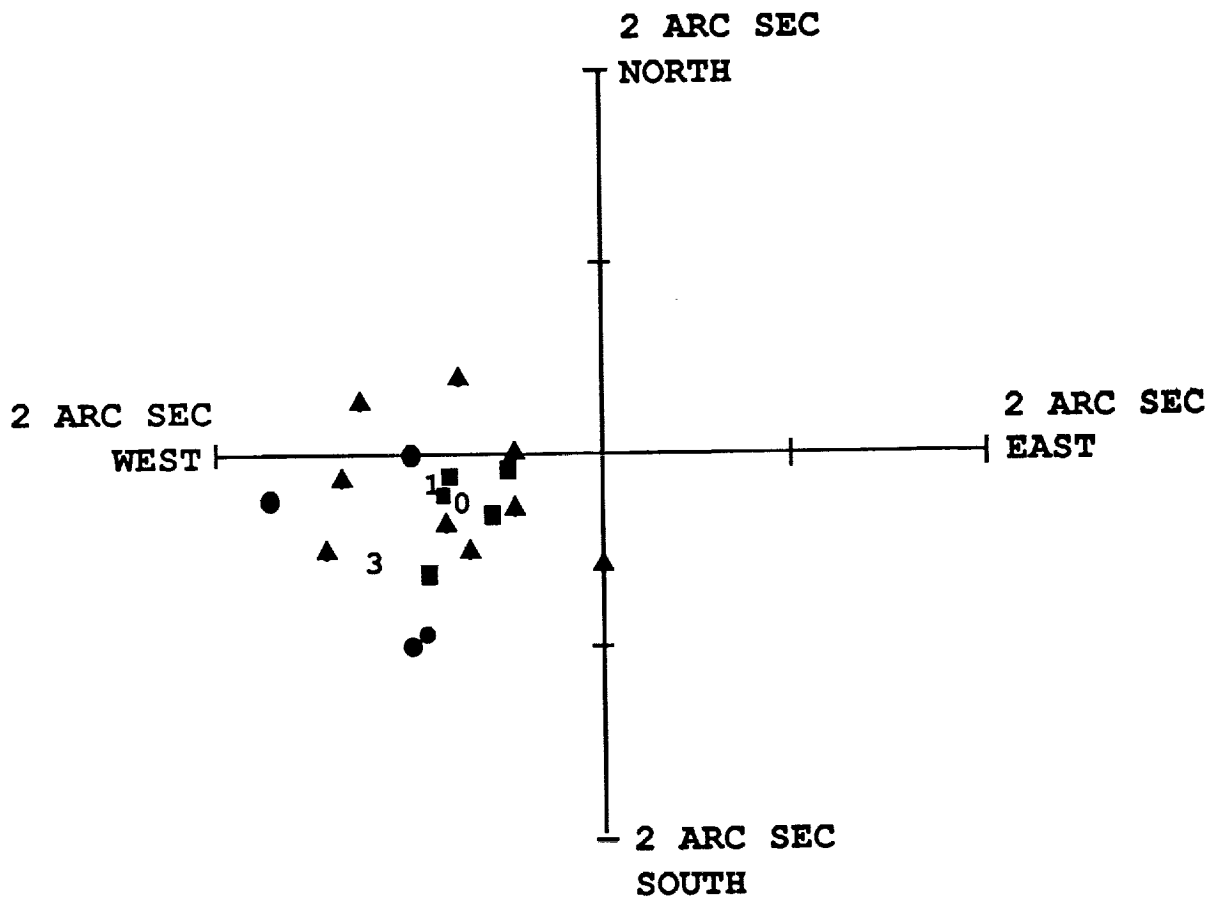


FIGURE 3. TDRS D RESIDUALS (OBS-CALC) ON
 ■ DECEMBER 10, 1990
 ▲ DECEMBER 11, 1990
 ● DECEMBER 13, 1990

0, 1, 3 MARKS MEAN RESIDUAL FOR
 DECEMBER 10, 11, 13

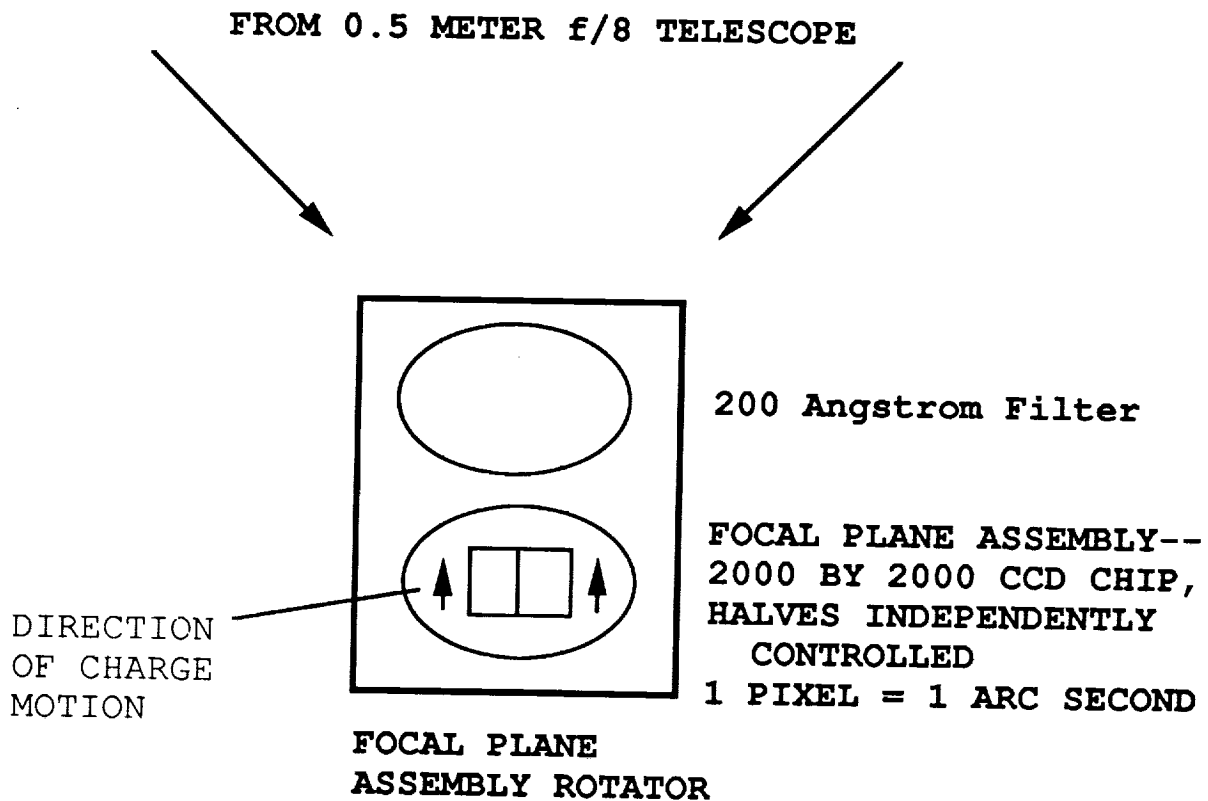


Figure 4. Focal Plane Assembly of Satellite Telescope

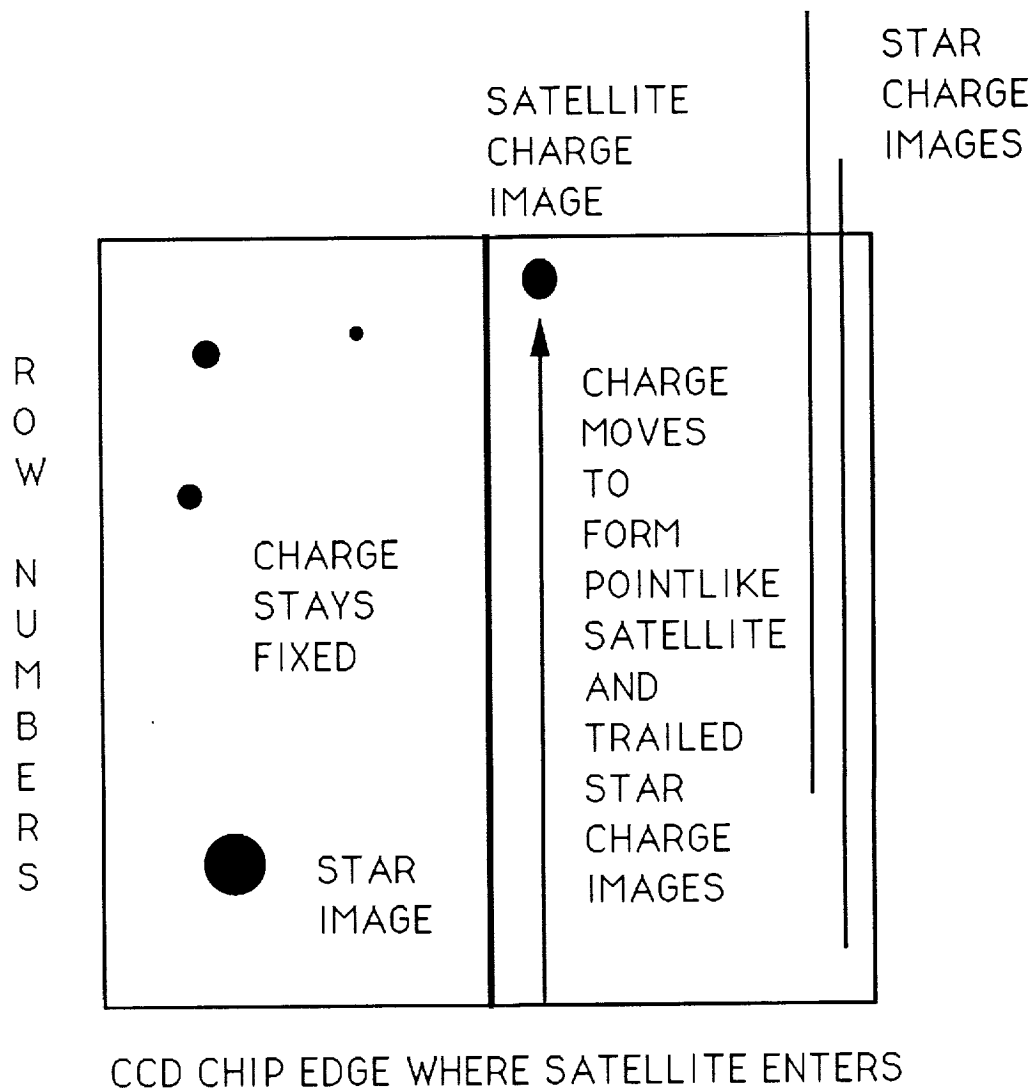


Figure 5. Operation of Focal Plane Assembly

FLIGHT MECHANICS/ESTIMATION THEORY SYMPOSIUM

MAY 21-23, 1991

SESSION 4

Testing of the High Accuracy Inertial Navigation System
in the Shuttle Avionics Integration Lab

Russell L. Strachan
James M. Evans
Guidance & Navigation Analyst
Rockwell Space Operations Co.
Houston, Texas

Abstract

This paper presents the description, results, and interpretation of comparison testing between the High Accuracy Inertial Navigation System (HAINS) and KT-70 Inertial Measurement Unit (IMU). The objective of the tests were to demonstrate the HAINS can replace the KT-70 IMU in the space shuttle Orbiter, both singularly and totally. This testing was performed in the Guidance, Navigation, and Control Test Station (GTS) of the Shuttle Avionics Integration Lab (SAIL) at the Johnson Space Center. GTS is a space shuttle simulator which is primarily utilized to evaluate and verify the flight software that operates the shuttle's five General Purpose Computers (GPC).

A variety of differences between the two instruments are explained. Besides being smaller and lighter, the HAINS has the capability to be internally torqued by commands from a GPC.

Four, 5-day test sessions were conducted varying the number and slot position of the HAINS and KT-70 IMUs. The various steps in the calibration and alignment procedure are explained.

Results and their interpretation are presented. The HAINS displayed a high level of performance accuracy previously unseen with the KT-70 IMU. The most significant improvement of performance came in the Tuned Inertial/Extended Launch Hold tests. The HAINS exceeded the 4-hour specification requirement. The results obtained from the SAIL tests were generally well beyond the requirements of the procurement specification.

The performance of the HAINS in the SAIL demonstrated the transparency of operation with respect to the KT-70 IMU. In addition, the concept of an internally compensated INS is compatible with the Orbiter avionics systems and flight software.

Purpose and Introduction

This paper presents the description, results, and interpretation of comparison testing between the High Accuracy Inertial Navigation System (HAINS) and the KT-70 Inertial Measurement Unit (IMU). The

objective of the tests were to demonstrate the HAINS can replace the KT-70 IMU in the Space Shuttle Orbiter, both singularly and totally. Both pieces of hardware are products of the Kearfott Guidance and Navigation Corp, Wayne, N.J.

Four test sessions were conducted during May, June, July, and August, 1990, in the Shuttle Avionics Integration Lab (SAIL) Guidance, Navigation, and Control Test Station (GTS) located at the Johnson Space Center, Houston, TX. GTS is a six degree-of-freedom space shuttle simulator which is primarily utilized to test the flight software that operates the shuttle's five, IBM AP101S General Purpose Computers (GPCs). These GPCs have a 256K bit memory and employ parallel processing of data.

The KT-70 IMU is presently in use aboard the three operational space shuttles. It provides accurate velocity and attitude information for use in the shuttle's GN&C systems. The inertial sensors contained in the four gimbal platform are two GYROFLEX gyroscopes and two force rebalance accelerometers. One and 8-speed resolvers are utilized to provide digital gimbal angle readouts. The KT-70 IMU consists of an all-attitude stabilized platform and associated electronics to supply output data. The Orbiter employs a triple redundant IMU configuration with skewed inertial clusters. This geometry provides failure detection and isolation techniques. The IMU Subsystem Operating Program (SOP) is software that functions during factory calibration/test, hanger calibration, and preflight calibration and alignment. In-orbit IMU updates are provided by on-board star trackers, which are mounted on a common navigation base. The IMU interface to the Orbiter's GPCs is accomplished via a multiplexed serial data line. The KT-70 IMUs are self-contained requiring only external power and cabin cooling air. Each instrument is 10.28 inches high, 11.5 inches wide and 22 inches long, weighing 58 pounds.

The Space Shuttle HAINS is a modified version of the USAF B-1B instrument. The HAINS contains an internal dedicated microprocessor with memory for processing and storing hardware compensation and scale factor data from the vendor's calibration. Therefore, the need to initial-load (I-load) over sixty parameters into the GPCs Mass Memory Unit (MMU) prior to a flight is reduced. The CPU software is called the Operational Flight Program (OFP). It includes Built-In-Test-Equipment (BITE) logic for the hardware and processed data. Navigational data are developed from self-contained inertial sensors consisting of a vertical accelerometer, two horizontal accelerometers, and two, 2-axis displacement GYROFLEX gyroscopes. The sensing elements are mounted in a four-gimbal, gyro stabilized inertial platform with the accelerometers (which are maintained in a known reference frame by

the gyroscopes) as the primary source of information. Attitude and heading information is obtained from resolver devices mounted between the platform gimbals. The HAINS is 9.24 inches high, 8.49 inches wide, and 22 inches long, weighing 43.5 pounds.

An inertial navigation system (INS) has: A) sensors that detect instantaneous vehicle linear acceleration along three orthogonal axes, and B) derives vehicle linear velocity and position and vehicle attitude and heading. The combination of these two features makes a self-contained system. With respect to the space shuttle, feature A is presently performed by the KT-70 IMU while feature B is performed by the GPCs.

Differences between the KT-70 IMU and HAINS

There are a variety of differences between these two pieces of hardware.

HAINS is smaller and lighter than the KT-70 IMU. HAINS has the capability to be internally torqued by its own microcomputer while the KT-70 IMU is externally torqued by commands from a GPC. The HAINS has one resolver for each axis while the KT-70 IMU has two resolvers per axis. The HAINS gyro error parameters are monitored by the self-contained CPU and transmitted to the GPCs through the MUX card and multiplexer. On the KT-70 IMU, these parameters are stored in and monitored by a GPC. The HAINS takes a longer amount of time than the KT-70 IMU to spin-up and spin-down due to braking circuit design. A Stat value of 3F, on the Ground IMU Control/Monitor display, indicates the IMUs are completely spun up. See Figure 1. The HAINS gyroscopes contain a gold plate that reduces gyro drift rate trending. Trending is the long term change in a parameter. The HAINS accelerometers allow for a tighter deadband. Not all of the HAINS capabilities are used in the Space Shuttle version because of the need to maintain transparency with the KT-70 IMU.

Initial-loads (I-loads) are predetermined values for various parameters (e.g., gyro errors). I-loads for the HAINS or KT-70 IMU vary from Orbiter Vehicle to Orbiter Vehicle.

Test Descriptions

Four test sequences, each consisting of five test cases, were conducted for approximately one week over the four month period of May, June, July, and August, 1990. The approach for the first three of the test sequences consisted of integrating one HAINS at a time into the GTS in combination with the KT-70 IMU, until a full complement of

three HAINS formed the test configuration for the third sequence. Test sequence 4 consisted of five special cases. See Table 1A and B. The GPCs were loaded with OI-8F flight software with both nominal and off-nominal (5-sigma) I-loads for the HAINS. For the KT-70 IMUs, the I-loads were determined at the ISL.

The IMU Redundancy Management (RM) routines were tested by inserting a delta bias into a HAINS during an IMU dilemma condition and observing the deselection of the appropriate IMU by RM.

May 1990 Testing Session

A) One HAINS (Slot 1) and Two KT-70 IMUs

B) All three instruments were controlled from the cockpit.

Because there was no Launch Data Bus, the Launch Processing System (LPS) only monitored downlisted data from the GPCs.

The LPS is a duplicate of the actual ground station equipment used at the Kennedy Space Center (KSC) from T-2.5 hours through countdown and liftoff.

June 1990 Testing Session

A) Two HAINS and 1 KT-70 IMU (Slot 3)

B) All three instruments were controlled from the cockpit except one test they were controlled from the LPS. Downlisted data from the GPC was monitored at the LPS.

July 1990 Testing Session

A) Three HAINS

B) All three instruments were controlled from the LPS through the Launch Data Bus (LDB). Downlisted data from the GPCs was monitored at the LPS. Raw redundant gyro data is what comes out of the IMU and contains noise. Compensated redundant gyro data is filtered (second ordered) by the GPC.

May, June and July Test Sessions

A) Test Case 1 : Orbiter Vehicle (OV) in horizontal position to simulate change out of units in the KSCs Orbiter Processing Facility (OPF)

B) Test Case 2 - 5 : OV in vertical position to simulate on-the-pad environment

August 1990 Testing Session

A) Two HAINS and 1 KT-70 IMU (Slot 1)

B) All three instruments were controlled from the LPS.

C) All five tests performed in the vertical position

Hanger Calibration A (HCA)

Each IMU is moved through 25 predefined cluster orientations. Using the measured acceleration and drift as measured by the accelerometers at each position, accelerometer biases, scale factors, symmetry, and misalignments as well as gyro bias scale factors, sensitivities, mass unbalances, drift and misalignments are calibrated. All three IMUs are commanded simultaneously in the operate mode. Item 20 on Spec 104 , the Ground IMU Control/Monitor Spec, is used to request initiation of this procedure that takes approximately six hours. See Figure 1. Item 28 on Operational Sequence (OPS) display 9011 (GPC Memory) indicates the position number (0001 - 0013) of the IMU cluster calibration being performed at that time. See Figure 2. During the hanger calibration, one of two sets of transformation matrices, describing desired platform orientations relative to the navigation base, is loaded into the GPC. Two distinct sets are available as a contingency provision to allow for alternate launch parameters.

Preflight Calibration A (PFCA)

Each IMU is sequenced through 13 platform or cluster positions, two times: the accelerometers are set in high gain for the first pass, and, in low gain in the second pass. All gyro calibration data and the high gain accelerometer calibration data are collected in the first pass. The second pass is to collect data for the low gain accelerometer calibration. A two minute delay is required for the accelerometers to stabilize following each gain change.

A subset of the accelerometer and gyro compensation parameters are updated. This procedure will calibrate all selected IMUs in the operate mode and takes approximately two hours. The launch pad preflight calibration is started no earlier than 15 hours prior to launch. The calibrated parameters are valid for 17 hours, thus providing at least two hours of on-orbit use before degradation. The IMUs will remain in the operate mode from the beginning of this calibration through launch.

Compensation Criteria (C-Crit)

The compensation criteria provides a basis for accepting or rejecting the results for an IMU calibration. It is used at the Kennedy Space Center to evaluate unit health. For example, the compensation criteria for the KT-70 IMU is 0.035 degrees per hour of drift while for the HAINS it is 0.006 degrees per hour.

Platform Positioning

The IMU gimbals are reoriented and then fixed (or caged) in place. The IMU-caged orientation is defined as the point at which all resolver outputs are zero. Physically, this causes the IMU platform to lie parallel to the nav base. Thus, the nav base and platform coordinate axes are parallel. This procedure takes approximately two minutes.

Attitude Determination

Resolver (attitude) and velocity data is used to determine the orientation of the navigation base to the North-West-Up (launch pad) coordinate frame for each operating IMU. A gyrocompassing technique is used to determine the position of north, west, and up relative to cluster position. This procedure, in conjunction with the gimbal angles, is used to define the navigation base to NWU transformation. The transformation is a prerequisite for running all subsequent options involving alignment and calibration. This procedure takes approximately four minutes. It is required whenever the Orbiter has been moved on the ground or the transformation data may have been destroyed in the GPC memory.

Preflight Platform Alignment

A preflight platform alignment, consisting of a gyrocompass alignment and velocity/tilt initialization, is performed for each IMU after the preflight calibration is completed. The purpose of this alignment is to position the platforms to the desired orientation for launch, to maintain this orientation until T-20 minutes (OPS 1 transition), and to provide platform orientation data to the GPCs. The gyrocompass phase of the preflight alignment positions the IMU platforms relative to the navigation base reference systems. The desired orientation loaded into the GPC during hanger calibration is used for this alignment. Since the navigation base orientation relative to the launch pad is known, this alignment actually positions the IMU platforms to a desired orientation relative to the NWU coordinate frame whose origin is at the launch pad.

Velocity/tilt initialization estimates the tilts and drifts experienced by the IMU's due to the Earth's rotation and gravity effects while awaiting the OPS 1 transition. Preflight platform alignment takes approximately 48 minutes.

Gyrocompass Alignment (GCA)

The platforms are moved to skewed launch orientations defined

with respect to the navigation base. The platform skewing is primarily for redundancy management purposes and also prevents more than one IMU experiencing gimbal flip at the same time. During this phase, the IMUs are placed in two orientations relative to the NWU coordinate system. These two orientations differ only in a 90 degree rotation about the up axis. Data is collected for 90 seconds by the accelerometers to remove any misalignment due to the reorientation. The accelerometers are used here because their accuracy is much better than the resolvers and the acceleration due to Earth rotation is definitely known. Therefore, any unexpected acceleration is due to IMU misalignment. Once this misalignment is nulled, the platform is torqued about the north axis to compensate for the Earth's rotation. Data is then collected for ten minutes to measure platform drifts. This sequence of data collecting is repeated at the second orientation. Also the relative attitude errors for each IMU pair are computed using resolver data. This is then repeated using accelerometer data. These two values are subtracted and transformed into body coordinates. A factory-calibrated relative resolver error term is then subtracted. At the end of the GCA, a relative gyrocompassing goodness test is performed on each IMU pair (1:2, 1:3, and 2:3). Failure to pass the goodness test will be indicated on the Ground IMU Control/Monitor display (FAIL will appear under GYROCOMP). Success of the goodness test is depicted on this display when the Hardware Bit Indicator changes from 8010 to 8000 thus signaling the switch of the Capacitive Reset Integrator (CAPRI) Scale Factor Gain Setting from high to low. See Figure 1. GC Fail = 0000, on GNA TOC display GC Align, also verifies a successful GCA. This procedure takes approximately 38 minutes. At the end of GCA, the software will automatically advance to Velocity/Tilt.

Velocity Tilt

The platforms are torqued at Earth's rotational rate, keeping the skewed launch orientations (set up by GCA) constant with respect to the navigation base. This establishes the drift experienced while waiting for the OPS 1 transition and amounts to less than 200 arcseconds per axis between IMUs. These drifts measured by the accelerometers are used to develop a compensation which is applied to the gyros from the OPS 1 transition to T- 12 seconds. They are also used to compute the current platform to M50 reference stable member matrix (REFSMMAT) at the OPS 1 transition. This procedure takes approximately ten minutes, at which point, CPLT appears under GYROCOMP on the Ground IMU

Control/Monitor display. VT Fail = 0000 indicates a successful completion of Velocity Tilt. At the same time, the software will begin performing a level axis tilt test on each platform three times per second.

Inertial Reference Alignment Monitoring System (IRAMS)

The IRAMS was designed to monitor IMU health, measure misalignments, predict launch hold time, and correct misalignments (if necessary) to avert a scrubbed mission. IRAMS determines IMU platform misalignment while holding on the launch pad. The IRAMS computes and displays values of gyro drift compensation needed to correct the misalignment over a specified period of time. IRAMS will monitor to determine if the misalignment was corrected. See Figure 3.

Inertial

This submode is requested by the crew using a keyboard item entry. It provides users with attitude and velocity data for flight computations. It also provides IMU torqueing to compensate for gyro drift. At the OPS 1 transition, the IMUs enter the "tuned inertial" drift compensation mode. It is "tuned" because a compensation factor, computed in the velocity tilt, is applied to the IMU gyro torqueing signals to account for the estimated drift, keeping the platforms aligned to the M50 coordinate system. The total accumulated IMU velocity data is compensated for accelerometer errors in order to support the navigation and redundancy management functions. The gimbal angles are compensated and made available to navigation and user interfaces. At T-12 seconds, this compensation is removed and the IMUs enter "free inertial" mode. The IMUs are now flight ready.

If a technical hold is imposed (launch delay encountered) between gyrocompass alignment and T-20 minutes, the inertial orientation of the IMU platforms computed from velocity tilt will differ from the current REFSMMAT expected for a nominal on-time launch. Since many ground systems supporting the Orbiter's GN&C functions use the current REFSMMAT, it is imperative that these ground systems incorporate the REFSMMAT computed by the Orbiter's Onboard Primary Flight Software at T-20 minutes. These REFSMMAT will be made available to the ground through telemetry (TLM) downlink.

If a technical hold is imposed after transition to OPS-1, the computed current REFSMMAT remains unchanged; however, velocity tilt drift compensation may be degraded with a resultant differ-

ence between the actual platform positions and the positions described by the current REFSMMATs. This status can be monitored from the ground and if limits are reached, the count must regress to some time prior to GCA in order to realign the IMU platforms.

Redundant Gyro Monitor (RGM)

For simulated on-orbit operation, a redundant gyro monitor test was performed for a roll, yaw, and pitch axis on the Dynamic Motion Simulator (DMS). This table and associated controls allowed for an all-attitude, unlimited rotation of the HAINS and KT-70 IMU in three orthogonal axes. By programming the slope of the frequency sweep, the angular acceleration and the time span of constant rate were accurately controlled. The DMS was tilted to a 45 degree angle from the reference position (launch orientation) in each axis. Starting from the horizontal position, the table was ramped to a rate of 13 degrees/second. It returned to zero degrees/second by the time the table reached a 45 degree incline. This procedure provided a means to calculate the staleness of the resolver angle data. It also checked the IMU's stability and performance under normal on-orbit maneuvering conditions. The table was ramped through a zero to thirty to zero degree/second cycle during testing in August. An IMU platform is capable of remaining inertial for vehicle rotations of up to 35 degrees/second and angular accelerations of 35 degrees per second squared.

Redundancy Management (RM)

The IMU RM scheme consists of a selection filter (SF) and fault detection, identification, and reconfiguration (FDIR) software. The SF selects the best data from the available IMUs. FDIR searches for faulty data, attempts to identify the IMU producing the data, and if successful, reconfigures the SF to exclude data from the faulty IMU.

The RM software is divided into two distinct areas, attitude RM and velocity RM. The purpose of the attitude SF is to choose one IMU as the attitude source for the GN&C software. The purpose of the velocity SF is to choose the best available data from the IMUs for use in propagating the Orbiter's state vector. Depending on the number of available IMUs, the SF uses different schemes to determine which IMU to use. Mid-select and averaging techniques are used in the data selection process.

On-Orbit IMU-to-IMU Alignment

When at least one IMU is already in alignment, this option is available to reposition any IMU(s) back to the desired cluster orientation with respect to inertial space. The aligned IMU is used as reference. Because the platforms are both slew and torqued, this type of alignment is fast and should be used when large misalignment angles are present. IMU-to-IMU alignments do not use star tracker or Crew Optical Alignment System data.

Results, Analysis, and Interpretation

Spin-up and spin-down time for the HAINS took 90 seconds while the KT-70 IMU took 37 seconds. The 53 second difference is due to the HAINS braking circuit design.

A total of ten Hanger Calibration A's were performed with excellent results. Three tests had the IMUs oriented horizontally to simulate the change out of units in the KSCs OPF. The other seven calibrations had the IMUs vertically oriented to simulate an on-the-pad environment. Three of these tests were initialized with 5-sigma off-nominal I-loads while the other four tests had nominal I-loads. Sample results are presented in Table 2. HCAs successfully calibrated the HAINS off-nominal 5-sigma I-loads.

A total of 16 PFCAs were performed with the IMUs in the vertical orientation with excellent results. The initial conditions for these PFCAs consisted of either nominal I-loads or previous SAIL calibrations via a Mass Memory read. Sample results are presented in Table 3.

A total of 38 preflight alignments were performed successfully. An example of HAINS GC results are presented in Table 4. Accelerometer and gyro performance was good. The requirement for the gyro restraint drift terms is 0.018 deg/hr over a year (3-sigma).

The Tuned Inertial/Extended Launch Hold tests perhaps best depicted the significant improvement of performance realized in the HAINS design. Holds of up to three hours in tuned inertial were successful. The IRAMS monitored platform drift and consistently predicted launch hold capability in excess of the four hour specification requirement.

Two series of OPS Trans were performed successfully. During simulated powered ascent (OPS 1, Liftoff through Orbit Circularization Maneuver Coast) and using the PASS, less torque commands were issued to the HAINS than KT-70 IMU. This decrease can be attributed to the HAINS gyro error parameters being internally compensated.

During each of three runs, one IMU was deselected and a large delta gyro bias was patched via a keyboard input to one of the remaining selected IMUs, in each case a HAINS. This tested the ability of PASS RM to properly fail a badly drifting HAINS in a RM attitude dilemma scenerio. With a delta bias of 4 deg/hour to the y-gyro (DFY) of IMU-3, RM correctly failed IMU-3. With a delta bias of 4 deg/hr input to the x-gyro (DFX) of IMU-2 resulted in the correct fail of IMU-2. With a delta bias of 4 deg/hr input to the z-gyro (DFZ) of IMU-3 resulted in the unexpected fail of IMU-2 instead of IMU-3 as intended. This result disclosed a shortcoming on the part of RM to detect a failure solely in the z-gyro axis. A RM dilemma occurred in about two minutes. For all three runs, the bias was removed followed by a successful IMU-to-IMU alignment and IMU reselection in MM201. The time required for realignment depends on how far the IMU was out. The maximum torque rate is 100 degrees/hour.

The RGM results show no consistent pattern in the data during the indicated disturbances to the DMS. The test attempted to detect disturbances to the redundant gyro when the DMS was rotated sequentially about each of its axes by a high step input command. Large rate step inputs to the DMS were not obviously discernible in the RGM output of either the HAINS or the KT-70 IMU, but the test did show that the HAINS RGM output was compatible with the KT-70 RGM output. It suggests that this parameter may be unreliable when used as a means of deselecting a drifting IMU during an attitude miscompare in the RM dilemma case.

A run with artificially introduced errors to drive the clusters off tested the IRAMS Uplink capability. This was accomplished with a patch to insert errors prior to the start of the Prelaunch sequence. The errors were as follows: IMU1 DIXE = 0.107 deg/hr, IMU2 DSXE = 0.207 deg/hr and IMU3 DSXE = 0.217 deg/hr. The test had two uplinks, the first being the IRAMS correction drift values and the second being the restoration of the initial I-load drift compensations. The performance was good and the uplink capability was adequately demonstrated. The maximum tilt error was 107 arcseconds in S/N 201 North tilt which was mostly due to the introduced drift errors. See Table 4.

There was a delay from the time the IRAMS correction values were determined and when they were actually applied. This accounted for the corrections of the misalignments not actually attaining zero.

Summary and Conclusions

This paper presented the description and explanation of comparison testing, as performed in the SAIL, between the HAINS and

the KT-70 IMU. The instruments were evaluated during various operational sequences and major modes of a space shuttle mission.

The HAINS performance in the SAIL demonstrated transparency of operation with respect to the KT-70 IMU. The concept of an internally compensated inertial navigation system is compatible with the Orbiter avionics system and flight software. The HAINS displayed a high level of performance accuracy previously unseen with the KT-70 IMU. The results obtained from the SAIL tests were generally well beyond the requirements of the procurement specification.

The HAINS will provide spares support, eventually phasing out the KT-70 IMUs. Flight rated HAINS will be swapped out with any KT-70 IMU that has failed in the three active Orbiters. The Endeavor, presently under construction in California, is being fitted with three HAINS. A full contingency (5) of IBM AP101S GPCs with OI-8 D/F PASS will fly on STS-42 in December, 1991. But no firm date has been established when an Orbiter will fly with 3 HAINS and 5 new GPCs.

Acknowledgement

The authors would like to recognize and thank Mr. Dan Harmon, of Lockheed Engineering and Systems Company, for his time, patience, technical expertise and assistance in the preparation of this paper.

They would also like to recognize Mr. Michael Tubielewicz, of Rockwell Space Operations Co., for his contribution in conducting these tests as well as Mr. George Larson of Rockwell International - Downey for his leadership in performing them.

References

- 1) IMU Workbook, NASA/Johnson Space Center, Houston, TX, July 1980 and April 1987
- 2) William L. Swingle and Dr. Youngkook Kang, The Shuttle Inertial System, AIAA Paper 82-1559, Aug. 1982
- 3) IMU Alignment Flight Procedures Handbook, NASA/Johnson Space Center, Houston, TX, April 1988
- 4) ISL Unit Test Evaluation of HAINS, NASA/Johnson Space Center, Houston, TX, Dec. 1989
- 5) KT-70 IMU and HAINS Description Brochure, Singer Electronics Systems Div., Little Falls, N.J., 1983
- 6) Space Shuttle Orbiter Operational Level C Functional Subsystem Software Requirements, No. 10 & 13, Redundancy Management & IMU SOP, Rockwell International, Space Systems Div., June 1987
- 7) HAINS SAIL Prelaunch Performance Evaluation, D.B. Harmon, Nov. 1990
- 8) Verification Test Report for HAINS, G.R. Larson, Nov. 1990

9011/104/		GND IMU CNRL/MON			4 366/23:59:59 000/00:00:00	
IMU		1	2	3		
X	1	121.23	4 -----	7 -----	SEL IMU 1	16
Y	2	121.23	5	8	2	17*
Z	3	.00	6	9	3	18
O		357.92				
M		1.15				
I		2.97				
IR		.02				
ΔV X		- .50			ATT DET	19*
Y		- .73			HNGR CAL A	20
Z		+ 1.43			B	21
ΔVRSS		1.68			C	22
					PREFLIGHT CAL	23
					GYROCOMP	24
B HDW	8000	8000	8000			
I S/W	00	00	00			
TSTAT	3 F	3 F	3 F			
					INERTIAL	25
					PLAT POS	26
					TERM/IDLE	27
PWR ON	*	*	*			
I/O	M		M			
STBY	10	11	12*		MM WRITE	28
OPER	13*	14*	15		READ	29

STRACHAN*006

Figure 1.- The GND IMU CNTRL/MON display.

Table 1A.- Test Case Description for Test Sequences 1, 2, & 3

Volume	Test Case Description*
1	KSC-OPF (Horiz); Nominal I-loads, HCA, PFCA, 3 GCAs
2	KSC-PAD (Vert); Nominal I-loads, HCA, PFCA, 3 GCAs
3	KSC-PAD (Vert); Nominal I-loads, PFCA, GCA, G9 Inertial, GCA, OPS Trans to MM101, 3 Hr Hold (IRAMS), OPS Trans to MM201, Delta Gyro Bias RM test, IMU-to-IMU Align
4	KSC-PAD (Vert); Off-nominal (5-sigma) HAINS I-loads, HCA, PFCA, GCA
5	KSC-PAD (Vert); Nominal I-loads, PFCA, GCA, OPS Trans to MM101, 2 Hr Hold (IRAMS), OPS Trans to MM201, DMS Step Inputs/RGM Noise test
<p>*Note: OPF - Orbiter Processing Facility GCA - Gyrocompass Alignment HCA - Hangar Calibration A OPS - Operational Sequence PFCA - Preflight Calibration A MM101 - Major Mode 101</p>	

STRACHAN*001

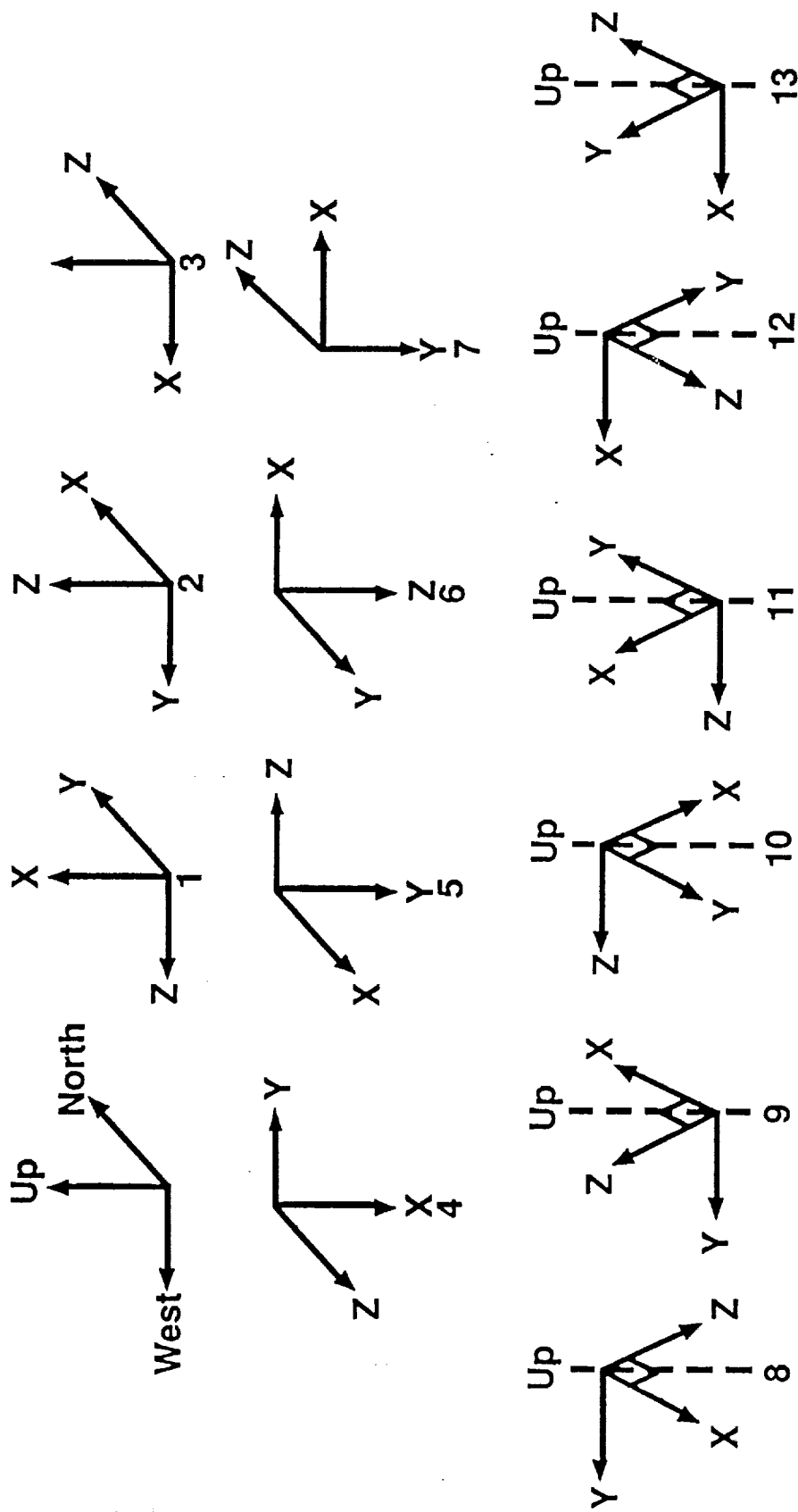
Table 1B.- Test Case Volumes for Sequence 4

Volume	Test Case Description
1	KSC-PAD (Vert); Generic I-loads, HCA, MM Write, PFCA, GCA, OPS Trans to MM101, 2 Hr Hold (IRAMS)
2	KSC-PAD (Vert); MM Read, PFCA, GCA, OPS to MM101, 2 Hr Hold (IRAMS), OPS to G9, GCA, OPS to MM101 3 Hr Hold (IRAMS), OPS to MM201, DES IMU-1, Input Delta DFZ to IMU-2, RM dilemma test
3	KSC-PAD (Vert); MM Read, PFCA, GCA, G9 Inertial, 1 Hr Hold, GCA, OPS to MM101, 3 Hr Hold, Des IMU-1, Input Delta KOX to IMU-2, Accel. RM test
4	KSC-PAD (Vert); MM Read, PFCA, GCA, OPS to MM101, 2 Hr Hold (IRAMS), OPS to G9, GCA, OPS to MM304, GPC-2 to Stby, Restraining IMU-2 to GPC-4, IMU-2 to IMU-3 Align*
5	KSC-PAD (Vert); Nominal I-loads, PFCA, GCA, BFS oneshot, OPS to MM101, 2 Hr Hold (IRAMS), Uplink IRAMS Gyro Bias, Ops to G9, Insert Misalign Patch, GCA, OPS MM101, 2 Hr Hold, Uplink IRAMS Gyro Bias
4*	KSC-PAD (Vert); MM Read, GCA, OPS to MM303, GPC-2 to Stby, Restraining IMU-2 to GPC-4, IMU-2, to IMU-3 Align.

***Note:** An abbreviated repeat of Vol. 4 was run due to procedural errors resulting in an unsuccessful IMU-to-IMU align. The repeated test was successful.

STRACHAN*002

Platform Positions for IMU Calibration



9100101

Figure 2

----- IRAMS PRELAUNCH ALIGNMENT PERFORMANCE ANALYSIS SUMMARY -----

MODE: INERTIAL OPR: NWU ALIGNMENT MONITORING
PAPAS TIME 229: 0:50:59 ALIGN ELAPSE 1:12: 2 SEQUENCE 10
FLT SYSTEM 230: 0:50: 9 OPS-1 ELAPSE 0:17:45 SEQUENCE TIME 145
ALIGN START 229:23:38: 7 OPS-1 TIME 230:0:32:23 OPS-1 COUNTS 1046

----- ALIGNMENT HOLD PREDICTIONS -----

REMAINING HOLD TIME 1:32:53 IMPACTING IMU 1
LAUNCH BY GMT 230: 2:35:17 IMPACTING REDLINE A

----- ALIGN ERROR (ARCS) ----- IMU HEALTH MONITOR -----

IMU	1	2	3	T-ERROR	COUNT	FAILS	OPS-1 TIME
				IMU	1 2 3	IMU	1 2 3
N	-142.	-24.	-57.	V-TILT MARG		V-TILT	
W	-19.	61.	2.	V-DROP OUT		ALIGN TEST	
U	28.	21.	54.	COUNTER		REDLINE	
N	-141.	-137.	3.	D-V ERROR		HOLD TIME	
W	-46.	-1.	12.	COUNTER		ACCEL	
U	47.	27.	19.	UPLINK LIMIT		GRYO DRIFT	

--- PAD/VEH/GC BIAS (ARCS) --- ACCEL ERROR (uG) --- D- ACCEL ERROR (uG/H) ---

U	-19.	-1.	66.	-15.	-13.	-11.	-7.	-3.	-19.
---	------	-----	-----	------	------	------	-----	-----	------

----- FILTERED ALIGN ERROR (ARCS) ----- DRIFT (D/H) -----

N	-120.	-129.	11.	6.	24.	19.	N-0.0126	0.0074	0.0016
W	-44.	34.	26.	2.	2.	-6.	W 0.0032	0.0033	-0.0072
U	36.	44.	10.	-36.	-44.	-10.	U-0.0294	-0.0242	-0.0140

--- DRIFT CORRECTIONS (D/H) --- ALIGN ERROR (ARCS) --- UNTUNED DRIFT (D/H) ---

X -0.479	0.006	0.014	A	6.	24.	19.	X-0.0114	-0.0089	-1.0135
Y -0.843	0.222	0.317	B	6.	24.	19.	Y-0.0385	0.0183	0.0123
Z 0.987	-0.533	0.110	C	-35.	-43.	-12.	Z-0.0004	-0.0266	0.0007

STRACHAN*005

Figure 3

TABLE 2 HAINS S/N 201 HCA TEST RESULTS

MSID	FSSR ATM	ONE SIGMA SHORT/LONG TERM	INITIAL I-LOAD	HCA(1) SIGMA	HCA(2) 6/12/90	HCA(3) 6/14/90	HCA(4) 7/16/90	HCA(4) SIGMA
V99A2520C	KIX	40/100 ppm	0	-0.24	-2.6430E+01	-2.6353E+01	-4.6825E+01	-0.47
V99A2523C	KIY	40/100 ppm	0	-0.17	-2.4226E+01	-2.2067E+01	-2.9574E+01	-0.30
V99A2526C	KIZ	40/100 ppm	0	-0.10	-1.9954E+01	-2.6029E+01	-3.9898E+01	-0.40
V99G2530C	KOX	50 ug	-1000	-0.56	-1.0278E+03	-1.0082E+03	-1.0368E+03	-0.74
V99G2533C	KOY	50 ug	-1000	1.28	-9.3594E+02	-9.7386E+02	-9.3150E+02	1.37
V99G2536C	KOZ	50 ug	-1000	0.08	-9.9578E+02	-9.9883E+02	-9.8615E+02	0.28
V99A2681C	KIXH	40/100 ppm	0	-0.25	-2.4532E+01	-2.9918E+01	-4.6846E+01	-0.47
V99A2684C	KIYH	40/100 ppm	0	-0.16	-1.6052E+01	-2.4938E+01	-3.0577E+01	-0.31
V99A2687C	KIZH	40/100 ppm	0	-0.14	-1.4185E+01	-2.7168E+01	-4.5126E+01	-0.45
V99G2670C	KOXH	50 ug	-1000	-0.57	-1.0287E+03	-1.0076E+03	-1.0365E+03	-0.73
V99G2673C	KOYH	50 ug	-1000	1.27	-9.3662E+02	-9.7104E+02	-9.3287E+02	1.34
V99G2676C	KOZH	50 ug	-1000	0.14	-9.9283E+02	-9.9242E+02	-9.8350E+02	0.33
V99G2500C	KTX	200 ppm	1	1.00000090	0.99990630	0.99989460	0.99997940	-0.10
V99G2503C	KIY	200 ppm	1	0.99998830	0.99995200	0.99996250	0.99998180	-0.09
V99G2506C	KTZ	200 ppm	1	0.99998210	0.99997940	0.99996850	0.99997060	-0.15
V99R2560C	DFX	0.015/0.035 deg/hr	0	4.4080E-04	-3.8530E-04	8.0980E-04	-2.8561E-03	-0.08
V99R2563C	DFY	0.015/0.035 deg/hr	0	5.2451E-03	2.0947E-03	4.5908E-03	8.4382E-03	0.24
V99R2566C	DFZ	0.015/0.035 deg/hr	0	1.1043E-02	1.1069E-02	1.1617E-02	2.1233E-02	0.61
V99U2576C	DSX	0.025 deg/hr/g	0	3.5980E-04	4.8790E-03	5.0761E-03	-3.4557E-03	-0.14
V99U2679C	DSZ	0.025 deg/hr/g	0	-2.8949E-03	-1.9229E-03	-2.6463E-03	-7.1613E-03	-0.29
V99U2570C	DIX	0.025 deg/hr/g	0	2.4635E-02	2.1472E-02	1.8147E-02	3.7506E-02	1.50
V99U2573C	DIZ	0.025 deg/hr/g	0	1.4686E-02	2.3771E-02	1.9203E-02	9.1388E-03	0.37
V99U2582C	DIZ	0.025 deg/hr/g	0	-7.7986E-03	-4.6654E-03	-4.4534E-03	-1.4644E-02	-0.59
V99A2510C	KSX	40/100 PPM	0	9.7693E+00	1.1827E+01	2.8502E+01	-1.0006E+00	-0.01
V99A2513C	KSY	40/100 PPM	0	4.5340E+00	1.3662E+00	1.0372E+00	1.0506E+01	0.11
V99A2516C	KSZ	40/100 PPM	0	5.7614E+00	1.1007E+01	9.8832E+00	1.7163E+01	0.17
V99H2540C	DELTX	21 arc sec	0	9.5252E-01	5.9505E-01	1.5619E+00	1.0619E+00	0.05
V99H2543C	DELTX	21 arc sec	0	1.6624E+00	-1.3442E+00	-1.0245E+00	1.6335E+00	0.08
V99H2546C	DELTY	21 arc sec	0	-1.0182E+01	-6.8366E+00	-6.4449E+00	-9.9831E+00	-0.48
V99H2590C	BXY	60 arc sec	0	-2.0549E+00	-1.3372E+00	7.1764E-01	-6.1347E-01	-0.01
V99H2593C	BXZ	60 arc sec	0	1.4037E+01	-1.3982E+00	-3.6988E-01	7.2053E+00	0.12
V99H2596C	BYX	60 arc sec	0	-4.9477E+00	3.7495E+00	2.4594E-01	-1.6939E+00	-0.03
V99H2599C	BYZ	60 arc sec	0	-1.4397E+01	-3.0179E+00	-4.0460E+00	-9.1887E+00	-0.15
V99H2602C	BZX	60 arc sec	0	3.8694E+00	-1.9737E+00	-1.3790E+00	1.9765E+00	0.03
V99H2605C	BZY	60 arc sec	0	6.0863E+00	4.8956E+00	4.8293E+00	7.8931E+00	0.13
V99U5870C	DOFR	0.05 deg/hr	0	-1.7047E-01	-1.8053E-01	-1.7335E-01	-1.6454E-01	-3.29
V99U5952C	DIFR	0.05 deg/hr	0	-8.3912E-02	-7.5130E-02	-6.7419E-02	-8.5529E-02	-1.71
V99U5955C	DIFR	0.05 deg/hr/g	0	2.5347E-02	2.8983E-02	3.3545E-02	4.5601E-03	0.09
V99U5958C	DOFR	0.05 deg/hr/g	0	1.2878E-02	1.4723E-02	1.7035E-02	2.3166E-03	0.05
V99U5961C	DOFR	0.05 deg/hr/g	0	3.7939E-02	4.6390E-02	4.5445E-02	3.3138E-02	0.05
V99U5964C	KXH	4000 ppm	0.891673	8.9706E-01	8.9765E-01	8.9728E-01	8.9827E-01	1.65
V99U5967C	KYH	4000 ppm	0.452609	4.5620E-01	4.5600E-01	4.5566E-01	4.5635E-01	0.94
V99U5970C	KZH	4000 ppm	0.008004	8.0850E-03	7.6935E-03	7.3224E-03	8.2554E-03	0.06

** 5 SIGMA I-LOAD

* ATP CRITERIA

TABLE 3 HAINS IMU S/N 201 PFCA TEST RESULTS

MNO	FSR ATJ	ONE SIGMA SHORT/LONG TERM	INITIAL I-LOAD	... PFCA(1) 6/12/90	PFCA(1) SIGMA	... PFCA(2) 6/13/90	PFCA(2) SIGMA	PFCA(3) 6/15/90	PFCA(3) SIGMA	PFCA(4) 7/17/90	PFCA(4) SIGMA
V99A2520C	KIX	40/100 ppm	0	-2.819e+01	-0.04	-4.3190e+01	-0.15	-2.8707e+01	-0.29	-4.8657e+01	0.01
V99A2523C	KIY	40/100 ppm	0	-2.8297e+01	-0.10	-4.0076e+01	-0.12	-2.3084e+01	-0.23	-3.9226e+01	-0.02
V99A2526C	KIZ	40/100 ppm	0	-2.2718e+01	-0.07	-4.0864e+01	-0.18	-2.8407e+01	-0.28	-5.5744e+01	-0.05
V99G2530C	KDX	50 ug	-1000	-1.0236e+03	-0.03	-1.0234e+03	0.00	-1.0537e+03	-1.07	-1.0020e+03	-0.03
V99G2533C	KDY	50 ug	-1000	-9.4857e+02	0.06	-9.4825e+02	0.01	-9.7906e+02	0.42	-9.5932e+02	-0.01
V99G2536C	KDZ	50 ug	-1000	-9.9885e+02	-0.03	-1.0020e+03	-0.06	-1.0126e+03	-0.25	-9.9316e+02	0.04
V99A2681C	KIXH	40/100 ppm	0	-2.7748e+01	0.05	-4.3108e+01	-0.15	-3.0616e+01	-0.31	-4.9548e+01	0.02
V99A2684C	KIYH	40/100 ppm	0	-2.8281e+01	-0.06	-3.8848e+01	-0.12	-2.3015e+01	-0.23	-3.9525e+01	-0.03
V99A2687C	KIZH	40/100 ppm	0	-2.6419e+01	0.02	-4.5050e+01	-0.19	-3.4272e+01	-0.34	-5.6099e+01	0.09
V99G2670C	KDXH	50 ug	-1000	-1.0239e+03	0.03	-1.0275e+03	-0.07	-1.0557e+03	-1.11	-1.0005e+03	0.03
V99G2673C	KDYH	50 ug	-1000	-9.5039e+02	-0.03	-9.4947e+02	0.02	-9.8123e+02	0.38	-9.5866e+02	-0.02
V99G2676C	KDZH	50 ug	-1000	-9.9773e+02	-0.01	-9.9945e+02	-0.03	-1.0111e+03	-0.22	-9.9157e+02	-0.07
V99G2500C	KIX	200 ppm	1								
V99G2503C	KIY	200 ppm	1								
V99G2506C	KIZ	200 ppm	1								
V99H2560C	IYX	0.015/0.035 deg/hr	0	2.2189e-03	0.17	2.7357e-03	0.01	-4.5430e-03	-0.13	-1.5302e-03	-0.11
V99H2563C	IY Y	0.015/0.035 deg/hr	0	3.4314e-03	0.09	9.9686e-03	0.19	3.7771e-03	0.11	9.0584e-03	-0.01
V99H2566C	IY Z	0.015/0.035 deg/hr	0	1.0743e-02	-0.02	1.1656e-02	0.03	1.1690e-02	0.33	2.1370e-02	0.00
V99U2576C	DSX	0.025 deg/hr/g	0	6.4297e-03	0.06	4.9968e-03	-0.06	1.9623e-03	0.08	4.0828e-03	-0.05
V99U2579C	DSZ	0.025 deg/hr/g	0	-3.0503e-03	-0.05	-2.1909e-03	0.03	-2.7649e-03	-0.11	-5.8681e-03	0.03
V99U2570C	DIX	0.025 deg/hr/g	0								
V99U2573C	DIZ	0.025 deg/hr/g	0								
V99U2582C	DOZ	0.025 deg/hr/g	0	-4.4903e-03	0.01	-4.1386e-03	0.01	-5.2449e-03	-0.21	-1.2842e-02	-0.03
V99A2510C	KSX	40/100 PPM	0								
V99A2513C	KSY	40/100 PPM	0								
V99A2516C	KSZ	40/100 PPM	0								
V99H2540C	DELTX	21 arc sec	0								
V99H2543C	DELTX	21 arc sec	0								
V99H2546C	DELTY	21 arc sec	0								
V99H2590C	BXY	60 arc sec	0	-1.5779e-01	0.45	-1.6740e-01	-3.35	-1.6574e-01	-3.31	-1.4965e-01	0.51
V99H2593C	BXZ	60 arc sec	0	-7.1385e-02	0.07	-6.6307e-02	0.10	-6.9245e-02	-1.38	-7.9636e-02	0.02
V99H2596C	BYX	60 arc sec	0	8.6649e-03	-0.41	2.3044e-02	0.29	3.7042e-02	0.74	-3.2634e-02	-0.08
V99H2599C	BYZ	60 arc sec	0	4.3950e-03	-0.21	1.1703e-02	0.15	1.8807e-02	0.38	-1.6560e-02	-0.43
V99H2602C	BZX	60 arc sec	0	4.2438e-02	-0.08	4.3253e-02	0.02	4.0863e-02	0.82	3.3216e-02	-0.46
V99H2605C	BZY	60 arc sec	0								
V99U5870C	DOFX	0.05 deg/hr	0								
V99U5920C	DHX	0.05 deg/hr	0								
V99U5955C	DIX	0.05 deg/hr/g	0								
V99U5958C	DIZ	0.05 deg/hr/g	0								
V99U5961C	DSX	0.05 deg/hr/g	0								
V99U5964C	KDX	4000 ppm	0.891673	8.9727e-01	-0.10	8.9795e-01	0.17	8.9734e-01	1.42	8.9724e-01	0.05
V99U5967C	KDY	4000 ppm	0.452609	4.5511e-01	-0.22	4.5603e-01	0.23	4.5561e-01	0.75	4.5530e-01	0.01
V99U5970C	KDZ	4000 ppm	0.008004	7.3059e-03	-0.10	7.1584e-03	-0.04	7.6741e-03	-0.08	7.7029e-03	0.01

* ATP CRITERIA

Table 4 Prelaunch Sequence Comparisons - Week 4

	DAY 6 RUN 1 (08/20/90)			DAY 6 RUN 2 (08/20/90)		
HAINS/IMU	18 (KT-70)	201 HAINS	202 HAINS	18	201	202
Gyrocompass						
Tilts:						
North	8.1	17.7	7.6	10.7	29.9	137.3
West	5.4	-0.4	-11.1	31.2	54.6	-49.1
Drifts:						
North	-0.0047	0.0122	-0.0024	-0.0012	0.0302	0.1784
West	0.0030	0.0025	-0.0072	0.0396	0.0737	-0.0779
Reslv/Acc:						
North	-47.6	-9.8	7.3	-63.2	-88.6	-4.2
West	-18.1	132.1	-5.1	-11.4	-7.5	-50.4
PHIT-Up:	-13.3	24.9	39.2	23.1	36.9	-2.4
Vel - Tilt						
Tilts:						
North	-10.8	5.6	-6.4	-8.0	20.9	133.1
West	2.9	-2.4	5.5	-23.7	-57.6	60.8
Drifts:						
North	-0.0034	0.0122	-0.0027	0.0006	0.0314	0.1773
West	-0.0068	0.0018	0.0163	-0.0420	-0.0746	0.0703
Reslv/Acc:						
North	-48.3	-34.5	48.7	-57.1	-104.9	122.2
West	-37.1	95.1	39.9	-15.3	-9.7	-23.1
PHIT-Up:	16.1	2.6	4.7	66.9	1.6	7.0
PAD BIAS:	-20.1	11.7	65.3	-9.0	17.5	67.7
Tuned Inert						
Init. Cond.						
Tilts:						
North	17.9	16.9	18.3	16.7	19.3	16.4
West	-0.7	-0.5	-0.2	-5.6	0.7	-3.7
Drifts:						
North	0.0069	0.0015	0.0003	0.0066	0.0030	-0.0017
West	0.0031	-0.0009	0.0004	0.0143	-0.0016	0.0002
Reslv/Acc:						
North	-29.3	-24.0	63.4	-43.4	-101.3	46.9
West	-29.4	45.6	53.3	-22.0	-93.0	11.5
PHIT-Up:	-2.8	5.2	-4.3	62.9	5.2	-3.3
Final Cond.						
Tilts:						
North	13.3	-15.3	35.6	-18.4	106.8	-90.5
West	27.7	7.9	24.2	-71.2	-15.6	-2.6
Drifts:						
North	-0.0079	-0.0034	-0.0010	-0.0031	0.0772	-0.0634
West	0.0136	0.0067	0.0030	0.0559	0.0106	0.0027
Reslv/Acc:						
North	14.4	-31.2	51.9	2.6	-112.1	33.8
West	-54.6	35.8	56.3	-47.6	-115.9	26.1
PHIT-Up:	-22.0	14.8	-10.2	102.3	-36.9	40.8

Effectiveness Of Large Booms As Nutation Dampers For Spin Stabilized Spacecraft

F. O. Eke*

Department of Mechanical,
Aeronautical and Materials Engineering
University of California
Davis, CA 95616

ABSTRACT

This paper discusses the issue of using long slender booms as pendulous nutation damping device on spinning spacecraft. Motivation for this work comes from experience with the Galileo spacecraft, whose magnetometer boom also serves as passive nutation damper for the spacecraft. Performance analysis of a spacecraft system equipped with such a device indicates that the nutation time constant of such systems are relatively insensitive to changes in the damping constant of the device. However, the size and arrangement of such a damper raises important questions concerning spacecraft stability in general.

INTRODUCTION

Most spin stabilized spacecraft are equipped with passive nutation damping devices that limit spacecraft nutation through on-board energy dissipation. The design of these devices is based on well established stability criteria for spinning bodies.¹⁻⁴ When disturbed slightly from its position of stable spin, a spacecraft with internal energy dissipation will recover faster than one without energy

* Assistant Professor

dissipation. This has led to the design of several passive devices that are triggered into dissipating energy on board of a spacecraft anytime that the spacecraft attitude motion is disturbed. Such devices have included simple mass-spring-dashpot systems, damped compound pendulum, viscous fluid in ring-shaped tubes, etc... The Galileo spacecraft features a passive nutation damper that differs markedly from any that has been flown to date. As shown in Fig.1, this dual-spin spacecraft consists essentially of a rotor, carrying a high gain antenna and three long booms, and a stator section that houses a probe and carries the scan platform containing most of the imaging instruments. The rotor is connected to the stator through a spin bearing assembly that allows one degree of freedom of relative motion that is controlled by the "clock" control loop. The ratio of the rotor spin inertia to the vehicle transverse inertia is greater than one (1.4), so that the spacecraft spin axis is also its axis of maximum inertia. The spacecraft's longest boom - its science/magnetometer boom - is also utilized as a passive nutation damper by connecting it to the rotor bus through a one degree of freedom hinge and a torsional spring and damper system, as shown schematically in Fig.2. Although this damper is of the pendulous type, its length (8.6m) far exceeds that of any such damper used in past missions. Furthermore, the mass center of the boom is outboard of its pivot point. This, again, is unusual for pendulum dampers.

In the remaining part of this paper, the effectiveness of this design is explored and compared with that of traditional dampers. This is done essentially by examining the shape of the damper time constant versus damping constant curve as well as by studying the overall attitude dynamics of the spacecraft in the presence of such a large boom.

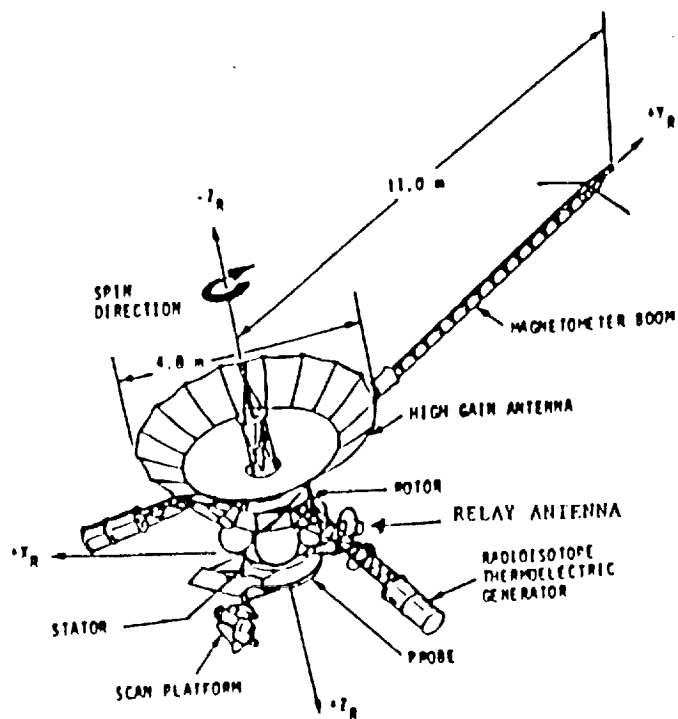


Fig. 1 Galileo Spacecraft

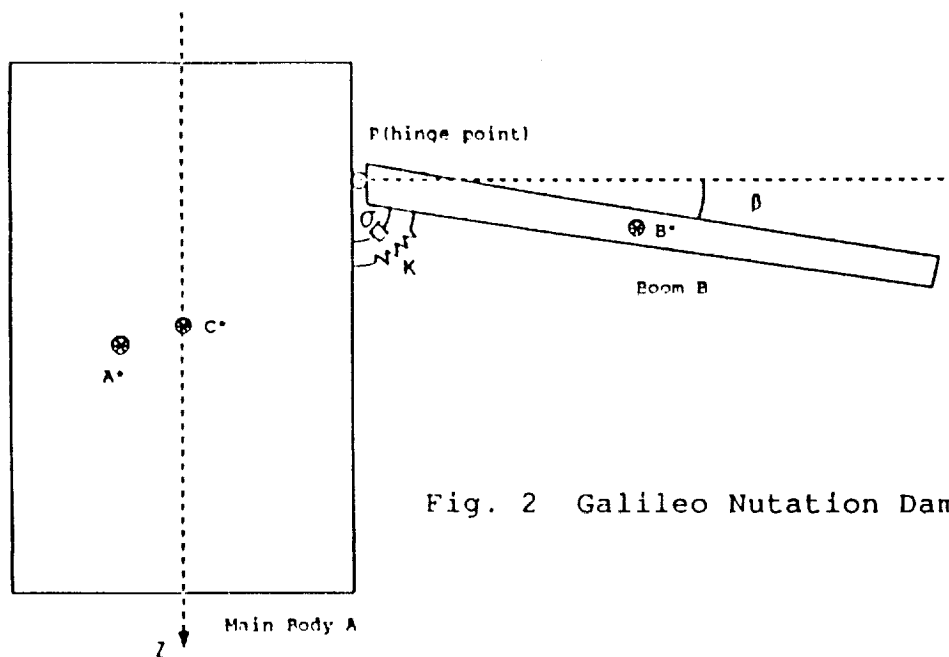


Fig. 2 Galileo Nutation Damper System

EQUATIONS OF ATTITUDE MOTION

To derive the dynamical equations of attitude motion of the spacecraft, the model shown in Fig.3 is used. The dual-spin nature of the spacecraft is ignored, and the system is assumed to be made up of a main rigid body A and a boom B. A^* and B^* are mass centers of A and B respectively, and S^* is the mass center of the combined system. The following simplifications are also made:

- S^* lies on the spin axis Z of the spacecraft and remains fixed in body A at all times;
- A^* , B^* and S^* all lie on a plane containing the Z axis;
- when $\beta = 0$, the central principal axes of the system for S^* are parallel to a_1, a_2 , and a_3 ;
- b_1, b_2, b_3 are parallel to central principal axes of B for B^* , and, for body B, $I_1 = I_3$, while $I_2 = 0$, where I indicates moment of inertia.

The equations of attitude motion of this system, as derived using AUTOLEV^{6,7}, are:

$$\begin{aligned}
 & \left\{ \left[(L_B \sin \beta + z_0)^2 + (L_B \cos \beta + y_0)^2 \right] m_B + (y_A^2 + z_A^2) m_A + (I_1^A + I^B) \right\} \dot{u}_1 + \\
 & \left\{ (L_B \sin \beta + z_0) L_B \sin \beta + (L_B \cos \beta + y_0) L_B \cos \beta \right\} m_B + I^B \dot{u}_4 - \\
 & \left[(u_1 + u_4) L_B \sin \beta + z_0 u_1 \right] u_1 + \\
 & (L_B u_2 \sin \beta - L_B u_3 \cos \beta + z_0 u_2 - y_0 u_3) u_2 + (u_1 + u_4) L_B \sin \beta u_4 \} (L_B \cos \beta + y_0) m_B + \\
 & \{ -[(u_1 + u_4) L_B \cos \beta + y_0 u_1] u_1 + [L_B (u_2 \sin \beta - u_3 \cos \beta) + z_0 u_2 - y_0 u_3] u_3 - \\
 & (u_1 + u_4) L_B \cos \beta u_4 \} (L_B \sin \beta + z_0) m_B - \{ [(z_A u_2 - y_A u_3) u_3 - y_A u_1^2] z_A + \\
 & [(z_A u_2 - y_A u_3) u_2 + z_A u_1^2] y_A \} m_A + (u_2 \cos \beta + u_3 \sin \beta) (u_3 \cos \beta - u_2 \sin \beta) I^B - \\
 & (I_2^A u_2 + I_{23}^A u_3) u_3 + (I_{23}^A u_2 + I_3^A u_3) u_2 = 0
 \end{aligned} \tag{1}$$

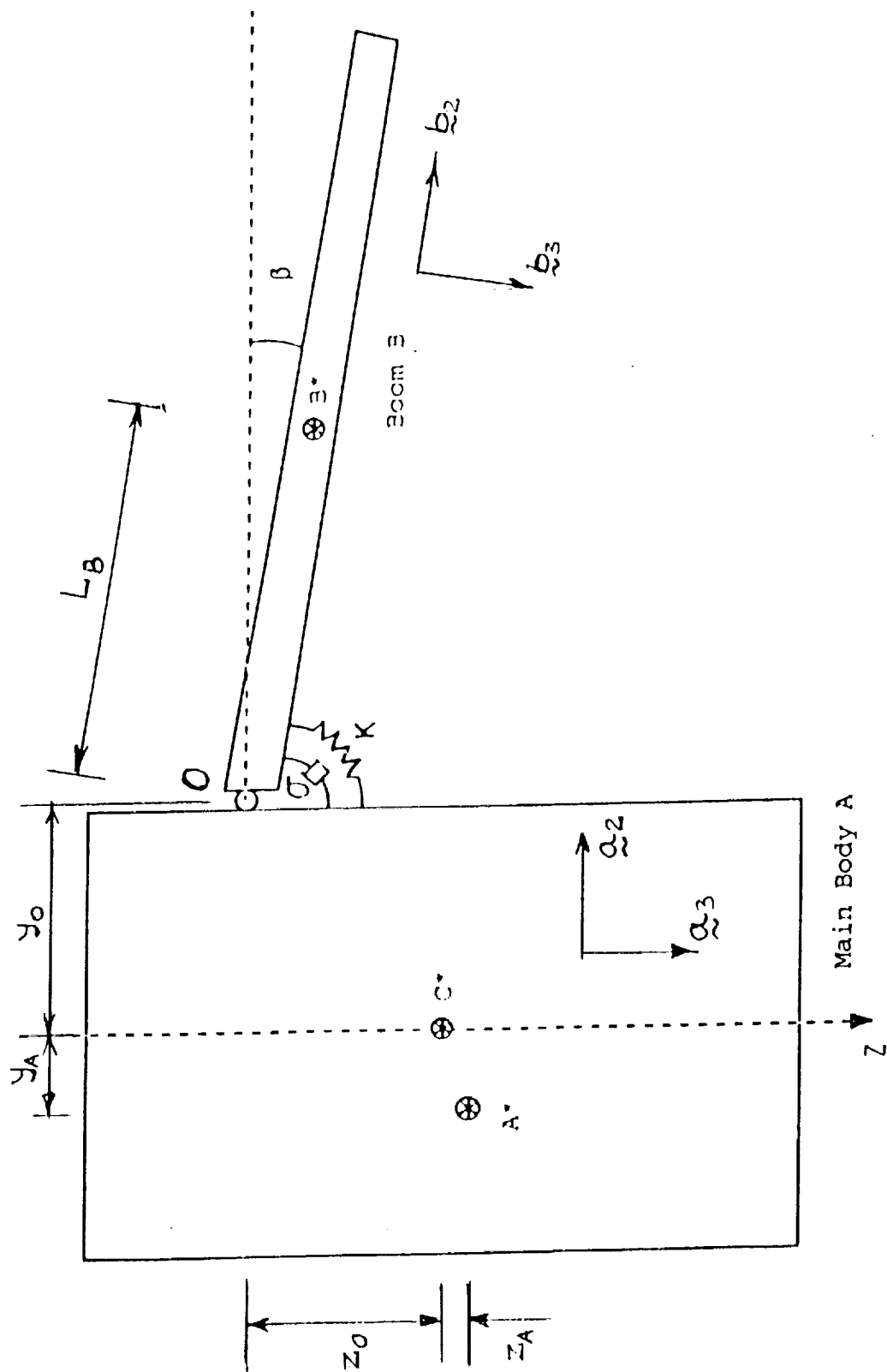


Fig. 3 Spacecraft Model

$$\begin{aligned}
& [(L_B \sin \beta + z_0)^2 m_B + (I_2^A + I^B \sin^2 \beta) + m_A z_A^2] \ddot{u}_2 - \\
& [(L_B \cos \beta + y_0)(L_B \sin \beta + z_0) m_B + I^B \sin \beta \cos \beta - I_{23}^A + m_A y_A z_A] \ddot{u}_3 + \\
& \{[(u_1 + u_4) L_B \cos \beta + y_0 u_1] u_2 + [(u_1 + u_4) L_B \sin \beta + z_0 u_1] u_3 + \\
& (u_2 \cos \beta + u_3 \sin \beta) L_B u_4\} (L_B \sin \beta + z_0) m_B + \{[(u_1 + u_4) u_3 - u_1 u_3] \sin \beta + \\
& [(u_1 + u_4) u_2 - u_1 u_2] \cos \beta\} I^B \sin \beta + (u_2 \cos \beta + u_3 \sin \beta) (u_1 + u_4) I^B \sin \beta - \\
& (I_{23}^A u_2 + I_3^A u_3) u_1 + (y_A u_1 u_2 + z_A u_1 u_3) m_A z_A + I_1^A u_1 u_3 = 0
\end{aligned} \tag{2}$$

$$\begin{aligned}
& [(L_B \cos \beta + y_0)(L_B \sin \beta + z_0) m_B + I^B \sin \beta \cos \beta - I_{23}^A + m_A y_A z_A] \ddot{u}_2 - \\
& [(L_B \cos \beta + y_0)^2 m_B + I^B \cos^2 \beta + I_3^A + m_A y_A^2] \ddot{u}_3 + \\
& \{[(u_1 + u_4) L_B \cos \beta + y_0 u_1] u_2 + [(u_1 + u_4) L_B \sin \beta + z_0 u_1] u_3 - \\
& L_B \cos \beta u_2 u_4 + L_B \sin \beta u_3 u_4\} (L_B \cos \beta + y_0) m_B + \{[(u_1 + u_4) u_3 - u_1 u_3] \cos \beta \sin \beta + \\
& [(u_1 + u_4) u_2 - u_1 u_2] \cos^2 \beta\} I^B + (u_2 \cos \beta + u_3 \sin \beta) (u_1 + u_4) I^B \cos \beta - \\
& (I_{23}^A u_3 + I_2^A u_2) u_1 + (y_A u_1 u_2 + z_A u_1 u_3) m_A y_A + I_1^A u_1 u_2 = 0
\end{aligned} \tag{3}$$

$$\begin{aligned}
& \{[(L_B \sin \beta + z_0) L_B \sin \beta + (L_B \cos \beta + y_0) L_B \cos \beta] m_B + I^B\} \ddot{u}_1 + (I^B + m_B L_B^2) \ddot{u}_4 - \\
& \{[(u_1 + u_4) L_B \sin \beta + z_0 u_1] u_1 + (L_B \sin \beta u_2 - L_B \cos \beta u_3 + z_0 u_2 - y_0 u_3) u_2 + \\
& (u_1 + u_4) L_B \sin \beta u_4\} L_B \cos \beta - \{[(u_1 + u_4) L_B \cos \beta + y_0 u_1] u_1 - \\
& (-L_B u_3 \cos \beta + L_B u_2 \sin \beta + z_0 u_2 - y_0 u_3) u_3 + \\
& (u_1 + u_4) L_B \cos \beta u_4\} L_B \sin \beta\} m_B + (u_2 \cos \beta + u_3 \sin \beta) (u_3 \cos \beta - u_2 \sin \beta) I^B + \\
& k \beta + \sigma u_4 = 0
\end{aligned} \tag{4}$$

where u_i ($i = 1, 2, 3$) are the components of the angular velocity of A along a_i , $u_4 = \beta$, m represents mass, I represents moment of inertia, k is spring stiffness, σ is damping constant, and the dimensions y_0, z_0, y_A, z_A, L_B are as shown in Fig.3.

NUTATION DAMPER TIME CONSTANT

A known equilibrium point of the system corresponds to the pure spin condition. That is the solution

$$u_1 = u_2 = 0, \quad u_3 = \Omega \text{ (const.)}, \quad u_4 = 0, \text{ and } \beta = 0.$$

This solution does satisfy Eqs.(1-4) provided that

$$I_{23}^A = m_A z_A y_A + m_B z_0 (L_B + y_0) \quad (5)$$

a condition that is indeed satisfied by the inertia related simplifying assumptions given earlier. When the full nonlinear dynamical equations given as Eqs(1-4) are linearized about the pure spin solution, the result is a set of first order differential equations that has the form

$$B \dot{x}^T = A x^T \quad (6)$$

where

$$x = [u_1 \ u_2 \ u_4 \ \beta] \quad (7)$$

and A and B are 4 by 4 matrices with the following elements:

$$A_{11} = A_{13} = A_{22} = A_{23} = A_{24} = A_{31} = A_{41} = A_{42} = A_{44} = 0 \quad (8)$$

$$A_{12} = [m_B (L_B + y_0)^2 + m_A (y_A^2 - z_A^2) + I^B - I_2^A + I_3^A] \Omega \quad (9)$$

$$A_{14} = -[I^B + m_B L_B (L_B + y_0)] \Omega^2 \quad (10)$$

$$A_{21} = -[I_1^A - I_3^A m_A z_A^2 + m_B z_0^2] \Omega \quad (11)$$

$$A_{32} = -[I^B + m_B L_B (L_B + y_0)] \Omega \quad (12)$$

$$A_{33} = -\sigma, \quad A_{43} = 1 \quad (13)$$

$$A_{34} = -[m_B L_B (L_B + y_0) \Omega^2 + k] \quad (14)$$

$$B_{11} = \{I_1^A + I^B + m_A (y_A^2 + z_A^2) + m_B [(L_B + y_0)^2 + z_0^2]\} \quad (15)$$

$$B_{12} = B_{14} = B_{21} = B_{23} = B_{24} = B_{32} = B_{34} = B_{41} = B_{42} = B_{43} = 0 \quad (16)$$

$$B_{13} = [I^B + m_B L_B (L_B + y_0)] \quad (17)$$

$$B_{22} = [I_2^A + m_A z_A^2 + m_B z_0^2] \quad (18)$$

$$B_{31} = [I^B + m_B L_B (L_B + y_0)] \quad (19)$$

$$B_{33} = I^B + m_B L_B^2 \quad (20)$$

$$B_{44} = 1 \quad (21)$$

The eigenvalues of the matrices A and B are found to have negative real parts for inertia property values corresponding to all mission phases of the spacecraft. Hence, the pure spin solution is a stable solution. The nutation angle time constant is the negative reciprocal of the eigenvalue corresponding to u_1 or u_2 .

RESULTS

Fig. 4 shows Galileo's nutation angle time constant plotted against the damping constant of the passive nutation damping device on board. The case shown corresponds to a damper spring stiffness of 335 N.m/rad, and spacecraft inertia property values near the beginning of the mission.

Two important facts emerge from this plot. First, there is an optimum damping constant corresponding to a given spring stiffness. The most remarkable thing about the curve shown is the fact that it is so flat; especially near the

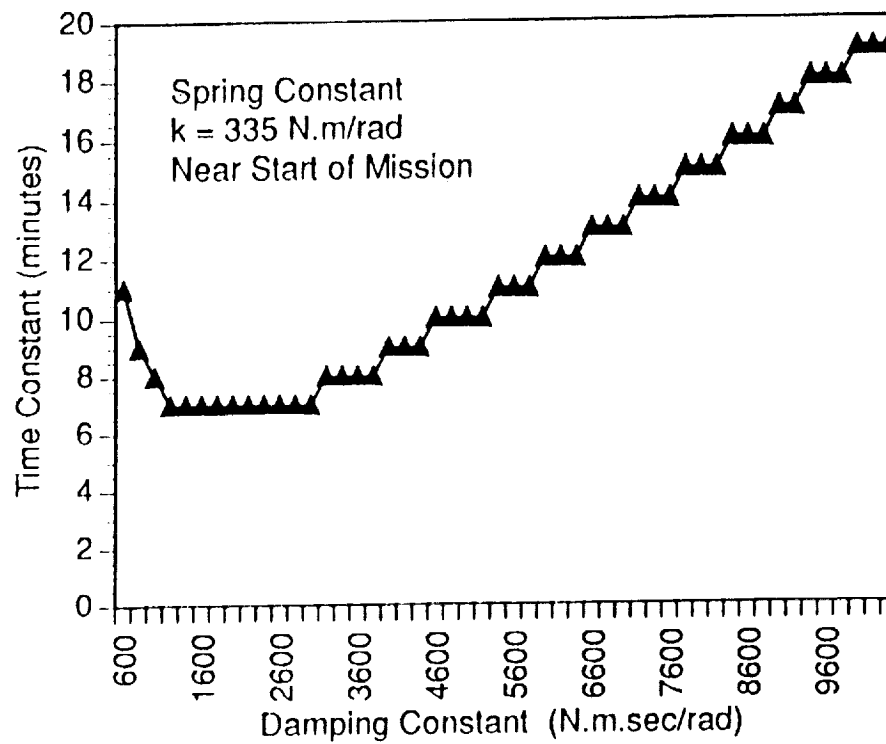


Fig. 4 Time Constant Vs. Damping Constant

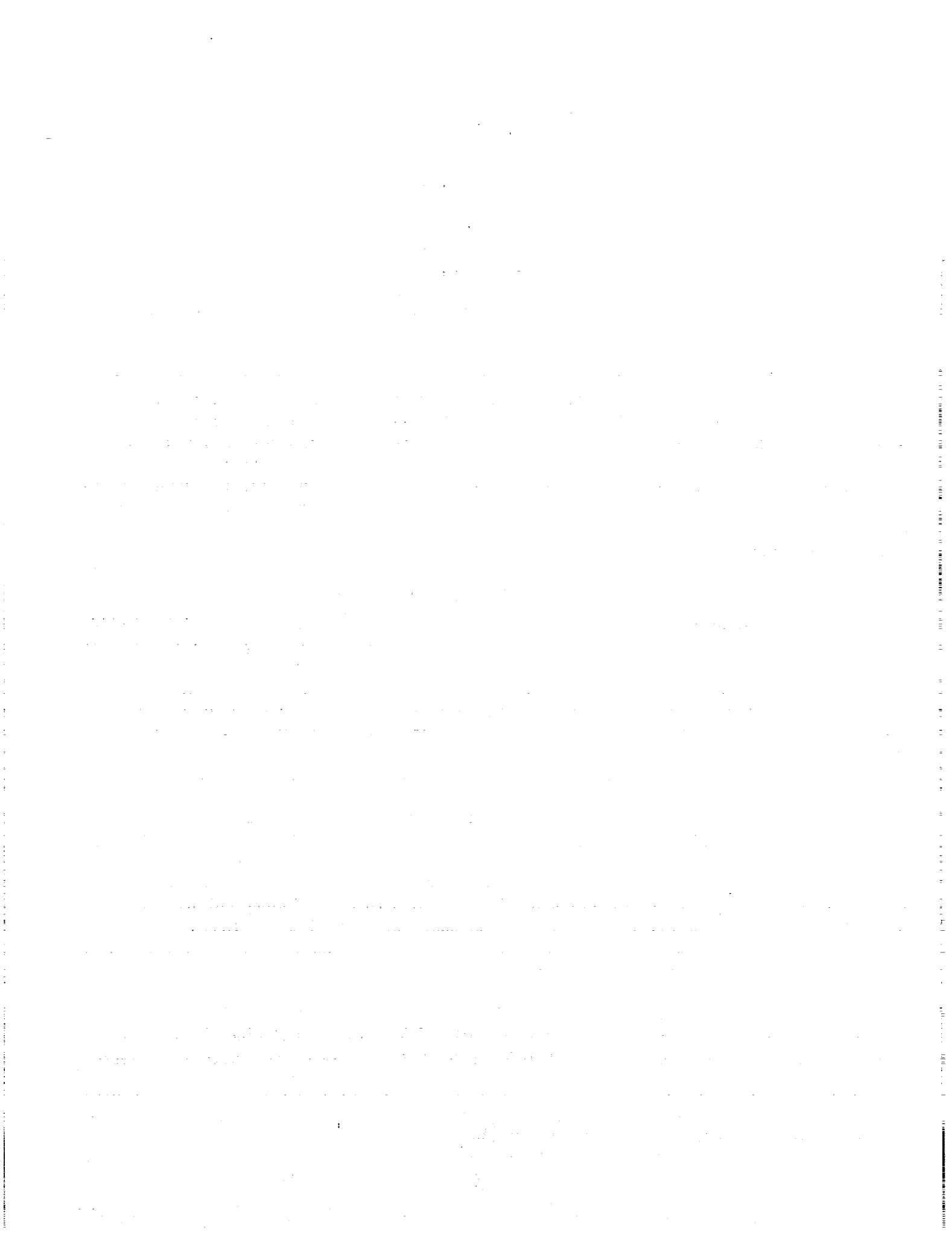
minimum time constant value. This means that there is a wide range of values of σ for which the time constant changes very little. This result is in great contrast with what obtains for traditional passive dampers, where such plots are not flat at all, and "tuning" of the damper is almost always a necessity if one desires reasonably small time constants. This relative insensitivity of the time constant to σ is particularly appropriate for interplanetary missions. This is because the viscosity of damper fluids is generally very sensitive to temperature, and, therefore, the damping constant can be expected to vary widely during a long interplanetary flight that takes a spacecraft through varied environments. It is thus advantageous to have a damper, whose performance will not be degraded by the inevitable fluctuations in damper fluid viscosity.

CONCLUSION

As exemplified by the design and performance analysis of the Galileo passive damper system, the use of long booms as nutation damper for spin stabilized spacecraft introduces a new and important advantage over traditional damping devices. It renders the system nutation angle time constant practically insensitive to the device damping constant, thereby drastically reducing the need for "tuning" of such dampers. The main disadvantage of such a large device is that it becomes an important factor in spacecraft stability. Furthermore, because of the small relative damper displacements that are to be expected from this design, factors such as stiction become important in the evaluation of the damper's performance, and may impose thresholds on the amount of nutation that can be damped out.

REFERENCES

1. Likins, P. W., "Attitude Stability Criteria for Dual-Spin Spacecraft," J. Spacecraft and Rockets, 4 (No. 12), (1967).
2. Mingori, D. L., "Effects of Energy Dissipation on the Attitude Stability of Dual-Spin Satellites," AIAA J., 7 (no. 1), (1969).
3. Auelmann, R. R., and Lane, P. T., "Design and Analysis of Ball-in-Tube Nutation Dampers," Proc. of the Symposium on Attitude Stabilization and Control of Dual-Spin Spacecraft, 1968..
4. Bainum, P. M., Fuechsel, P. G., and Mackison, D. L., "Motion and Stability of a Dual-Spin Satellite with Nutation Damping," J. Spacecraft and Rockets, 7 (No. 6), (1970).
5. Yeates, C. M. and Clarke, T. C., "The Galileo Mission to Jupiter," Astronomy, 10 (No. 1), 1982.
6. Schaechter, D. B. and Levinson, D. A., "Interactive Computerized Symbolic Dynamics for the Dynamicist," J. of the Astronautical Sciences, 36 (No. 4), 1988.
7. Levinson, D. A. and Kane, T. R., "AUTOLEV - A New Approach to Multibody Dynamics," Multibody Systems Handbook, Springer Verlag, Berlin, 1990.



AN ANALYSIS OF THE HUBBLE SPACE TELESCOPE FINE GUIDANCE SENSOR FINE LOCK MODE*

L. G. Taff

Space Telescope Science Institute
3700 San Martin Drive
Baltimore, MD 21218

ABSTRACT

There are two guiding modes of the Hubble Space Telescope used for the acquisition of astronomical data by one of its six scientific instruments. The more precise one is called Fine Lock. Command and control problems in the on-board electronics has limited Fine Lock to brighter stars, $V < 13.0$ mag, instead of fulfilling its goal of $V = 14.5$ mag. Consequently, the less precise guiding mode of Coarse Track (~ 40 milli-arc seconds) has to be used fairly frequently. Indeed, almost half of the celestial hemisphere has stars too faint to support a Fine Lock guidance mode. Hence, some of the scientific observations to have been made with the Hubble Space Telescope will be compromised. In this paper I report on the only realistic or extensive simulations of the Fine Lock guidance mode. The theoretical analysis underlying the Monte Carlo experiments and the numerical computations clearly show both that the control electronics are severely under-engineered and how to adjust the various control parameters to successfully extend Fine Lock guiding performance back to $V = 14.0$ mag and sometimes beyond.

1. INTRODUCTION

This paper is complementary to Taff (1990a) in which the Coarse Track mode of the Hubble Space Telescope Fine Guidance Sensors was analyzed. The motivation for that paper was the desire to considerably shorten Guide Star acquisition times—thereby significantly enhancing the efficiency of Hubble Space Telescope operations—without a loss of scientific information. The key issue was a realistic estimate of the Coarse Track guiding mode pointing stability, methods to improve upon it, and whether or not this level of pointing stability would compromise the scientific content of some Hubble Space Telescope observations.

The real Optical Telescope Assembly—because of manufacturing errors, wavefront calibration analysis errors, and the tilt and decenter of the secondary mirror—is seriously degrading the guiding performance of the Fine Guidance Sensors. Instead of a 17–20 milli-arc second Coarse Track pointing precision, we more typically experience a 40 milli-arc second (mas) pointing instability. Instead of Fine Lock to $V = 14.5$ mag, operationally successful Fine Lock stops at $V = 13.0$ mag. The implication of a thirteenth magnitude Fine Lock limit is, in effect, no Hubble Space Telescope observations, with Fine Lock, beyond a galactic latitude limit of $|b| = 30^\circ$. This means excluding half of the celestial hemisphere and most of the extra-galactic part of the sky. Thus, a complete investigation of the Fine Lock algorithm was undertaken in an attempt to rapidly make the maximum improvements. This paper summarizes that effort.

The next section of the main text addresses the limiting magnitude issue in more depth. With a clearer understanding of the importance of the Fine Lock limiting magnitude, I then briefly review the Fine Guidance Sensor electro-optical system (§3) and the principles of Fine Guidance Sensor guidance operation (§4). Section 5 summarizes a theoretical analysis of Fine Lock and extensive

* Based on observations with the NASA/ESA Hubble Space Telescope, obtained at the Space Telescope Science Institute, which is operated by the Association of Universities for Research in Astronomy, Inc., under NASA contract NAS5-26555.

computer simulations of Fine Lock. The latter are based on empirical Fine Guidance Sensor Transfer Functions.

2. GUIDE STAR PHOTOMETRIC STATISTICS

The operational problem faced during the latter half of 1990 was the unreliability of the Fine Lock process of the Hubble Space Telescope (HST) Fine Guidance Sensors (FGSs) operating under the Pointing Control System.¹ Without now going into the detail which will be provided in Section 4, the Fine Lock mode is the ultimate in the control of the spacecraft. The successful attainment and maintenance of this state is crucial for reaching some of the scientific goals of the HST mission for only with the pointing stability of Fine Lock (~ 7 milli-arc seconds) can some of the instrumental modes function optimally. This became even more important when the spherical aberration in the primary mirror degraded the pointing stability of the Coarse Track mode by a factor of two, from ~ 20 milli-arc seconds to ~ 40 mas. The Guide Star Catalog, a catalog of stars from which guiding targets for the FGSs are to be chosen, typically reaches $V = 14.5$ mag for this was the specified limit of a successfully achieved and maintained Fine Lock state. Unfortunately, the real performance of the hardware and Perkin-Elmer Corp.'s utilization of it limited a stable Fine Lock state to $V < 13.0$ mag and Fine Lock was routinely unobtainable beyond $V = 13.0$ mag. These poor results, the improvement of which is the main subject of this paper, would have placed severe limitations on the scientific operational capabilities of the HST.

To understand how a significantly brighter limiting magnitude for Guide Stars affects the scientific mission of the HST we must understand how the Guide Star Catalog was created. The stellar density goals were ~ 500 stars per square degree, uniformly over the entire celestial sphere, to a fixed limiting magnitude. Our location in the Milky Way, the spiral nature of the Galaxy, and the underlying galactic luminosity distribution all conspire to prevent one from attaining this goal. As the constructors of the Guide Star Catalog moved towards the galactic poles they were forced to go fainter and fainter to maintain a constant stellar density. Not knowing, in advance, where the General Observers who would use the HST might want to point it, allowance had to be made for all-sky coverage with a uniform areal density. The apparent magnitude distributions for three galactic latitudes are shown in Fig. 1 wherein the faintward shift at higher galactic latitudes can be seen. However, since the Guide Star Catalog is not a complete catalog, the limiting magnitude does not decrease as rapidly with increasing absolute value of galactic latitude as the true stellar density decreases. Figure 2 provides an integrated (over galactic latitude) apparent magnitude distribution for the entire Guide Star Catalog. There is a displacement of ~ 0.6 mag between the two celestial hemispheres because of a color term between the $\sim V$ sensitivity of the northern hemisphere Schmidt plates and the $\sim J$ sensitivity of the southern hemisphere Schmidt plates used to construct the Guide Star Catalog.

To achieve Fine Lock in two of the three FGSs, which is what is necessary for the Pointing Control System to be satisfied, we require two stars brighter than the limiting magnitude of Fine Lock guidance. If, instead of being able to avail ourselves of the full $V = 14.5$ mag limit of the Guide Star Catalog we are forced to retreat to $V = 13.0$ mag, then the *a priori* probability of being able to achieve Fine Lock—solely because of the lack of suitable Guide Stars—drops to 0.44 of the nominal level. Moreover, almost all the lost portion of the celestial sphere is beyond 30° from the galactic equator. An increase in the improvement in the Fine Lock guiding process to $V = 13.5$ mag raises this probability to 0.60. Thus, the rate at which sky coverage is regained is a slowly varying function

¹ The Pointing Control System logic implemented by Lockheed Missiles Corp. discards three-quarters of the photons acquired by the telescope. This egregious procedure reduces the effective limiting magnitude by 1.5 mag from the one otherwise attainable. This represents a separate, additional problem not dealt with herein.

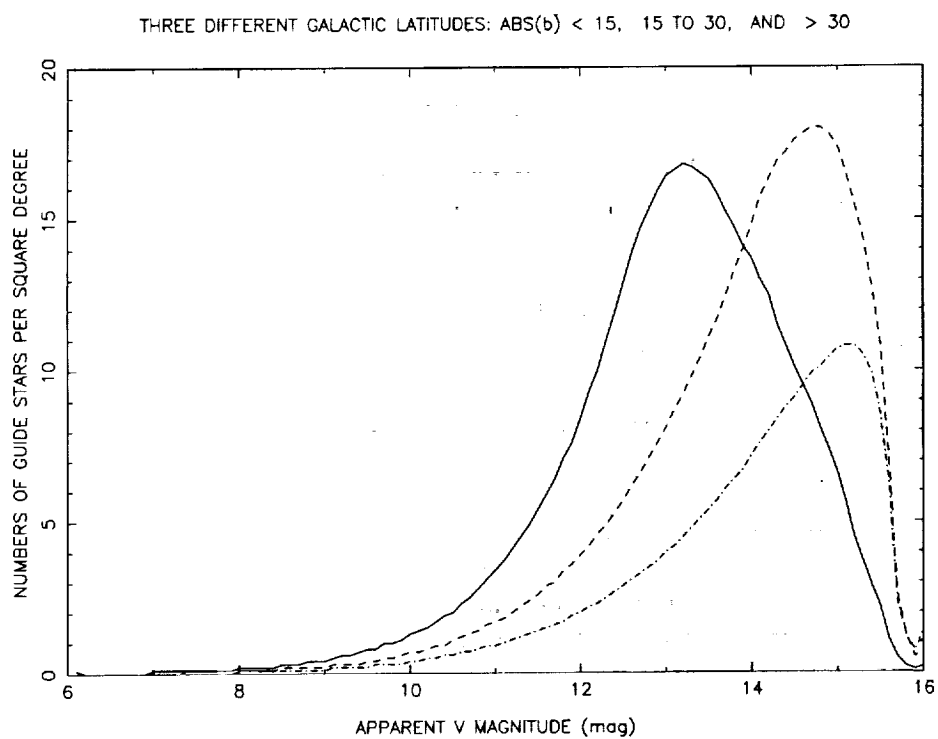


Figure 1. Guide Star Catalog number distributions vs. apparent magnitude at three galactic latitudes.

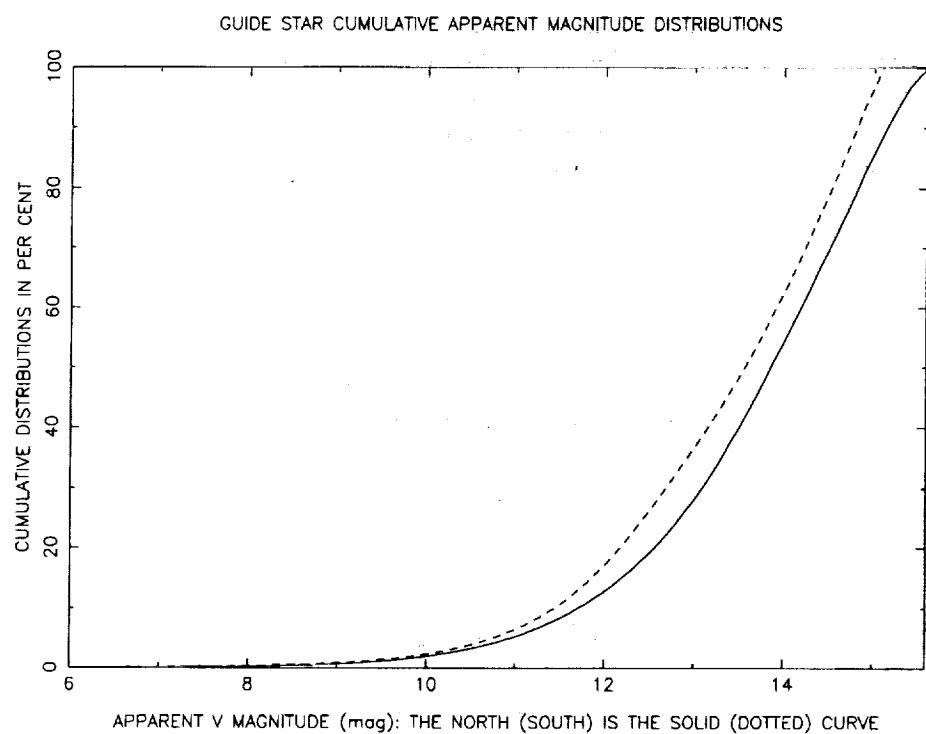


Figure 2. Guide Star Catalog cumulative numbers vs. apparent magnitude.

of the limiting magnitude primarily because the current limiting magnitude is so bright. Finally, retrieving $V = 14.0$ mag performance, as I suggest can be routinely done, brings us back to 79% of the $V = 14.5$ mag level.

3. THE DESIGN AND FUNCTIONING OF AN FGS

3.1 Optical System

The optical train of a Fine Guidance Sensor (FGS) is displayed in Fig. 3 (see also Taff 1990b). The Optical Telescope Assembly (OTA) system of the HST is a Ritchey-Chretien Cassegrain design. Before the prime focus of the OTA is a plane pickoff mirror which deflects light into the FGS. The FGS total field-of-view is defined by this mirror. Light diverging from the pickoff mirror hits an off-axis aspheric mirror which nearly collimates the beam. A collimated beam is required for sensing wavefront tilt at the Koester's prism (see below). The beam then travels to the first "Star Selector" known as Star Selector A. It rotates about its optical shaft encoder axis; the angle of rotation is denoted by θ_A .

A ray striking Star Selector A, parallel to its rotation axis, will be (nominally) deviated by 406.2 arc minutes. Star Selector A acts in concert with a second star selector, B (whose rotation angle is θ_B). It too accomplishes a (nominal) 6.77 degree deviation. Together they move the $5'' \times 5''$ instantaneous field-of-view of an FGS about its total field-of-view.

In between the two star selectors is a five element corrector group; this corrector group is placed just before the first pupil and its function is to provide better collimation. Also, this refractive group corrects for field curvature and astigmatism (which are characteristics of the Ritchey-Chretien design of the OTA). In addition, it corrects for *design* spherical aberration, coma, and the small amounts of astigmatism found in the collimating asphere. (The corrector group rotates with Star Selector A as one mechanical assembly.) The corrector group does *not* correct for the mis-shapen primary mirror *nor* does it correct for improper tilt or decenter of the secondary mirror *nor* for mechanical displacements of FGS optical components.

The polarizing beam splitter after the filter wheel divides the light into two equal intensity beams in mutually orthogonal directions. Each beam is also plane polarized. Two beams—hence two Koester's prisms—are required since a Koester's prism only senses wavefront tilt in one axis. The light bundle is next incident onto the face of a Koester's prism. Within the prism it is divided by a dielectric beam splitter which performs a wavefront division of the incident ray. These two channels are denoted by A and B. The dielectric coating retards the transmitted beam by a quarter of a wavelength while the reflected light is unaffected.

Located beyond the Koester's prism is a set of duplex reimaging optics, one for the A and one for the B channels. The first part of each unit, the doublet, images the star onto the field stop. The lens/field stop assembly is located in the back focal plane of the doublet. The lens produces the pupil image on the sensitive surface of the photocathode tube. The $5''$ by $5''$ (object space) field stop provides the boundaries for the FGS instantaneous field-of-view. There is a photomultiplier tube for each channel of each Koester's prism, hence, four photomultiplier tubes reside in each FGS. The response of the photomultiplier tube is similar to that of the S-20 tube.

3.2 The FGS Transfer Function and the Fine Error Signal

3.2.1 The Transfer Function

Before discussing the algorithms contained in the Fine Guidance Electronics (FGE), it is important to describe the FGS Transfer Function. Figure 4 shows two situations. In the top picture there exists zero tilt in the wavefront at the face of the prism. That is, a combination of re-positioning the spacecraft and the Star Selectors has placed the target Guide Star onto the combined optical axis. Therefore, each photomultiplier tube for this prism senses the same amount of light. In the

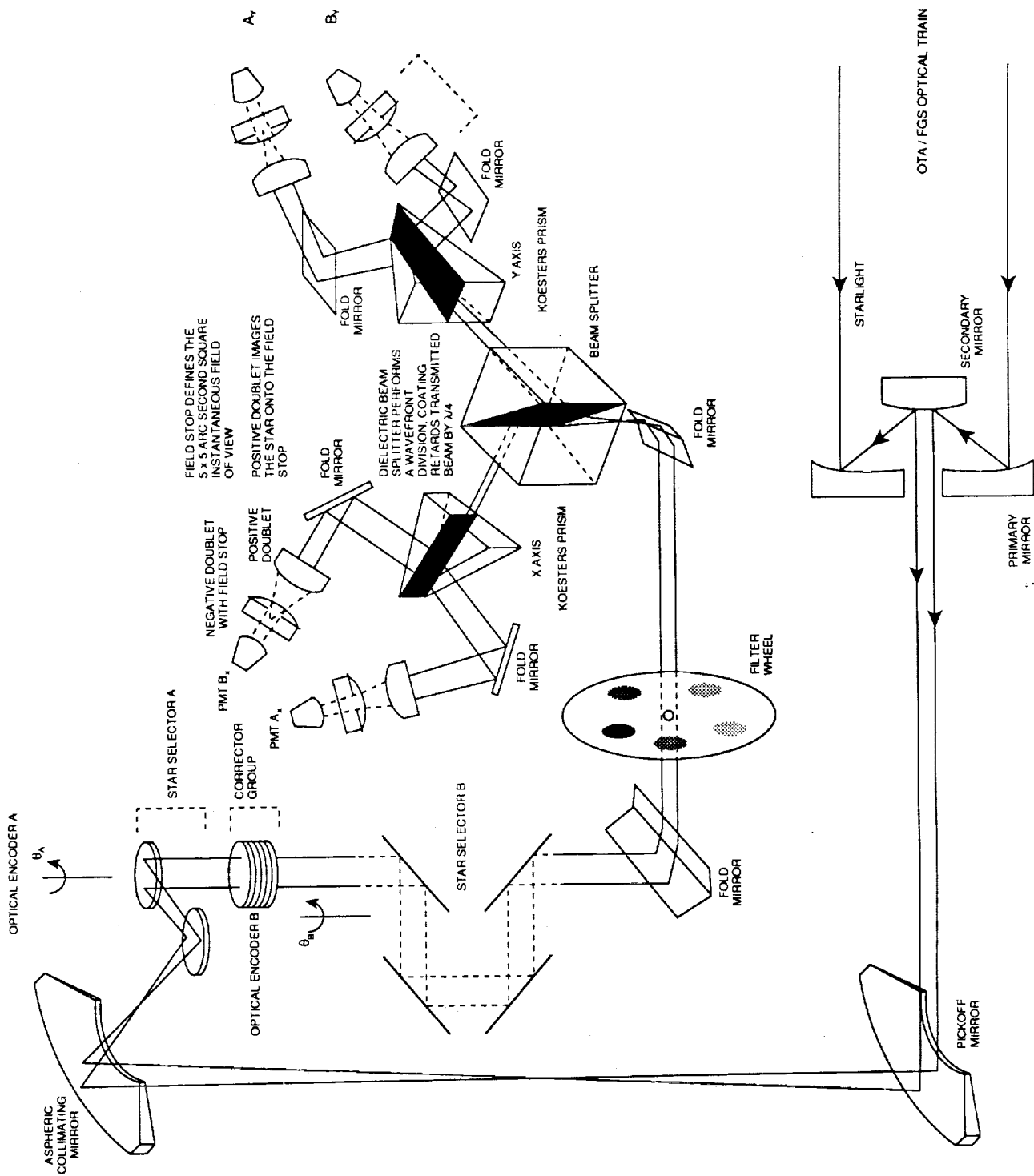


Figure 3. FGS Optical Train Schematic.

lower part of the figure the wavefront has a quarter wave tilt. As the beam exits the left side of the Koester's prism constructive interference occurs. (The wavefront which is transmitted through the beam splitter is additionally retarded by $\lambda/4$.) The right side will experience destructive interference. Hence, the counts for the left side photomultiplier tube are greater than those in the right side photomultiplier tube. A graph of the counts versus tilt angle is known as the Transfer Function (TF). See Fig. 5.

In more mathematical detail, for a monochromatic ray of light with angular frequency ω , the resultant of one component of its electromagnetic field will be of the form

$$I \cos(\omega t - \phi) + I \cos\left(\omega t - \phi + \frac{\pi}{2}\right) = 2I \cos \frac{\pi}{4} \cos\left(\omega t - \phi + \frac{\pi}{4}\right)$$

where ϕ is the initial phase. The resultant intensity is proportional to $2I^2$. More generally, with some angle of incidence of the ray normal with respect to the Koester's prism face of θ at a distance r out from the optical axis, the resultant component of the electromagnetic field has the form

$$I \cos(\omega t - \phi + 2\pi\delta_{L,R}\theta r/\lambda) + I \cos\left(\omega t - \phi + 2\pi\delta_{L,R}\theta r/\lambda + \frac{\pi}{2}\right).$$

The wavelength associated with ω is λ and $\delta_{L,R}$ is ± 1 depending on whether the ray passed through the lefthand or righthand side face of the Koester's prism. Ignoring the temporal modulation, the net energy is proportional to

$$E_{L,R} = 2I^2 \cos^2\left(2\pi\delta_{L,R}\theta r/\lambda + \frac{\pi}{4}\right).$$

The FGE combines the counts from the A and B channels of the Koesters prism to form the TF (see Fig. 5). That is,

$$S = \frac{A - B}{A + B} \quad (1)$$

in which A and B are the counts in the A and B channels. In terms of $E_{L,R}$, A and B are proportional to

$$e_{L,R} = \int_0^R 2I^2 \cos^2\left(2\pi\delta_{L,R}\theta r/\lambda + \frac{\pi}{4}\right) dr = \int_0^R E_{L,R} dr$$

where R is the radius of the primary mirror. Thus,

$$S = \frac{e_L - e_R}{e_L + e_R} = \sin^2 z/z, \quad z = 2\pi\theta R/\lambda. \quad (2)$$

This is the Green's function for the FGS optical system and we may build up a theoretical TF by integrating it over a hypothetical stellar spectrum, angular disc with limb darkening, actual photomultiplier responsivity, and so on (see Taff 1991).

3.2.2 Fine Error Signal

Once the FGS is locked onto a star, the Fine Error Signal is used to update the Star Selector positions so that the wavefront maintains zero tilt at the face of the Koester's prism. This process maintains the high precision pointing required for HST guiding. As can be seen from Fig. 5, the core part of the TF is approximately linear from -10 to $+10$ mas. While the slope of the TF does change with stellar color index, this does not represent a significant variation.

The Fine Error Signal is defined in the FGE as

$$R_x = K_{1x} * S_x + K_{0x}, \quad R_y = K_{1y} * S_y + K_{0y} \quad (3)$$

where S_x and S_y are the FGE TFs for the x and y axes ala Eq. (1). K_{1x} and K_{1y} are the signal gains for each axis and are dependent upon stellar magnitude and background brightness [see Eq. (10)].

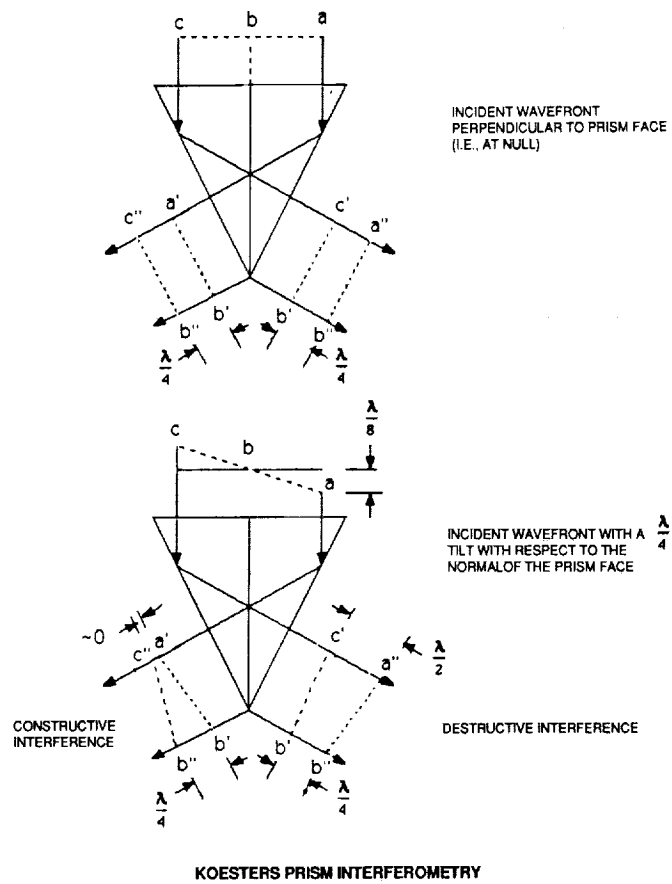


Figure 4. Koester's prism interferometry without wavefront tilt (top) and with $\lambda/4$ tilt (bottom).

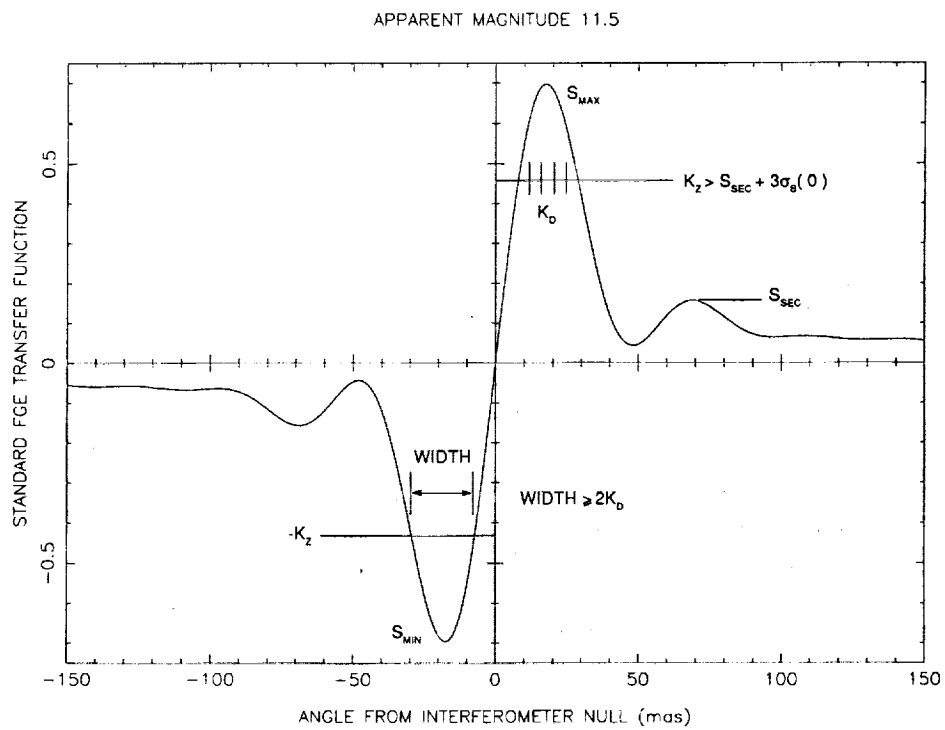


Figure 5. Theoretical Transfer Function (TF).

K_{0x} and K_{0y} are offsets whose initial purpose should be the equalization of the probability of a successful threshold detection whether one approaches the null of the interferometer from the left or the right [see Eq. (11)]. Values for these, and other, parameters can be changed via uplink telemetry.

The 'FGE Transfer Function' differs from that in Eq. (1) in two respects. First, to reduce sensitivity to photon noise, a mean value of $A + B$ is used to normalize S . This average is taken over the first sixteen samples after the Coarse Track phase has successfully terminated and just before the commencement of the 'walkdown' (the walkdown is described in §4.3). In addition, the mean, over these same 16 samples, of $A - B$ is computed, call it Δ_{AB} , and subtracted from the numerator of S in Eq. (1), as in Eq. (4) below. This adjusts for any A vs. B photomultiplier tube bias.

4. FGS GUIDANCE OPERATION

4.1 Search Mode

Search mode is entered into when the spacecraft's main computer issues a Search/Track "On" command to the Fine Guidance Electronics (FGE). The FGE will generate the appropriate Star Selector servo commands, at a 40 hertz rate, to move the $5'' \times 5''$ instantaneous field-of-view of the FGS in an outward spiral (there is nominally a 30% overlap in coverage from one spiral line to the next). The purpose of Search mode is to search for a specific target (*i.e.*, the Guide Star in this scenario). Success is based upon the photomultiplier tube count rate exceeding a lower limit threshold.

4.2 Coarse Track Mode

Once the target Guide Star has been detected in Search mode, the FGE will command the Star Selectors such that the instantaneous field-of-view will circle about the target at a once per second rate. The nominal nutation circle radius is 2.706 arc seconds; the number of nutations is variable. The FGE algorithm for Coarse Track updates the position of that center every 25 milliseconds nominally for 12 complete circuits (although only every fourth sample is accepted by the Pointing Control System; there is no integration). Coarse Track produces an error signal based on the combined photomultiplier tube counts it senses in each of the four quadrants of the nutation circle (see Taff 1990a for a fuller explanation). This signal then produces a new estimate for the center of nutation. The objectives of Coarse Track are to stabilize the still-drifting spacecraft (after a slew) and to determine the star's position to approximately 20 mas. Then a transition-stage, known as the 'walkdown', is used to reach the Fine Lock state.

4.3 Fine Lock Mode

The geometry of the approach to Fine Lock mode is shown in Fig. 6. The orthogonal intersection of the interferometers is commanded to a position K_B arc seconds away from the target position (and midway in between them) which was determined in Coarse Track. Thus, approach can only occur along a diagonal and there is no provision for anisotropy (*e.g.*, a K_{bx} and a K_{by}). The star selector encoders will be commanded by the FGE to approach the target position in at most K_5 steps, with each step being K_D arc seconds in length (no K_{dx} nor K_{dy}). The process of stepping down to the star colloquially referred to as the 'walkdown.'

The number of walkdown steps may vary up to 765. The nominal walkdown step size was 0.009 arc seconds (it is now 6.5 mas). When the target Guide Star is "detected" in one of the interferometer axes, the step size for that axis is halved to prevent overshoot. Detection occurs when the interferometer signal exceeds a predetermined threshold (K_Z ; no K_{zx} nor K_{zy}) for three consecutive 0.025 second samples (this is colloquially referred to as the 'three-hit algorithm'). Once a Guide Star is acquired, then the FGE control system will position the Star Selectors such that it will be simultaneously maintained in the linear region (at or near the null) of the interferometer axes (Sec. 3.2.2).

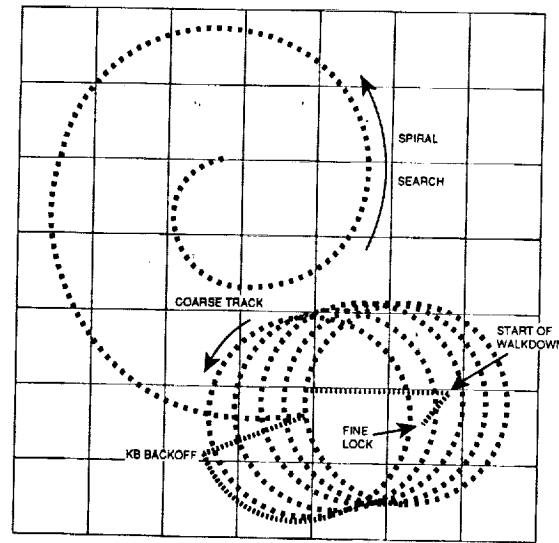


Figure 6. Schematic Coarse Track/Fine Lock Process

4.4 Discussion

To obtain the Fine Lock state on both axes of the two orthogonal Koester's prisms there are seven parameters available to us. (There should be at least two sets of seven for minimal flexibility.) The septuplet consists of K_5 (or K_B ; $K_5 K_D = K_B / \sqrt{2}$), K_D , K_Z , K_{1x} and K_{1y} , and K_{0x} and K_{0y} . After defining these parameters and illustrating the role(s) they play in the Fine Lock process, I provide a theoretical analysis of maximizing the probability of reaching the Fine Lock state. Note that being in the Fine Lock state as far as the FGE is concerned refers to a successful passage through the 'three-hit' algorithm. It does not necessarily say anything regarding the location of the Guide Star with respect to the optical axis. For instance, on a faint Guide Star we might 'lock' onto noise with the star still far away from the interferometer null(s). (This has, in fact, happened with the real FGSs.) Whenever the 'three-hit' algorithm is satisfied, the Fine Lock condition, in the sense that the relevant flag in the FGE is reset, is established.

Remembering the general discussion of FGS operations (for guidance) given above, after the Coarse Track state has been maintained for K_Y (~ 12) circuits of the nutation circle the position of the photocenter has been reliably ascertained and the spacecraft drift stabilized. The FGE then commands the star selector servos to place the star a certain distance away from the photocenter's location (*i.e.*, the backoff distance K_B) and at an orientation 45° with respect to the interferometer axes. (An orientation of 225° is also possible.) Once at this point we commence the 'walkdown' process towards the photocenter and, if we are successful at passing the 'three-hit' algorithm, an eventual Fine Lock state. K_5 is the maximum number of steps that can be taken on the 'walkdown'. K_5 must be large enough to ensure that we can pass through both the Transfer Function extrema. Because of the reduction of the step size once the threshold test has been successfully passed (by 50%, see the K_D discussion below), K_5 must be larger than (total distance to the other side of the

Transfer Function)/(step size/2). (Any bias between the Coarse Track photocenter position and the interferometer null positions should have been incorporated into the original offset from the Coarse Track photocenter position, *i.e.*, in K_B . Such a systematic difference could arise for a number of reasons not dealt with herein. These causes need not maintain—and indeed have not maintained—symmetry with respect to the x and y axes. Therefore, there should have been provision for a K_{5x} and a K_{5y} as well as a K_{bx} and K_{by} .)

You might wonder at the need for a K_5 at all. Given that the Coarse Track/Fine Lock offset vector has been well-determined (which is not yet the case at the beginning of 1991), we might adjust the Coarse Track backoff from the interferometer nulls to be between the two maxima (or minima for the other polarity) of the TF. This is the place marked S_{SEC} in Fig. 5. Even if this were done we still need a maximum number of attempts at passing the ‘three-hit’ algorithm else we might never exit from the ‘walkdown’ state. Claiming that this is a Guide Star, and that therefore something is known regarding the star’s surroundings and its apparent V magnitude, does not vitiate the argument. The photometric precision of the Guide Star Catalog is only ± 0.4 mag and there is a color term between the northern and southern celestial hemispheres [*i.e.*, $J = V + 0.72(B - V)$]. This has been adjusted for, on the average, by assuming that the typical Guide Star is a K or M dwarf (so $J \simeq V + 0.6$ mag). A less common spectral type will not be correctly handled with respect to the color index term.

The need for a parameter which fulfills the function of K_5 does not address the issue of why the ‘walkdown’ commences so far from the interferometer nulls. The alleged reason is that the TF can not merely be $(A - B)/(A + B)$ for this does not incorporate different sensitivities or responsivities between the photomultiplier tubes on the A and B channels. This bias, say Δ_{AB} , is subtracted from the difference term in the numerator so that

$$S = \frac{A - B - \Delta_{AB}}{\langle A + B \rangle}. \quad (4)$$

(Remember that S is normalized by the *mean* value of the first 16 samples, hence the angular brackets in the denominator.) Δ_{AB} is calculated at the start of the ‘walkdown’. Thus, this position must be far enough from the interferometer nulls that the uncorrected value of the TF [*i.e.*, $(A - B)/(A + B)$] would almost vanish were the two photomultiplier tubes perfectly matched. (Sixteen 0.025 sec samples are used to compute Δ_{AB} .) By this mechanism the photomultiplier tube mismatch is always made local—in time in case of aging of the tubes, in place on the celestial sphere in case of a variation in the celestial background, and for this particular star in case it has an atypical color index. Even more importantly, this procedure allows for the failure of one of the photomultiplier tubes without destroying the capability of obtaining and maintaining Fine Lock. However, the real reason a large K_B is necessary is that the field stops in front of the photomultipliers have become displaced. The net instantaneous field-of-view is the intersection of the four stops. This causes a significant Coarse Track/Fine Lock bias, up to one arc second.

As we step towards the interferometer nulls from the Coarse Track backoff position, we do so with steps of size K_D . (Perkin-Elmer Corp. originally used a value of 9 mas but it was since reduced, as a result of this analysis, to near the optimum of 6 mas.) The smaller K_D is the longer it will take to execute the ‘walkdown’, the larger K_5 must be, and the more danger there is that the position-to-rate converter, the piece of software in the FGE that actually computes the settings for the star selector encoders, will stall. Remember that the star selectors are being commanded to move on the surface of a sphere across a domain that has the shape of the FGS total field-of-view. Hence, the geometry is non-planar and there is the possibility that a desired *linear* step will result in a very small projected step. Since the position-to-rate converter is inhibited from taking very small steps—it has a ‘least significant bit criterion’ of 3 bits (nominally; this is also adjustable)—too small a value of K_D may bring about this situation. Thus, the same portion of the TF will be repeatedly sampled. This is actually a good thing to occur when we have a faint star and we are trying to satisfy the ‘three-hit’

algorithm. Since the step we take is halved whenever we pass the above-threshold query after not having passed it during the last 25 milli-second photon integration period, the possibility of a stall increases as we decrease K_D just where, with respect to the TF, we want it to. Hence, the decision to lower K_D from its initial value when the poor performance of the Fine Lock process became apparent, especially on fainter stars.

There are other bounds on K_D . In particular, the above-threshold portion of the TF must be at least $2K_D$ wide and should preferably be $4K_D$ across. Table 1 gives the two solutions to the equation $S(x) = K_Z$, for the $S > 0$ portion of the curve (the theoretical curve has odd parity) for a variety of values of K_Z expressed as a percentage of the maximum value of the TF. To understand the reasoning behind the $2K_D$ and $4K_D$ lower bounds to the width of the above-threshold portion of the TF (see Fig. 5 again), consider the first step into the above-threshold portion of the curve from the right. The largest this advance could be is K_D . Suppose that this is the case and that we pass the K_Z threshold test. Then the step size would be halved and we would penetrate $K_D/2$ further. Suppose that once more the K_Z threshold test is satisfied. We would take one more $K_D/2$ step, presumably pass the K_Z threshold once again—now satisfying the ‘three-hit’ algorithm—and then enter the null maintenance logic in the FGE. The total distance we traversed was $2K_D$. More realistically we might want the width of the above-threshold portion of the TF to be large enough to allow for one failing of the K_Z test and still guarantee overall success at the ‘three-hit’ algorithm. In the worst circumstances this requires an additional minimum distance of $2K_D$ whence the $4K_D$ realistic lower limit. For the nominal (*i.e.*, Perkin-Elmer Corp.) threshold setting the width of the above-threshold portion of the theoretical TF was 22.4 mas or just less than $2.5K_D$ for a K_D of 9 mas. Since we can assume that the entrance into the above-threshold portion of the TF is randomly and uniformly distributed, $4K_D$ becomes $3.5K_D$ in the mean or 21 mas ($= 2.3$ the Perkin-Elmer Corp. value of K_D).

Table 1. Fine Lock Values

X_L (mas)	X_U (mas)	$K_z \cdot S_{MAX}$	K_z	Width (mas)
5.68	31.93	0.356	0.5	26.25
6.99	29.92	0.427	0.6	22.93
8.44	27.89	0.498	0.7	19.45
10.12	25.71	0.570	0.8	15.59
12.26	23.13	0.641	0.9	10.87

In addition, in the presence of excessive spacecraft jitter, we want both K_D and K_Z to be as small as possible. The reason is, once the jitter per axis becomes comparable to K_D itself we have too high a probability of being thrown outside the above-threshold portion of the TF by a bodily movement of the spacecraft. Thus, we will (on the average) fail the K_Z threshold test more often when the jitter is larger. Within the FGE the only method we have of countering this is to maximize the number of opportunities we can have to exceed the threshold. Lowering the threshold K_Z widens the above-threshold portion of the curve and lowering K_D maximizes the number of chances of testing against the threshold. Finally, if optical imperfections in the OTA or the FGSs cause the empirical TF to narrow with respect to the theoretical one, once again our only means of combating this within the FGE is to reduce K_D . Of course neither spacecraft jitter nor optical defects have to be symmetrical with respect to the faces of the Koester’s prisms, so there should have been a provision for a K_{dx} and a K_{dy} .

K_Z is the much talked about threshold value. Since the most likely place to falsely declare the 'Fine Lock' state is when we traverse the secondary peaks in the TF (at the place marked S_{SEC} in Fig. 5), the optimum value of K_Z which will prevent this is $|S(X_{SEC})| + 3\sigma_S(x=0)$. I have used the value of the standard deviation of the TF at the null because it is largest there. Such a three sigma criterion, built on the highest possible non-peak pedestal, ought to safely prevent a satisfaction of the 'three-hit' algorithm almost everywhere during the 'walkdown' process. Uncritically using this value can not be done because it gives no weight to how much of the above-threshold portion of the TF peak we will cut off. As discussed in detail above, the minimum width of the above-threshold portion of the TF is $3.5K_D$. A simplified model of the photon-noise induced variation in the TF predicts that the standard deviation of the TF counts per axis from the star, the sky background, and the dark current noise in the photomultiplier tubes is ≈ 0.05 hence, the lower limit to K_Z can be safely met. Finally, because the imperfections in the OTA and the FGSs are not required to affect the x and y axis TFs in an identical manner, there should have been a provision for a K_{zx} and a K_{zy} .

The remaining two K-factors are used to adjust the instrumental TF, given in Eq. (4), into one that will allow the FGE to succeed in the task of achieving the 'Fine Lock' state as per Eqs. (3). The first one I shall discuss removes any bias. Suppose that owing to optical imperfections, movements of the optical elements as a consequence of the exigencies of launch, deployment, or out-gassing, or so on the positive peak of the instrumental TF is larger in magnitude than the negative peak of the instrumental TF on the same axis. Then, we would not have an equal chance of passing the 'three-hit' algorithm as we approached the interferometer null from the left and right sides. The purpose of K_{0x} and K_{0y} is to offset any such bias so that the TF the FGE has to deal with is symmetrical with respect to the probability of 'three-hit' algorithm passage. Thus, S in Eq. (4) becomes

$$S = \frac{A - B - \Delta_{AB}}{\langle A + B \rangle} + K_0 \quad (5)$$

Of course there is now a S_x and a S_y because there is provision for a K_{0x} and a K_{0y} . The simplistic value of K_0 is clearly the peak-to-peak distance minus half the absolute value of one of the extrema, viz.

$$K_0 = [S_{MAX} - S_{MIN}] - S_{MAX}/2. \quad (6)$$

This is the correct value for K_0 when we are trying to maintain the fine lock state with the Guide Star at the null of the interferometer. The reason is that this value of K_0 makes it equally difficult to climb over either extrema of the TF. This value for K_0 does *not* equalize the probability of success at the 'three-hit' algorithm [see §5.1, particularly just above Eq. (11)].

The two remaining K-factors, K_{1x} and K_{1y} , unfortunately are forced to serve quadruple roles! Their first two functions are to correct the instrumental TF for the effect visible in Fig. 7. Because of the addition of the two channel photon counts in the denominator of S , as in Eq. (4) or (5), while they are subtracted in the numerator, the 'noise' component of the signal—namely the sky background and the dark current noise in the photomultiplier tubes—is compounded in the denominator but is eliminated in the numerator (on the average). Thus, as the Guide Star we are attempting to attain the 'Fine Lock' state on gets fainter, the instrumental TF naturally has a decreased fringe visibility. With K_z fixed as a percentage of S_{MAX} , we may never pass the 'three-hit' algorithm for a fainter star. The initial purpose of K_1 is to boost the instrumental TF so that the K_z threshold can be successfully passed even for fainter stars. Thus, K_1 must be a function of the apparent magnitude of the star as well as be different for each axis and each FGS. Whence, the final FGE version of the TF is given by

$$Q = K_1 \left\{ \frac{A - B - \Delta_{AB}}{\langle A + B \rangle} \right\} + K_0 \quad (7)$$

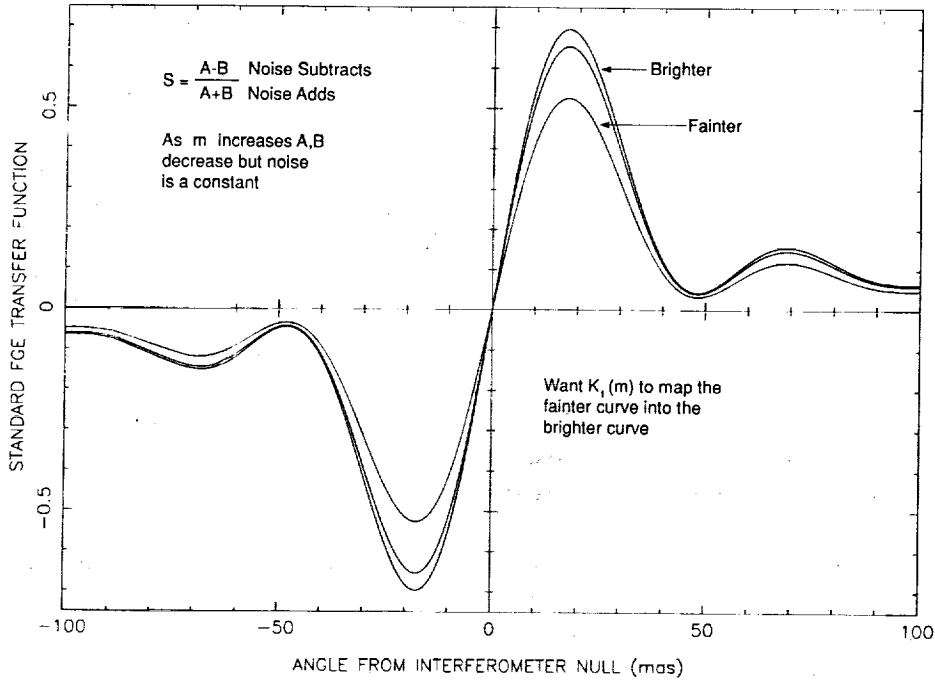


Figure 7. Decrease in fringe visibility with apparent magnitude.

Knowing what K_1 is supposed to do, it is easy to compute its value (although this is not the Perkin-Elmer Corp. procedure). The other three roles of K_1 are more fully discussed in the next section. Briefly, K_1 is used during the walkdown to prevent a false lock, it is used in the Fine Lock state to prevent a loss of lock, and it is simultaneously used in the Fine Lock state to minimize spacecraft pointing errors.

Finally, with definitions for K_0 and K_1 we can refine the constraint on K_Z discussed above and shown in Fig. 5. The real version of this is

$$|K_1(m)[S_{SEC} + 3\sigma_S(0)] + K_0| < K_Z$$

to prevent a false fine lock during the walkdown. Conversely, the constraint

$$|K_1(m)K_Z + K_0| > K_Z$$

must also be satisfied else passing the "three-hit" algorithm will not occur. Perkin-Elmer Corp. always uses a zero value for K_0 and $K_1(m)$ given by Eqs. (9) and (10) is always near 1.1, so these refinements have little practical effect.

5. ANALYSIS

5.1 Theory

Let us start with the 'walkdown.' We need to be far away from the secondary maximum (minimum; we shall assume that the polarity is such that we are approaching from the right in Fig. 5) of the TF in order for $\Delta_{AB} = \langle A - B \rangle$ to have meaning. From Fig. 5 any value of $K_B \gtrsim 200$ mas will

do (*i.e.*, less than half the Perkin-Elmer Corp. value). (Actually we can start as close as $K_B = 50$ mas if we use K_0 to remove the bias.) Until we encounter the maximum of the TF we are only interested in not falsely locking. The place a false lock is most likely to occur is at the secondary maximum; hence, a threshold value of K_Z in excess of $|S_{SEC}| + 3\sigma_S(0)$ is desirable.

Throughout, and especially during passage through the maximum (minimum), we want to correct for the effect in Fig. 7. The proper role of $K_1 = K_1(m)$ then, is to map the fainter curve into the brighter curve. Specifically, imagine that we have a reference TF S obtained on a very bright star of magnitude m_S . We can assume that we have used both ends of the empirical curve to obtain a statistically secure value for $\Delta_{AB} = \langle A - B \rangle$. Similarly we can use the entire curve to obtain a noise-free estimate of $C = \langle A + B \rangle$; whence

$$S = \frac{A - B - \Delta_{AB}}{C}. \quad (8)$$

Now A is composed of both reference star photon counts A_S and 'noise' counts. The latter arise from the sky background and the dark current noise. Symbolize the sum of the latter two components, which we can not easily separate, by D . Therefore,

$$A = A_S + D, \quad B = B_S + D.$$

Thus, on the average, we may recover A_S and B_S from Eq. (8),

$$A_S = C(1 + S)/2 + SD/2, \quad B_S = C(1 - S)/2 - SD/2.$$

Now, for a Guide Star of apparent magnitude m , A_S and B_S become α and β where

$$\alpha = \kappa A_S, \quad \beta = \kappa B_S \text{ with } \kappa = \text{dex}[-0.4(m - m_S)].$$

Similarly $C_S = A_S + B_S$ becomes $\gamma = \kappa C_S$ and S becomes σ ,

$$\sigma = \frac{\alpha - \beta}{\gamma + D}.$$

Clearly, then, the optimal value for $K_1(m)$ is just

$$K_1(m)\sigma = S \quad (9)$$

for *this* value of K_1 transforms the faint star TF into the (bright) reference star TF *everywhere*. The solution for K_1 may be written as

$$K_1 = 1 + D(1/\kappa - 1)/C. \quad (10)$$

For real photomultiplier tube performance and realistic values of C ($\simeq 4$ per photomultiplier tube per 0.025 sec), K_1 ranges from 1.017 to 1.18 as m ranges from 12.5 mag to 15.0 mag.

Before we leave the 'walkdown' and the possibility of false lock, if a real TF has a bias, then it has to be counteracted. Perkin-Elmer's theoretical value of K_0 was given in Eq. (6) and it only adjusts the extrema (in practice they always set K_0 equal to zero). As this value has to offer an equal probability of success at the 'three-hit' algorithm, this is too simplistic. In order to understand this I must digress a bit further.

Irregular bodily motions of the spacecraft, that is jitter, are deadly to the probability of success of the 'three-hit' algorithm. When compounded by too large a value of K_D , too high a value of K_Z , or an instrumentally narrowed set of above-threshold widths W_+ and W_- , the problem becomes even more acute. (W_{\pm} are the linear widths of the above-threshold portions of the TF on the positive and

negative sides of the interferometer null.) Now, with a jitter amplitude $\gtrsim 1.5 K_D$ or $\gtrsim W_+/2$ or $W_-/2$, there is a reasonably high probability of being thrown out of the above-threshold portion of the TF even though the Star Selector encoders have been properly commanded to keep us within the desirable portion of the curve. Once on the shoulders of the extrema of the TFs the probability of passing the K_Z threshold test is much diminished, hence no Fine Lock state.

One cure for this is to double our chances of achieving Fine Lock by attempting to pass the 'three-hit' algorithm criteria on both extrema of the TF. [Indeed the real FGE accepts above-threshold crossings from both extrema sequentially (should this occur).] Hence, the desire to have both halves of the curve be symmetrical with respect to this point. Clearly the sense in which they need to be made symmetrical is that the two widths be made equal; $W_+ = W_-$ and not that $S_{MAX} = |S_{MIN}|$. Thus, the implicit criterion defining K_0 is just

$$W_+ = W_- \quad (11)$$

So far we have fixed K_0 , K_1 , and K_B . K_D should be as small as possible such that once it is halved, it will not cause the Star Selector servos to stall (K_{11} determines the least significant bit criterion in the position-to-rate converter). K_Z must be determined by actually simulating the 'walkdown' and threshold-crossing process with an overall figure of merit, for the entire procedure, in mind. $K_Z \simeq 0.45$ is typically optimal.

This brings us to another essential point not considered by Perkin-Elmer Corp. In assessing the performance of a complicated electro-optical system such as an FGS, especially in a situation wherein the device is remotely located and it is (effectively) impossible to repair or alter it, the maximum amount of flexibility must be built in *after* a thorough analysis of the entire system's operation has been conducted. Such an analysis should include all of the obvious things which might go wrong as well as a few of the things which can not possibly (sic) go wrong. In the end, the non-linear optimization has to be decided on by an overall figure of merit. None of this is evident in Perkin-Elmer Corp. documentation. As a specific example consider the Fine Lock process we have been discussing. There are four different functions to successfully perform during the Fine Lock process: (i) Avoid a false lock during the 'walkdown'; (ii) Achieve success at the 'three-hit' algorithm and do these two things reliably for $V \simeq 14.5$ mag stars; (iii) Once Fine Lock is achieved maintain a position near the interferometer null, that is avoid a loss of lock; and (iv) Maximize the pointing system's stability. Perkin-Elmer makes one value of K_1 try to perform all four of these things with no thought given to an overall optimization. (In fact, they choose K_1 solely to satisfy the no loss-of-lock criterion.)

5.2 Numerical Experiments

Late in 1990 a single bright star (Upgren 62, $V = 9.55$ mag) was placed in nine different locations of each FGS field-of-view and five transfer scans obtained. From these nonets two curves per axis per FGS were selected; one as "typical" and one as "unusual". For this set of a dozen single axis TFs a detailed simulation of the walkdown, three-hit algorithm, and null maintenance aspects of Guide Star acquisitions were simulated. Some generalities followed, to wit: (1) Spacecraft jitter, above 5 mas per axis on a 0.025 second timescale, is deadly to three-hit algorithm satisfaction. Fortunately real spacecraft jitter does not have high frequency components of this amplitude. All further simulations were performed with a real spacecraft jitter file rather than a 40 Hz Gaussian as previously. (2) K_B needs to be as small as the Coarse Track/Fine Lock bias will allow. A larger value of K_B just increases the probability of a lock on photon noise during the walkdown stage. (3) K_D should be just larger than twice the position-to-rate converter stall value. This greatly helps the probability of success at the three-hit algorithm while only minimally extending the time interval necessary to accomplish the walkdown stage. (4) $K_0 = K_0(K_Z)$ is a complex function whose utilization has still not been thoroughly explored. (5) Real TFs are asymmetrical and the inability to have even a quartet

of directional options will diminish the probability of fulfilling the scientific goals of the HST mission; and (6) Large, rapidly fluctuating jitter is deadly to the maintenance of fine lock, especially for fainter stars.

Before the large set of numerical experiments mentioned above were conducted, theoretical TFs, such as those shown in Fig. 5, were used to test and debug the tripartite simulator software. Even before I had real TFs and real jitter files, the above list of generalities was plainly evident. Thus, only a very limited subset of all the results so far obtained are presented below.

Table 2 shows the results of a more focused set of numerical experiments ($K_D = 6$ mas, $K_0 = 0$, real spacecraft jitter). There are twelve sets of results in Table 2, four for each FGS. The origin of these quartets are two doublets, one for each axis (i.e., x or y) in each FGS. Each component of the doublet is chosen from among the nine points in the aforementioned engineering test. After manual evaluation of the TFs at each of those nine places two were selected; one being close to the pre-launch theoretical expectation and one being typically realistic for that axis in that FGS. The full FGE software simulator, with a real jitter file, was executed on each of the dozen curves and the various probabilities of success were computed. In no case, for reasonable values of the K factors, was a loss of lock ever encountered for a (simulation) time duration of 10 minutes (i.e., $40 \times 60 \times 10$ executions of the null maintenance logic given a randomly placed start in between the extrema of the TF). Thus, the probability of a loss of lock, with this jitter file, is zero and will not be further discussed. A more indepth analysis of the jitter file shows it to be a little more quiet than is typical, hence it is still premature to say that we know how to prevent a loss of lock during non-terminator crossing induced disturbances. (One reason this jitter file was chosen was that it was a very long one—this selection effect biased it towards being unusually uneventful too.)

Table 2 contains the probability of success of the three-hit algorithm during threshold crossing P_t , the probability of success of the three hit-algorithm during the walkdown stage, P_w , and the overall probability of success

$$P_{tot} = (1 - P_w) * P_t * (1 - P_{lol})$$

where P_{lol} is the loss of lock probability. There are two rows per Guide Star apparent V magnitude, one for the highest value of P_{tot} and one for the second highest value (as the K factors were varied). By giving both of these one can evaluate the sensitivity of the optimal state with regard to perturbations. Each apparent magnitude also has two columns, one for each direction of approach that the FGE allows.

Perusing Table 2 one can rapidly conclude that guidance on fainter Guide Stars than we are currently using is eminently probable if one controls the FGS in a rationally determined manner. There is also a marked asymmetry in some of the results so that the direction of approach is an important variable and should not merely be left at the pre-launch (default) value. The asymmetry in the TF is a non-linear combination of primary mirror misfiguring, secondary mirror misplacement (both in tilt and in decenter), and in individual FGS mechanical and optical defects. None of this, beyond the existence and magnitude of the primary mirror spherical aberration, is understood nor capable of even being modeled (at the moment; the model I have suggested for the optical aberrations Perkin-Elmer Corp. refuses to even numerically attempt). In particular, if one starts at the outer edge of the FGS in Radial Bay #1 and moves across its field-of-view towards the FGS in Radial Bay #2 there is a continous change in the shape of the TFs which carries over to the next FGS, through its field-of-view, and then into the next FGS. This marked, field dependent, shape deformation can only arise in the OTA and can not be *spherical* aberration!

What does the software simulator have to say about the current K factor settings? These results are in Table 3 along with the my best overall success probabilities for the same apparent magnitudes (remember that Table 3 includes a significantly reduced value of K_D so that the probability of false lock during the walkdown stage is a little increased and that the probability of a successful lock

Table 2. FGE Simulator Results

V	K_Z	K_1	Left P_t	P_w	P_{tot}	K_Z	K_1	Right P_t	P_w	P_{tot}
<i>FGS1-X1</i>										
13.25	0.45	0.90	100.0	0.0	100.0	0.55	0.90	99.5	0.5	99.0
	0.55	1.00	99.5	0.0	99.5	0.55	1.00	99.5	1.0	98.5
14.00	0.55	0.80	93.0	3.5	89.7	0.65	1.00	95.5	3.5	92.1
	0.65	1.00	92.5	4.5	88.3	0.55	0.80	92.0	2.5	89.7
14.75	0.65	0.80	79.5	16.5	66.4	0.65	0.80	68.0	28.0	49.0
	0.65	0.90	87.5	36.5	55.6	0.75	0.90	63.0	27.0	46.0
<i>FGS1-X2</i>										
13.25	0.65	1.00	98.0	2.5	95.6	0.65	1.00	99.5	7.5	92.0
	0.55	0.90	100.0	4.5	95.5	0.65	0.90	94.5	3.0	91.7
14.00	0.65	0.80	84.5	8.0	77.7	0.65	0.80	82.5	19.0	66.8
	0.75	0.90	76.5	7.0	71.1	0.65	0.90	95.5	32.0	64.9
14.75	0.75	0.80	53.0	38.5	32.6	0.75	0.80	61.0	44.0	34.2
	0.65	0.80	78.0	67.5	25.4	0.75	0.90	75.0	74.0	19.5
<i>FGS1-Y1</i>										
13.25	0.45	0.80	100.0	0.0	100.0	0.45	0.80	100.0	0.0	100.0
	0.55	0.80	100.0	0.0	100.0	0.45	0.90	100.0	0.0	100.0
14.00	0.55	0.90	100.0	1.5	98.5	0.55	0.80	99.5	1.0	98.5
	0.65	1.00	98.5	0.5	98.0	0.55	0.80	98.0	0.5	97.5
14.75	0.65	0.90	90.0	10.5	80.6	0.65	0.90	93.0	9.0	84.6
	0.65	0.80	80.0	1.0	79.2	0.75	1.00	89.0	9.0	81.0
<i>FGS1-Y2</i>										
13.25	0.45	0.80	100.0	0.0	100.0	0.45	0.80	100.0	0.0	100.0
	0.55	1.00	100.0	0.0	100.0	0.55	1.00	100.0	0.0	100.0
14.00	0.55	0.80	97.0	0.0	97.0	0.55	0.90	100.0	3.0	97.0
	0.65	1.00	97.5	1.5	96.0	0.65	1.00	96.5	0.0	96.5
14.75	0.55	0.80	95.0	17.5	78.4	0.65	0.90	87.5	33.0	58.6
	0.75	1.00	80.5	7.5	74.5	0.75	1.00	77.5	24.5	58.5
<i>FGS2-X1</i>										
13.25	0.55	0.80	93.5	93.0	6.5	0.55	0.80	94.0	85.0	14.1
	0.45	0.80	98.5	98.5	1.5	0.55	0.90	99.5	97.5	2.5
14.00	0.55	0.80	93.5	99.5	0.5	0.45	0.80	100.0	100.0	0.0
	0.45	0.80	100.0	100.0	0.0	0.45	0.90	100.0	100.0	0.0
14.75	0.45	0.80	100.0	100.0	0.0	0.45	0.80	100.0	100.0	0.0
	0.55	0.80	99.5	100.0	0.0	0.55	0.80	100.0	100.0	0.0

Table 2. Continued

V	K_Z	K_1	Left P_t	P_w	P_{tot}	K_Z	K_1	Right P_t	P_w	P_{tot}
<i>FGS2-X2</i>										
13.25	0.55	0.80	98.0	1.5	96.5	0.55	0.80	99.5	1.5	98.0
	0.65	1.00	98.0	2.0	96.0	0.65	1.00	100.0	4.0	96.0
14.00	0.65	0.80	85.0	10.5	76.1	0.65	0.80	83.5	17.0	69.3
	0.65	0.90	93.0	38.0	57.7	0.65	0.90	90.0	34.5	59.0
14.75	0.65	0.80	85.5	74.5	21.8	0.65	0.80	76.5	70.0	23.0
	0.65	0.90	91.5	91.5	7.8	0.65	0.90	84.0	90.0	8.4
<i>FGS2-Y1</i>										
13.25	0.65	0.80	91.5	1.0	90.6	0.65	0.80	89.0	7.0	82.8
	0.65	0.90	94.5	6.0	88.8	0.65	0.90	98.5	16.0	82.7
14.00	0.75	0.80	72.0	11.5	63.7	0.65	0.80	90.0	40.5	53.6
	0.65	0.80	87.5	32.5	59.1	0.75	0.80	64.0	21.5	50.2
14.75	0.75	0.80	64.0	83.5	10.6	0.75	0.80	63.5	89.5	6.7
	0.75	0.90	78.5	96.5	2.7	0.65	0.80	85.0	97.0	2.6
<i>FGS2-Y2</i>										
13.25	0.55	0.80	95.0	17.0	78.9	0.65	0.80	81.0	9.0	73.7
	0.75	1.00	85.5	8.0	78.7	0.65	0.90	89.0	24.5	67.2
14.00	0.75	0.80	61.0	29.0	43.3	0.75	0.80	61.5	25.5	45.8
	0.75	0.90	75.0	52.5	35.6	0.75	0.90	73.5	38.0	45.6
14.75	0.75	0.80	68.0	88.0	8.2	0.75	0.80	63.0	77.5	14.2
	0.75	0.90	78.0	95.5	3.5	0.75	0.90	68.0	95.5	3.1
<i>FGS3-X1</i>										
13.25	0.55	0.90	100.0	0.0	100.0	0.45	0.80	100.0	0.0	100.0
	0.55	0.80	99.5	0.0	99.5	0.55	0.80	99.5	0.0	99.5
14.00	0.55	0.80	98.0	6.5	91.6	0.65	0.90	93.0	2.0	91.1
	0.65	0.90	93.5	2.0	91.6	0.55	0.80	97.5	8.0	89.7
14.75	0.75	0.90	75.5	14.0	64.9	0.65	0.80	88.5	24.5	66.8
	0.65	0.80	75.0	14.5	64.1	0.75	0.90	82.5	20.0	66.0
<i>FGS3-X2</i>										
13.25	0.45	0.80	100.0	0.0	100.0	0.55	0.80	100.0	0.5	99.5
	0.45	0.90	100.0	0.0	100.0	0.65	1.00	99.5	0.0	99.5
14.00	0.55	0.80	98.0	2.0	96.0	0.55	0.80	97.5	2.0	95.6
	0.65	0.90	97.0	1.5	95.5	0.65	1.00	98.0	3.0	95.1
14.75	0.65	0.80	76.5	15.0	65.0	0.65	0.80	86.0	6.0	80.8
	0.65	0.90	86.0	29.0	61.1	0.65	0.90	90.5	14.0	77.8

Table 2. *Continued*

V	K_Z	K_1	Left P_t	P_w	P_{tot}	K_Z	K_1	Right P_t	P_w	P_{tot}
<i>FGS3-Y1</i>										
13.25	0.45	0.80	99.5	0.0	99.5	0.45	0.90	100.0	0.5	99.5
	0.65	1.10	98.5	0.0	98.5	0.45	0.80	99.5	0.5	99.0
14.00	0.55	0.90	95.0	6.5	88.8	0.45	0.80	98.0	14.0	84.3
	0.65	1.10	96.0	7.5	88.8	0.55	0.90	89.0	7.5	82.3
14.75	0.55	0.80	77.0	29.5	54.3	0.55	0.80	75.0	28.5	53.6
	0.65	0.90	72.0	22.5	55.8	0.55	0.90	80.0	50.0	40.0
<i>FGS3-Y2</i>										
13.25	0.45	0.80	100.0	0.0	100.0	0.45	0.80	100.0	0.0	100.0
	0.55	0.90	100.0	0.0	100.0	0.45	0.90	100.0	0.0	100.0
14.00	0.65	1.20	100.0	0.0	100.0	0.55	0.90	99.0	1.0	98.0
	0.75	1.20	100.0	0.0	100.0	0.55	1.00	99.5	1.5	98.0
14.75	0.55	0.80	94.0	7.5	90.0	0.55	0.80	90.5	18.5	73.8
	0.65	1.00	93.0	8.0	85.6	0.65	0.90	84.5	10.0	76.1

during the threshold crossing stage is dramatically increased). Two things stand out in Table 3; Perkin-Elmer Corp.'s K_1 is much too large and, as a consequence, their probability of false lock during the walkdown often reaches certainty. The real cause of this is that the TFs which led to the $P_w = 100\%$ values are double humped; they are so deformed that to speak of a maximum and secondary maximum, as illustrated in Fig. 5 is very misleading. The height of the 'secondary' peak is sometimes more than half that of the primary. Thus, when an excessively large value of K_1 is used, it becomes almost a certainty that lock will occur on the secondary peak (as long as the direction of approach is such that this must be encountered; since it is rare to have both secondary extrema pronounced, this is another reason to vary the direction of approach with each FGS). Remember too that the K_1 values in Table 3 are real whereas those in Table 2 are relative to the nominal value of K_1 given by Eq. (10). As the nominal value is typically 1.1, Perkin-Elmer Corp.'s values of K_1 are 2-3 times larger than the ones I would suggest.

This has severe operational consequences. First of all, when viewed as a successful or unsuccessful lock it gets counted as a successful one. It is rarely a stable one because jitter has a much easier job driving the FGE over the secondary hump. When this happens we are so far away from the true null that automatic recovery will almost never succeed. Similar remarks apply to a photon-noise induced loss of lock from the secondary null. A second negative consequence of locking on the secondary peak is that the telescope is mis-pointed by the distance between the two nulls. This is fatal to astrometry and fairly important for general target acquisition since the FGS to Science Instrument aperture alignment will be thrown off. This can easily amount to 50 mas. All of the above, easily predictable, consequences have frequently occurred with the real spacecraft. Now there is a straightforward, unified, explanation for them.

Table 3. FGE P-E Simulator Results

V	K_Z	K_1	P_t	P_w	P_{tot}	LGT P_{tot}
13.00	0.42	1.86	100.0	15.5	84.5	99.0
14.00	0.42	2.04	97.5	71.5	27.8	92.2
13.00	0.42	1.86	0.0	100.0	0.0	91.7
14.00	0.42	2.04	0.0	100.0	0.0	66.8
13.00	0.42	1.56	100.0	1.5	98.5	100.0
14.00	0.42	1.62	100.0	17.0	83.0	100.0
13.00	0.42	1.56	100.0	2.0	98.0	100.0
14.00	0.42	1.62	97.0	18.0	79.5	97.0
13.00	0.42	1.98	0.0	100.0	0.0	14.1
14.00	0.42	2.22	0.0	100.0	0.0	0.0
13.00	0.42	1.98	0.0	100.0	0.0	98.0
14.00	0.42	2.22	0.0	100.0	0.0	69.3
13.00	0.42	2.46	0.0	100.0	0.0	82.3
14.00	0.42	2.70	0.0	100.0	0.0	53.6
13.00	0.42	2.46	0.0	100.0	0.0	73.7
14.00	0.42	2.70	0.0	100.0	0.0	45.8
13.00	0.42	1.50	97.5	3.5	94.0	100.0
14.00	0.42	1.68	90.5	24.5	68.3	91.1
13.00	0.42	1.50	0.0	100.0	0.0	99.5
14.00	0.42	1.68	0.0	100.0	0.0	95.6
13.00	0.42	1.62	11.5	2.5	11.2	99.0
14.00	0.42	1.74	13.0	21.5	10.2	82.3
13.00	0.42	1.62	100.0	1.5	98.5	100.0
14.00	0.42	1.74	99.5	32.0	67.7	98.0

REFERENCES

- L. G. Taff, "An Analysis of the Hubble Space Telescope Fine Guidance Sensor Coarse Track Mode," *Exp. Astr.*, vol. 1, pp. 237-226, 1990a.
- L. G. Taff, "The Astrometric Calibration of the Hubble Space Telescope Fine Guidance Sensors," *Astrophys. J.*, vol. 365, pp. 407-418, Dec. 1990b.
- L. G. Taff, "Expanding the Scientific Role of the Hubble Space Telescope Fine Guidance Sensors," in press in *Adv. Space Res.*, 1991.

**THE IN-FLIGHT CALIBRATION
OF THE HUBBLE SPACE TELESCOPE ATTITUDE SENSORS**

Gary L. Welter
Computer Sciences Corporation
1100 West Street, Laurel MD 20707, U.S.A.

ABSTRACT

This paper presents a detailed review of the in-flight calibration of the Hubble Space Telescope attitude sensors. The review, which covers the period from the April 24, 1990, launch of the spacecraft until the time of this writing (June 1991), describes the calibrations required and accuracies achieved for the four principal attitude sensing systems on the spacecraft: the magnetometers, the fixed-head star trackers, the gyroscopes, and the fine guidance sensors (FGSs). In contrast to the other three sensor groups, the Hubble Telescope's FGSs are unique in the precision and performance levels being attempted; spacecraft control and astrometric research at the near-milliarcsecond level are the ultimate goals. FGS calibration accuracies at the 20-milliarcsecond level have already been achieved, and plans for new data acquisitions and reductions that should substantially improve these results are in progress. This paper presents a summary of the basic attributes of each of the four sensor groups with respect to its usage as an attitude measuring system, followed by a discussion of the calibration items of interest for that group. The calibration items are as follows: for the magnetometers, the corrections for the spacecraft's static and time-varying magnetic fields; for the fixed-head star trackers, their relative alignments and use in performing onboard attitude updates; for the gyroscopes, their scale factors, alignments, and drift rate biases; and for the FGSs, their magnifications, optical distortions, and alignments. The discussion covers the procedures used for each calibration, as well as the order of the calibrations within the general flow of orbital verification activities. It also includes a synopsis of current plans for the eventual calibration of the FGSs to achieve their near-milliarcsecond design accuracy. The conclusions include a table indicating the current and predicted ultimate accuracies for each of the calibration items.

I. INTRODUCTION

The ultimate scientific goals of the Hubble Space Telescope (HST) mission require relative pointing accuracy on the order of a few milliarcseconds for target objects within the telescope's 1/2-degree-diameter field-of-view (FOV). This high accuracy is to be achieved using the spacecraft's fine guidance sensors (FGSs), manufactured by Hughes Danbury Optical Systems, which allow the spacecraft to maintain pointing relative to a preselected set of guide stars. The milliarcsecond accuracy requirements for use of the FGSs dictate equally demanding accuracy requirements for their calibration. One of the purposes of this paper is to present an overview of the multistage procedure used for the calibration of the FGSs and the results obtained to date for that procedure. Another purpose is to describe the broader, sensor calibration context within which the calibration of the FGSs fits. The FGS FOVs are restricted to the outer 4-arcminute annulus of the telescope's full FOV. Because of the small size of the FGS FOVs, as well as the significant amount of time required to find guide stars using the FGSs, auxiliary systems are required for determining and controlling attitude at coarser levels. The principal auxiliary attitude determination sensors are the HST magnetic sensing system (MSS), manufactured by the Schonstedt Instrument Company; the fixed-head star trackers (FHSTs), manufactured by Ball Aerospace Systems Division; and the rate gyro assemblies (RGAs), manufactured by Allied Signal Aerospace Corporation. Use of these "auxiliary" systems, sometimes as the principal attitude sensing devices, has been common on many previous spacecraft (see Reference 1). This paper reports on the procedures used for the in-flight calibration of each of these auxiliary sensor groups for the HST mission. The description of the calibration of the FGSs follows that of the auxiliary sensors, paralleling the actual sequence of events followed during the orbital verification phase of the HST mission.

The data reduction and analysis algorithms used for the sensor calibration activities described in this paper have been implemented within the HST Payload Operations Control Center (POCC) Applications Software Support (PASS) system developed by Computer Sciences Corporation (CSC) under contract to the National Aeronautics and Space Administration / Goddard Space Flight Center (NASA/GSFC). The requirements for the PASS system, which continues to evolve, are documented in Reference 2. It is primarily from the author's perspective as a developer and user of the PASS system that this paper is written.

II. OVERVIEW OF HST AND ITS ATTITUDE SENSORS

Figure 1 shows the general layout of HST, including the locations of some of the important systems. The reader should note in particular the locations of the indicated magnetometer, magnetic torquer (MT), FHST, RGA, and FGS. (Companion instruments of each type are located symmetrically about the spacecraft.) The figure also indicates the locations of the optical telescope assembly (OTA), which comprises the primary and secondary mirrors and their mounting system, and one of the scientific instruments (SIs). In addition, it illustrates the standard reference frame of the spacecraft, with axes (V1,V2,V3), where V1 is along the primary viewing direction of the satellite, V2 is along the axis of the port side solar array, and V3 is along the upper high-gain antenna boom. [These are only approximate definitions; in actual operations the spacecraft axes are defined by the selected alignment matrix for FGS-2 (the FGS indicated in Figure 1). All other reference frames of interest are then measured relative to this fiducial frame.]

The four HST sensing systems of principal concern in this paper, the MSS, FHSTs, RGAs, and FGSs, are discussed in Sections IV, V, VI, and VII, respectively. Calibration of the sensors proceeds in essentially the same order in which they are discussed here. As an indication of the challenge involved with the full calibration, a few ballpark numbers are worth mentioning at this point. As noted in Section I, the design accuracy of the FGSs is a few milliarcseconds. The prelaunch errors in FGS calibration were estimated to be large enough to cause errors of up to 10 arcseconds in measured relative star separations. The relative mounting error between distinct sensors was estimated to be approximately 5 arcminutes. Finally, the error in HST attitude at the time of spacecraft release from the shuttle's remote manipulator system, as well as the attitude error during spacecraft recovery from a software sunpoint safemode situation, were estimated to be on the order of 6 degrees. HST's attitude determination and sensor calibration requirements thus range over a factor of nearly 10^7 in pointing resolution. Calibration of the MSS provides the capability to determine spacecraft attitudes to within approximately 3 degrees. This is sufficiently accurate to allow identification of stars observed by the FHSTs. Attitudes determined with the FHSTs prior to calibration of their relative alignments were good to approximately 10 arcminutes (the extra factor of 2 entering because of the geometry of the relative mountings of the trackers). Following alignment calibration, attitudes can be determined with FHST data to within approximately 20 arcseconds. Using FHST data to determine spacecraft attitudes, the RGAs can

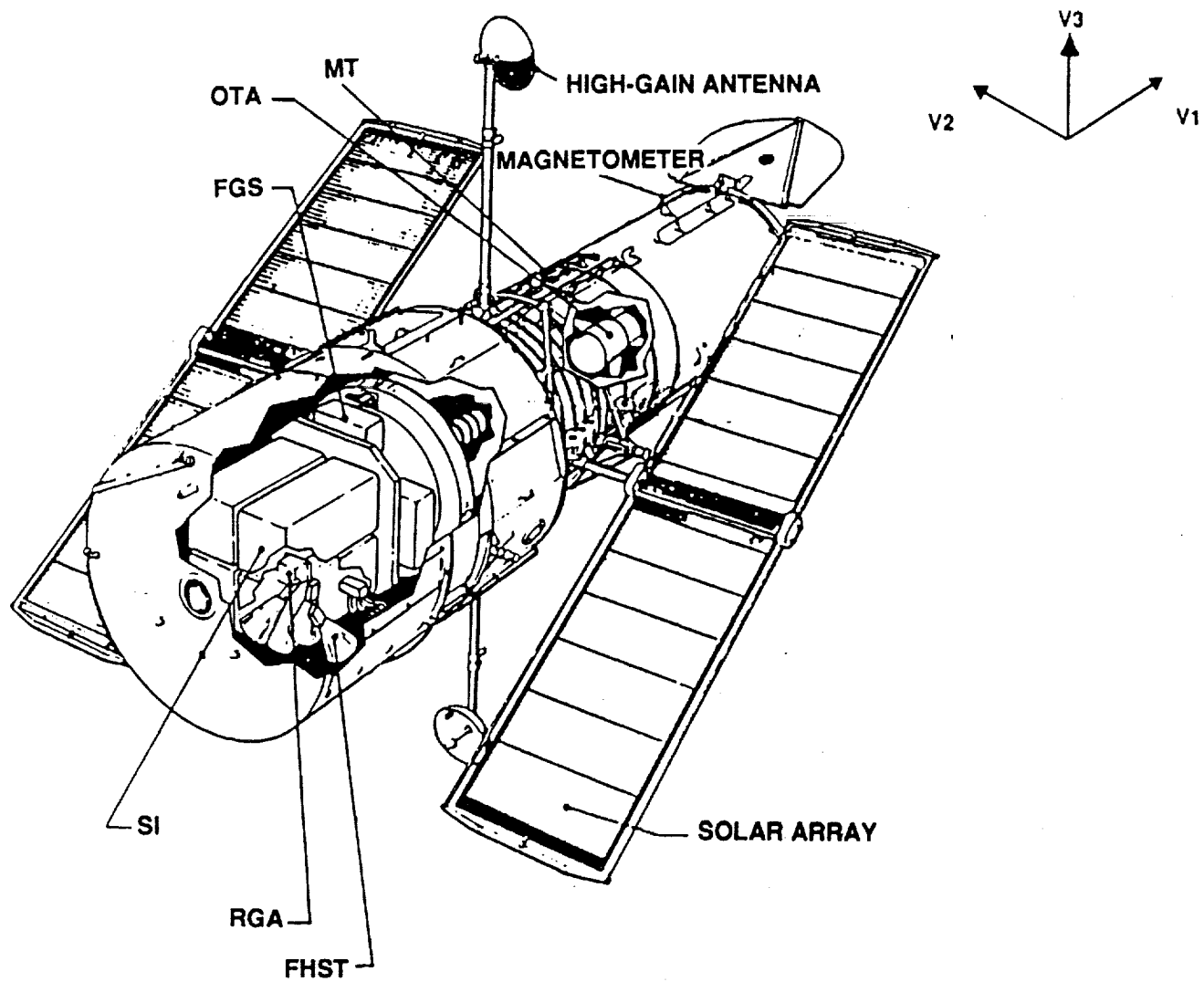


Figure 1. Hubble Space Telescope

be calibrated well enough to allow large-angle maneuvers with an accuracy of better than 60 arc-seconds. The accuracy of FHST attitudes also puts the system in the domain of the FGSs, at least after FGS calibration has proceeded through its initial stages. Detailed FGS calibration prepares the satellite to undertake its scientific objectives. A more detailed overview of each of these levels of calibration is given in the following sections.

III. GENERIC ATTITUDE DETERMINATION AND SENSOR ALIGNMENT

Much of the work described in this paper relies on the determination of either spacecraft attitude or sensor orientation based on a comparison of sensor-detected direction vectors (i.e., star direction vectors or geomagnetic field directions) to a known reference for those vectors. The mathematical problem is to find the attitude transformation matrix, A , that minimizes the loss function

$$L(A) = 1/2 \sum [(|W_i - AX_i| / \sigma_i)^2] \quad (1)$$

where

- W_i = i-th observation vector
- X_i = associated reference vector [in geocentric inertial (GCI) coordinates]
- σ_i = associated angular uncertainty

and the sum is over all observations. For the sensors discussed in this paper, X_i is obtained either from a star catalog (when FHST or FGS data are being used) or a geomagnetic field model (when MSS data are being used). Solving for the attitude matrix A requires a minimum input of two noncolinear observation vectors, with best results achieved for cases where substantial angular variation between vectors is involved. The algorithm used in PASS for the determination of the matrix A is one originally developed by P. Davenport and refined by M. Shuster. A complete discussion of the algorithm can be found in Reference 3.

The loss function of Equation 1 can be used as the basis of an algorithm for the determination of the relative alignments of two independent vector-direction sensors, or the relative attitude change of a given sensor over a period of time. Indeed, the PASS system uses this approach in certain of its algorithms. Another possible approach for the determination of a set of transformation matrices, $\{T_1, T_2, \dots, T_N\}$, that link a set of N sensors to a common reference frame is to minimize the loss function

$$L(T_1, T_2, \dots, T_N) = 1/2 \sum [(C_{W,(\mu i)(vj)} - C_{X,(\mu i)(vj)})^2 / (S_{(\mu i)(vj)})^2] \quad (2)$$

where

$$\begin{aligned} C_{W,(\mu i)(vj)} &= (W_{\mu i} \cdot W_{vj}) \\ C_{X,(\mu i)(vj)} &= (T_{\mu} X_{\mu i} \cdot T_v X_{vj}) \\ W_{\mu i}, W_{vj} &= i\text{-th and } j\text{-th observation vectors in sensors } \mu \text{ and } v, \text{ respectively} \\ X_{\mu i}, X_{vj} &= \text{associated reference vectors} \\ (S_{(\mu i)(vj)})^2 &= (\sigma_{\mu i}^2 + \sigma_{vj}^2) (W_{\mu i} \times W_{vj})^2 \\ \sigma_{\mu i}, \sigma_{vj} &= \text{angular uncertainty for the } i\text{-th and } j\text{-th observations in sensors} \\ &\quad \mu \text{ and } v, \text{ respectively} \end{aligned}$$

and the sum is performed over all pairs of unique observations between distinct sensors. (Note that $(S_{(\mu i)(vj)})^2$ is the variance associated with $C_{X,(\mu i)(vj)}$.) The PASS procedure for solving for the set $\{T_1, T_2, \dots, T_N\}$ in the case of relative FHST-to-FHST or FHST-to-FGS alignment determination is documented in Reference 2.

IV. CALIBRATION AND USE OF THE MAGNETOMETERS

The HST MSS consists of two magnetometers mounted on the outer hull of the satellite near the forward aperture. The magnetometers are designed to have a range of approximately -0.6 to +0.6 gauss, with a resolution of 0.0048 gauss per count. The MSS can be used to measure the local geomagnetic field in the spacecraft reference frame. These measurements, if taken over a sufficiently long period of time (i.e., at sufficiently many distinct positions in the spacecraft orbit) to

allow significant variation of the sampled geomagnetic field, can be used in conjunction with a geomagnetic field model (e.g., Reference 4) to determine the spacecraft attitude. Empirically it has been found that 20 minutes of MSS data allow determination of the attitude to within approximately 3 degrees, sufficient to allow attitude determination with the FHSTs.

The achievement of 3-degree attitude accuracy with MSS data requires some in-flight calibration of the MSS, part of which must be done before an accurate estimate of the spacecraft attitude has been determined. The most important in-flight calibrations of the MSS pertain to the magnetometers' response to the magnetic field generated by the spacecraft itself. This field may be divided into two parts: (1) a static bias produced by the magnetization of the spacecraft as a whole (including any intrinsic magnetometer bias) and (2) a time-varying field produced by the spacecraft's magnetic torquing system (MTS), which is part of HST's momentum management system. (The MTS field is used to couple the spacecraft to the Earth's magnetic field, which allows the dumping of excess spacecraft angular momentum to the Earth's field.) Both of these field components must be either eliminated or compensated for before application of the attitude determination algorithm will yield accurate results. The MTS-generated field can be removed by the deactivation of the MTS, a procedure that was used during the acquisition of MSS data shortly after HST's release from the shuttle's remote manipulator system. With all time variation of the measured magnetic field being due to motion of the spacecraft through the geomagnetic field, it is possible to determine the static spacecraft magnetic bias without knowledge of the spacecraft's attitude; the algorithm used by the PASS system for this initial bias determination is presented in Reference 5. The magnitude of HST's static field at the locations of the two magnetometers at the start of the mission was found to be roughly 0.020 gauss, with an uncertainty of 0.006 gauss. With the static bias determined, the MSS data were then reprocessed to provide an estimate of the spacecraft's attitude accurate to the aforementioned 3 degrees. This in turn allowed use of the FHSTs to commence.

Given an independent means of determining the attitude of the spacecraft (i.e., using the FHSTs), it is possible to calibrate the MSS for better estimates of its sensitivity to static bias and MTS-generated fields. The currently implemented algorithm for correcting MSS data for the effects of the MTS-generated magnetic fields is based on the MTS model used by the onboard computer for its momentum management computations. MTS field strengths at the locations of the magnetometers are estimated to be typically about 0.05 gauss. For the purposes of HST's momentum

management needs, it was found that the MTS field can be represented as a simple time-varying magnetic dipole at the center of the satellite. This approximation was incorporated into the ground-based attitude determination software to correct MSS data for the effects of the MTS field. In-flight calibration of the MSS to account for the two spacecraft field sources is calculable via the minimization of the loss function

$$L_{\mu} = \sum (B_{\mu i} - b_{\mu} - T_{\mu} D_i - A_i R_i)^2 \quad (3)$$

where

- $B_{\mu i}$ = magnetic field vector measured by magnetometer μ at time i
- b_{μ} = static bias vector at magnetometer μ (to be solved for)
- T_{μ} = MTS coupling matrix for magnetometer μ (to be solved for)
- D_i = MTS dipole moment vector at time i
- A_i = GCI-to-HST attitude transformation matrix at time i
- R_i = geomagnetic reference field at HST's location at time i

The loss function used in PASS for the determination of b_{μ} and T_{μ} is actually somewhat more complicated than that of Equation 3 in that it also allows for an adjustment of the magnetometer alignment matrices. The details of the algorithm used to minimize the loss function are documented in Reference 2. A preliminary, "full" MSS calibration was performed a few months after launch. Approximately 600 data points, taken at 30 well-distributed attitudes and over the full range of MTS current readings (-2000 to + 2000 amperes \cdot meters²), were used in the calibration. The accuracy for the postcalibration correction for static and time-varying magnetic fields as sensed at the magnetometers was found to be approximately 0.005 gauss. Empirically it has been found that, for data taken within a few weeks of the calibration, use of the in-flight calibration parameters allows attitude determination with the MSS to within about 3 degrees even with the MTS active. In contrast, if in-flight calibration values for the static bias are applied, but prelaunch values for the MTS coupling matrix are used, the determined attitudes are accurate to only about 6 degrees. A subsequent review of the accuracy of MSS-derived attitudes has suggested a secular variation of the static bias. The details of this secular variation remain under investigation.

A refinement to the model for representing the MTS-generated field is being considered. The MTS consists of four magnetic torquer bars whose separations from each other are about one-third their separations from the magnetometers. For this reason it has been suggested that a better MTS model would use four dipoles, each centered at the location of one of the bars. When time permits, this enhancement to the representation of the MTS field may be incorporated into the PASS system.

V. CALIBRATION AND USE OF THE FIXED-HEAD STAR TRACKERS

The HST FHST system consists of three star cameras, each having an 8-degree-by-8-degree FOV and capable of detecting stars within the visual magnitude range of approximately 2 to 6 m_v . As indicated in Figure 1, the FHST FOVs are directed significantly away from the principal axis of the telescope. FHST-1 is mounted so as to have its boresight approximately along the -V3-axis. FHST-2 and FHST-3 are mounted so as to point downwards and backwards in the spacecraft reference frame. Their boresight direction-vectors are located within a plane rotated approximately 45 degrees about the V2-axis away from the V2/V3 plane, the individual boresight directions being 30 degrees to either side of the V1/V3 plane. The HST design imposes the operational restriction that only two FHSTs can be active simultaneously. The one-sigma accuracy of the HST star trackers is estimated to be approximately 11 arcseconds. This 11-arcsecond accuracy for a single FHST is obtained after distortion effects have been removed. FHST distortion is a function of position with the FOV, ambient temperature and magnetic field conditions within the tracker, and brightness of the observed star. Calibration of the FHSTs for distortion was performed on the ground, will not be repeated in orbit, and will not be further discussed in this paper.

The FHSTs operate in a number of modes, two of which are relevant to the discussions of this paper. The first, map mode, simply causes a given FHST to scan across its entire FOV and record all stars that it detects. When operating in map mode, the FHSTs are typically configured to have an observing rate of approximately one star every 20 seconds per active tracker. Ground-based attitude determination is performed using map mode data and the least-squares algorithm associated with Equation 1. It is by means of such ground-determined attitudes that the onboard computer's attitude knowledge is initialized (e.g., after spacecraft release from the shuttle or during spacecraft

recovery from a safemode situation). The accuracy of such computed attitudes was restricted at the beginning of the mission by the uncertainty in the relative alignments of the FHSTs, which were known only to about 5 arcminutes. An iterative algorithm using the loss function of Equation 2 is used by PASS to determine the relative alignments of the FHSTs; the details of the algorithm are presented in Reference 2. Because of the restriction that only two FHSTs can be active simultaneously, a minimum of three sets of data (one for each pair of trackers) is required to obtain a good alignment determination for the complete triad. The use of multiple data sets for each tracker pair is the standard procedure. Typically, from 5 to 10 fairly well-distributed stars are found in each tracker FOV during alignment calibration work. At 20 seconds per star, this implies an observing period of approximately 3 minutes to map the star fields for each pair of trackers. Proper alignment calibration therefore requires that the spacecraft gyroscopes have been sufficiently well calibrated to hold the spacecraft steady (or correct ground calculations) to significantly better than about 4 arcseconds per minute. Because the estimated prelaunch gyro bias uncertainty was approximately this value, iteration between gyroscope calibration and FHST alignment calibration at the beginning of the mission was required. Given the large number of star observations used in the tracker alignment procedure, statistical reduction of errors yields alignment accuracies a few times better than the 11-arcsecond accuracy level for a single observation. After alignment calibration is completed, it is the accuracy of the individual FHSTs coupled with the geometry of the tracker mountings, rather than the accuracy of the alignment determination, that sets a limit on the accuracy of the spacecraft attitudes that can be derived based on tracker data. Given N star measurements in each of two trackers with a separation angle of α between the trackers, the derived attitude would have a one-sigma "roll" uncertainty of $\sim \{ 11 / [(2N)^{1/2} \cdot \sin(\alpha/2)] \}$ arcseconds about the axis bisecting the chord connecting the trackers. Taking $N \sim 5$, this corresponds to about 7 arcseconds for the HST trackers.

The second mode of operation, update mode, uses one star in each FHST in operation. These data are used by the onboard computer to determine any adjustments to the spacecraft attitude required to reposition to the scheduled attitude. In practice, such attitude corrections are essentially always required after large vehicle maneuvers. The onboard algorithm for attitude error correction (details of which may be found in Reference 6) incorporates a simplifying approximation; it effectively assumes that the observed stars are near the FHST boresights. This approximation introduces an error on the order of $\beta \cdot [1 - \cos(\gamma)]$, where β is the true attitude error (i.e., deviation from desired

attitude), and γ is angular distance of the observed star from the center of the tracker. HST is currently operated with a restriction of 300 arcseconds on the value of β correctable by the onboard computer, whereas γ is restricted by the size of the FHST FOV to be less than about 5 degrees. This yields a maximum $\beta \cdot [1 - \cos(\gamma)]$ error of order 1 arcsecond. This is significantly smaller than the 20-arcsecond (one-sigma) error level inherent in FHST data having just one star per tracker (i.e., the onboard algorithm is effectively as accurate as a least-squares algorithm).

Although the update mode algorithm is, in principle, as accurate as a least-squares algorithm, significant difficulties in the use of update mode were encountered in actual operations. During the months immediately after launch, approximately 15 percent of scheduled FHST updates failed to properly correct the spacecraft attitude. The result was usually an inability to acquire FGS guide stars and a subsequent loss of scientific observations. Because of the criticality of successful FHST updates, a special analysis team was organized to study the causes of FHST update failures and to make recommendations for modifications to the ground and onboard algorithms so as to reduce the update failure rate. To a substantial extent, the difficulties with updates were found to have arisen as a consequence of (1) limitations of the update mode operation of the tracker hardware, (2) inexact specifications of FHST operating parameters, and (3) a few oversights in the original software package used for selection of FHST update stars. Update mode requires each of two FHSTs to find a preselected star in the FHST FOV. To this end, the FHST restricts its scanning operation to a 1.5-degree-by-1.5-degree reduced FOV (RFOV), accepting only stars brighter than a user-specified threshold. The center of the RFOV is not arbitrarily selectable, but rather is restricted to be one of a set of grid points spaced such that the set of all RFOVs covers the full FOV with overlap. Similarly, the star brightness threshold is not arbitrarily specifiable, but rather is restricted to one of four FHST response values corresponding to approximately 3, 4, 5, and 6 m_v . (Strictly speaking, the last "threshold" corresponds to all detectable stars.) It is one of the purposes of the PASS mission scheduling subsystem to select pairs of stars for FHST updates that are isolatable within FHST RFOV and brightness boundaries. The details of the algorithm for the selection of update pairs are beyond the scope of this paper; suffice it to say that the distribution of stars in brightness and position about the celestial sphere makes the problem an extremely nontrivial one. (Details may be found in Reference 2.) Careful tuning of input parameters is a necessity. Among those items studied and (where appropriate) tuned by the FHST anomaly analysis team are (1) the sensitivity response of each FHST as a function of FOV position, star

brightness, and star color, (2) the exact dimensions of the FHSTs' RFOVs, (3) the precision of the star brightness threshold limits, (4) reference star parameters (e.g. variability or incorrectly documented magnitude) for those stars used in unsuccessful updates, (5) command timing for FHST update executions, (6) FHST response error due to stray light (e.g., sunlight reflected from spacecraft components), (7) FHST plate scale response, (8) the possibility of enhancing an FHST's star isolation capability by means of an "error box" algorithm that will reject stars observed to be too far removed from the preselected position, and (9) the possibility of enhancing the probability of successfully updating the spacecraft attitude by scheduling multiple updates after major maneuvers. Modifications to ground or onboard systems have been made with respect to items 1 through 5; these modifications have already reduced the FHST update failure rate to approximately 4 percent. No significant correlation of update failures with spacecraft attitude or orbit position were found; this led to the dismissal of stray light (item 6) as a likely cause of update problems. Plate scale response (item 7) has been found to be nonnominal for FHST-3; starting in January 1991, that tracker has been minifying angular separations by about 0.25 percent. The cause of this anomalous scale behavior remains under investigation; correcting it will certainly prevent the recurrence of certain update difficulties that have recently been encountered. Recommendations for enhancements to onboard and ground software have been made with respect to items 8 and 9. Although improvement of system performance is anticipated upon implementation of each item, an exact determination of the degree of improvement -- particularly with respect to item 9 -- cannot be made at this time.

VI. CALIBRATION AND USE OF THE RATE GYRO ASSEMBLIES

HST's gyroscope system comprises three RGAs, each of which consists of two independently operable gyroscopes. The purpose of the RGAs is twofold: (1) to allow the spacecraft to remain at a fairly constant attitude while not using stars for guidance control and (2) to allow the spacecraft to perform large-angle slews with sufficient accuracy. In this context, "sufficient accuracy" means such that FHST updates can be performed after slews and thereby leave the spacecraft with an attitude good to within 60 arcseconds (three-sigma) of that intended. The basic design properties of the HST gyros are as follows. The mounting of the gyros is summarized via the matrix equation

$$\begin{array}{rcl}
|\omega_1| & | & -\sin(\alpha) \quad 0 \quad -\cos(\alpha) | \quad |\Omega_1| \\
|\omega_2| & | & -\sin(\alpha) \quad 0 \quad \cos(\alpha) | \quad |\Omega_2| \\
|\omega_3| & = & | -\cos(\alpha) \sin(\beta) \quad -\cos(\alpha) \cos(\beta) \quad -\sin(\alpha) | \quad |\Omega_3| \\
|\omega_4| & | & | \cos(\alpha) \sin(\beta) \quad \cos(\alpha) \cos(\beta) \quad -\sin(\alpha) | \\
|\omega_5| & | & | -\cos(\alpha) \sin(\beta) \quad \cos(\alpha) \cos(\beta) \quad -\sin(\alpha) | \\
|\omega_6| & | & | \cos(\alpha) \sin(\beta) \quad -\cos(\alpha) \cos(\beta) \quad -\sin(\alpha) |
\end{array}$$

where ω_i represents a rotation about the i -th gyroscope, and Ω_j represents a rotation about spacecraft axis V_j . The design values for the angles α and β are 31.7 degrees and 43.5 degrees, respectively, α being a characterization of the mounting of the gyro with its RGA and β being a characterization of the RGAs' mounting on HST. The gyros can operate in two modes. The high-rate mode has a range of ± 1800 degrees per hour with a resolution of 7.5 milliarcseconds per 40-hertz sample. The low-rate mode has a range of ± 20 degrees per hour with a resolution of 0.125 milliarcsecond per 40-hertz sample. The three-sigma slew accuracy of the RGAs after calibration is estimated to be ~ 1 arcsecond per degree. The relative alignments of the HST gyroscopes is such that any three may be used to completely sample rotations of the spacecraft. The onboard control system is configured to use four gyros simultaneously, keeping the remaining two as backups. The active configuration immediately after launch was the set consisting of gyros 3, 4, 5, and 6. In December 1990, 8 months after launch, gyro 6 failed and was replaced in the control configuration by gyro 2. This configuration continues in use at the time of this writing.

The algorithm used within PASS for the calibration of an active gyro combination is presented in References 1 and 7. The basic thrust of the algorithm is to compare the responses produced by the gyros during a series of maneuvers with the known attitude changes across the maneuvers as determined using data from the FHSTs before and after each maneuver. (In principle, asymmetrically improved RGA calibrations can be achieved using attitudes determined with both FHST and FGS data. At present FGS data are not used.) If applied to a combination of three gyroscopes, the calibration procedure can yield information on the scale factor, alignment, and drift rate bias of the individual gyros. The one-sigma accuracy of the high-rate mode scale factor calibration is about 20 arcseconds per 90-degree maneuver, with roughly equal contributions coming from FHST attitude uncertainties and RGA nonlinearities. (The low-rate mode scale factors are not recalibrated

on orbit, but rather are assumed to be unchanged from their preflight values.) The alignment calibration is good to about 20 arcseconds, and the drift rate bias to about 5 arcseconds per hour for both high- and low-rate mode. The drift rate bias, for both high- and low-rate modes, has been found to vary at about 7 arcseconds per hour per day. As a consequence, the low-rate mode bias is recalibrated every 2 days and the high-rate mode bias every 7 days.

As indicated earlier, an asymmetric improvement in gyro calibration accuracy can, in principle, be achieved if FGS data are included along with the FHST data for attitude determination. This follows because the pitch/yaw accuracy of an attitude determined using FGS data is very good, restricted essentially by the accuracy of the ground-based catalog coordinates, which can be made good to better than an arcsecond. The HST astrometry team made a special effort to supply the HST orbital verification planning team with well-measured coordinates for stars in a set of 14 positions around the sky for use in this gyro calibration effort. Ultimately, at least as of this writing, the extreme difficulty in scheduling simultaneous FGS and FHST observations around the occultation patterns dictated by the calibration slews, coupled with the significant temporal variation of the drift rate bias, has led to a decision to restrict RGA calibration efforts to using only FHST-derived attitudes.

VII. CALIBRATION AND USE OF THE FINE GUIDANCE SENSORS

The heart of HST's pointing control system is the set of FGSs manufactured specifically for use on HST by Hughes Danbury Optical Systems. The FOVs of the FGSs are within the outer part of the full FOV of HST's primary optics. Each FGS FOV consists of an arc with an azimuthal range of 82 degrees and a radial range extending from approximately 10 arcminutes to 14 arcminutes relative to the primary optical axis of the telescope. Figure 2 illustrates the FOVs of the FGSs as they look out to the celestial sphere. The magnitude range for guide stars usable by the FGSs is approximately 9 to 16 m_v . The FGSs are designed to have an accuracy in determining relative star positions of approximately 3 milliarcseconds when fully calibrated (an accuracy not yet achieved at the time of this writing). The precision of the system follows from the design of an FGS as an amplitude interferometer using Koester's prisms combined with photomultiplier tubes. As with the

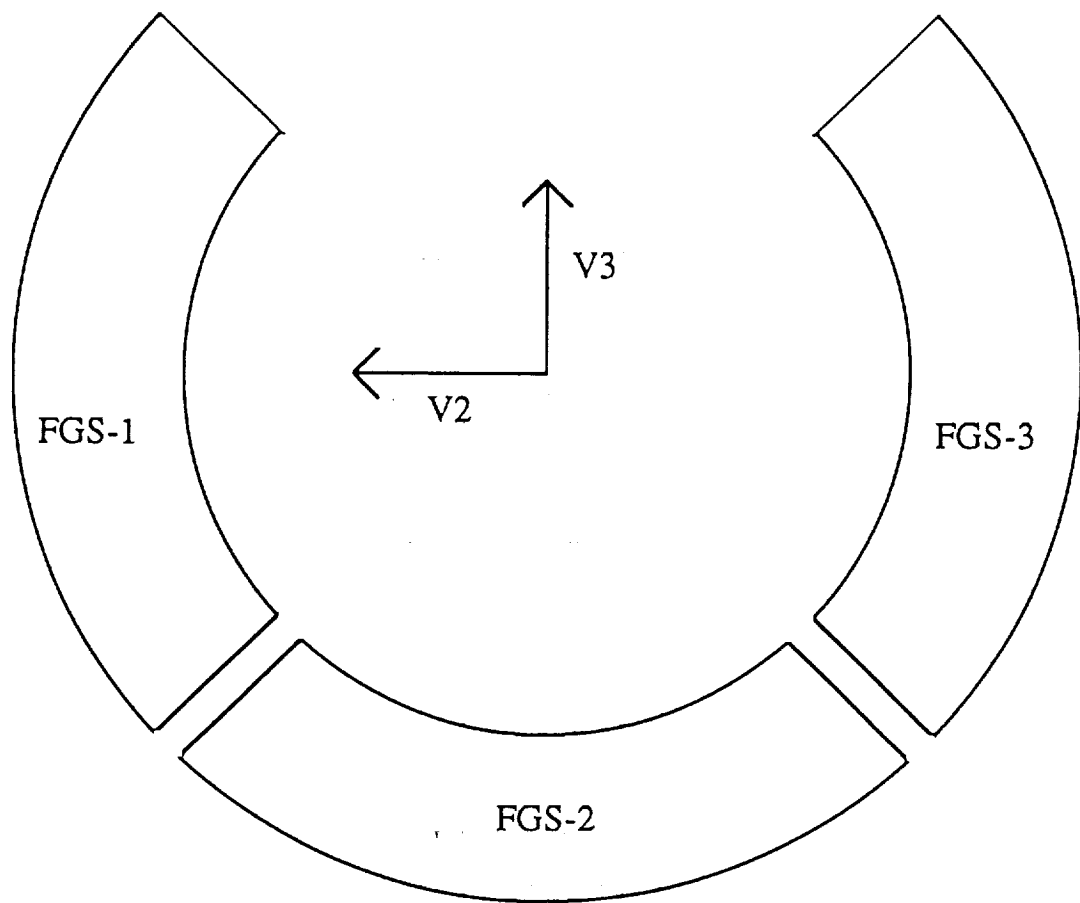


Figure 2. Fine Guidance Sensor Fields-of-View

FHSTs, an FGS can measure the position of only one star at a time. Each FGS has a 5-arcsecond-by-5-arcsecond instantaneous field of view (IFOV) that can be commanded to a selected position within the total FGS FOV. A star image falling within the inner 20 milliarcseconds of the IFOV will produce a significant interferometric signal. The FGS is said to be in fine lock when so measuring a star's direction. A second mode of FGS operation, coarse track mode, is also available. In this mode the center of the IFOV is commanded to nutate about the true star position in such a way that the edges of the IFOV cut across the image of the star in a symmetric pattern. The estimated design accuracy of determining star positions using coarse track mode is approximately 20 milliarcseconds. Because coarse track mode is less sensitive to spacecraft jitter than is fine lock mode, particularly for faint stars, it is expected that coarse track will regularly be used in observing situations in which extreme pointing precision is not required. Standard pointing control procedure during scientific observations is to use two of the FGSs to maintain guidance of the spacecraft, one for pitch/yaw stability and the other for roll stability. The remaining FGS is available for precise astrometric observations. This short description of the characteristics of the FGSs will suffice for the purposes of this paper. A more detailed description of the design and operation of the FGSs is available in Reference 8; indepth descriptions may be found in Reference 9.

The in-flight calibration of the FGSs consists of two major stages: external calibration and internal calibration. External calibration pertains to the alignment of the FGS triad to the rest of the spacecraft, whereas internal calibration pertains to the nonalignment-related parameters of the individual FGSs and the alignments of the individual FGSs relative to each other. External alignment is performed by gathering simultaneous data for FHSTs and FGSs and thereafter minimizing the loss function of Equation 2 while treating the FGSs as a single sensor. The most difficult aspect of the alignment effort pertained to the identification of the first stars observed with the FGSs. This initial alignment calibration of the FGS triad was done by pointing the telescope toward the open star cluster NGC 3532, commanding the guide FGSs to locate one star each in their FOVs for guidance, commanding the astrometry FGS to scan its FOV for as many stars as it could find within a specified magnitude range in the time available, and then attempting to match the pattern of stars found with stars in a reference catalog. Each FGS was used as the astrometry FGS three times during the exercise, with each astrometry scan covering a region of approximately 14 square arcminutes. In practice, this resulted in approximately six astrometry stars per scan. Practical

difficulties encountered during actual operations (certain of them related to the uncalibrated state of the FGSs at that time) led to modifications in the observing plans that ultimately made the star identification procedure and subsequent alignment calibration effort more laborious than anticipated. In particular, the lower limit on star brightness was set to 14 m_v , which is significantly fainter than the limit of the special NGC 3532 catalog provided by the HST astrometry team. This caused a certain degree of confusion and difficulty in identifying the observed star patterns. Approximately half of the observations were ultimately found in the original catalog. This allowed a preliminary determination of the relative alignments of the FGSs to the FHSTs -- preliminary in that most of the guide stars were unidentified and therefore the various baselines for FGS star separations were often no longer than about 6 arcminutes. The identification of the subset of observed stars, together with the FGS FOV coordinates for the whole set of observations, allowed the HST astrometry team to study specific regions on their NGC 3532 photographic plate and thereby provide catalog coordinates for the remaining stars. This enhancement allowed a final alignment calibration of the FGS triad to the FHSTs using FGS star separations that spanned the entire 28-arcminute-diameter FOV of the triad.

The internal calibration of the FGSs is divided into two phases. Phase 1 is intended to bring the calibration of the FGS system to an accuracy commensurate with ground-based astrometric observations. It does so by using such observations as reference points. Phase 2 goes beyond the limitations of ground-based astrometric work, the goal being to achieve the full near-milliarcsecond design capabilities of the FGS system. This second phase takes HST beyond any previously achieved ground or spacecraft calibration accuracies and requires extraordinary planning for both calibration programming and data acquisition. The basic goals of both phases of the on-orbit internal calibration of the FGSs are the determination of (1) the optical field angle distortion (OFAD) function for each FGS, (2) the magnification factor for each FGS, (3) the systematic offset between star positions determined in coarse track and those determined in fine lock for each FGS, and (4) the relative alignments of the FGSs. The details of the FGS calibration algorithms, particularly those for the phase 2 OFAD calibration, are of such complexity and demanding of such precision that a special analysis team was formed to analyze and develop the algorithm details. The team included representatives from CSC, GSFC, Hughes Danbury Optical Systems, Marshall Space Flight Center, and the University of Texas Astronomy Department. CSC personnel concurrently conducted an extensive feasibility and verification study of the FGS calibration algorithms as

part of their implementation. The details of the algorithms as implemented are documented in Reference 2; the results of the study are presented in Reference 10. An overview of each of the algorithms is presented below. The essential results of the study are that, based on certain assumed smoothness properties of the OFAD functions, the implemented algorithms are capable of determining the calibration parameters well enough to allow relative angular determinations to within a few milliarcseconds across each FGS FOV and between pairs of FGS FOVs. Independently, the astrometry teams at the University of Texas and Yale University have implemented versions of HST FGS calibration software for their own astrometric studies; these are being used for independent analysis of the FGS calibration data.

The algorithm used for OFAD calibration is a constrained two-dimensional least-squares algorithm based on the least-squares technique presented in Reference 11. The essential idea is to minimize a loss function, L , subject to certain constraints applied to the associated state vector. The loss function can be expressed (slightly nonrigorously) as

$$L = \sum \{ [W_{ij} - D(W_{ij}, S) - A_j X_i]^2 / \sigma_{ij}^2 \} \quad (4)$$

where

- W_{ij} = observation of star i in observation set j
- $D(W_{ij}, S)$ = OFAD correction vector function
- S = OFAD correction function parameter set (to be solved for)
- A_j = attitude transformation matrix between attitude frame j and a selected standard reference frame (to be solved for)
- X_i = "true" direction vector for star i in the standard reference frame (after correction for velocity aberration effects)
- σ_{ij} = measurement uncertainty for observation of star i in set j (may include error associated with X_i)

and the summation is done over all stars and observation sets. For HST OFAD calibration, the correction function $D(W_{ij}, S)$ has been parameterized as separate polynomials in the x and y Cartesian projections of W . The set S is therefore a set of polynomial coefficients. The phase 1

OFAD calibration procedure solves for a state vector $\{S, A_j (j=1,n) \}$, where n is the number of observation sets. The vector set $\{X_i\}$ is provided as a priori knowledge from ground-based observations. The ground-based observations need be accurate only differentially; any systematic errors in $\{X_i\}$ will be absorbed in the matrices $\{A_j\}$. The selected constraints, applied to the set S , are that the operator D should apply no net affine transformations to the vectors $\{W_{ij}\}$. Specifically, there should be no systematic shift in centroid location, rotation, or scale of $\{W_{ij}\}$. (Optionally, the constraints can be applied to an integration across the FGS FOV rather than the set of observations.) This calibration can, in principle, be performed using a single set of data (i.e., with each star observed only once). The phase 2 OFAD extends the phase 1 procedure so as to include $\{X_i\}$ as part of the state vector, thereby eliminating any errors associated with ground observations from the solution. Unlike the phase 1 calibration, that of phase 2 requires multiple observation sets and significant variation of the spacecraft attitude. It is by moving the various target stars through locally different distortion variation in the FGS FOV that the relative distortion across the entire FOV becomes observable at FGS accuracy levels.

The algorithm used for magnification calibration is substantially simpler than that used for OFAD calibration. Angular separations as imaged in the FGS detector space (hereafter "image space") are magnified by a factor of approximately 57.2 over their true (or "object space") values. In a zeroth order (i.e., small-angle) approximation, the magnification calibration could be performed simply by computing the ratio of the measured image space angular separation of two sources to the object space separation. The magnification, which works along radial arcs intersecting the optical axis, produces a sufficiently large image space FOV as to invalidate any small-angle approach. The following algorithm is therefore used for FGS magnification calibration. Let (ψ_i, ρ_i) be the image space polar coordinates for the i -th star observed, ρ_i being the "radial" angular separation from the optical axis, and ψ_i being the azimuthal distance from an arbitrary reference direction. The object space angular separation, Θ_{ij} , between two points with coordinates (ψ_i, ρ_i) and (ψ_j, ρ_j) is given by the spherical trigonometric relation (see Reference 12)

$$\cos(\Theta_{ij}) = \sin(\rho_i / M) \sin(\rho_j / M) \cos(\psi_i - \psi_j) + \cos(\rho_i / M) \cos(\rho_j / M) \quad (5)$$

where M is the magnification factor. Given an independent determination (e.g., from ground-based measurements) of the true angular separation, θ_{ij} , and an estimate, $M_{ij,n}$, for the magnification, an improved estimate for the magnification can be obtained using the relations

$$(M_{ij,n+1})^{-1} = (M_{ij,n})^{-1} - F(M_{ij,n}) / F'(M_{ij,n}) \quad (6)$$

$$F(M) = \cos(\Theta_{ij}) - \cos(\theta_{ij}) \quad (7)$$

where $F'(M)$ is the derivative of $F(M)$ with respect to M^{-1} . This process can be repeated until M_{ij}^{-1} converges to an acceptable accuracy. The full iteration can be repeated for all observation pairs within a given observation set. Finally, a weighted average over all such estimates of M^{-1} can be obtained using the equation

$$\langle M^{-1} \rangle = \Sigma [M_{ij}^{-1} (\theta_{ij} / \sigma_{ij})^2] / \Sigma [(\theta_{ij} / \sigma_{ij})^2] \quad (8)$$

where σ_{ij} is the root-mean-square uncertainty associated with the i - j pair, and the sum is over all observation pairs. The phase 1 magnification calibration can be performed using the same data set as the phase 1 OFAD calibration, with the θ_{ij} values being taken from ground-based observations. The phase 2 calibration requires a more accurate determination of θ_{ij} . The plan is to perform this calibration using observations of an asteroid moving across the FGS FOV and to obtain the required θ_{ij} estimates using high-precision numerical calculations of the asteroid ephemeris. Studies of asteroids suggest that variations of order 10 milliarcseconds in the separation of center-of-light and center-of-mass may result due to asteroid tumbling. Center-of-light variations will be compensated for by allowing θ_{ij} to be modeled in the form

$$\theta_{ij} = \theta_{i1} - \theta_{j1} \quad (9)$$

$$\theta_{i1} = \theta_{i1}(\text{center-of-mass}) + \alpha + \epsilon \sin[\omega(t_i - t_1) + \phi] \quad (10)$$

where α , ϵ , ω , and ϕ are selected to give a best least-squares fit between Θ_{i1} and θ_{i1} , and t_i is the time of the i -th observation. (The model neglects center-of-light variation perpendicular to the direction of asteroid motion and asteroid motion curvature in the FOV.) Solutions for $\langle M^{-1} \rangle$ and $\{\alpha, \epsilon, \omega, \phi\}$ are performed separately and iteratively.

The FGS-to-FGS alignment algorithm uses a two-part procedure. Part 1 establishes the angular separations between stars for every pair of stars in a selected reference set. During phase 1 of FGS calibration these angular separations are determined using ground-based observations. In contrast, during phase 2 the angular separations are determined using a single FGS in astrometry mode while the spacecraft is held at a constant attitude. With these angular separations specified, part 2 uses them to determine the relative alignments of two FGSs by means of an algorithm that is essentially equivalent to the minimization of Equation 2. Although there are no a priori restrictions as to which FGSs must be involved in the alignment procedure for the phase 1 calibration, phase 2 calibration requires that FGS-2 be used. This follows because the reference angular separations are restricted to being no greater than the maximum viewable by a single FGS at a fixed attitude; the minimum angular separation between FGS-1 and FGS-3 exceed this restriction. Optimal alignment results will be achieved if the FGS used for the determination of the reference angular separations during part 1 is positioned so as to give equal coverage to the star fields to be observed by the two FGSs during part 2; i.e., the spacecraft should be reoriented between parts 1 and 2 by means of a 45-degree roll about the V1-axis.

The algorithms implemented within PASS do not solve for the coarse-track-to-fine-lock (CT/FL) position offset. That such calibration would be required was not fully realized until shortly before HST's launch. One of the goals of the FGS calibration team has been to establish an appropriate parameterization for the bias. The dominant source of CT/FL offset is believed to be field stop misalignment within the FGS optics, which would show itself predominantly as a systematic offset throughout the FOV. Variation of the CT/FL offset as a function of field position may occur, a possible cause being optical vignetting near the edges of the FGS FOVs. Recent data has in fact shown that there are both systematic as well as field dependent components to the CT/FL offsets for all three FGSs.

To date, FGS calibration efforts have been essentially restricted to phase 1 calibration efforts. A catalog of ground-based star coordinates for the open cluster NGC 5617 has been provided by the Yale University astrometry team for this phase of calibration. The data reduction analysis for these observations, which were taken using the Mount Stromlo 26-inch refractor telescope, are described in Reference 13. The estimated one-sigma accuracy of the catalog is 30 milliarcseconds. Two sets

of data have been taken for the purpose of distortion and plate scale calibration, the time periods being the final week of December 1990 and the final week of May 1991. For each set, HST was commanded to make a series of astrometric observations of the target cluster. In what follows, "frame" will refer to the data taken in a single orbit, during which a single pair of guide stars were used in controlling the vehicle's attitude. The December observations consisted of five frames of data for each FGS, each frame consisting of approximately 17 stars. Each frame was taken at slightly adjusted telescope pointings, the adjustments being made as ± 1 -arcminute maneuvers in pitch and yaw. The May observations consisted of a set of 7 frames of roughly 15 stars apiece per FGS. Between frame adjustments by means of ± 1 -arcminute pitch and yaw maneuvers were also made, with the extra two frames being adjusted by means of ± 15 -degree roll maneuvers. The actual number of unique stars in each data set was approximately 25; however, not all stars in the set were observed in every frame. The combined optical distortion and magnification one-sigma residuals (i.e., the residuals between catalog star coordinates and FGS star coordinates after the latter have been corrected for distortion and magnification) for the December data reduction were found to be approximately 70 milliarcseconds. These errors were subsequently found to be best explainable as systematic color- and magnitude-dependent distortion effects in the catalog data. These systematic catalog errors have been corrected using the FGS data as a comparison. FGS calibration work with the new catalog produces solutions with residuals of approximately 35 milliarcseconds. The calibration results demonstrated reasonable consistency between the true and design coefficients characterizing the FGS distortion curves. In contrast, the calibration results suggest strongly that the relative rotational offset between two optical elements in each of FGSs 2 and 3 differ significantly from their design values of zero. Specifically, for the benefit of readers familiar with References 8 and 9, the relative offset between the star selector A and B measurements has been found to be 0.57 degrees for FGS-2 and -0.63 degrees for FGS-3. These values are significantly larger than the design uncertainty for the offset angles; possible reasons for this discrepancy remain under investigation. The distortion and magnification calibrations were repeated for each FGS using the data taken in May. The calibration results show significant differences between the two calibration dates, particularly with respect to magnification. The magnification factor was found to increase for all three FGSs, the fractional increases being $1.2 \cdot 10^{-4}$, $7.5 \cdot 10^{-5}$, and $2.4 \cdot 10^{-5}$ for FGSs 1, 2, and 3, respectively. For FGS-1, this corresponds to a 100 milliarcsecond change in relative star separation for stars 14 arcminutes apart. A small fraction of this change, about 13 milliarcseconds, may be accounted for as due to known differences in the primary to secondary mirror spacing; the bulk of the change is unexplained.

differences in the primary to secondary mirror spacing; the bulk of the change is unexplained. The May data set was specifically designed to allow for a determination of the CT/FL offset. Each star in the astrometric FGS was observed for 30 seconds in coarse track prior to the transition to fine lock mode. This provided approximately 100 points distributed throughout each FGS FOV from which CT/FL offset could be determined. Analysis of the data indicates that the offset for each FGS is well represented by a linear model. The magnitude of the constant component of the offset ranges between 0.2 and 0.8 arcseconds for the three FGSs, while the field dependent component introduces offset changes of approximately 80 milliarcseconds across the 18-arcminute range of an individual FGS. The accuracy of the CT/FL offset correction is estimated to be approximately 5 milliarcseconds, although significant and systematic departures from the fit were observed for certain individual stars (i.e., the offset can be dependent on specific star properties).

Data specifically for phase 1 FGS relative alignment determination were also taken during the December observing period. The data consist of 17 frames of observations, each frame consisting of approximately 10 star observations in FGS-2 (used in astrometry mode) and one guide star in each of the other FGSs. Because of operational difficulties (e.g., the then unresolved solar array jitter problem), the data were taken with the guide FGSs (1 and 3) using coarse track mode. The locations of the stars within the FGS FOVs were selected so as to provide complete coverage when the data sets are combined. The data were processed, and corrections within each FGS for distortion, magnification, and CT/FL offset were applied. Relative FGS-to-FGS alignment calibrations were then performed. The postcalibration one-sigma residuals for the difference between measured and reference star separations between FGSs were found to be approximately 35 milliarcseconds, i.e., basically consistent with the estimated accuracy of the reference catalog. The implied accuracy for the alignment calibration is about 10 milliarcseconds. In order to verify these alignment calibrations, the May FGS 2 distortion data acquisitions were specifically designed with guide star distributions appropriate for an FGS-to-FGS alignment determination. These alignment results produced one-sigma residuals of approximately 54 milliarcseconds, with an implied alignment accuracy of about 20 milliarcseconds. Unexpectedly, the alignment solutions for the May data differed significantly from those for the December data, the differences being approximately 200 milliarcseconds. A third FGS data set appropriate for alignment determination was available from the end of January, 1991. These data also produced internally self-consistent alignment solutions with one-sigma residuals of about 50 milliarcsecond and accuracy of about

20 milliarcseconds. The January alignments are about 100 milliarcseconds different from either of the other two. At this point we have no physical explanation for the variations in the alignment solutions; the cause of the variability remains under investigation.

The two data sets accumulated for each FGS for phase 1 OFAD/magnification analysis have allowed a restricted amount of phase 2 OFAD processing. This admittedly very preliminary analysis has resulted in OFAD solutions with one-sigma residuals on the order of 7 to 10 milliarcseconds. Comparison of these phase 2 solutions with the phase 1 results indicates that the phase 2 software package is more robust than originally expected, and that reasonably accurate results for OFAD calibration can be obtained (at least for the central region of an FGS FOV) with as few as five frames of data. The ultimate OFAD phase 2 analysis will require approximately five times as much data for at least one of the FGSs. (Phase 1 OFAD processing can thereafter be applied to the other two FGSs using reference data from their well-calibrated sibling, thereby achieving full accuracy at a phase 2 level for all three FGSs.) Current plans place full phase 2 FGS calibrations no earlier than the last 2 months of 1991.

VIII. OPTICS CALIBRATION AND SCIENTIFIC INSTRUMENT ALIGNMENT

Two major calibration activities closely related to the calibration of the attitude sensors are not covered by this paper: the optics calibration and the calibration of the alignments of the apertures of the SIs. The optics calibration consists of the measurements and analysis performed in connection with the adjustment of the relative positions of the secondary and primary mirrors. It touches upon the topic of this paper in that the performance of the FGSs and their effective alignments relative to the other HST attitude sensors are functions of the relative configuration of the two mirrors. Adjustments to the tilt or decenter of the secondary mirror therefore necessitate recalibrations of the relative alignments of the other sensors to the FGSs. (In practice, only the FHST and RGA alignment matrices need respecification.) It was within the context of performing an optical calibration that representatives of Hughes Danbury Optical Systems (the mirror manufacturer) discovered the spherical aberration of the primary mirror. Because the FGSs are afocal systems, the manufacturer believes that the spherical aberration of HST's primary mirror will not significantly degrade the accuracy of the FGSs.

The aperture directions of the various SIs are located interior to the annulus of the FGS FOVs. Operationally, the SI aperture alignments are measured relative to a reference frame defined by the FGSs. The alignment calibration for any given SI is performed by taking simultaneous measurements with the SI and at least two of the FGSs, then comparing these measurements with accurate astrometric coordinates for the observed stars. This procedure clearly places a limit on the accuracy obtainable for the determined SI aperture direction; i.e., the alignment accuracy can be no better than the calibration accuracy of the FGSs. Because the ground system does not currently correct for the CT/FL offset, the SI aperture alignment accuracy is thus currently restricted by the operational FGS accuracy of about 0.8 arcsecond imposed by the uncompensated CT/FL offset in FGS 2. As the effective FGS accuracies improve, through both software upgrades to the operational system and actual improvements in the FGS calibration, operational improvements in the pointing of the SIs will result.

IX. SUMMARY

This paper has presented a review of the calibration algorithms and accuracies for the four principal attitude determination sensing systems aboard HST. Table 1 summarizes the current and ultimately expected accuracies for each of the calibration items discussed. Final calibration accuracy has essentially been achieved for the MSS, the FHSTs, and the RGAs; significant progress has been made in the calibration of the FGSs. Significant work continues with respect to tuning and enhancing the FHST update capability. Regular recalibration of the RGA drift rate bias is required because of its temporal variation. Periodic recalibration of the FHST and RGA alignments is required because of redefinitions of the spacecraft reference frame that result from (1) improved FGS calibration and (2) adjustments to the tilt or decenter of the secondary mirror. Significant progress has been made in the calibration of the FGSs, accuracies on the order of 10 to 20 milliarcseconds seem obtainable for a data set localized in time. An unexplained variation of the FGS magnifications and relative alignments, with effects on the order of a few hundred milliarcseconds, has been observed; this variation remains under investigation. Plans are being made for the acquisition of data designed for FGS calibrations accurate to the level of a few milliarcseconds.

Table 1. Attitude Sensor Calibration Accuracies

<u>Sensor</u>	<u>Calibration Item</u>	<u>Current Accuracy</u>	<u>Expected Accuracy</u>	<u>Typical Value</u>	<u>Units</u>
MSS	Static bias	~ 0.004	~ 0.004	~ 0.02	Gauss
	MTS coupling	~ 0.004	~ 0.004	~ 0.05	Gauss
FHST	Distortion	~ 11	~ 11	~ 60	Arcseconds
	Alignments	~ 4	~ 4	—	Arcseconds
RGA	Alignment (to FHSTs)	~ 30	~ 30	—	Arcseconds
	Scale factor (high-rate mode)	~ 0.4	~ 0.4	—	Arcseconds per degree
	Drift rate bias	~ 5	~ 5	~ 10000	Arcseconds per hour
	Bias change rate (high- and low-rate modes)	~ 4	~ 4	~ 7	Arcseconds per hour per day
FGS	Alignment (to FHSTs)	~ 10	~ 10	—	Arcseconds
	Distortion / (Magnification)	~ 0.010	~ 0.003	~ 5 (57.2)	Arcseconds (unitless)
	Alignment to FGSs	~ 0.015	~ 0.006	—	Arcseconds
	CT/FL offset	~ 0.010	~ 0.010	~ 0.5	Arcseconds
	Unexplained Variation			~ 0.2	Arcseconds

X. CALIBRATION TEAMS AND SUPPORTING ORGANIZATIONS

The following persons and organizations have been closely involved with HST sensor data analysis and calibration during the first year of the HST mission. The MSS / FHST / RGA data analysis team for the first few months of orbital verification consisted of John Boia^c, William Collier^c, Martin Gakenheimer^a, Edward Kimmer^a, Matthew Nadelman^c, Cherie Schultz^c, and Gary Welter (superscripts refer to organization affiliation; see list below). Responsibility for the periodic recalibration of these sensors has been turned over to the PASS operations contractor -- primarily Messrs. Gakenheimer and Kimmer, with most of the MSS calibration analysis being performed by Sidney Broude^a. Individuals participating in the analysis of FHST update anomalies included Michael Brunofski^a, W. Collier, Paul Davenport^c, Larry Dunham^g, M. Gakenheimer, Theresa Gaston^g, Kevin Grady^d, Lou Hallock^d, Joseph Hennessy^d, Jeffery Karl^c, E. Kimmer, Raymond Kutina^c, Robert McCutcheon^c, M. Nadelman, William Ochs^d, Thomas Pfarr^c, Milton Phenneger^c, G. Welter, and Michael Wright^d. NGC 3532 catalog star coordinates for the initial FGS alignment calibration were provided by George Benedict^k, Otto Franz^f, Lawrence Fredrick^l, Darrell Story^k, and Lawrence Wasserman^f. The FGS calibration team consists of Linda Abramowicz-Reed^e, William Brady^e, Todd Burr^e, Roger Doxsey^j, Terrence Girard^m, Arun Guha^b, L. Hallock, William Jefferys^k, E. Kimmer, Young-Wook Lee^m, Bruce Lowenberg^e, Olivia Lupie^{cj}, William Van Altena^m, Qiangguo Wang^k, G. Welter, and Robert Zarba^e. Numerous other individuals from many organizations provided extensive support for the activities described in this paper. These organizations include

- | | |
|--|---|
| a. Allied Signal Aerospace Corporation | i. Marshall Space Flight Center |
| b. AKG, Incorporated | j. Space Telescope Science Institute |
| c. Computer Sciences Corporation | k. The University of Texas Astronomy
Department |
| d. Goddard Space Flight Center | l. The University of Virginia Astronomy
Department |
| e. Hughes Danbury Optical Systems | m. Yale University Astronomy Department |
| f. Lowell Observatory | |
| g. Jackson and Tull | |
| h. Lockheed Missiles and Space Company | |

Many other individuals were involved with activities in prelaunch preparation for the calibration of the HST attitude sensors. Of particular note for their support in this area are Paul Davenport, whose analytic insights provided the basis for, or extensions of, many of the algorithms in the PASS system; Gerald Abshire^c, who coordinated the software development effort for the original implementation of most of the PASS sensor calibration algorithms; and Robert Coulterⁱ, who coordinated the intricate prelaunch scheduling of the early orbital verification activities. The calibration of HST will be an ongoing effort, with varying degrees of intensity, throughout the lifetime of the telescope. It is, and will continue to be, an interesting and stimulating intellectual challenge.

The work reported in this article was supported in part by NASA contract NAS-5-31500, which enables CSC to provide general systems engineering and analysis support to NASA/GSFC, including specific support for the HST mission.

REFERENCES

1. J. Wertz (ed.), Spacecraft Attitude Determination and Control. Dordrecht, Holland: D. Reidel Publishing Company, 1978
2. Computer Sciences Corporation, CSC/TM-82/6045, Space Telescope POCC Applications Software Support (PASS) Requirements Specification (Revision E), L. Hallock et al., September 1987
3. M. Shuster and S. Oh, *Three-Axis Attitude Determination from Vector Observations*, Journal of Guidance and Control, January 1981, vol. 4, no. 1, p. 70
4. National Space Science Data Center, Goddard Space Flight Center, Code 633.4, *International Geomagnetic Reference Field Revision 1987*
5. P. Davenport, W. Ruml, and G. Welter, *In-flight Determination of Spacecraft Magnetic Bias Independent of Attitude*, GSFC Flight Mechanics / Estimation Theory Symposium, May 1988

6. Computer Sciences Corporation, CSC/TM-88/6103. Hubble Space Telescope (HST) Flight Software Examination for the Pointing Control Subsystem (PCS), L. Hallock, March 1990
7. P. Davenport and G. Welter, *Algorithm for In-flight Gyroscope Calibration*, GSFC Flight Mechanics / Estimation Theory Symposium, May 1988
8. A. Bradley, L. Abramowicz-Reed, D. Story, G. Benedict, and W. Jefferys, *The Flight Hardware and Ground System for Hubble Space Telescope Astrometry*, Publications of the Astronomical Society of the Pacific, 1991, vol. 103, p. 317
9. Marshall Space Flight Center, SMO-1040, Hubble Space Telescope Astrometry Operations Handbook, March 1987
10. K. Luchetti, G. Abshire, L. Hallock, and R. McCutcheon, *The Optical Field Angle Distortion Calibration Feasibility Study for the Hubble Space Telescope Fine Guidance Sensors*, GSFC Flight Mechanics / Estimation Theory Symposium, May 1988
11. W. Jefferys, *On the Method of Least Squares*, The Astronomical Journal, February 1980, vol. 85, no. 2, p. 177
12. W. Smart, Text-Book on Spherical Astronomy. Cambridge, England: Cambridge University Press, 1971
13. T. Girard, C. Heisler, Y.-W. Lee, C. Lopez, W. van Altena, and P. Ianna, *Astrometric Calibration Regions with Proper Motion Membership Estimates in the Open Clusters NGC 188 and NGC 5617*, Poster Presentation at the January 1990 Meeting of the American Astronomical Society held in Washington D.C.

FLIGHT MECHANICS/ESTIMATION THEORY SYMPOSIUM

MAY 21-23, 1991

SESSION 5

N92-14091

**AN EXTENDED KALMAN FILTER
FOR SPINNING SPACECRAFT
ATTITUDE ESTIMATION**

by

David F. Baker

NASA - Goddard Space Flight Center
Attitude Analysis Section (554.1)
Greenbelt, MD 20771

ABSTRACT

An extended Kalman filter for real-time ground attitude estimation of a gyro-less spinning spacecraft has been developed and tested. The filter state vector includes the angular momentum direction, phase angle, inertial nutation angle, and inertial and body nutation rates. The filter solves for the nutating three-axis attitude and accounts for effects due to principle axes offset from the body axes. The attitude is propagated using the kinematics of a rigid body symmetric about the principle spin axis; disturbance torques are assumed to be small. Filter updates consist only of the measured angles between celestial objects (Sun, Earth, etc.) and the nominal spin axis, and the times these angles were measured.

Both simulated data and real data from the Dynamics Explorer -A (DE-A) spacecraft were used to test the filter; the results are presented. Convergence was achieved rapidly from a wide range of a priori state estimates, and sub-degree accuracy was attained. Systematic errors affecting the solution accuracy are discussed, as are the results of an attempt to solve for sensor measurement angle biases in the state vector.

1. INTRODUCTION

The Kalman filter presented here was developed as part of a continuing effort in the Attitude Analysis Section (Code 554.1) at NASA/Goddard to investigate the potential of sequential filters for spacecraft ground attitude estimation. The filter was developed primarily to provide accurate real-time attitude determination for spinning spacecraft to complement the batch estimators that have been used up until now. Use of this filter or a successor is planned in support of upcoming spinning spacecraft missions such as SAMPEX/FAST.

Kalman filtering has the potential for obtaining attitude estimates of comparable, if not superior, accuracy to currently-used batch methods, since, like batch methods, it can use large numbers of measurements in its solution, while, unlike them, it also models dynamic noise. Moreover, it has the potential for doing this in real-time with minimal human operator involvement, unlike batch methods. The filter presented here was coded and run on a 286-class IBM PC clone, in part to demonstrate the potential of personal computers for computation-intensive attitude estimation.

A complete modeling of the dynamics of an asymmetrical, rigid spacecraft could probably be incorporated into a Kalman filter, using, for example, the equations given in Melvin (1989). Due to their complexity, however, it is not obvious that these equations could be propagated quickly enough for real-time attitude estimation using a PC. To retain a high degree of accuracy while ensuring real-time performance, the highly linear dynamics model used by Markley, et.al. (1988), which models the nutational motion of an axisymmetrical rigid body, has been used.

Measurement equations are developed which, given a sensor complement of a single Sun sensor and a single Earth sensor, permit the filter to solve for the nutating three-axis attitude of a spinning spacecraft. A discussion of systematic errors affecting the spin axis estimate is given last, and those errors which may be compensated for or solved for in the filter are noted.

2. DYNAMICS MODEL

Spinning spacecraft are usually designed to spin about a nominal spin axis, taken here as the body Z axis, Z_b . The deployment process usually imparts a nutational motion to the spacecraft, however, which causes the nominal spin axis to move on an elliptical cone about the spacecraft angular momentum vector L at the inertial nutation rate w_1 . If the principle axis of the spacecraft Z_p is offset from Z_b , it is Z_p that nutates about L , while Z_b revolves on a circular cone about Z_p at the body nutation rate w_b in a motion called "coning" (Wertz, p.489). Since the angular measurements returned by the attitude sensors are referenced to Z_b , its motion must be modeled for accurate attitude estimation. It should be noted that most spacecraft have nutation dampers to reduce inertial nutation, but this motion is present to some degree most of the time.

The attitude of the spacecraft, given as the attitude matrix A_{pi} which transforms a vector in an inertial frame into the spacecraft principle axis frame, may be represented as the product:

$$A_{pi}(t) = A_{p1}(t) A_{1i}(t) \quad (1)$$

$$\begin{aligned} \text{where} \quad A_{1i}(t) &= A_2(\pi/2-\delta) A_3(\alpha) \\ A_{p1}(t) &= A_3(\psi) A_1(\theta) A_3(\phi) \end{aligned}$$

and where $A_j(\Gamma)$ represents a rotation Γ about the j th body axis (Markley, et.al., (1988)). Matrix A_{1i} , which transforms a vector into an intermediate frame with the spacecraft angular momentum vector along its Z axis, is introduced to separate the motions of L and Z_p . This is done since, for most spinning spacecraft, the spin rate is chosen so that the integrated magnitude of all disturbance torques acting on the spacecraft is negligible compared to the magnitude of the angular momentum vector L . In this case, the direction of L remains essentially constant, and A_{1i} is therefore constant as well; the spin axis attitude of the spinning spacecraft is generally defined as the angular momentum direction. Note that if the angular momentum direction were to change rapidly, this motion could be modeled with a variation of parameters approach (Kraige and Junkins (1976)).

Angles ϕ , θ , and ψ , which define the nutational motion of the spacecraft about L , are given by complicated elliptic

functions in time for the general case of a spacecraft with unequal transverse principle moments of inertia (those perpendicular to the spin axis) (Melvin (1989)). In the interest of filter run-time performance, the filter presented here models only the axisymmetrical case, in which the two transverse principle moments of inertia are equal.

With the spacecraft assumed to be an axisymmetrical rigid body experiencing negligible external torques, the attitude and dynamics of the spacecraft may be described by the following state vector equations (Markley, et.al. (1988)):

$$\mathbf{x} = [\alpha, \delta, \phi, \theta, \psi, w_1, w_p]^T \quad (2)$$

$$\dot{\mathbf{x}} = [0, 0, w_1, 0, w_p, 0, 0]^T \quad (3)$$

where

α, δ = the right ascension and declination of the angular momentum vector in geocentric inertial (GCI) coordinates;

ϕ, θ, ψ = three 3-1-3 Euler angles specifying the attitude of the nutating spacecraft with respect to the angular momentum reference frame, where θ is the constant nutation angle and where ϕ and ψ are (for small nutation angles) basically rotations about the spin axis; the sum $\phi + \psi$ is approximately equal to the "phase angle";

w_1 = the inertial nutation rate at which \mathbf{z}_p nutates about the angular momentum vector \mathbf{L} ;

w_p = the body nutation rate at which \mathbf{z}_b cones about \mathbf{z}_p .

3. MEASUREMENT MODEL

This analysis assumes that all attitude measurements received by the spacecraft are represented as the angle between the nominal spacecraft spin axis, \mathbf{z}_b , and a sensed reference vector, \mathbf{V} , known precisely in the inertial frame. The time of this angular measurement is also used. While this model is a simplification of measurements obtained by real sensors, it

captures the essential attitude information and permits the results to be compared easily with other vector-based approaches, such as that, for example, given by Schuster (1983).

For each angle/time pair received from a each sensor, three measurements are calculated as follows:

$$z_1 = \cos(\Omega) \quad (4)$$

$$z_2 = 0. \quad (5)$$

$$z_3 = 2\pi / (t_2 - t_1). \quad (6)$$

where

Ω = measured angle between \mathbf{V} and \mathbf{Z}_b

t_2 = time of measurement

t_1 = time of previous measurement of \mathbf{V}_i by same sensor

The first measurement corresponds to the measured angle itself, the second to the sine of a reference phase angle at the measurement time, and the third to the total spin rate.

These actual measurements received from the sensors are compared to three corresponding expected measurements calculated by the filter from the propagated state estimate as follows:

$$\begin{aligned} h_1 &= \mathbf{V}_i \cdot \mathbf{Z}_{b,i} \\ &= \mathbf{V}_i^T [\mathbf{A}_{il}(\alpha, \delta)] [\mathbf{A}_{lp}(\phi, \theta, \psi)] \mathbf{Z}_{b,p} \end{aligned} \quad (7)$$

$$\begin{aligned} h_2 &= \mathbf{V}_i \cdot \mathbf{T}_i \\ &= \mathbf{V}_i^T [\mathbf{A}_{il}(\alpha, \delta)] [\mathbf{A}_{lp}(\phi, \theta, \psi)] \mathbf{T}_p \end{aligned} \quad (8)$$

$$h_3 = w_1 + w_b \quad (9)$$

where $\mathbf{T}_p = (\mathbf{B}_p \times \mathbf{Z}_{b,p}) / |\mathbf{B}_p \times \mathbf{Z}_{b,p}|$

and

- \mathbf{A}_{il} -- the angular momentum-to-inertial attitude matrix
- \mathbf{A}_{lp} -- the principle-to-angular momentum attitude matrix
- \mathbf{T}_p -- the measurement "trigger vector", principle frame
- \mathbf{B}_p -- Sensor boresight vector, principle frame
- $\mathbf{Z}_{b,p}$ -- the body Z axis \mathbf{Z}_b in the principle axes frame
- $\mathbf{Z}_{b,i}$ -- the body Z axis \mathbf{Z}_b in the inertial frame

Note: all the vectors above are of unit length.

The difference $h-z$ between the expected and actual measurements is used to update the filter state and covariance. Note that the measurement equations are non-linear in the state parameters. Because of this, the notation and equations for the extended Kalman filter have been used here.

4. KALMAN FILTER ALGORITHM

In this study, the standard extended Kalman filter equations have been used, given as follows (Gelb, p.188):

State estimate and error covariance dynamic propagation:

$$\dot{\mathbf{x}}(t) = \mathbf{f}(\mathbf{x}(t), t) \quad (10)$$

$$\dot{\mathbf{P}}(t) = \mathbf{F}(\mathbf{x}(t), t)\mathbf{P}(t) + \mathbf{P}(t)\mathbf{F}^T(\mathbf{x}(t), t) + \mathbf{Q}(t) \quad (11)$$

State estimate and error covariance measurement update:

$$\mathbf{x}_k(+) = \mathbf{x}_k(-) + \mathbf{K}_k [\mathbf{z}_k - \mathbf{h}_k(-)] \quad (12)$$

$$\mathbf{P}_k(+) = [\mathbf{I} - \mathbf{K}_k \mathbf{H}_k(-)] \mathbf{P}_k(-) [\mathbf{I} - \mathbf{K}_k \mathbf{H}_k(-)]^T + \mathbf{K}_k \mathbf{R}_k \mathbf{K}_k^T \quad (13)$$

where

$$\mathbf{K}_k = \mathbf{P}_k(-) \mathbf{H}_k^T(-) [\mathbf{H}_k(-) \mathbf{P}_k(-) \mathbf{H}_k^T(-) + \mathbf{R}_k]^{-1} \quad (14)$$

For a complete development of the theory and meaning of these equations, see the Gelb reference. The Joseph update in equation (13) was found to be necessary for numerical stability, while iterating the measurement update (Gelb, p.190) was found useful for converging large errors in the a priori estimate.

5. FILTER PERFORMANCE WITH SIMULATED DATA

A truth model was developed to provide realistic measurements to the filter for a range of attitudes and dynamics for testing purposes. The true spacecraft attitude and dynamics were given by:

$$\mathbf{x} = [\alpha, \delta, \phi, \theta, \psi, w_1, w_p]^T \quad (15)$$

$$\dot{\mathbf{x}} = [0, 0, w_1, 0, w_p, 0, 0]^T + \mathbf{U} \quad (16)$$

basically the same model used in the filter, except with U , the dynamic noise, added (Markley, et.al., (1988)). While this truth model does not account for the effects of external torques and does not model the dynamics of non-axisymmetrical spacecraft, it does permit the testing of the filter without the interference of modeling error.

A battery of filter runs were performed to test the convergence of the filter from a variety of a priori state estimates. For these tests, only the data from a single Sun sensor and a single Earth sensor were used to update the state estimate. The covariance results of these tests showed that state parameters ϕ , ψ , w_1 , and w_p were in all cases highly correlated, to the largest degree in the tests where the nutation angle θ was small. Because of this high correlation, the filter was able to estimate the angles ϕ and ψ to only within about 5° at best.

Because of measurements h_2 and h_3 on the phase angle and spin rate, respectively, the filter was however able to estimate the sums $\phi+\psi$ (the phase angle) and w_1+w_p (the spin rate) quite accurately. Since most spinning spacecraft may be supported adequately without the need for knowing the phase angle, much less the component angles ϕ and ψ , the above observability problem would probably not be an operational concern as long as the attitude would be solved for adequately. Indeed, despite the 5° error in ϕ and ψ , the filter solves for the spin axis attitude in terms of α and δ to sub-degree accuracy in all the test cases that were run.

An explanation for the observability problem noted above follows. The phase angle $\phi+\psi$ and spin rate w_1+w_p are estimated quickly and accurately by measurements h_2 and h_3 , respectively. The only information to distinguish between ϕ and ψ and between w_1 and w_p , however, comes from measurement h_1 , the cosine of the angle between the body Z axis and the sensed reference vector. The measured angle will oscillate sinusoidally with amplitude θ and angular rate w_1 as the spacecraft principle Z axis rotates about the angular momentum vector at the inertial nutation rate. Also, the location of the angle on this sinusoidal curve permits only two possibilities for angle ϕ . For larger nutation angles θ the filter can isolate both ϕ and w_1 using the variation in h_1 , allowing for a fairly accurate determination of ϕ , ψ , w_1 , and w_p when combined with measurements h_2 and h_3 . For cases of small

nutations angles or large measurement noise on h_1 , however, the sinusoidal variation in h_1 becomes difficult to distinguish and the uncertainty in ϕ , ψ , w_1 , and w_p becomes larger. In contrast to a 5° best-case uncertainty in ϕ and ψ , the uncertainty may grow to 30° or more for the smallest nutation angles. Simulations have shown, however, that when the nutation angle becomes small enough to cause large errors in ϕ and ψ , it is also so small that it does not significantly affect the spin axis determination either.

5.1 SAMPLE CONVERGENCE RESULTS

Figures 1 to 3 illustrate how the state estimate converges from three different large a priori state errors. The true state is compared to the Kalman filter estimate, and two error terms are calculated. The spin axis error is approximated by:

$$SAE = [d^2(\alpha) + d^2(\delta)]^{.5} \quad (17)$$

while the error in a "reduced state" with components $\phi+\psi$ and w_1+w_p , instead of ϕ , ψ , w_1 , w_p , is given by:

$$RSE = [d^2(\alpha) + d^2(\delta) + d^2(\phi+\psi) + d^2(\theta) + d^2(w_1+w_p)]^{.5} \quad (18)$$

In these equations, $d^2()$ represents the square of the difference between the estimated and actual values of the parameter in parentheses.

The initial conditions for these runs are given in the Appendix. Figure 1 shows that the filter almost immediately solves for the spin axis to an uncertainty of only about 0.1° from an a priori state with a 20° error. A more realistic convergence scenario is illustrated in Fig. 2 for an a priori estimate with errors on the order of 70° for ϕ and ψ , and on the order of 20° for their sum. In practice, these angles should be the most difficult state initialization parameters to calculate, so these large errors are appropriate. Figure 2 shows that the filter takes substantially longer to converge, but solves for the spin axis to the same 0.1° uncertainty level after about a minute.

Figure 3 illustrates convergence from an a priori state with errors on the order on 5 deg/sec for w_1 and w_p and 2 deg/sec for their sum. The filter has the most difficulty converging with

large nutation rate errors, because they generate large errors in ϕ and ψ , as well, during convergence. This difficulty is reflected in Figure 3, which shows that the filter requires over five minutes to converge to a 0.1° spin axis attitude uncertainty. The large value of the error in the reduced state is caused by the filter converging to a negative value of the nutation angle θ ; this result is perfectly acceptable, and serves to illustrate that angle ϕ was driven 180° from its a priori value due to the high a priori rate errors. It should be noted that a priori rate errors as large as these should never have to be input into the filter, since w_1 and w_p can be calculated accurately beforehand, given the spin rate and moments of inertia of the spacecraft (Wertz, p.490).

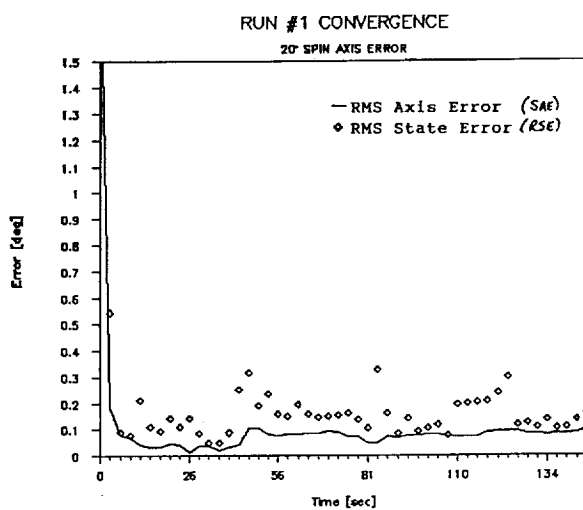


Figure 1.
Large A Priori Spin Axis Attitude Error

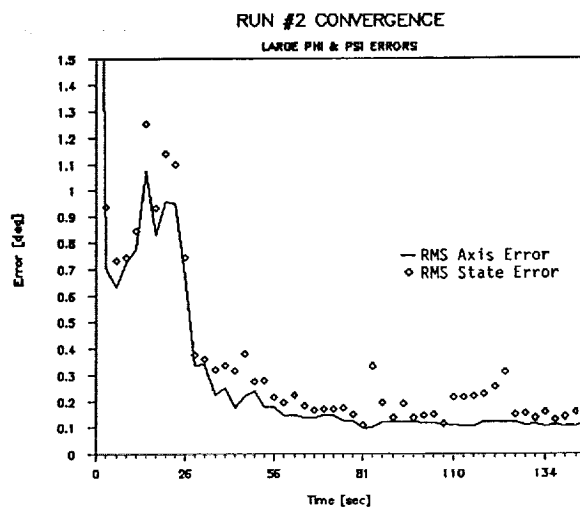


Figure 2.
Large A Priori ϕ and ψ Errors

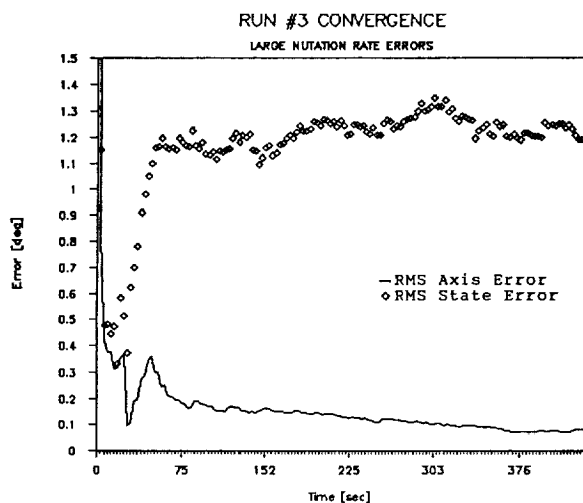


Figure 3.
Large A Priori Nutation Rate Errors

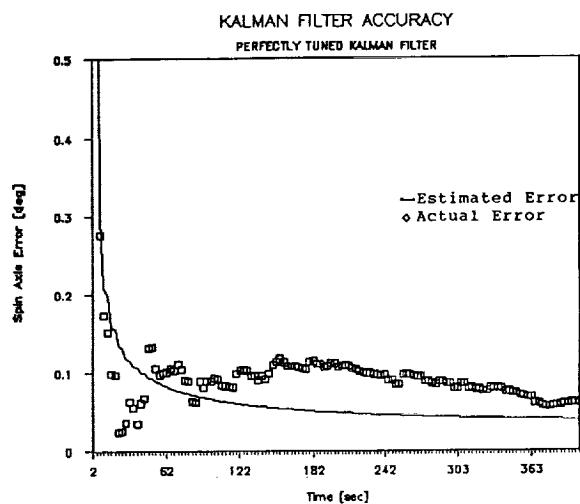


Figure 4.
Perfectly Tuned Kalman Filter

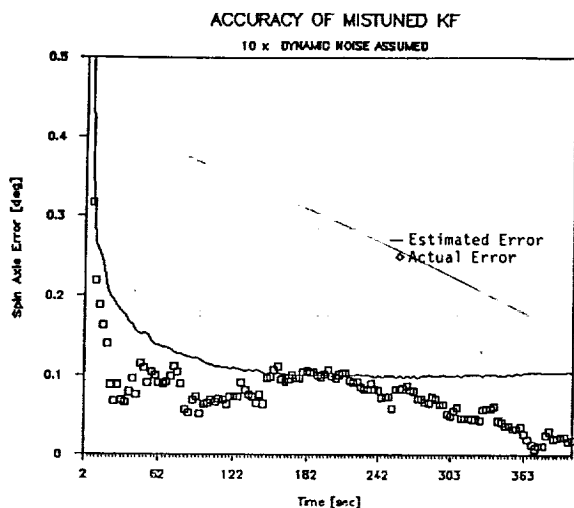


Figure 5.
Assumed Dynamic Noise 10x Too Large

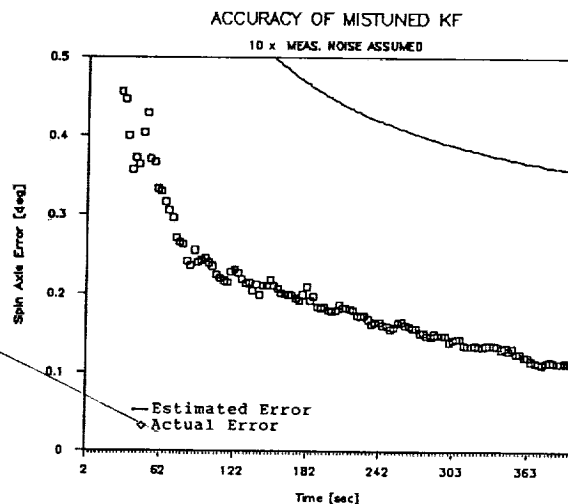


Figure 6.
Assumed Measurement Noise 10x Too Large

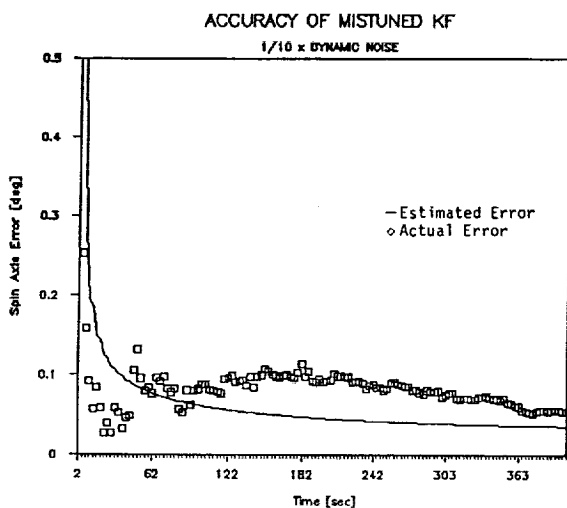


Figure 7.
Assumed Dynamic Noise 10x Too Small

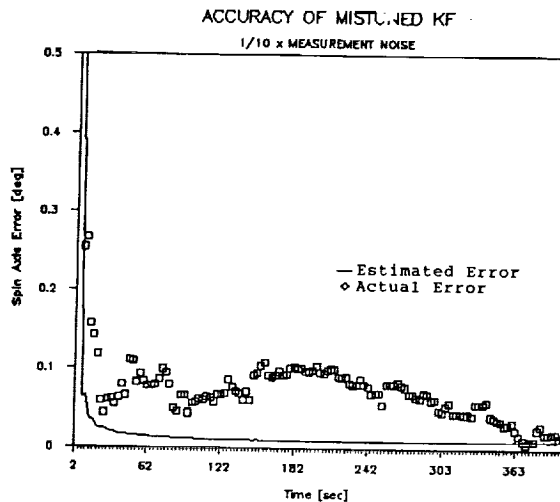


Figure 8.
Assumed Measurement Noise 10x Too Small

5.2 ACCURACY RESULTS

The user of a Kalman filter is required to make an estimate the magnitude of the dynamic and measurement noise affecting the system and the data being filtered. The magnitude of this noise is usually not known exactly, especially in the case of the dynamic noise, and may not even be known to within an order of magnitude. Since the magnitude estimate of these noise terms is always in error to some degree, it is interesting to see how such "mistuning" effects the filter results. The truth model enables the actual error in the state estimate to be compared against the

Kalman filter covariance, which indicates how well the filter believes it is estimating the state.

Figures 4 through 8 plot as a function of time both the actual spin axis error, approximated by equation (17) (the difference between the true values and the KF estimates), and the Kalman filter covariance corresponding to the same error. Figure 4 gives these results for a perfectly tuned filter, Figures 5 and 6 for assumed values for dynamic and measurement noise 10 times too high, respectively, and Figures 7 and 8 for those same respective noises assumed to be 10 times too low. While the actual and estimated errors do not agree exactly, even in the perfectly tuned case, an overriding tendency can be noted: the accuracy of the Kalman filter covariance seems to be much more sensitive to the assumed measurement noise magnitude than to the assumed dynamic noise magnitude. This is fortunate, since the properties of the dynamic noise are usually known less well than those of the measurement noise.

The parameters used the accuracy runs above are given in the Appendix. In additional runs not shown here, for which the dynamic noise and measurement noise were set to zero in both the truth model and the Kalman filter, the actual and estimated errors were both extremely low, as would be expected, since the filter and truth model both use the same dynamics model.

5.3 FILTER SPEED

Besides achieving sub-degree accuracy, the Kalman filter for the runs above was able to propagate and update in real time. This was achieved by choosing an appropriate value for the propagation step size; this step size could be set quite large because of the linearity of the dynamics. Since the test cases above were run assuming a spacecraft spin rate of about 10 rpm, and since two measurements were assumed to be received each spin period (a Sun angle and an Earth angle), the filter had to process a measurement update every 3 seconds on the average to operate in real time. The runs were executed on a 12 MHz 286-class IBM PC clone. Use of a faster 386-class machine would permit smaller dynamic propagation steps to be taken, or, alternatively, a larger number of measurements to be processed per spin period.

6. PERFORMANCE WITH ACTUAL SPACECRAFT DATA

Attitude sensor data were obtained from the DE-A spacecraft in order to test the potential of the Kalman filter for actual spacecraft ground attitude determination. The author was unable to obtain data for a period with significant nutational motion, however, so the following results only validate the filter's performance for the nutationally-damped case.

Data from a single Earth sensor and a single Sun sensor were entered into the Kalman filter as input. Nadir angles had to be calculated beforehand from the original DE-A Earth sensor data, and precalculated biases were subtracted from the Sun angles before they were input, as well.

TABLE 1 -- KF INPUT FOR DE-A DATA RUN

$\mathbf{x}_0 = [1.1968, -.17216, 0., 0., -1.3209, -1.9568, .89226]^T$
 Dynamic noise = $[.001, .001, .005, .002, .005, .002, .002]^T$
 Measurement noise = $[.0002, .01, .0002]^T$
 \mathbf{z}_b , principle frame = $[0., 0., 1.]^T$
 Uncert. in $\mathbf{x}_0 = [.03, .03, 1.0, .005, 1.0, .001, .001]^T$

The filter input parameters for the run are given in Table 1. The estimated filter spin axis right ascension and declination are plotted in Figures 9 and 10, with the batch solution plotted as the straight line on the same plots. As Table 2 shows, the difference between the Kalman filter and batch spin axis directions is within the 0.21 degree uncertainty given by both the Kalman filter and batch methods. The fact that the Kalman filter and batch covariances agree so closely suggests that level of dynamic noise, which the batch method does not model, is of negligible significance in this data as compared with the level of measurement noise.

TABLE 2 -- COMPARISON OF KF & BATCH SOLUTIONS

	<u>Batch</u>	<u>KF</u>	<u>Difference</u>
Spin Axis RA [deg]	68.2610	68.35	+0.089
Spin Axis Dec [deg]	-9.4650	-9.54	-0.075
Spin Axis Att [deg]			0.116
Att. Uncert. [deg]	0.2178	0.21	

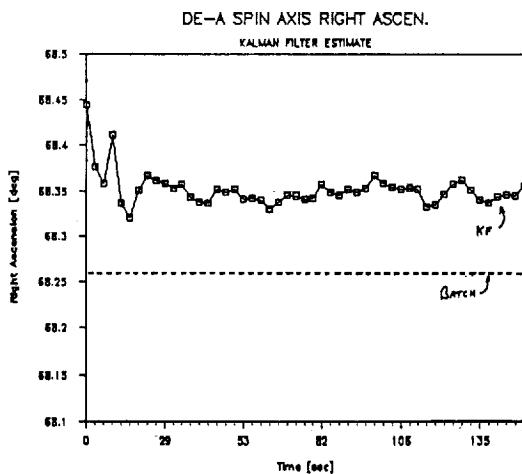


Figure 9.

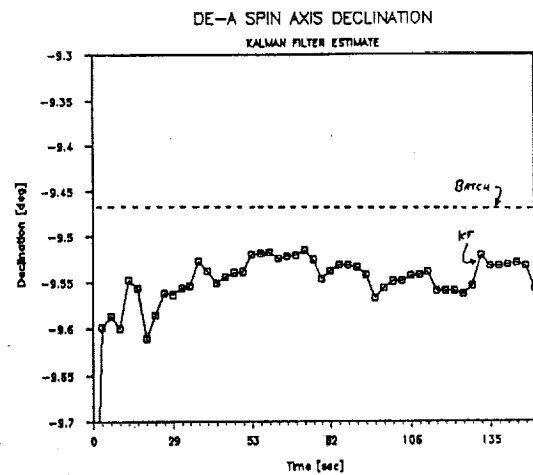


Figure 10.

7. UNMODELED ERROR SOURCES

7.1 SPACECRAFT ASYMMETRY EFFECTS

The Kalman filter described above successfully solves for the nutating 3-axis attitude of an axisymmetrical spinning spacecraft. No spacecraft is truly axisymmetrical, however, since the two principle moments of inertia perpendicular to the spin axis are always unequal to some degree. The Kalman filter estimate will therefore suffer from modeling error when real data from a nutating spacecraft is filtered. The Kalman filter should in this case try to model the elliptical path of \mathbf{Z}_p about \mathbf{L} for the real spacecraft with a circular path. The modeling error would depend on the extent of the spacecraft asymmetry, and would cause both an increase in the uncertainty of the spin axis attitude uncertainty and a shift in the solved-for spin axis direction (Wertz, p.541). This error source could be removed by correctly modeling the dynamics of an asymmetric spacecraft, perhaps with a state based on the dynamics model of Melvin (1989).

7.2 SENSOR BIASES AND MISALIGNMENTS

If not compensated for, sensor biases and misalignments can cause large shifts in the solved-for spin axis direction. A bias or misalignment that systematically changes the measured angle between the spacecraft body Z axis and the reference vector may cause a shift in the estimated spin axis direction: using the analogy of the cone method attitude solution (Wertz, p.363) for an Earth and Sun sensor, the spin axis direction, lying along the intersection of the Sun and Earth cones, changes as the Sun and Earth angles change from their true to their biased values. As discussed below, attempts to solve for Sun and Earth angle biases by adding them to the state vector were not successful. The filter given above could easily compensate for precalculated angle biases, however, by subtracting these biases from the measured angles before using them in the update equations.

The relative misalignment of sensors in the plane perpendicular to the body Z axis would change the timing of the angular measurements, affecting the accuracy of the estimated ϕ and ψ angles, the w_1 and w_p nutation rates, and, to a much lesser extent, the spin axis direction, as well.

7.3 Z_p OFFSET FROM Z_b

If the principle Z axis, Z_p , of the spacecraft is offset from the body Z axis, Z_b , due to non-zero products of inertia I_{xz} and I_{yz} , then Z_b will "cone" about Z_p at the body nutation rate (see Wertz, p.490). This coning motion will add a sinusoidally-varying error to measurements taken at a rate other than the spin rate (e.g., from a magnetometer), but will simply add a constant bias to measurements taken at the spin rate (e.g., from a Sun or Earth sensor) since the direction of Z_b relative to Z_p and the sensed reference vector V is the same for subsequent measurements.

This bias may result in a systematic error in the estimated spin axis direction for filters that assume Z_b and Z_p are collinear. The effects of the Z_b/Z_p offset may be removed in this Kalman filter, however, simply by entering the value of Z_b in the spacecraft principle reference frame into the measurement equations (7) and (8). Vector Z_b in the principle frame may be calculated from the mass moment of inertia matrix.

8. SENSOR MISALIGNMENT ESTIMATION PROBLEM

An attempt was made to solve for the angular biases noted above in the Kalman filter, in hopes of removing this major source of spin axis attitude error. A Sun angle bias and an Earth angle bias were added to the state and dynamics model, and the measurement equations were modified to account for the bias terms. The truth model then produced simulated angular measurements shifted by specified Sun and Earth biases, and the Kalman filter was applied to the data to solve for the specified biases along with the attitude.

The filter was unable to solve for the applied biases, however, due to high correlations between these biases and the attitude parameters. In particular, the filter was unable to differentiate between the angular biases and errors in the spin axis direction. A covariance analysis was performed using the Attitude Determination Error Analysis System (ADEAS) (Nicholson, et.al. (1988)) to determine to what accuracy the biases could be expected to be solved for. The ADEAS results suggested that for normal noise levels the biases could not be determined in the Kalman filter to a useful level of accuracy.

9. CONCLUSION

In this paper, a new Kalman filter has been presented that solves for the nutating 3-axis attitude of a spinning spacecraft in real-time on a 286-class IBM PC clone to an accuracy comparable to or better than the batch methods currently used. The filter has been tested both with simulated data and with real data from the DE-A spacecraft. Although a modified version of the filter was unsuccessful in solving for biases on the measured angles, the filter could compensate for these errors if biases calculated in some other way were to be input into the filter. Similarly, the filter can remove errors due a $\mathbf{z}_p/\mathbf{z}_b$ offset by using the easily-calculated $\mathbf{z}_{b,p}$ vector as input.

Attitude errors due to unequal spacecraft transverse moments of inertia cannot be compensated for in this filter. Further work on removing this error source by properly modeling the general motion of an asymmetrical rigid body would be valuable.

REFERENCES

- Dynamics Explorer -A and -B Attitude System Functional Specifications and Requirements, OAO Corporation, Beltsville, Maryland, under contract No. NASA-25534, December, 1979.
- Fang, B.T., "Mathematical Specifications for an Attitude/Orbit Error Analysis System", Planetary Sciences Dept., Report No. 009-74 under Contract No. NAS 5-20098, October, 1974.
- Gelb, A., ed., Applied Optimal Estimation, The MIT Press, 1974.
- Kraige, L.G., and J.L. Junkins, "Perturbation Formulations for Satellite Attitude Dynamics", Celestial Mechanics, Vol 13. (1976), pp. 39-64.
- Markley, F.L., E. Seidewitz, and M. Nicholson, "A General Model for Attitude Determination Error Analysis", Proceedings of the Flight Mechanics/Estimation Theory Symposium, May 1988.
- Melvin, P.J., "A New Method for Generation of Torque Free Motion of a Satellite", AIAA Paper No. 89-0546.
- Nicholson, M., F.L. Markley, and E. Seidewitz, Attitude Determination Error Analysis (ADEAS) Mathematical Specifications Document, CSC/TM-88/6001, Computer Sciences Corporation, October 1988.
- Schuster, M.D., "Efficient Algorithms for Spin Axis Attitude Estimation", The Journal of the Astronautical Sciences, Vol. 31, No. 2, pp. 237-249, April-June, 1983.
- Wertz, J.R., ed., Spacecraft Attitude Determination and Control, D. Reidel Publishing Company, Boston, 1978.

APPENDIX

CONVERGENCE TEST PARAMETERS

Truth Model Input: ($\mathbf{x} = [\alpha, \delta, \phi, \theta, \psi, w_1, w_p]^T$)

$$\mathbf{x}_0 = [1.222, -.349, 1., .01, 1., 1.925, -.8777]^T$$

$$\text{Dynamic noise} = [.00001, .00001, .005, .0002, .005, .003, .003]^T$$

$$\text{Measurement. noise} = [.002, .002, .002]^T$$

$$\mathbf{z}_b, \text{ principle frame} = [0., 0., 1.]^T$$

Base Parameters for KF Runs:

$$\mathbf{x}_0 = [1.172, -.399, .83, .0, .915, 1.915, -.8727]^T$$

$$\text{Dynamic noise} = [.000015, .000015, .0075, .0003, .0075, .0045, .0045]^T$$

$$\text{Measurement. noise} = [.003, .003, .003]^T$$

$$\mathbf{z}_b, \text{ principle frame} = [0., 0., 1.]^T$$

$$\text{Uncert. in } \mathbf{x}_0 = [.05, .05, .17, .02, .17, .01, .01]^T$$

Run #1 -- Large A Priori Spin Axis Attitude Error

$$\mathbf{x}_0 = [1.469, -.596, .83, .0, .915, 1.915, -.8727]^T$$

$$\text{Uncert. in } \mathbf{x}_0 = [.25, .25, .17, .02, .17, .01, .01]^T$$

Run #2 -- Large A Priori ϕ and ψ Errors

$$\mathbf{x}_0 = [1.172, -.399, -.2, 0., 2.6, 1.915, -.8727]^T$$

$$\text{Uncert. in } \mathbf{x}_0 = [.05, .05, 1.5, .02, 1.5, .01, .01]^T$$

Run #3 -- Large A Priori Nutation Rate Errors

$$\mathbf{x}_0 = [1.172, -.399, .83, .0, .915, 1.82, -.8077]^T$$

$$\text{Uncert. in } \mathbf{x}_0 = [.05, .05, .17, .02, .17, .2, .2]^T$$

(Units: angles in radians, rates in radians/second)

ACCURACY TEST PARAMETERS

Truth Model Input: ($\mathbf{x} = [\alpha, \delta, \phi, \theta, \psi, w_1, w_p]^T$)

$\mathbf{x}_0 = [1.222, -.349, 1., .01, 1., 1.925, -.8777]^T$

Dynamic noise = $\mathbf{D} =$
 $[.00001, .00001, .005, .0002, .005, .003, .003]^T$

Measurement noise = $\mathbf{M} = [.002, .002, .002]^T$

\mathbf{z}_b , principle frame = $[0., 0., 1.]^T$

Base Parameters for KF Runs:

$\mathbf{x}_0 = [1.172, -.399, .83, .0, .915, 1.915, -.8727]^T$

\mathbf{z}_b , principle frame = $[0., 0., 1.]^T$

Uncert. in $\mathbf{x}_0 = [.05, .05, .17, .02, .17, .01, .01]^T$

Run #1 -- Perfectly tuned KF

Dynamic noise = \mathbf{D}

Measurement noise = \mathbf{M}

Run #2 -- Assumed Measurement Noise 10x Too Large

Dynamic noise = \mathbf{D}

Measurement noise = 10. x \mathbf{M}

Run #3 -- Assumed Dynamic Noise 10x Too Large

Dynamic noise = 10. x \mathbf{D}

Measurement noise = \mathbf{M}

Run #4 -- Assumed Measurement Noise 10x Too Small

Dynamic noise = \mathbf{D}

Measurement noise = .10 x \mathbf{M}

Run #5 -- Assumed Dynamic Noise 10x Too Small

Dynamic noise = .10 x \mathbf{D}

Measurement noise = \mathbf{M}

(Units: angles in radians, rates in radians/second)

QUATERNION NORMALIZATION IN ADDITIVE EKF
FOR SPACECRAFT ATTITUDE DETERMINATION

by

I.Y. Bar-Itzhack^{*}, J. Deutschmann⁺, and F.L. Markley[#]

Abstract

This work introduces, examines and compares several quaternion normalization algorithms, which are shown to be an effective stage in the application of the additive extended Kalman filter (EKF) to spacecraft attitude determination, which is based on vector measurements. Two new normalization schemes are introduced. They are compared with one another and with the known brute force normalization scheme, and their efficiency is examined. Simulated satellite data are used to demonstrate the performance of all three schemes. A fourth scheme is suggested for future research.

Although the schemes were tested for spacecraft attitude determination, the conclusions are general and hold for attitude determination of any three dimensional body when based on vector measurements, and use an additive EKF for estimation, and the quaternion for specifying the attitude.

* Professor, Faculty of Aerospace Engineering, Technion - Israel Institute of Technology, member Technion Space Research Institute, Haifa, Israel 32000. Tel. (972)4-293196.

+ Aerospace Engineer, Attitude Analysis Section, Flight Dynamics Analysis Branch, NASA Goddard Space Flight Center, Greenbelt, MD 20771. Tel. (301) 286-9033.

Assistant Head, Guidance and Control Branch, NASA Goddard Space Flight Center, Greenbelt, MD 20771. Tel. (301) 286-8333.

I. INTRODUCTION

Attitude determination of spacecraft usually utilizes vector measurements such as Sun, center of Earth, star, and magnetic field direction to update the quaternion which determines the spacecraft orientation with respect to some reference coordinates in the three dimensional space [1,2,3]. These measurements are usually processed by an extended Kalman filter (EKF) which yields an estimate of the attitude quaternion [4-8].

Two EKF versions for quaternion estimation were presented in the literature; namely, the multiplicative EKF [4-6] and the additive EKF [5,7,8]. In the multiplicative EKF it is assumed that the error between the correct quaternion and its *a-priori* estimate is, by itself, a quaternion that represents the rotation necessary to bring the attitude which corresponds to the *a-priori* estimate of the quaternion into coincidence with the correct attitude. The EKF basically estimates this quotient quaternion and then the updated quaternion estimate is obtained by the *product* of the *a-priori* quaternion estimate and the estimate of the difference quaternion. In the additive EKF it is assumed that the error between the *a-priori* quaternion estimate and the correct one is an algebraic difference between two four-tuple elements and thus the EKF is set to estimate this difference. The updated quaternion is then computed by *adding* the estimate of the difference to the *a-priori* quaternion estimate.

If the quaternion estimate converges to the correct quaternion, then, naturally, the quaternion estimate has unity norm. This fact was utilized in the past to obtain superior filter performance by applying normalization to the filter measurement update of the quaternion [7]. It was observed for the additive EKF that when the attitude changed very slowly between measurements, normalization merely resulted in a faster convergence [7,8]; however, when the attitude changed considerably between measurements, without filter tuning or normalization, the quaternion estimate diverged. However, when the quaternion

estimate was normalized, the estimate converged faster and to a lower error than with tuning only.

In the next section we introduce the additive EKF for attitude determination. The role of quaternion normalization in the additive EKF is explained in Section III. In Section IV we discuss the brute force (BF) normalization scheme and examine its performance. In the following sections we introduce the quaternion pseudo-measurement (QPM), and the magnitude pseudo-measurement (MPM). Test results of the application of all normalization algorithms discussed in this work to simulated Earth Radiation Budget Satellite (ERBS) data is presented in Section VII. In Section VIII we introduce the linearized orthogonalized matrix (LOM) normalization scheme as a suggestion for future investigation. Finally, the conclusions of this work are discussed in Section IX.

II. THE ADDITIVE EKF FOR QUATERNION ESTIMATION

Attitude determination from vector observations using the additive EKF is explained as follows. Suppose that a sequence $\underline{v}_{bm,i}$ $i=0,1,2,\dots$ of vector measurements performed in body, b , coordinates are given. Given are also these vectors in the reference coordinate system r . Denote the latter vectors by $\underline{v}_{r,i}$ $i=0,1,2,\dots$. The vector $\underline{v}_{bm,i}$ is a column matrix whose elements are the components of a vector \bar{v} measured at time t_i and coordinatized in the body coordinate system. Similarly, the corresponding $\underline{v}_{r,i}$ vector is a column matrix whose elements are the components of the same vector \bar{v} coordinatized in the reference coordinate system. Our aim is to estimate the quaternion \underline{q} which expresses the body attitude with respect to the reference coordinate system. To meet this end we define an *effective measurement* \underline{y} as follows

$$\underline{y}_i = \underline{v}_{bm,i} - A(\hat{\underline{q}})\underline{v}_{r,i} \quad (2.1)$$

where A is the direction cosine matrix (DCM) which transforms vectors from r to b , and where \hat{q} is the latest estimate of q . The vector $v_{bm,i}$ which is a result of a measurement, contains all the error associated with the instrumentation, such as instrument misalignments, scale factor error, bias, white noise etc. The vector $v_{r,i}$ is taken from the almanac and is assumed to be perfectly known. We observe that when the measurement is error free and when the quaternion estimate is accurate, y_i is zero. On the other hand, when these assumptions do not hold, then y_i is a, generally non-linear, function of the instrument and attitude errors.

The measured vector $v_{bm,i}$ can be expressed as follows

$$v_{bm,i} = v_{b,i} + \left. \frac{\partial v}{\partial e} \right|_{v_{b,i}} (\delta e + n_i) \quad (2.2)$$

where $v_{b,i}$ is the error-free value of \bar{v} when coordinatized in the b system. the Jacobian matrix

$$H_{e,i} \triangleq \left. \frac{\partial v}{\partial e} \right|_{v_{b,i}} \quad (2.3)$$

is the sensitivity matrix of the error associated with the measurement $v_{bm,i}$ as a function of the instrument errors. The latter are expressed as a sum of a narrow spectrum error vector, δe , and a wide spectrum error vector n_i , which is modeled as a white noise error vector. The vector e contains all the instrumentation errors mentioned before, while δe denotes the difference between e and its compensation value which is the latest estimate of e denoted by \hat{e} .

Define δq as follows

$$\delta q = q - \hat{q} \quad (2.4)$$

then

$$A(q) = A(\hat{q} + \delta q) \quad (2.5)$$

therefore, based on the assumption that $\delta \underline{q}$ is small such that $\hat{\underline{q}}$ is close enough to \underline{q} , $A(\underline{q})$ can be approximated as follows

$$A(\underline{q}) = A(\hat{\underline{q}}) + \sum_{j=1}^4 \left. \frac{\partial A(\underline{q})}{\partial q_j} \right|_{\hat{\underline{q}}} \delta q_j \quad (2.6)$$

consequently

$$A(\hat{\underline{q}}) \underline{v}_{-r,1} = A(\underline{q}) \underline{v}_{-r,1} - \sum_{j=1}^4 \left. \frac{\partial A(\underline{q})}{\partial q_j} \right|_{\hat{\underline{q}}} \delta q_j \quad (2.7)$$

Define

$$G_j = G_j(\hat{\underline{q}}) = \left. \frac{\partial A(\underline{q})}{\partial q_j} \right|_{\hat{\underline{q}}} \quad (2.8)$$

Since

$$A(\underline{q}) = \begin{bmatrix} q_1^2 - q_2^2 - q_3^2 + q_4^2 & 2(q_1 q_2 + q_3 q_4) & 2(q_1 q_3 - q_2 q_4) \\ 2(q_1 q_2 - q_3 q_4) & -q_1^2 + q_2^2 - q_3^2 + q_4^2 & 2(q_2 q_3 + q_1 q_4) \\ 2(q_1 q_3 + q_2 q_4) & 2(q_2 q_3 - q_1 q_4) & -q_1^2 - q_2^2 + q_3^2 + q_4^2 \end{bmatrix} \quad (2.9)$$

then

$$G_1 = 2 \begin{bmatrix} \hat{q}_1 & \hat{q}_2 & \hat{q}_3 \\ \hat{q}_2 & -\hat{q}_1 & \hat{q}_4 \\ \hat{q}_3 & -\hat{q}_4 & -\hat{q}_1 \end{bmatrix} \quad (2.10a)$$

$$G_2 = 2 \begin{bmatrix} -\hat{q}_2 & \hat{q}_1 & -\hat{q}_4 \\ \hat{q}_1 & \hat{q}_2 & \hat{q}_3 \\ \hat{q}_4 & \hat{q}_3 & -\hat{q}_2 \end{bmatrix} \quad (2.10b)$$

$$G_3 = 2 \begin{bmatrix} -\hat{q}_3 & \hat{q}_4 & \hat{q}_1 \\ -\hat{q}_4 & -\hat{q}_3 & \hat{q}_2 \\ \hat{q}_1 & \hat{q}_2 & \hat{q}_3 \end{bmatrix} \quad (2.10c)$$

$$G_4 = 2 \begin{bmatrix} \hat{q}_4 & \hat{q}_3 & -\hat{q}_2 \\ -\hat{q}_3 & \hat{q}_4 & \hat{q}_2 \\ \hat{q}_2 & -\hat{q}_1 & \hat{q}_4 \end{bmatrix} \quad (2.10d)$$

Define

$$\underline{h}_j = G_{j-r,i} v_{j-r,i} \quad (2.11)$$

and

$$H_{q,i} = \begin{bmatrix} \underline{h}_1 | \underline{h}_2 | \underline{h}_3 | \underline{h}_4 \end{bmatrix} \quad (2.12)$$

then using (2.12), (2.7) can be written as

$$A(\hat{q}) v_{-r,i} = A(\underline{q}) v_{-r,i} - H_{q,i} \delta \underline{q} \quad (2.13)$$

Finally from (2.1), (2.2), (2.3) and (2.13) we obtain

$$\underline{y}_i = \underline{v}_{b,i} + H_{e,i} \delta \underline{e} + H_{e,i} \underline{n}_i - A(\underline{q}) v_{-r,i} + H_{q,i} \delta \underline{q} \quad (2.14)$$

Since $\underline{v}_{b,i}$, $A(\underline{q})$ and $\underline{v}_{-r,i}$ are error-free, it is clear that

$$\underline{v}_{b,i} = A(\underline{q}) v_{-r,i} \quad (2.15)$$

therefore (2.14) can be written as

$$\underline{y}_i = H_{e,i} \delta \underline{e} + H_{q,i} \delta \underline{q} + \underline{n}_i^* \quad (2.16)$$

where

$$\underline{n}_i^* = H_{e,i} \underline{n}_i \quad (2.17)$$

Note that (2.16) can be written as

$$\underline{y}_i = \begin{bmatrix} H_{q,i} | H_{e,i} \end{bmatrix} \begin{bmatrix} \delta \underline{q} \\ \delta \underline{e} \end{bmatrix} + \underline{n}_i^* \quad (2.18)$$

The propagation of the vector $[\delta \underline{q}^T | \delta \underline{e}^T]^T$ (where T denotes the transpose) in time can be expressed by the linear equation [8]

$$\frac{d}{dt} \begin{bmatrix} \delta \underline{q} \\ \delta \underline{e} \\ \delta \underline{p} \end{bmatrix} = \begin{bmatrix} F \end{bmatrix} \begin{bmatrix} \delta \underline{q} \\ \delta \underline{e} \\ \delta \underline{p} \end{bmatrix} + \underline{w} \quad (2.19)$$

where $\delta \underline{p}$ contains additional states necessary to express (2.19) as a linear equation driven by a white noise vector \underline{w} . For compatibility with (2.19), (2.18) is extended to include $\delta \underline{p}$ as follows

$$\underline{y}_i = [H_{q,i} | H_{e,i} | 0] \begin{bmatrix} \delta \underline{q} \\ \delta \underline{e} \\ \delta \underline{p} \end{bmatrix} + \underline{n}_i \quad (2.20)$$

The set (2.19) and (2.20) can be written as

$$\dot{\underline{x}} = F \underline{x} + \underline{w} \quad (2.21a)$$

$$\underline{y}_i = H_i \underline{x} + \underline{n}_i^* \quad (2.21b)$$

where $H_i = [H_{q,i} | H_{e,i} | 0]$. The latter equations can be used in an EKF to compute $\hat{\underline{x}}_i$, the estimate of \underline{x} at time t_i .

Let $\underline{X}^T = [\underline{q}^T | \underline{e}^T | \underline{p}^T]$ then according to the EKF algorithm, $\hat{\underline{x}}_i(-)$, the a-priori estimate of \underline{x} at time t_i is used to calculate H_i which is needed to obtain the a-posteriori estimate $\hat{\underline{x}}_i(+)$. The latter is then used to update the entire state estimate as follows

$$\hat{\underline{x}}_i(+) = \hat{\underline{x}}_i(-) + \hat{\underline{x}}_i(+) \quad (2.22)$$

Using (2.21a), $\hat{\underline{x}}_i(+) is propagated in time to become $\hat{\underline{x}}_{i+1}(-)$, the a-priori entire state estimate at time t_{i+1} . The dynamics matrix for the propagation of $\hat{\underline{x}}_i(+) is denoted by A (see (2.23a). The covariance which is needed for computing the Kalman gain necessary for evaluating $\hat{\underline{x}}_i(+) is computed according to the ordinary Kalman filter algorithm. To sum it up, the full EKF algorithm is as follows$$$

Between measurements

Solve from t_i to t_{i+1}

$$\dot{\underline{\hat{x}}} = A[\underline{\hat{x}}(t), t] \underline{\hat{x}} \quad (2.23a)$$

$$\dot{P} = A[\underline{\hat{x}}(t), t] P + P A^T[\underline{\hat{x}}(t), t] + Q(t) \quad (2.23b)$$

with the initial conditions $\hat{X}_0 = \hat{X}_1(+)$, $P_0 = P_1(+)$. The solutions at t_{i+1} are denoted by $\hat{X}_{i+1}(-)$ and $P_{i+1}(-)$ respectively. $Q(t)$ is the spectral density matrix [9] of \underline{w} .

Across measurements

$$K_{i+1} = P_{i+1}(-)H_{i+1}^T [H_{i+1}P_{i+1}(-)H_{i+1}^T + R_{i+1}]^{-1} \quad (2.23c)$$

$$\hat{\underline{x}}_{i+1}(+) = K_{i+1}\underline{y}_{i+1} \quad (2.23d)$$

$$\hat{\underline{x}}_{i+1}(+) = \hat{\underline{x}}_{i+1}(-) + \hat{\underline{x}}_{i+1}(+) \quad (2.23e)$$

$$P_{i+1}(+) = [I - K_{i+1}H_{i+1}] P_{i+1}(-) [I - K_{i+1}H_{i+1}]^T + K_{i+1}R_{i+1}K_{i+1}^T \quad (2.23f)$$

where R_{i+1} is the covariance of \underline{n}_{i+1}^* .

Compensation

In computing (2.23a) and (2.23b) we need to use the gyro output vector \underline{w} which contains errors. Those errors are estimated as a part of $\hat{\underline{p}}$. Before each time (2.23a,b) are used, the errors have to be appropriately compensated using their estimate. Similarly, $\underline{v}_{bm,i}$, which is used in (2.1) to obtain \underline{y}_i , contains errors which constitute \underline{e} . Before each time \underline{y}_i is computed (for use in (2.23d)), the errors in $\underline{v}_{bm,i}$ have to be compensated using their estimate.

III. THE ROLE OF QUATERNION NORMALIZATION

The state measurement update given in (2.23e) can be written in an explicit form as follows:

$$\begin{bmatrix} \hat{\underline{q}}(+) \\ \hat{\underline{e}}(+) \\ \hat{\underline{p}}(+) \end{bmatrix}_{i+1} = \begin{bmatrix} \hat{\underline{q}}(-) \\ \hat{\underline{e}}(-) \\ \hat{\underline{p}}(-) \end{bmatrix}_{i+1} + \begin{bmatrix} \delta\hat{\underline{q}}(+) \\ \delta\hat{\underline{e}}(+) \\ \delta\hat{\underline{p}}(+) \end{bmatrix}_{i+1} \quad (3.1)$$

Unless convergence has been attained, $\hat{\underline{q}}_{i+1}(+)$ is not necessarily normal even if $\hat{\underline{q}}_{i+1}(-)$ is. We know, however, that the quaternion which the algorithm is trying to estimate is necessarily normal. We can then enforce normalization on $\hat{\underline{q}}_{i+1}(+)$ with the hope that the enforcement of this quality of the correct quaternion will direct the estimated quaternion in the right track and will enhance its convergence. Indeed, it was found in the past [7,8] that normalization is helpful. In particular, it was found that when the attitude varies very slowly between measurements, normalization, although not necessary, resulted in a faster convergence; however, when the attitude changed rapidly between measurements either filter tuning or normalization were necessary to avoid divergence. The use of normalization is superior to tuning because, first, tuning involves a tedious trial and error process, second, tuning is not a robust solution, and third, with quaternion normalization the final attitude estimate is closer to the correct quaternion.

Four normalization schemes are discussed next.

IV. BRUTE FORCE (BF) NORMALIZATION

The BF normalization is performed as follows [7]. After $\hat{\underline{x}}_{i+1}(+)$ has been computed in (2.23e) the quaternion part of the state (see (3.1)) is normalized as follows

$$\hat{\underline{q}}_{i+1}^*(+) = \hat{\underline{q}}_{i+1}(+) / \|\hat{\underline{q}}_{i+1}(+)\| \quad (4.1)$$

and then, the normal quaternion, $\hat{\underline{q}}_{i+1}^*(+)$, is used to re-form $\hat{\underline{x}}_{i+1}(+)$ as follows

$$\hat{\underline{x}}_{i+1}(+) = \begin{bmatrix} \hat{\underline{q}}^*(+) \\ \hat{\underline{e}}(+) \\ \hat{\underline{p}}(+) \end{bmatrix}_{i+1} \quad (4.2)$$

This straightforward mode of normalization constitutes an outside interference in the EKF algorithm which has to be accounted for in order to avoid filter divergence. It was shown [7] that the normalization operation of (4.1) is tantamount to the following computation of $\hat{q}_{i+1}^*(+)$

$$\hat{q}_{i+1}^*(+) = \left[\hat{q}_{i+1}(-) + \delta \hat{q}_{i+1}(+) \right] - \hat{q}_{i+1}(-) \hat{q}_{i+1}^T(-) \delta \hat{q}_{i+1}(+) \quad (4.3)$$

Therefore, while the EKF algorithm presented in Section II assumes that the a-priori quaternion estimate is updated according to (2.23e) as follows

$$\hat{q}_{i+1}(+) = \hat{q}_{i+1}(-) + \delta \hat{q}_{i+1}(+) \quad (4.4)$$

in reality, due to the normalization, it is updated according to (4.3). The difference is then in the term $-\hat{q}_{i+1}(-) \hat{q}_{i+1}^T(-) \delta \hat{q}_{i+1}(+)$. Because of this residual term, the full reset implied by (4.4) does not hold anymore. Therefore, following the logic of the EKF algorithm, the residual term, $-\hat{q}_{i+1}(-) \hat{q}_{i+1}^T(-) \delta \hat{q}_{i+1}(+)$ has to be propagated in time. It was shown [7] that this mode of normalization does not affect the covariance computation of the EKF; therefore, only the state computation has to be modified. In view of the normalization operation of (4.1), the following changes have to be made in the EKF algorithm presented in Section II. Between measurements, in addition to the computation of $\hat{x}_{i+1}(-)$ and $P_{i+1}(-)$, compute also $\delta \hat{q}_{i+1}(-)$ as follows. Solve from t_i to t_{i+1} the differential equation

$$\dot{\delta \hat{q}} = F_q [\hat{x}(t), t] \delta \hat{q} \quad (4.5)$$

where F_q is the 1,1 submatrix of F , with the initial condition $\delta \hat{q}_0 = \hat{q}_1(-) \hat{q}_1^T(-) \delta \hat{q}_1(+)$ and denote the solution at t_{i+1} by $\delta \hat{q}_{i+1}(-)$. Then form

$$\hat{x}_{i+1}^T(-) = [\delta \hat{q}_{i+1}^T(-), 0^T, 0^T] \quad (4.6)$$

and change (2.23d) to read

$$\hat{\underline{x}}_{i+1}(+) = \hat{\underline{x}}_{i+1}(-) + K_{i+1}[\underline{y}_{i+1} - H_{i+1}\hat{\underline{x}}_{i+1}(-)] \quad (4.7)$$

The BF normalization algorithm has all the expected advantages mentioned in Section III; however, it is not elegant in the sense that the normalization constitutes an outside interference in the EKF algorithm which has to be compensated. This compensation adds a certain complication to the algorithm presented in Section II. Therefore we propose the following QPM normalization scheme.

V. QUATERNION PSEUDO-MEASUREMENT (QPM) NORMALIZATION

According to this algorithm the updated quaternion $\hat{\underline{q}}_{i+1}(+)$ is used to form a pseudo-measurement as follows

$$\underline{y}_{n,i+1} = \hat{\underline{q}}_{i+1}(+) / || \hat{\underline{q}}_{i+1}(+) || \quad (5.1)$$

It is then assumed that the quaternion is measured by an imaginary device, say "quaternion-meter", and the output of this device is $\underline{y}_{n,i+1}$ plus a small white measurement error. Following this rationale a measurement update is performed which is based on the quaternion measurement. To accomplish that we realize from (3.1) that $\underline{y}_{n,i+1}$ is related to the state vector as follows

$$\underline{y}_{n,i+1} = H_{n,i+1} \underline{x}_{i+1} + \underline{n}_{n,i+1} \quad (5.2)$$

where

$$\underline{x}_{i+1}^T = [\underline{q}^T | \underline{e}^T | \underline{p}^T]_{i+1} \quad (5.3)$$

$$H_{n,i+1} = \left[\begin{array}{cccc|c|c} 1 & 0 & 0 & 0 & 0 & 0 \\ 0 & 1 & 0 & 0 & 0 & 0 \\ 0 & 0 & 1 & 0 & 0 & 0 \\ 0 & 0 & 0 & 1 & 0 & 0 \end{array} \right] \quad (5.4)$$

and $R_{n,i+1}$, the covariance of $\underline{n}_{n,i+1}$, is the diagonal matrix

$$R_{n,i+1} = \text{diag}[r^2, r^2, r^2, r^2] \quad (5.5)$$

and where r is a small number. The a-priori state estimate for this measurement update is, of course, $\hat{x}_{i+1}^{(-)}$. Note that the output of this update is the full state vector and not just the estimate of, x , the difference between \hat{x}_{i+1} and its estimate $\hat{x}_{i+1}^{(-)}$. This pseudo-measurement update is performed after the computation in (2.23f) has been carried out. The pseudo-measurement update algorithm is as follows. $K_{n,i+1}$ is computed according to (2.23c) where H_{i+1} and $P_{i+1}^{(-)}$ and R_{i+1} are replaced by $H_{n,i+1}$, $P_{i+1}^{(-)}$ and $R_{n,i+1}$ respectively. The state update is then re-computed as follows

$$\hat{x}_{i+1}^{(+)} = \hat{x}_{i+1}^{(-)} + K_{n,i+1} [y_{n,i+1} - H_{n,i+1} \hat{x}_{i+1}^{(-)}] \quad (5.6)$$

and $P_{i+1}^{(+)}$ is re-computed according to (2.23f) where K_{i+1} , H_{i+1} and $P_{i+1}^{(-)}$ are replaced by $K_{n,i+1}$, $H_{n,i+1}$ and $P_{i+1}^{(-)}$ respectively. The new estimate and its covariance are then propagated in time as before.

The QPM normalization performs quite well and achieves the expected benefits of quaternion normalization provided r is well tuned. If this is not the case, the attitude estimate may reach a wrong value, and if the attitude changes between vector measurements, it may even diverge. The reason for this is described next.

For the normalization to be effective one is tempted to choose a small r in which case the filter practically replaces the stored quaternion estimate by the normalized quaternion. However, the small "measurement noise", r , reduces the variance of the quaternion estimation error considerably. Therefore, the filter assigns a very high credibility to the normalized quaternion estimate even though it is not yet the correct quaternion. Consequently, the filter does not allow new vector measurements to alter the quaternion estimate and the latter is stuck on a wrong value. If the quaternion changes now due to attitude change

then the quaternion estimate diverges. In order to avoid this phenomenon one has to tune the value of r which constitutes an additional design burden. Therefore although, unlike the BF normalization, the QPM normalization blends naturally into the EKF algorithm, the required tuning constitutes a considerable disadvantage. To alleviate this problem we proposed the following magnitude pseudo-measurement normalization scheme.

VI. MAGNITUDE PSEUDO-MEASUREMENT (MPM) NORMALIZATION

Unlike the previous scheme, where we assumed that we "measured" the normalized quaternion, here we assume that we "measure" the square of the quaternion Euclidean norm whose magnitude is assumed to be 1. This imaginary "norm meter" yields the reading z where

$$z_{n,i+1} = 1 + v_{n,i+1} \quad (6.1)$$

and where $v_{n,i+1}$ is assumed to be a white measurement noise whose variance is r . Note that the "measured" quantity is a non-linear function of the quaternion components; therefore, we compute the *effective* measurement, $y_{n,i+1}$, as

$$y_{n,i+1} = z_{n,i+1} - \left[\hat{q}(+)_{1,i+1}^2 + \hat{q}(+)_{2,i+1}^2 + \hat{q}(+)_{3,i+1}^2 + \hat{q}(+)_{4,i+1}^2 \right] \quad (6.2)$$

Using (6.1) and (2.4), (6.2) can be written as

$$y_{n,i+1} = 1 - \sum_{j=1}^4 \left[q_{j,i+1} - \delta q_{j,i+1} \right]^2 + v_{n,i+1} \quad (6.3)$$

Neglecting products of $\delta q_{j,n+1}$, (6.3) can be written as

$$y_{n,i+1} = 1 - \left[\sum_{j=1}^4 q_{j,i+1}^2 - 2 \sum_{j=1}^4 q_{j,i+1} \delta q_{j,i+1} \right] + v_{n,i+1} \quad (6.4)$$

and since

$$\sum_{j=1}^4 q_{j,i+1}^2 = 1 \quad (6.5)$$

then (6.4) can be written as

$$y_{n,i+1} = \left[2q_{1,i+1} \middle| 2q_{2,i+1} \middle| 2q_{3,i+1} \middle| 2q_{4,i+1} \right] \begin{bmatrix} \delta q_{1,i+1} \\ \delta q_{2,i+1} \\ \delta q_{3,i+1} \\ \delta q_{4,i+1} \end{bmatrix} + v_{n,i+1} \quad (6.6)$$

Since $q_{j,i+1}$ $j=1,2,3,4$ is unknown, we follow the common practice of replacing the quaternion components by their estimate, thus

$$y_{n,i+1} = \left[2\hat{q}(+)_{1,i+1} \middle| 2\hat{q}(+)_{2,i+1} \middle| 2\hat{q}(+)_{3,i+1} \middle| 2\hat{q}(+)_{4,i+1} \right] \begin{bmatrix} \delta q_{1,i+1} \\ \delta q_{2,i+1} \\ \delta q_{3,i+1} \\ \delta q_{4,i+1} \end{bmatrix} + v_{n,i+1} \quad (6.7)$$

The latter is the measurement equation which is used to perform a magnitude pseudo-measurement normalization update. The sequence of operations is similar to that performed when the QPM normalization update is carried out (see the preceding section). The only difference is that now

$$y_{n,i+1} = 1 - \sum_{j=1}^4 \hat{q}(+)_{j,i+1}^2 \quad (6.8)$$

$$H = \left[2\hat{q}(+)_{1,i+1} \middle| 2\hat{q}(+)_{2,i+1} \middle| 2\hat{q}(+)_{3,i+1} \middle| 2\hat{q}(+)_{4,i+1} \right] \quad (6.9)$$

and

$$R_{n,i+1} = r \quad (6.10)$$

We realize that the fact that r is very small does not imply that the

measurement of \underline{q} is precise. It only implies that the measurement of $\|\underline{q}\|$ is precise. Therefore, now the variances of the quaternion states do not increase to a value close to r and thus the estimates of the quaternion components do not cling to wrong values and stay there like they do when the preceding QPM normalization is applied with a small r .

VII. TEST RESULTS

The algorithms presented in this paper were and still are being tested now. In these tests the EKF is applied to simulated as well as to real Earth Radiation Budget Satellite (ERBS) data. Partial results are presented as follows.

Quaternion normalization speeds up the convergence of the additive EKF when used to estimate spacecraft attitude from vector measurements. Moreover, if the attitude changes considerably between vector measurements, quaternion normalization replaces filter tuning which is necessary to avoid divergence. In the latter case, quaternion normalization also reduces the final attitude estimation error.

In Table 7.1 we see the final attitude estimation error when the EKF is applied to simulated ERBS data. The initial attitude error is 30° and the value of r used in the QPM and MPM algorithms is 10^{-5} .

Table 7.1: Final Attitude Error in Degrees at 100 sec, $r=10^{-5}$

	Normalization Algorithm			
	Without Normalization	BP	QPM	MPM
Yaw	.0048	.0074	.0057	.0069
Roll	.0022	-.0002	.0019	.0039
Pitch	.0170	.0060	-.0009	-.0033
RMS	0.0178	0.0095	0.0061	0.0086

Note that the BF algorithm implies no measurement update therefore no r is used in this run. We turn to Table 7.2 to see the advantage of the MPM over the QPM algorithm. We realize that while for $r=10^{-5}$ both algorithms exhibit identical accuracy, the QPM algorithm fails when $r=10^{-11}$. The reason for this difference was mentioned at the end of Section V.

Table 7.2: Final Attitude Error in Degrees at 100 sec, $r=10^{-11}$

	Normalization Algorithm	
	QPM	MPM
Yaw	3.2387	.0045
Roll	10.3660	.0083
Pitch	-0.7451	.0127

VIII. SUGGESTED FUTURE RESEARCH

Although the MPM normalization performed satisfactorily we suggest to investigate an algorithm of implied normalization which does not really use normalization. This algorithm is presented next.

In Section II we presented the development of the additive EKF for quaternion estimation. In that development we derived the linearized relationship between the vector measurement error and the quaternion estimation error which are summarized in (2.16). To meet this end we differentiated the matrix $A(\underline{q})$ given in (2.9). The differentials were partial differentials with respect to the elements of \underline{q} . As a result of the differentiations we obtained the matrices G_j , $j=1,2,3,4$ which are listed in (2.10).

When \underline{q} is indeed of unit length, $A(\underline{q})$ is an orthonormal matrix; that is, its columns (rows) are orthogonal to one another and are of unit length. If, however, \underline{q} is not of unit length, then the columns (rows) of $A(\underline{q})$ are still orthogonal to one another, but their length is not a unit anymore. It was proven

in [10] that the matrix $A^*(\hat{q})$ computed as follows

$$A^*(\hat{q}) = \frac{1}{\|\hat{q}\|^2} A(\hat{q}) \quad (8.1)$$

is not only orthonormal, but it is also the "closest" orthonormal matrix to $A(\underline{q})$; that is, of all possible orthonormal matrices, the distance between $A^*(\hat{q})$ and $A(\underline{q})$ is the smallest where by distance we mean the Euclidean norm of the difference matrix $A^*(\underline{q}) - A(\underline{q})$. It can be argued that if we use $A^*(\hat{q})$ rather than $A(\hat{q})$, we practically enforce normalization. This is so because normalizing \hat{q} first and then using the normalized quaternion to compute $A(\hat{q})$ is identical to the computation of $A^*(\hat{q})$ as given in (8.1). The partial differentiation of (8.1) with respect to the quaternion components yields

$$\Gamma_j = \Gamma_j(\hat{q}) = \left. \frac{\partial A^*(\underline{q})}{\partial q_j} \right|_{\hat{q}} = - \frac{2\hat{q}_j}{\|\hat{q}\|^4} A(\hat{q}) + \frac{1}{\|\hat{q}\|^2} G_j(\hat{q}) \quad (8.2)$$

where $G_j(\hat{q})$ is given in (2.10). The final algorithm is as given in Section II with Γ_j replacing G_j in (2.11). We call this normalization scheme the linearized orthogonalized matrix (LOM) algorithm.

Finally, in the future we intend to apply all the normalization schemes discussed here to real ERBS data.

IX. CONCLUSIONS

It was found again that quaternion normalization in the additive EKF for attitude determination from vector measurement has the following advantages. If the attitude changes slowly, normalization speeds up estimation convergence. If attitude changes rapidly between measurements and no normalization is applied then filter tuning has to be used in order to avoid divergence. However, if normalization is applied, convergence is achieved without filter tuning. Moreover, the final attitude estimation error is smaller. There is then a clear

advantage to quaternion normalization. Three quaternion normalization algorithms were tested. The conclusions with regard to the use of each one of them is listed next.

- The brute force (BF) normalization algorithm works well and exhibits the normalization benefits described before.
- The quaternion pseudo-measurement (QPM) algorithm performs well only after tuning.
- The magnitude pseudo-measurement (MPM) algorithm performs well and needs no tuning.

Finally, we suggest the investigation of the linearized orthogonal matrix (LOM) normalization whose development was presented in Section VII. All the normalization schemes will be tested on real ERBS data.

References

1. Wertz, J.R., *Spacecraft Attitude Determination and Control*, D. Reidel Publishing Company, Dordrecht, Holland, 1988.
2. Shuster, M.D., "Approximate Algorithm for Fast Optimal Attitude Computation," *AIAA Guidance and Control Conference*, Palo Alto, CA, Aug. 7-9, 1978, Paper 78-1249.
3. Shuster, M.D. and Oh, S.D., "Three Axis Attitude Determination from Vector Observation," *Journal of Guidance and Control*, Vol. 4, Jan.-Feb., 1981, pp. 70-77.
4. Murrell, J. W., "Precision Attitude Determination for Multimission Spacecraft," *AIAA Guidance and Control Conference*, Palo Alto, CA, Aug. 7-9, 1978, Paper 78-1248.
5. Lefferts, E.J., Markley, F.L., and Shuster, M.D., "Kalman Filtering for Spacecraft Attitude Estimation," *Journal of Guidance Control, and Dynamics*, Vol. 5, Sept-Oct. 1982, pp. 417-429.
6. Gai, E.G., Daly, K.C., Harrison, J.V., and Lamos, L., "Star-Sensor-Based Satellite Attitude/Attitude Rate Estimator," *Journal of Guidance, Control, and Dynamics*, Vol. 8, Sept.-Oct. 1985, pp. 560-565.
7. Bar-Itzhack, I.Y., and Oshman, Y., "Attitude Determination from Vector Observations: Quaternion Estimation," *IEEE Transactions on Aerospace and Electronic Systems*, Vol. AES-21, Jan., 1985, pp. 128-135.

8. Bar-Itzhack, I.Y. and Deutschmann, J., "Extended Kalman Filter for Attitude Estimation of the Earth Radiation Budget Satellite," *Astrodynamics Conference*, Portland, OR, Aug. 20-22, 1990, paper 90-2964.
9. Gelb, A., *Applied Optimal Estimation*, M.I.T. Press, Cambridge, MA, 1988, p. 75.
10. Giardina, C.R., Bronson, R., and Wallen, I., "An Optimal Normalization Scheme," *IEEE Transactions on Aerospace and Electronic Systems*, Vol. AES-11, July 1975, pp. 443-446.

COLORED NOISE EFFECTS ON BATCH ATTITUDE ACCURACY ESTIMATES¹

By Stephen Bilanow
General Sciences Corporation
6100 Chevy Chase Drive
Laurel, Maryland 20707

Abstract

This paper investigates the effects of colored noise on the accuracy of batch least squares parameter estimates with applications to attitude determination cases. The standard approaches used for estimating the accuracy of a computed attitude commonly assume uncorrelated (white) measurement noise, while in actual flight experience measurement noise often contains significant time correlations and thus is "colored." For example, horizon scanner measurements from low Earth orbit have been observed to show correlations over many minutes in response to large scale atmospheric phenomena.

A general approach to the analysis of the effects of colored noise is investigated, and interpretation of the resulting equations provides insight into the effects of any particular noise color and the worst case noise coloring for any particular parameter estimate. It is shown that for certain cases, the effects of relatively short term correlations can be accommodated by a simple correction factor. The errors in the predicted accuracy assuming white noise and the reduced accuracy due to the suboptimal nature of estimators that do not take into account the noise color characteristics are discussed. The appearance of a variety of sample noise color characteristics are demonstrated through simulation, and their effects are discussed for sample estimation cases. Based on the analysis, options for dealing with the effects of colored noise are discussed.

1. INTRODUCTION

A requirement for flight dynamics support is the estimation of the accuracy of attitude and orbit solutions, and this requires a knowledge of the measurement noise characteristics. Often, the measurement errors are assumed to be independent and identically distributed, what engineers commonly call "white" noise. One reason this assumption is made is simply that noise of this nature is easy to handle in estimation algorithms. However, this is not always a correct assumption for real spacecraft data. This paper investigates the implications of that assumption, discusses a formulation for calculating the true parameter uncertainty when the noise is not white, and shows how to interpret the effects of various noise colors in some representative cases.

"Colored" noise refers to any noise that is not white, i.e., that has correlations related to the time between measurements of the same type. "Batch" refers to the computation of fixed parameters using data over a given time span in a single solution.

1.1 COLORED NOISE IN SPACECRAFT DATA

Spacecraft horizon scanner data provides a clear example of measurement noise that is obviously non-white, and for which an explanation for long term correlations of various frequencies is apparent. Figure 1 shows a sample scanner data from Seasat and Landsat. In the Seasat mission, the bumps in the data were directly correlated with the infrared scanner "seeing" a high altitude cloud in the threshold adjust region of the horizon detection logic (Reference 1). Thus large scale atmospheric phenomena contributed a low-frequency "noise" to the scanner measurements. In the Landsat mission, the "bumps" could not be correlated with specific cloud features; however long term correlations are clearly present (note that the highest frequency component of the Landsat data noise was filtered by 128 point averaging for data volume reduction; the remaining noise variations clearly have longer correlations than white noise.) For Landsat some of the very long term variability was associated with seasonal

1. This work was supported by the NASA Small Business Innovation Research (SBIR) program

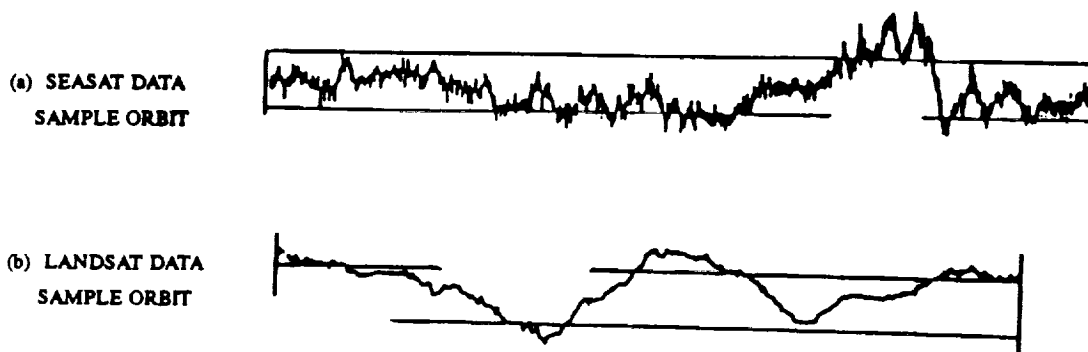


Figure 1. Sample Horizon Scanner Data from Seasat and Landsat

random stratospheric temperature variations (Reference 2). Ever since horizon scanners have first been built, manufacturers have worked to make them less sensitive to clouds in the lower atmosphere and to trigger on the more stable stratosphere, but yet it seems natural that this sensor may remain sensitive to large scale "weather" phenomena to some extent and thus have long term correlations in the data.

Other sources of long term correlations in sensor measurements can include any modeling uncertainties such as sensitivities to stray light, magnetic field changes (external or internally generated), or temperature variations. Certainly the line between noise and systematic errors can become blurred, but the low frequency noise model for some types of possible modeling errors can be useful. Another source of effective low frequency noise can be spacecraft dynamics modeling uncertainties or the effects of gyro noise. However, the similarity of the effects of these noise types with low frequency measurement noise will not be developed in this paper.

1.2 BRIEF LITERATURE REVIEW

The equations for treating colored noise in batch least squares estimation have long been known and are given in numerous textbooks. It is a matter of applying an optimal data weighting based on the expected correlations. However, as a practical matter, many actual estimation systems simply assume white noise. Although every relevant text reviews the optimal, maximum likelihood weighting, and the simplification with the white noise assumption, there is surprisingly little discussion of the impact of this simplifying assumption and what it can mean in practical batch estimation problems. Furthermore, there is a relatively simple formula for computing the accuracy of an estimator that assumes white noise while actual correlations are present. This formula does not seem to be noted, let alone its relevance emphasized, in most texts on estimation. The general form of this equation, giving the errors due to a difference between any assumed and actual noise covariance, is given in the mathematics for the general model for attitude determination error analysis developed at GSFC (Reference 3). However, in the current system implementation based on this analysis, only white noise assumptions are allowed (Reference 4). References 5 and 6 both mention this formula and discuss the implications briefly by an example. It is likely that more attention to this problem may be contained in the broad literature on estimation in various fields, but its consideration (particularly for flight dynamics applications) seems to be very infrequent.

There is notable available literature on handling colored noise in Kalman filter applications. Problems in handling colored noise in continuous time filters were first presented and resolved by Bryson and Johansen in 1965 (Reference 7), and further developments were provided and a few practical applications were discussed in papers that followed (References 8 through 12). Sections on handling "colored noise" in Kalman filters are found in books on estimation (e.g., References 5, and 13 through 15) published in the early 70's. These references give prescriptions for optimally filtering the data given colored noise. However, these references do not generally address a sensitivity analysis to the "suboptimal" white noise assumption in covariance analysis, which is the problem discussed in this paper in the batch estimation case.

Estimation and the spectral analysis of data in general is a field with a long history, wide application, and considerable development. Today, voluminous literature on spectral analysis and estimation is found in communications engineering, statistical time series analysis, time standards stability, and speech data processing, among other fields. Although effort was made to locate relevant references, an exhaustive survey is by no means claimed.

2. MATHEMATICAL DEVELOPMENT

2.1 OPTIMAL WEIGHTED LEAST SQUARES

We assume a linearized model of our measurements, z ,

$$z = Hx + \epsilon \quad (1)$$

where H is the matrix of partials of the measurements with respect to the state parameters, x is the state vector of parameters, and ϵ is the vector of measurement errors. Basic weighted batch least squares provides an estimate of the state parameters, \hat{x} ,

$$\hat{x}_0 = (H^T W H)^{-1} H^T W z \quad (2)$$

This estimate is optimal if the weight matrix is the inverse of the measurement noise covariance matrix

$$W = R^{-1} \quad (3)$$

where R is the expected noise covariance

$$R = E \begin{bmatrix} \epsilon & \epsilon^T \end{bmatrix} \quad (4)$$

The accuracy of an estimate is given by the state covariance matrix

$$P_0 = (H^T W H)^{-1} \quad (5)$$

These equations are the maximum likelihood estimate, or best linear unbiased estimate, and they are equivalent to the Bayesian estimate if no a priori uncertainty information is available.

2.2 WHITE NOISE/UNWEIGHTED LEAST SQUARES

If we know that our measurements are independent and uncorrelated, then R is a diagonal matrix. If we make the additional assumption that all the measurements have the same variance, then we may write R as a scalar times the identity matrix, I .

$$R = \sigma_m^2 I \quad (6)$$

and

$$W = \frac{1}{\sigma_m^2} I \quad (7)$$

In this case the estimator (2) simplifies to

$$\hat{x} = (H^T H)^{-1} H^T z \quad (8)$$

and the covariance of our estimate is given by

$$P_u = \sigma_m^2 (H^T H)^{-1} \quad (9)$$

This simplification is commonly made in many systems, including those for attitude determination. Two reasons often given are: (1) A priori measurement statistics may not be available, and it is often just assumed that independence of the measurements is a good model, and (2) It is also sometimes observed that optimal weighting requires computing the inverse of the measurement noise covariance, and this may not be practical when handling large amounts of data. This is an additional motivation for assuming equal weighting is good enough. (It is not widely noted that one basic colored noise model does have an exact form for its inverse – see Equation 23.)

It is the purpose of this paper to investigate the impact of this simplification on the expected covariance of our estimate. This can be particularly important for prelaunch studies when we want to predict how well our estimator will perform. It also can be of importance for postlaunch analysis if we want to use the estimators predicted covariance as an indicator of the actual attitude accuracy.

2.3 UNWEIGHTED ESTIMATOR WITH COLORED NOISE

The expected variance of the unweighted least squares estimator in the presence of correlated measurements may be derived directly by taking the expected covariance of estimator (8) assuming noise covariance R .

$$P_s = (H^T H)^{-1} H^T R H (H^T H)^{-1} \quad (10)$$

Thus if we have a model for the actual noise covariance, R , we can directly compute the error of our unweighted estimator. This is the main formula used to derive results presented in this paper. As observed in the literature review, it is remarkable how seldom this equation is noted.

As we shall see, interpreting results from this formula requires some careful attention. Note that there are as many terms in the noise covariance as there are points being fit in the least squares estimation. This gives a tremendous amount of power in terms of possible assumptions about our noise model. For example, this formula can be used to evaluate the effects of random biases as well as noise in the traditional sense.

In the terminology often used in error analysis, the unweighted least squares is considered a suboptimal estimator in the context that actual correlations are present in the noise (and hence the choice of subscript). Note however that we are not primarily concerned here with the actual performance of this suboptimal estimator relative to the optimal one, although we will make observations about this difference ($P_s - P_o$). Instead we will be concerned mainly about the erroneous prediction of the suboptimal estimator accuracy assuming white noise relative to its actual accuracy given colored noise ($P_s - P_w$). As we shall see, this suboptimal estimator does not generally do badly relative to the optimal one, but the prediction of its accuracy erroneously assuming white noise can be quite unrealistic.

It is noted that a more general equation for error analysis can be obtained by taking the expected covariance for the weighted least squares estimator when the true noise covariance is different than the expected noise covariance. We will not, however, look at that more general problem here.

2.4 CORRECTION FACTOR INTERPRETATION

A very interesting and elegant interpretation can be made of the correction factor between white noise predicted accuracy and accuracy in colored noise. We take Equation (10) and break it into two parts, one giving the white noise predicted covariance, P_w , and a correction matrix C , so that

$$P_s = \left[\sigma_w^2 (H^T H)^{-1} \right] \cdot \left[\sigma_w^{-2} H^T R H (H^T H)^{-1} \right] = P_w C \quad (11)$$

For simplicity, consider estimating a single parameter from a single time series of correlated measurements. Let σ_t^2 be the true variance of the measurements and $\rho(k)$ be the autocorrelation as where k gives the sample lag. ρ is normalized so $\rho_0 = 1$, and $\rho(k) = \rho(-k)$ due to the properties of the autocorrelation function (see Section 3 for more discussion of noise properties). The measurement noise covariance is

$$R = \sigma_t^2 \begin{bmatrix} 1 & \rho_1 & \dots & \rho_N \\ \rho_1 & 1 & & \\ \vdots & & \ddots & \\ \vdots & & & \rho_1 \\ \rho_N & & & \rho_1 & 1 \end{bmatrix} \quad (12)$$

and the partials matrix H is now a vector which we shall call h and refer to as our "basis vector" since it is the function we are fitting in a least squares sense. Thus our scalar correction factor is

$$c = \frac{1}{\sigma_m^2} h^T R h (h^T h)^{-1} \quad (13)$$

Written out as a summation, we can write

$$c = \frac{\sigma_t^2}{\sigma_m^2} \sum_{i=-N}^N \rho_i \frac{\sum_{j=0}^{N-1} h_j h_{j+1}}{\sum_{j=0}^N h_j^2} \quad (14)$$

In this form, the inner sum in the numerator may be recognized as the convolution of the basis vector with its reflection, or equivalently as the autocovariance function for the basis vector. The sum shown in the denominator normalizes the basis vector autocovariance to unity at zero lag, and thus this whole expression may be considered as a "basis vector autocorrelation" sequence, which we will label η . The correction factor is the ratio of the actual to expected variance times the dot product or projection of two normalized sequences: the true noise autocorrelation, ρ , and the basis vector autocorrelation, η .

$$c = \frac{\sigma_t^2}{\sigma_m^2} (\vec{\rho} \cdot \vec{\eta}) \quad (15)$$

The ratio of variances is just a correction for the assumed and true noise variance. If we had assumed the correct variance, but had ignored the correlations at non-zero lags, the correction would be just the indicated projection.

This projection may be interpreted in the frequency domain as well. Using Parseval's theorem as applied to finite series, the product of terms in the time domain is related to the product in the frequency domain. This is a special case of the fact that the product in the time domain is a convolution in the frequency domain, but where we are concerned the "DC" component in the time domain which is given by the spectrum evaluated at zero frequency. Let the Discrete Fourier Transform be defined as

$$\text{DFT}(f_n) = \sum_{h=0}^{N-1} f_n e^{-j \frac{2\pi n k}{N}} \quad (16)$$

Using Parseval's theorem gives

$$\vec{\rho} \cdot \vec{\eta} = \frac{1}{N} \overrightarrow{\text{DFT}(\rho)} \cdot \overrightarrow{\text{DFT}(\eta)} \quad (17)$$

The transform of the autocorrelation is the power spectrum. Thus the correction factor is related to the projection of the true noise power spectrum and what we may define as the "basis vector power spectrum."

The easiest way to apply this interpretation to a multiple parameter case is to choose a set of orthogonal basis vectors so that P_w , C , and P_i are all diagonal matrices and the parameter estimates can be decoupled. The use of this interpretation of the correction factor will be discussed with some specific examples in Sections 4 and 5.

2.5 LINEAR COMBINATIONS OF COLORS

At times it will be useful to consider the noise covariance as the combination of two different noise types. In this case, since Equation (10) is linear in R , we have

$$\begin{aligned} P_s &= (H^T H)^{-1} H^T (R_1 + R_2) H (H^T H)^{-1} \\ &= (H^T H)^{-1} H^T R_1 H (H^T H)^{-1} + (H^T H)^{-1} H^T R_2 H (H^T H)^{-1} \end{aligned} \quad (18)$$

Thus if the effects of two independent noise sources are evaluated, the total effect from both can be computed as the linear sum of the variances due to their separate effects. (Note that the combination is linear in the variance, not linear in the standard deviation of the noise.)

3. COLORED NOISE SAMPLES

This section defines some specific types of colored noise for analysis and provides examples for illustration.

3.1 NOISE SIMULATION AND CHARACTERIZATION

Stationary noise of any desired spectrum can be obtained by passing white noise through an appropriate filter. Any stable time invariant linear filter will color a white noise input according to its frequency response. Since there are as many possible "colors" to noise as there are frequency response curves, which is an uncountable infinity of curves, we will necessarily restrict our attention to a few simple classes of coloring for illustrating specific cases. The theory of digital filtering and time series analysis is covered in numerous texts (e.g. Ref. 16-19). For this discussion we will simply provide a few definitions to clarify the noise models that will be used in the sample cases that follow.

In the time domain, a linear filter is defined by its impulse response which when convolved with its input, in our case white noise, produces the system output, colored noise. The variance of the output noise from a filter will be given by the sum of squares of the impulse response sequence. In the examples shown we will routinely normalize the output variance to unity and have the plot scales cover ± 3 standard deviations for consistency.

The most efficient way to generate colored noise for fairly simple processes is through linear difference equations. Care must be given to the initial conditions in the noise generation to assure immediately stationary realization in a statistical sense (Reference 19), otherwise the noise must be simulated for a period to reach a steady state (particularly for long lag process simulations).

A stationary stochastic (noise) process is characterized by its autocovariance function or alternatively by the Fourier transform of the autocovariance function which is its power spectral density (PSD). The autocovariance is defined as

$$\gamma(k) = E \left[x(n) x(n+k) \right] \quad (19)$$

We will refer to the autocorrelation function (ACF), which is the autocovariance normalized by its value at zero lag (which is its variance),

$$\rho(k) = \frac{\gamma(k)}{\gamma(0)} \quad (20)$$

Since this is the noise characterization that enters directly into our formulas for evaluation of the colored noise effects on a least squares estimation accuracy, we note the autocorrelation functions for the sample noise processes presented below.

3.2 WHITE NOISE

Figure 2 shows the appearance of white noise with uniform and Gaussian probability distributions, both of which are familiar to those with data processing experience. As stated earlier our definition of stationary white noise is just that the data samples are independent and identically distributed. The most common assumption about the distribution is that it is Gaussian because of the tractable statistical properties. We will use the Gaussian noise as input to filters to simulate the colored noise shown here, but it is noted that the choice of uniform or Gaussian input distributions does not noticeably affect the appearance of the filtered noise. A result of the central limit theorem is that the more heavily filtered the noise is, the more the output distribution will approach Gaussian no matter what the input distribution.

Note also that the number of data samples plotted and the plot scaling impacts the visual appearance of any noise. We use 400 points for each of the plots shown here for uniformity. The plot scales are set at the expected value for three standard deviations. Data quantization can also significantly impact the appearance, but we will not simulate quantization here.

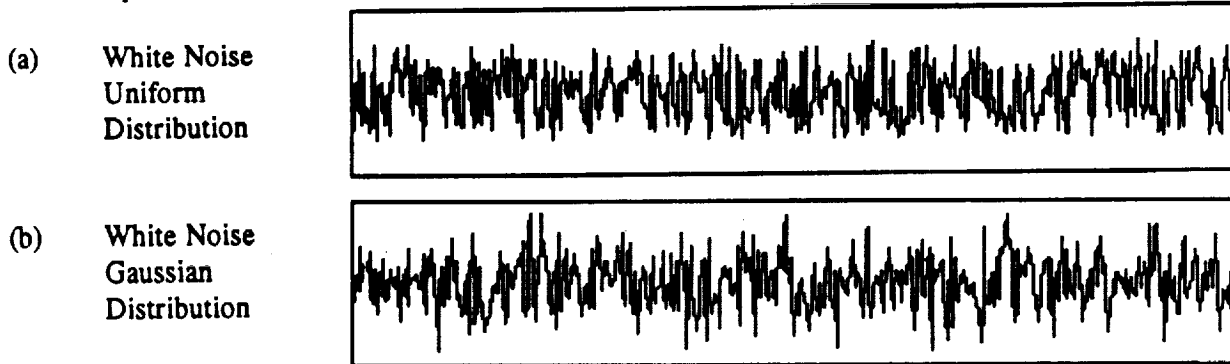


Figure 2. Sample White Noise with Uniform and Gaussian Distributions

3.3 LOWPASS NOISE

A simple single pole lowpass filter of white noise, $w(n)$, is specified by the linear difference equation:

$$x(n) = \phi x(n-1) + w(n) \quad (21)$$

where ϕ is the pole location. This is known as a first order autoregressive process (AR(1))—a label we will use for brevity. It is also commonly called a first order stationary Markov process. The autocorrelation for this process is given by

$$\rho(k) = \phi^{|k|} \quad (22)$$

Thus ϕ gives the correlation between consecutive samples. Samples of this type of noise for selected values of the ϕ are shown in Figure 3. The values of ϕ shown correspond to effective "time constants - τ " (for the correlation to decay to $1/e$) of 2, 15, and 100 samples duration.

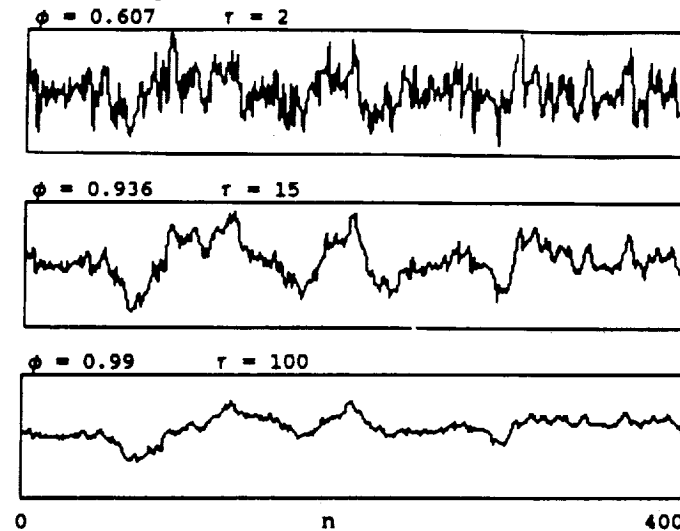


Figure 3. Sample Lowpass Noise with Selected Time Constants (400 Samples Plotted)

Since the general difficulty of inverting the noise covariance matrix R is sometimes cited as a reason for not attempting the optimal weighting, it is interesting to note that for this particular noise model, the noise covariance matrix has an exact inverse:

$$\begin{array}{cc}
 \text{Noise Covariance} & \text{Optimal Weighting} \\
 R = \begin{bmatrix} 1 & \phi & \phi^2 & \dots & \phi^N \\ \phi & 1 & \phi & & \\ \phi^2 & \phi & 1 & & \\ \vdots & & & \ddots & \\ \phi^N & \dots & & & 1 \end{bmatrix} & W = R^{-1} = \frac{1}{1-\phi^2} \begin{bmatrix} 1 & -\phi & & & 0 \\ -\phi & 1+\phi^2 & -\phi & & \\ & -\phi & 1+\phi^2 & \ddots & \\ & & \ddots & \ddots & 1+\phi^2 & -\phi \\ 0 & & & -\phi & 1 \end{bmatrix}
 \end{array} \quad (23)$$

Another type of lowpass filter is a simple N -point running average filter. The autocorrelation function is a finite triangular shaped sequence:

$$\rho(k) = 1 - \frac{|k|}{N}, \quad |k| < N, \quad 0 \text{ otherwise} \quad (24)$$

A sample 23-point running average filter of the same input white noise sequence is shown in Figure 4. Note the similarity with the AR(1) process with $\phi = .936$. This similarity was emphasized by choosing the number of points so that the above finite autocorrelation function was a simple linear approximation to the AR(1) exponential decay curve. This illustrates how the appearance of many of the general visual features in the filtered noise are the same for filters with basically the same short term correlations. The long tail in the AR(1) process does not significantly influence the visual appearance of the noise.

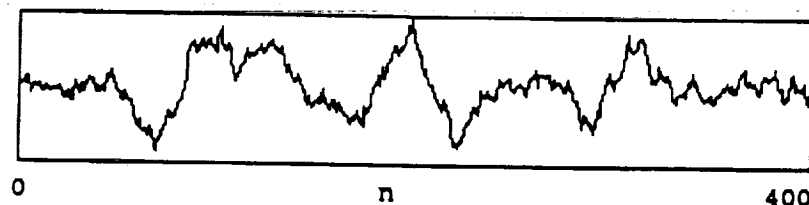


Figure 4. Sample 23-point Running Average Filter of White Noise

3.4 HIGHPASS NOISE

The AR(1) lowpass filter becomes a simple highpass filter for ϕ less than zero. A sample highpass noise plot is shown in Figure 5.

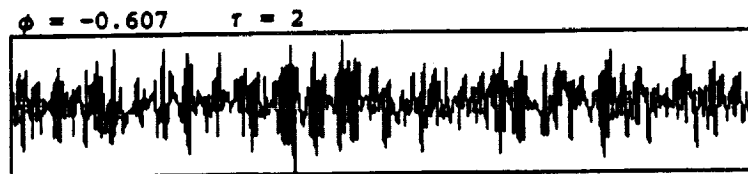


Figure 5. Sample Highpass Noise, $\phi = -0.607$

3.5 BANDPASS NOISE

To generate noise with a selected frequency emphasis, we will utilize a simple two pole filter with complex conjugate roots so that our impulse response function remains real. This noise process is a second order autoregressive AR(2) model or second order stationary Markov process. In terms of pole locations at radius r and angle θ around the unit circle, the linear difference equations for generating this noise are given by

$$x(n) = w(n) + 2r \cos\theta x(n-1) - r^2 x(n-2) \quad (25)$$

The autocorrelation function is given by

$$\rho(k) = r^k \left[\cos(k\theta) + \frac{\cos\theta}{\sin\theta} \frac{1-r^2}{1+r^2} \sin(k\theta) \right] \quad (26)$$

Two samples of noise generated in this way are shown in Figure 6 for a relatively high and relatively low frequency emphasis.

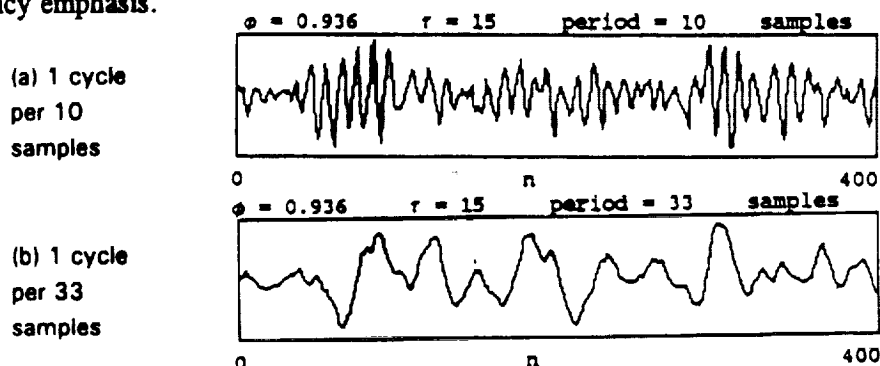


Figure 6. Bandpass Filter Noise with Two Different Frequencies Emphasized

3.6 COMBINED NOISE MODELS

Noises of any particular types can be combined and it is important to note that a low amplitude of one "color" can be hidden by the dominance of another, although it seems that human eye and brain do a pretty good job of discriminating patterns. For example, Figure 7 shows a combination of independent white noise of standard deviation 0.8 with the moderate lag lowpass noise, AR(1), ϕ equal to 0.936, of standard deviation 0.6 (the total variance is $(0.6)^2 + (0.8)^2 = 1.0$). The total effect on estimation accuracy will equal the combination of their separate effects as noted in Section 2.5.

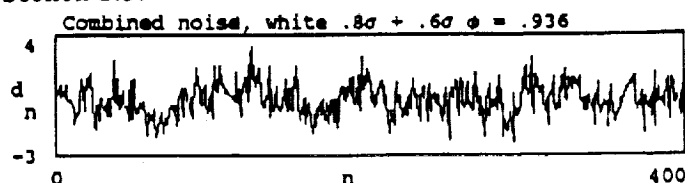


Figure 7. Combined Noise Sample

4. ESTIMATION OF THE MEAN

It is instructive to start with the simplest of cases in order to understand the effects of colored noise on estimation. Thus we begin by reviewing the effects of colored noise in the estimation of the mean of a single sequence of measurements. Although this is a simple case it can be considered as basically applicable to some attitude estimation cases, for example if a spacecraft is inertially pointing and collecting star measurements under basically the same geometry. Further, when several parameters are being estimated, one of the parameters, a measurement bias for example, may essentially be computed from the mean of the measurements.

4.1 ACCURACY vs SAMPLES IN LOWPASS NOISE

We will start with the simplest lowpass filter noise, a first order autoregressive process (AR(1)) or simple Markov process as defined in Equation 21. The partials of all measurements w.r.t the mean is 1, so the basis vector contains all 1's, and the unweighted estimate of the mean is the sample average. One can derive a formula for the uncertainty in the average as an estimator of the mean directly through slightly tedious algebra and recognition of the proper series summations. One obtains

$$\sigma_{\text{AVG}}^2 = \frac{1}{N} \left\{ \frac{1+\phi}{1-\phi} - \frac{2\phi}{N} \frac{1-\phi^N}{(1-\phi)^2} \right\} \quad (27)$$

One can also compute the optimally weighted (or maximum likelihood) estimate of the mean, using the exact inverse noted in Equation (23) to obtain:

$$\sigma_{\text{OPT}}^2 = \frac{1}{N} \left\{ \frac{1+\phi}{1-\phi + \frac{2\phi}{N}} \right\} \quad (28)$$

Results of the uncertainty in these various estimates of the mean are shown in Figure 8. Two different values for the correlation between samples are illustrated. Both the unweighted and weighted (suboptimal and optimal) estimates of the mean are less accurate in the lowpass noise. It is interesting to note that the unweighted estimate of the mean is almost as accurate as the optimally weighted estimate even when the correlation between samples is fairly high. (The relative weighting of data points is give by the sum of the columns in the weight matrix (see Equation 23), so it is interesting to note that the optimal weighting for this noise model simply adds more weight to the end points. One interpretation of this is that the end points carry more information because of correlations with the data beyond the end points.) On the other hand, the white noise estimate of the accuracy is unrealistically optimistic when significant lowpass noise is present.

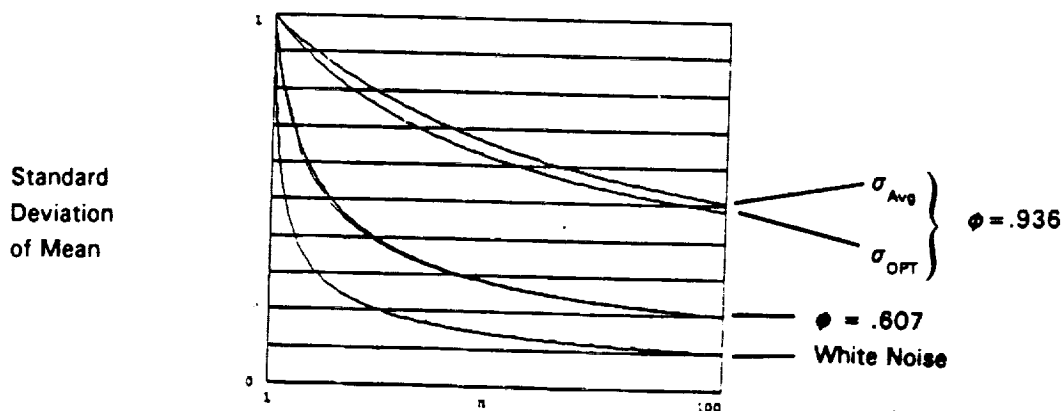


Figure 8. Standard Deviation of Mean vs Number of Samples, in Simple Lowpass Noise

4.2 ASYMPTOTIC RESULTS

A feature to note in Figure 8 is that the ratio of actual accuracy to that predicted by white noise appears consistent as the number of samples gets large. In fact, it can be seen from the formulas (27) and (28) that ratio of the accuracy of both the estimators to the accuracy assuming white noise converges to a limit for large N, which is given by:

$$\lim_{N \rightarrow \infty} \frac{\sigma_{AVG}^2}{\sigma_w^2} = \lim_{N \rightarrow \infty} \frac{\sigma_{OPT}^2}{\sigma_w^2} = \frac{1+\phi}{1-\phi} \quad (29)$$

This convergence ratio, which applies to both the unweighted and weighted least squares estimates, is shown in Figure 9 as a function of the correlation between samples, ϕ . Here the range of ϕ is allowed to go from -1 to 1 to illustrate effects from extreme highpass to extreme lowpass noise. This illustrates how the accuracy in the estimate of the mean is lower in lowpass

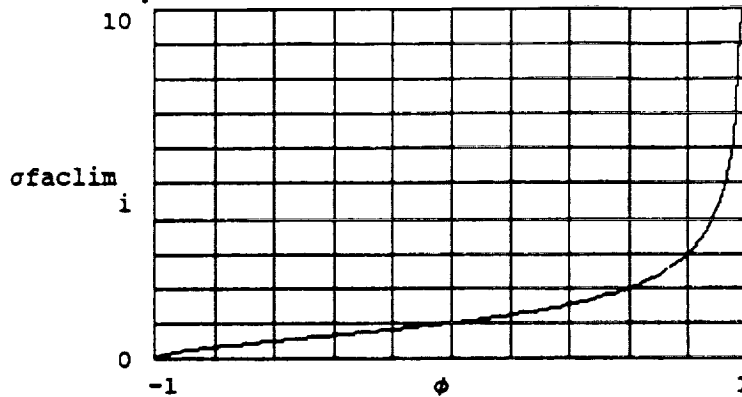


Figure 9. Asymptotic Ratio for Colored vs White Noise Accuracy

noise, but higher in highpass noise. In the extreme case for highpass noise, the data may be oscillating back and forth, but the expected value of the midpoint is nevertheless exactly the mean. The extreme case for lowpass noise is a random bias which we will discuss more later. In this case, the ratio goes to infinity because the white noise accuracy converges to zero. We will later see that for certain well behaved general multiparameter cases this convergence ratio will apply approximately to all the parameters.

4.3 PROJECTION INTERPRETATION

Now let us take a first look at the correction factor interpretation previously discussed as it applies in this case. We will examine it in the time domain and make a brief note about the corresponding results in the frequency domain. Figure 10 illustrates the noise autocorrelation for this process and the basis vector autocorrelation for a short, medium and long data span. The basis function is a constant, the convolution with itself makes the autocorrelation a triangular pulse that is stretched out for longer data spans. Underneath each of the basis autocorrelation vectors is the product whose sum gives us the correction factor relative to the white noise accuracy. As the data span goes to infinity, the correction factor converges to the sum of the noise autocorrelation values which is a convergent geometric series.

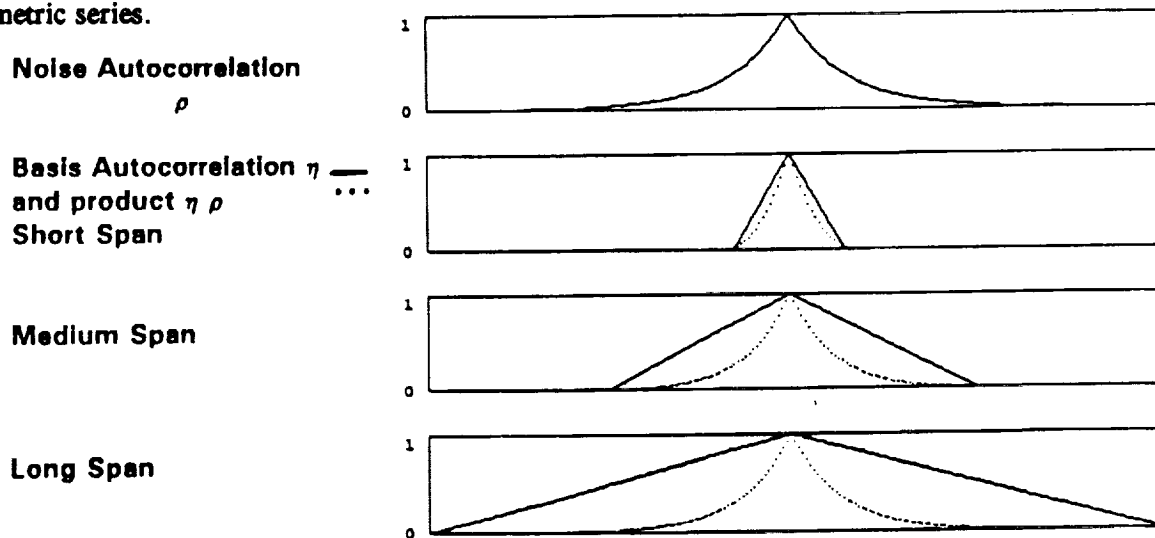


Figure 10. Projection Interpretation for Correction Factor to Estimate of the Mean

It is easy to see from geometric arguments presented in this case that, more generally, the correction factor for the estimation of the mean will converge for any finite autocorrelation (MA or FIR process), or any process where the sum of the autocorrelation terms is finite. This sum is in fact finite for any ARMA stationary process. A proof of this asymptotic convergence ratio for the estimation of the mean is given in Reference 19 (Chapter 7).

4.4 INCREASING SAMPLES IN A FIXED DATA SPAN

Another aspect of the difference between white noise and colored noise is illustrated by considering an increasing number of sample points taken over a fixed data span. Under the ideal white noise model, no matter how close in time the samples are taken they are still independent, so the variance decreases as the inverse of the number of samples. In actual practice however, one expects that as samples become very close in time, they become highly dependent so that at some number of samples little additional accuracy can be obtained.

Figure 11 illustrates this for the sampling of an AR(1) process to estimate the mean. As the time between samples decreases, the correlations increase. The correlation as a function of time for the AR(1) process is modeled as an exponential. Let τ be a time constant for the process, so the correlation between consecutive samples in a data span of length T divided into N samples is given by

$$\phi(N) = e^{-T/\tau N} \quad (30)$$

Putting this expression for ϕ in our formula for the variance of the average and taking the limit as N goes to infinity, we obtain:

$$\lim_{N \rightarrow \infty} \sigma_{\text{AVG}}^2 = \frac{2\tau}{T} - \frac{2 \left[1 - e^{-T/\tau} \right] \tau^2}{T^2} \quad (31)$$

The limit for the optimally weighted estimate is

$$\lim_{N \rightarrow \infty} \sigma_{\text{OPT}}^2 = \frac{2\tau}{T} \quad (32)$$

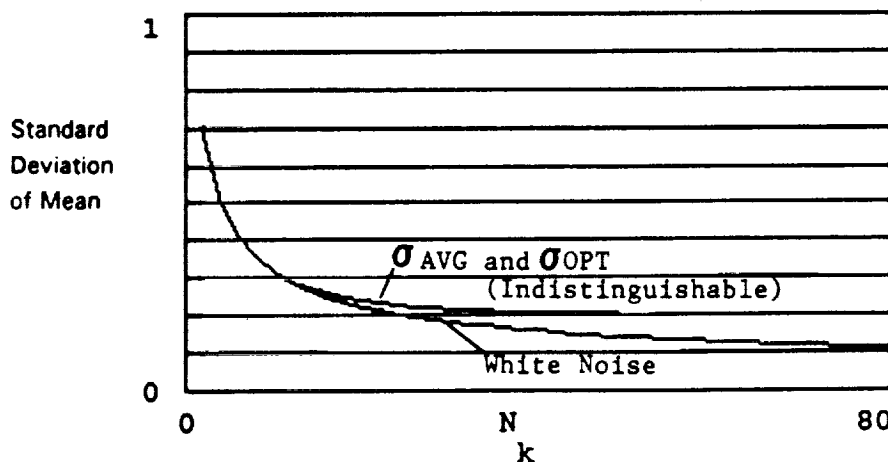


Figure 11. Increasing the Number of Samples in a Fixed Data Span

5. SPIN AXIS ESTIMATION

We now apply the analysis to a case of estimating the spin axis attitude from a single data span of roll measurements which may be from a horizon scanner. We will assume a simple geometry for the problem to permit easier understanding of the results. The general nature of the results described can, however, be applied to a

variety of similar attitude estimation scenarios. For example, it is similar to the computation of roll and yaw for an Earth pointing spacecraft with calibrated gyro data.

5.1 GEOMETRY FOR SAMPLE CASES

The geometry for our sample cases is shown in Figure 12. We will assume a circular orbit and have the satellite spin axis pointed at orbit normal, which idealizes a common mission geometry. To use round numbers (but without loss of generality), we assume a 100 minute period orbit, so that a data span of 10 minutes, is one tenth of an orbit. In order to apply convenient labels to the attitude, we will assume a polar orbit, so right ascension and declination define the spin axis in the equatorial plane without any high declination scaling concerns.

It is convenient for interpretation to choose orthogonal axes for the attitude state parameters which are oriented so that there is no coupling of the errors. This axis selection to decouple the parameters can be done in any least squares estimate. For our sample cases will make those axes correspond to right ascension and declination (labeled RA and DEC), by choosing our data span so that it is symmetric about the north pole point in the orbit. Thus the major axis of the error ellipse for the spin axis will always be in the RA direction and the minor axis will be in the DEC direction. To achieve generality for the orbit position one can read, instead of "RA" and "DEC," "the axis of greatest uncertainty", and "the axis of least uncertainty," respectively.

Based on this geometry, the matrix of partials of the roll measurements with respect to RA and DEC state parameters is simply a sine and cosine function of the orbit angle relative to the middle of the data span at the North pole.

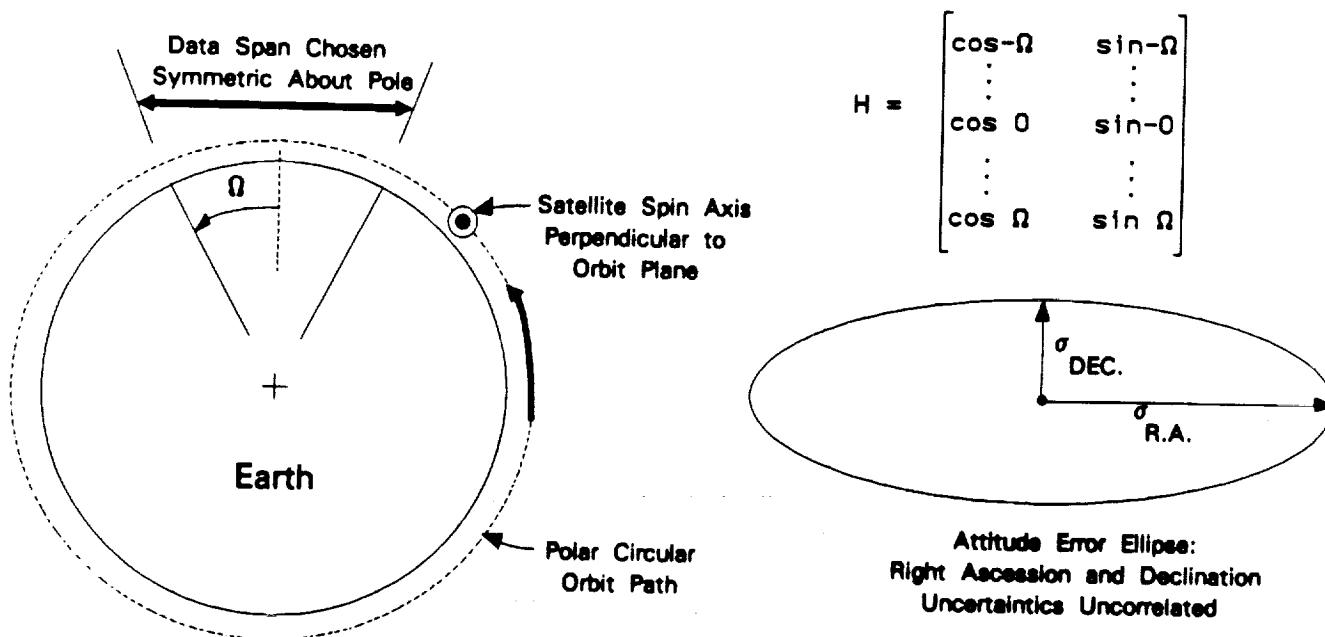


Figure 12. Geometry for Spin Axis Estimation Sample Cases

5.2 SPIN AXIS ACCURACY VERSUS TIME IN LOWPASS NOISE

Figure 13 shows the DEC and RA accuracy versus time for 100 samples taken over ten minutes (1/10 orbit) where the correlation between consecutive samples is 0.607 (see Figure 7 for noise sample plot.) This corresponds to a 12 second time constant on the lowpass noise. The accuracy predicted in white noise is shown for comparison, and also shown is the optimally weighted estimator accuracy which is hardly different from the unweighted estimator accuracy in this case.

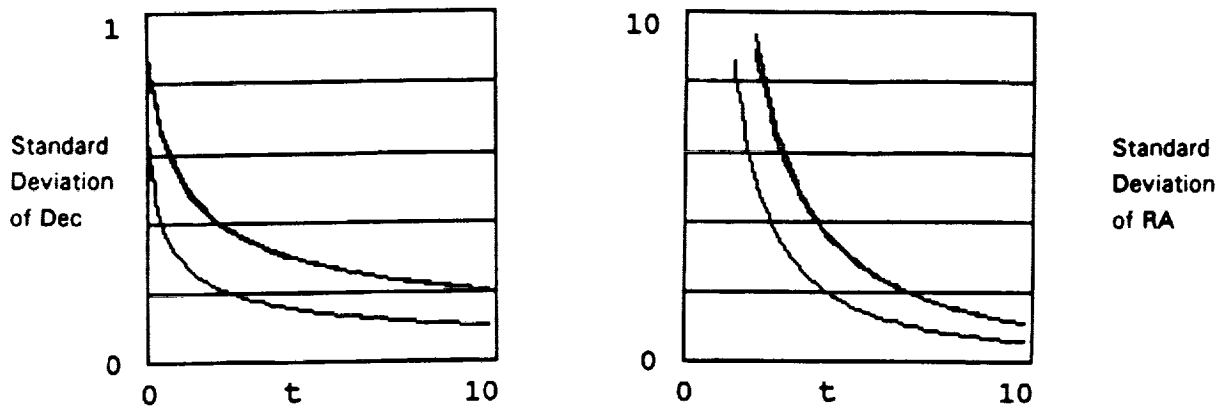


Figure 13. DEC and RA Accuracy Versus Time Over 10 Minutes

Notice that the DEC accuracy decreases in nearly exactly the same manner as the estimate for the mean illustrated for the same correlation between samples in Figure 8. This is not surprising since the basis vector for the DEC over this span, a small piece of a cosine wave, is very much like a constant.

The RA accuracy improves with the increasing data span as expected from the improved geometry that makes RA observable. Notice that the correction factor that applies to DEC estimates applies practically just as well to the RA estimates in this case.

Figure 14 illustrates the equivalent results for an extreme lowpass noise case (see Figure 7 for sample of noise). Here, something very interesting happens to the RA accuracy at very short data spans, where it is better than the accuracy predicted in white noise. An interpretation of what is happening in this case shows how the lowpass noise actually does provide better RA information. For a short data span the RA information is essentially acquired from the slope which is fit to series of observations, since the RA basis vector is a small piece of a sine wave. When the noise is highly filtered, a little piece of the data actually carries more reliable information about the slope than a group of completely random white noise measurements. In the limiting case where $\phi = 1$, the data has a random bias, but a sequence of points still retains the proper slope which will be fit properly in a least squares procedure. This limiting case is discussed further below.

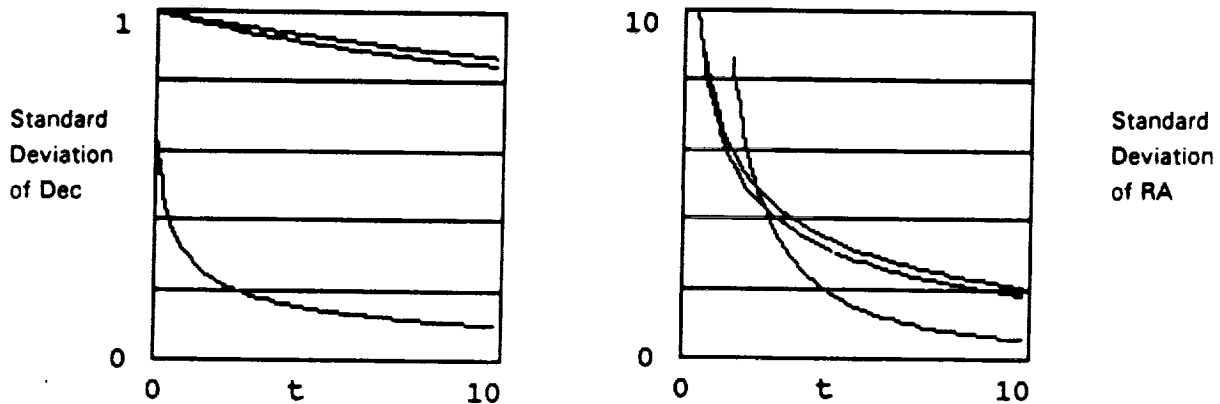


Figure 14. DEC and RA Accuracy for Extreme Lowpass Noise Case, $\phi = .99$

5.3 EFFECT OF A RANDOM BIAS ON ACCURACY

In the limiting case where the correlation term $\phi = 1$, the noise model provides the effect of a random bias (a bias that is random for each data span). To the first order, a bias affects DEC by exactly the size of the bias, but does not impact RA at all. Thus Equation 10 gives exactly this result.

Since Equation 10 is valid for linear combinations of noise types, it is noteworthy that one can include a bias uncertainty along with any colored noise model for computing the estimation accuracy. An illustration of this is the limiting case of a combination of two AR(1) noise processes: one with a very short lag and one with a very long lag. In the limit, one may consider this as white noise plus a constant correlation term which is effectively a bias term. If one normalizes the overall noise autocorrelation function to unity with this model, one will find that the RA accuracy actually improves relative to the white noise case, but it is important to recognize that one is just effectively using a smaller white noise component along with the bias component which doesn't impact the RA accuracy at all. If one is careful to scale for a unity white noise component along with a bias term, the RA accuracy will improve exactly as without the bias, while the DEC accuracy, which is sensitive to the bias, will improve with more observations but reach a limiting accuracy at the bias term. This result makes sense because a very long term correlation must be expected to be exactly like a bias for a finite data span.

This highlights the point that whatever noise spectrum may be worst for one parameter will not be worst for all the parameters. A very long term lag is worst for estimation of the mean, and is worst for the DEC estimation in a relatively short data span as discussed above, but it is certainly not the worst effect on RA. Furthermore since RA is the most uncertain axis for this data span, long lags do not give the worst type of noise impact on the overall spin axis accuracy. We will discuss the type of noise spectrum that can be worst on the overall accuracy, but it will be helpful to do that after we review the insights that can be gained from our projection interpretation.

5.4 PROJECTION INTERPRETATIONS

Figure 15 shows the basis vector autocorrelation and basis vector power spectral densities for the RA and DEC in the 10 minute data span. The basis function for DEC, a small piece of a cosine wave, is very much like a constant, so the autocorrelation looks much like that for estimation of the mean as shown in Figure 9. The basis vector power spectral density (literally the discrete Fourier transform of the sampled autocorrelation) is practically a Kronecker delta function. The basis function for RA, a small piece of a sine wave like a linear constant slope line, gives the "mustache shaped" autocorrelation shown. The power spectral density is zero at the zero frequency, indicating the zero mean of the autocorrelation, and shows a peak at the lowest sampling frequency of the Discrete Fourier Transform, and falls off rapidly with higher frequency. (Note the sampling frequencies of the DFT correspond to sine waves with integer numbers of cycles of the data period). The DFT highlights the essentially low frequency content of these basis functions.

One can see how any fairly short period correlation would cause similar effects in RA and DEC to the correction factor to the white noise effects. Note that white noise is a delta function in the time domain and a constant in the frequency domain. Thus a slightly broader noise autocorrelation in the time domain makes a correction factor slightly greater than one.

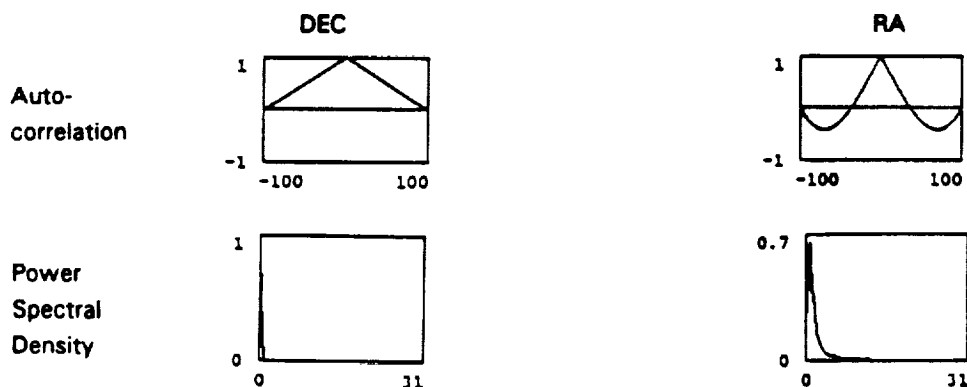


Figure 15. Autocorrelation and Power Spectral Density for DEC and RA Basis Vectors for 10 Minute Span

It is easy to see the expected effect of random bias on RA and DEC using the projection interpretation. Note that a random bias autocorrelation function corresponds to constant value of 1 while the PSD is a Kronecker delta function (times N). Thus the bias has no effect on RA, while having maximum effect on DEC.

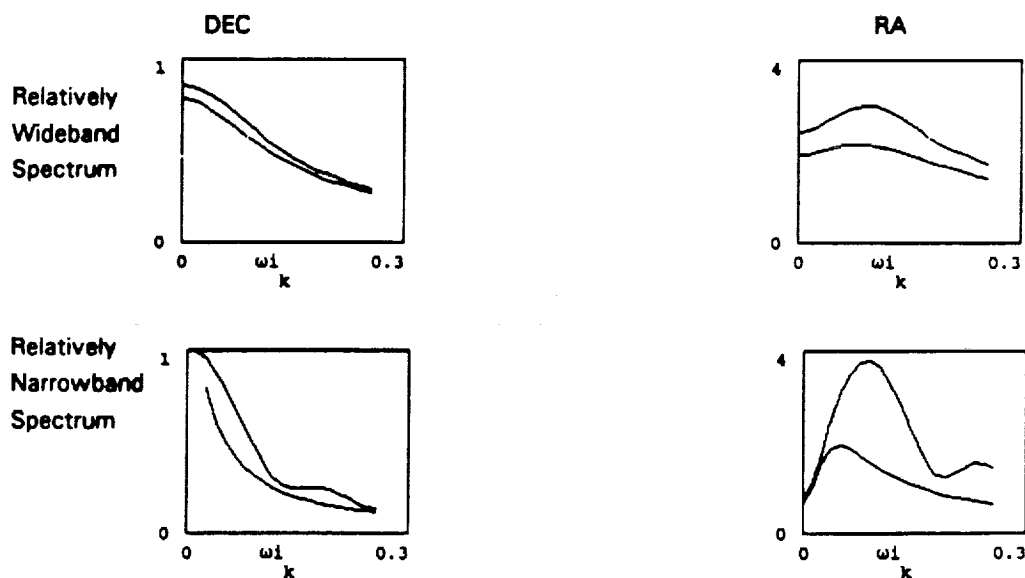
One can also use the projection interpretation to develop a sense of the worst type of noise to impact a parameter. In general, one can select a noise model that has similar frequency content as the basis vector to maximum errors. An extreme worst case might be a sine wave of exactly the dominant frequency of the basis. The autocorrelation function for a sine wave of random phase is a cosine function of the same frequency. In particular for RA in this case one can note by inspection of the basis autocorrelation that the worst frequency would have a period of about $2/3$ of the data span length (it would change sign at the same point as the RA basis autocorrelation).

5.5 UNCERTAINTY VERSUS NOISE COLOR

We will apply the noise model generated by a simple 2 pole filter in order to show the sensitivity of our parameter estimates to the frequency emphasis of the noise. We choose complex conjugate roots to define a real impulse response. The closeness of the poles to the unit circle roughly defines the narrowness of the passband, so we will keep this distance fixed as we move the poles apart and around the unit circle to vary the peak frequency response. We are interested in the low frequency effects that we have predicted to impact our RA estimates. Thus we will vary the peak frequency from near zero to about twice the frequency corresponding to the data span duration. The autocorrelation function corresponding to this noise process is given by Equation (26).

The attitude accuracy in RA and DEC in response to a moderately narrowband noise and to an extremely narrowband noise is shown in Figure 16. The extremely narrowband noise may be thought of practically as a sine wave of fixed frequency and unit amplitude but random phase. As predicted by the discussion in the previous subsection, the frequencies near $2/3$ of the data span frequency have the worst effect on RA accuracy. The DEC accuracy, on the other hand, improves as the dominant frequencies get higher.

The accuracies that would result from the optimal data weighting are included in Figure 16, illustrating that in this colored noise case the weighting can make a significant difference to the estimator accuracy.



(Upper curve for suboptimal/unweighted estimator; lower curve for optimal/weighted estimator)

Figure 16. Standard Deviation Uncertainty Versus Low Frequency Noise From 0 to 2 Cycles Per Data Span

5.6 EXPECTED EFFECTS FOR LONGER DATA SPANS

By looking at how the basis vector autocorrelation and power spectral density change as the data span increases, it is possible to make some general predictions about the effects that may be expected from colored noise and biases as longer data spans are used. Figure 17 shows the RA and DEC basis vectors and their autocorrelation functions for selected lengths of data spans. The characteristic shapes seen in Figure 15 for the short span is still seen until more than about half an orbit is accumulated. Thus RA remains most sensitive to noise periods of about 2/3 of the data span and DEC remains most sensitive to random biases. As the data span gets beyond one orbit the autocorrelation functions for RA and DEC undergo a transition in their shapes so that for two or more orbits both are similar: a cosine function shaped by a triangular window in amplitude. (In the limit of long spans, this illustrates how the cosine wave is the autocorrelation for a signal with random phase.) The power spectral density likewise undergoes transition from DEC sensitive to the zero frequency and RA sensitive to just the two lowest non-zero frequencies in the discrete transform, evolving to both RA and DEC sensitive primarily to the orbit frequency.

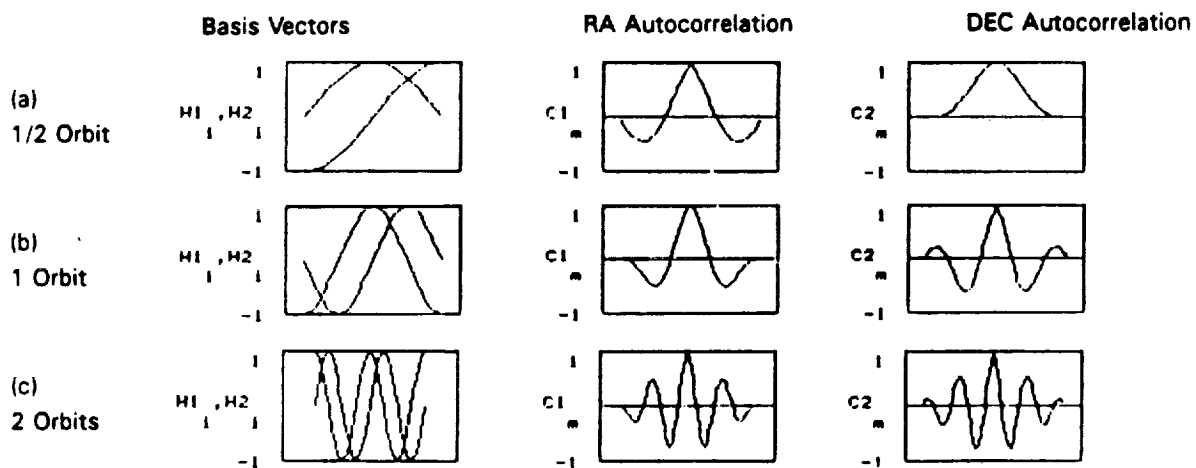


Figure 17. Basis Vectors and Their Autocorrelation Function for Longer Data Spans

Thus in multi-orbit data spans, neither RA nor DEC is sensitive to a random bias, and both are most sensitive to noise frequencies at orbital frequency. Since many physical phenomena occur at orbit frequencies (e.g., spacecraft temperatures, orbit altitude, atmospheric drag, magnetic field changes, and science instrument operations), it is a useful to remember that any unmodeled or random aspects of their effects on sensor measurements are a potential source of noise with frequency content to which attitude solutions are most sensitive.

The effects of relatively short term correlations, on the other hand, can be shown to remain quite constant in terms of a correction factor as the data span increases. To understand this, keep in mind that the time scales are increasing in Figures 17 (a) through (c), and an autocorrelation function representing short term correlations stays (squeezed with the time scale) inside the main central peak which is always found. Thus the correction factor from the projection can be expected to converge quickly.

6. BRIEF DISCUSSION OF GENERAL RESULTS

The results described above can be generalized for what we can call "well behaved cases:" those where the basis vector frequency content is low relative to the data sampling frequency. This would apply, for example, to any set of orthogonal low order polynomials. An ideal set of basis vectors from the frequency analysis standpoint is a finite Fourier series; then the basis vector power spectral densities are spikes at each of the lowest frequencies in the discrete transform. Polynomials would show a similar behavior with each term of higher order showing a

For these cases we can expect that the effects of short period correlations can be accommodated by a correction factor in predicting the estimator accuracy, and unweighted least squares will perform almost as well as optimal weighting. Cases where short term correlations can still impact the accuracy significantly will occur, for example, in cases where the discrimination of two basis vectors relies heavily on a relatively few observations close in time.

7. CONCLUSIONS

Techniques for analyzing the effects of colored noise on unweighted least squares accuracy have been explored, and an illuminating interpretation of the effects has been presented. These techniques were applied to some simple but representative sample cases to show the colored noise impacts. More work remains to be done to apply these techniques to additional and more complex cases, but nevertheless certain important conclusions may be drawn from the general analysis and the cases already explored.

1. If a model for the actual noise correlations is available, the actual accuracy of the unweighted estimator can be evaluated directly (without requiring a matrix inverse). This is recommended.
2. In certain commonly encountered well behaved cases (moderately lowpass noise and very low frequency content in the basis functions), the effects of relatively short period correlations can be accommodated by a simple correction factor to the white noise accuracy. This can be applied as a correction to the assumed white noise standard deviation.
3. In these well behaved cases the optimally weighted estimator does not perform a lot better than the unweighted estimator. In this sense the unweighted least squares can be justified with colored noise, but the proper formula should be used to compute the expected uncertainty of the parameter estimates.
4. In general noise frequencies that are concentrated near the frequencies of the basis functions have the greatest impact on the accuracy of the corresponding parameter, as might be expected. This is quantified mathematically in the frequency domain projection interpretation of the white noise correction factor.
5. Noise frequencies with corresponding periods of about $2/3$ the data span length have the worst impact when an approximately linear (constant slope) term is being fit to the data.
6. Shorter data spans can be expected to be more sensitive to noise correlations particularly because correlations with time constants on the order of the data span are more likely.
7. The techniques described here can also be used to consider the effects of random biases on the solution accuracy.

Much further work can be done to extend the above results more generally and also more specifically to relevant applications. The author believes there is yet more to be explored in the relationship between spectral analysis and least squares solution accuracy. Since noise spectral content is shown to have a notable effect on the predicted accuracy of data fits, a key to improved knowledge of actual accuracies is improved knowledge of the spectral content of sensor noise.

REFERENCES

1. Bilanow, S. and M. Phenneger, *The Response of the SEASAT and MAGSAT Infrared Horizon Scanners to Cold Clouds*, Proceedings of the Fifth Annual Flight Mechanics/Estimation Theory Symposium, Goddard Space Flight Center, Greenbelt, 1980.
2. Bilanow, Stephen, Lily C. Chen, Davis W. Minor, and John P. Stanley, *LANDSAT-4 Horizon Scanner Performance Evaluation*, GSC-TR8401, General Sciences Corporation, prepared for Goddard Space Flight Center, 1984.
3. Markley, F. Landis, Ed, Seidewitz, and Mark Nicholson, *A General Model for Attitude Determination Error Analysis*, Proceedings of the Flight Mechanics/Estimation Theory Symposium, Goddard Space Flight Center, 1988.
4. Nicholson, M, F. Markley, and E. Seidewitz, *Attitude Determination Error Analysis System (ADEAS) Mathematical Specifications Document*, CSC/TM-88/6001, Computer Sciences Corporation, 1987.
5. Johnston, J, *Econometric Methods*, 2nd Edition, McGraw-Hill Kogakusha, Ltd. Tokyo, 1963.
6. Sage, Andrew P. and James L. Melsa, *Estimation Theory with Applications to Communications and Control*, Information and Control Sciences Center, Institute of Technology, Southern Methodist University, McGraw-Hill Book Company, 1971.
7. Bryson, A.E., Jr. and D.E. Johansen, *Linear Filtering for Time-Varying Systems Using Measurements Containing Colored Noise*, 1964.
8. Bryson, A.E., Jr. and L.J. Henrikson, *Estimation Using Sampled Data Containing Sequentially Correlated Noise I*, Spacecraft, Vol. 5, No. 6, 1968.
9. Stear, Edwin B. and Allen R. Stubberud, *Optimal filtering for Gauss-Markov noise*, Int. J. Control, Vol. 8, No. 2, pp. 123-130, 1968.
10. Mehra, Raman K., and Arthur E. Bryson, Jr., *Linear Smoothing Using Measurements Containing Correlated Noise with an Application to Inertial Navigation*, IEEE Transactions on Automatic Control, Vol. AC-13, No. 5, 1968.
11. Johnson, Donald J., *Application of a Colored Noise Kalman Filter to a Radio-Guided Ascent Mission*, J. Spacecraft, Vol. 7, No. 3, 1970.
12. Kailath, Thomas and Roger A. Geesey, *An Innovations Approach to Least-Squares Estimation--Part V: Innovations Representations and Recursive Estimation in Colored Noise*, IEEE Transactions on Automatic Control, 1973.
13. Nahi, Nasser E., *Estimation Theory and Applications*, John Wiley & Sons, Inc., 1969.
14. Gelb, Arthur, ed., *Applied Optimal Estimation*, The M.I.T. Press, 1974.
15. Bryson, Arthur E., Jr. and Yu-Chi Ho, *Applied Optimal Control Optimization, Estimation, and Control*, Hemisphere Publishing Corp., 1975.

16. Oppenheim, Alan V. and Ronald W. Schaffer, *Digital Signal Processing*, Prentice-Hall, Inc., 1975.
17. Tretter, Steven A., *Introduction to Discrete-Time Signal Processing*, John Wiley & Sons, 1976.
18. Box, George, E.P. and Gwilym M. Jenkins, *Time Series Analysis forecasting and control*, Holden-Day, 1976.
19. Brockwell, Peter J. and Richard A. Davis, *Time Series: Theory and Methods* Springer-Verlag, 1987.
20. Kay, Steven M., *Efficient Generation of Colored Noise*, Proceedings of the IEEE, Vol. 69, No. 4, 1981.

Correlation Techniques To Determine Model Form In Robust Nonlinear System Realization/Identification

Greselda I. Stry¹ and D. Joseph Mook²

**Department of Mechanical and Aerospace Engineering
State University of New York at Buffalo
Buffalo, New York 14260
716-636-3058**

ABSTRACT

The fundamental challenge in identification of nonlinear dynamic systems is determining the appropriate form of the model. A robust technique is presented in this paper which essentially eliminates this problem for many applications.

The technique is based on the Minimum Model Error (MME) optimal estimation approach. A detailed literature review is included in which fundamental differences between the current approach and previous work is described. The most significant feature of the current work is the ability to identify nonlinear dynamic systems without prior assumptions regarding the form of the nonlinearities, in contrast to existing nonlinear identification approaches which usually require detailed assumptions of the nonlinearities. Model form is determined via statistical correlation of the MME optimal state estimates with the MME optimal model error estimates. The example illustrations indicate that the method is robust with respect to prior ignorance of the model, and with respect to measurement noise, measurement frequency, and measurement record length.

¹ Graduate Research Assistant; NASA Graduate Researcher

² Assistant Professor

INTRODUCTION

The widespread existence of nonlinear behavior in many dynamic systems is well-documented, e.g., Thompson and Stewart [1]; Nayfeh and Mook [2]. In particular, virtually every problem associated with orbit estimation, flight trajectory estimation, spacecraft dynamics, etc., is known to exhibit nonlinear behavior. Many excellent methods for analyzing nonlinear system models have been developed. However, a key practical link is often overlooked, namely: How does one obtain an accurate mathematical model for the dynamics of a particular complicated nonlinear system? General methods for actually obtaining accurate models for real physical systems are not nearly as widespread or well developed as are the techniques available for analyzing models.

Accurate dynamic models are necessary for many tasks, including basic physical understanding, analysis, performance prediction, evaluation, life cycle estimation, control system design, etc. For example, most filter design assumes white process noise, yet many nonlinear effects are inherently non-zero mean; e.g., quadratic nonlinearities are always positive. In order to obtain a model with truly zero mean process noise for filter design purposes, all of the quadratic terms (and many other nonlinearities) must be well modeled. However, the complexity of many real systems greatly diminishes the possibility of accurately constructing a dynamic model purely from analysis using the laws of physics.

Identification is the process of developing an accurate mathematical model for a system, given a set of output measurements and knowledge of the input. Many well developed and efficient identification algorithms already exist for linear systems (e.g., [3]-[7]). These often may be employed to model nonlinear systems when the system nonlinearities are small, and/or the system operates in a small linear regime. However, linearization does not work well (if at all) in every application, and even when it does provide a reasonable approximation, the approximation is normally limited to a small region about the operating point of linearization. Consequently, there is a real need for nonlinear identification algorithms. If nonlinearities are a predominant part of a system's behavior, using a linear model to describe such a system leads to inconsistencies ranging from inaccurate numerical results to misrepresentation of the system's qualitative behavior. Many important characteristics of nonlinear behavior, such as multiple steady-states, limit cycles, hysteresis, softening or hardening systems, chaos, etc., have no linear equivalent. Since nonlinearities are seldomly easily characterized, identification techniques may prove beneficial in developing accurate mathematical representations of nonlinear systems.

Numerous methods for the identification of nonlinear systems have been developed in the past two decades. Many of these techniques are reviewed in Natke, Juang and Gawronski [8], Billings [9], and Bekey [10]. Most methods fall into one of the following categories:

- ☐ describing the nonlinear system using a linear model
- ☐ the direct equation approach
- ☐ representing the nonlinear system in a series expansion, and obtaining the respective coefficients either by using a regression estimation technique, by minimizing a cost functional, by using correlation techniques, or by some other approach

- obtaining a graphical representation of the nonlinear term(s), then finding an analytical model for the nonlinearity

With such diversity of nonlinear identification techniques, the choice of a particular algorithm may be based on criteria such as: the degree to which prior assumptions of the model form affect the user's effort in applying the algorithms; the number of iterations required; the sensitivity to the presence of measurement noise in the data; the number of state measurements needed; whether or not knowledge of the initial conditions is required; the kind of forcing input(s) required or permitted (step, white gaussian noise, sinusoidal, etc.); the ability to handle hysteretic or discontinuous nonlinearities; the degree of a priori knowledge of system properties required; and the computational requirements. Most algorithms differ widely in at least some of these comparisons; the choice of a particular technique depends on the needs of the particular application.

Among the methods which linearize the nonlinear system are those presented by Jedner and Unbehauen [11] and Ibanez [12]. Jedner and Unbehauen represent a nonlinear system, which may often operate in small regions around a number of operating points, by an equivalent number of linear submodels. It is assumed that the system operates at only a few points. Although the model may work well for controller design, the points at which the system is operating must be known and the linear models apply only within the operating regions. Ibanez takes a slightly different approach by assuming the system response to be periodic at the forcing frequency. An approximate transfer function is constructed. The transfer function is dependent on the amplitude as well as on the exciting frequency and is valid only within the region of exciting frequencies.

The direct equation approach is used by Yasuda, Kawamura and Watanabe [13], [14]. The input and output measurements of a dynamic process are expressed in a Fourier Series using, for example, an FFT algorithm. The system nonlinearity is represented as a sum of polynomials with unknown coefficients. Applying the principle of harmonic balance, the polynomial coefficients as well as the other system parameters are obtained accurately. Knowledge of the nonlinearity is needed to construct the polynomial. Truncation in the Fourier Series expansion of the input or output may lead to error.

The regression estimation approach is used by Billings and Voon [15] and Greblick and Pawlak [16]. Billings and Voon use the NARMAX model (Nonlinear Auto Regressive Moving Average model with eXogenous inputs) to represent the nonlinear system. A stepwise regression method determines the significant terms in the NARMAX model. Then a prediction-error algorithm provides optimal estimates of the final model parameters. Greblick and Pawlak represent the linear dynamic submodel by an ARMA model and the nonlinearities by a Borel function. A non-parametric kernel regression estimation is employed to obtain the final analytical model.

Kortman and Unbehauen [17] and Distefano and Rath [18] use the minimization of an error cost function as a means of obtaining the coefficients of the functions used to represent the nonlinearities. The method presented by Kortman and Unbehauen uses only system input and output information to estimate the polynomial representing the nonlinearities and the parameters

of the linear components. It is robust in the presence of noise, although iteration is necessary. Distefano and Rath present two techniques, a non-iterative direct identification and an iterative direct identification. In the first technique, measurement of all variables is required and the model parameters are obtained through the minimization of an error function. In the second technique, iteration is used to minimize a cost function yielding the system parameters in addition to the state trajectories. In Distefano and Rath, the nonlinear model form is also taken to be known.

In other techniques, as in statistical linearization, a nonlinear relation is replaced by a linear equivalent gain. Broersen [19] extends the technique of statistical linearization by representing the nonlinearity as a linear combination of a number of arbitrary functions. Correlation techniques are then used to determine the coefficients of these functions. The number and type of functions selected depends on the desired accuracy as well as some knowledge of the system nonlinearity. Reasonable accuracy is obtained in the presence of noise and no iterations are necessary. Although some of the basic properties of the true nonlinear output are preserved, it is limited to only random excitation, and knowledge of all states and forcing terms is required.

In the method of multiple scales (Hanagud, Mayyappa and Craig [20]), a perturbation solution to the nonlinear equation of motion is obtained. An objective function is built employing an integral least squares approach. The minimization of the functional yields the unknown parameters. Data on only one field variable is necessary, and the method is effective in the presence of high noise. The method of multiple scales, however, is restricted to systems with small damping and slight nonlinearities and, as in most other methods, the form of the nonlinearity is assumed a priori. The method typically requires some algebraic manipulations which may be quite involved, and these manipulations are only valid for a particular assumed nonlinear form. If the assumed nonlinear form is changed, the algebra must be repeated.

Several techniques describe the nonlinear system using the Volterra or Wiener kernels. The Volterra series consists of the summation of impulse responses of increasing dimensionality. The Wiener series is also a set of orthogonal functions in which the input is white gaussian noise. Marmarelis and Udwadia [21], for example, estimate the first and higher order kernels appearing in the Volterra series using correlation techniques. Chen, Ishii and Suzumura [22] use cross-correlation functions in addition to the Volterra and Wiener series to describe nonlinear models and to show the relation between the system inner structure and the series. Although weakly nonlinear systems can be described by the first few kernels, for strongly nonlinear systems these series give accurate numerical results only at the expense of an excessive number of coefficients. This renders the analytical model impractical for control applications.

Other popular series used in nonlinear identification are orthogonal polynomials such as Legendre (Wang and Chan [23]), Chebyshev, and Jacobi (Horn and Chou [24]). Horn and Chou expand the variables of the system into a shifted Jacobi series, reducing the nonlinear state equation into a linear algebraic matrix equation. The unknown parameters of the nonlinear system are then estimated using least squares. Even though the algorithm works well in the presence of noise, the nonlinear form must be known a priori.

Methods for the identification of nonlinear systems have also been developed based on the extended Kalman filter. The extended Kalman filter is the linear Kalman filter applied to nonlinear systems by linearizing the nonlinear model into a Taylor series expansion about the estimated state vector. Yun and Shinozuka [25] apply the extended Kalman filter for the parameter estimation of a quadratic term. The state vector is augmented by including the unknown parameters in addition to the state variables. Through a series of iterations, the response, as well as the unknown parameters, are estimated by the Kalman filter. Among its disadvantages are high sensitivity to initial conditions, in particular if the initial conditions are barely known. The nonlinear form must be chosen a priori in order to estimate the corresponding parameter(s).

Hammond, Lo and Seager-Smith [26] use an optimal control technique based on optimal control methods employed for linear system deconvolution. The form of the linear model is assumed to be known as well as the input and the output. A cost functional consisting of the weighted sum of the square of the error (between the actual and estimated output) yields an optimal estimated input. The estimated input and the actual input are used to obtain the nonlinearity as a function of the state variables. Although no previous assumption is made of the nonlinearities, there is no provision to deal with noise.

All of the techniques outlined above have proven useful in certain applications. However, all of them are subject to one or more of the following shortcomings:

1. The form of the nonlinearity (quadratic, cubic, exponential, etc.) must be assumed a priori. This is a very serious drawback, because the identification algorithm can only attempt to find the best model in the assumed form. If the form is assumed incorrectly, the resulting model may be so poor as to be useless, or it may appear to fit the data well enough that the user erroneously concludes that the correct model has been obtained. Also, for many techniques of this type, the effort required to test a given form is considerable, which greatly diminishes the effectiveness since multiple form tests are less likely to be conducted.
2. Techniques which attempt to avoid the problem of a priori model form assumption through the use of series expansions generally eliminate any possibility of understanding the underlying physics. Thus, although a good fit of the data might be achieved using a sufficient number of terms in the series, physical insight is lost. Moreover, large systems and/or particularly complicated behavior may require that a very large number of terms be used to obtain a given level of accuracy.
3. The presence of noise in the measurement data is not rigorously treated, yet noise is generally unavoidable.
4. Initial conditions must be known in order to implement the algorithm.
5. The algorithm can only be implemented if the data is obtained using very specific system excitations.

The algorithm of the current paper compares favorably with existing algorithms in most of the categories listed above. It is robust with respect to measurement noise; does not require knowledge of the initial conditions; is independent of the forcing (but, like all methods, assumes that it is known); is not computationally prohibitive; and, most importantly, it requires minimal

a priori assumptions regarding the form of the model or the system properties. In fact, using the correlation technique outlined in the next section, the algorithm essentially eliminates the need to ever assume the nonlinear model form.

The identification algorithm is based on a combination of Minimum Model Error (MME) state estimation, correlation techniques, and least squares. MME was first described by Mook and Junkins [27]. The MME combines the available measurements and an assumed model of the system to produce optimal estimates of the states and the model error. The assumed model represents an initial attempt to model the system using direct analysis, but may be extremely poor. Given the noisy output measurements of the system, MME estimates the state histories as well as the error in the assumed model. In previous work, the correct form and corresponding parameters of the nonlinear model were then estimated in a trial-and-error fashion, by assuming a nonlinear (in the states) form of the error terms, and then determining the best least-squares fit between the state estimates and the model error estimates. Thus, although the MME portion of the algorithm did not require the model form to be assumed, the subsequent least-squares fit between the state estimates and the model error estimates did. In Mook [28] it was shown that this approach could accurately identify terms in a Duffing oscillator, in the presence of noise and sparse measurements. The method worked well even when only a crude model of the dynamic system was assumed, and the error model used for the least-squares fit contained numerous terms in addition to the correct one(s). Later, in Mook and Stry [29], a simple harmonic oscillator with quadratic feedback was simulated on an analog computer. The algorithm was shown to accurately identify the nonlinear model from analog measurements.

In this paper, the identification of the model from the MME-produced state and model error estimates is improved by using correlation techniques to select the form of the correction terms. The correction terms, when added to the initially assumed model, yield the true model of the system. The correction terms may consist of a combination of linear and nonlinear functions. An extensive library of linear and nonlinear functions has been assembled. The correlation technique is used to select the true forms from the library. Even when the true form of the nonlinearity was not present in the library, the correlation technique picks the closest form(s), typically, the first term(s) in the Taylor Series expansion. Once the forms have been selected by the correlation algorithm, least-squares is used to determine the model parameters.

IDENTIFICATION ALGORITHM

In this section, the identification algorithm is explained. First, the MME technique is briefly reviewed, and then the correlation technique used to automate the model form determination is explained in detail.

The MME may be summarized as follows (a more detailed explanation may be found in Mook and Junkins [27]). Suppose there is a nonlinear system whose exact analytical representation is unknown, but for which output measurements are available. Using whatever means are available (analysis, finite elements, etc.), a system model is constructed. As shown in [27]-[29], the MME works well even if this system model is poor. The MME combines the

assumed model with the measurements to produce optimal estimates of (i) the state trajectories, and (ii) the error in the model. In the present work, these state and model error estimates are used for system identification.

Consider a forced nonlinear dynamic system which may be modeled in state-space form by the equation

$$\dot{\underline{x}}(t) = A\underline{x}(t) + \underline{F}(t) + \underline{f}(\underline{x}(t), \dot{\underline{x}}(t)) \quad (1)$$

where $\underline{x}(t)$ is the $n \times 1$ state vector consisting of the system states, A is the $n \times n$ state matrix, $\underline{F}(t)$ is an $n \times 1$ vector of known external excitation, and $\underline{f}(\underline{x}(t), \dot{\underline{x}}(t))$ is an $n \times 1$ vector which includes all of the system nonlinearities. State-observable discrete time domain measurements are available for this system in the form

$$\underline{\tilde{y}}(t_k) = \underline{g}_k(\underline{x}(t_k), t_k) + \underline{v}_k, \quad t_0 \leq t_k \leq t_f \quad (2)$$

where $\underline{\tilde{y}}(t_k)$ is an $m \times 1$ measurement vector at time t_k , \underline{g}_k is the accurate model of the measurement process, and \underline{v}_k represents measurement noise. \underline{v}_k is assumed to be a zero-mean, gaussian distributed process of known covariance R_k . The measurement vector $\underline{\tilde{y}}(t_k)$ may contain one or more of the system states. To implement MME, assume that a model, which is generally not the true system model because of the difficulties inherent in obtaining the true system model, is constructed in state-vector form as

$$\dot{\underline{x}}(t) = A\underline{x}(t) + \underline{F}(t) \quad (3)$$

Here, we show a linear model because in practice, linearization is the most common approach to modeling nonlinear systems. MME uses the assumed linear model in Eq. (3) and the noisy measurements in Eq. (2) to find optimal estimates of the states and of the model error.

The model error, which includes the unknown nonlinear terms of the system, is represented by the addition of a term to the assumed linear model as

$$\dot{\underline{x}}(t) = A\underline{x}(t) + \underline{F}(t) + \underline{d}(t) \quad (4)$$

where $\underline{d}(t)$ is the $n \times 1$ model error to be estimated along with the states.

A cost functional, J , that consists of the weighted integral square of the model error term plus the weighted sum square of the measurement-minus-estimated measurement residuals, is formed:

$$J = \sum_{k=1}^M \left\{ [\underline{\tilde{y}}(t_k) - \underline{g}_k(\hat{\underline{x}}(t_k), t_k)]^T R_k^{-1} [\underline{\tilde{y}}(t_k) - \underline{g}_k(\hat{\underline{x}}(t_k), t_k)] \right\} + \int_{t_0}^{t_f} \underline{d}(\tau)^T W \underline{d}(\tau) d\tau \quad (5)$$

where M is the number of measurement times, $\hat{\underline{x}}(t_k)$ is the estimated state vector and W is a weight matrix to be determined.

J is minimized with respect to the model error term, $\underline{d}(t)$. The necessary conditions for the minimization lead to the following two point boundary value problem (TPBVP), (see Geering [30]),

$$\dot{\underline{x}}(t) = A\underline{x}(t) + \underline{F}(t) + \underline{d}(t) \quad (5a)$$

$$\dot{\underline{\lambda}}(t) = -A^T \underline{\lambda}(t) \quad (5b)$$

$$\underline{d}(t) = -\frac{1}{2}W\underline{\lambda}(t) \quad (5c)$$

$$\underline{\lambda}(t_k^+) = \underline{\lambda}(t_k^-) + 2H_k R_k^{-1} [\tilde{y}(t_k) - \underline{g}_k(\hat{\underline{x}}(t_k), t_k)] \quad (5d)$$

$$H_k = \frac{\delta g}{\delta \underline{x}} \big|_{\hat{\underline{x}}(t_k), t_k}$$

$$\underline{x}(t_o) = \underline{x}_o \quad \text{or} \quad \underline{\lambda}(t_o) = 0 \quad (5e)$$

$$\underline{x}(t_f) = \underline{x}_f \quad \text{or} \quad \underline{\lambda}(t_f) = 0 \quad (5f)$$

where $\underline{\lambda}(t)$ is a vector of costates (Lagrange multipliers). Estimates of the states and of the model error are produced by the solution of this two-point boundary value problem. The estimates depend on the particular value of W . The solution is repeated until a value of W is obtained which produces state estimates which satisfy the "covariance constraint", explained next.

According to the covariance constraint, the measurement-minus-estimated measurement residual covariance matrix must match the measurement-minus-truth error covariance matrix. This may be written as

$$[\tilde{y}(t_k) - \underline{g}_k(\hat{\underline{x}}(t_k), t_k)]^T [\tilde{y}(t_k) - \underline{g}_k(\hat{\underline{x}}(t_k), t_k)] \approx R_k \quad (6)$$

During the minimization, the weight W is varied until the state estimates satisfy the covariance constraint, i.e., the left hand side of Eq. (6) is approximately equal to the right hand side. The model error is, therefore, the minimum adjustment to the model required for the estimated states to predict the measurements with approximately the same covariance as the measurement error.

The TPBVP represented by Eqs. (5a) to (5f) contains jumps in the costates and, consequently, in the model error. As evident from Eq. (5d), the size of the jump is directly proportional to the measurement residual at each measurement time. The noisier the measurements, the larger the jump size. A multiple shooting algorithm, developed by Mook and Lew [31], converts this jump-discontinuous TPBVP into a set of linear algebraic equations which may be solved using any linear equation solver. Multiple shooting also facilitates the analysis of a large number of measurements, by processing the solution at the end of every set of jumps.

Correlation is a measure of the relationship that exists between two variables. The more highly correlated two variables are, the more closely will the change in one variable correspond to a change in the other variable. The cross-correlation coefficient between two discrete variables, say x and y , is defined as (see Newland [32] or Witte [33])

$$C(x, y) = \frac{\sum_{i=1}^n (x_i - \bar{x})(y_i - \bar{y})}{\sigma_x \sigma_y n} \quad (7)$$

where n is the number of data points and the overbar denotes the mean of those n points. σ_x is the standard deviation of the variable x and is defined as

$$\sigma_x = \sqrt{\frac{\sum_{i=1}^n (x_i - \bar{x})^2}{n}}$$

$C(x, y)$ is a measure of the linear relationship between variables x and y . The value of $C(x, y)$ lies in the range $-1 < C(x, y) < 1$. If, for instance, changes in the value of x correspond to perfectly predictable (linearly) changes in the value of y , where the changes in both variables are of the same sign, then the value of $C(x, y)$ is 1. If the changes are of opposite sign but still perfectly predictable, then the value of $C(x, y)$ is -1. If changes in the values of x and y tend to correspond in sign but are not perfectly predictable, then $0 < C(x, y) < 1$. If changes in the values of x and y tend to be of opposite sign but are not perfectly predictable, then $-1 < C(x, y) < 0$. If there is no linear relationship between the values of x and y , then $C(x, y) = 0$. For example, suppose x and y are multiples of each other, $x = K * y$, where K is an arbitrary constant of proportionality. Then

$$C(x, y) = \frac{\sum_{i=1}^n K(x_i - \bar{x})^2}{\sum_{j=1}^n K(x_j - \bar{x})^2} = 1.0 \quad (8)$$

The true functional form of the model error can be found by calculating the correlation of the MME model error estimates with functions of the MME state estimates. If the functional form of the actual system is used, and if the estimates from MME are perfect, then $C(x, y) = 1.0$. Thus, an algorithm may be constructed which performs nonlinear system identification by (i) utilizing the MME to process the available measurements and the initial model in order to produce state estimates and model error estimates, and (ii) testing the correlation between the state estimates and the model error estimates using a "sufficient number" of functional forms so that the actual form is included among those tested. The MME does not require that the correct form of the model be known a priori. The correlation tests may be performed using an existing library of nonlinear functional forms, without input from the user. Thus, if the library is complete (in the sense that it contains the actual model form), the identification of the nonlinear model is accomplished, yet at no point in the algorithm is the user required to assume the correct model form.

The success of the algorithm is determined by the ability of the MME to produce accurate state and model error estimates, and by the completeness of the library of nonlinear functions to be used in the correlation test. We now address these issues in order.

The MME has been shown to consistently produce state and model error estimates of high accuracy in the presence of high measurement noise, low measurement frequency, and poor initial model [27–29]. Generally, however, some noise is still present in both the state estimate and the model error term, although these noise levels are considerably less than the noise in the original data. Let the model error term be given by $x_{\text{correction}} = x + \xi$ where ξ is the noise.

The cross-correlation between the error term and the test function y becomes

$$C(x, y) = \frac{\sum_{i=1}^n (x_i - \bar{x})(y_i - \bar{y}) + \sum_{j=1}^n \xi(y_j - \bar{y})}{n\sigma_y \sqrt{\sigma_x^2 + \frac{1}{n} \sum_{k=1}^n (2\xi(x - \bar{x}) + \xi^2)}} \approx 1.0 \quad (9)$$

As long as the noise is negligible all terms containing ξ are small and affect the result only slightly. Thus, the correlation calculated for the actual function is close to, but not exactly equal to, 1, while the correlation calculated for incorrect terms remains close to 0. If the level of noise is excessive, say, of comparable magnitude to one or more of the actual nonlinear model terms, then the ability of the correlation test to distinguish this term from similar terms may be greatly reduced or eliminated. However, subsequent least-squares fit of the terms has, in every case tested, correctly selected the actual nonlinear function from among those which the correlation test could not distinguish. An example of this is shown in the next section.

The issue of completeness of the library is now addressed. The error term may be composed of more than one function from the library, or the actual function may be missing from the library. Consider first the case where the actual error is a combination of library terms, say, two terms. The error term may be written $x_{\text{correction}} = x_1 + x_2$ and the cross-correlation has the form

$$C(x, y) = \frac{\sum_{i=1}^n (x_{1i} - \bar{x}_1)(y_i - \bar{y}) + \sum_{j=1}^n (x_{2j} - \bar{x}_2)(y_j - \bar{y})}{n\sigma_y \sqrt{\sigma_{x_1}^2 + \sigma_{x_2}^2 + \frac{1}{n} \sum_{k=1}^n 2(x_{1k} + \bar{x}_1)(x_{2k} + \bar{x}_2)}} \quad (10)$$

The cross-correlation is highest for the term which constitutes the largest part of the error. Thus, it is desirable to execute the algorithm iteratively. The library term which constitutes the largest portion of the actual model error is identified first and then added to the MME model. The entire process (including MME) is then repeated, so that new state and model error estimates are obtained (note that the change in state estimates should be minimal, while the change in model error estimates should be a large reduction in magnitude). The largest term remaining in the model error is identified in each pass, then added to the initial MME model.

An alternative to iterative application of the algorithm is to test the correlation of combinations of the library functions. An algorithm can be constructed which tests every possible combination of the functions explicitly contained in the library. This approach has not been attempted in the examples which follow.

If the actual model error is not present in the library, then test cases show that the highest correlation values are calculated for the terms in the series expansion of the actual function. Thus, for example, if the actual model error was of the form $\sin(x)$, but $\sin(x)$ was not present in the library, the correlation coefficients are highest for the terms x , x^3 , x^5 , etc. However, the test described by Eq. 7 is very fast, so the library may contain a very large number of terms.

The final step in the identification procedure is to use a least-squares algorithm to fit the model error to the functional forms (i.e., perform parameter identification once the true nonlinear form has been determined). The error term is expanded into a combination of the functional forms such as

$$d(t) = \alpha f_1(\underline{x}(t)) + \beta f_2(\underline{x}(t)) + \gamma f_3(\underline{x}(t)) + \dots \quad (11)$$

where $\alpha, \beta, \gamma, \dots$ are unknown coefficients to be determined by least squares, and f_1, f_2, f_3, \dots are functions which are selected as a result of the correlation test (often, however, only one function is used at a time). Other parameters may be present inside the functions (such as, for example, coefficients of exponents). Eq. (11) may be sampled repeatedly (using the MME estimates) to obtain

$$\begin{aligned} d(t_1) &= \alpha f_1(\underline{x}(t_1)) + \beta f_2(\underline{x}(t_1)) + \gamma f_3(\underline{x}(t_1)) + \dots \\ d(t_2) &= \alpha f_1(\underline{x}(t_2)) + \beta f_2(\underline{x}(t_2)) + \gamma f_3(\underline{x}(t_2)) + \dots \\ &\vdots \\ d(t_l) &= \alpha f_1(\underline{x}(t_l)) + \beta f_2(\underline{x}(t_l)) + \gamma f_3(\underline{x}(t_l)) + \dots \end{aligned}$$

or, in matrix form,

$$\underline{D}_{l \times 1} = \underline{M}_{l \times p} \underline{P}_{p \times 1} \quad (12)$$

where $\underline{P} = [\alpha \ \beta \ \gamma \ \dots]^T$ is the vector of coefficients for the terms in $d(t)$. Since estimates of $d(t)$ are available continuously throughout the time domain, the parameter l may be chosen quite large to improve the least squares fit. Generally, because of the potential jump discontinuities in the model error estimates at the measurement times, it is desirable to pick the least squares sampling times in Eq. (12) at points other than the measurement times. The least squares estimate is found by minimizing the following cost functional with respect to \underline{P} :

$$\Phi = [\underline{D} - \underline{M}\underline{P}]^T [\underline{D} - \underline{M}\underline{P}] \quad (13)$$

The solution is given by

$$\underline{P} = (\underline{M}^T \underline{M})^{-1} \underline{M}^T \underline{D} \quad (14)$$

If the functions include parameters to be estimated, the equivalent nonlinear least-squares problem is constructed.

The multiple shooting algorithm presented by Mook and Lew [31] was used to obtain the MME solutions used in the tests presented in this paper. It was assumed in the examples that MME obtained the dynamic error term without knowledge of the boundary conditions on \underline{x} , so some distortion of the correction term at the initial and final times was expected due to the constraints of Eqs. (5e-5f), i.e., by assuming no state knowledge is available at t_0 or t_f , we constrain $\lambda(t_0) = 0$ and $\lambda(t_f) = 0$. Therefore, in all test cases, the initial and final ten percent of the correction term data was ignored in the least squares fit.

EXAMPLES

For illustrative purposes, the true system was chosen as a simple harmonic oscillator with various forms of nonlinear feedback. The true system can be modeled as

$$\begin{pmatrix} \dot{x} \\ \dot{v} \end{pmatrix} = \begin{pmatrix} 0 & 1 \\ -1 & 0 \end{pmatrix} \begin{pmatrix} x \\ v \end{pmatrix} + \begin{pmatrix} 0 \\ f(x, v) \end{pmatrix} \quad (15)$$

where x is position, v is velocity and the dot indicates differentiation with respect to time. For simplicity, the system was unforced. The term $f(x, v)$ represents the nonlinear terms to be identified by the MME-based identification algorithm. Measurements were generated from the true system, Eq. (15), with different kinds of nonlinear functions $f(x, v)$. The ability of the identification algorithm to identify the model with no prior knowledge of $f(x, v)$ is tested. Table 1 shows the functions used in each simulation. Note that the unknown error term may be a combination of linear and nonlinear functions. Table 1 also shows the initial conditions and the amount of noise used to generate measurements for each test. The noise levels represent the percentage of the peak system response (actual percentages are higher for the majority of the measurements since the response is only at peak amplitude for brief periods).

Table 1
SUMMARY OF TEST CASES

TEST #	TRUE ERROR: $f(x, v)$	$x(0)$	$v(0)$	NOISE
1	$3.0*x*x$	0.175	0	0
2	$-0.1*x*x*v$	0.175	0	0
3	$-0.5*\cos(x)*\cos(v)$	0.175	0	0
4	$-1.0*v*\sin(x)$	0.175	0	0
5	$-1.0*x*x - 0.25*v$	0.350	0	0
6	$-1.0*x*x*x - 0.1*\tan(v)$	0.873	0	0
7	$-1.0/\cos(x) - 1.0*\sin(v)$	1.750	0	0
8	$3.0*x*x$	0.175	0	10%
9	$-1.0*x*x - 0.25*v$	0.350	0	10%
10	$-1.0*x*x*x - 0.1*\tan(v)$	0.873	0	10%

The assumed model used for the MME analysis consisted of the undamped linear oscillator part of the system,

$$\begin{pmatrix} \dot{x} \\ \dot{v} \end{pmatrix} = \begin{pmatrix} 0 & 1 \\ -1 & 0 \end{pmatrix} \begin{pmatrix} x \\ v \end{pmatrix} \quad (16)$$

For each test, 200 measurements of position were obtained from the digital simulation of Eq. (15) at a sampling rate of 10 Hz. The functional form of the dynamic error, $f(x, v)$, was determined solely from the least-squares fit of the functions identified during the correlation tests on the MME state and model error estimates obtained using only the model in Eq. (16).

A library of functions was built consisting of approximately 300 of the most commonly found nonlinear and linear forms. For a particular test, after the model error term was found

from MME, it was correlated with each one of the functions in the library. The correlation test of the entire library of functions did not take more than a few seconds to execute, since the calculations are simple. The functional form of the unknown nonlinear term was chosen as the one for which the absolute value of the cross-correlation coefficient was closest to 1. Table 2 shows the results for all 10 tests, including the true dynamic error, the highest cross-correlation coefficient obtained, the corresponding functional form, and the respective coefficient computed from the least squares fit. The star (*) indicates tests performed from noisy measurements.

Table 2.
IDENTIFICATION RESULTS FOR EACH TEST CASE

TEST#	TRUE ERROR(S)	$C(d(t), f)$	SELECTED	L.S.
1	$3.0*x*x$	0.999	$x*x$	2.99
2	$-0.1*x*x*v$	0.999	$x*x*v$	-0.10
3	$-0.5*\cos(x)*\cos(v)$	0.999	$\cos(x)*\cos(v)$	-0.49
4	$-1.0*v*\sin(x)$	0.999	$v*\sin(x)$	-1.00
5	$-1.0*x*x$	0.999	$x*x$	-0.99
	$-0.25*v$	0.746	v	-0.24
6	$-1.0*x*x*x$	0.936	$x*x*x$	-1.00
	$-0.1*\tan(v)$	0.999	$\tan(v)$	-0.10
7	$-1.0/\cos(x)$	0.927	$1/\cos(x)$	-0.99
	$-1.0*\sin(v)$	0.999	$\sin(v)$	-1.00
8*	$3.0*x*x$	0.797	$x*x$	3.12
9*	$-1.0*x*x$	0.937	$x*x$	-0.90
	$-0.25*v$	0.772	v	-0.22
10*	$-1.0*x*x*x$	0.838	$x*x*x$	-0.98
	$-0.1*\tan(v)$	0.583	$\tan(v)$	-0.10

For tests 1, 2, 3, and 4, the exact form of the nonlinearity was contained in the library and the measurements did not contain noise. The calculated value of $C(d(t), f)$ was 1 for the true forms. In test 8, the library contained the exact form of the nonlinearity but the measurements contained significant noise. The correlation for the correct term was much higher than for any other term, but was approximately 0.8 instead of 1 due to the noise. In the cases where the error term consisted of two functions but the measurements were noise-free (tests 5, 6 and 7), $C(d(t), f)$ was close to one for both functions after applying the algorithm iteratively as described in the previous section.

When noise and more than one function was present in the dynamic error term (tests 9 and 10), the maximum value of the cross-correlation coefficients dropped significantly and in some cases did not immediately identify the actual form over other similar forms. As an example,

Table 3 shows the top five cross-correlation values for the identification of the $\tan(v)$ term in test case 10. Note that the functions with the highest cross-correlation values are all similar in form to $\tan(v)$, and the corresponding correlation coefficients are of similar magnitude. Since $C(d(t), f)$ did not clearly identify $\tan(v)$ as the missing term, the five functions yielding the highest $C(d(t), f)$ values were individually least-squares fit to the model error term. In all cases (i.e., repeating this test for a number of different random noise samples), the function with the smallest least squares error cost was the correct function ($\tan(v)$). Thus, the least-squares fit of the parameters to the functional forms also serves as a second test if the correlation test is inconclusive due to high noise levels.

Table 3.
HIGHEST CROSS-CORRELATION COEFFICIENTS
OBTAINED FOR THE TAN(V) TERM OF TEST CASE 10

FUNCTION	$C(d(t), f)$	L.S.	L.S. cost
$\tan(v)$	0.583	-0.104	0.588
v	0.584	-0.119	0.623
$v \cdot \cos(x) \cdot \cos(v)$	0.584	-0.150	0.659
$v \cdot \cos(x)$	0.586	-0.126	0.607
$\sin(v) \cdot \cos(x)$	0.586	-0.133	0.621

The number of data points used in the MME algorithm was irrelevant as long as there were enough points to reasonably span the qualitative aspects of the system (e.g., sinusoidal terms cannot be identified if the data only spans a small fraction of the period).

If the exact functional form of the dynamic error term was not in the function library, the correlation procedure would pick the first term in the Taylor Series expansion of the exact form. For example in a test case where the dynamic error term corresponded to $x \cdot \sin(v)$ and $x \cdot \sin(v)$ was deleted from the library, the function with the largest $C(d(t), f)$ was $x \cdot v$. Similarly, in several examples which are not shown the magnitude of the states, x and v , were small. Thus, the trigonometric functions of position and velocity were approximately equal to the first term in their Taylor Series expansions, i.e., $\cos(x) \approx 1.0$, $\sin(x) \approx x$, $\cos(v) \approx 1.0$ and $\sin(v) \approx v$. In these cases, assumptions of linearity are clearly valid, and are not of interest in the present work.

SUMMARY AND CONCLUSIONS

In this paper, an algorithm based on the MME estimation technique, coupled with correlation tests and least squares, has been developed for identification of nonlinear systems. The results of the examples indicate that the correlation technique applied to the MME-produced state and

model error estimates enables the form of the model to be accurately determined, thus eliminating the requirement that the form be assumed a priori. Once the form is determined, the least-squares fit provides excellent parameter identification. In cases of high noise, where the correlation test may not be able to distinguish the actual form from similar forms, the least-squares fit also proved to be a reliable second test for determining the actual form.

At no point in the algorithm is the user required to assume the form of the model, representing a tremendous advantage over existing techniques, including the previous MME-based work. The MME does not require an accurate model in order to produce accurate state and model error estimates, and the correlation tests are automatically performed on a large existing library of functions. Additional functions and more sophisticated methods of combining existing functions can be added to the correlation testing portion of the algorithm (the authors are currently pursuing this), virtually eliminating the likelihood that the actual model error terms are not tested.

REFERENCES

1. Thompson, J.M.T., and Stewart, H.B., *Nonlinear Dynamics and Chaos*, Wiley, New York, 1986.
2. Nayfeh, A. H., and Mook, D. T., *Nonlinear Oscillations*, Wiley, New York, 1979.
3. Ibrahim, S.R., and Mikulcik, E.C., "A Method for the Direct Identification of Vibration Parameters from the Free Response," *Shock and Vibration Bulletin*, No. 47, Pt. 4, pp. 183-198, Sept. 1977.
4. Rajaram, S., and Junkins, J.L., "Identification of Vibrating Flexible Structures", *AIAA Journal of Guidance, Control, and Dynamics*, Vol. 8, No. 4, pp. 463-470, July-Aug. 1985.
5. Hendricks, S.L., et. al., "Identification of Mass, Damping, and Stiffness Matrices for Large Linear Vibratory Systems", *AIAA Journal of Guidance, Control, and Dynamics*, Vol. 7, No. 2, pp. 244-245, March-April 1984.
6. Chen, J.C., et.al., "Direct Structural Parameter Identification by Modal Test Results", *24th Structures, Structural Dynamics, and Materials Conference*, Pt. 2, 1983.
7. Juang, J.-N., and Pappa, R.S., "An Eigensystem Realization Algorithm (ERA) for Modal Parameter Identification and Model Reduction", *AIAA Journal of Guidance, Control, and Dynamics*, Vol. 8, No. 5, pp. 620-627, Sept.-Oct. 1985.
8. Natke, H.G., Juang, J.-N., and Gawronski, W., "Identification of Nonlinear Mechanical Systems: A Brief Review," NASA Langley Research Center, Hampton, VA, U.S.A. .
9. Billings, S.A., "Identification of Nonlinear Systems-a Survey," *IEE Proc.*, Vol. 127, Pt. D, No. 6, 1980, pp.272-285.
10. Bekey, G.A., "System Identification-an Introduction and a Survey," *Simulation*, October 1970, pp. 151-166.
11. Jedner, U., and Unbehauen, H., "Identification of a Class of Nonlinear Systems by Parameter Estimation of a Linear Multi-Model," *IMACS, Modeling and Simulation for Control of Lumped and Distributed Parameter Systems*, June 3-6, 1986, pp. 11-15.

12. Ibanez, P., "Identification of Dynamic Parameters of Linear and Non-Linear Structural Models from Experimental Data," *Nuclear Engineering and Design*, Vol. 25, 1973, pp. 32-41.
13. Yasuda, K., Kawamura, S., and Watanabe, K., "Identification of Nonlinear Multi-Degree-of-Freedom Systems (Identification Under Noisy Measurements)," *JSME International Journal*, Vol. 3, No. 1, 1988, pp. 502-509.
14. Yasuda, K., Kawamura, S., and Watanabe, K., "Identification of Nonlinear Multi-Degree-of-Freedom Systems (Presentation of an Identification technique)," *JSME International Journal*, Vol. 3, No. 1, 1988, pp. 8-14.
15. Billings, S.A., and Voon, W.S.F., "A Prediction-Error and Stepwise Regression Estimation Algorithm for Nonlinear Systems," *Int. J. Control*, Vol. 44, No. 3, 1986, pp. 803-822.
16. Greblick, W., and Pawlak, M., "Hammerstein System Identification by Non-Parametric Regression Estimation," *Int. J. Control*, Vol. 45, No. 1, 1987, pp. 343-354.
17. Kortmann, M., and Unbehauen, H., "Application of a Recursive Prediction Error Method to the Identification of Nonlinear Systems Using the Weiner Model," *IMACS, Modeling and Simulation for Control of Lumped and Distributed Parameter Systems*, June 3-6, 1986, pp. 3-9.
18. Distefano, N., and Rath, A., "System Identification in Nonlinear Seismic Dynamics," *Computer Methods in Applied Mechanics and Engineering*, Vol. 5, 1975, pp. 353-372.
19. Broersen, P.M.T., "Estimation of Parameters of Non-Linear Dynamical Systems," *Int. J. Non-Linear Mechanics*, Vol. 9, 1974, pp. 355-361.
20. Hanagud, S.V., Meyyappa, M., and Craig, J.I., "Method of Multiple Scales and Identification of Nonlinear Dynamical Systems," *AAIA J.*, Vol. 23, No. 5, 1985, pp. 802-807.
21. Marmarelis, P.Z., and Udawadia, F.E., "The Identification of Building Structural Systems-PartII: The Nonlinear Case," *Bulletin of the Seismological Society of America*, Vol. 66, 1979, pp. 153-171.
22. Chen, H., Ishii, N., and Suzumura, N., "Structural Classification of Non-Linear Systems by Input and Output," *Int. J. Systems Sci.*, Vol. 17, No. 5, 1986, pp. 741-774.
23. Wang, M.L., and Chang, R.Y., "Model Reduction and Control System Design by Shifted Legendre Polynomial Functions," *A.S.M.E. J. Dynam. Sys. Meas. Control*, Vol. 105, 1983, pp. 52-55.
24. Horn, I-R., and Chou, J-H., "Analysis and Identification of Non-Linear Systems via Shifted Jacobi Series," *Int. J. Control*, Vol. 45, No. 1, 1987, pp. 279-290.
25. Yun, C-B., and Shinozuka, M., "Identification of Nonlinear Structural Dynamic Systems," *J. Struct. Mech.*, Vol. 8, No. 2, 1980, pp. 187-203.
26. Hammond, J.K., Lo, H.R., and Seager-Smith, E.J., "Identification of Nonlinearities in Vibrating Systems Using Optimal Control Techniques," *IMAC*, 1987, pp. 1467-1473.
27. Mook, D.J., and Junkins, "Minimum Model Error Estimation for Poorly Modeled Dynamic Systems", *AIAA Journal of Guidance, Control, and Dynamics*, Vol. 11, No. 3, 1988, pp. 256-261.
28. Mook, D.J., "Estimation and Identification of Nonlinear Dynamic Systems," *AIAA Journal*,

Vol. 27, No. 7, 1989, pp. 968–974.

29. Mook, D.J., and Stry, G.I., "An Analog Experimental Study of Nonlinear System Identification," to appear, *Nonlinear Dynamics*.
30. Geering, H.P., "Continuous Time Optimal Control Theory for Cost Functionals Including Discrete State Penalty Terms," *IEEE Trans. A. C.*, Vol. AC-21, 1976, pp. 86–869.
31. Mook, D.J., and Lew, J-H., "Solution of Linear Two-Point Boundary Value Problems with Jump Discontinuities," to appear in the *IEEE Trans. A.C.* .
32. Newland, D.E., "(An Introduction to) Random Vibrations and Spectral Analysis," 3rd. ed., Longman, Great Britain, 1980, pp. 29.
33. Witte, R.S., "*Statistics*," Holt, Rinehart and Winston, New York, USA, 1980, pp. 75.

Minimum Fuel Coplanar Aeroassisted Orbital Transfer
Using Collocation and Nonlinear Programming

By

Yun Yuan Shi* and D. H. Young**
McDonnell Douglas Space System Company
Huntington Beach, California

ABSTRACT

The fuel optimal control problem arising in coplanar orbital transfer employing aeroassisted technology is addressed. The mission involves the transfer from high energy orbit (HEO) to low energy orbit (LEO) without plane change. The basic approach here is to employ a combination of propulsive maneuvers in space and aerodynamic maneuvers in the atmosphere.

The basic sequence of events for the coplanar aeroassisted HEO to LEO orbit transfer consists of three phases. In the first phase, the transfer begins with a deorbit impulse at HEO which injects the vehicle into a elliptic transfer orbit with perigee inside the atmosphere. In the second phase, the vehicle is optimally controlled by lift and drag modulation to satisfy heating constraints and to exit the atmosphere with the desired flight path angle and velocity so that the apogee of the exit orbit is the altitude of the desired LEO. Finally, the second impulse is required to circularize the orbit at LEO. The performance index is maximum final mass.

Simulation results show that the coplanar aerocapture is quite different from the case where orbital plane changes are made inside the atmosphere. In the latter case, the vehicle has to penetrate deeper into the atmosphere to perform the desired orbital plane change. For the coplanar case, the vehicle needs only to penetrate the atmosphere deep enough to reduce the exit velocity so the vehicle can be captured at the desired LEO. The peak heating rates are lower and the entry corridor is wider. From the thermal protection point of view, the coplanar transfer may be desirable. Parametric studies also show the maximum peak heating rates and the entry corridor width are functions of maximum lift coefficient.

The problem is solved using a direct optimization technique which uses piecewise polynomial representation for the states and controls and collocation to represent the differential equations. This converts the optimal control problem into a nonlinear programming problem which is solved numerically by using a modified version of NPSOL. Solutions were obtained for the described problem for cases with and without heating constraints. The method appears to be more robust than other optimization methods. In addition, the method can handle complex dynamical constraints.

* Staff Manager, and ** Senior Specialist, Advance Flight System, Advanced Technology.

NOMENCLATURE

A	: $Sp_s/2$
C_D	: drag coefficient
C_{DO}	: zero-lift drag coefficient
C_L	: lift coefficient
C_{LR}	: lift coefficient for maximum lift-to-drag ratio
D	: drag force
g	: gravitational acceleration
g_s	: gravitational acceleration at surface level
H	: altitude
J	: performance index
K	: induced drag factor
L	: lift force
m	: vehicle mass
R	: distance from Earth center to vehicle center of gravity
R_a	: radius of the atmospheric boundary
R_c	: radius of the low Earth orbit (LEO)
R_d	: radius of the high Earth orbit (HEO)
R_E	: radius of Earth
S	: aerodynamic reference area
t	: time
V	: velocity
T	: thrust
β	: inverse atmospheric scale height
γ	: flight path angle
ψ	: heading angle
σ	: bank angle
θ	: down range angle or longitude
ϕ	: cross range angle or latitude
μ	: gravitational constant of Earth
ρ	: density
Δi	: orbital plane changes
ΔV	: characteristic velocity
subscripts	
c	: subscript for circularization or reorbit
d	: subscript for deorbit
s	: subscript for surface level

1. INTRODUCTION

In order to have a viable and affordable space program, advanced technology must be exploited and new design concepts must be developed to reduce the size and cost of transportation elements for supporting new mission requirements. One of the new

concepts that has evolved in recent years to advance the cost effectiveness of space transportation systems is the aerodynamically assisted orbit transfer. Such an orbital transfer vehicle is designed with an aerodynamic configuration which can utilize the planetary atmosphere for the purpose of energy management. Numerous studies have demonstrated that the use of the aerobraking can significantly reduce the propulsive velocity requirements for certain class of orbit transfers. Excellent review papers were given by Warberg (Reference 1) and Mease (Reference 10).

In our earlier studies, the fuel optimal control problem arising in a typical nonplanar orbit transfer from HEO to LEO as discussed in most recent publications was addressed. As discussed in References 2 and 15, the aeroassisted orbit transfer vehicle (AOTV) maneuver involves three phases with three propulsive burns or impulses as sketched in Fig.1. The orbital plane change was assumed to perform entirely inside the atmosphere with aeroassistance. Unlike References 2 and 15, the more general formulation given in Reference 17 does not restrict the orbital plane change to be performed entirely inside the atmosphere. In the first phase, the orbital transfer begins with a deorbit impulse at HEO which injects the vehicle into an elliptic transfer orbit with a plane change at HEO and with the perigee inside the atmosphere. In the second phase, the vehicle is inside the atmosphere and is optimally controlled by the lift and bank angle modulations to perform another orbital plane change and to satisfy the heating rate and other physical constraints. Because of the energy loss during the atmospheric maneuvers, an impulse is required to initiate the third phase to boost the vehicle back to the final orbital altitude. Finally, the third impulse is applied to circularize the orbit at LEO. Additional plane changes are allowed at the atmospheric exit and the final orbit circulation. In summary, there are three propulsive plane changes associated with three propulsive burns outside the atmosphere and an aeroassisted orbital plane change inside the atmosphere. In Reference 17, simulation results for the general formulation were obtained under the assumption that all trajectories enter the atmosphere at the same ϕ_e , ψ_e , and θ_e . In addition, simulation results were compared with those obtained in Reference 2 and 15, where orbital plane changes are performed entirely inside the atmosphere. These studies provided necessary data base and essential information concerning the effective use of aeroassisted orbital plane changes.

In this paper, the fuel optimal control problem arising in a typical coplanar aeroassisted orbit transfer is addressed. The mission involves the transfer from high energy orbit (HEO) to low energy orbit (LEO) without plane change. The basic approach here is to employ a combination of propulsive maneuvers in space and aerodynamic maneuvers inside the atmosphere. The aeroassisted orbital transfer problem is formulated under the assumption that no orbital plane change is needed. Similar to Reference 15 and 17, the basic sequence of events consists of three phases but only two impulses are needed. In the first phase, the transfer begins with a deorbit impulse at GEO which injects the vehicle into an elliptic transfer orbit with perigee inside the atmosphere. In the second phase, the vehicle is optimally controlled by lift and drag modulation to satisfy heating and other physical constraints and to exit the atmosphere with the desired flight path angle and velocity so that the apogee of the exit orbit is the altitude of the desired LEO. Finally, in the third phase, the second impulse is required to circular the orbit at LEO. The optimal control solutions were all obtained by using the Hermite polynomial and collocation technique

to convert the optimal control problem into a corresponding nonlinear programming (NP) problem which is solved numerically using the optimization code, NZSOL (cf. Reference 12) provided by Gill, which is an improved version of NPSOL (cf. Reference 6), developed at Stanford. This solution method is different from the indirect method such as those discussed in Reference 2,4,7 and 8. Simulation results were then compared with those obtained earlier for different orbital inclination changes in Reference 15 and 17. The details are presented and discussed here. In this paper, simulation results were actually obtained for returns from geosynchronous orbit (GEO) to space station orbit (SSO). It is important that in the future these simulations be extended to include all other realistic flight constraints and to establish baseline optimum trajectory characteristics for GEO to Space station or shuttle, lunar and Mars missions.

2. DIRECT TRAJECTORY OPTIMIZATION WITH COLLOCATION AND HERMITE POLYNOMIALS

In the direct collocation with nonlinear programming approach, the trajectory is approximated by piecewise polynomials, which represent the state and control variables at a number of discrete time points, i.e., nodes. For a given state variable, the state trajectory over a given "segment" between two nodes is taken to be the unique Hermite cubic which goes through the end points of the segments with the appropriate derivatives that are dictated by the differential equations of motion at the endpoints. This is the "Hermite cubic" since it is determined by the states and their derivatives. A collocation is taken at the center of the segment where the derivative given by the Hermite cubic is compared to the derivative obtained from the evaluation of the equations of motion. The difference is termed the "defect" and is a measure of how well the equations of motion are satisfied over the segments. If all the defects are zero, then the differential equations are satisfied at the center collocation points as well as at the endpoints. Figure 2 shows the typical defects between node 1 and node 2.

Let the system of equations of motion be given as

$$\dot{X}' = f(X,U,D) \quad (2-1a)$$

where X is the state vector, U is the control vector, D is the design parameter vector and (\cdot) denotes the differentiation with respect to the time. Let the time over a given segment be T . For the problems mentioned above, one can show that

$$\begin{aligned} X &= (x, y, z, x', y', z', m) \\ U &= (C_L, \sigma) \\ D &= (\Delta i_1, \Delta i_2, \Delta i_3) \end{aligned} \quad (2-1b)$$

where design parameters are defined here as unknown constants (i.e., three propulsive plane changes) to be determined by the optimization processes. Then the Hermite interpolated x-component of the state vector X at the center point is

$$x_c = (1/2) (x_1 + x_r) + (T/8) [f(X_1, U_1) - f(X_r, U_r)] \quad (2-2)$$

where x_1 and x_r are respectively the x-component of the state vector X at the left and the right nodes. The derivative of the interpolating Hermite cubic at the center point is

$$x_c' = -3/(2T) (x_1 - x_r) - (1/4) [f(X_1, U_1) + f(X_r, U_r)] \quad (2-3)$$

The defect vector is then calculated as

$$d = f(X_c, U_c) - x_c' \quad (2-4)$$

If x_1 , u_1 , x_r , and u_r are chosen such that the elements of the defect vector, d , are sufficiently small, the "Hermite polynomials" become an accurate approximation to the

solution of the differential equations of motion (by implicit integration). With the above approach, the differential equations are converted into nonlinear algebraic constraint equations and the optimal control problem can then be solved using the nonlinear programming techniques.

3. BASIC EQUATIONS FOR OPTIMAL AEROASSISTED ORBITAL TRANSFER

The aeroassisted orbital transfer can be analyzed in three phases, i.e., deorbit, aeroassist (or atmospheric flight), boost and reorbit (or circularization). In each of the phases, a particular set of equations of motion apply.

3.1 Deorbit

Initially, the spacecraft is moving with a circular velocity $V_d = \sqrt{\mu/R_d}$ in a circular orbit of radius R_d , well outside the Earth's atmosphere. Deorbit is accomplished at point D by means of an impulse ΔV_d to transfer the vehicle from a circular orbit to an elliptic orbit and with perigee low enough for the trajectory to intersect the dense part of the atmosphere. Since the elliptic velocity at D is less than the circular velocity at D , the impulse ΔV_d is executed so as to oppose the circular velocity V_d . In other words, at point D , the velocity required to put the vehicle into elliptic orbit is less than the velocity required to maintain it in circular orbit. The deorbit impulse ΔV_d causes the vehicle to enter the atmosphere at radius R_a with a velocity V_e and flight path angle γ_e . It is known that the optimal energy loss maneuver from the circular orbit is simply the Hohmann transfer and the impulse is parallel and opposite to the instantaneous velocity vector.

After applying the deorbit impulse and before entering the atmosphere at R_a , the deorbit trajectory is a coasting arc and known integrals of the equations of motion can be used to relate the state vectors at R_a , the entry into atmosphere to the state vectors right after the deorbit impulse at R_d . Using the principle of conservation of energy and angular momentum at the deorbit point D and the atmospheric entry point E , we get

$$V_e^2 / 2 - \mu / R_a = V_1^2 / 2 - \mu / R_d \quad (3-1)$$

$$R_a V_e \cos(-\gamma_e) = R_d V_1 \quad (3-2)$$

where V_1 is the magnitude of the velocity right after the deorbit impulse ΔV_d and from the above equations we can solve for V_1 and then compute ΔV_d to get

$$V_1 = \sqrt{2\mu(1/R_a - 1/R_d) / [(R_d/R_a)^2 / \cos^2 \gamma_e - 1]} \quad (3-3a)$$

and

$$\Delta V_d = V_d - V_1 \quad (3-3b)$$

It is easily seen that the minimum deorbit impulse ΔV_{dm} obtained for $\gamma_e = 0$, corresponds to an ideal transfer with the space vehicle grazing the atmospheric boundary. To ensure proper atmospheric entry, the deorbit impulse ΔV_d must be higher than the following minimum deorbit impulse ΔV_{dm}

$$V_{1m} = \sqrt{2\mu(1/R_a - 1/R_d) / [(R_d/R_a)^2 - 1]} \quad (3-4a)$$

$$\Delta V_{dm} = V_d - V_{1m} \quad (3-4b)$$

Physically, the second term of the above equation corresponds to the apogee velocity of an elliptic transfer orbit with perigee radius R_a and apogee radius R_d . This elliptic transfer orbit is tangent to the atmosphere boundary at perigee. It will be shown later that the nonlinear constraint equations (3-15) at the atmospheric entry point can also be derived from equations (3-1 and 2).

3.2 Aeroassist

During the atmospheric flight, the vehicle can be optimally controlled by the lift and bank angle modulations to achieve the necessary velocity reduction (due to the atmospheric drag) and the orbital plane change if needed. In the present formulation, only the aeroassisted atmospheric flight need be solved by using the collocation and nonlinear programming techniques discussed earlier in this paper. The solutions in the other phases are provided by the known integral relations of the equations of motion because these arcs are coasting arcs.

Consider a vehicle with the point mass m , moving about a rotating spherical planet. The atmosphere surrounding the planet is assumed to be at rest, and the central gravitational field obeys the usual inverse square law. The equations of motion for the vehicle are given by (Figure 1),

$$\dot{r} = V \sin \gamma \quad (3-5a)$$

$$\dot{\theta} = \frac{V \cos \gamma \cos \psi}{r \cos \phi} \quad (3-5b)$$

$$\dot{\phi} = \frac{V \cos \gamma \sin \psi}{r} \quad (3-5c)$$

$$\dot{v} = \frac{(\eta T \cos \epsilon - D)}{m} - \frac{\mu \sin \gamma}{r^2} + \omega^2 r \cos \phi (\sin \gamma \cos \phi - \cos \gamma \sin \psi \sin \phi) \quad (3-5d)$$

$$\dot{\gamma} = \frac{(\eta T \sin \epsilon + L) \cos \sigma}{mV} - \frac{\mu \cos \gamma}{V r^2} + \frac{V \cos \gamma}{r} + 2\omega \cos \psi \cos \phi + \frac{\omega^2 r \cos \phi}{V} (\cos \gamma \cos \phi + \sin \gamma \sin \psi \sin \phi) \quad (3-5e)$$

$$\dot{\psi} = \frac{(\eta T \sin \epsilon + L) \sin \sigma}{mV \cos \gamma} - \frac{V \cos \gamma \cos \psi \tan \phi}{r} + 2\omega (\tan \gamma \sin \psi \cos \phi - \sin \phi) + \frac{\omega^2 r \cos \psi \sin \phi \cos \phi}{V \cos \gamma} \quad (3-5f)$$

$$\dot{m} = -f(r, V, \eta) \quad (3-5g)$$

where for a given vehicle, the drag D and the lift L are

$$D = \frac{S}{2m} \rho V^2 C_D \quad (3-5h)$$

$$L = \frac{S}{2m} \rho V^2 C_L \quad (3-5i)$$

and the drag and lift coefficients obey the drag-polar relation

$$C_D = C_{D0} + KC_L^2 \quad (3-5j)$$

Also, for an exponential atmosphere, one has

$$\rho = \rho_s \exp(-H\beta) \quad \text{and} \quad H = R - R_E \quad (3-5k)$$

Simulation results obtained here were using the U.S. standard Atmosphere 1976.

For aeroassisted orbital transfer problems considered here, one assumes that, inside the atmosphere, the vehicle is optimally controlled by the aerodynamic forces only. It is assumed that the thrust T is absent and the point mass is constant in this region. Furthermore, no earth rotation was assumed. The later is equivalent to consider the motion with respect to an earth fixed inertial coordinate system (ECI). The plane change or the orbit inclination, i , is related to the cross range ϕ and the heading angle ψ as

$$\cos i = \cos \phi \cos \psi \quad t_e \leq t \leq t_f \quad (3-6)$$

For coplanar orbital transfer problems considered here, the orbit inclination is assumed to be constant throughout the atmospheric flight.

3.3 Boost and Reorbit

During the atmospheric flight, the vehicle is optimally controlled by the lift and drag modulation to satisfy the heating constraints and to exit the atmosphere with the desired flight path angle and velocity so that the apogee of the exit orbit is the altitude of the desired LEO. Thus, no impulse is required at the exit from the atmosphere to boost the vehicle back to the final orbital altitude at LEO. The vehicle exits the atmosphere at point F , with a velocity V_f and the flight path angle γ_f . The additional impulse ΔV_b , required at the exit point F for boosting the vehicle into an elliptic transfer orbit with apogee radius R_c is assumed to be zero and the reorbit (or circularization) impulse ΔV_c , required to insert the vehicle into a circular orbit are obtained by using the principle of conservation of energy and angular momentum at the exit point F and the reorbit or circularization point C . Thus, we have

$$V_f^2 / 2 - \mu / R_a = V_3^2 / 2 - \mu / R_c \quad (3-7)$$

$$V_f R_a \cos \gamma_f = R_c V_3 \quad (3-8)$$

where V_f is the velocity at the exit from the atmosphere and V_3 is the velocity at the reorbit point C just before the circularization burn ΔV_c .

Solving for V_f and V_3 from the above equations (3-7) and (3-8) yields

$$V_2 - \sqrt{2\mu(1/R_a - 1/R_c) / [1 - (R_a/R_c)^2 \cos^2 \gamma_f]} = 0 \quad (3-9)$$

$$V_3 = \sqrt{2\mu(1/R_a - 1/R_c) / [(R_c/R_a)^2 / \cos^2 \gamma_f - 1]} \quad (3-10)$$

and ΔV_c can be computed as follows

$$\Delta V_b = 0 \quad (3-11)$$

$$\Delta V_c = V_c - V_3 \quad (3-12)$$

It is interesting to note that V_3 is maximum for $\gamma_f = 0$ and therefore the reorbit impulse ΔV_c is minimum for $\gamma_f = 0$. It will be shown later that boundary conditions and nonlinear constraint equations at the exit point F, can be derived in terms of the final orbit characteristics and the final state vectors at the exit as shown in (3-16, 17, & 18).

3.4 Performance Index

It is known that the change in speed, ΔV , also called the characteristic velocity, is a convenient parameter to measure the fuel consumption. For minimum-fuel maneuver, the objective is then to minimize the total characteristic velocity. A convenient performance index is the sum of the characteristic velocities for deorbit, boost, and reorbit, as

$$\begin{aligned} J &= \Delta V_d + \Delta V_c \\ &= \Delta V_d(R_d, \Delta i_1, V_e, \gamma_e) + \Delta V_c(R_c, \Delta i_3, \gamma_f, V_f) \end{aligned} \quad (3-13)$$

Where, ΔV_d and ΔV_c are the deorbit, and reorbit characteristic velocities respectively, and are given by (3-3, and 12) respectively. Note that for a given final circular orbit, the impulse ΔV_c are completely determined by the state variables V_f and γ_f at the exit of the atmospheric portion of the trajectory. The velocity V_e and the flight path angle γ_e at the atmospheric entry point are dependent only on the magnitude of the deorbit impulse ΔV_d . It follows that the optimal control problem needs to consider only the trajectory segment within the atmosphere subject to the nonlinear constraints and boundary conditions at the atmospheric entry and exit points. In addition, other path constraints such as the peak heating rate have to be satisfied.

3.5 Boundary conditions and constraints

The boundary conditions and constraints for the optimal control problem can be summarized as follows:

- At the entry into atmosphere, the following initial constraints must be satisfied.

$$R = R_a ; \quad \gamma_e \leq 0 \quad (3-14a)$$

$$\phi_e = 0, \quad \psi_e = 0, \quad \theta_e = 0, \quad (3-14b)$$

$$\frac{V_e^2}{2} \left[1 - \left(\frac{R_a}{R_d} \right)^2 \cos^2(\gamma_e) \right] - \mu \left(\frac{1}{R_a} - \frac{1}{R_d} \right) = 0 \quad (3-15)$$

The first initial constraint is required to ensure the vehicle enters the atmosphere. The second set of boundary conditions assumes that all trajectories enter the atmosphere at the same ϕ_e , ψ_e and θ_e . In the present formulation, the initial velocity and the flight path angle are unknown and to be determined by the optimization processes subject to the constraint equation (3-15).

- At the exit from atmosphere, the following constraints must be satisfied.

$$R = R_a ; \quad \gamma_f \geq 0 \quad (3-16)$$

$$\frac{V_2^2}{2} \left(1 - \frac{R_a^2}{R_c^2} \cos^2 \gamma_f \right) - \mu \left(\frac{1}{R_a} - \frac{1}{R_c} \right) = 0 \quad (3-17)$$

$$\cos i_f = \cos \phi_f \cos \psi_f = \cos i_0 \quad (3-18)$$

Equation (3-16) is required to ensure the vehicle exit the atmosphere. The second constraint (3-17) must be imposed to determine the correct V_f and γ_f if ΔV_b is assumed to be zero as in the coplanar case discussed here. The third constraint (3-18) is required to ensure the orbital transfer is coplanar.

In addition, there are other path constraints ,i.e., constraints must be satisfied along the trajectory such as stagnation point heating rate constraints, altitude constraints, bounds on the control variables abd others

4. STRUCTURE AND SOLUTION OF THE NONLINEAR PROGRAMMING PROBLEM

The direct collocation and Hermite polynomial procedures described above convert optimal control problems into corresponding nonlinear programming problems. Ordinary differential equations are converted into corresponding nonlinear algebraic equations (or nonlinear "defects" constraint equations). These problems can then be solved using nonlinear programming codes.

The variables for the nonlinear programming problem are the collected state vectors and control vectors at the nodes and the time duration of phases. These quantities are assembled into the NLP state vectors

$$X^T = [X_1^T, U_1^T, \dots, X_n^T, U_n^T, t_1, t_2, \dots, t_k] \quad (4-1)$$

where n is the number of nodes and k is the number of phases on the trajectory. The defects and other physical and mathematical constraints are collected into the NLP constraint vector C

$$C^T = [d_1^T, d_2^T, \dots, d_n^T, w_1^T, w_2^T, w_3^T, \dots, w_j^T] \quad (4-2)$$

where d_i is the defect vector and w is a vector of additional problem constraints.

The nonlinear programming code used here is the NZSOL (Reference 12). The NZSOL is an improved version of the NPSOL (Reference 6) , developed by the Stanford Optimization Laboratory and designed to minimize a smooth nonlinear function subject to a set of constraints which may include simple bounds on the variables, linear constraints, and smooth nonlinear constraints. The problem is assumed to be stated in the following form:

NP

$$\begin{aligned} &\text{minimize} && F(x) \\ &x \in R^n \end{aligned}$$

$$\text{subject to} \quad \ell \leq \begin{Bmatrix} x \\ A_L x \\ c(x) \end{Bmatrix} \leq u, \quad (4-3)$$

where the objective function $F(z)$ is a nonlinear function, A_L is an $m_L, x n$ constant matrix of general linear constraints, and $c(x)$ is an m_N - vector of nonlinear constraint

functions. the objective function F and the constraint functions are assumed to be smooth, i.e., at least twice-continuously differentiable. (The method of NPSOL will usually solve NP if there are only isolated discontinuities away from the solution).

Note that upper and lower bounds are specified for all the variables and for all the constraints. This form allows full generality in specifying other types of constraints. In particular, the i -th constraint may be defined as an equality by setting $\ell_i = u_i$. If certain bounds are not present, the associated elements of ℓ or u can be set to special values that will be treated as $-\infty$ or $+\infty$.

Here we briefly summarize the main features of the method of NZSOL and NPSOL as discussed in Reference 6 because Reference 12 is not available to general public. At a solution of NP, some of the constraints will be active, i.e., satisfied exactly. An active simple bound constraint implies that the corresponding variable is fixed at its bound, and hence the variables are partitioned into fixed and free variables. Let C denote the $m \times n$ matrix of gradients of the active general linear and nonlinear constraints. The number of fixed variables will be denoted by n_{FX} , with n_{FR} ($n_{FR} = n - n_{FX}$) the number of free variables. The subscripts "FX" and "FR" on a vector or matrix will denote the vector or matrix composed of the components corresponding to fixed or free variables. The details are discussed in Reference 11.

A point x is a first-order Kuhn-Tucker point for NP if the following conditions hold:

- (i) x is feasible;
- (ii) there exist vectors ζ and λ (the Lagrange multiplier vectors for the bound and general constraints) such that
$$g = C^T \lambda + \zeta, \quad (4-4a)$$

where g is the gradient of F evaluated at x , and $\zeta_j = 0$ if the j -th variable is free.
- (iii) The Lagrange multiplier corresponding to an inequality constraint active at its lower bound must be non-negative, and non-positive for an inequality constraint active at its upper bound.

Let Z denote a matrix whose columns form a basis for the set of vectors orthogonal to the rows of C_{FR} ; i.e., $C_{FR}Z = 0$. An equivalent statement of the condition in terms of Z is

$$Z^T g_{FR} = 0 \quad (4-4b)$$

The vector $Z^T g_{FR}$ is termed the projected gradient of F at x . Certain additional conditions must be satisfied in order for a first-order Kuhn-Tucker point to be a solution of NP.

4.1 The Quadratic Programming Subproblem

Similar to NPSOL, the basic structure of NZSOL involves major and minor iterations. The major iterations generate a sequence of iterates (x_k) that converge to x^* , a first-order Kuhn-Tucker point of NP. At a typical major iteration, the new iterate \bar{x} is defined by

$$\bar{x} = x + \alpha p, \quad (4-5a)$$

where x is the current iterate, the non-negative scalar α is the step length, and p is the search direction. Also associated with each major iteration are estimates of the Lagrange multipliers and a prediction of the active set.

The search direction p is the solution of a quadratic programming subproblem of the form

$$\begin{aligned} & \underset{p}{\text{minimize}} && g^T p + \frac{1}{2} p^T H p \\ & \text{subject to} && \bar{l} \leq \begin{Bmatrix} p \\ A_{LP} \\ A_{NP} \end{Bmatrix} \leq \bar{u}, \end{aligned} \quad (4-5b)$$

where g is the gradient of F at x , the matrix H is a positive-definite quasi-Newton approximation to the Hessian of the Lagrangian function and A_N is the Jacobian matrix of c evaluated at x .

The estimated Lagrange multipliers at each major iteration are the Lagrange multipliers from the subproblem (and similarly for the predicted active set) and provide information about the sensitivity of these NLP problems.

Certain matrices associated with the QP subproblem are relevant in the major iterations. Let the subscripts "FX" and "FR" refer to the predicted fixed and free variables, and let C denote the $m \times n$ matrix of gradients of the general linear and nonlinear constraints in the predicted active set. First, we have available the TQ factorization (Reference 11) of C_{FR} :

$$C_{FR} Q_{FR} = (0 \quad T), \quad (4-6)$$

where T is a nonsingular $m \times m$ reverse-triangular matrix (i.e., $t_{ij} = 0$ if $i + j < m$), and the non-singular $n_{FR} \times n_{FR}$ matrix Q_{FR} is the product of orthogonal transformations. Second, we have the upper-triangular Cholesky factor R of the transformed and re-ordered Hessian matrix

$$R^T R = H_Q \equiv Q^T \bar{H} Q, \quad (4-7)$$

where \bar{H} is the Hessian H with rows and columns permuted so that the free variables are first, and Q is the $n \times n$ matrix

$$Q = \begin{pmatrix} Q_{FR} & \\ & I_{FX} \end{pmatrix}, \quad (4-8)$$

with I_{FX} the identity matrix of order n_{FX} . If the columns of Q_{FR} are partitioned so that

$$Q_{FR} = (Z \quad Y), \quad (4-9)$$

the n_Z ($n_Z \equiv n_{FR} - m$) columns of Z form a basis for the null space of C_{FR} . The matrix Z is used to compute the projected gradient $Z^T g_{FR}$ at the current iterate.

As discussed in Reference 6 and 11, a theoretical characteristic of SQP methods is that the predicted active set from the QP subproblem is identical to the correct active set in a neighborhood of x^* . In NPSOL, this feature is exploited by using the QP active set from the previous iteration as a prediction of the active set for the next QP

subproblem, which leads in practice to optimality of the subproblems in only one iteration as the solution is approached. Separate treatment of bound and linear constraints in NPSOL also saves computation in factorizing C_{FR} and H_Q .

4.2 The merit function

Detailed discussions of the merit function are given in Reference 14. In NZSOL and NPSOL, once the search direction p has been computed, the major iteration proceeds by determining a steplength α that produces a "sufficient decrease" in the augmented Lagrangian merit function

$$L(x, \lambda, s) = F(x) - \sum_i \lambda_i (c_i(x) - s_i) + \frac{1}{2} \sum_i \rho_i (c_i(x) - s_i)^2, \quad (4-10)$$

where x , λ and s vary during the line search. The summation terms involve only the nonlinear constraints. The vector λ is an estimate of the Lagrange multipliers for the nonlinear constraints of NP. The non-negative slack variable $\{s_i\}$ allow nonlinear inequality constraints to be treated without introducing discontinuities. The solution of the QP subproblem (4-5) provides a vector triple that serves as a direction of search for the three sets of variables.

4.3 The quasi-Newton updated

Before going into the detailed discussions, it is important to point out that both the NZSOL and NPSOL start by initializing the Hessian matrix H = Identity matrix. Thus at the beginning, the search direction is in the steepest decent direction. No initial curvature information is computed and the curvature information is accumulated through the BFGS quasi-Newton updates. The matrix H in (4-5) is a positive-definite quasi-Newton approximation to the Hessian of the Lagrangian function. At the end of each major iteration, a new Hessian approximation \bar{H} is defined as a rank-two modification of H . In NPSOL the BFGS quasi-Newton update is used:

$$\bar{H} = H - \frac{1}{s^T H s} H s s^T H + \frac{1}{y^T s} y y^T, \quad (4-11)$$

where $s = \bar{x} - x$ (the change in x).

Rather than modifying H itself, the Cholesky factor of the transformed Hessian H_Q (4-7) is updated, where Q is the matrix from (4-8) associated with the active set of the QP subproblem. The update (4-11) is equivalent to the following update to H_Q :

$$\bar{H}_Q = H_Q - \frac{1}{s_Q^T H_Q s_Q} H_Q s_Q s_Q^T H_Q + \frac{1}{y_Q^T s_Q} y_Q y_Q^T, \quad (4-12)$$

where $y_Q = Q^T y$ and $s_Q = Q^T s$. This update may be expressed as a rank-one update to \bar{H} and is used to incorporate new curvature information obtained in the move from x to \bar{x} .

4.4 NZSOL, NPSOL 4.02, and NPSOL 2.1

For those who are interested in applying these NLP codes, there are two published versions of NPSOL. The NPSOL 4.02 was developed after the NPSOL 2.1 and therefore more reliable and efficient algorithm were incorporated according to Gill (

Reference 12). However, in updating the Cholesky factor, the NPSOL 4.02 updates the whole or complete R while the NPSOL 2.1 updates only the part associated with the Z-space or null space of R. For the problem formulated here ,usually several hundred variables are involved and the NPSOL 2.1 converges in less computing time. The NZSOL (Reference 12) incorporates not only latest efficient and reliable algorithm but also updates only the part of R associated with the null space of R only. In addition to improve the algorithm of NPSOL, it also adopts the best parts of both NPSOL 2.1 and 4.02.

Finally, it may be interesting to point out that the matrices in the present formulation using collocation and Hermite polynomial are large and fairly sparse. For computational efficiency, it is important to incorporate NLP codes such as MINOS (Reference 13) to take advantage of the special characteristic of the collocation formulation discussed here.

5. NUMERICAL RESULTS AND DATA

The data used in the numerical experiments presented here (c.f. Reference 2 and 9) are summarized as follows:

$$C_{DO} = 0.1 \quad ; \quad K = 1.111 \quad ; \quad m/S = 300 \text{ kg/m}^2 \quad (5-1)$$

and the drag polar is

$$C_D = C_{DO} + K * C_L^2 \quad (5-2)$$

and other useful data are

$$\begin{aligned} \rho_a &= 1.225 \text{ kg / m}^3; \mu = 3.986 \times 10^{14} \text{ m}^3 / \text{sec}^2 \\ \beta &= 1/6900 \text{ m}^{-1}; R_E = 6378 \text{ km} \\ H_a &= 120 \text{ km} \end{aligned} \quad (5-3)$$

Using the above mentioned data, simulations were carried out

For an AOTV returning from the geosynchronous orbit (GEO) to the space station orbit (SSO) , one has $R_d = 42240 \text{ km}$ and $R_c = 6934 \text{ km}$. Simulation results were obtained for the following parametric studies for different values of C_{LM} .

a) Case 1 (Reference Case). For this reference case , simulation results were obtained under the general formulation that no orbital plane changes are allowed at deorbit, boost, and reorbit impulses and inside the atmosphere. This reference case has the following entry and exit status

$$\begin{aligned} \text{Entry status:} \quad H_e &= 120 \text{ km}; \quad V_e = 10.315 \text{ km/sec} \\ \gamma_e &= -3.727 \text{ degrees}; \quad \phi_e = 0; \quad \psi_e = 0 \end{aligned} \quad (5-4)$$

$$\begin{aligned} \text{Exit status:} \quad H_f &= 120 \text{ km}; \quad V_f = 7.952 \text{ km/sec} \\ \gamma_f &= 0.91 \text{ deg}; \quad \phi_f = 0 \text{ deg} \\ \psi_f &= 0 \text{ deg}; \quad \text{total flight time} = 769.25 \text{ sec} \end{aligned} \quad (5-5)$$

The characteristic velocities are 1489 meters per seconds and 132 meters per second at the deorbit and the reorbit respectively. The total characteristic velocity is 1621 meters per second. The C_{LMax} is assumed to be 3.0.

b) Case 2 : Simulation results were also obtained for the case where the maximum lift coefficient is assumed to be 4.5. Similar to the reference case, no orbital plane change is allowed. The entry and exit status are summarized as follows:.

Entry status: $H_e = 120 \text{ km}; V_e = 10.3118 \text{ km/sec}$
 $\gamma_e = -3.576 \text{ degrees}; \phi_e = 0; \psi_e = 0$ (5-6)

Exit status: $H_f = 120 \text{ km}; V_f = 7.9518 \text{ km/sec}$
 $\gamma_f = 3.576 \text{ deg}; \phi_f = 0 \text{ deg}$ (5-7)
 $\psi_f = 0 \text{ deg}; i_f = 0 \text{ degree , total flight time} = 673.38 \text{ sec}$

The deorbit characteristic velocity is 1488.91 meters per second and the recirculation characteristic velocity is 131.61 meters per second. The total characteristic velocity is 1620.517 meters per second. It is interesting to observe that all the characteristic velocities are almost the same as those obtained in case 1.

c) Case 3 : Similar to Case 2 , the optimal control solution has a maximum lift coefficient of 2.3 and has the following entry and exit status.

Entry status: $H_e = 120 \text{ km}; V_e = 10.3115 \text{ km/sec}$
 $\gamma_e = -3.814 \text{ degrees}; \phi_e = 0; \psi_e = 0$ (5-8)

Exit status: $H_f = 120 \text{ km}; V_f = 7.9515 \text{ km/sec}$
 $\gamma_f = 0.917 \text{ deg}; \phi_f = 0.\text{deg}; i_f = 0.0 \text{ deg}$
 $\psi_f = 0.0 \text{ deg; total flight time} = 857.34 \text{ sec}$ (5-9)

d) Case 4. Similar to Case 2, the optimal control solution has a maximum lift coefficient of 0.9 and has the following entry and exit status.

Entry status: $H_e = 120 \text{ km}; V_e = 10.3117 \text{ km/sec}$
 $\gamma_e = -4.154 \text{ degrees}; \phi_e = 0; \psi_e = 0$ (5-10)

Exit status: $H_f = 120 \text{ km}; V_f = 7.9509 \text{ km/sec}$
 $\gamma_f = 0.954 \text{ deg}; \phi_f = 0.\text{deg}; i_f = 0.0 \text{ deg}$
 $\psi_f = 0.0 \text{ deg; total flight time} = 1450.67 \text{ sec}$ (5-11)

Again, all the characteristic velocities associated with the deorbit, and reorbit impulses for Case 3 and Case 4 are almost the same as Case 1 and Case 2.

Time histories of altitude, velocity, flight path angles, lift coefficient, lift to drag ratio, dynamical pressure, atmospheric density and heating rate for all three cases (Case 1, 2, & 3.) are shown in Figure 3-10. It is important to point out that for the vehicle

considered here, the maximum lift coefficient is 0.9. However, for the simulation results shown here, the maximum lift coefficient is set to be less than 4.5 for parametric studies.

An interesting observation from the simulation results as shown in Figs. 3 to 10 is that although the total characteristic velocity is insensitive to the variation of the maximum lift coefficient, the optimal trajectory is very sensitive. The higher the maximum lift coefficient is the less the vehicle penetrates into the atmosphere and the less the time of flight is needed. The vehicle was flying at the maximum lift coefficient in contrast to previous simulation where the vehicle was flying at the maximum lift to drag ratio as shown in Reference 15 and 17. Simulation results shows that for the coplanar orbital transfer the vehicle has only to penetrate the atmosphere deep enough to reduce the exit velocity so that the vehicle will exit the atmosphere at the desired velocity and flight path angle so that the apogee of the exit orbit is the altitude of the desired final LEO.

The heating rate Q_r , along the atmospheric trajectory, is computed for the stagnation point of a sphere of radius of one meter, according to the following relation (Reference 2 and 6)

$$Q_r = K_r \rho^{0.5} V^{3.08} \quad (5-12)$$

where the ρ is the atmospheric density in kg/km^3 , V is the velocity in km/sec and the K_r is the proportionality constant equal to 0.000308. The time history of heating rates for the reference case (Case 1), Case 2, Case 3, and Case 4 were shown in Fig. 6. These simulation results presented provided enough information that the peak heating rate for coplanar case will be much less than those for cases aeroassisted orbital plane changes are made. As shown in References 15 and 17, one needs less thermal protection materials and more fuel consumption to fly the heat constrained trajectories and therefore by taking into account the weight of thermal protection materials one may find an optimal design to minimize the total vehicle weight.

Another interesting observation from previous simulation results (cf. Reference 15 and 17) is that for given HEO and LEO, the deorbit impulse is almost the same for all the cases simulated here. The total characteristic velocity for a given optimal trajectory is almost completely determined by the boost and the recirculation. In fact, the boost velocity contributes the most to the variation of the total characteristic velocity. Physically, it is obvious as the vehicle makes a larger turn it also loses more energy and therefore needs more velocity to boost it back to the final orbital altitude. Although the total characteristic velocity is insensitive to the magnitude of deorbit impulse, the optimal trajectory is very sensitive to ΔV_d . In the coplanar aeroassisted orbit transfer here, the boost impulse is not needed and the deorbit and recirculation impulses are almost the same for all the cases simulated here. Thus the total characteristic velocity is not sensitive to the variation of the maximum lift coefficient. However, the depth of penetration was shown as a function of the maximum lift coefficients.

6. CONCLUDING REMARKS

An excellent survey of the subject was given in Reference 1. Walberg reviewed the problem of optimal aeroassisted orbital transfer with plane change. In a recent paper

by Naidu (c.f. Reference 2), fuel optimal trajectories of aeroassisted orbital transfer with plane change were presented using the so-called multiple shooting method for the case without heating rate constraints and under the assumption that all the plane change was performed entirely in the atmosphere. A brief review of the progress made in this field was also given in Reference 2. In Reference 15, a similar problem for cases with and without peak stagnation point heating rate constraints was solved using the collocation and nonlinear programming technique. This method is especially suitable for parametrical studies because of its relative insensitivity to initial guesses.

In Reference 17, simulation results were obtained under a more general formulation that not all the orbital plane changes are made in the atmosphere. It must be noted that the AOTV transfer can be made more efficient propulsively if the plane change is performed partly in the atmosphere and partly in space and the propulsive plane change in space is subdivided into components associated with various impulsive points. All these plane changes were automatically determined by the optimization processes discussed in Reference 17.

The above studies provided necessary data bases and essential information concerning how to use and how to combine the propulsive and aeroassisted orbital plane changes effectively. In this paper, another group of problems under the assumption no orbital plane change is allowed are investigated. In fact, the present investigation is closely related to the problem of returning from GEO to space station assuming all plane changes are made propulsively outside the atmosphere. As discussed, the characteristics of the flight is quite different from the cases where the orbital plane changes are made inside the atmosphere. In the latter case, the vehicle has to penetrate deeper into the atmosphere to perform the the desired orbital plane change. On the other hand, for the coplanar case, the vehicle needs only to penetrate the atmosphere deep enough to reduce the exit velocity so that the vehicle can be capture at the desired LEO.

It should be mentioned that the collocation and nonlinear programming technique discussed here was recently applied to another group of orbital transfer problem by Enright and Conway in Reference 3 and the relative insensitivity of this method to the initial guesses was also observed by them. Our basic simulation test bed is the OTIS codes (Reference 5) with an improved and updated nonlinear programming code (NZSOL). All physical models used were documented in Reference 5. Of course, necessary modifications and corrections have to be incorporated to simulate the aerobraking problems discussed here.

It may be worthwhile mentioning that the present problem was actually solved by guessing the initial state and control variables at four selected points, i.e., the initial point, the final point and two other nodal points along the trajectory inside the atmosphere. The initial state and control variables at other nodes or grid points were simply obtained by linear interpolation. These initial guesses do not have to satisfy either the governing equations or the nonlinear constraints including the defects. Only rough guesses are needed at these four points. Converged solutions were obtained with relative ease. Once a converged solution is obtained, optimal solutions for other cases with different inclination changes or different peak heating rate constraints can

be obtained using this converged solution as initial guesses. However, it is important to point out proper scaling of the defects, constraints and variables are essential to get converged solutions. For simulations discussed here, converged solutions were obtained by using as little as 50 nodes. However, in some cases, converged solutions were obtained using 100 nodes. As far as we know, this may be the first time converged solutions were obtained for so many independent variables and nonlinear constraint equations. This also illustrates how powerful the nonlinear programming code and the collocation and Hermite polynomial technique are.

Finally, it is important to mention again that aeroassisted orbital transfer introduces a strong coupling between the vehicle design and the trajectory design as indicated by the simulation data. A trajectory that minimizes fuel mass, without attention to heating, may require the vehicle to have heavy thermal protection systems. As shown here, an optimal design for the total vehicle weight may be obtained as discussed earlier. However, if the aeroassisted transfer is to be preferred to all propulsive transfer, it must offer a reduction in fuel mass greater than the increase in thermal protection mass. As far as minimum fuel is concerned, the reference cases investigated in Reference 17 provided more fuel savings as expected. But for the over all trade-off studies, the peak heating rate, dynamical pressure, maximum g forces, and fuel mass have to be considered. May be, it is also important to point out that the problems investigated here is to assume that all plane changes are propulsive and outside the atmosphere and that the aeroassisted atmospheric flight is planar. This case is most beneficial from the thermal protection point of view and must be considered in the over all trade-off studies.

7. REFERENCES

1. Walberg, G. A., "A Survey of Aeroassisted Orbit Transfer", Journal of Spacecraft and Rockets, Vol. 22, Jan-Feb. 1985, pp 3-18.
2. Naidu, D. S., "Fuel-optimal Trajectories of Aeroassisted Orbital Transfer with Plan Change" AIAA Guidance, Navigation & Control Conference, Boston, MA., August 14-16, 1989.
3. Enright, P. J. and Conway, B. A., "Optimal Finite Thrust Spacecraft Trajectories Using Collocation and Nonlinear Programming", Paper AAS 89-350, AAS/AIAA Astrodynamics Specialist Conference, Stowe, Vermont, August 7-10, 1989.
4. Shi, Y. Y., "Matched Asymptotic Solution For Optimum Lift Controlled Atmospheric Entry", AIAA JOURNAL, VOL. 9, 1971, PP. 2229-2238.
5. Hardgraves, C. R. and Paris, S. W., "OTIS-Optimal Trajectories by Implicit Integration", Boeing Aerospace Co., Contract No. F33615-85-C-3009, 1988.
6. Gill, P.E., Murray, W., Sanders, M.A., and Wright, M.H., "User's Guide For NPSOL (Version 4.0) : A Fortran Package For Nonlinear Programming", System Optimization Laboratory, Department of Operation Research, Stanford University, Stanford, California, 1986.
7. Shi, Y. Y., Pottsepp, L., and M. C. Eckstein. "Optimal lift Control of a Hypersonic Lifting Body During Atmospheric Entry", AIAA Journal, Vol.7, No.12, December, 1969..
8. Shi, Y. Y. and Eckstein, M. C., "An Exact Solution for Optimum Controlled Soft Lunar Landing", Astronautica Acta, Vol.16, pp. 9-18, Pergamon Press, New York, 1971.

9. Mease, K.D. and Vinh, N. X., "Minimum-Fuel Aeroassisted Coplanar Orbit Transfer Using Lift-Modulation", AIAA Journal of Guidance and Control, Vol.8, No.1, Jan-Feb. 1985.
10. Mease, K.D., "Optimization of Aeroassisted Orbital Transfer : Current Status", The Journal of the Astronautical Sciences, Special Issue On Hypervelocity Flight, Volume 36, Nos.1/2, January-June, 1988.
11. Gill, P.E., and Wright, M.H., "Practical Optimization", Academic press, London and New York, 1981.
12. Gill, P.E., "NZSOL: An Improved Version of NPSOL", Private Communications, Huntington Beach, California, 1989-90.
13. Murtagh, B. A. and Saunders, M.A., "MINORS 5.0 User's Guide", Report SOL 83-20, Department of Operation Research, Stanford Research, California, 1983.
14. Gill, P.E., Murray, W., Sanders, M.A., and Wright, M.H., "Some Theoretical Properties of An Augmented Lagrangian Merit Function", Technical Report SOL 86-6R, System Optimization Laboratory, Department of Operation Research, Stanford University, Stanford, California, 1986.
15. Shi, Y. Y., Nelson, R., L., and Young, D., H., "Optimal Aeroassisted Orbital Transfer With Plane Change Using Collocation and Nonlinear Programming", Proceedings of 1990 Flight Mechanics / Estimation Theory Symposium, NASA Goddard Space Flight Center, Greenbelt, Maryland, May 22-24, 1990.
16. Jezewski, D. J., "An Efficient Method For Calculating Optimal Free Space, N-Impulse Trajectory", AIAA Journal, Vol. 6, No. 11, November, 1968.
17. Shi, Y. Y., Young, D., H., & Nelson, R., L., "Minimum-Fuel Aeroassisted Nonplanar Orbital Transfer Using Collocation and Nonlinear Programming", Proceedings of the 1990 AIAA/AAS Astrodynamics Specialist Conference, Portland, Oregon, August 22-24, 1990.

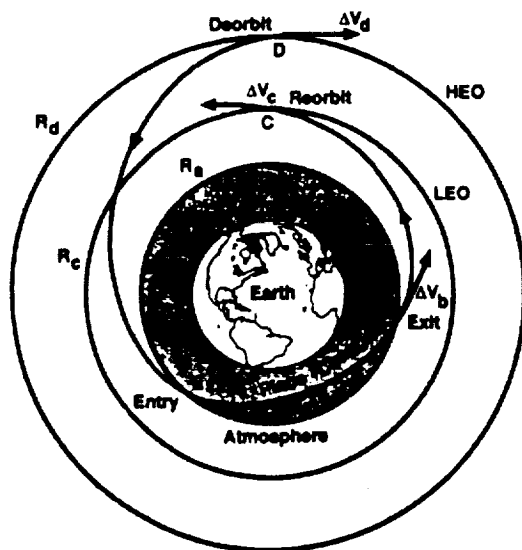


Fig. 1 Aeroassisted Orbital Plane Change

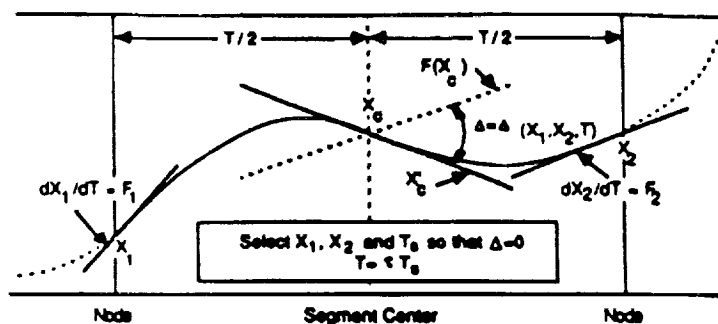


Fig. 2 Collocation and Hermite Approximation

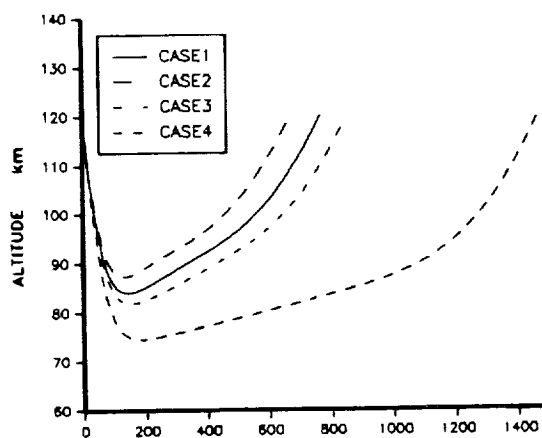


Fig. 3 Time History of Altitude

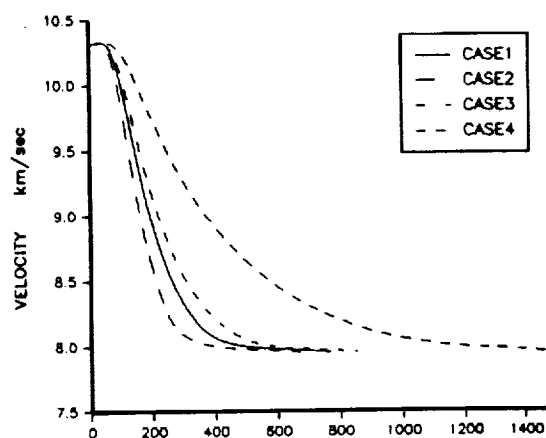


Fig. 4 Time History of Velocity

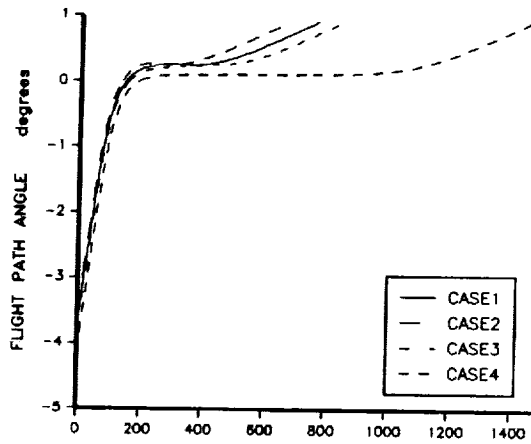


Fig.5 Time History of Flight Path Angle

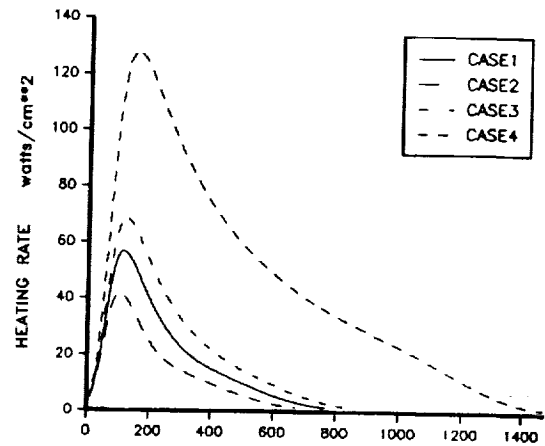


Fig.6 Time History of Heating Rate

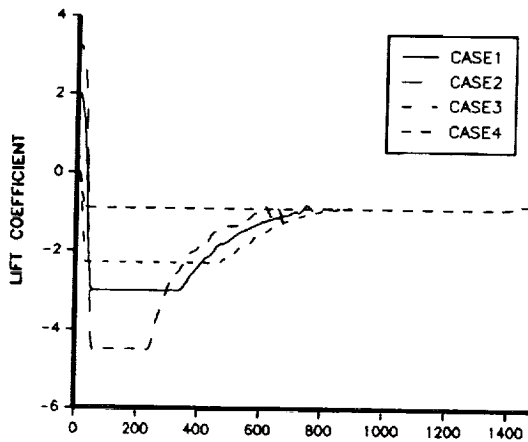


Fig.7 Time History of Lift Coefficient

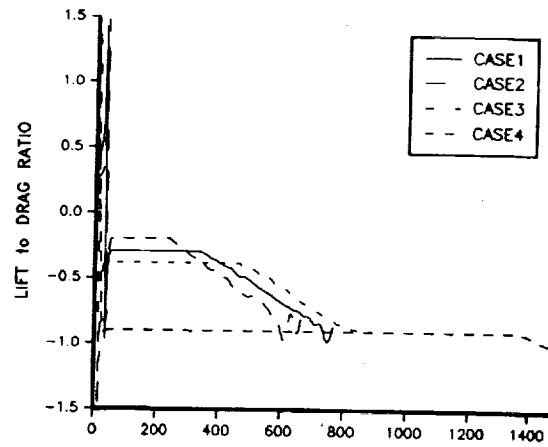


Fig.8 Time History of Lift to Drag Ratio

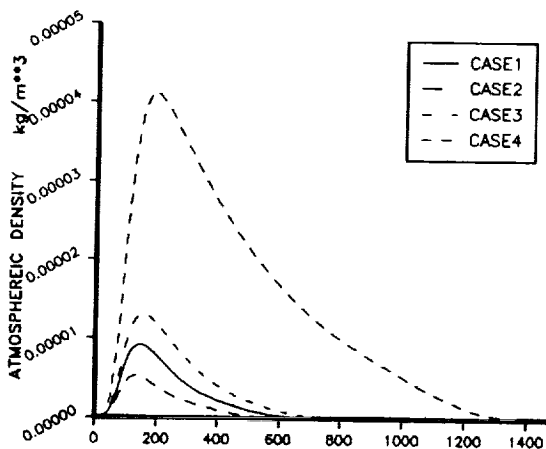


Fig.9 Time History of Atmospheric Density

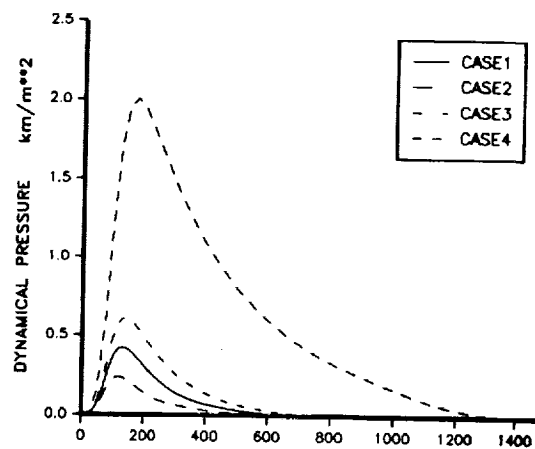


Fig.10 Time History of Dynamical Pressure

Propellant-Remaining Modeling

S. Torgovitsky
COMPUTER SCIENCES CORPORATION (CSC)

ABSTRACT

A successful satellite mission is predicated upon the proper maintenance of the spacecraft's orbit and attitude. One requirement for planning and predicting the orbit and attitude is the accurate estimation of the propellant remaining onboard the spacecraft. For geosynchronous satellites, a precise propellant-remaining estimation is of particular importance. Twenty kilograms (kg) of propellant can add a year to the operational lifetime of a satellite such as the Geostationary Operational Environment Satellite (GOES)-I. Moreover, the geosynchronous ring is becoming cluttered with propellant-depleted satellites; therefore, an extra 3 to 4 kg of fuel may be required to deorbit an expiring satellite out of the geosynchronous ring. For GOES-I, which is loaded with over 670 kg of oxidizer and over 420 kg of fuel, accounting for 20 kg of propellant requires accuracy in propellant-remaining estimation of within 2 percent. Budgeting for the 3 kg of propellant at the end of the mission requires a method with an accuracy of within 0.5 percent.

This paper focuses on the three methods that were developed for calculating the propellant budget: in particular, the errors associated with each method and the uncertainties in the variables required to determine the propellant remaining that contribute to these errors. Based on these findings, a strategy will be developed for improved propellant-remaining estimation. The first method is based on Boyle's law, which relates the values of pressure, volume, and temperature (PVT) of an ideal gas. The PVT method is used for both the monopropellant and the bipropellant engines. The second method is based on the engine performance tests, which provide data that relate thrust and specific impulse (I_{sp}) associated with a propellant tank to that tank's pressure. Two curves representing thrust and specific impulse as functions of pressure are then generated using a polynomial fit on the engine performance data. The third method involves a computer simulation of the propellant system. The propellant flow is modeled by creating a conceptual model of the propulsion system configuration, taking into account such factors as the propellant and pressurant tank characteristics, thruster functionality, and piping layout.

Finally, this paper presents a thrust calibration technique that uses differential correction with the computer simulation method of propellant-remaining modeling. Thrust calibration will provide a better assessment of thruster performance and therefore enable a more accurate estimation of propellant consumed during a given maneuver.

1. METHODS OF COMPUTING PROPELLANT REMAINING

Introduction

Before presenting the detailed descriptions of the propellant estimation methods, a brief introduction on the propulsion system operation during a spacecraft mission is in order.

For the liquid propellant/gas pressurant system considered in this paper two modes of operations are feasible: blowdown and pressure regulated. In blowdown mode, the propellant tank is pressurized by the gas pressurant and then during the mission the propellant tank pressure is allowed to decay as propellant is "blown out" of the tank when the thrusters are firing. In pressure regulated mode, the propellant tank pressure is maintained constant by supplying additional pressurant gas into the propellant tank during the thruster firing. The advantage of the pressure regulated mode is the constant propellant flow rate which is necessary to maintain in a bipropellant type engine to ensure constant mixture ratio for optimum thruster performance (see Section I, Method 1).

The propellant estimation methods described here can be used to model an engine operating in both blowdown and pressure regulated mode, blowdown mode only, and pressure regulated mode only (Methods 1, 2, and 3 respectively).

Two phases of the mission are mentioned in this paper: the transfer orbit phase—when the satellite is maneuvered to achieve mission orbit; and the station keeping phase—when the satellite is maneuvered to maintain the mission orbit. For GOES-I, 86 percent of the propellant is used during the transfer orbit phase (NASA phase). GRO on the other hand is inserted into the mission orbit by the launch vehicle; therefore, ideally, 100 percent of propellant is used for station keeping and controlled reentry.

Method 1: Pressure, Volume, Temperature

The PVT method is based on an assumption of ideal gas behavior of the pressurant gas. Since the pressurant gas is helium, the ideal gas approximation is valid. Boyle's law is then used to estimate the propellant remaining based on the amount of pressurant that was forced into the propellant tank. The procedure is as follows:

Suppose that the volume of propellant displaced from the tank is equal to the volume of pressurant forced into the tank, given that pressurant and propellant do not mix and that the tank volume does not change. Then,

$$dM_f = \rho_{of} \cdot dV_{He,f} \quad (1-1)$$

where dM_f = propellant forced out of the tank
 ρ_{of} = propellant density
 $dV_{He,f}$ = volume of pressurant forced into the tank

Using Boyle's law to compute the pressurant volume and writing the propellant density as a function of tank temperature, we have

$$dV_{He,f} = \frac{R \cdot dm_{He} \cdot Z_{He} \cdot T_{He}}{P_{He}} \quad (1-2)$$

where R = pressurant (helium) gas constant
 dm_{He} = mass of pressurant forced into the propellant tank
 Z_{He} = pressurant compressibility
 T_{He} = pressurant temperature
 P_{He} = pressurant pressure

and

$$\rho_{of} = b_0 + b_1 \cdot T + b_2 \cdot T^2 \quad (1-3)$$

where T = propellant tank temperature
 b_0, b_1, b_2 = propellant density coefficients

Since pressurant and propellant are in the same tank and do not mix,

$$T_{He} = T \quad (1-4)$$

and

$$P_{He} = P - P_{sat} \quad (1-5)$$

where P = propellant tank pressure
 P_{sat} = propellant saturation pressure

Propellant saturation pressure may be expressed as a function of temperature, T ,

$$P_{sat} = 10^{(a_0 - a_1/T - a_2/T^2)} \quad (1-6)$$

where a_0, a_1, a_2 = propellant saturation pressure coefficients

Pressurant compressibility may be expressed as a function of pressurant pressure, P_{He} , and temperature, T_{He} ,

$$Z_{He} = 1 + P_{He} \cdot [\beta + \Gamma \cdot (T - T_s)] \quad (1-7)$$

where β, Γ = pressurant compressibility coefficients
 T_s = pressurant standard temperature

The expression for propellant used may then be rewritten as a function of tank pressure and temperature and the mass of pressurant forced into the propellant tank,

$$dM_f = R \cdot dM_{He} \cdot [b_0 + b_1 \cdot T + b_2 \cdot T^2] \cdot \left[\frac{T}{P - 10^{(a_0 - a_1/T - a_2/T^2)}} + \beta \cdot T + \Gamma \cdot T^2 - \Gamma \cdot T_s \cdot T \right] \quad (1-8)$$

The accuracy of the propellant estimation using this method is only as good as the certainty in the values of P, T , and dM_{He} . The uncertainty in the tank pressure and temperature is based on the ratings of the pressure transducers and the temperature sensors, as well as the telemetry signal resolution. The uncertainty in the pressurant mass forced into the propellant tank can be considered at most as great as the uncertainty in the pressurant mass leaving the pressurant tank (assuming there are no leaks), which is a function of the loading conditions and the telemetry readings of the pressure and temperature of the pressurant tank.

Since pressurant gas behaves as an ideal gas, Boyle's law applies as follows:

$$\frac{P_o \cdot V_o}{m_o \cdot Z_{He,o} \cdot T_o} = \frac{P_{He} \cdot V_{He}}{m_{He} \cdot Z_{He} \cdot T_{He}} \quad (1-9)$$

where P_o = loading pressurant tank pressure
 T_o = loading pressurant tank temperature
 V_o = loading pressurant tank volume
 m_o = loading pressurant mass
 $Z_{He,o}$ = loading pressurant compressibility
 P_{He} = pressurant tank pressure
 T_{He} = pressurant tank temperature
 V_{He} = pressurant tank volume
 m_{He} = pressurant mass
 Z_{He} = pressurant compressibility

Using the fact that pressurant tank volume is a function of pressurant tank pressure and temperature,

$$V_o = V_h + q_1 \cdot (P_o - P_h) + q_2 \cdot (T_o - T_h) \quad (1-10)$$

$$V_{He} = V_h + q_1 \cdot (P_{He} - P_h) + q_2 \cdot (T_{He} - T_h) \quad (1-11)$$

where V_h = standard pressurant tank volume
 P_h = standard pressurant tank pressure
 T_h = standard pressurant tank temperature
 q_1 = pressure coefficient
 q_2 = temperature coefficient

and the fact that compressibility is also a function of tank pressure and temperature, Equation (1-7), the amount of pressurant forced into the propellant tank may be expressed as follows:

$$dM_{He} = m_o - m_{He} \quad (1-12)$$

or

$$dM_{He} = m_o \cdot \left\{ 1 - \frac{P_{He} \cdot T_o}{P_o \cdot T_{He}} \cdot \frac{V_h + q_1 \cdot (P_{He} - P_h) + q_2 \cdot (T_{He} - T_h)}{V_h + q_1 \cdot (P_o - P_h) + q_2 \cdot (T_o - T_h)} \right. \\ \left. \cdot \frac{1 + P_o \cdot [\beta + \Gamma \cdot (T_o - T_s)]}{1 + P_{He} \cdot [\beta + \Gamma \cdot (T_{He} - T_s)]} \right\} \quad (1-13)$$

The error in propellant estimation may be expressed in terms of the uncertainties in propellant tank temperatures and pressures obtained from telemetry and the uncertainty in the pressurant mass forced into the propellant tank. Therefore, the error in propellant estimation due to these variables can be defined in standard fashion as

$$Error_P = \frac{\delta (dM_f)}{\delta (P)} \cdot P_{uncertainty} \quad (1-14a)$$

$$Error_T = \frac{\delta (dM_f)}{\delta (T)} \cdot T_{uncertainty} \quad (1-14b)$$

$$\text{Error}_{dM_{He}} = \frac{\delta (dM_f)}{\delta (dM_{He})} \cdot dM_{He_{uncertainty}} \quad (1-14c)$$

The uncertainty in pressurant mass can be expressed as 1σ error in the pressurant mass due to the uncertainties in the pressurant tank loading conditions and telemetry uncertainty in pressurant tank pressure and temperature:

$$dM_{He_{uncertainty}} = \sqrt{(\text{Error}_{P_{He}})^2 + (\text{Error}_{T_{He}})^2 + (\text{Error}_{P_o})^2 + (\text{Error}_{T_o})^2 + (\text{Error}_{m_o})^2} \quad (1-14d)$$

where

$$\text{Error}_{P_{He}} = \frac{\delta (dM_{He})}{\delta (P_{He})} \cdot P_{He_{uncertainty}} \quad (1-14e)$$

$$\text{Error}_{T_{He}} = \frac{\delta (dM_{He})}{\delta (T_{He})} \cdot T_{He_{uncertainty}} \quad (1-14f)$$

$$\text{Error}_{P_o} = \frac{\delta (dM_{He})}{\delta (P_o)} \cdot P_{O_{uncertainty}} \quad (1-14g)$$

$$\text{Error}_{T_o} = \frac{\delta (dM_{He})}{\delta (T_o)} \cdot T_{O_{uncertainty}} \quad (1-14h)$$

$$\text{Error}_{m_o} = \frac{\delta (dM_{He})}{\delta (m_o)} \cdot m_{O_{uncertainty}} \quad (1-14i)$$

Blowdown mode operation may be simulated by assuming that there is no change in pressurant mass in the propellant tank (i.e., pressurant tank is shut off). Then, the propellant remaining becomes a function of the propellant tank pressure and temperature change where $dM_{He} = \text{constant}$.

In a bipropellant propulsion system such as the one in GOES-I, the pressurant forced into a given tank is a function of the split ratio (the ratio of pressurant mass forced into the two tanks) as well as a function of the pressurant mass leaving the pressurant tank. The split ratio is, in turn, a function of the pressures and temperatures of the two propellant tanks and the mixture ratio (the ratio of the mass flow rates of the two propellants). The pressures and the temperatures are obtained from telemetry; the mixture ratio is defined by the manufacturer to ensure the optimum thruster performance. The expression for the split ratio in terms of the above quantities is derived as follows:

$$\text{Split Ratio} = \frac{dM_{He1}}{dM_{He2}} \quad (1-15)$$

where dM_{He1} = mass of pressurant forced into propellant tank 1
 dM_{He2} = mass of pressurant forced into propellant tank 2

Combining Equations (1-1) and (1-2) and introducing subscripts to distinguish between the two propellant tanks,

$$\frac{dM_{f1}}{dM_{He1}} = \rho_{o f1} \cdot \frac{R \cdot Z_{He1} \cdot T_{He1}}{P_{He1}} \quad (1-16a)$$

and

$$\frac{dM_{f2}}{dM_{He2}} = \rho_{f2} \cdot \frac{R \cdot Z_{He2} \cdot T_{He2}}{P_{He2}} \quad (1-16b)$$

Then, using the definition of the mixture ratio (MR) and Equations (1-3) and (1-7) for propellant densities and pressurant compressibility, respectively,

$$\begin{aligned} \text{Split Ratio} = \text{MR} \cdot \frac{b_{f0} + b_{f1} \cdot T_2 + b_{f2} \cdot T_2^2}{b_{o0} + b_{o1} \cdot T_1 + b_{o2} \cdot T_1^2} \cdot \frac{P_{He1}}{P_{He2}} \cdot \frac{T_{He2}}{T_{He1}} \\ \cdot \frac{1 + P_{He2} \cdot [\beta + \Gamma \cdot (T_2 - T_s)]}{1 + P_{He1} \cdot [\beta + \Gamma \cdot (T_1 - T_s)]} \end{aligned} \quad (1-17)$$

where pressurant partial pressure can be expressed in terms of the pressure and temperature of the propellant tank using Equations (1-5) and (1-6). Then the pressurant forced into either propellant tank as a function of the total pressurant leaving the pressurant tank and the split ratio is

$$dM_{He1} = dM_{He} \cdot \frac{\text{Split Ratio}}{(\text{Split Ratio} + 1)} \quad (1-18a)$$

$$dM_{He2} = dM_{He} \cdot \frac{1}{(\text{Split Ratio} + 1)} \quad (1-18b)$$

Therefore, the set of error equations (Equation (1-14)) for a given propellant tank (1 or 2) must be expanded to include the errors in pressurant mass forced into the propellant tank due to the uncertainties in the mixture ratio and the uncertainties in pressure and temperature of the other propellant tank in the system. That is,

$$\text{Error}_{P1} = \frac{\delta(dM_{He})}{\delta(P_1)} \cdot P1_{\text{uncertainty}} \quad (1-19a)$$

$$\text{Error}_{T1} = \frac{\delta(dM_{He})}{\delta(T_1)} \cdot T1_{\text{uncertainty}} \quad (1-19b)$$

$$\text{Error}_{P2} = \frac{\delta(dM_{He})}{\delta(P_2)} \cdot P2_{\text{uncertainty}} \quad (1-19c)$$

$$\text{Error}_{T2} = \frac{\delta(dM_{He})}{\delta(T_2)} \cdot T2_{\text{uncertainty}} \quad (1-19d)$$

$$\text{Error}_{MR} = \frac{\delta(dM_{He})}{\delta(MR)} \cdot MR_{\text{uncertainty}} \quad (1-19e)$$

The 1σ error in pressurant forced into a given propellant tank then becomes

$$dM_{He_{uncertainty}} = [(Error_{P_{He}})^2 + (Error_{T_{He}})^2 + (Error_{P_o})^2 + (Error_{T_o})^2 + (Error_{m_o})^2 + (Error_{P_1})^2 + (Error_{T_1})^2 + (Error_{P_2})^2 + (Error_{T_2})^2 + (Error_{MR})^2]^{1/2} \quad (1-19f)$$

Using the data for the GOES-I propellant system operating in pressure regulated mode as an example: given nominal operating propellant tank pressures and temperatures (indexes 1 and 2 indicate the oxidizer and the fuel tanks, respectively) of

$$P_1 = P_2 = 230 \text{ psi} \quad T_1 = T_2 = 20^\circ \text{ C}$$

and pressurant tank loading mass, pressure, and temperature

$$P_o = 3300 \text{ psi} \quad T_o = 21^\circ \text{ C} \quad m_o = 2.54 \text{ lbm}$$

and assuming the operating pressurant tank temperature remains constant

$$T_{He} = T_o$$

the pressurant tank pressure at the end of NASA phase is reduced to

$$P_{He} = 200 \text{ psi}$$

and the optimum mixture ratio as supplied by the manufacturer is

$$MR = 1.610$$

Assuming that there are no uncertainties in loading conditions of the pressurant tank and mass, the partials are computed to be

$$\frac{\delta(dM_f)}{\delta(P_2)} = -1.4 \text{ lbm/psi} \quad \frac{\delta(dM_f)}{\delta(T_2)} = 0.57 \text{ lbm/}^\circ \text{ K} \quad \frac{\delta(dM_f)}{\delta(dM_{He2})} = 339.5$$

The partials to compute the uncertainty in pressurant mass forced into the fuel tank are

$$\begin{aligned} \frac{\delta(dM_{He2})}{\delta(P_{He})} &= -0.0004 \text{ lbm/psi} & \frac{\delta(dM_{He2})}{\delta(T_{He})} &= +0.003 \text{ lbm/}^\circ \text{ K} \\ \frac{\delta(dM_{He2})}{\delta(P_1)} &= -0.002 \text{ lbm/psi} & \frac{\delta(dM_{He2})}{\delta(T_1)} &= +0.002 \text{ lbm/}^\circ \text{ K} \\ \frac{\delta(dM_{He2})}{\delta(P_2)} &= +0.002 \text{ lbm/psi} & \frac{\delta(dM_{He2})}{\delta(T_2)} &= -0.001 \text{ lbm/}^\circ \text{ K} \\ \frac{\delta(dM_{He2})}{\delta(MR)} &= -0.3 \text{ lbm} \end{aligned}$$

The uncertainties in pressure and temperature due to the telemetry resolution are

$$P1_{\text{uncertainty(telem)}} = \pm 0.4 \text{ psi} \quad T1_{\text{uncertainty(telem)}} = \pm 1.0^\circ \text{ K}$$

$$P2_{\text{uncertainty(telem)}} = \pm 0.4 \text{ psi} \quad T2_{\text{uncertainty(telem)}} = \pm 1.0^\circ \text{ K}$$

$$PHe_{\text{uncertainty(telem)}} = \pm 0.4 \text{ psi} \quad THe_{\text{uncertainty(telem)}} = \pm 1.0^\circ \text{ K}$$

The uncertainty in pressure due to the transducer accuracy and the resulting total root-mean-square uncertainty in pressure readings are

$$P1_{\text{uncertainty(trans)}} = \pm 1.35 \text{ psi} \quad P1_{\text{uncertainty(tot)}} = \pm 1.41 \text{ psi}$$

$$P2_{\text{uncertainty(trans)}} = \pm 1.35 \text{ psi} \quad P2_{\text{uncertainty(tot)}} = \pm 1.41 \text{ psi}$$

$$PHe_{\text{uncertainty(trans)}} = \pm 1.35 \text{ psi} \quad PHe_{\text{uncertainty(tot)}} = \pm 1.41 \text{ psi}$$

The uncertainty in the mixture ratio as supplied by the manufacturer is

$$MR_{\text{uncertainty}} = \pm 0.024$$

Thus, the errors in fuel used associated with the resulting uncertainties in the fuel tank pressure, temperature, and amount of pressurant forced into the fuel tank (3σ error in pressurant forced into the fuel tank is $\pm 0.027 \text{ lbm}$) are

$$\text{Error}_{P2} = 2.0 \text{ lbm} \quad \text{Error}_{T2} = 0.57 \text{ lbm} \quad \text{Error}_{dMHe} = 9.17 \text{ lbm}$$

This shows that the fuel-used estimate for the GOES-I spacecraft in the pressure-regulated mode has a 3σ uncertainty of $\pm 28.2 \text{ lbm}$. Thus, given a 911.6 lbm estimated fuel usage, the relative error in fuel-remaining estimation is 3.1 percent.

Method 2: Thrust and Specific Impulse Performance Data

This section presents the mathematical argument for the thrust and specific impulse (I_{sp}) curves method of computing the propellant consumed from a tank during a specified time interval. These curves describe thrust and I_{sp} as functions of pressure and temperature. The method assumes that the propellant system behaves according to the thrust and I_{sp} performance curves derived through empirical testing of the propellant system. The equations to describe these curves are derived through polynomial fitting and take on the following form when the first three terms of the polynomial are used:

$$F = c0 + c1 \cdot P - c2 \cdot P^2 \cdot \left[\frac{T}{T_{\text{ref}}} \right]^{c3 + c4 \cdot P} \quad (1-20)$$

$$I_{sp} = d0 + d1 \cdot P - d2 \cdot P^2 \cdot \left[\frac{T}{T_{\text{ref}}} \right]^{d3 + d4 \cdot P} \quad (1-21)$$

where F = thrust
 I_{sp} = specific impulse
 P = propellant tank pressure
 T = inlet propellant temperature
 T_{ref} = inlet propellant temperature at which the data were taken
 c_0, c_1, c_2, c_3, c_4 = thrust polynomial coefficients
 d_0, d_1, d_2, d_3, d_4 = I_{sp} polynomial coefficients

(Note that if T and T_{ref} are equal, then thrust and I_{sp} are functions of tank pressure only.)

Given thrust and I_{sp} , the propellant flow rate is easily determined:

$$\dot{\omega} = F/I_{sp} \quad (1-22)$$

where $\dot{\omega}$ = propellant flow rate.

The propellant mass escaping the tank during a certain time period is

$$dM_f = \int_{t_0}^{t_1} \dot{\omega} \cdot dt \quad (1-23)$$

where dt = time period.

Substituting Equations (1-20) and (1-21) into Equation (1-22), integrating with respect to pressure and temperature, dividing by the change in pressure and temperature to obtain the average flow rate, and then substituting into Equation (1-23), we find that

$$dM_f = \int_{t_0}^{t_1} \frac{\int_{P_0}^{P_1} \frac{\int_{T_0}^{T_1} \dot{\omega} dT}{T_1 - T_0} dP}{P_1 - P_0} dt \quad (1-24)$$

where P_{t_0} = tank pressure at t_0
 P_{t_1} = tank pressure at t_1
 T_{t_0} = tank temperature at t_0
 T_{t_1} = tank temperature at t_1

Note that when there is no change in temperature or pressure in a given time interval, the flow rate is constant with respect to that variable over this time interval, and therefore, the integration step with respect to the unchanging variable should be omitted.

Since thrust and I_{sp} method depends on tank pressure variation, it is meaningful to use this method only in the blowdown mode of operation when a significant change in tank pressures can be observed.

The errors associated with this method are inherent to the instruments used in deriving thrust and I_{sp} data points, as well as the data regularity required to produce a close polynomial fit. Assuming that thrust and I_{sp} are well-behaved functions and that the instruments used to take the data are extremely accurate, the error in determining the propellant flow rate is then a function of uncertainties in the burn start and stop time and of the uncertainties in tank pressure and temperature at burn start and stop time.

$$\text{Error}_{P0} = \frac{\delta (dM_f)}{\delta (P0)} \cdot P0_{\text{uncertainty}} \quad (1-25a)$$

$$\text{Error}_{P1} = \frac{\delta (dM_f)}{\delta (P1)} \cdot P1_{\text{uncertainty}} \quad (1-25b)$$

$$\text{Error}_{T0} = \frac{\delta (dM_f)}{\delta (T0)} \cdot T0_{\text{uncertainty}} \quad (1-26a)$$

$$\text{Error}_{T1} = \frac{\delta (dM_f)}{\delta (T1)} \cdot T1_{\text{uncertainty}} \quad (1-26b)$$

$$\text{Error}_{t0} = \frac{\delta (dM_f)}{\delta (t0)} \cdot t0_{\text{uncertainty}} \quad (1-27a)$$

$$\text{Error}_{t1} = \frac{\delta (dM_f)}{\delta (t1)} \cdot t1_{\text{uncertainty}} \quad (1-27b)$$

The following example for the Gamma Ray Observatory (GRO) satellite, which operates in blowdown mode, shows the calculations of the fuel used from a tank given that tank's pressures at start and end of burn and the burn duration.

Using GRO main satellite thrusters performance coefficients and assuming that the tank temperature remains the same as the reference temperature during which the curves data were taken:

$$F = (3.3502 \text{ lbf}) + (0.39898 \text{ lbf/psi}) \cdot P - (0.0001463 \text{ lbf/psi}^2) \cdot P^2$$

$$I_{sp} = (222.52 \text{ s} \cdot g) + (0.064329 \text{ s} \cdot g) \cdot P - (0.0000672 \text{ s} \cdot g) \cdot P^2$$

where the units of thrust and I_{sp} coefficients are as appropriate, and, given a 2-minute ascent maneuver and propellant tank pressures at the start and end of the maneuver of

$$dt = 120 \text{ sec}$$

$$P0 = 400 \text{ psi}$$

$$P1 = 334 \text{ psi}$$

the partials are computed to be

$$\frac{\delta(dM_f)}{\delta(P0)} = 0.072 \text{ lbf/psi} \quad \frac{\delta(dM_f)}{\delta(t0)} = 0.548 \text{ lbf/sec}$$

$$\frac{\delta(dM_f)}{\delta(P1)} = 0.071 \text{ lbf/psi} \quad \frac{\delta(dM_f)}{\delta(t1)} = -0.548 \text{ lbf/sec}$$

The uncertainties in pressure and time due to the telemetry resolution are

$$P_{0\text{uncertainty}} = \pm 3.0 \text{ psi} \quad t_{0\text{uncertainty}} = \pm 0.256 \text{ sec}$$

$$P_{1\text{uncertainty}} = \pm 3.0 \text{ psi} \quad t_{1\text{uncertainty}} = \pm 0.256 \text{ sec}$$

This shows that the fuel-used estimate from a GRO tank during an ascent maneuver has a 3σ uncertainty of ± 1.1 lbm. Thus, computing that the total fuel used during the ascent from that tank is 65.8 lbm, the relative error in the fuel-remaining estimation is 1.7 percent. Note that this method is an approximation that relies on engine performance to follow the curves obtained during ground testing.

Method 3: Conceptual Model of the Propulsion System

A conceptual model of the propulsion system involves creating a schematic representing the layout of the propellant piping, tank, and thruster configuration. Then a set of mathematical expressions must be developed to describe the physics of this system, using the data obtained from the manufacturers on such system characteristics as the flow resistance through the piping, characteristic propellant velocity and thrust coefficients for all thrusters, the throat areas of the thrusters, and the temperature and pressure of the tanks. A good example of the development of such a model is the GOES-I bipropellant system model.

The GOES-I propellant system consists of a pressurant tank, a fuel tank, an oxidizer tank, one main satellite thruster (MST), and 12 attitude and orbit control thrusters (AOCT) arranged in strings A and B, each containing six AOCTs.

A model representation of the bipropellant system consisting of only one thruster (e.g., the MST) may be used to derive the following set of governing equations representing the physics of the system (Figure 1):

$$P_c = P_f - \sum K_f \dot{\omega}_f^2 \quad (1-28a)$$

$$P_c = P_o - \sum K_o \dot{\omega}_o^2 \quad (1-28b)$$

$$F = A_t C_f P_c \quad (1-28c)$$

$$F = (\dot{\omega}_o + \dot{\omega}_f) I_{sp} \quad (1-28d)$$

$$F = A + B \cdot I_{sp} \quad (1-28e)$$

where

- $\sum K_o$ = line resistances (oxidizer)
- $\sum K_f$ = line resistances (fuel)
- A_t = throat area
- A, B = coefficients in Equation (1-28e)
- P_o = oxidizer tank pressure
- C_f = orifice coefficient
- P_f = fuel tank pressure

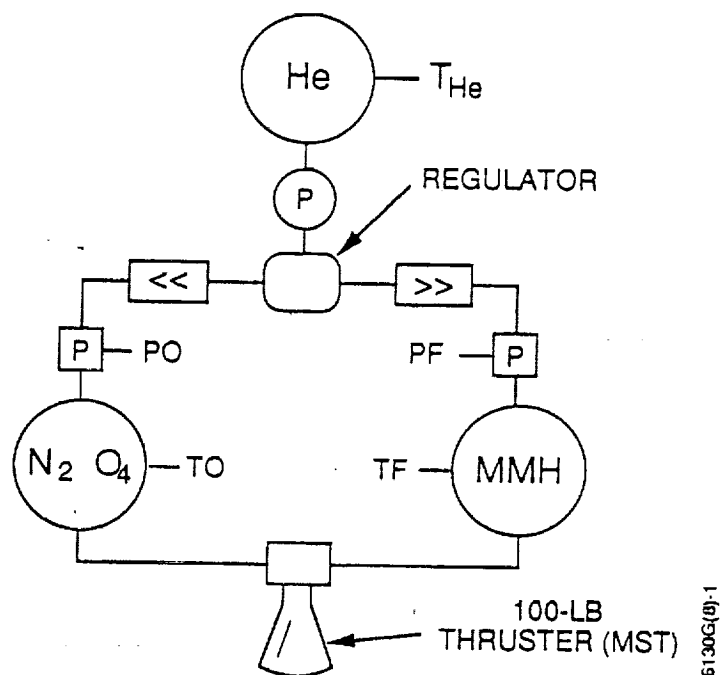


Figure 1. Schematic of the Simplified Bipropellant System Containing Only the Main Satellite Thruster

- $\dot{\omega}_f$ = fuel flow rate
- $\dot{\omega}_o$ = oxidizer flow rate
- P_c = chamber pressure
- F = thrust
- I_{sp} = specific impulse

This simple model can then be expanded to include the entire system. The conceptual model representing the system functionalities is shown in Figure 2.

Using the conceptual model in conjunction with the propellant system's physical constants, a set of governing equations relating propellant flow rates and thruster chamber pressure can be derived for each of the 13 thrusters in the same manner as for MST.

Then the mathematical representation of the functionality of the whole system is accomplished in combining the above equations for AOCTs and MST by applying a physical constraint of propellant flow continuity inherent to the system. That is, propellant mass flowing into a junction is equal to propellant mass flowing out of that junction. For example

$$\dot{\omega}_{ft} = \dot{\omega}_f + \dot{\omega}_{fA} + \dot{\omega}_{fB} \quad (1-29)$$

Solving the system of equations described above will give the propellant flow rates through each thruster and the chamber pressure of each thruster. Propellant used due to each thruster is then the product of the flow rate and thruster on time. The propellant remaining may also be calculated by using the chamber pressure in the thrust and I_{sp} performance data curves for each thruster.

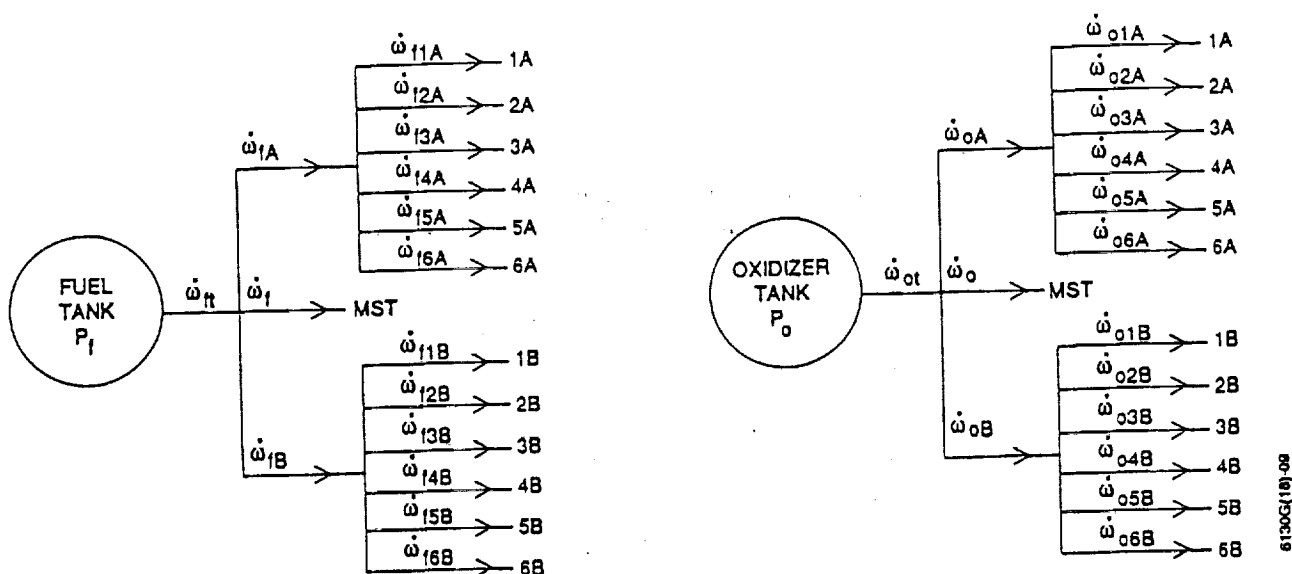


Figure 2. Conceptual Schematic of the GOES-I Propulsion System

Currently, this model is used for propellant estimation in pressure regulated mode of operation. However, by solving the system of equations for each new pressure reading in the propellant tanks, this model may be used for propellant estimation in blowdown mode.

The uncertainty in the conceptual model method comes mainly from the error in the flow resistance and thruster coefficients, tank pressure and temperature, and thruster on time. Also, there is added error in any method chosen to solve the system of nonlinear equations.

The error due to the method of solving the equations is simply the smallest tolerances of the variable under which the method converges to a solution. The error due to flow resistance and thruster coefficients, tank pressure, and temperature is determined by adding maximum error to these variables and then solving the equations to see the amount by which the solution under maximum error deviates from the nominal solution obtained by using nominal values of these variables. The error due to time uncertainty is simply the product of the time uncertainty and the computed propellant flow rate.

The following is an example of error in GOES-I MST firing in pressure regulated mode propellant-used prediction as computed by the bipropellant engine model using nominal propellant flow resistance and thrust coefficients as supplied by SS/Loral and assuming nominal tank pressures and temperatures

$$K_o = 110.713 \text{ lbf} \cdot \text{s}^2/\text{lbm} \cdot \text{in}^5 \quad K_f = 190.944 \text{ lbf} \cdot \text{s}^2/\text{lbm} \cdot \text{in}^5$$

$$C_F = 1.865 \quad P_o = P_f = 230 \text{ psi} \quad T_o = T_f = 21.3^\circ \text{ C}$$

and based on the following uncertainties: uncertainty in fuel and oxidizer tank pressures due to transducer accuracy and telemetry resolution (total pressure uncertainty is root-mean-squared of these two); uncertainty in temperatures due to telemetry resolution,

$$\begin{aligned} P_{\text{uncertainty(tele)}} &= \pm 0.4 \text{ psi} & T_{\text{uncertainty}} &= \pm 1.0^\circ \text{ K} \\ P_{\text{uncertainty(trans)}} &= \pm 1.35 \text{ psi} & P_{\text{uncertainty(tot)}} &= \pm 1.41 \text{ psi} \end{aligned}$$

and uncertainty in MST propellant flow resistance (K_o and K_f) and thrust (C_F) coefficients as given by SS/Loral (Reference 1)

$$\begin{aligned} K_{o\text{uncertainty}} &= \pm 0.541 \text{ lbf} \cdot \text{s}^2/\text{lbm} \cdot \text{in}^5 \\ K_{f\text{uncertainty}} &= \pm 2.583 \text{ lbf} \cdot \text{s}^2/\text{lbm} \cdot \text{in}^5 \\ C_{F\text{uncertainty}} &= \pm 0.00236 \end{aligned}$$

The resulting fuel and oxidizer flow rates and 1σ errors in the flow rates due to the above uncertainties combined with 0.00001 convergence tolerance of the flow rates when solved for using Runge-Kutta method are

$$\begin{aligned} \dot{\omega}_o &= 0.21857 \text{ lbm/s} & \text{Error}_{\dot{\omega}_o} &= 0.00090 \text{ lbm/s} \\ \dot{\omega}_f &= 0.13566 \text{ lbm/s} & \text{Error}_{\dot{\omega}_f} &= 0.00087 \text{ lbm/s} \end{aligned}$$

The uncertainty in MST on time due to the telemetry resolution is

$$t_{\text{uncertainty}} = \pm 0.023 \text{ sec}$$

Assuming the nominal GOES-I first two apogee maneuver firings, the total MST on time is 96 minutes (5,760 sec). Then the fuel and oxidizer masses used (as computed by the bipropellant engine model) are

$$\begin{aligned} dM_o &= 0.21857 \text{ lbm/s} \cdot 5760 \text{ s} = 1258.96 \text{ lbm} \\ dM_f &= 0.13566 \text{ lbm/s} \cdot 5760 \text{ s} = 781.40 \text{ lbm} \end{aligned}$$

The errors in the propellant-used computations are:

from errors in flow rates:

$$\text{Error}_{dM_o, \dot{\omega}_o} = \pm 5.18 \text{ lbm}$$

$$\text{Error}_{dM_f, \dot{\omega}_f} = \pm 5.01 \text{ lbm}$$

from errors in thruster on time:

$$\text{Error}_{dM_o, t} = 0.005 \text{ lbm}$$

$$\text{Error}_{dM_f, t} = 0.003 \text{ lbm}$$

Thus, based on the total propellant used during the burn, the 3σ error in fuel used is ± 15.03 lbm, the 3σ error in oxidizer used is ± 15.54 lbm, the relative error in the fuel-used estimation is 1.9 percent, and the relative error in the oxidizer-used estimate is 1.2 percent.

2. CALIBRATION TECHNIQUES

The models discussed in Part 1 of this document neglect to take advantage of the actual performance data of the spacecraft during the mission, which can be determined from the actual orbit achieved after the burn or the status of the orbit during the burn. That is, actual thrust delivered by the engines can be deduced from the orbital data available through tracking. This section presents a method of calibrating the conceptual propellant system model by using the actual thrust of the GOES-I satellite as determined from the orbit achieved.

Biprop differential corrector is a FORTRAN program that modifies the parameters of the GOES Bipropellant engine model (developed using the algorithm described in Part 1; see Reference 2) until the solution for total thrust obtained by the model matches the observed total thrust produced by the GOES propulsion system. The correction applied to the parameters is based on the information, according to SS/Loral, that the engine components most likely to vary during a burn are the propellant flow resistance coefficients for the MST section of the piping. Since the propellant piping is such that there are no isolated thrusters, the AOCTs are also affected by the varying MST resistance coefficients. However, the AOCTs are not affected when the MST is off, because MST off indicates zero propellant flow to the piping with varying resistance coefficients. Thus, Biprop differential corrector is used only when the MST is on—that is, during the NASA phase of the mission. In summary, the Biprop differential corrector is designed to correct for total thrust produced by the MST and the AOCTs combinations by adjusting the propellant (both oxidizer and fuel) flow resistance coefficients of the MST piping. The single constraint on varying the MST fuel and oxidizer resistance coefficients, given by SS/Loral, is that the mixture ratio (the ratio of the oxidizer flow rate and the fuel flow rate) for the MST must equal a predetermined constant. This section discusses (1) calculation of total thrust and average MST mixture ratio taking into account the AOCT duty cycles; (2) differential corrector requirements; (3) the differential corrector algorithm; and (4) some examples to illustrate the function and performance of the Biprop differential corrector program.

2.1 CALCULATION OF TOTAL AVERAGE THRUST AND AVERAGE MST MIXTURE RATIO

During a burn, the AOCTs are usually fired for a shorter time period than the MST. The on time of the AOCTs is described by a duty cycle (percentage of the burn time that the AOCTs are on). The MST stays on for the entire burn period. The equation for the total thrust is the average of all thrusters that are firing weighted according to each thruster's on time. As was shown in the study of the effects of multiple thruster firing on thruster performance (see Reference 3), for the total thrust magnitude calculations it is valid to assume an average duty cycle for all the AOCTs that are on. Likewise, it is valid to assume that all AOCTs that are on are firing at the same time and at the beginning of the burn. Therefore, the equation for total weighted average thrust is a sum of two parts: one for the MST firing alone and another for the MST firing together with the AOCTs. Hence,

$$T_{av} = T_{MST(off)} \cdot (1 - \text{Duty Cycle}/100) + (T_{MST(on)} + \sum T_{AOC}) \cdot (\text{Duty Cycle}/100) \quad (2-1)$$

where T_{av} = total weighted average thrust
 $T_{MST(off)}$ = MST thrust while AOCTs are off
 $T_{MST(on)}$ = MST thrust while AOCTs are on
 $\sum T_{AOC}$ = total thrust produced by AOCTs
Duty Cycle = percent of the burn time that the AOCTs are on

The mixture ratio used in the differential corrector must also be averaged, taking into account the duty cycles. The mixture ratio in the MST changes when the AOCTs go on, because the flow rates to the MST are changed. Therefore, the average MST mixture ratio must be calculated in a fashion similar to average, total thrust calculations. The formula for the weighted average MST mixture ratio is

$$MR_{av} = MR_{MST(off)} \cdot (1 - \text{Duty Cycle}/100) + MR_{MST(on)} \cdot (\text{Duty Cycle}/100) \quad (2-2)$$

where MR_{av} = average weighted MST mixture ratio
 $MR_{MST(off)}$ = MST mixture ratio while AOCTs are off
 $MR_{MST(on)}$ = MST mixture ratio while AOCTs are on

This average mixture ratio is constrained to equal a predetermined value.

2.2 DIFFERENTIAL CORRECTOR REQUIREMENTS

The differential corrector algorithm has two requirements for the function that describes the system:

1. The function must be continuous over a chosen interval.
2. The function must be differentiable on this interval.

Both of these requirements must be true for total thrust and MST mixture ratio as functions of the MST flow resistance coefficients. Since the system being modeled is a physical system, the thrust produced by the system must be directly related to the propellant flow in the system. From the governing equations of the bipropellant engine model (see Reference 4) we have for any given thruster

$$P_c = P_f - \sum (K_{f(i)} \cdot \dot{\omega}_{f(i)}^2) \quad (2-3)$$

$$P_c = P_o - \sum (K_{o(i)} \cdot \dot{\omega}_{o(i)}^2) \quad (2-4)$$

$$T = (A_t \cdot C_f) \cdot P_c \quad (2-5)$$

where P_c = chamber pressure
 P_f = fuel pressure
 P_o = oxidizer pressure
 K_f = fuel resistance coefficient
 K_o = oxidizer resistance coefficient
 $\dot{\omega}_f$ = fuel flow rate
 $\dot{\omega}_o$ = oxidizer flow rate
 T = thrust
 A_t = throat area of the thruster
 C_f = thrust coefficient

Therefore, from Equations (2-3) and (2-4), $P_c(K_f)$ and $P_c(K_o)$ are linear functions. Since T is proportional to P_c , $T(K_f)$ and $T(K_o)$ are also linear functions. Thus, taking $K_{f(MST)}$ and $K_{o(MST)}$ to be variable resistances for the MST, the functions that relate these resistances to the total thrust, $T(K_{f(MST)})$ and $T(K_{o(MST)})$, are linear by the above argument, and thereby meet the requirements of the differential corrector algorithm.

Intuitively, there must be a smooth relationship between the flow resistance coefficients and the flow rates. That is, the flow rate of a propellant in a pipe is smoothly related to the resistance of the pipe's interior surface. The mixture ratio is simply the oxidizer flow rate divided by the fuel flow rate. Also, the flow rates are never zero, since the MST is always on when the differential corrector is required. Therefore, the mixture ratio is a smooth function of the oxidizer and fuel resistance coefficients, and thus meets the requirements of the differential corrector algorithm.

2.3 DIFFERENTIAL CORRECTOR ALGORITHM

The problem of thrust correction is defined by two variables and two constraints. The two variables are the fuel resistance coefficient and the oxidizer resistance coefficient. The two constraints are that the computed thrust must equal the actual thrust and that the computed mixture ratio must equal the actual mixture ratio. The requirement that mixture ratio be fixed implies that the actual mixture ratio is equal to the nominal mixture ratio within a specified tolerance. The following procedure must be used in performing the differential correction on the bipropellant engine model:

1. Obtain the actual mixture ratio (MR_a) using bipropellant engine model with nominal flow resistance coefficients supplied by the manufacturer.
2. Obtain the actual, total thrust magnitude from the calibrated maneuver mode.
3. Until the computed total thrust (T_n) and the computed mixture ratio (MR_n) are within the specified tolerance of the constraints, iterate with

$$K_{f(MST)}(i+1) = K_{f(MST)}(i) + \Delta K_{f(MST)} \quad (2-6)$$

$$K_{o(MST)}(i+1) = K_{o(MST)}(i) + \Delta K_{o(MST)} \quad (2-7)$$

where $\Delta K_{f(MST)}$ and $\Delta K_{o(MST)}$ are obtained via the differential corrector method

$$\begin{bmatrix} \Delta K_{o(MST)} \\ \Delta K_{f(MST)} \end{bmatrix} = \begin{bmatrix} \delta T / \delta K_{o(MST)} & \delta T / \delta K_{f(MST)} \\ \delta MR / \delta K_{o(MST)} & \delta MR / \delta K_{f(MST)} \end{bmatrix}^{-1} \begin{bmatrix} T_a - T_n \\ MR_a - MR_n \end{bmatrix} \quad (2-8)$$

where $\delta K_{o(MST)}$, $\delta K_{f(MST)}$ = perturbation applied to the coefficients

δT , δMR = $(T_{pert} - T_n)$, $(MR_{pert} - MR_n)$ respectively

T_{pert} , MR_{pert} = thrust and mixture ratio, respectively, computed by BIPROP using perturbed coefficients $K_{f(MST)}(i) + \delta K_{f(MST)}$, $K_{o(MST)}(i) + \delta K_{o(MST)}$

T_n , MR_n = thrust and mixture ratio, respectively, computed by BIPROP using unperturbed coefficients

2.4 EXAMPLES OF BIPROP DIFFERENTIAL CORRECTOR

Table 1 gives some examples of the differential corrector performance. The numbers used for the actual thrust (T_a) were chosen only for the testing purposes. The nominal resistance coefficients were part of the data given by the manufacturer for testing the bipropellant engine model software. As shown in the table, the differential correction makes good progress in only two to three iterations with relative error for thrust and mixture ratio specified at under 0.5 percent. Note that in Case 2 we find significantly higher resistance than in Case 1, although the difference between actual and total thrust in both cases is almost the same. This may be understood as follows:

Let

$$DT_{MST} = T_{MST(off)} - T_{MST(on)} \quad (2-9)$$

so the DT_{MST} is the change in the MST thrust caused by AOCTs firing. Then, substituting DT_{MST} into Equation (2-1), we get

$$T_{av} = T_{MST(off)} + (\text{Duty Cycle}/100) \cdot (\sum T_{AOC} - DT_{MST}) \quad (2-10)$$

Table 1. Differential Corrector Performance

C A S E	Thrusters Firing	Nominal resistance coefficients as supplied by FACC		Nominal total thrust computed by BIPROP	Actual average mixture ratio computed by BIPROP	Actual total thrust from calibrated manuever mode	Actual resistance coefficients computed by Differential Corrector to obtain actual thrust		Total number of iterations performed by Differential Corrector to obtain the actual thrust
		Oxidizer ($K_o(MST)$)	Fuel ($K_f(MST)$)				Oxidizer ($K_o(MST)$)	Fuel ($K_f(MST)$)	
#	names			(T_n)	(MR_a)	(T_a)			#
1	MST only	110.713	190.944	108.876	1.611	93.6	176.079	297.618	3
2	MST, 2A	110.713	190.944	110.748	1.644	95.0	178.624	303.305	2
3	MST, west face AOCs	110.713	190.944	112.613	1.643	102.0	141.416	255.606	2
4	MST, all AOCs	110.713	190.944	116.034	1.642	140.0	53.046	95.709	3

NOTE: For the examples here, the differential corrector uses the following inputs:

Specified Relative Error for T_a and MR_a : 0.5%

Duty Cycle: 10%

Burn Time: 3,000 sec

Although $DT_{MST} > 0$, we observe that $(\sum T_{AOC} - DT_{MST}) > 0$. Also, from Equations (2-3), (2-4), and (2-5), we know that $T_{MST(off)}$ decreases with increasing resistances. Likewise, from Equation (2-10), we have

$$T_{MST(off)} = T_{av} - (\text{Duty Cycle}/100) \cdot (\sum T_{AOC} - DT_{MST}) \quad (2-11)$$

This shows $T_{MST(off)} < T_{av}$ in Case 2, while $T_{MST(off)} = T_{av}$ in Case 1. Therefore, we expect Case 2 to require higher resistances. Moreover, as the resistances increase, the flow rates to the MST decrease; and, from continuity conditions, the flow rates to AOCTs must increase. Thus, $(\text{Duty Cycle}/100) \cdot (\sum T_{AOC} - DT_{MST})$ increases as resistances increase. Similarly, $(\text{Duty Cycle}/100) \cdot (\sum T_{AOC} - DT_{MST})$ increases as the number of the AOCTs firing or the Duty Cycle increases. That is, the increase in required resistances to obtain the same average thrust becomes more marked as the number, or the duty cycle, of the AOCTs firing with the MST increases.

Case 4 shows that the resistance coefficients may also be decreased in order to account for a better thruster performance than expected.

When such a calibration technique is used, the propellant flow rates and the chamber pressure of each thruster that was firing during the burn are adjusted in the process to reflect more closely the actual performance of the thrusters. Using the information of case 1 from Table 1 as an example, if the actual thruster performance is 86 percent of the predicted performance then the difference in fuel used computed using nominal and calibrated flow resistance coefficients is 107 lbm. For GOES-I 107 lbm is equivalent to 2.5 years of mission lifetime. Therefore, the propellant-remaining calculations derived by the conceptual model of the system are more realistic, since the model reflects the actual performance of the propellant system as observed during the mission.

REFERENCES

1. Ford Aerospace, Space Systems Division, SSD-TR10817A, *GOES IJK/LM Propulsion Requirements Analysis*, DRL 303-01, June 1988
2. Computer Sciences Corporation, SEAS Quick Note No. GOES-468-89020, *Expanding the Bipropellant Model to Include 12 AOC Thrusters*, prepared by S. Torgovitsky, May 12, 1989
3. —, SEAS Quick Note No. GOES-468-89006, *Effects of Multiple Thruster Firing on Thruster Performance and Fuel Remaining*, prepared by S. Torgovitsky, December 7, 1988
4. —, CSC/TR-89/6003, *Geostationary Operational Environmental Satellites (GOES)-I/M Flight Dynamics Support System (FDSS) Volume II: Functional Specifications, Revision 1*, C. Audain et al., February 22, 1989

Report Documentation Page

1. Report No. NASA CP-3123		2. Government Accession No.		3. Recipient's Catalog No.	
4. Title and Subtitle Flight Mechanics/Estimation Theory Symposium - 1991				5. Report Date October 1991	
				6. Performing Organization Code 554	
7. Author(s) Thomas Stengle, Editor				8. Performing Organization Report No. 91B00133	
				10. Work Unit No.	
9. Performing Organization Name and Address Goddard Space Flight Center Greenbelt, Maryland 20771				11. Contract or Grant No.	
				13. Type of Report and Period Covered Conference Publication	
12. Sponsoring Agency Name and Address National Aeronautics and Space Administration Washington, D.C. 20546-0001				14. Sponsoring Agency Code	
15. Supplementary Notes Thomas Stengle is Head, Attitude Analysis Section, Flight Dynamics Analysis Branch, Goddard Space Flight Center, Greenbelt, Maryland					
16. Abstract This conference publication includes 26 papers and abstracts presented at the Flight Mechanics/Estimation Theory Symposium on May 21-23, 1991. Sponsored by the Flight Dynamics Division of Goddard Space Flight Center, this symposium features technical papers on a wide range of issues related to orbit-attitude prediction, determination, and control; attitude sensor calibration; attitude dynamics; and orbit decay and maneuver strategy. Government, industry, and the academic community participated in the preparation and presentation of these papers.					
17. Key Words (Suggested by Author(s)) Flight Mechanics Spacecraft Dynamics Estimation Theory Orbit Determination Attitude Determination Mission Analysis				18. Distribution Statement Unclassified Subject Category 13	
19. Security Classif. (of this report) Unclassified		20. Security Classif. (of this page) Unclassified		21. No. of pages 508	
				22. Price A22	